Exploration, Synthesis, and Characterization of Bioinspired Iron–Imide and Iron–Amide Clusters

by

Justin Shmordok

A thesis
presented to the University of Waterloo
in fulfillment of the
thesis requirement for the degree of
Doctor of Philosophy
in
Chemistry

Waterloo, Ontario, Canada, 2025

© Justin Shmordok 2025

Examining Committee Membership

External Examiner	Prof. Samuel A. Johnson Professor Department of Chemistry University of Windsor, Windsor, ON, Canada
Supervisor	Prof. Sonny C. Lee Associate Professor Department of Chemistry University of Waterloo, Waterloo, ON, Canada
Internal Member	Prof. J. Michael Chong Professor Department of Chemistry University of Waterloo, Waterloo, ON, Canada
Internal Member	Prof. Holger Kleinke Professor Department of Chemistry University of Waterloo, Waterloo, ON, Canada
Internal-external Member	Prof. Brian Kendall Associate Professor Department of Earth and Environmental Sciences University of Waterloo, Waterloo, ON, Canada

Author's Declaration

I hereby declare that I am the sole author of this thesis. This is a true copy of the thesis, including any required final revisions, as accepted by my examiners.
I understand that my thesis may be made electronically available to the public.

Abstract

Iron-sulfur clusters with high-spin irons play a crucial role in various biological processes. These clusters are found in enzymes such as ferredoxins, aconitase, and nitrogenase, where they function as redox cofactors or active sites for catalysis. One particularly significant transformation is the reduction of atmospheric dinitrogen to ammonia, which occurs at a complex iron-sulfur cluster with core composition [MFe_7S_9C] where M = Mo, V or Fe**.** Notably, this cluster features a μ_6-carbide, whose function in the cluster remains unclear.

In synthetic iron-sulfur chemistry, Fe_4S_4 clusters have been extensively studied with various ligands and core compositions. To explore the effects of light 2p-element ligation, nitrogen anions in amide or imide motifs can be employed. Research in the Lee group has led to the synthesis of a series of iron-imide-sulfide clusters $[Fe_4(N^tBu)_nS_{4-n}Cl_4]^z$ (n = 1-4). This class of compounds extends from [Fe_4S_4] to [$Fe_4(N^tBu)_4$] cores, with intermediate species in the series containing a mixture of imide and sulfide ligands.

The [$Fe_4(N^tBu)_4$] core is synthesized via the reaction of $FeCl_3$ with two equivalents of $LiNH^tBu$, yielding $[Fe_4(N^tBu)_4Cl_4]^{1-}$, $Fe_4(N^tBu)_4Cl_3(N^tBu)$ and $FeCl_2(NH_2{}^tBu)_2$ as the primary iron-containing products, with an approximate combined *in-situ* yield of 50% based on starting iron content. The $[Fe_4(N^tBu)_4Cl_4]^{1-}$ species can be isolated in 24% yield and undergoes both chemical oxidation and reduction to form [$Fe_4(N^tBu)_4Cl_4$] and $[Fe_4(N^tBu)_4Cl_4]^{2-}$, respectively. The $[Fe_4(N^tBu)_4Cl_4]^z$ series has been characterized using a range of spectroscopic and structural techniques to elucidate its solid-state and solution phase properties.

$LiNH^tBu$ is synthesized via the lithiation of $^tBuNH_2$ with one equivalent of *n*-BuLi. Upon workup, this reaction affords white crystals which display an octameric ladder structure with eight molecules of $LiNH^tBu$ in the solid state. When excess $^tBuNH_2$ (ca. 1.1 equivalents) is used, a white colloidal solution forms, yielding an infinite polymeric ladder structure in the solid state. The cyclic ladder structure was determined to be the metastable polymorph and the infinite polymer ladder structure was determined to be the thermodynamic polymorph using DSC analysis and synthetic procedures. The cyclic ladder

structure can be converted to the infinite polymer structure by heat or by addition of a donor ligand to catalyze the transformation

The $[Fe_4(N^tBu)S_3Cl_4]^{2-}$ cluster is synthesized via a controlled synthetic protocol involving the formation of an iron-amide dinuclear intermediate, $Fe_2(\mu\text{-}NH^tBu)_2[N(SiMe_3)_2]_2$. This intermediate arises from the protonolysis reaction of $Fe[N(SiMe_3)_2]_2$ with $^tBuNH_2$. Notably, this transformation is unusual, as analogous reactions with $Fe[N(SiMe_3)_2]_2$ typically proceed with ligands that are more acidic than $HN(SiMe_3)_2$. To explore the scope of this reactivity, a series of amines with varying acidity, steric hindrance and nitrogen substitution patterns were examined. The products that can form from reactivity of $Fe[N(SiMe_3)_2]_2$ with amines include a mononuclear amine adduct, di– and tri–substituted dinuclear complexes and homo– and heteroleptic trinuclear complexes. The type of complex formed depended on the stoichiometry of amine to $Fe[N(SiMe_3)_2]_2$ and the acidity, nitrogen substitution and steric hindrance around the nitrogen.

Finally, the reduction of $[Fe_4(N^tBu)S_3(SPh)_4]^{2-}$ was attempted. Although reduction to the $z = 3-$ cluster was achieved, the resulting product proved unstable in CD_3CN, decomposing into a new species accompanied by thiolate release. Upon oxidation of the decomposition product, $[Fe_4(N^tBu)S_3(SPh)_4]^{2-}$ was regenerated, indicating that the $Fe_4(N^tBu)S_3$ core likely remains intact. Further ligand tuning revealed that the use of *p*-methylbenzene thiolate allowed for the isolation of the reduced cluster; however, purification was hindered by its limited solubility. The synthesis of the oxidized, $[Et_4N][Fe_4(N^tBu)S_3(SMes)_4]$ cluster was achieved by oxidization of the $z = 2-$ cluster by ferrocenium. Surprisingly, the oxidized cluster displayed a ground spin state of $S = 3/2$.

Acknowledgements

I would like to acknowledge all the wonderful people I have had the chance to work with during graduate school.

First and foremost, I would like to thank Dr. Sonny Lee. Thank you for entertaining the idea of me working in your lab as second-year student who scored a 45% on the first CHEM 212 midterm. Thank you for not only taking a chance on me but providing invaluable knowledge, patience and guidance over the past several years. You have taught me so much about inorganic chemistry and the due diligence required to do good science. These are skills I will be using for the rest of my academic career.

I would like to thank my committee members: Dr. Mike Chong, Dr. Holger Kleinke and Dr. Kathryn Preuss. Thank you all for being a part of my journey. Mike, thank you for all the chemicals you have lent me over the years and for sharing your deep knowledge of organic chemistry. Holger, thank you for all our chats about random topics and for your patience with discussing techniques I was unfamiliar with. Kathryn, thank you for sharing your expertise on the system with me and for being someone I have truly enjoyed learning from.

I would also like to thank other faculty members in the department, including Dr. Mónica Barra, Dr. Dara Gilbert, Dr. Thorsten Dieckmann, Dr. John Corrigan. Mónica, thank you for believing in me when I didn't believe in myself. Your support and mentorship have helped me become the person I am today. Thank you for being my teaching role model–I don't think I would be the teacher I am today without sitting in your CHEM 400 course. Dara, thank you for our endless chats throughout during grad school. I have truly enjoyed our conversations about teaching and, of course, our gossip sessions. Thorsten and John, thank you both for supporting me in my EDI endeavours with CGSS and throughout the Faculty of Science. Our graduate community wouldn't be what it is without your guidance and encouragement.

Now, to the Lee group. I would like to thank all the lab members I've had the chance to work alongside: Lay Ling Tan, Max Hamilton, Tommy Ma, Dion Grobe, Amanda Kwan, Desmond Ng, Emma Fantin, Nathan Cheng, Jay Bhagat, Jessica Zhang, Sandra Salic, Grace

Tseng, Petra Thorpe and Emily Robinson. A huge shoutout is in order for Max Hamilton. Anyone reading my thesis who knows me will agree Max deserves a second PhD just for dealing with me for the past five-plus years. Thank you, Max, for being both a great lab mate and a wonderful friend. I have cherished our thousands of discussions over the years about chemistry, relationships, politics, and life.

I would like to thank members of the Chemistry department, specifically, Dr. Blossom Yan, Dr. Jalil Assoud, Madeleine Blauel and Leanne Racicot. Blossom, you deserve a huge shoutout here. Thank you for motivating me to bring more EDI awareness to the department. I also appreciate you challenging my viewpoints and providing crucial perspectives that helped shape the person I am today. Oh, and of course, thank you for teaching me advanced NMR techniques! Your expertise in NMR spectroscopy has been invaluable in my PhD. To Jalil, thank you for teaching me about X-ray Diffraction Analysis. I apologize for all the samples that didn't survive when you cut into them, but I'm truly grateful for your willingness to teach me every step of the way. Madeleine, thank you for all the daily chats over the past two years–I've always looked forward to them. Leanne, thank you for being a mentor and a friend over the years. Talking to you always made me feel better when chemistry (and life) took a dip.

Now, to my friends. First and foremost, thank you to Emily Wedde, Avery To, Amanda Kwan and Dion Grobe for proofreading and editing my thesis. Your help has been invaluable. I would also like to thank the entire Chemistry Graduate Student Society. You've all made a significant impact on my graduate career, and I am incredibly proud of how we've grown this graduate club into the force it is today. A special thanks to the following individuals: Herbert (Ben, Benny Boo Bear, LGB) Voss, Emily Wedde (again), Madi Donohoe, Tristan Licskai, Natasha Evans, Una Hogen, Carlee Montgomery, Annie Li, Dion Grobe (again), Harjeet Dhuga and Iain McDonald. You guys have been great friends to me throughout these years. I would also like to thank my friends since high school, Veronica (Vron) Magnaye and Sarah Prpic. Thank you both for sticking by me for the last decade.

Dedication

This thesis is dedicated to my family who have made sacrifices to get me to where I am today.

Table of Contents

Examining Committee Membership ii
Author's Declaration iii
Abstract iv
Acknowledgements vi
Dedication viii
List of Figures xii
List of Tables xx
List of Abbreviations xxiii
List of Schemes xxvi
List of Equations xxvii
List of Compounds xxviii
Chapter 1 : Introduction 1
1.1 Iron-Sulfur Clusters in Biochemistry 1
1.2 Nitrogen Ligated Clusters 3
1.3 Mixed Imide/Amide-Sulfide 4
1.4 Scope of Thesis 5
Chapter 2 : Improved Synthesis and Characterization of Iron-Alkylimide Clusters 6
2.1 Introduction 6
2.2 Results and Discussion 11
2.2.1 Reactivity of Ferric Chloride with Lithium *tert*-Butylamide 11
2.2.2 Purification of 2 19
2.2.3 Redox Behaviour 20
2.2.4 Cluster Structures 23
2.2.5 Characterization 28
2.2.6 Characterization of Mononuclear By-Product 36
2.2.7 Chapter Summary 40
2.3 Experimental Section 42
2.3.1 General Experimental Details 42
2.3.2 Preparation of Compounds 42
2.3.3 X-Ray Crystallography 44
2.3.4 Electrochemical Analysis 45
2.3.5 ^{1}H qNMR Analysis 46
Chapter 3 : Polymorphism of Lithium *tert*-Butylamide 47
3.1.1 Introduction 47
3.1.2 Lithium *tert*-butylamide 50
3.2 Results and Discussion 52
3.2.1 Synthesis of Lithium *tert*-Butylamide 52
3.2.2 Single Crystal X-ray Diffraction Analysis 53
3.2.3 Conversion of Polymorphs 59
3.2.4 Powder X-ray Diffraction Analysis 61
3.2.5 Differential Scanning Calorimetry Analysis 63
3.2.6 ^{1}H NMR Spectroscopy 66
3.2.7 In Solution Molecular Mass Determination 67

3.3 Experimental Section 78
3.3.1 General Experimental Details 78
3.3.2 Preparation of Compounds 78
3.3.3 Elemental Analysis 79
3.3.4 X-Ray Crystallography 79
3.3.5 Other Physical Measurements 80
Chapter 4 : Synthesis of Di- and Trinuclear Iron (II) Complexes with Mixed Amide Ligation 82
4.1 Introduction 82
4.2 Results and Discussion 87
4.2.1 Synthetic Summary 87
4.2.2 Protonolysis by Alkylamines 93
4.2.2 Protonolysis by Arylamines 100
4.2.3 Protonolysis by *N*-methylamines 103
4.2.4 Complex Structures 104
4.2.5 Isomers 115
4.2.6 Spectroscopic Properties 118
4.2.7 Reactivity 135
4.2.8 Chapter Summary 147
4.3 Experimental Section 148
4.3.1 General Experimental Details 148
4.3.2 Preparation of Compounds 149
4.3.3 X-Ray Crystallography 153
Chapter 5 : Synthesis and Stability Study of Oxidized and Reduced Iron-Imide-Sulfide Clusters 156
5.1 Introduction 156
5.1.1 Cofactors in nitrogenases 156
5.1.2 Nitrogenase active site 158
5.1.3 Synthetic Analogues 160
5.1.4 Synthetic Analogues of FeMoco 161
5.2 Results and Discussions 163
5.2.1 Synthesis of Starting Material 163
5.2.2 Thiolate Ligation of $Fe_4(N^tBu)S_3$ Clusters 166
5.2.3 Spectroscopic Properties 167
5.2.4 X-ray Crystallography 169
5.2.5 Redox Properties 172
5.2.6 Synthesis of Oxidized Clusters 176
5.2.7 Synthesis and Stability Studies of $[Fe_4S(N^tBu)(SPh)_4]^{3-}$ 179
5.2.8 Synthesis and Stability Studies of $[Fe_4S_4(SR)_4]^{1+}$ Clusters 186
5.2.9 Synthesis and Stability Studies of $[Fe_4S_3(N^tBu)(SAr)_4]^{3-}$ Clusters 190
5.2.10 Ground Spin State Determination 196
5.2.11 Chapter Summary 203
5.3 Experimental Section 204
5.3.1 General Experimental Details 204

5.3.2 Preparation of Compounds 204
5.3.3 X-ray Crystallography 208
Chapter 6 : Synthesis of Iron-Imide-Sulfide Complexes with Bulky Thiolate Ligands 210
6.1 Introduction 210
6.1.1 Site Differentiation of Fe_4S_4 Clusters 210
6.1.2 Bulky thiolates 212
6.1.3 Proposal 216
6.2 Results and Discussion 217
6.2.1 Reactivity with $^{-}$STriph 218
6.2.2 Reactivity of Fe_4NS_3 with 2,6-dimesitylbenzene thiolate 219
6.2.3 Future Work 222
6.3 Experimental Section 222
6.4 Final Words 223
References 225
Appendix A: Reactivity of $[Ph_4P]2$ with KC_8 237
Appendix B: $FeCl_2(NH_2{}^tBu)_2$ Titration Data 240
Appendix C: ^{1}H DOSY Data 251

List of Figures

Figure 1.1. Iron-sulfur complexes found in rubredoxin, ferredoxins and aconitase. 1
Figure 1.2. Metallocofactors found in the Mo– and V– nitrogenase enzymes. 3
Figure 1.3. Iron-imide/amide complexes synthesized within the Lee group.[22–27] 4
Figure 1.4. Mixed iron-imide/amide-sulfide complexes.[26,28] 5
Figure 2.1. Reported molecular structures of iron-imide cubane clusters: variations in core and terminal ligation. [22–24,29–34] 7
Figure 2.2. Molecular structures of the iron-imide-sulfide series ($[Fe_4(N^tBu)_nS_{4-n}Cl_4]^z$ (n = 0-4)).[26] 10
Figure 2.3. Structure of dianion $[Fe_2(\mu\text{-}N^tBu)_2Cl_4]^{2-}$ 12
Figure 2.4. Crude ^{1}H NMR(300 MHz, 25 °C) spectra of $FeCl_3$ and 2 equivalents of $LiNH^tBu$ in CD_3CN under various conditions: (**A**) ether insoluble material (**B**) ether soluble material, (**C**) toluene soluble material generated at 80 °C, (**D**) toluene soluble material generated at rt, (**E**) THF soluble material generated at 90 °C and (**F**) THF soluble material generated at rt. 14
Figure 2.5. ^{1}H NMR (300 MHz, 25 °C) spectra with varying equivalents of $LiNH^tBu$ to $FeCl_3$. Spectra were either collected in CD_3CN or C_6D_6 with residual protio signal assigned with *. (**A**) 4 equivalents in C_6D_6, (**B**) 4 equivalents in CD_3CN, (**C**) 3 equivalents in C_6D_6, (**D**) 3 equivalents in CD_3CN, (**E**) 2 equivalents in CD_3CN, (**F**) 1.5 equivalents in CD_3CN and (**G**) 1 equivalent in CD_3CN. 17
Figure 2.6. ^{1}H NMR (CD_3CN), 300 MHz, 25 °C) spectra of (**A**) pure $[Ph_4P]$2, (**B**) DCM extract and (**C**) crude of $FeCl_3$ and 2 equivalents of $LiNH^tBu$ in THF heated to 90 °C over 16 hours. 20
Figure 2.7. Cyclic voltammogram (0.1 M $(n\text{-}Bu_4N)ClO_4$ supporting electrolyte in MeCN, 100 mV/s scan rate) of $[Ph_4P]_2$**6**. 22
Figure 2.8. Structure of cluster dianion of $(Ph_4P)_2[Fe_4(\mu_3\text{-}N^tBu)_4Cl_4]$ ($[Ph_4P]_2$**6**) showing non-hydrogen atoms (50% probability thermal ellipsoids). 24
Figure 2.9. ^{1}H NMR (300 MHz, 25 °C) spectra of **1**, $[Ph_4P]$**2**, and $[Ph_4P]_2$**6**). * represents residual protio solvent resonance (C_6D_6 for top and CD_3CN for middle and bottom spectra). 29
Figure 2.10. Solution UV-vis absorption spectra of $[Fe_4(N^tBu)_4Cl_4]$ (**1**, green), $[Ph_4P][Fe_4(N^tBu)_4Cl_4]$ ($[Ph_4P]$**2**, blue) and $[Ph_4P]_2[Fe_4(N^tBu)_4Cl_4]$ ($[Ph_4P]_2$**6**, red) 31
Figure 2.11. X-band EPR spectrum (10 K, 0.2 M TBAP/MeCN) of $[Ph_4P]$**2**. 32
Figure 2.12. Mössbauer spectra (T = 70 K) of polycrystalline $[Fe_4(N^tBu)_4Cl_4]$ (**1**, green), $[Ph_4P][Fe_4(N^tBu)_4Cl_4]$ ($[Ph_4P]$**2**, blue) and $[Ph_4P]_2[Fe_4(N^tBu)_4Cl_4]$ ($[Ph_4P]_2$**6**, red). Solid black lines are spectral simulations based on preliminary parameters indicated on the left of the spectra. 33
Figure 2.13. Temperature dependence plot of the magnetic susceptibilities of polycrystalline $[Fe_4(N^tBu)_4Cl_4]$ (**1**, green), $[Ph_4P][Fe_4(N^tBu)_4Cl_4]$ ($[Ph_4P]$**2**, blue) and $[Ph_4P]_2[Fe_4(N^tBu)_4Cl_4]$ ($[Ph_4P]_2$**6**, red) 35
Figure 2.14. Temperature dependence plot of the reciprocal magnetic susceptibility of polycrystalline $[Ph_4P][Fe_4(N^tBu)_4Cl_4]$ ($[Ph_4P]$**2**). The solid line indicates the linear least-squares fit (y = 1.85 x +2.96; C = 0.375 emu K/mol, θ = –1.60 K) to the data between T = 2 – 50 K. Data is consistent with a S=1/2 ground spin state. 36

Figure 2.15. ^{1}H NMR titration of $FeCl_2$ in MeCN with ^{t}BuNH$_2$ in CD_3CN. Concentration of $FeCl_2$ is 15.8 mM. Concentration of total ^{t}BuNH$_2$ found on the sides of the spectra. 39
Figure 3.1. Common structure types of lithium amides characterized by single crystal X-ray diffraction analysis. Structure types include (**A**) mononuclear, (**B**) dinuclear, four-membered rings, (**C**) trinuclear, six-membered rings, (**D**), tetranuclear, eight-membered rings, (**E**) six membered, cyclic ladder (**F**) eight membered, cyclic ladder (**G**) four-rung ladder and (**H**) polymeric ladder. Nitrogen R groups omitted for clarity. 49
Figure 3.2. Published structure of [(LiNH^{t}Bu)$_8$·C$_6$H$_{14}$] (**8**). Barnett, N. D. R.; Clegg, W.; Horsburgh, L.; Lindsay, D. M.; Liu, Q.-Y.; Mackenzie, F. M.; Mulvey, R. E.; Williard P. G., *Chem. Commun.*, 1996, *5*, 231–2322, with permission from The Royal Society of Chemistry. 50
Figure 3.3. Crystal structures of other (^{t}BuHN)$^-$ compounds, [(NaNH^{t}Bu)$_3$^{t}BuNH$_2$]$_\infty$ and [(LiNa[NH^{t}Bu]$_2$)$_2$(TMEDA)$_2$]. Reproduced from Clegg, W.; Henderson, K. W.; Horsburgh, L.; Mackenzie, F. M.; Mulvey, R. E., *Chem. Eur. J.,* 1998, 4 (1), 53–56, with permission from Wiley-VCH. 51
Figure 3.4. Structure of (LiNH^{t}Bu)$_\infty$ (**9**) with thermal ellipsoids (50% probability level) and selected atom labels. For clarity, ^{t}Bu hydrogen atoms are not shown. One unit of LiNH^{t}Bu is present in the asymmetric unit with other atoms generated by crystallographic 2-fold rotation. 54
Figure 3.5. Structure of (LiNH^{t}Bu)$_8$ (**10**) with thermal ellipsoids (50% probability level) and selected atom labels. For clarity, ^{t}Bu hydrogen atoms are not shown. Four molecules of LiNH^{t}Bu are present in the asymmetric unit with other atoms generated by crystallographic 2-fold rotation. 55
Figure 3.6. Superposition of the 16 atom Li_8N_8 core of **8** (green) and **10** (purple). 57
Figure 3.7. Crystal structures of other $^-$(NH^{t}Bu) compounds, [(NaNH^{t}Bu)$_3$^{t}BuNH$_2$]$_\infty$ and [(LiNa[NH^{t}Bu]$_2$)$_2$(TMEDA)$_2$]. Reproduced from Clegg, W.; Henderson, K. W.; Horsburgh, L.; Mackenzie, F. M.; Mulvey, R. E., *Chem. Eur. J.,* 1998, 4 (1), 53–56, with permission from Wiley-VCH. 57
Figure 3.8. Fitted PXRD Data for (LiNH^{t}Bu)$_8$ (**8**) and (LiNH^{t}Bu)$_\infty$ (**9**). Experimental data shown as blue points, while the green line represents the calculated PXRD pattern based on single crystal X-ray diffraction data. The red line indicates the baseline correction, and the teal line shows the difference between the experimental and calculated patterns. 62
Figure 3.9. DSC curve at 10 °C/min for (LiNH^{t}Bu)$_\infty$ (**9**). Parameters for run A: Mass of 9 was 3.6 mg, starting temperature set to 40 °C and ramp rate was 10.00 °C/min. Parameters for run B: Mass of 9 was 3.7 mg, starting temperature set to 40 °C and ramp rate was 10.00 °C/min. 63
Figure 3.10. DSC curve at 10 °C/min for (LiNH^{t}Bu)$_8$ (**8**). Mass of 8 was 3.5 mg. Starting temperature was 40 °C and ramp rate was 10.00 °C. 1 represents first heating and cooling cycle to 200 °C and 2 represents second heating and cooling cycle to 270 °C. 64
Figure 3.11. ^{1}H NMR (300 MHz, 25 °C) spectra of **8** in C$_6$D$_6$ and THF-d_8 and **9** in THF-d_8. * represents residual protio solvent resonance. 67
Figure 3.12. Likely structures of LiNH^{t}Bu in toluene-d_8 consistent with ^{6}Li and ^{15}N isotopic labelled NMR experiments. Reprinted (adapted) with permission from Aubrecht, K. B.;

Lucht, B. L.; Collum, D. B. *Organometallics* 1999, *18* (16), 2981–2987. Copyright 1999 American Chemical Society. 68
Figure 3.13. ^{1}H DOSY spectrum of **8** and four internal references in THF-d_8..... 70
Figure 3.14. Stejskal-Tanner plot of 1-tetradecene in THF-d_8 72
Figure 3.15. log D vs log MW DOSY molecular weight calibration curve. 73
Figure 3.16. Structures consistent with the molecular mass of **8** and **9** in THF-d_8. 76
Figure 4.1. Structurally characterized transition metal (bistrimethylsilylamide) complexes. 82
Figure 4.2. Select examples of di- and trinuclear complex from the protolytic ligand substitution reaction of **11** with ligands with acidic protons. 86
Figure 4.3. Structures of various amines tested in this study..... 88
Figure 4.4. Molecular structures of *n*-butylamine, *n*-octylamine, cyclohexylamine, and diethylamine..... 98
Figure 4.5. Structure of $Fe(NH(CH_2)_5)[N(SiMe_3)_2]_2$ (**12-pip**) with thermal ellipsoids (50% probability level) and selected atom labels. Hydrogen atoms are not shown. 105
Figure 4.6. Structure of $Fe(NH(^iPr)_2)[N(SiMe_3)_2]_2$ (**12-DIPA**) with thermal ellipsoids (50% probability level) and selected atom labels. Hydrogen atoms are not shown. The asymmetric unit contains half of the **12-DIPA** molecule, with the remaining atoms generated by a crystallographic 2-fold rotation..... 105
Figure 4.7. Structure of $Fe_2(\mu\text{-}N(CH_2)_5)(\mu\text{-}N(SiMe_3)_2)[N(SiMe_3)_2]_2$ (**13-pip**) with thermal ellipsoids (50% probability level) and selected atom labels. Hydrogen atoms are not shown. 107
Figure 4.8. Structure of $Fe_2(\mu\text{-}NH^tAm)(\mu\text{-}N(SiMe_3)_2)[N(SiMe_3)_2]_2$(**13-^{t}Am**) with thermal ellipsoids (50% probability level) and selected atom labels. Hydrogen atoms are not shown. 107
Figure 4.9. Structure of $Fe_2(\mu\text{-}NHMes)(\mu\text{-}N(SiMe_3)_2)[N(SiMe_3)_2]_2$(**13-Mes**) with thermal ellipsoids (50% probability level) and selected atom labels. Hydrogen atoms are not shown. Half the molecule of **13-Mes** present in the asymmetric unit with other atoms generated by crystallographic 2-fold rotation..... 108
Figure 4.10. Structure of $Fe_2(\mu\text{-}2,6\text{-}C_6H_3{}^iPr_2)(\mu\text{-}N(SiMe_3)_2)[N(SiMe_3)_2]_2$(**13-DIPAni**) with thermal ellipsoids (50% probability level) and selected atom labels. Hydrogen atoms are not shown. 108
Figure 4.11. Structure of $Fe_3(\mu\text{-}N(CH_2)_5)_4[N(SiMe_3)_2]_2$ (**15-pip)** with thermal ellipsoids (50% probability level) and selected atom labels. Hydrogen atoms are not shown. 111
Figure 4.12. Structure of $Fe_3(\mu\text{-}NHMes)_4[N(SiMe_3)_2]_2$ (**15-Mes**) with thermal ellipsoids (50% probability level) and selected atom labels. Hydrogen atoms are not shown. 111
Figure 4.13. Structure of $Fe_3(\mu\text{-}N(Me)Ph)_4N(SiMe_3)_2]_2$ (**15-NMePh**) with thermal ellipsoids (50% probability level) and selected atom labels. Hydrogen atoms are not shown. 112
Figure 4.14. Structure of $Fe_3(\mu\text{-}N(Me)Bn)_4N(SiMe_3)_2]_2$ (**15-NMeBn**) with thermal ellipsoids (50% probability level) and selected atom labels. Hydrogen atoms are not shown. Half the molecule of **15-NMeBn** is present in the asymmetric unit with other atoms generated by crystallographic 2-fold rotation..... 112
Figure 4.15. Structure of $Fe_3(\mu\text{-}NH(2,6\text{-}C_6H_3{}^iPr_2)_4[NH(2,6\text{-}C_6H_3{}^iPr_2)]_2$ (**16-DIPAni**) with thermal ellipsoids (50% probability level) and selected atom labels. Hydrogen atoms are not shown. 113

Figure 4.16. Structures of isolated heteroleptic dinuclear complexes (**14-^{t}Bu** and **14-^{t}Am**). Cis and trans configuration of the disubstituted, dinuclear complexes. 116
Figure 4.17. All possible diastereomers of the trinuclear complexes. 117
Figure 4.18. ^{1}H NMR spectra (298 K, 300 MHz) of **12-DIPA** and **12-pip** in C_6D_6. Residual protio signal indicated by *. 119
Figure 4.19. ^{1}H NMR titration of **11** with varying equivalents of DIPA in C_6D_6. 120
Figure 4.20. Chemical shift comparison of **11** in C_6D_6 with varying equivalents of DIPA. 121
Figure 4.21. ^{1}H NMR spectra (298 K, 300 MHz) of **13-^{t}Bu**, **14-^{t}Bu**, **13-^{t}Am**, and **14-^{t}Am** in C_6D_6. Residual protio signal indicated by *. 122
Figure 4.22. ^{1}H NMR spectrum (298 K, 300 MHz) of **13-Bn** and **13-pip** in C_6D_6. Residual protio signal indicated by *. 123
Figure 4.23. ^{1}H NMR spectra (298 K, 300 MHz) of **13-DIPAni** and **13-Mes** in C_6D_6. Residual protio signal indicated by *. 124
Figure 4.24. ^{1}H NMR spectra (298 K, 300 MHz) of **13-Ph**, **13-*p*-Tol** and **13-*o*-Tol**. Residual protio signal indicated by *. 125
Figure 4.25. ^{1}H NMR spectra (298 K, 300 MHz) of **13-NMePh** and **13-NMeBn** in C_6D_6. Residual protio signal indicated by *. 125
Figure 4.26. ^{1}H NMR spectrum (298 K, 300 MHz) of **15-^{t}Bu** in C_6D_6 contaminated with 14-^{t}Bu. Residual protio signal indicated by * 126
Figure 4.27. ^{1}H NMR spectrum (298 K, 300 MHz) of **15-pip** in C_6D_6. Residual protio signal indicated by *. 127
Figure 4.28. ^{1}H NMR spectrum (298 K, 300 MHz) of a single crystal of **15-Mes** in C_6D_6. Residual protio signal indicated by *. 128
Figure 4.29. ^{1}H NMR spectra (298 K, 300 MHz) of a single crystal of **15-NMePh** (bottom) and **15-NMeBn** (top). Residual protio signal indicated by *. 129
Figure 4.30. (top) ^{1}H NMR spectra (298 K, 300 MHz) of the crude reaction of **11** and **1.33** equivalents of 2,6-diisopropylaniline. (bottom) ^{1}H NMR spectra (298 K, 300 MHz) of single crystals of **16-DIPAni** in C_6D_6. 130
Figure 4.31. Electronic absorption spectra of **15-pip** (black), **13-pip** (red) and **12-pip** (blue) in *n*-pentane. 132
Figure 4.32. Electronic absorption spectra of **15-Mes** (black) and **13-Mes** (red) in *n*-pentane. 133
Figure 4.33. Electronic absorption spectra of **14-^{t}Bu** (green) and **13-^{t}Bu** (red) in *n*-pentane. 133
Figure 4.34. Electronic absorption spectra of **14-^{t}Am** (green) and **13-^{t}Am** (red) in *n*-pentane. 134
Figure 4.35. Electronic absorption spectra of **13-DIPAni** (red) in *n*-pentane. 134
Figure 4.36. Electronic absorption spectra of **12-DIPA** (blue) in *n*-pentane. 135
Figure 5.1. Metalloclusters found in Mo-nitrogenase and V-nitrogenase. 157
Figure 5.2. Structure of FeMoco under turnover conditions. Figure A and C taken from Reference 150. Figure B: Reprinted with permission from Spatzal, T.; Perez, K. A.; Einsle. O; Howard, J. B.; Rees, D. C, *Science*, 2014, *345*, 1616–1620. © 2020 The Authors, some rights reserved, exclusive licensee American Association for the Advancement of Science. Figure D and E: Reprinted with permission from Kang, W.; Lee, C. C.; Jasniewski, A. J.;

Ribbe, M. W.; Hu, Y., *Science*, 2020, *368*, 1381–1385. © 2020 The Authors, some rights reserved, exclusive licensee American Association for the Advancement of Science. Figure F taken from Reference 153. 159
Figure 5.3. Structures of synthetic analogues of FeMoco in historical order. 161
Figure 5.4. Superposition of the [Fe_4S_3N] core and the [Fe_4S_3C] subunit of FeMoco. The RMSD is 0.047 Å for the eight core atoms. Reprinted (adapted) with permission from Chen, X. D.; Zhang, W.; Duncan, J. S.; Lee, S. C. *Inorg. Chem.* 2012, *51* (23), 12891–12904. Copyright 2012 American Chemical Society. 162
Figure 5.5. Thiolates utilized as ligands in this chapter. Thiolates include mesityl thiolate (SMes), 4-methylbenzene thiolate (S-*p*-Tol), benzene thiolate (SPh), 4-chlorobenzene thiolate (SCBT), and 2,6-dichlorobenzene thiolate (SDCBT). 166
Figure 5.6. ^{1}H NMR Spectra (298 K, 300 MHz) of $[Ph_4P]_2$**20-Ph**, $[Et_4N]_2$**20-*p*Tol**, $[Et_4N]_2$**20-Mes**, $[Et_4N]_2$**20-CBT**, and $[Et_4N]_2$**20-DCBT**. Residual protio signals of CD_3CN are marked by *. Resonances corresponding to ligand environments bound to the three equivalent Fe sites are indicated in red; those corresponding to the unique Fe site are indicated in green. 168
Figure 5.7. Solution UV-vis absorption spectra of $[Ph_4P]_2[Fe_4(N^tBu)S_3Cl_4]$ ($[Ph_4P]_2$**19**, black), $[Ph_4P]_2[Fe_4(N^tBu)S_3(SPh)_4]$ ($[Ph_4P]_2$**20-Ph**, orange), $[Et_4N]_2[Fe_4(N^tBu)S_3(S(4\text{-}C_6H_4Me))_4]$ ($[Et_4N]_2$**20-*p*Tol**, red), and $[Et_4N]_2[Fe_4(N^tBu)S_3(S(2,6\text{-}C_6H_3Cl_2))_4]$ ($[Et_4N]_2$**20-DCBT**, blue) in pentane. 169
Figure 5.8. Structure of anion in $[Et_4N]_2[Fe_4(N^tBu)S_3(S(2,6\text{-}C_6H_3Cl_2))_4]$ ($[Et_4N]_2$**20-DCBT**) with thermal ellipsoids (50% probability level) and selected atom labels. For clarity, hydrogen atoms are not shown. 170
Figure 5.9. Structure of anion in $[Et_4N]_2[Fe_4(N^tBu)S_3(S(4\text{-}C_6H_4Me))_4]$ ($[Et_4N]_2$**20-*p*Tol**) with thermal ellipsoids (50% probability level) and selected atom labels. For clarity, hydrogen atoms are not shown. 170
Figure 5.10. Cyclic voltammograms (0.1 M (n-Bu_4N)ClO_4 supporting electrolyte in MeCN, 100 mV/s scan rate) of $[Et_4N]_2$**20-Ph** and $[Et_4N]_2$**20-Mes**. 173
Figure 5.11. Cyclic voltammogram (0.1 M (n-Bu_4N)ClO_4 supporting electrolyte in MeCN, 100 mV/s scan rate) of $[Et_4N]_2$**20-CBT**. 174
Figure 5.12. Cyclic voltammogram (0.1 M (n-Bu_4N)ClO_4 supporting electrolyte in MeCN, 100 mV/s scan rate) of $[Et_4N]_2$**20-*p*Tol**. 175
Figure 5.13. Cyclic voltammogram (0.1 M (n-Bu_4N)ClO_4 supporting electrolyte in MeCN, 100 mV/s scan rate) of $[Et_4N]_2$**20-DCBT**. 175
Figure 5.14. ^{1}H NMR spectra (298 K, 300 MHz) of $[Et_4N]$21-Mes in CD_3CN. Residual protio signal indicated by *. Counterion resonances indicated by **. Resonances corresponding to ligand environments bound to the three equivalent Fe sites are indicated in red; those corresponding to the unique Fe site are indicated in green. 178
Figure 5.15. ^{1}H NMR spectrum (298 K, 300 MHz) of $[Et_4N]_2$**20-Ph** with 1.2 equivalents of Cp_2*Co in CD_3CN. Residual protio signal indicated by *. Counterion resonances indicated by **. Resonances corresponding to ligand environments bound to the three equivalent Fe sites are indicated in red; those corresponding to the unique Fe site are indicated in green. 182
Figure 5.16. (**A**) ^{1}H NMR (298 K, 300 MHz) spectrum of $[Ph_4P]_2$**20-Ph**. (**B**) ^{1}H NMR (298 K, 300 MHz) spectrum of $[Ph_4P]_2$**20-Ph** and 1.1 equivalents of Cp^*_2Co. (**C**) ^{1}H NMR (298 K, 300 MHz) spectrum of the oxidation of (B) with $Fc(PF_6)$. Residual protio signal indicated

by *. Counterion resonances indicated by **. Resonances corresponding to ligand environments bound to the three equivalent Fe sites are indicated in red; those corresponding to the unique Fe site are indicated in green. 183
Figure 5.17. (**A**) ^{1}H NMR spectrum (298 K, 300 MHz) of $[Ph_4P]_2$**20-Ph** (**B**) ^{1}H NMR (298 K, 300 MHz) spectra of $[Ph_4P]_2$**20-Ph** and 1.1 equivalents of Cp^*_2Co producing $[Ph_4P][Cp^*_2Co]_2$22-Ph. (**C**) ^{1}H NMR spectrum of B after 16 h. (**D**) ^{1}H NMR spectrum after oxidation with 1.1 equivalents of $Fc(PF_6)$. Residual protio signal indicated by *. Counterion resonances indicated by **. Resonances corresponding to ligand environments bound to the three equivalent Fe sites are indicated in red; those corresponding to the unique Fe site are indicated in green. 185
Figure 5.18. (**A**) ^{1}H NMR spectrum (298 K, 300 MHz) of $[Et_4N]_2$**23-Ph**. (**B**) ^{1}H NMR spectrum (298 K, 300 MHz) of $[Et_4N][Cp^*_2Co]$**24-Ph** generated from reduction of $[Et_4N]_2$23-Ph with Cp^*_2Co. (**C**) ^{1}H NMR spectrum (298 K, 300 MHz) of $[Et_4N]_2$**23-Ph** generated from oxidation of B with $Fc(PF_6)$. Residual protio signal indicated by *. Counterion resonances indicated by **. 187
Figure 5.19. (**A**) ^{1}H NMR spectrum (298 K, 300 MHz) of $[Et_4N]_2$**23-Ph**. (**B**) ^{1}H NMR spectrum (298 K, 300 MHz) of $[Et_4N][Cp^*_2Co]$**25** generated from reduction of $[Et_4N]_2$**23-Ph** with Cp^*_2Co. (**C**) ^{1}H NMR spectrum (298 K, 300 MHz) of C after 16 hours. (**D**) ^{1}H NMR spectrum (298 K, 300 MHz) of $[Et_4N]_2$**23-Ph** generated from oxidation of C with $Fc(PF_6)$. Residual protio signal indicated by *. Counterion resonances indicated by **..... 189
Figure 5.20. (**A**) ^{1}H NMR spectrum (298 K, 300 MHz) of $[Et_4N]_2$**23-Bn**. (**B**) ^{1}H NMR spectrum (298 K, 300 MHz) of $[Et_4N]_3$**24-Bn** generated from reduction of $[Et_4N]_2$**23-Bn** with Cp^*_2Co after 30 minutes. (**C**) ^{1}H NMR spectrum (298 K, 300 MHz) of $[Et_4N]_3$**24-Bn** generated from reduction of $[Et_4N]_2$23-Bn with Cp^*_2Co after 16 hours. Residual protio signal indicated by *. Counterion resonances indicated by **. 190
Figure 5.21. Reduction and oxidation of $[Et_4N]_2$**20-DCBT** in CD_3CN (298 K, 300 MHz). (**A**) ^{1}H NMR spectrum of $[Et_4N]_2$**20-DCBT**. (**B**) Addition of 1 equivalent of Cp^*_2Co. (**C**) Addition of 2nd equivalent of Cp^*_2Co. (**D**) Addition of 1 equivalent of $Fc(PF_6)$. (**E**) Addition of a 2nd equivalent of $Fc(PF_6)$. Residual protio signal indicated by *. Counterion resonances indicated by **. Resonances corresponding to ligand environments bound to the three equivalent Fe sites are indicated in red; those corresponding to the unique Fe site are indicated in green. 191
Figure 5.22. (**A**) ^{1}H NMR spectrum (298 K, 300 MHz) of $[Et_4N]_2$**23-DCBT**. (**B**) ^{1}H NMR spectrum (298 K, 300 MHz) of $[Et_4N]_2$**23-DCBT** and 1 equivalent Cp^*_2Co after 15 minutes. (**C**) ^{1}H NMR spectrum (298 K, 300 MHz) of $[Et_4N]_2$**23-DCBT** and 1 equivalent Cp^*_2Co after 16 hours. Residual protio signal indicated by *. Counterion resonances indicated by **.... 192
Figure 5.23. (**A**) ^{1}H NMR (298 K, 300 MHz) spectrum of the reaction of $(Ph_4P)_2$**19** and 4.1 equivalents of $Na(4\text{-}C_6H_4Cl)$. (**B**) ^{1}H NMR (298 K, 300 MHz) spectrum after addition of one equivalent of Cp^*_2Co. Residual protio signal indicated by *. Counterion resonances indicated by **. Resonances corresponding to ligand environments bound to the three equivalent Fe sites are indicated in red; those corresponding to the unique Fe site are indicated in green. 194
Figure 5.24. (**A**) ^{1}H NMR (298 K, 300 MHz) spectrum of crystalline $[Et_4N]_3$**22-*p*To**l in CD_3CN after 15 minutes. (**B**) ^{1}H NMR (298 K, 300 MHz) spectrum of crystalline $[Et_4N]_3$**22-**

***p*Tol** in CD_3CN after 16 hours. Residual protio signal indicated by *. Counterion resonances indicated by **. 196
Figure 5.25. Temperature dependence plot of the magnetic susceptibilities of polycrystalline $[Et_4N]_2[Fe_4(N^tBu)S_3(SMes)_4]$ ($[Et_4N]_2$**20-Mes**, blue) and $[Et_4N][Fe_4(N^tBu)S_3(SMes)_4]$ ($[Et_4N]$**21-Mes**, purple). The magnet moment of $[Et_4N]$**21-Mes** is plotted in black. 197
Figure 5.26. Temperature dependence plot of the reciprocal magnetic susceptibility of polycrystalline $[Et_4N][Fe_4(N^tBu)S_3(SMes)_4]$ ($[Et_4N]$**21-Mes**). The solid line indicates the linear least-squares fit ($y = 0.51\ x + 0.88$; $C = 2.00$ emu K/mol, $\theta = -1.75$ K) to the data between $T = 2 - 50$ K. Data is consistent with a S=3/2 ground spin state. 198
Figure 5.27. X-band EPR spectrum (4 K, 0.2 M TBAP/DMF) of $[Et_4N]$**21-Mes**. 199
Figure 5.28. (**A**) Conceptualization of the delocalization in $[Fe_4S_4]^{2+}$ clusters. (**B**) Delocalization and localization patterns in $[Fe_4S_4]^{1+/2+/3+}$ clusters. 200
Figure 5.29. Conceptual fragmentation of $[Et_4N]$**21-Mes** into Fe^{2+} and $[Fe_3(N^tBu)S_4]$. 201
Figure 5.30. ^{1}H NMR (298 K, 300 MHz) spectra of $[Et_4N]_2$**20-Ph** (A), $[Et_4N]_2[Cp^*_2Co]$**22-Ph** (B), $[Et_4N]_2$**20-Mes** (C) and $[Et_4N]$**21-Mes** (D). Resonances corresponding to ligand environments bound to the three equivalent Fe sites are indicated in red; those corresponding to the unique Fe site are indicated in green. 202
Figure 5.31. Literature model with Ni^{2+} and Fe_3S_4 fragmentation 203
Figure 6.1. Schematic of a site differentiated iron-sulfur cluster from the Holm group. Reprinted (adapted) with permission from Rao, P. V.; Holm, R. H. *Chem. Rev.* 2004, *104*, 527–559. Copyright 2004 American Chemical Society. 211
Figure 6.2. Synthesis of site-differentiated Fe_4S_4 cluster with bulky NHC ligation. Reprinted (adapted) with permission from Brown, A. C.; Suess, D. L. M., *Inorg. Chem.* 2019, *58*, 5273–5280. Copyright 2019 American Chemical Society. 211
Figure 6.3. Schematic of CO and N_2 bound to synthetic iron-sulfur and iron-molybdenum-sulfur cubane clusters. Top figure: reprinted (adapted) from Brown, A. C.; Thompson, N. B.; Suess, D. L. M. *J. Am. Chem. Soc.* 2022, *144* (20), 9066–9073. Copyright 2022 American Chemical Society. Bottom figure: reproduced with permission from McSkimming et al., *Nature Chemistry*, 2021, *13(7)* , 666–670, Springer Nature. 212
Figure 6.4. Structures of mononuclear iron complexes ligated with $^-$SDmp. Reproduced from Ellison, J. J.; Ruhlandt-Senge, K.; Power, P. P., *Angew. Chem. Int. Ed.*, 1994, 33, 1178–1180, with permission from Wiley-VCH. 213
Figure 6.5. Synthesis of site differentiated Fe_4S_4 clusters with $^-$SDmp. Reproduced from Ohki, Y.; Tanifuji, K.; Yamada, N.; Imada, M.; Tajima, T.; Tatsumi, K. *PNAS* 2011, *108*, 12635–12640. Copyright 2011 National Academy of Sciences. 214
Figure 6.6. Crystal structures of $[Fe_4S_4(SDmp)_4]^z$ in five charge states (z = 0 to 4–). Reproduced from Grunwald, L.; Clémancey, M.; Klose, D.; Dubois, L.; Gambarelli, S.; Jeschke, G.; Wörle, M.; Blondin, M.; Mougel, V. *PNAS* 2022, *119 (31).* Copyright 2022 National Academy of Sciences. 216
Figure 6.7. Thiolate ligands utilized within this chapter. 218
Figure 6.8. ^{1}H NMR (298 K, 300 MHz) spectrum of $[Et_4N]_2$**20-Triph** and $[Et_4N]$**21-Triph** in CD_3CN. Residual protio signal indicated by *. Counterion resonances indicated by **. 219
Figure 6.9. All possible substitution patterns with $^-$SDmp onto the Fe_4NS_3 core. Shorthand denotes which iron site (proximal vs. distal) is substituted. 220

Figure 6.10. Stoichiometry investigation of $[Et_4N]_2$**19** with varying equivalents of $^-$SDmp in CD_3CN. Residual protio signal indicated by *. Counterion resonances indicated by **. 221
Figure A.1. ^{1}H NMR spectra of $[Ph_4P]$**2** and 3 equivalents of KC_8 in CD_3CN. Signal set for the new species highlighted with peak positions shown. 237
Figure A.2. ^{1}H NMR spectra (300 MHz, 298 K) of residual oil from THF collected from SPS in $CDCl_3$. 238
Figure B.1. Titration 1 residuals contour map. 245
Figure B.2. Titration 2 residuals contour map. 246
Figure B.3. Titration 3 residuals contour map. 246
Figure B.4. Residual plot for titration 1. 247
Figure B.5. Residual plot for titration 2. 247
Figure B.6. Residual plot for titration 3. 248
Figure B.7. Calibration plot of Fe^{2+} in MeCN. 249
Figure C.1. Stejskal-Tanner plot of benzene in THF-d_8. 251
Figure C.2. Stejskal-Tanner plot of 1-tetradecene in THF-d_8. 252
Figure C.3. Stejskal-Tanner plot of cyclooctene in THF-d_8. 252
Figure C.4. Stejskal-Tanner plot of squalene in THF-d_8. 253
Figure C.5. Stejskal-Tanner plot of **9** in THF-d_8. 253
Figure C.6. Stejskal-Tanner plot of cyclooctene in THF-d_8. 254
Figure C.7. Stejskal-Tanner plot of benzene in THF-d_8. 254
Figure C.8. Stejskal-Tanner plot of squalene in THF-d_8. 255
Figure C.9. Stejskal-Tanner plot of **8** in THF-d_8. 255
Figure C.10. log D vs log MW DOSY molecular weight calibration curve. 256
Figure C.11. Stejskal-Tanner plot of **8** in toluene-d_8. 257
Figure C.12. Stejskal-Tanner plot of 1-tetradecene in toluene-d_8. 257
Figure C.13. Stejskal-Tanner plot of cyclooctene in toluene-d_8. 258
Figure C.14. Stejskal-Tanner plot of squalene in toluene-d_8. 258
Figure C.15. log D vs log MW DOSY molecular weight calibration curve. 259

List of Tables

Table 2.1. Redox potentials ($E_{1/2}$) for $[Fe_4(N^tBu)_4Cl_4]^z$ 22
Table 2.2. Selected interatomic distances (Å) and angles (°) for $[Ph_4P]_2$**6** 24
Table 2.3. Selected mean distances (A˚) and angles (deg) for $[Ph_4P]_2$**6** 25
Table 2.4. Selected averaged interatomic distances (Å) and Angles (º) in $Fe_4(\mu_3\text{-}N^tBu)_4Cl_4$ (**1**), $[Ph_4P][Fe_4(\mu_3\text{-}N^tBu)_4Cl_4]$ (**2**) and $[Ph_4P]_2[Fe_4(\mu_3\text{-}N^tBu)_4Cl_4]$ (**6**) 26
Table 2.5. Selected interatomic distances (Å) and angles (º) in $Fe_4(NPh)_4(SMes)_4$, $Fe_4(N\text{-}p\text{-}Tol)_4(SMes)_4$, $[Fe(THF)_6][Fe_4(N\text{-}p\text{-}Tol)_4\text{-}(SDMP)_3(N\{SiMe_3\}_2)]_2$ and $[Li(DME)_3]_2[Fe_4(NPh)_4Cl_4]$ 27
Table 2.6. Selected Interatomic Distances (Å) and Angles (º) in $[Et_4N][Fe_4(N^tBu)_3SCl_4]$, $[Et_4N]_2[Fe_4(N^tBu)_2S_2Cl_4]$ and $[Et_4N]_2[Fe_4(N^tBu)S_3Cl_4]$ 28
Table 2.7. Spectroscopic data for $Fe_4(\mu_3\text{-}N^tBu_4)Cl_4$ (**1**), $(Ph_4P)[Fe_4(\mu_3\text{-}N^tBu)_4Cl_4]$ ($[Ph_4P]$**2**), and $(Ph_4P)_2[Fe_4(\mu_3\text{-}N^tBu)_4Cl_4]$ ($[Ph_4P]_2$**6**) 28
Table 2.8. ^{1}H NMR chemical shifts of $[Fe_4(N^tBu)_3SCl_4]^{1-}$, $[Fe_4(N^tBu)_2S_2Cl_4]^{2-}$ and $[Fe_4(N^tBu)S_3Cl_4]^{2-}$ in CD_3CN 30
Table 2.9. Mössbauer isomer shifts of members of the $[Fe_4(N^tBu)_nS_{4-n}Cl_4]^z$ series 34
Table 2.10. Equilibrium constants and chemical shifts for $FeCl_2(^tBuNH_2)$ and $FeCl_2(^tBuNH_2)_2$ 40
Table 2.11. Selected crystallographic data for $FeCl_2(NH_2{}^tBu)_2$ (**4**) 45
Table 2.12. Crystallographic data summary for $[Ph_4P]_2[Fe_4(N^tBu)_4Cl_4]$ ($[Ph_4P]_2$**6**) 45
Table 3.1. Selected distances (Å) and angles (º) for $(LiNH^tBu)_\infty$ (**9**) and $(LiNH^tBu)_8$ (**10**).... 53
Table 3.2. Selected averaged distances (Å) and angles (º) for $(LiNH^tBu)_8C_6H_{14}$ (**8**), $(LiNH^tBu)_\infty$ (**9**) and $(LiNH^tBu)_8$ (**10**) 56
Table 3.3. Selected interatomic distances (Å) and angles (°) of $[(NaNH^tBu)_3{}^tBuNH_2]_\infty$ and $[(LiNa[NH^tBu]_2)_2(TMEDA)_2]$ 58
Table 3.4. Polymorph conversion data of **8** to **9** using various methods 60
Table 3.5. Calorimetry data for $(LiNH^tBu)_8$ (**8**) and $(LiNH^tBu)_\infty$ (**9**) 65
Table 3.6. ^{1}H NMR data for $(LiNH^tBu)_8$ (**8**/**10**) and $(LiNH^tBu)_\infty$ (**9**) 66
Table 3.7. Percent differences of the actual and calculated molecular mass of benzene, cyclooctene, 1-tetradecene and squalene 73
Table 3.8. Calculated diffusion coefficients and molecular masses of internal standards and **8** in THF-d_8 and toluene- d_8 and **9** in THF-d_8 74
Table 3.9. Calculated MW for **8** in toluene-d_8 and THF-d_8 and **9** in THF-d_8 using ^{1}H DOSY MW analysis 75
Table 3.10. Crystallographic data for (LiNHtBu)∞ (**9**) and (LiNHtBu)8 (**10**) 80
Table 4.1. Summary of outcomes in the reaction of **11** with various amines 92
Table 4.2. Selected Distances (Å) and Angles (º) for $Fe(NH(CH_2)_5)[N(SiMe_3)_2]_2$ (**12-pip**) and $Fe(NH(^iPr)_2)[N(SiMe_3)_2]_2$ (**12-DIPA**) 106
Table 4.3. Selected Distances (Å) and Angles (º) for $Fe_2(\mu\text{-}N(CH_2)_5)(\mu\text{-}N(SiMe_3)_2)[N(SiMe_3)_2]_2$ (**13-pip**) and $Fe_2(\mu\text{-}NH^tAm)(\mu\text{-}N(SiMe_3)_2)[N(SiMe_3)_2]_2$ (**13-^{t}Am**) 109
Table 4.4. Selected Distances (Å) and Angles (º) for $Fe_2(\mu\text{-}NHMes)(\mu\ N(SiMe_3)_2)[N(SiMe_3)_2]_2$ (**13-Mes**) 109

Table 4.5. Selected Distances (Å) and Angles (º) for $Fe_2(\mu\text{-}NH(2,6\text{-}C_6H_3{}^iPr_2)(\mu\text{-}N(SiMe_3)_2)[N(SiMe_3)_2]_2$ (**13-DIPAni**) 110
Table 4.6. Selected Distances (Å) and Angles (º) for $Fe_3(\mu\text{-}NHMes)_4[N(SiMe_3)_2]_2$ (15-Mes) and $Fe_3(\mu\text{-}N(Me)Ph)_4N(SiMe_3)_2]_2$ (**15-NMePh**) 113
Table 4.7. Selected Distances (Å) and Angles (º) for $Fe_3(\mu\text{-}N(CH_2)_5)_4[N(SiMe_3)_2]_2$ (**15-pip**) and $Fe_3(\mu\text{-}NH(2,6\text{-}C_6H_3{}^iPr_2)_4[NH(2,6\text{-}C_6H_3{}^iPr_2)]_2$ (**15-DIPAni**) 114
Table 4.8. Selected Distances (Å) and Angles (º) for $Fe_3(\mu\text{-}N(Me)Bn)_4N(SiMe_3)_2]_2$ (15-NMeBn) 115
Table 4.9. ^{1}H NMR data for $Fe_2(\mu\text{-}NH{}^tBu)_2[N(SiMe_3)_2]_2$ (**14-^{t}Bu**), $Fe_2(\mu\text{-}NH{}^tBu)(\mu\text{-}N(SiMe_3)_2)[N(SiMe_3)_2]_2$ (**13-^{t}Bu**), $Fe_3(\mu\text{-}NH{}^tBu)_4[N(SiMe_3)_2]_2$ (**15-^{t}Bu**), $Fe_2(\mu\text{-}NH{}^tAm)(\mu\text{-}N(SiMe_3)_2)[N(SiMe_3)_2]_2$ (**13-^{t}Am**), $Fe_2(\mu\text{-}NH{}^tAm)_2[N(SiMe_3)_2]_2$ (**14-^{t}Am**), $Fe(NH({}^iPr)_2)[N(SiMe_3)_2]_2$ (**12-DIPA**), $Fe(NH(CH_2)_5)[N(SiMe_3)_2]_2$ (**12-pip**), $Fe_2(\mu\text{-}N(CH_2)_5)(\mu\text{-}N(SiMe_3)_2)[N(SiMe_3)_2]_2$ (**13-pip**), $Fe_3(\mu\text{-}N(CH_2)_5)_4[N(SiMe_3)_2]_2$ (**15-pip**), $Fe_2(\mu\text{-}NHBn)(\mu\text{-}N(SiMe_3)_2)[N(SiMe_3)_2]_2$ (**13-Bn**), $Fe_3(\mu\text{-}NHPh)_4[N(SiMe_3)_2]_2$ (**13-Ph**), $Fe(\mu\text{-}NH(4\text{-}C_6H_4(Me)))(\mu\text{-}N(SiMe_3)_2)[N(SiMe_3)_2]_2$ (**13-*p*-Tol**), $Fe(\mu\text{-}NH(o\text{-}C_6H_4(Me)))(\mu\text{-}N(SiMe_3)_2)[[N(SiMe_3)_2]_2$ (**13-*o*-Tol**), $Fe_2(\mu\text{-}NHMes)(\mu\text{-}N(SiMe_3)_2)[N(SiMe_3)_2]_2$ (**13-Mes**), $Fe_3(\mu\text{-}NHMes)_4[N(SiMe_3)_2]_2$ (**15-Mes**), $Fe_2(\mu\text{-}N(Me)Ph)(\mu\text{-}N(SiMe_3)_2)[N(SiMe_3)_2]_2$ (**13-NMePh**), and $Fe_2(\mu\text{-}N(Me)Bn)(\mu\text{-}N(SiMe_3)_2)[N(SiMe_3)_2]_2$ (**13-NMeBn**) 151
Table 4.10. UV-vis Data for $Fe_2(\mu\text{-}NH{}^tBu)_2[N(SiMe_3)_2]_2$ (**14-^{t}Bu**), $Fe_2(\mu\text{-}NH{}^tBu)(\mu\text{-}N(SiMe_3)_2)[N(SiMe_3)_2]_2$ (**13-^{t}Bu**), $Fe_2(\mu\text{-}NH{}^tAm)(\mu\text{-}N(SiMe_3)_2)[N(SiMe_3)_2]_2$ (**13-^{t}Am**), $Fe_2(\mu\text{-}NH{}^tAm)_2[N(SiMe_3)_2]_2$ (**14-^{t}Am**), $Fe(NH({}^iPr)_2)[N(SiMe_3)_2]_2$ (**12-DIPA**), $Fe(NH(CH_2)_5)[N(SiMe_3)_2]_2$ (**12-pip**), $Fe_2(\mu\text{-}N(CH_2)_5)(\mu\text{-}N(SiMe_3)_2)[N(SiMe_3)_2]_2$ (**13-pip**), $Fe_3(\mu\text{-}N(CH_2)_5)_4[N(SiMe_3)_2]_2$ (**15-pip**), $Fe_2(\mu\text{-}NHMes)(\mu\text{-}N(SiMe_3)_2)[N(SiMe_3)_2]_2$ (**13-Mes**), $Fe_3(\mu\text{-}NHMes)_4[N(SiMe_3)_2]_2$ (**15-Mes**) and $Fe_2(\mu\text{-}NH(2,6\text{-}C_6H_3{}^iPr_2)(\mu\text{-}N(SiMe_3)_2)[N(SiMe_3)_2]_2$ (13-DIPAni) 152
Table 4.11. Crystallographic data for $Fe(NH({}^iPr)_2)[N(SiMe_3)_2]_2$ (**12-DIPA**) and $Fe(NH(CH_2)_5)[N(SiMe_3)_2]_2$ (**12-pip**) 153
Table 4.12. Crystallographic data for $Fe_2(\mu\text{-}NH{}^tAm)(\mu\text{-}N(SiMe_3)_2)[N(SiMe_3)_2]_2$ (**13-^{t}Am**), $Fe_2(\mu\text{-}N(CH_2)_5)(\mu\text{-}N(SiMe_3)_2)[N(SiMe_3)_2]_2$ (**13-pip**), $Fe_2(\mu\text{-}NHMes)(\mu\text{-}N(SiMe_3)_2)[N(SiMe_3)_2]_2$ (**13-Mes**), and $Fe_2(\mu\text{-}NH(2,6\text{-}C_6H_3{}^iPr_2)(\mu\text{-}N(SiMe_3)_2)[N(SiMe_3)_2]_2$ (**13-DIPAni**) 154
Table 4.13. Crystallographic data for $Fe_3(\mu\text{-}NHMes)_4[N(SiMe_3)_2]_2$ (**15-Mes**), $Fe_3(\mu\text{-}N(CH_2)_5)_4[N(SiMe_3)_2]_2$ (**15-pip**), $Fe_3(\mu\text{-}N(Me)Bn)_4N(SiMe_3)_2]_2$ (**15-NMeBn**), $Fe_3(\mu\text{-}N(Me)Ph)_4N(SiMe_3)_2]_2$ (**15-NMePh**), and $Fe_3(\mu\text{-}NH(2,6\text{-}C_6H_3{}^iPr_2)_4[NH(2,6\text{-}C_6H_3{}^iPr_2)]_2$ (**16-DIPAni**) 154
Table 5.1. Selected Distances (Å) and Angles (º) for $[Et_4N]_2[Fe_4(N{}^tBu)S_3(S(2,6\text{-}C_6H_3Cl_2))_4]$ ($[Et_4N]_2$**20-DCBT**) and $[Et_4N]_2[Fe_4(N{}^tBu)S_3(S(4\text{-}C_6H_4Me))_4]$ ($[Et_4N]_2$**20-*p*Tol**) 171
Table 5.2. Selected mean distances (Å) and angles (º) for $[Et_4N]_2$**20-DCBT** 172
Table 5.3. Selected mean distances (Å) and angles (º) for $[Et_4N]_2$**20-*p*Tol**..... 172
Table 5.4. Electrochemical data for select $[Fe_4S_4]$ clusters, $[Fe_4(N{}^tBu)S_3]$ clusters and redox agents (vs. SCE). Solvent is MeCN unless otherwise noted..... 176
Table 5.5. ^{1}H NMR data for $[Ph_4P]_2[Fe_4(N{}^tBu)S_3Cl_4]$ ($[Ph_4P]_2$**19**), $[Ph_4P]_2[Fe_4(N{}^tBu)S_3(SPh)_4]$ ($[Ph_4P]_2$**20**), $[Et_4N]_2[Fe_4(N{}^tBu)S_3(SMes)_4]$ ($[Et_4N]_2$**20-Mes**), $[Et_4N]Fe_4(N{}^tBu)S_3(SMes)_4]$ ($[Et_4N]$**21-Mes**), $[Et_4N]_2[Cp^*{}_2Co][Fe_4(N{}^tBu)S_3(SPh)_4]$

([Et_4N]$_2$[Cp*$_2$Co]22-Ph), [Et_4N]$_2$[Fe_4S_4(SPh)$_4$] ([Et_4N]$_2$**23-Ph**), [Et_4N]$_3$[Fe_4S_4(SPh)$_4$] ([Et_4N]$_3$24-Ph), [Et_4N]$_2$[Fe_4S_4(SBn)$_4$] ([Et_4N]$_2$**23-Bn**), [Et_4N]$_2$[Cp*$_2$Co][Fe_4S_4(SBn)$_4$] ([Et_4N]$_2$[Cp*$_2$Co]**24-Bn**), [Et_4N]$_2$[Fe_4(N^{t}Bu)S_3(S(2,6-$C_6H_3Cl_2$))$_4$] ([Et_4N]$_2$**20-DCBT**), [Ph_4P]$_2$[Fe_4S_4(S(2,6-$C_6H_3Cl_2$)$_4$] ([Ph_4P]$_2$**23-DCBT**), [Et_4N]$_2$[Fe_4(N^{t}Bu)S_3(S(4-C_6H_4Cl))$_4$] ([Et_4N]$_2$**20-CBT**), [Et_4N]$_2$[Fe_4(N^{t}Bu)S_3(S(4-C_6H_4Me))$_4$] ([Et_4N]$_2$**20-*p*Tol**) 207
Table 5.6. UV-vis Data for [Ph_4P]$_2$[Fe_4(N^{t}Bu)S_3Cl_4] ([Ph_4P]$_2$**19**), [Ph_4P]$_2$[Fe_4(N^{t}Bu)S_3(SPh)$_4$] ([Ph_4P]$_2$**20-Ph**), [Et_4N]$_2$[Fe_4(N^{t}Bu)S_3(S(2,6-$C_6H_3Cl_2$))$_4$] ([Et_4N]$_2$**20-DCBT**) and [Et_4N]$_2$[Fe_4(N^{t}Bu)S_3(S(4-C_6H_4Me))$_4$] ([Et_4N]$_2$**20-*p*Tol**) 208
Table 5.7. Crystallographic data summary for [Et_4N]$_2$[Fe_4(N^{t}Bu)S_3(S(2,6-$C_6H_3Cl_2$))$_4$] ([Et_4N]$_2$**20-DCBT**) and [Et_4N]$_2$[Fe_4(N^{t}Bu)S_3(S(4-C_6H_4Me))$_4$] ([Et_4N]$_2$**20-*p*Tol**) 209
Table 6.1. ^{1}H NMR data for likely $^-$SDmp ligated species 222
Table B.1. Averaged and independent calculated titration data 241
Table B.2. Amounts and concentrations of $FeCl_2$ and ^{t}BuNH$_2$ for each titration run 242
Table B.3. Calculated data for titration 1 242
Table B.4. Calculated data for titration 2 243
Table B.5. Calculated data for titration 3 244
Table B.6. Tabulated absorbances 249
Table C.1. Masses, volumes and NMR parameters 251
Table C.2. Percent differences of the actual and calculated molecular mass of benzene, cyclooctene, 1-tetradecene and squalene 256
Table C.3. Percent differences of the actual and calculated molecular mass of benzene, cyclooctene, 1-tetradecene and squalene 259

List of Abbreviations

^1H	Proton
ACN	Acenaphthalene
Ar	Aromatic
Å	Angstrom
Bn	Benzyl
CBT	4-chlorobenzene thiolate
CD_3CN	Acetonitrile-d_3
COSY	Correlation Spectroscopy
Cp	Cyclopentadienyl
Cp*	Pentamethylcyclopentadienyl
Cy	Cyclo
DCBT	2,6-dichlorobenzene thiolate
DCM	Dichloromethane
DIPA	Diisopropylamine
DIPAni	2,6-diisopropylaniline
DMB	Dimethylbenzene
DMF	Dimethylformamide
DME	1,2-dimethoxyethane
DOSY	Diffusion Ordered Spectroscopy
DSC	Differential Scanning Calorimetry
SDmp	2,6-dimesitylbenzene thiolate
$E_{1/2}$	Redox potential
Equiv.	Equivalents
EPR	Electron Paramagnetic Resonance
Et	Ethyl
Et_2O	Diethyl ether
Fc	Ferrocene
Fc^+	Ferrocenium

Fe–S	Iron sulfur
FeMoco	Iron molybdenum cofactor
FeVco	Iron vanadium cofactor
g	g-value
h	Hour
HMBC	Heteronuclear multiple bond correlation
HMQC	Heteronuclear multiple quantum correlation
HMDS	Bis(trimethylsilyl)amide
HMDSA	Hexamethyldisilazane
HMDSO	Hexamethyldisiloxane
HMPA	Hexamethylphosphoramide
I	Intensity
^{i}Pr	*iso*-propyl
K	Kelvin
LDA	lithium diisopropylamide
MeCN	Acetonitrile
Me	Methyl
Mes	Mesityl
Min	Minute
n.a.	Not applicable
n.o.	Not observed
NMR	Nuclear Magnetic Resonance
nr	No reaction
p-Tol	*p*-Tolyl
Ph	Phenyl
Pip	Piperidine
PXRD	Powder X-ray Diffraction Analysis
qNMR	Quantitative Nuclear Magnetic Resonance
RMSD	Root-mean Squared Deviation
rt	Room Temperature

SCE	Saturated Calomel Electrode
SPS	Solvent Purification System
T	Temperature
TBAP	Tetrabutylammonium perchlorate
T_e	onset temperature
^{t}Am	*tert*-amyl
^{t}Bu	*tert*-butyl
THF	Tetrahydrofuran
THF-d_8	Tetrahydrofuran-d_8
STipp	2,4,6-triisopropylbenzene thiolate
TMEDA	N,N,N′,N′-tetramethylethylenediamine
TMS	Trimethylsilyl
Tol	Toluene
T_p	Maximum temperature
STriph	2,4,6-triphenylbenzene thiolate
UV-Vis	Ultraviolet-visible
vs.	versus
XRD	X-ray diffraction analysis
Xy	Xylene
z	Charge
δ	Chemical shift
δ	Diffusion gradient length
Δ	Diffusion time
ε	Molar absorptivity
λ	Wavelength
μ	Bridging
υ	Scan rate
º	Degree
ºC	Degrees Celsius

List of Schemes

Scheme 2.1. Reaction of $FeCl_3$ and 2 equivalents of $LiNH^tBu$ in THF heated to 70 °C for 6 hours with observed reaction product distribution. 7
Scheme 2.2. Flow chart of work performed by Dr. Jeremiah Duncan in the synthesis of $[Fe_4(\mu_3\text{-}N^tBu)_4Cl_4]$ (**1**), $[Ph_4P][Fe_4(\mu_3\text{-}N^tBu)_4Cl_4]$ ($[Ph_4P]$**2**) and $Fe_4(\mu_3\text{-}N^tBu)_4Cl_3(N^tBu)$ (**3**). 9
Scheme 2.3. Proposed reactivity of $[Fe_4(N^tBu)_3SCl_4]^{1-}$ with thiolate ligands. 11
Scheme 2.4. Improved reaction conditions to produce [Li]**2**. 14
Scheme 2.5. Redox transformation of the $[Fe_4(\mu_3\text{-}N^tBu)_4Cl_4]^z$ series. 21
Scheme 2.6. Synthesis of **4** 37
Scheme 3.1. Common reactions in the formation of alkali metal organoamide compounds . 48
Scheme 3.2. General example of ring-laddering 49
Scheme 3.3. Literature synthesis of $(LiNH^tBu)_8$ (**8**) 52
Scheme 3.4. Synthesis of $(LiNH^tBu)_\infty$ (**9**) 53
Scheme 4.1. Original synthesis of $Fe(N(SiMe_3)_2)_2$ (**11**) 83
Scheme 4.2. Selected examples of 11 used in double protolytic substitution reactions. 84
Scheme 4.3. Selected example of 11 reacting in a single protolytic substitution reaction 85
Scheme 4.4. Synthesis of $Fe_2(\mu\text{-}NH^tBu)_2[N(SiMe_3)_2]_2$ (**14-^{t}Bu**) 86
Scheme 4.5. Synthesis of $[Fe_4(N^tBu)S_3Cl_4]^{2-}$ 87
Scheme 4.6. Ideal stoichiometries to form complexes observed 90
Scheme 4.7. Reactivity of **12-pip** 137
Scheme 4.8. Reaction of **13-pip** and **15-pip** 138
Scheme 4.9. Reactivity of **13** with the same amine 142
Scheme 4.10. Reactivity of **13** with various amines 143
Scheme 4.11. Intercluster reactivity of **13** 145
Scheme 4.12. Selected **13** and **14** complexes in THF-d_8 146
Scheme 4.13. Oxidative addition reactions with sulfur 147
Scheme 5.1. Synthesis of $[Fe_4(N^tBu)S_3Cl_4]^{2-}$ (**19**) 163
Scheme 5.2. Counterion metathesis reaction 165
Scheme 5.3. Ligand exchange reaction of **19** with arylthiolate 166
Scheme 5.4. Oxidation of $[Et_4N]_2$**20-Mes** with $Fc(PF_6)$ 177
Scheme 5.5. Synthetic methods to synthesize $[Fe_4S_4(SPh)_4]^{3-}$ 180
Scheme 5.6. Previous reduction and oxidation work by Tan 181
Scheme 5.7. Reduction of $[Et_4N]_2$**20-Ph** in CD_3CN with 1 equivalent of Cp^*_2Co and subsequent oxidation with $Fc(PF_6)$ 182
Scheme 5.8. (A) Reduction of **$[Et_4N]_2$20-Ph** in CD_3CN with 1 equivalent of Cp^*_2Co. (B) Oxidation of reduced solution with 1 equivalent of $Fc(PF_6)$. 184
Scheme 5.9. Reduction of $[Et_4N]_2$**23-Ph** in CD_3CN with 1 equivalent of Cp^*_2Co and subsequent oxidation with $Fc(PF_6)$ 187
Scheme 5.10. (A) Reduction of $[Et_4N]_2$**23-Ph** in CD_3CN with 1 equivalent of Cp^*_2Co in C_6D_6. (B) Oxidation of (A) with 1 equivalent of $Fc(PF_6)$ in CD_3CN 188
Scheme 6.1. Proposed reactivity of $[Et_4N]_2$**19** with NaSDmp 217

List of Equations

Equation 2.1 8
Equation 2.2 38
Equation 2.3 38
Equation 2.4 38
Equation 2.5 38
Equation 2.6 38
Equation 3.1. 69
Equation 3.2. 69
Equation 3.3. 69
Equation 3.4. 71
Equation 3.5. 71
Equation 4.1. 83
Equation 4.2. 87
Equation 5.1 156
Equation 5.2. 163

List of Compounds

Compound Number	Formula
1	$Fe_4(\mu_3\text{-}N^tBu_4)Cl_4$
[Li]**2**	$Li[Fe_4(\mu_3\text{-}N^tBu)_4Cl_4]$
$[Ph_4P]$**2**	$[Ph_4P][Fe_4(\mu_3\text{-}N^tBu)_4Cl_4]$
3	$Fe_4(\mu_3\text{-}N^tBu)_4Cl_3(N^tBu)$
4	$FeCl_2(NH_2{}^tBu)_2$
5	$FeCl_3((THF)_2)_2$
$[Ph_4P]_2$**6**	$[Ph_4P]_2[Fe_4(\mu_3\text{-}N^tBu)_4Cl_4]$
$[Ph_4P][Cp^*_2Co]$**6**	$(Ph_4P)(Cp^*_2Co)[Fe_4(\mu_3\text{-}N^tBu)_4Cl_4]$
7	$[Fe_4(\mu_3\text{-}N^tBu)_4Cl_3(THF)_2]^z$
8	$(LiNH^tBu)_8\cdot C_6H_{12}$
9	$(LiNH^tBu)_\infty$
10	$(LiNH^tBu)_8$
11	$Fe[N(SiMe_3)_2]_2$
12-DIPA	$Fe(NH(^iPr)_2)[N(SiMe_3)_2]_2$
12-pip	$Fe(NH(CH_2)_5)[N(SiMe_3)_2]_2$
13-^{t}Bu	$Fe_2(\mu\text{-}NH^tBu)(\mu\text{-}N(SiMe_3)_2)[N(SiMe_3)_2]_2$
13-^{t}Am	$Fe_2(\mu\text{-}NH^tAm)(\mu\text{-}N(SiMe_3)_2)[N(SiMe_3)_2]_2$
13-pip	$Fe_2(\mu\text{-}N(CH_2)_5)(\mu\text{-}N(SiMe_3)_2)[N(SiMe_3)_2]_2$
13-Bn	$Fe_2(\mu\text{-}NHBn)(\mu\text{-}N(SiMe_3)_2)[N(SiMe_3)_2]_2$
13-Ph	$Fe_2(\mu\text{-}NHPh)(\mu\text{-}N(SiMe_3)_2)[N(SiMe_3)_2]_2$
13-*p*-Tol	$Fe(\mu\text{-}NH(4\text{-}C_6H_4(Me))(\mu\text{-}N(SiMe_3)_2)[\ [N(SiMe_3)_2]_2$
13-*o*-Tol	$Fe(\mu\text{-}NH(2,6\text{-}C_6H_4(Me))(\mu\text{-}N(SiMe_3)_2)[\ [N(SiMe_3)_2]_2$
13-Mes	$Fe_2(\mu\text{-}NHMes)(\mu\text{-}N(SiMe_3)_2)[N(SiMe_3)_2]_2$
13-DIPAni	$Fe_2(\mu\text{-}NH(2,6\text{-}C_6H_3{}^iPr_2)(\mu\text{-}N(SiMe_3)_2)[N(SiMe_3)_2]_2$
13-NMePh	$Fe_2(\mu\text{-}N(Me)Ph)(\mu\text{-}N(SiMe_3)_2)[N(SiMe_3)_2]_2$
14-^{t}Bu	$Fe_2(\mu\text{-}NH^tBu)_2[N(SiMe_3)_2]_2$
14-^{t}Am	$Fe_2(\mu\text{-}NH^tAm)_2[N(SiMe_3)_2]_2$
14-pip	$Fe_2(\mu\text{-}N(CH_2)_5)_2[N(SiMe_3)_2]_2$
15-^{t}Bu	$Fe_3(\mu\text{-}NH^tBu)_4[N(SiMe_3)_2]_2$
15-pip	$Fe_3(\mu\text{-}N(CH_2)_5)_4[N(SiMe_3)_2]_2$
15-Mes	$Fe_3(\mu\text{-}NHMes)_4[N(SiMe_3)_2]_2$
15-NMePh	$Fe_3(\mu\text{-}N(Me)Ph)_4N(SiMe_3)_2]_2$
15-NMeBn	$Fe_3(\mu\text{-}N(Me)Bn)_4N(SiMe_3)_2]_2$
16-DIPAni	$Fe_3(\mu\text{-}NH(2,6\text{-}C_6H_3{}^iPr_2)_4[NH(2,6\text{-}C_6H_3{}^iPr_2)]_2$
17	$Fe_2(\mu\text{-}NH^tBu)_2S[N(SiMe_3)_2]_2$
$[Et_4N]_2$**18**	$[Et_4N]_2[Fe_4S_4Cl_4]$
$[Ph_4P]_2$**18**	$[Ph_4P]_2[Fe_4S_4Cl_4]$
$[Et_4N]_2$**19**	$[Et_4N]_2[Fe_4(N^tBu)S_3Cl_4]$
$[Ph_4P]_2$**19**	$[Ph_4P]_2[Fe_4(N^tBu)S_3Cl_4]$
$[Ph_4P]_2$**20-Ph**	$[Ph_4P]_2[Fe_4(N^tBu)S_3(SPh)_4]$

$[Et_4N]_2$**20-Ph**	$[Et_4N]_2[Fe_4(N^tBu)S_3(SPh)_4]$
$[Et_4N]_2$**20-Mes**	$[Et_4N]_2[Fe_4(N^tBu)S_3(SMes)_4]$
$[Et_4N]$**21-Mes**	$[Et_4N]Fe_4(N^tBu)S_3(SMes)_4]$
$[Et_4N]_2[Cp^*_2Co]$**22-Ph**	$[Et_4N]_2[Cp^*_2Co][Fe_4(N^tBu)S_3(SPh)_4]$
$[Et_4N]_2$**23-Ph**	$[Et_4N]_2[Fe_4S_4(SPh)_4]$
$[Et_4N]_3$**24-Ph**	$[Et_4N]_3[Fe_4S_4(SPh)_4]$
$[Et_4N]_2$**23-Bn**	$[Et_4N]_2[Fe_4S_4(SBn)_4]$
$[Et_4N]_3$**23-Ph**	$[Et_4N]_3[Fe_4S_4(SBn)_4]$
$[Et_4N]_2$**20-DCBT**	$[Et_4N]_2[Fe_4(N^tBu)S_3(S(2,6\text{-}C_6H_3Cl_2))_4]$
$[Ph_4P]_2$**23-DCBT**	$[Ph_4P]_2[Fe_4S_4(S(2,6\text{-}C_6H_3Cl_2)_4]$
$[Et_4N]_2$**20-CBT**	$[Et_4N]_2[Fe_4(N^tBu)S_3(S(4\text{-}C_6H_4Cl))_4]$
$[Et_4N]_2$**20-*p*Tol**	$[Et_4N]_2[Fe_4(N^tBu)S_3(S(4\text{-}C_6H_4Me))_4]$
$[Et_4N]_3$**22-*p*Tol**	$[Et_4N]_3[Fe_4(N^tBu)S_3(S(4\text{-}C_6H_4Me))_4]$
$[Et_4N]_2$**20-Triph**	$(Et_4N)_2[Fe_4(N^tBu)S_3(STriph)_4]$
$[Et_4N]$**21-Triph**	$(Et_4N)[Fe_4(N^tBu)S_3(STriph)_4]$
0:1	$(Et_4N)_2[Fe_4(N^tBu)S_3(SDmp)Cl_3]$
1:1	$(Et_4N)_2[Fe_4(N^tBu)S_3(SDmp)_2Cl_2]$
2:1	$(Et_4N)_2[Fe_4(N^tBu)S_3(SDmp)_3Cl_1]$
3:1	$(Et_4N)_2[Fe_4(N^tBu)S_3(SDmp)_4]$

Chapter 1: Introduction

1.1 Iron-Sulfur Clusters in Biochemistry

Iron sulfur (Fe-S) clusters constitute an essential class of cofactors in biological systems.[1–3] These complexes are ubiquitous in nature, serving as electron transport mediators and active sites for various biochemical transformations. Notable examples include rubredoxin[4,5], ferredoxin[6,7], aconitase[8,9] and nitrogenase[10–13] where Fe–S clusters function as necessary cofactors. Figure 1.1 illustrates examples of mono–, di–, tri–, and tetranuclear Fe–S clusters found in biological systems. These clusters feature tetrahedral, high-spin iron centres coordinated by bridging sulfide ligands and terminal ligands typically consisting of cysteine thiolates. These complexes generally exhibit high-spin Fe(II)/Fe(III) formal oxidation states, although other iron redox states have also been observed.

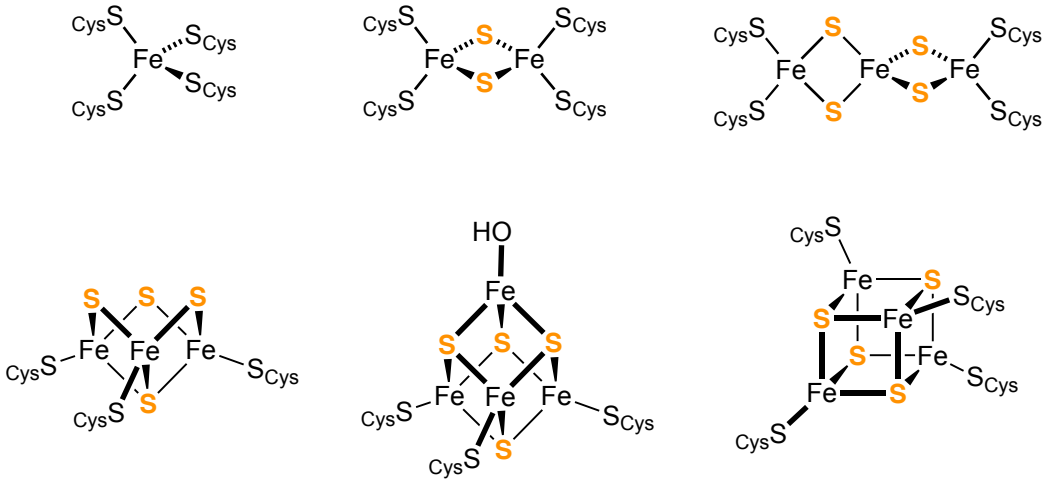

Figure 1.1. Iron-sulfur complexes found in rubredoxin, ferredoxins and aconitase.

The first synthetic iron-sulfur cluster was reported by Holm and coworkers in 1972, in which the compound $(Et_4N)_2[Fe_4S_4(SCH_2Ph)_4]$ was prepared.[14] Although the terminal ligands in this synthetic model are not cysteine thiolates, the charge equivalence between the benzyl thiolate and cysteine thiolate enabled this complex to serve as a model for studying the properties of biological tetranuclear Fe–S clusters. This work has been crucial in

advancing the study of other Fe-S containing clusters, as well as in the synthesis of their redox derivatives. The clusters shown in Figure 1.1 have been successfully prepared synthetically with SAr/SR groups.[14–20] Research in this field has spanned over 50 years, with significant efforts dedicated not only to the synthesis of these clusters but also to the characterization of their properties using a wide array of physical techniques.

More complex iron-sulfur clusters found in biological systems are present in the cofactors of the nitrogenase enzymes. These enzymes are responsible for biological nitrogen fixation, the conversion of atmospheric dinitrogen into biologically accessible ammonia. The process of biological nitrogen fixation is discussed in more detail in Chapter 5. There are three known types of nitrogenase enzymes: Mo-nitrogenase, V-nitrogenase, and Fe-only nitrogenase. The Mo- and V-nitrogenases have been characterized crystallographically and the structures of these cofactors are shown in Figure 1.2. The three cofactors found in the nitrogenase enzymes are the F-cluster, P-cluster and M-cluster. The P- and M-cluster in nitrogenase are more intricate than those found in aconitase and ferredoxins, as these cluster can be viewed as two vertex fused cubanes. In all examples, the iron centers adopt a tetrahedral geometry and high-spin electronic configuration, with sulfides or cysteine thiolates as the primary ligands. The active site for biological nitrogen fixation is believed to be on the M-cluster (FeMo-co for the Mo-nitrogenase and FeV-co for the V-nitrogenase).

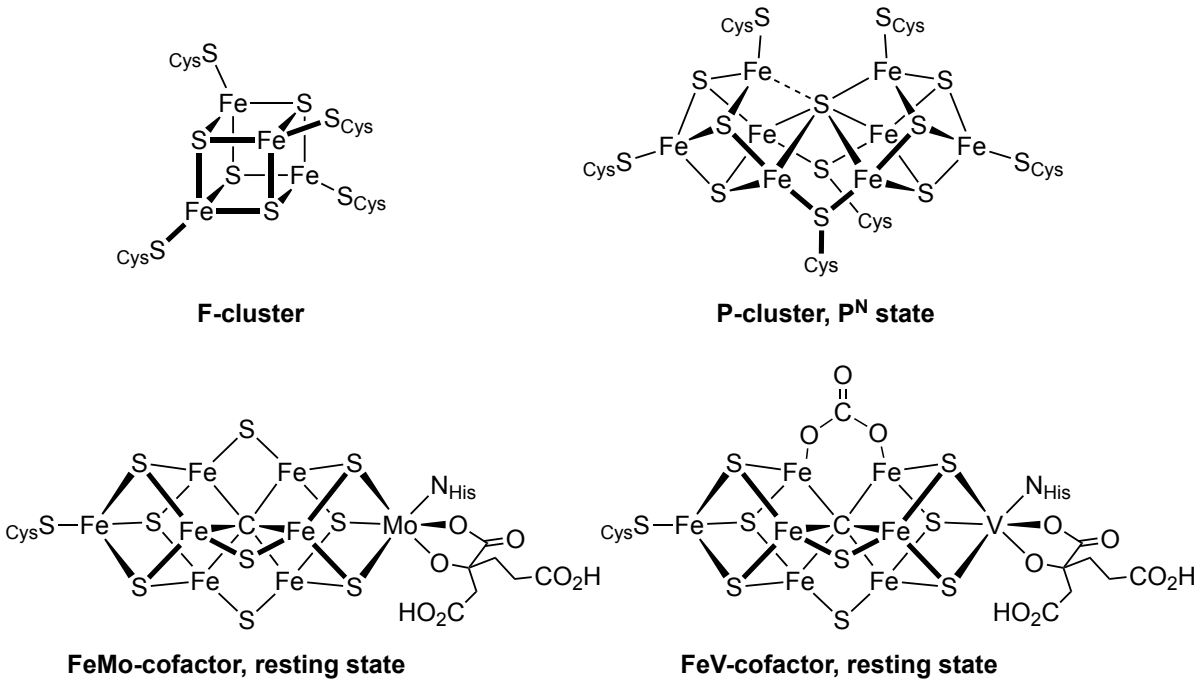

Figure 1.2. Metallocofactors found in the Mo– and V– nitrogenase enzymes.

Model compounds resembling the double-fused cubane structure of the P-cluster have been synthesized; however, work is still ongoing to develop models of the M-cluster.[21] ne challenge in synthesizing models that accurately replicate the M-cluster is the incorporation of the central carbide. It is believed that biological systems achieve this process using the radical S-adenosylmethionine (SAM) enzyme family, which facilitates the insertion of a carbide into the biosynthetic assembly of FeMo-co. To better understand the role of the carbide, Fe-S models that contain a light 2p element should be investigated.

1.2 Nitrogen Ligated Clusters

The investigation of iron-sulfur clusters ligated with nitrogen-based anions is motivated by the carbide ligand in nitrogenase and dinitrogen serving as a substrate for these enzymes. Research in the Lee group has led to the synthesis and characterization of a diverse array of [high-spin, Fe(II)/Fe(III)] iron-amide and iron-imide complexes, exhibiting varying nuclearity and structural motifs.[22–27] These structural motifs include mononuclear species, four-membered dinuclear rings, linear trinuclear complexes, and tetranuclear assemblies, as

shown in Figure 1.3. The formation of Fe–N bonds with different protonation states of nitrogen provides valuable benchmarks for elucidating aspects of biological nitrogen fixation. It can be postulated that the donation ability of imides to smaller iron fragments resemble the donation ability of the bridging carbide to the M-cluster of nitrogenase.

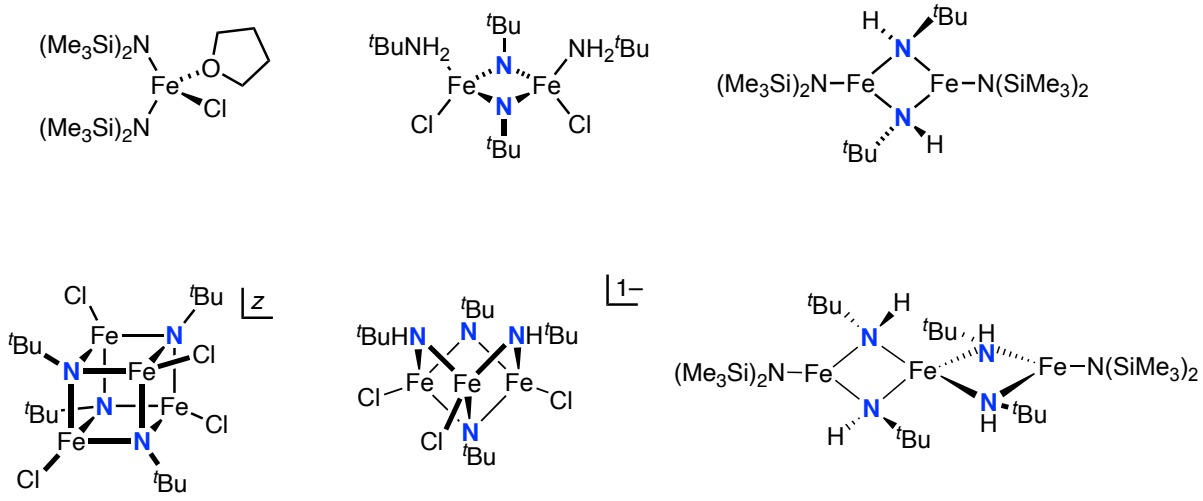

Figure 1.3. Iron-imide/amide complexes synthesized within the Lee group.[22–27]

1.3 Mixed Imide/Amide-Sulfide

The incorporation of both sulfides and nitrogen anions in high-spin iron complexes has been achieved by the Lee group, as shown by examples in Figure 1.4.[26,28] The imide ligand $(N^tBu)^{2-}$, is isoelectronic with sulfide $(S)^{2-}$ but differs in its donor properties as $(N^tBu)^{2-}$ is a stronger donor due to its greater basicity compared to $(S)^{2-}$. The synthesis of the dinuclear heteroleptic species has facilitated the formation of tetranuclear complexes, which adopt a cubane-like structural motif analogous to the tetranuclear Fe–S clusters (e.g. F-cluster). The incorporation of each $(N^tBu)^{2-}$ ligand modulates the physical properties of the clusters, enabling the investigation of the impact of the imide ligation and the hopes to uncover more information about biological nitrogen fixation.

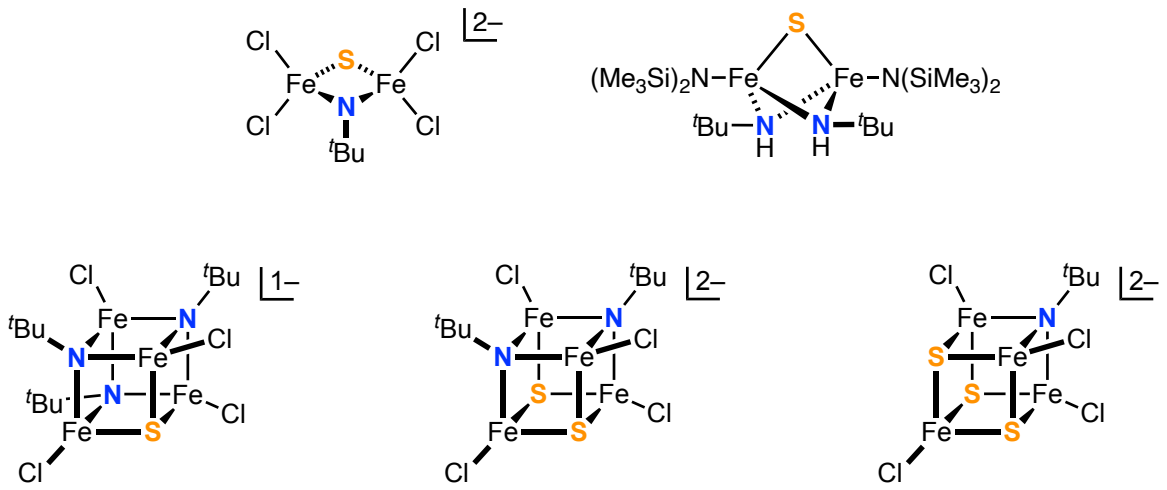

Figure 1.4. Mixed iron-imide/amide-sulfide complexes.[26,28]

1.4 Scope of Thesis

The work detailed in this thesis expands on the field of high-spin iron complexes, with a particular focus on the synthesis, characterization and reactivity of iron-amide, iron-imide and iron-imide-sulfide clusters. Each chapter presents distinct research objectives, with Chapters 2, 3 and 4 serving as stand-alone studies. Chapter 2 describes the synthesis and characterization of iron-alkylimide cubane-like clusters, providing a more in-depth investigation of tetranuclear clusters. This study establishes benchmarks for comparison with mixed iron-imide-sulfide and iron-sulfide analogues. Chapter 3 explores the discovery of a second form of lithium *tert*-butylamide, a reagent utilized in Chapter 2, which exhibits distinct properties that may impact its use in synthetic applications. Chapter 4 examines the protolytic ligand substitution reaction of a common iron(II) synthon with less acidic protio-ligands, leveraging previous work in the Lee group to investigate the scope of such ligand exchanges. Chapters 5 and 6 focus on the synthesis of reduced iron-imide-sulfide clusters, which serve as synthetic analogues of the nitrogenase active site. This study highlights the instability of reduced $[Fe_4(N^tBu)S_3]^{3-}$ cubane-core clusters, possibly providing insight into the role of the bridging carbide in nitrogenase function. Collectively, the research presented in this thesis contributes to a deeper understanding of iron-cluster chemistry and nitrogen anion ligation.

Chapter 2: Improved Synthesis and Characterization of Iron-Alkylimide Clusters

2.1 Introduction

Iron-imide cubane clusters, characterized by an $Fe_4(NR)_4$ core, represent a limited subset of iron cubane clusters (Fe_4Q_4), with only a few examples reported in the literature.[22–24,29–34] This small subset of iron-imide cubane clusters contrasts with the extensively studied iron-sulfur cubane clusters, for which dozens of compounds with the Fe_4S_4 core have been reported.[35–38] This difference can be attributed to the ubiquity of Fe_4S_4 clusters in biological chemistry. Although Fe_4N_4 clusters are not found in biological systems, the potential remains to utilize these clusters in physical and chemical applications. $Fe_4(NR)_4$ clusters exhibit charge similarities to the Fe_4S_4 clusters, as the core bridging ligands $(N\text{-}R)^{2-}$ are isoelectronic with bridging S^{2-}. However, the limited study of $Fe_4(NR)_4$ clusters leaves the chemical and physical property differences between these cluster types poorly understood.

The general structural motif of $Fe_4(NR)_4$ clusters consist of four tetrahedral iron atoms coordinated to four μ_3-imide ligands in the cluster core, with four terminal ligands bound to the iron atoms. Iron-imide clusters can be divided into two categories: (1) iron-alkylimide and (2) iron-arylimide clusters. The iron-alkylimide category includes four clusters, while the iron–arylimide category includes three clusters, as depicted in Figure 2.1. The primary difference between these two categories lies in the donating ability of the bridging imide ligand. Alkylimide ligands are more basic than arylimide ligands, making them stronger donors and leading to different chemical properties. The clusters that are the focus of this chapter are the alkylimide ligated $[Fe_4(\mu_3\text{-}N^tBu)_4Cl_4]^z$ series.[1]

---

[*] The work presented in this chapter is built from work performed by Dr. Jeremiah Duncan[25] and Matthew Traub[56]. Dr. Paul Dube (McMaster), Dr. Ben Brennessel (Rochester), Dr. Harald Kelm (Kaiserslautern) and Prof. Dr. Hans Jörg Krüger (Kaiserslautern) are all acknowledged for collecting magnetic susceptibility (McMaster), elemental analysis (Rochester), EPR (Kaiserslautern) and Mössbauer (Kaiserslautern) measurements.

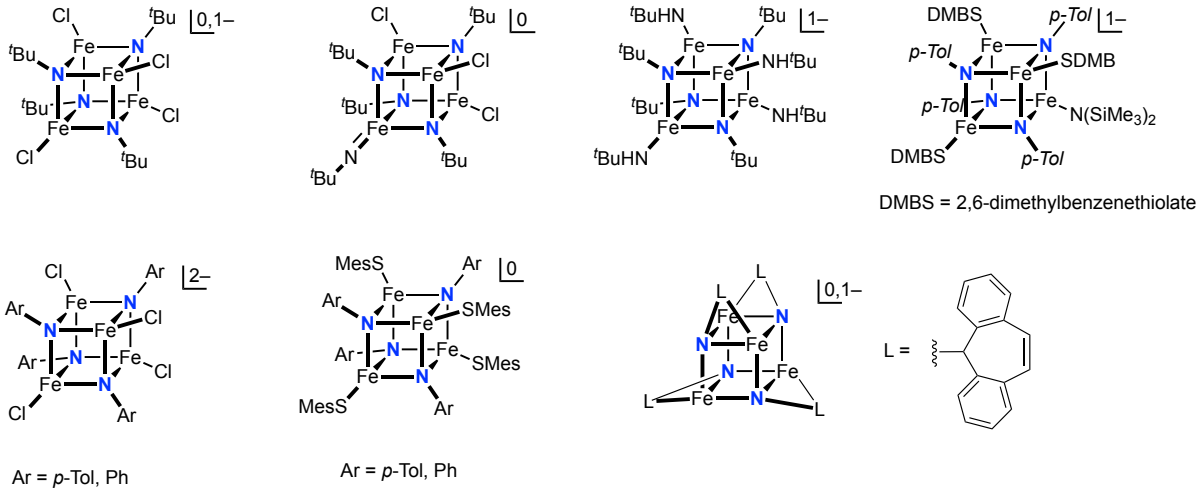

Figure 2.1. Reported molecular structures of iron-imide cubane clusters: variations in core and terminal ligation. [22–24,29–34]

The synthesis of $Fe_4(\mu_3\text{-}N^tBu)_4Cl_4$ (**1**) was previously reported by our laboratory and the laboratory of Fenske under different reaction conditions. In the earlier communication by the Lee group, the synthesis of iron-imide clusters was achieved via the reaction of $FeCl_3$ and 2 equivalents of $LiNH^tBu$ in THF at 70 °C for 6 hours, as shown in Scheme 2.1. The reaction workup involved evaporation under vacuum, extraction with pentane, and fractional crystallization to isolate **1** with a yield of ~1%. Other iron-containing compounds, $[Fe_4(\mu_3\text{-}N^tBu)_4Cl_4]^-$ (**2**) and $Fe_4(\mu_3\text{-}N^tBu)_4Cl_3(N^tBu)$ (**3**), were obtained in low isolated yields of 1–2% and were characterized to a limited extent. Compounds **1** and **2** have the same atom composition and connectivity but differ in iron oxidation states. Compound **3** has the same $Fe_4(N^tBu)_4$ core composition as **1** and **2** but contains a terminal *tert*-butylimide ligand.

Scheme 2.1. Reaction of $FeCl_3$ and 2 equivalents of $LiNH^tBu$ in THF heated to 70 °C for 6 hours with observed reaction product distribution.

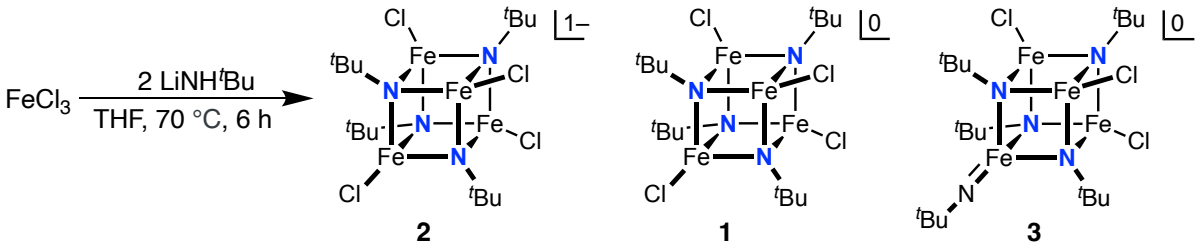

A balanced chemical equation can be written for the reaction of $FeCl_3$ with 2 equivalents of LiNH^{t}Bu. The theoretical product of this reaction is $Fe_4(\mu_3\text{-N}^t\text{Bu})_4Cl_4$ (**1**), as illustrated in Equation 2.1 with 4 equivalents of ^{t}BuNH$_2$ and 8 equivalents of LiCl generated as coproducts. Experimentally however, the reaction of $FeCl_3$ and 2 equivalents of LiNH^{t}Bu does not lead to **1** being the sole iron-containing species; instead, multiple iron containing species are formed.

Equation 2.1

$$4\ FeCl_3 + 8\ LiNH^tBu \longrightarrow Fe_4(N^tBu)_4Cl_4 + 4\ ^tBuNH_2 + 8\ LiCl$$

Almost simultaneously, Fenske and coworkers synthesized **1** and **2** using a different protocol. Specifically, **2** was prepared in a 26% yield via the reaction of $FeCl_3$ and 1.22 equivalents of LiNH^{t}Bu at –80 °C in toluene. Compound **1** was synthesized in a 29% yield from a reaction of $FeCl_2$ and 1.5 equiv of LiNH^{t}Bu at –78 °C in THF in the presence of PEt_3. Details of the reaction conditions, choice of stoichiometry and reagents were not discussed.

A previous member of the Lee group, Dr. Jeremiah Duncan, further investigated the synthesis of iron-alkylimide cubane clusters.[25] Duncan's work followed similar initial reaction conditions to the Lee group communication with the reaction time, temperature and extraction protocols modified as summarized in Scheme 2.2. Duncan utilized a benzene extraction and pentane wash to separate non-polar and neutral species from the polar and charged species. Compound [Li]**2** which resided in the benzene insoluble fraction, was oxidized to **1** in MeCN and recrystallized in pentane/HMDSO to yield **1** in an isolated yield of 24.3%. The work performed by Duncan led to the reliable isolation of **1** but not the direct isolation of the main product, [Li]**2**. The work presented in this chapter has led to the direct isolation of **2** from the crude reaction mixture, a more thorough analysis of optimized reaction conditions, and further characterization of the $[Fe_4(\mu_3\text{-N}^t\text{Bu})_4Cl_4]^z$ compound class.

Scheme 2.2. Flow chart of work performed by Dr. Jeremiah Duncan in the synthesis of $[Fe_4(\mu_3\text{-}N^tBu)_4Cl_4]$ (**1**), $[Ph_4P][Fe_4(\mu_3\text{-}N^tBu)_4Cl_4]$ ($[Ph_4P]$**2**) and $Fe_4(\mu_3\text{-}N^tBu)_4Cl_3(N^tBu)$ (**3**)

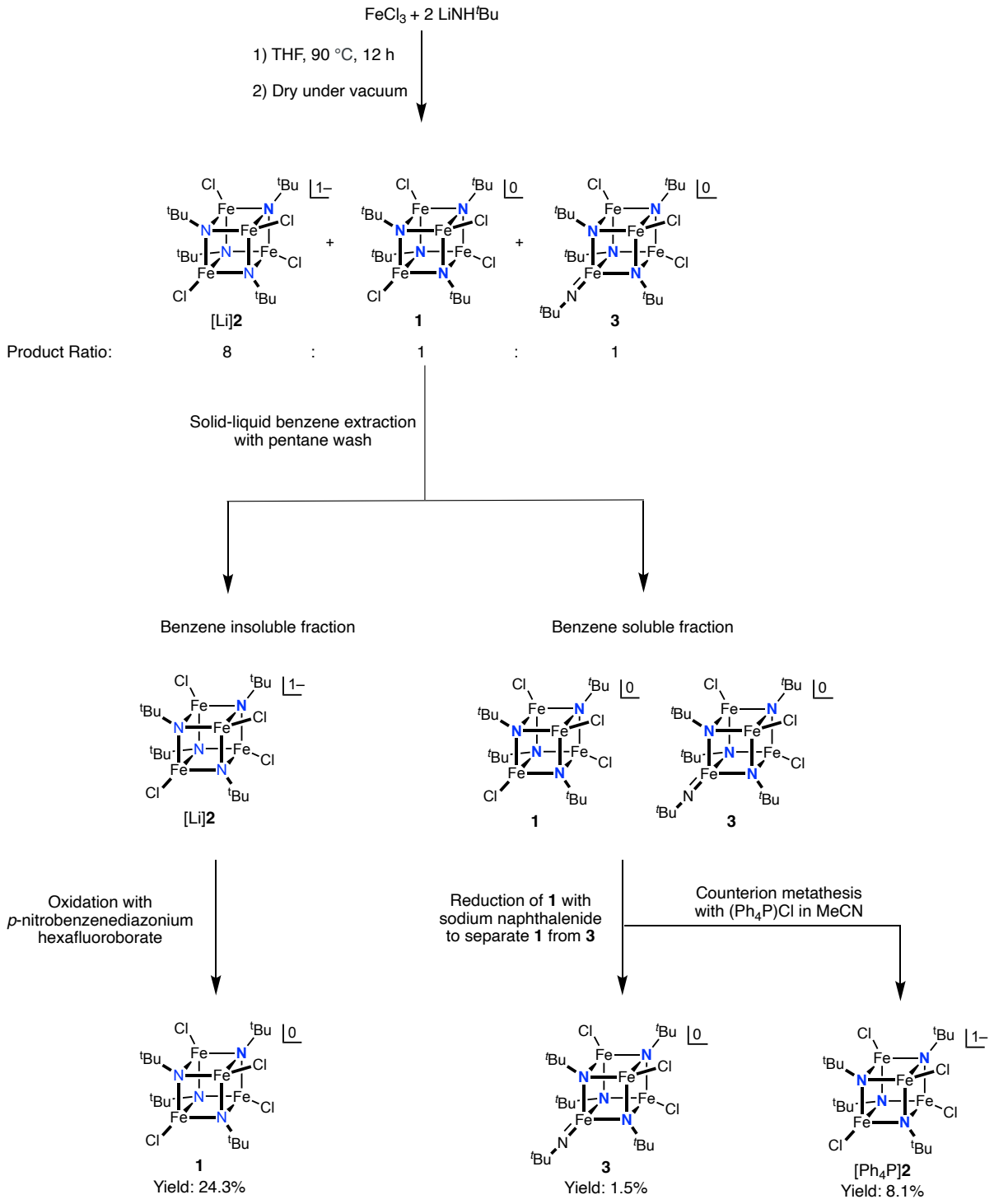

The primary purpose of the current re-examination of this class of compounds is to enable their use as a basis for comparison with related systems. Work conducted in the Lee group resulted in the synthesis and characterization of imide and imide-sulfide cubane-like clusters with the general formula $[Fe_4(N^tBu)_nS_{4-n}Cl_4]^z$ (n = 1-4) as shown in Figure 2.2.[26] The synthesis of the terminal members of the series (n = 0), $[Fe_4S_4Cl_4]^{2-}$, was first reported by Holm and coworkers with the $[Fe_4S_4]^z$ cluster core being extensively studied and analyzed. Heteroleptic cluster cores (n = 1 – 3) were reported in 2011 and utilized controlled, synthetic methods to produce these mixed imide-sulfide cubane clusters.

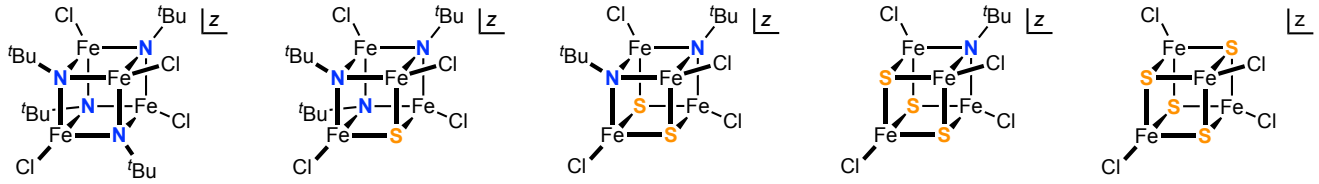

Figure 2.2. Molecular structures of the iron-imide-sulfide series ($[Fe_4(N^tBu)_nS_{4-n}Cl_4]^z$ (n = 0-4)).[26]

Further study of the terminal member of the series $[Fe_4(N^tBu)_nS_{4-n}Cl_4]^z$ (n = 4) is useful in understanding the effect of increasing the number of μ_3-imides in the cluster core. This research becomes potentially valuable in the study of $[Fe_4(N^tBu)_3SCl_4]^z$, which adopts C_{3V} symmetry and contains two distinct iron sites. The first site consists of three iron atoms proximal to the μ_3-sulfide, while the second unique site is the unique iron atom distal to the μ_3-sulfide. This distal iron atom is coordinated by three μ_3-N^tBu ligands, creating a steric environment similar to that of all iron atoms in $[Fe_4(\mu_3\text{-}N^tBu)_4Cl_4]^z$. Ligand substitution studies on $[Fe_4(\mu_3\text{-}N^tBu)_4Cl_4]^z$ provide a valuable preliminary framework for understanding the reactivity of $[Fe_4(N^tBu)_3SCl_4]^z$, as the latter requires more complex and lengthy synthetic procedures to obtain usable material. Research in the group has focused on leveraging the unique iron site in $[Fe_4(N^tBu)_3SCl_4]^z$ for novel chemical transformations. Achieving this requires passivating the three equivalent iron atoms with ligands of sufficient steric bulk to prevent coordination to the unique iron site as shown in Scheme 2.3. Reactivity studies on $[Fe_4(\mu_3\text{-}N^tBu)_4Cl_4]^z$ serve as a foundation for this work, as the extent of ligand substitution and the substitution rates can provide insight into the potential effects on $[Fe_4(N^tBu)_3SCl_4]^z$.

Consequently, the development of reliable synthetic methods for $[Fe_4(\mu_3\text{-}N^tBu)_4Cl_4]^z$ is crucial to facilitate these investigations.

Scheme 2.3. Proposed reactivity of $[Fe_4(N^tBu)_3SCl_4]^{1-}$ with thiolate ligands.

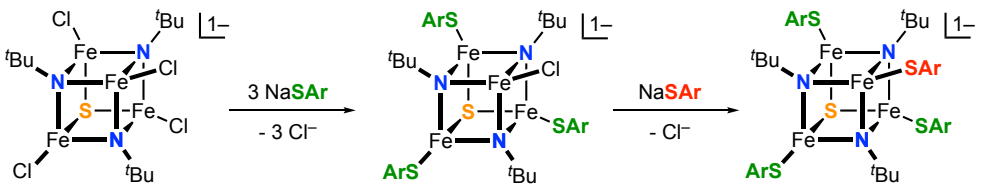

The work detailed in this chapter describes a more in-depth study into the reaction of $FeCl_3$ and $LiNH^tBu$ with reaction solvent, stoichiometry, reaction temperature and purification protocols altered to optimize the yield of **2**. The properties of **2** and redox derivatives were collected and analyzed to provide benchmarks for the other members of the $[Fe_4(N^tBu)_nS_{4-n}Cl_4]^z$ series.

2.2 Results and Discussion

2.2.1 Reactivity of Ferric Chloride with Lithium *tert*-Butylamide

2.2.1.1 Effect of Reaction Solvent

The reaction of $FeCl_3$ with two equivalents of $LiNH^tBu$, performed in THF at room temperature over 16 hours, led to $[Fe_4(\mu_3\text{-}N^tBu)_4Cl_4]^{1-}$ ([Li]**2**), $FeCl_2(NH_2{}^tBu)_2$ (**4**) and four unknown, less predominant, broad signals when analyzed in CD_3CN using ^1H NMR spectroscopy as shown in Figure 2.4 (F). The *in-situ* yield of [Li]**2** was determined to be 10% based on $FeCl_3$. The other signals in the ^1H NMR spectrum appear at 10.37, 8.43, 7.90, 7.62, 7.35 and 5.31 ppm. The signals at 10.37 and 8.43 ppm correspond to roughly 7.5% of the peak area of [Li]**2**, and the signal at 5.31 ppm is roughly half the peak area of [Li]**2**. The three peaks overlapping in the 7.89-7.35 ppm region had a combined peak area of around 1.37 times of [Li]**2**. These broad signals are likely dinuclear iron-imide complexes based on chemical shift positions and peak broadness when compared to known Fe(III) di-imide dinuclear complexes.[23] One of the signals in the 7 ppm region is likely $[Fe_2(\mu\text{-}N^tBu)_2Cl_4]^{2-}$

based on ^{1}H NMR chemical shift of pure $[Fe_2(\mu\text{-}N^tBu)_2Cl_4]^{2-}$. The structure of $[Fe_2(\mu\text{-}N^tBu)_2Cl_4]^{2-}$ shown in Figure 2.3.

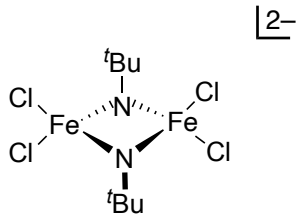

Figure 2.3. Structure of dianion $[Fe_2(\mu\text{-}N^tBu)_2Cl_4]^{2-}$.

$Fe_4(\mu_3\text{-}N^tBu)_4Cl_3(N^tBu)$ (**3**) was not present in the crude reaction mixture when performed in THF at room temperature for 18 hours. The addition of a room temperature solution of $LiNH^tBu$ in THF to a suspension of $FeCl_3$ in THF at –78 °C led to a similar result as if the reaction had been performed at room temperature. These observations suggest that heat plays a crucial role in the formation of **3**.

When the reaction of $FeCl_3$ and 2 equivalents of $LiNH^tBu$ was performed in diethyl ether (Et_2O), large amounts of insoluble material were produced that led to a diethyl ether soluble and insoluble fraction, with the two fractions being almost mass equivalent. The Et_2O soluble fraction display many paramagnetic signals (around twelve broad signals) when analyzed by ^{1}H NMR spectroscopy, with all signals having similar peak areas, as shown in Figure 2.4 (B), and no signals could be attributed to a predominant species, These signals appeared between -7 and 20 ppm with [Li]**2** being one of the signals present, based on the limiting chemical shift of [Li]**2**. The Et_2O insoluble fraction contained three ^{1}H NMR active products likely being $[Fe_2(\mu\text{-}N^tBu)_2Cl_4]^{2-}$, **4** and trace amounts of [Li]**2** as shown in Figure 2.4 (A). Stirring of the Et_2O insoluble fraction in THF or DME for 6 hours led to an increased amount of [Li]**2** and a decreased amount of $[Fe_2(\mu\text{-}N^tBu)_2Cl_4]^{2-}$, and **4**. Moreover, the spectrum of the THF/DME treated Et_2O insoluble fraction resembled the crude spectrum of the reaction performed in THF at room temperature (rt). This observation highlights the influence of solvent on complex formation. Notably, when the material is redissolved in THF or DME —more polar, ethereal solvents—and subsequently dried under vacuum and analyzed in CD_3CN, the resulting signal set and the ratio between signals match those

observed when the reaction of $FeCl_3$ and 2 equivalents of LiNH^{t}Bu is conducted at room temperature in THF (Figure 2.4 (F)).

The reaction performed in toluene, similarly to Et_2O, led to many signals with the predominant species being **4**, based on the large signal upfield relative to the smaller signals downfield. Extracting the toluene crude with benzene and rinsing with pentane led to a benzene/pentane soluble and insoluble fraction. The benzene extract contained predominantly **3** and **1**, while the benzene insoluble residue contained $[Fe_2(\mu\text{-N}^t\text{Bu})_2Cl_4]^{2-}$, **4** and [Li]**2**. Performing the reaction in toluene with heat (80 °C) did not lead to a different spectrum or a drastic change in product ratios compared to performing the reaction in toluene without heat.

2.2.1.2 Effect of Reaction Temperature

When the reaction of $FeCl_3$ with 2 equivalents of LiNH^{t}Bu was performed at 90 °C over 12 to 16 hours, the signals in the NMR spectrum in THF-d_8 or CD_3CN are consistent with [Li]**2**, **3**, and **4**, with the [Li]**2** to **3** ratio being 6:1. Heating the reaction to 90 °C for over 12 hours led to only three iron containing products when probed using ^{1}H NMR spectroscopy. The product distribution and yield based on iron content for these reaction conditions are highlighted in Scheme 2.4. Based on *q*NMR analysis, the amount of [Li]**2** and **1** produced was 44% and 6.5% respectively, based on total iron content. The crude reaction was characterized in both THF-d_8 and CD_3CN, as CD_3CN was chosen as the NMR solvent because relatively polar and charged species are soluble in CD_3CN while THF-d_8 was to ensure there were no solvent effects following the dissolution of the crude material in CD_3CN. The yield based on the starting iron content of [Li]**2** becomes 44%, which is four times higher in yield compared to the reaction performed at room temperature. This increase in *in-situ* yield and disappearance of the signals at 8.43, 7.90, 7.62, 7.35 and 5.31 ppm are consistent with the dinuclear species being intermediates to [Li]**2**.

Scheme 2.4. Improved reaction conditions to produce [Li]**2**

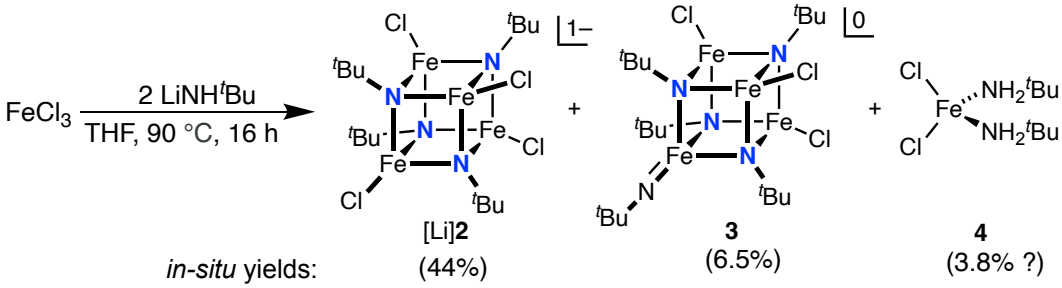

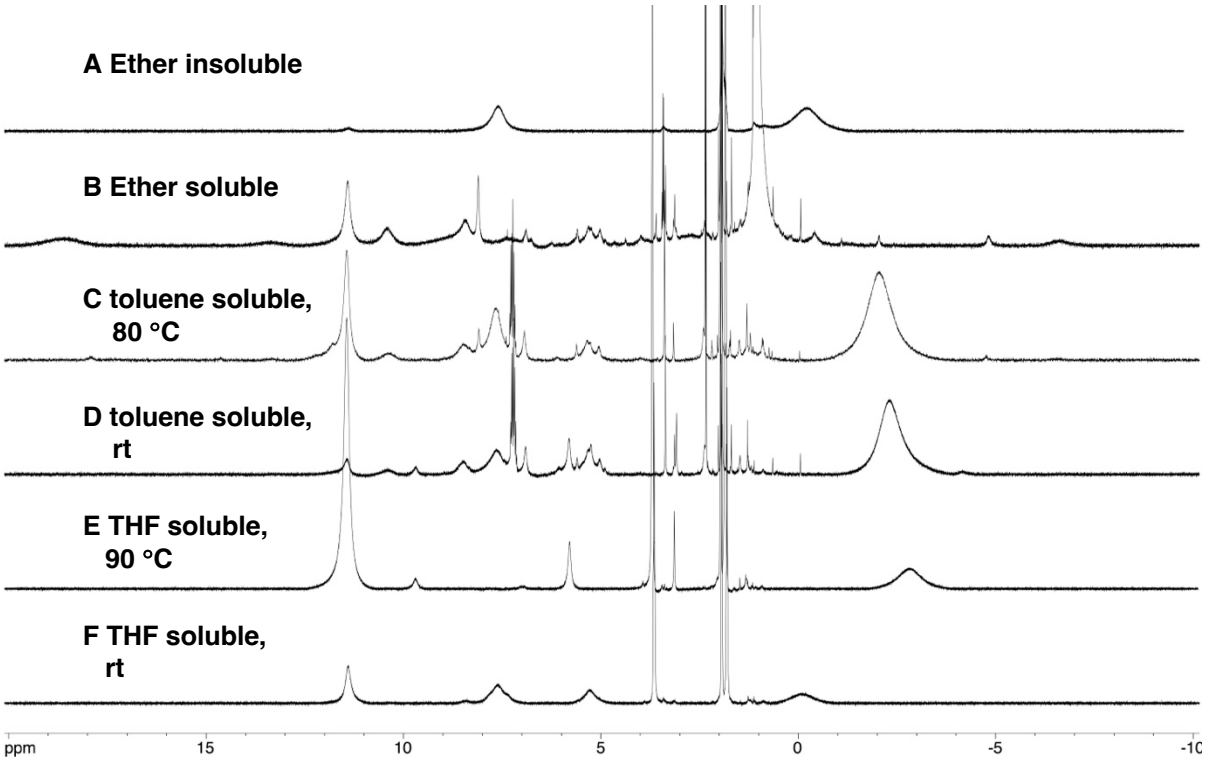

Figure 2.4. Crude ^{1}H NMR(300 MHz, 25 °C) spectra of $FeCl_3$ and 2 equivalents of LiNH^{t}Bu in CD_3CN under various conditions: (**A**) ether insoluble material **(B**) ether soluble material, (**C**) toluene soluble material generated at 80 °C, (**D**) toluene soluble material generated at rt, (**E**) THF soluble material generated at 90 °C and **(F**) THF soluble material generated at rt.

The addition of $FeCl_3$ to THF was exothermic and led to an amber suspension. It has been observed that if the rate of addition of solid $FeCl_3$ to THF is not controlled, it may lead to the ring opening and polymerization of THF.[39] It was unclear whether this dissolution step contributed to cluster decomposition or facilitated the production of [Li]**2**. To remove this variable, $FeCl_3(THF)_2$ (**5**) was synthesized from the dissolution of $FeCl_3$ in THF. The initial reaction produced an amber suspension, which was filtered to yield a transparent, light green solution. Light green crystals were present upon volume reduction and storage of the solution in the freezer for 2 hours at –20 °C. These crystals displayed the same unit cell as the published structure of **5**, providing structural evidence that **5** was synthesized.[40] Dissolving the crystals of **5** in C_6D_6 led to two ^{1}H NMR signals, consistent with a THF adduct. These crystals were stable in the solid state over months and in solution at room temperature for at least a day. Using $FeCl_3(THF)_2$ as the Fe(III) source while following the same protocol (concentration, reaction conditions) led to the same amount of [Li]**2** produced, meaning the initial dissolution step did not interfere with the reaction chemistry.

2.2.1.3 Stoichiometry Investigation

The preparation of [Li]**2** used 2 equivalents of LiNH^{t}Bu, as this represents the ideal stoichiometry in forming **1**. The work presented in this section displays the stoichiometry effect on the reaction of $FeCl_3$ and LiNH^{t}Bu. Altering the stoichiometry to 1, 1.5, 3 and 4 equivalents of LiNH^{t}Bu resulted in changes in the observed products and their distribution. The reaction observations described here pertain to the reaction of $FeCl_3$ with varying equivalents of LiNH^{t}Bu at similar concentrations and reaction times, with the reaction heated to 90 °C. After solvent removal *in vacuo*, these reactions were analyzed using ^{1}H NMR spectroscopy in CD_3CN or C_6D_6. The stoichiometry investigation validated that 2 equivalents of LiNH^{t}Bu was the ideal stoichiometry in producing [Li]**2** as lower equivalents led to less [Li]**2** produced and more equivalents led to more signals observed, likely being $^-$(NH^{t}Bu) ligated Fe_4N_4 clusters. The outcome of the stoichiometry investigation is described below.

When 1 equivalent of LiNH^{t}Bu was used and the reaction was heated for 19 hours, the solution became a deep, opaque green. After removing THF under vacuum, the resulting brown solid was redissolved in CD_3CN, producing an opaque brown solution and complete

dissolution of the crude material. The predominant signal in the ^{1}H NMR spectrum was consistent with **4** at –6.32 ppm, with additional signals observed at 7.19. 7.75, 10.44 and 11.42 ppm as shown in Figure 2.5 (G). The signal at 11.42 ppm is consistent with [Li]**2** with a total yield of 1% based on the amount of starting $FeCl_3$.

When 1.5 equivalents of LiNH^{t}Bu were used and the reaction was heated for 16 hours, the solution turned a deep, opaque brown color, like the color observed with 2 equivalents. After THF removal *in vacuo*, the resulting brown solid was redissolved in CD_3CN, producing an opaque brown solution with small amounts of white insoluble material. The predominant signals in the ^{1}H NMR spectrum corresponded to **4** and [Li]**2** with the total yield of [Li]**2** being 14%, as shown in Figure 2.5 (F). At 1.5 equivalents, the signal set at 7.75 and 10.44 is still present, representing approximately 20% of the peak area of [Li]**2**. Compound **4** was observed at a 1:20 ratio of **4** : [Li]**2** which is substantially lower than the ratio observed at 2 equivalents.

When 3 equivalents of LiNH^{t}Bu were used and the reaction was heated for 18 hours, the solution developed a deep, opaque golden-brown color. After THF removal *in vacuo*, the resulting brown solid was redissolved in CD_3CN, forming a dilute brown solution with a significant amount of CD_3CN insoluble material. Dissolution of the crude in C_6D_6 led to less black insoluble material and a concentrated brown solution. The ^{1}H NMR spectrum in CD_3CN revealed numerous minor paramagnetically shifted signals with [Li]**2** not found in the spectrum as shown in Figure 2.5 (D). The predominant signal in CD_3CN appeared at 1.08 ppm, likely corresponding to the product of LiNH^{t}Bu reacting with CD_3CN. The ^{1}H NMR in C_6D_6 displayed many signals from –7.38 ppm to 22.72 ppm as shown in Figure 2.5 (C)

When 4 equivalents of LiNH^{t}Bu were used and the reaction was heated for 18 hours, the solution developed a deep, opaque, reddish black. Following the removal of THF under vacuum, the resulting brown solid was dissolved in CD_3CN and in C_6D_6 for analysis by ^{1}H NMR spectroscopy. Dissolution in both solvents led to opaque reddish black solutions, accompanied by grey/black insoluble material. The ^{1}H NMR spectrum in CD_3CN displayed one broad signal at 7.95 ppm and a sharp signal at 1.08 ppm, likely the product of LiNH^{t}Bu reacting with CD_3CN. The ^{1}H NMR spectrum in C_6D_6 displayed multiple (10-12) broad signals from 0.98 ppm to 11.38 ppm.

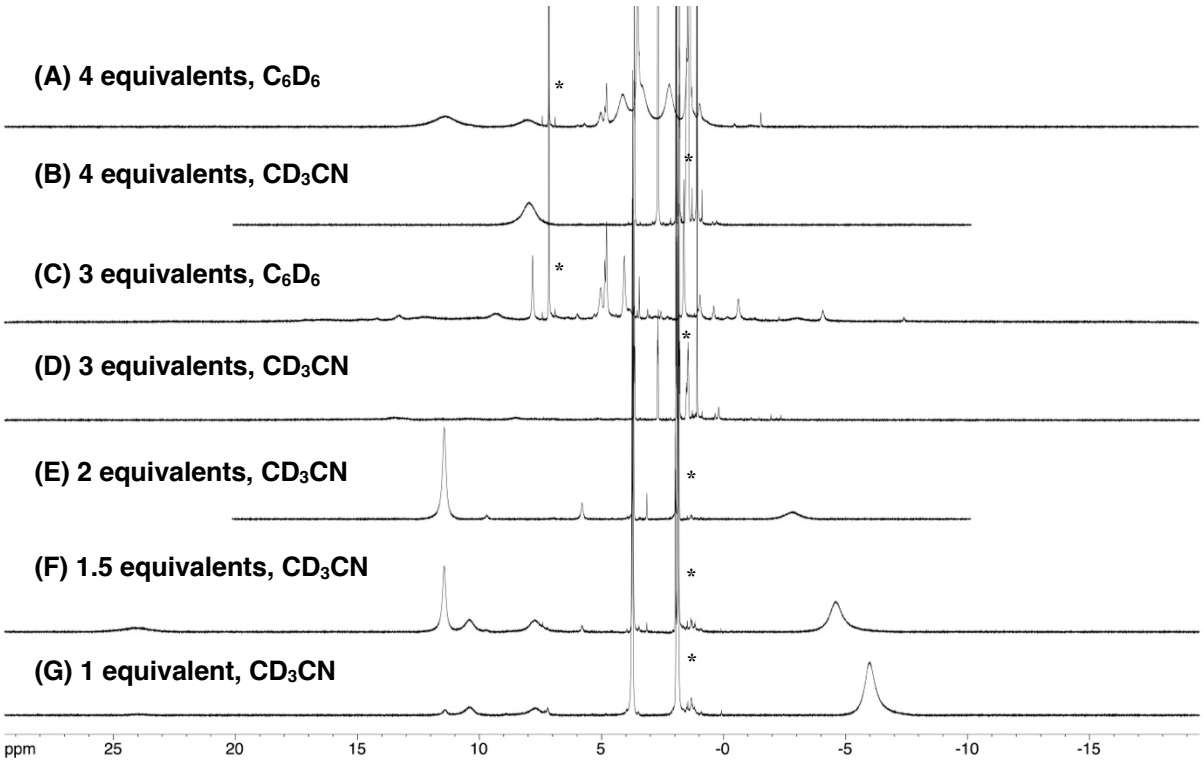

Figure 2.5. ^{1}H NMR (300 MHz, 25 °C) spectra with varying equivalents of LiNH^{t}Bu to $FeCl_3$. Spectra were either collected in CD_3CN or C_6D_6 with residual protio signal assigned with *. (**A**) 4 equivalents in C_6D_6, (**B**) 4 equivalents in CD_3CN, (**C**) 3 equivalents in C_6D_6, (**D**) 3 equivalents in CD_3CN, (**E**) 2 equivalents in CD_3CN, (**F**) 1.5 equivalents in CD_3CN and (**G**) 1 equivalent in CD_3CN.

2.2.1.4 Effect of Extraction Solvents

Purification of the crude mixture of $FeCl_3$ with 2 equivalents of LiNH^{t}Bu in THF at 90 °C overnight by solvent extraction was studied. The crude product mixture, containing **4**, **3** and [Li]**2**, can be partitioned into two fractions based on polarity and charge using organic solvents. Organic solvents tested included MeCN/CD_3CN, DCM, benzene, pentane and THF-d_8. Extraction with MeCN (or CD_3CN) resulted in a deep brown solution with light colored solid, likely LiCl, and yielded a ^{1}H NMR spectrum showing the presence of [Li]**2**, **3** and **4** in CD_3CN. Notably, the same amount of [Li]**2** was observed in the MeCN extract as in the crude, suggesting that all [Li]**2** was extracted in MeCN. Extraction with DCM produced a similar outcome to MeCN but with the ^{t}Bu signal shifted upfield to 10.5 ppm, approaching the chemical shift of **1** in CD_3CN. This chemical shift aligns with a redox equilibrium of

1/[Li]**2**, where exchange is fast on the NMR timescale. Extraction using benzene and pentane yielded a black solution with significant amounts of insoluble material. The ^{1}H NMR spectrum of the benzene/pentane extract in C_6D_6 revealed the presence of only **1** and **3**, whereas the insoluble residue contained [Li]**2** and **4**, confirmed by ^{1}H NMR spectroscopy in CD_3CN. Analysis of the reaction mixture of $FeCl_3$ and 2 equivalents of LiNH^{t}Bu (using the optimized protocol to synthesize [Li]**2**) in THF-d_8 by ^{1}H NMR spectroscopy demonstrated [Li]**2** as the sole $[Fe_4N(^tBu)_4Cl_4]^z$ cluster produced. This was further verified by spiking the NMR solution with [Ph_4P]**2**, which caused no changes to the chemical shift of Li[**2**]. Since the crude reaction in THF-d_8 displayed the [Li]**2** signal at 11.4 ppm rather than 7 ppm, the change in redox state is likely due to extraction into non-polar solvents. The conversion of **2** to **1** during extraction with non-polar solvents is attributed to unreacted $FeCl_3$ oxidizing **2**.

2.2.1.5 Redox Equilibrium

The ^{t}Bu chemical shifts of the $[Fe_4N(^tBu)_4Cl_4]^z$ series are highlighted and discussed in Section 2.2.5.1. Notably, a mixture of z = 0/1– and 1–/2– clusters result in a single observed ^{t}Bu signal in the ^{1}H NMR spectrum, appearing as a weighted average of both species in solution. The observation of a single signal for a mixture of redox states is attributed to a fast redox equilibrium on the NMR timescale. This indicates that if the ^{t}Bu signal deviates from the authentic chemical shift position, a mixture of redox states is likely present, necessitating caution in assigning chemical shifts to species. For example, the chemical shift of $[Fe_4N(^tBu)_4Cl_4]^0$ is 7.7 ppm and the chemical shift of $[Fe_4N(^tBu)_4Cl_4]^{1-}$ is 11.4 ppm in CD_3CN. A ^{t}Bu signal at 10.4 ppm suggests that most of the species in solution is the reduced (z = 1–) cluster, while the upfield shift can be attributed to partial oxidation and the presence of some oxidized (z = 0) cluster.

2.2.1.6 Summary

Altering synthetic parameters such as the Fe(III) precursor, temperature, stoichiometry, reaction solvent and purification protocol has revealed that the ideal parameters for this reaction have been determined by Duncan. Performing the reaction at 90 °C, over 16 hours at a 1:2 $FeCl_3$:LiNH^{t}Bu in THF leads to the most Li[**2**] produced.

2.2.2 Purification of 2

The synthesis of [Li]**2** and **1** in the original report had low isolated quantities (~1-2%), which were attributed to challenges in purifying [Li]**2** from the contaminating LiCl by–product and difficulties in separating **1** from **3**, as both compounds exhibit similar solubility in organic solvents. As discussed in Chapter 2.2.1, **1** is not directly produced during the synthesis of [Li]**2** but likely forms because of purification solvents, thereby facilitating the oxidation of some Li[**2**] to **1**. Despite varying crystallization conditions, [Li]**2** could not be fully separated from contaminating LiCl. To address this issue, extraction of the iron-containing species in DCM was performed, resulting in the removal of a light tan solid, likely LiCl, and a deep brown solution. Surprisingly, [Li]**2** exhibited solubility in DCM, which was likely due to the solvation of $(Li)^+$ with at least two THF molecules as validated by ^{1}H NMR analysis. Pure [Ph_4P]**2** was obtained via counterion metathesis with PPh_4Cl, which produced highly crystalline [Ph_4P]**2**. The counterion metathesis to form [Ph_4P]**2** resulted in large, dark crystalline material contaminated with a light, colourless solid, likely LiCl. Small amounts of THF likely facilitated the solubility of some LiCl in DCM. The light, colourless solid was separated from the large, dark crystals of [Ph_4P]**2** via manual flotation in Et_2O followed by successive washes of the dark crystals with Et_2O. The isolated yield of [Ph_4P]**2** was approximately 20% lower than the *in-situ* yield due to the additional purification steps required. Shown in Figure 2.6 are the resulting ^{1}H NMR spectra of the crude reaction, post DCM extraction and of pure [Ph_4P]**2**.

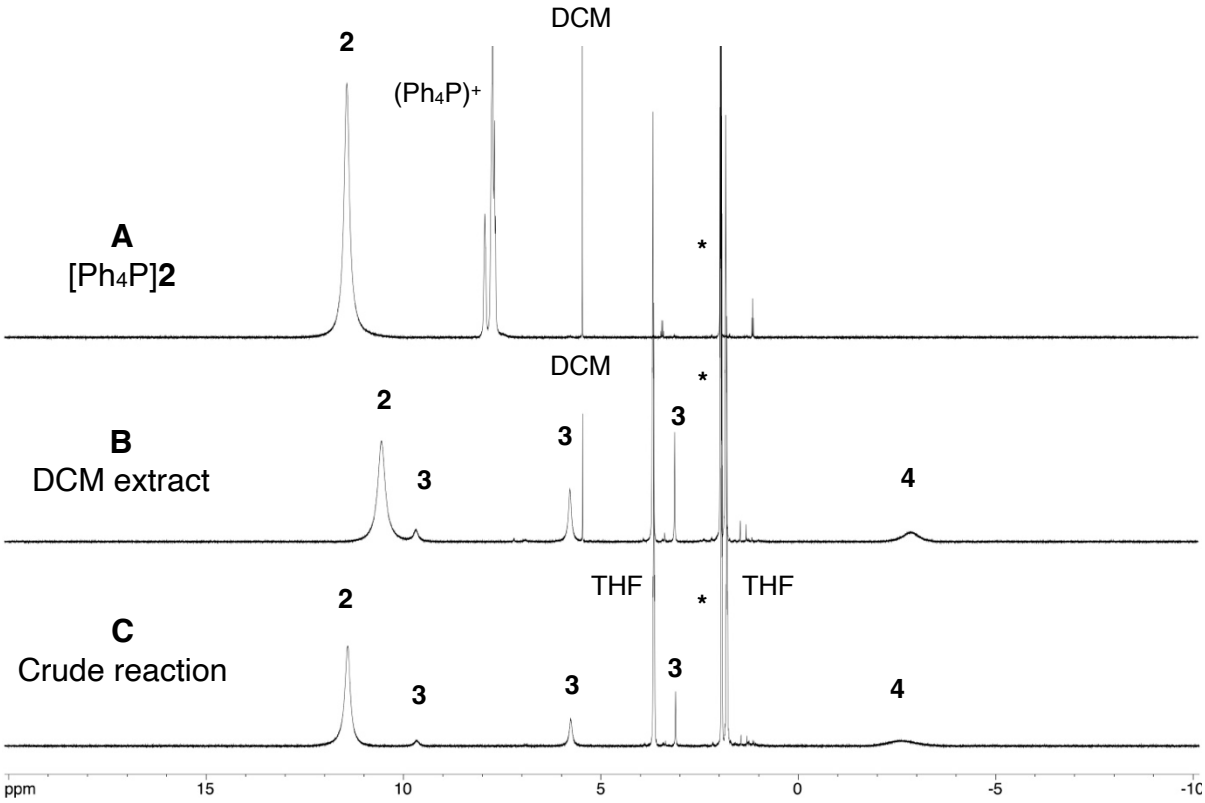

Figure 2.6. ^{1}H NMR (CD_3CN), 300 MHz, 25 °C) spectra of (**A**) pure $[Ph_4P]$**2**, (**B**) DCM extract and (**C**) crude of $FeCl_3$ and 2 equivalents of LiNH^{t}Bu in THF heated to 90 °C over 16 hours.

2.2.3 Redox Behaviour

Two redox members of the $[Fe_4(N^tBu)_4Cl_4]^z$ series (z = 0, 1–) have been previously isolated. A third redox state (z = 2–), previously identified electrochemically, is synthesized and described herein. Compounds **1** and $[Ph_4P]_2$**6** were synthesized through the oxidation of [Li]**2** and the reduction of $[Ph_4P]$**2**, respectively. The solubility of these clusters is as follows: $[Ph_4P]$**2** is soluble in DCM, MeCN and THF; **1** is soluble in non-polar solvents such as benzene and hydrocarbons with some solubility in DCM and MeCN; and $[Ph_4P]_2$**6** is soluble in MeCN. The oxidation of [Li]**2** to **1** was performed in MeCN, followed by solvent removal under reduced pressure. Compound **1** was then extracted into *n*-pentane, ensuring that any unreacted $[Ph_4P]$**2** remained as an insoluble solid. The reduction of $[Ph_4P]$**2** to $[Ph_4P]_2$**6** was carried out in THF with the addition of Ph_4PCl, leading to the precipitation of crystalline $[Ph_4P]_2$**6** from the solution. Each redox member in this series can be interconverted using appropriate oxidants and reductants, as shown in Scheme 2.5. For example, the oxidation of

[Li]**2** to **1** can be achieved using *p*-nitrobenzenediazonium or $Ag(PF_6)$ in MeCN. The reduction of **1** to $[Ph_4P]$**2** and $[Ph_4P]$**2** to $[Ph_4P]_2$**6** can be performed with $Na[Ph_2CO]$ and Cp^*_2Co.

Scheme 2.5. Redox transformation of the $[Fe_4(\mu_3\text{-}N^tBu)_4Cl_4]^z$ series.

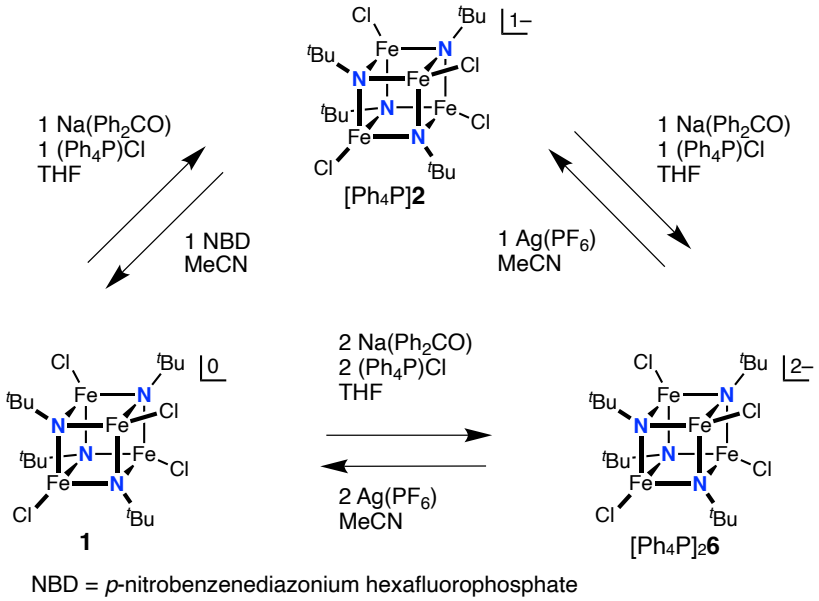

The least stable member of the $[Fe_4(\mu_3\text{-}N^tBu)_4Cl_4]^z$ redox series is $[Ph_4P]_2$**6**. It has been observed that storing solid $[Ph_4P]_2$**6** at –18 °C over two weeks led to the counterion (PPh_4) displaying two broad signals for the aromatic protons instead of the multiplets observed with freshly prepared $[Ph_4P]_2$**6** when analyzed in CD_3CN using ^1H NMR spectroscopy. $[Ph_4P]$**2** is more stable compared to $[Ph_4P]_2$**6** with solid state stability over months when stored at –18 °C, showed decomposition behaviour to $[Ph_4P]_2$**6** when analyzed in CD_3CN using ^1H NMR spectroscopy. The broadness and loss of features of the $(PPh_4)^+$ counterion in both $[Ph_4P]$**2** and $[Ph_4P]_2$**6** was attributed to magnetic iron contamination from cluster decomposition.

The cyclic voltammogram of the newly isolated redox member, $[Ph_4P]_2[Fe_4(N^tBu)_4Cl_4]$ ($[Ph_4P]_2$**6**), exhibits a reversible (z = 0/1–) redox potential and (z = 1–/2–) redox potentials at 0.17 V vs. SCE and –0.95 V vs. SCE, respectively in MeCN, as

shown in Figure 2.7 and tabulated in Table 2.1. The z = 1–/0 oxidation and z = 1–/2– reduction potentials are electrochemically reversible with i_{pa}/i_{pc} = 1 for υ = 10 to 1000 mV/s and $E_{1/2}$ and ΔEp largely independent of υ when analyzed on a sample of $[Ph_4P]_2$**6**. Cyclic voltammograms of the neutral **1** and singly reduced $[Ph_4P]$**2** were acquired by Dr. Jeremiah Duncan and show almost identical features to $[Ph_4P]_2$**6** except the 1–/2– coupling being quasi reversible.

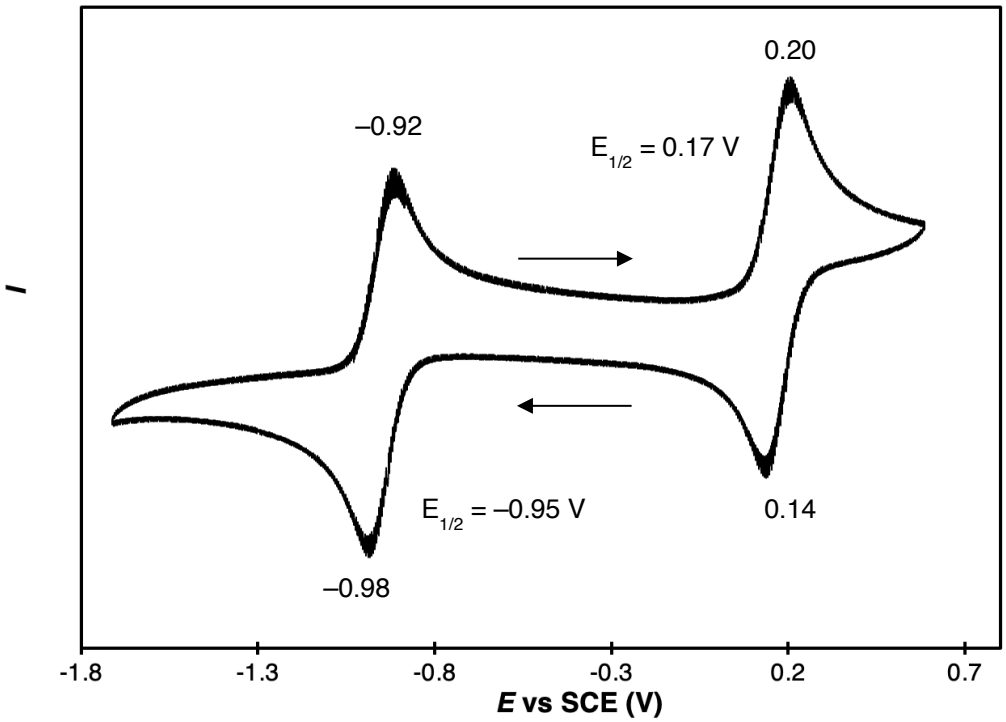

Figure 2.7. Cyclic voltammogram (0.1 M (n-Bu_4N)ClO_4 supporting electrolyte in MeCN, 100 mV/s scan rate) of $[Ph_4P]_2$**6**.

Table 2.1. Redox potentials ($E_{1/2}$) for $[Fe_4(N^tBu)_4Cl_4]^z$ measured from $[Ph_4P]_2$**6**

Compound	0/1– (vs. SCE)	1–/2– (vs. SCE)
$[Ph_4P]_2$**6**	0.17	-0.95

Jeremiah S. Duncan collected CV data for **1** and $[Ph_4P]$**2**. $Fc^{+/0}$ = +0.38 V vs SCE in 0.1 M TBAP/MeCN

The members of the $[Fe_4(N^tBu)_4Cl_4]^z$ series can be isolated in three redox states (z = 0, 1– and 2–). The related, all sulfide, $[Fe_4S_4Cl_4]^z$ motif, has two accessible redox states (z = 2–, 3–).[41,42] The more oxidized redox states observed with $[Fe_4(N^tBu)_4Cl_4]^z$ was attributed to

the donating ability of the N-dianion stabilizing the oxidized states and the steric bulk of the ^{t}Bu protecting the oxidized states from nucleophilic solvent attack on the [$Fe_4(N^tBu)_4$] core. It was observed in the synthesis of oxidized Fe_4S_4 clusters that ligands with sufficient steric bulk were necessary for the stability and isolation of these clusters, as shown in the synthesis of (Bu_4N)[$Fe_4S_4(S(2,4,6\text{-}C_6H_2(^iPr)_3)_4)$] (Further discussed in Chapter 5).[43] The cyclic voltammogram of [Ph_4P]**2** showed an irreversible 2–/3– reduction potential at –1.93 V vs. SCE that is negatively shifted compared to the nearly reversible $[Fe_4S_4Cl_4]^z$ z = 2–/3– potential at around –0.82 V vs. SCE. The z = 2–/3– couple for $[Fe_4S_4Cl_4]^z$ was determined in MeCN with the supporting electrode including a 0.1 M solution of n-Bu_4NCl in MeCN. The different supporting electrolyte in the cyclic voltammetry measurement of $[Fe_4S_4Cl_4]^{2-}$ compared to $[Ph_4P]_2$**6** is attributed to the z = 2–/3– potential for $[Fe_4S_4Cl_4]^{2-}$ being quasi-reversible unless in the presence of excess chloride. It was observed that the excess chloride stabilized $[Fe_4S_4Cl_4]^{3-}$ in the timescale of the cyclic voltammetry experiment.

2.2.4 Cluster Structures

2.2.4.1 Cluster Metrics of $[Ph_4P]_2$6

Members of the $[Fe_4(\mu_3\text{-}N^tBu)_4Cl_4]^z$ series have been characterized using single crystal X-ray diffraction analysis to establish solid state structural motifs. The z = 1– ([Ph_4P]**2**) and z = 0 (**1**) members of the redox series were collected and analyzed by Dr. Jeremiah Duncan.[25] The newest member synthesized from the series, z = 2– was collected by Dr. Jalil Assoud. The structure of $[Ph_4P]_2$**6** is shown in Figure 2.8 with the selected interatomic distances and angles tabulated in Table 2.2 and averaged selected interatomic distances and angles tabulated in Table 2.3.

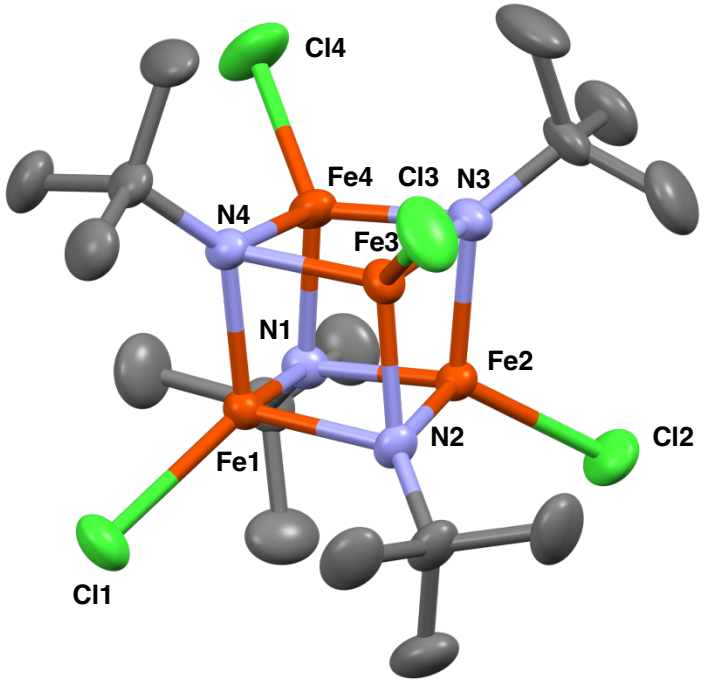

Figure 2.8. Structure of cluster dianion of $(Ph_4P)_2[Fe_4(\mu_3\text{-}N^tBu)_4Cl_4]$ ($[Ph_4P]_2$**6**) showing non-hydrogen atoms (50% probability thermal ellipsoids).

Table 2.2. Selected interatomic distances (Å) and angles (°) for $[Ph_4P]_2$**6**

	$[Ph_4P]_2$**6**
Fe(1)–N(1/2/4)	1.970(3)/1.978(3)/1.975(3)
Fe(2)–N(1/2/3)	1.970(3)/1.976(3)/1.973(3)
Fe(3)–N(2/3/4)	1.972(3)/1.982(3)/1.961(3)
Fe(4)-N(1/3/4)	1.979(3)/1.975(4)/1.997(3)
Fe(1/2/3/4)–Cl(1/2/3/4)	2.2728(12)/2.2533(11)/ 2.2725(13)/2.2664(14)
N(2/4/4)–Fe(1)–N(1/1/2)	96.02(14)/96.23(14)/98.27(14)
N(1/1/3)–Fe(2)–N(3/2/2)	98.33(14)/96.41(13)/ 95.94(14)
N(2/4/4)–Fe(3)–N(3/3/2)	95.79(14)/97.12(14)/ 98.92(13)
N(1/3/3)–Fe(4)–N(4/4/1)	95.54(13)/96.18(14)/97.97(14)
Fe(2/2/4)–N(1)–Fe(4/1/1)	81.66(13)/ 83.27(12)/83.62(13)
Fe(3/3/2)–N(2)–Fe(2/1/1)	83.46(13)/81.02(12)/83.17(13)

	$[Ph_4P]_2$**6**
Fe(2/2/4)–N(3)–Fe(4/3/3)	81.70(13)/83.30(13)/82.82(13)
Fe(3/3/1)–N(4)–Fe(1/1/4)	81.39(12)/82.77(12)/83.31(12)
Fe(1)···Fe(2/3/4)	2.6247(8)/2.5663(8)/2.6397(8)
Fe(2)···Fe(3/4)	2.6284(8)/ 2.5823(8)
Fe(3)···Fe(4)	2.6169(9)
N(1)···N(2/3/4)	2.942(5)/2.982(4)/2.944(5)
N(2)···N(3/4)	2.933(5)/2.989(4)
N(3)···N(4)	2.956(5)

Table 2.3. Selected averaged distances (Å) and angles (deg) for $[Ph_4P]_2$**6**

	***n*[a]**	**Mean[b]**	**Range**
Fe–N (Å)	12	1.977(8)	1.961(3)-1.997(3)
Fe–Cl (Å)	4	2.266(9)	2.2533(11)-2.2728(11)
Fe···Fe (Å)	6	2.610(29)	2.5663(8)-2.6397(8)
N···N (Å)	6	2.959(24)	2.933(5)-2.989(4)
N–Fe–N (°)	12	97(1)	95.54(13)-98.92(13)
Fe–N–Fe (°)	12	82.57(96)	81.02(12)-83.62(13)

[a] Number of independent values corresponding to the metric type. [b] Arithmetic mean, with uncertainty representing the standard deviation from the mean.

2.2.4.2 Metric Comparison of $[Fe_4(\mu_3\text{-}N^tBu)_4Cl_4]^z$ Series

The metrics of the three members of the $Fe_4(N^tBu)_4]^z$ series are shown below (Table 2.4). Based on literature data on Fe_4S_4 clusters, increasing the total charge state of the cluster will lead to an overall increase in the bond lengths.[44] As the $[Fe_4(N^tBu)_4]$ core is reduced, the Fe–N and Fe–Cl bond lengths, and N–Fe–N bond angles of the cluster increase while the Fe–N–Fe bond angles decrease. The Fe–N bond length increases by 0.030 Å from **1** to $[Ph_4P]_2$**6**. The Fe–Cl bond length changes the most drastically, increasing of 0.1 Å from **1** to $[Ph_4P]_2$**6**. Surprisingly, the Fe···Fe separation does not increase as the cluster becomes more reduced

while the N···N separation does increase with the separation increasing by 0.060 Å from **1** to $[Ph_4P]_2$**6**.

Table 2.4. Selected averaged interatomic distances (Å) and Angles (º) in $Fe_4(\mu_3\text{-}N^tBu)_4Cl_4$ (**1**), $[Ph_4P][Fe_4(\mu_3\text{-}N^tBu)_4Cl_4]$ (**2**) and $[Ph_4P]_2[Fe_4(\mu_3\text{-}N^tBu)_4Cl_4]$ (**6**)

	1	$[Ph_4P]$**2**	$[Ph_4P]_2$**6**
Fe–N	1.948(10)	1.956(4)	1.977(8)
Fe–Cl	2.160(6)	2.204(6)	2.266(9)
Fe···Fe	2.608(11)	2.610(11)	2.610(29)
N···N	2.890(21)	2.906(12)	2.959(24)
N–Fe–N	95.8(7)	95.95(53)	97(1)
Fe–N–Fe	84.1(6)	83.71(43)	82.57(96)

Structural data was provided by Jeremiah S. Duncan for **1** and $[Ph_4P]$**2**.

2.2.4.3 Metric Comparison with Iron-Arylimide Clusters

The iron-arylimide cluster series represents another group of clusters featuring core imide ligation. Metric comparison (Table 2.5) with this set of clusters showcases the effect of alkylimide vs. arylimide ligation. Comparing the metrics of **1** with $Fe_4(NPh)_4(SMes)_4$ and $Fe_4(N\text{-}p\text{-}Tol)_4(SMes)_4$, $[Ph_4P]$**2** with $[Fe(THF)_6][Fe_4(N\text{-}p\text{-}Tol)_4\text{-}(SDMP)_3(N\{SiMe_3\}_2)]_2$ and $[Ph_4P]_2$**6** with $[Li(DME)_3]_2[Fe_4(NPh)_4Cl_4]$, the main difference found is in the Fe–N bond lengths.[23,30] The Fe–N bond lengths of **1** and $[Ph_4P]$**2** are shorter by 0.01 to 0.02 Å respectively compared to iron-arylimide clusters at the same redox state. The Fe–N bond lengths of $[Ph_4P]_2$**6** are similar in length compared to those of $[Li(DME)_3]_2[Fe_4(NPh)_4Cl_4]$.

Table 2.5. Selected averaged interatomic distances (Å) and angles (º) in $Fe_4(NPh)_4(SMes)_4$, $Fe_4(N\text{-}p\text{-}Tol)_4(SMes)_4$, $[Fe(THF)_6][Fe_4(N\text{-}p\text{-}Tol)_4\text{-}(SDMP)_3(N\{SiMe_3\}_2)]_2$ and $[Li(DME)_3]_2[Fe_4(NPh)_4Cl_4]$

	$Fe_4(NPh)_4(SMes)_4$	$Fe_4(N\text{-}p\text{-}Tol)_4(SMes)_4$	$[Fe(THF)_6][Fe_4(N\text{-}p\text{-}Tol)_4\text{-}(SDMP)_3(N\{SiMe_3\}_2)]_2$	$[Li(DME)_3]_2[Fe_4(NPh)_4Cl_4]$
Fe–N	1.963(13)	1.962(12)	1.98(3)	1.983(9)
Fe···Fe	2.63(2)	2.62(2)	2.66(8)	2.65(4)
N···N	2.904(12)	2.91(2)	2.93(4)	2.941(3)
N–Fe–N	95.4(7)	95.7(8)	95(3)	96(1)

2.2.4.4 Metric Comparison with Fe_4S_4 Clusters

The next metric comparison is with the homoleptic sulfide cluster, $[Fe_4S_4X_4]^z$ (where X = anionic ligand) systems. The general structures of **1**, $[Ph_4P]$**2** and $[Ph_4P]_2$**6** show idealized T_d geometry and no evidence of cluster core distortion to D_{2d} as seen with some $[Fe_4S_4X_4]^z$ systems at the z = 2– and 3– redox states.[45–48] The cluster core tetragonal elongation or compression in $[Fe_4S_4X_4]^z$ was observed by the comparison of Fe–S bond lengths. It can be seen for $[Fe_4S_4X_4]^z$ at z = 2– and 3– that four of the twelve Fe–S bond lengths which are approximately parallel to the idealized S_4 axis are either shorter or longer compared to the other eight Fe–S bond lengths which are perpendicular to the idealized S_4 axis. This deviation was observed by a 3% increase in the elongated Fe–S bond lengths. The imide cubanes are more compact compared to sulfide cubanes which was attributed to shorter Fe–N bond lengths and are more cubic in shape as the Fe_2N_2 rhombs interior angles approach 90 º. The Fe···Fe separations are slightly shorter by approximately 0.1 Å as compared to $[Fe_4S_4X_4]^z$ clusters of the same oxidation states.

2.2.4.5 Metric Comparison with the NS Series

The metrics of the $[Fe_4(\mu_3\text{-}N^tBu)_4Cl_4]^z$ series (Table 2.6) can then be compared to the other members of the $[Fe_4(N^tBu)_nS_{4\text{-}n}Cl_4]^z$ series at the same redox state.[26] The presence of one sulfide in $[Fe_4(N^tBu)_3SCl_4]^{1-}$ compared to $[Ph_4P]$**2** correlates to the slight decrease in

Fe–Cl and Fe–N bond length of 0.007 Å and 0.008 Å respectively. The Fe–N bond length of $[Ph_4P]_2$**6** is longer by 0.025 Å when compared to the bond length found in $[Fe_4(N^tBu)_2S_2Cl_4]^{2-}$ and $[Fe_4(N^tBu)S_3Cl_4]^{2-}$. The Fe–Cl bond length of $[Ph_4P]_2$**6** is longer by 0.028 and 0.039 Å when compared to $[Fe_4(N^tBu)_2S_2Cl_4]^{2-}$ and $[Fe_4(N^tBu)S_3Cl_4]^{2-}$ [26], respectively.

Table 2.6. Selected Averaged Interatomic Distances (Å) and Angles (º) in $[Et_4N][Fe_4(N^tBu)_3SCl_4]$, $[Et_4N]_2[Fe_4(N^tBu)_2S_2Cl_4]$ and $[Et_4N]_2[Fe_4(N^tBu)S_3Cl_4]$

	$[Fe_4(N^tBu)_3SCl_4]^{1-}$	$[Fe_4(N^tBu)_2S_2Cl_4]^{2-}$	$[Fe_4(N^tBu)S_3Cl_4]^{2-}$
Fe–Cl	2.197(9)	2.238(5)	2.227(8)
Fe–N	1.946(8)	1.95(4)	1.953(9)

2.2.5 Characterization

The characterization data for the $[Fe_4(\mu_3\text{-}N^tBu)_4Cl_4]^z$ series was compared with reported data for the $[Fe_4(N^tBu)_nS_{4-n}Cl_4]^z$ series. This comparison enabled a direct comparison to the effect of increased imide content in the cluster core.

2.2.5.1 Spectroscopic Properties

Spectroscopic data for **1**, (Ph_4P)**2**, and $(Ph_4P)_2$**6** are summarized in Table 2.7.

Table 2.7. Spectroscopic data for $Fe_4(\mu_3\text{-}N^tBu_4)Cl_4$ (**1**), $(Ph_4P)[Fe_4(\mu_3\text{-}N^tBu)_4Cl_4]$ ($[Ph_4P]$**2**), and $(Ph_4P)_2[Fe_4(\mu_3\text{-}N^tBu)_4Cl_4]$ ($[Ph_4P]_2$**6**)

Compound	^{1}H NMR, ppm	UV-vis	Mössbauer
	δ	λ, nm (ε_M, $L\cdot mol^{-1}\cdot cm^{-1}$)	δ ($\lvert\Delta E_Q\rvert$), mm/s
1	7.85 (CD_3CN) 7.72 (C_6D_6)	217 (26 700), 234 (27 300), 274 (25 200)	0.34 (0.54)
$[Ph_4P]$**2**	11.44 (CD_3CN) 11.32 (THF-d_8)	232 (38 100), 255 (19 200), 270 (15 500). 276 (13 700)	0.43 (0.28)
$[Ph_4P]_2$**6**	7.68 (CD_3CN)	226 (27 600), 259 (9 000), 269 (9 300), 277 (8 000)	0.54 (0.71)

^{1}H NMR measurements were conducted on a 300 MHz spectrometer at rt. UV-Vis measurements were conducted in pentane for **1** and MeCN for $[Ph_4P]$**2** and $[Ph_4P]_2$**6.** Mössbauer measurements were conducted on pure polycrystalline solid.

The clusters in the $[Fe_4(N^tBu)_4Cl_4]^z$ series can be identified in solution using ^{1}H NMR spectroscopy as shown in Figure 2.9. The clusters display a single ^{t}Bu signal, consistent with the highest possible symmetry (T_d) of the complex and free rotation of the ^{t}Bu substituents. The ^{t}Bu signal is isotropically shifted compared to equivalent signals of ^{t}BuNH$_2$ and LiNH^{t}Bu due to the paramagnetism of the clusters at room temperature. The ^{t}Bu signal of $[Ph_4P]$**2** is more downfield compared to **1** and $[Ph_4P]_2$**6**, which is attributed to $[Ph_4P]$**2** exhibiting a non-zero ground spin state, whereas both **1** and $[Ph_4P]_2$**6** exhibit a zero (diamagnetic) ground spin state (see Section 2.2.5.2).

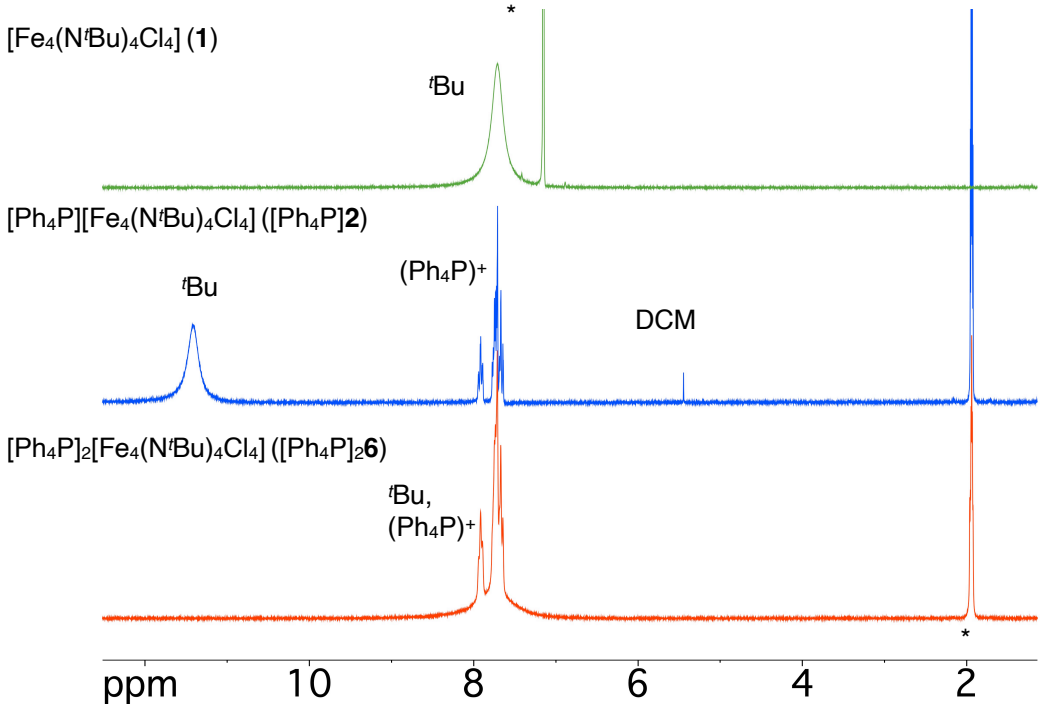

Figure 2.9. ^{1}H NMR (300 MHz, 25 °C) spectra of **1**, $[Ph_4P]$**2**, and $[Ph_4P]_2$**6**). * represents residual protio solvent resonance (C_6D_6 for top and CD_3CN for middle and bottom spectra).

The ^{1}H chemical shifts for the $[Fe_4(N^tBu)_4Cl_4]^z$ series are compared to members of the $[Fe_4(N^tBu)_nS_{4-n}Cl_4]^z$ series at the same charge state. The chemical shift of $[Ph_4P]$**2** can be compared to $[Fe_4(N^tBu)_3SCl_4]^{1-}$ while the chemical shifts of $[Ph_4P]_2$**6** can be compared to $[Fe_4(N^tBu)_2S_2Cl_4]^{2-}$ and $[Fe_4(N^tBu)S_3Cl_4]^{2-}$. In Table 2.8 are the respective ^{1}H chemical shifts of the $[Fe_4(N^tBu)_nS_{4-n}Cl_4]^z$ series analyzed in CD_3CN. Increasing the sulfide content in the cluster core correlates with the ^{t}Bu signal shifting upfield.

Table 2.8. ^{1}H NMR chemical shifts of $[Fe_4(N^tBu)_3SCl_4]^{1-}$, $[Fe_4(N^tBu)_2S_2Cl_4]^{2-}$ and $[Fe_4(N^tBu)S_3Cl_4]^{2-}$ in CD_3CN

Cluster	^{1}H NMR Chemical Shift
$[Ph_4P]$**2**	11.44
$[Fe_4(N^tBu)_3SCl_4]^{1-}$	10.51
$[Ph_4P]_2$**6**	7.68
$[Fe_4(N^tBu)_2S_2Cl_4]^{2-}$	7.02
$[Fe_4(N^tBu)S_3Cl_4]^{2-}$	5.51

Compounds **1**, $[Ph_4P]$**2** and $[Ph_4P]_2$**6** exhibit characteristic electronic absorption features typical of iron cubane clusters as displayed in Figure 2.10. The spectra display intense features in the near-UV-to-visible regions. A blue shift is observed in the UV-vis absorption spectra with changes in oxidation state (from z = 0 to 2–), like the blue shift observed in $[Fe_4S_4(N(SiMe_3)_2)_4]^z$ (z = 0 – 2–).[49] The $[Fe_4S_4(N(SiMe_3)_2)_4]^z$ (z = 0 – 2–) series contains members of the same oxidation state as the $[Fe_4(N^tBu)_4Cl_4]^z$ series, making the comparison useful. The spectra for $[Ph_4P]$**2** and $[Ph_4P]_2$**6** also display relatively sharp features corresponding to $(Ph_4P)^+$ at 275, 268 and 228 nm based on the UV-vis spectrum of PPh_4Cl in MeCN.

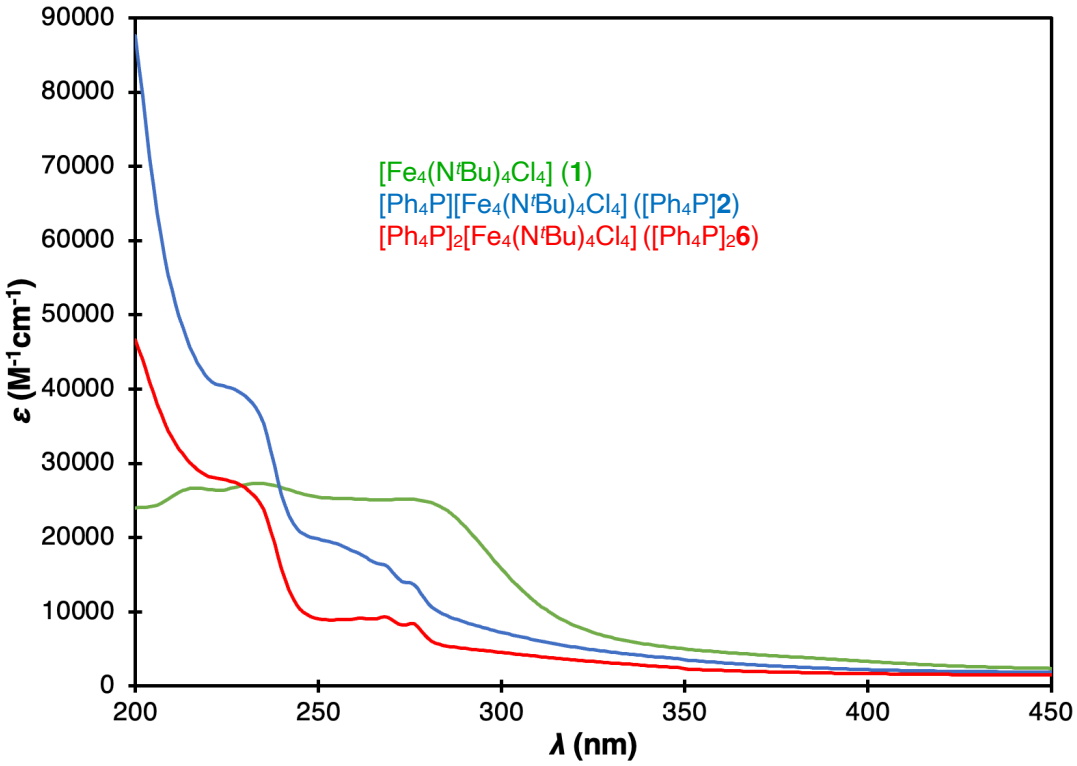

Figure 2.10. Solution UV-vis absorption spectra of $[Fe_4(N^tBu)_4Cl_4]$ (**1**, green), $[Ph_4P][Fe_4(N^tBu)_4Cl_4]$ ($[Ph_4P]$**2**, blue) and $[Ph_4P]_2[Fe_4(N^tBu)_4Cl_4]$ ($[Ph_4P]_2$**6**, red) $[Ph_4P]$**2** and $[Ph_4P]_2$**6** were measured in MeCN and **1** was measured in pentane.

The odd-spin cluster $[Ph_4P]$**2** displays an EPR signal at $g = 2.02$ in 0.2 M TBAP/MeCN glass at X-band frequency at 10 K (Figure 2.11), consistent with a ground spin state of S = ½. The signal shape at 10 K is isotropic but broad, like the EPR shape observed with $[Fe_4(N^tBu)_3SCl_4]^{1-}$, another S= ½ cluster reported by our laboratory.

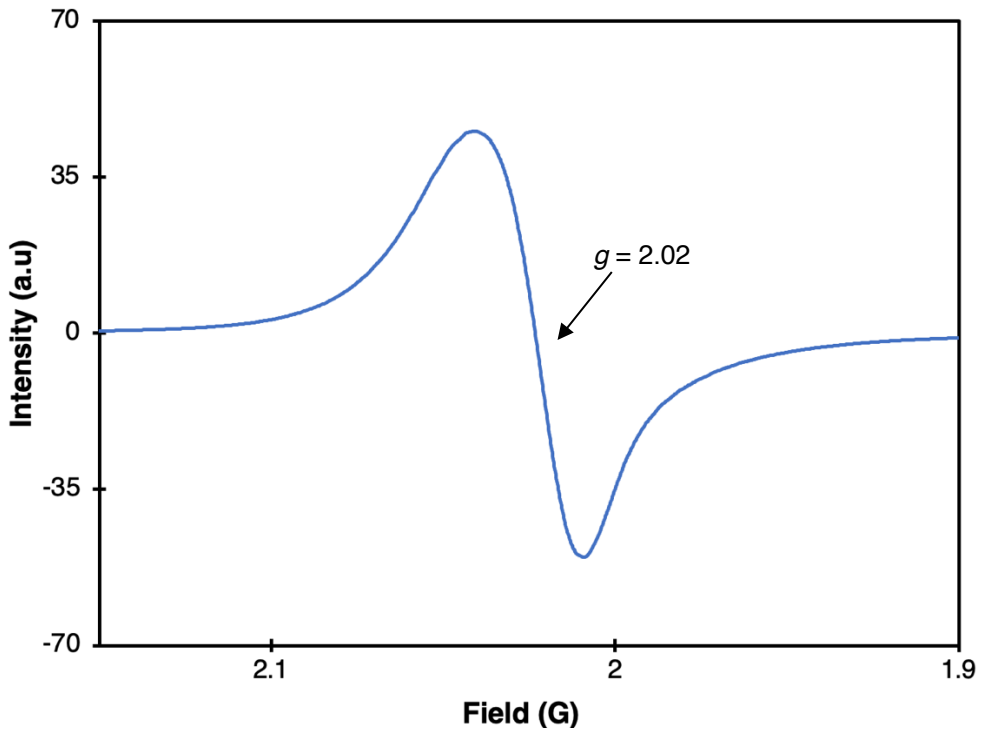

Figure 2.11. X-band EPR spectrum (10 K, 0.2 M TBAP/MeCN) of $[Ph_4P]$**2**.

Additional electronic information was obtained by ^{57}Fe Mossbauer measurements on polycrystalline **1**, $[Ph_4P]$**2** and $[Ph_4P]_2$**6**, shown in Figure 2.12. Measurements in zero applied field at 70 K reveal symmetric doublets for **1** and $[Ph_4P]_2$**6**, while $[Ph_4P]$**2** exhibits an asymmetric absorption.

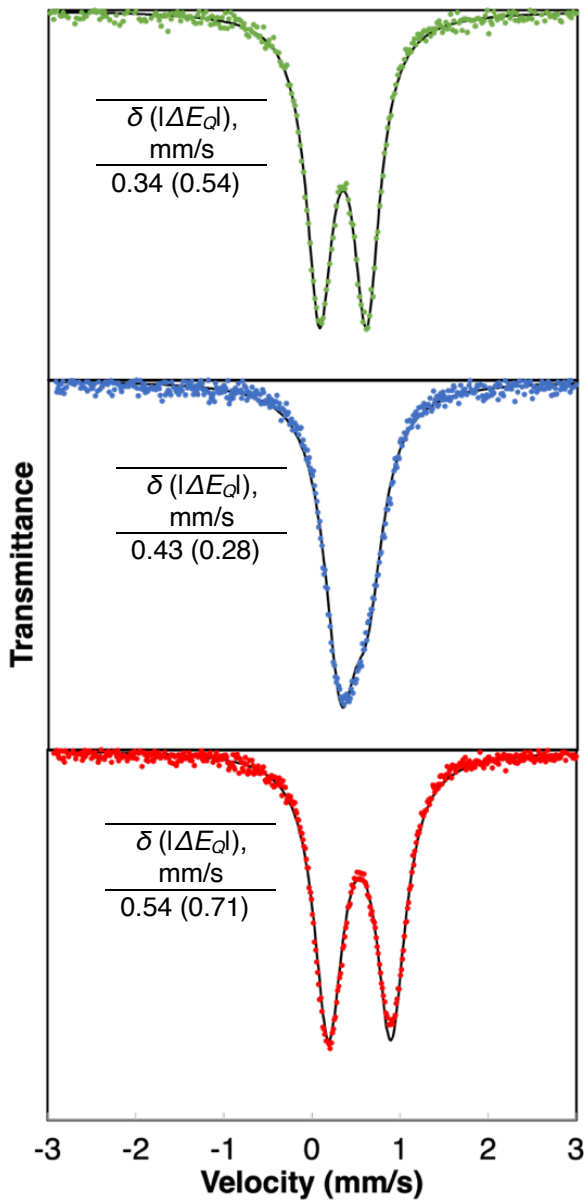

Figure 2.12. Mössbauer spectra (T = 70 K) of polycrystalline $[Fe_4(N^tBu)_4Cl_4]$ (**1**, green), $[Ph_4P][Fe_4(N^tBu)_4Cl_4]$ ($[Ph_4P]$**2**, blue) and $[Ph_4P]_2[Fe_4(N^tBu)_4Cl_4]$ ($[Ph_4P]_2$**6**, red). Solid black lines are spectral simulations based on preliminary parameters indicated on the left of the spectra.

Mössbauer isomer shifts for members of the $[Fe_4(N^tBu)_nS_{4-n}Cl_4]^z$ series are shown in Table 2.9. The isomer shift for $[Ph_4P]_2$**6** is 0.54 mm/s, like that of iron-sulfide and iron-imide-sulfide clusters with the same iron oxidation state (2 Fe(II)/2 Fe(III)). The isomer shifts for $[Fe_4S_4Cl_4]^{2-}$ is 0.51 mm/s at 77 K and the isomer shift $[Fe_4(N^tBu)S_3Cl_4]^{2-}$ and

$[Fe_4(N^tBu)_2S_2Cl_4]^{2-}$ is 0.50 mm/s at 130 K. The isomer shifts for $[Ph_4P]$**2** and **1** are reduced relative to that of $[Ph_4P]_2$**6**, consistent with the clusters being more oxidized (formally Fe(II)/3Fe(III) and 4Fe(III) respectively). The isomer shift for $[Ph_4P]$**2** is 0.43 mm/s at 70 K which is the same as the isomer shift for $[Fe_4(N^tBu)_3SCl_4]^{1-}$, which is 0.43 mm/s at 130 K.

Table 2.9. Mössbauer isomer shifts of members of the $[Fe_4(N^tBu)_nS_{4-n}Cl_4]^z$ series

Cluster	Isomer Shifts
$[Ph_4P]$**2**	0.42 mm/s
$[Fe_4(N^tBu)_3SCl_4]^{1-}$	0.43 mm/s
$[Ph_4P]_2$**6**	0.54 mm/s
$[Fe_4(N^tBu)_2S_2Cl_4]^{2-}$	0.50 mm/s

The Mössbauer spectrum of $[Ph_4P]$**2** can be fit as an asymmetric doublet with small quadruple splitting. The asymmetric doublet was found to be temperature independent as decreasing the temperature from 150 K to 8 K did not resolve the asymmetric features. We attribute the temperature independent asymmetry of $[Ph_4P]$**2** to slower spin-spin relaxation times at the timescale of the Mössbauer experiment.[50–55] If the spin-spin relaxation time was faster, the peak shape would be a symmetric doublet, as we see with **1**. It is believed that the slower spin-spin relaxation is correlated to the distances between high spin Fe(III) and neighbouring paramagnetic metal ions.

2.2.5.2 Other Physical Measurements

Magnetic susceptibility measurements were performed on polycrystalline **1**, $[Ph_4P]$**2** and $[Ph_4P]_2$**6** as shown in Figure 2.13. Both **1** and $[Ph_4P]_2$**6** exhibit a decrease in magnetic susceptibility with decreasing temperature, reaching a minimum at 55 K for **1** and 60 K for $[Ph_4P]_2$**6**, followed by a sharp increase in susceptibility towards 2 K, indicative of magnetic contamination. The low magnetic susceptibility values for **1** and $[Ph_4P]_2$**6** (1.47×10^{-3} emu/mol and 4.17×10^{-3} emu/mol) and the magnetic moments of 0.41 BM and 0.71 BM at 2 K, respectively, are consistent with antiferromagnetically coupled iron atoms at low temperatures and an $S = 0$ ground spin state. The magnetic moment calculated for $[Ph_4P]$**2** at 2 K is 1.93 BM.

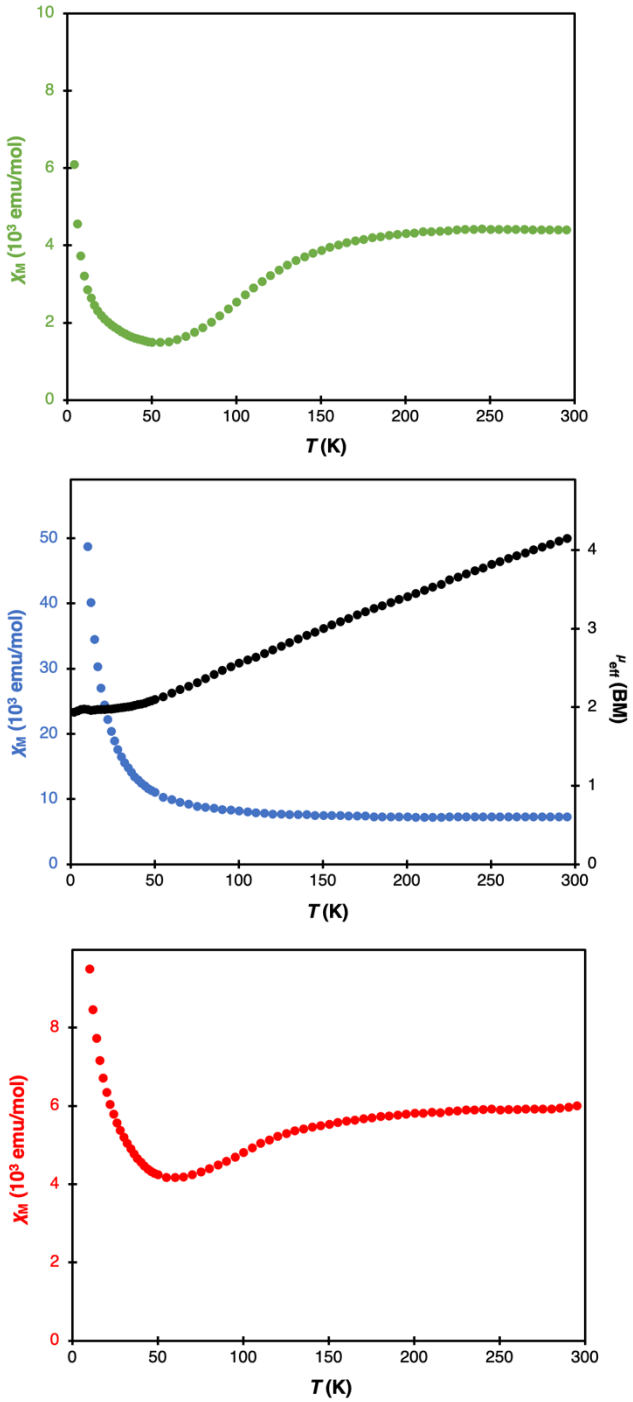

Figure 2.13. Temperature dependence plot of the magnetic susceptibilities of polycrystalline $[Fe_4(N^tBu)_4Cl_4]$ (**1**, green), $[Ph_4P][Fe_4(N^tBu)_4Cl_4]$ ($[Ph_4P]$**2**, blue) and $[Ph_4P]_2[Fe_4(N^tBu)_4Cl_4]$ ($[Ph_4P]_2$**6**, red)

Magnetic susceptibility measurements of [Ph_4P]**2** follow a linear Curie-Weiss relationship ($\chi^M = C/(T-\theta)$; C = 0.54 emu K/mol, θ = –1.60 K) at low temperatures (2-50 K) but deviate above 50 K likely due to the accessibility of higher spin states (Figure 2.14). This relationship is consistent with the iron atoms being antiferromagnetically coupled, with a ground spin state of S = 1/2 (ideal spin-only C=0.375 emu K/mol assuming g =2). The magnetic moment derived from the Curie-Weiss analysis is 2.07 BM. The Curie constant observed for [Ph_4P]**2** is the same as calculated for $[Fe_4S_4(N(SiMe_3)_2)_4]^{1-}$.

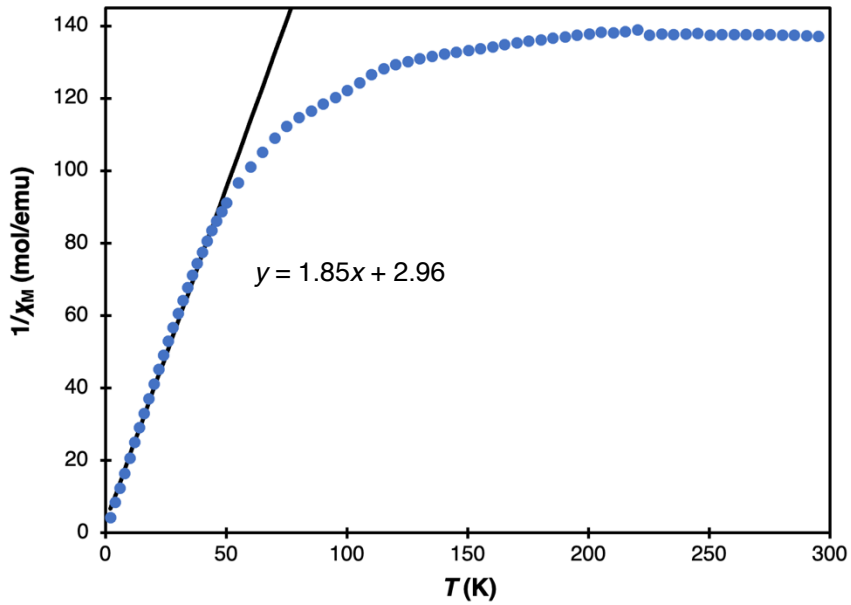

Figure 2.14. Temperature dependence plot of the reciprocal magnetic susceptibility of polycrystalline [Ph_4P][$Fe_4(N^tBu)_4Cl_4$] ([Ph_4P]**2**). The solid line indicates the linear least-squares fit (y = 1.85 x +2.96; C = 0.375 emu K/mol, θ = –1.60 K) to the data between T = 2 – 50 K. Data is consistent with a S=1/2 ground spin state.

2.2.6 Characterization of Mononuclear By-Product

2.2.6.1 Synthesis of 4

Compound **4**, the byproduct observed in the synthesis of [Ph_4P]**2**, was initially isolated from the ether insoluble fraction of the reaction with $FeCl_3$ and 2 equivalents of $LiNH^tBu$ in Et_2O by Matthew Traub.[56] Traub dissolved the precipitate in MeCN, and Et_2O was diffused into the solution, leading to colourless stacked fused plates of **4** which revealed the novel mononuclear Fe (II) complex coordinated by two chlorides and two $^tBuNH_2$

ligands. Duncan claimed excess $^{t}BuNH_2$ was necessary in the synthesis of **4** as the $^{t}BuNH_2$ ligand is weakly coordinated to the Fe(II) center, leading to a dynamic exchange in solution. The preparation of **4** performed by Duncan required a three-day reaction time, two filtrations over celite and a yield of 40%. Improvements to the synthesis of **4** include a shorter reaction time of 6 hours, only one filtration and a yield of 69% (Scheme 2.6). Compound **4** has solubility in MeCN, THF and partial solubility in DCM and $CDCl_3$.

Scheme 2.6. Synthesis of **4**

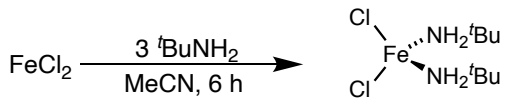

4
69%

Crystals of **4**, isolated from the ether insoluble fraction of $FeCl_3$ and 2 equivalents of $LiNH^{t}Bu$ in Et_2O were subjected to single crystal X-ray diffraction analysis to establish the solid-state structure. Crystals of **4**, synthesized from the reaction of $FeCl_2$ and 3 equivalents of $^{t}BuNH_2$, were also analyzed by X-ray diffraction analysis, which resulted in the same unit cell as the original crystal structure confirming **4** was synthesized.

2.2.6.2 Evidence for Dynamic Equilibrium

The chemical shift of the ^{t}Bu resonance in **4** can be observed between 1.1 ppm to –6 ppm depending on the concentration of **4**, $^{t}BuNH_2$ and $FeCl_2$ present in solution. An observed chemical shift closer to 1 ppm, indicates an excess of free $^{t}BuNH_2$ in solution, while a more upfield shift suggests stoichiometric or substoichiometric amounts of $^{t}BuNH_2$ relative to $FeCl_2$. As a result, quantitation of **4** solely based on signal integration is not feasible, as the observed signal represents **4** and free $^{t}BuNH_2$ found in solution. The presence of a single ^{t}Bu resonance suggests that $^{t}BuNH_2$ is weakly coordinating to the Fe (II) center and undergoes rapid dynamic exchange on the NMR time scale. Dissolution of varying amounts of pure **4** in CD_3CN resulted in corresponding changes in the ^{t}Bu chemical shift, further supporting the presence of dynamic exchange. To more accurately estimate the amount of **4** in solution, equilibrium constants were determined through ^{1}H NMR titration experiments (*vide infra*).

2.2.6.3 Equilibrium Binding Model

The dynamic exchange phenomenon was modeled using a 1:2 metal to ligand, stepwise binding equilibrium with select equations shown in Equation 2.2 to 2.6.[57] In this model, the binding of $^{t}BuNH_2$ to the Fe (II) center occurs sequentially: the first molecule of $^{t}BuNH_2$ binds initially, followed by a second molecule. This stepwise binding model was selected based on the solid-state structure of **4**, which reveals a mononuclear complex with two $^{t}BuNH_2$ ligands. The equilibrium expressions of this model are presented below:

Let M represent $FeCl_2(CD_3CN)_x$ and L represent $^{t}BuNH_2$

Equation 2.2

$$\mathrm{M} + \mathrm{L} \rightleftharpoons \mathrm{ML}$$

Equation 2.3

$$\mathrm{ML} + \mathrm{L} \rightleftharpoons \mathrm{ML_2}$$

Equation 2.4

$$K_1 = \frac{[\mathrm{ML}]}{[\mathrm{M}][\mathrm{L}]}$$

Equation 2.5

$$K_2 = \frac{[\mathrm{ML_2}]}{[\mathrm{ML}][\mathrm{L}]}$$

As only one signal is observed in the ^{1}H NMR spectrum of **4**, that signal is a weighted average of all $^{t}BuNH_2$ containing species in solution which include **4**, $FeCl_2(^{t}BuNH_2)$, and $^{t}BuNH_2$ which is expressed in Equation 2.5.

Equation 2.6

$$\delta_{obs} = \frac{[\mathrm{L}]}{[\mathrm{L}^0]}\delta_L + \frac{[\mathrm{ML}]}{[\mathrm{L}^0]}\delta_{ML} + \frac{2[\mathrm{ML_2}]}{[\mathrm{L}^0]}\delta_{ML_2}$$

^{1}H NMR titration experiments were executed to provide sufficient data to determine the equilibrium constants and chemical shifts for $FeCl_2(^{t}BuNH_2)$ and **4**. Titration experiments

were performed by keeping the concentration of $FeCl_2$ constant and varying the amount of $^tBuNH_2$ as displayed in Figure 2.15. These experiments were performed in triplicate to account for experimental error and followed best practices for determining equilibrium constants. Dissolution of $FeCl_2$ in MeCN was performed and verified spectrophotometrically with 1,10-phenanthroline as the indicator to ensure complete dissolution of $FeCl_2$ as the solubility of $FeCl_2$ in MeCN has not been directly explored. Full ^1H NMR titration and spectrophotometrically titration data, experimental protocols and processed data found in Appendix B.

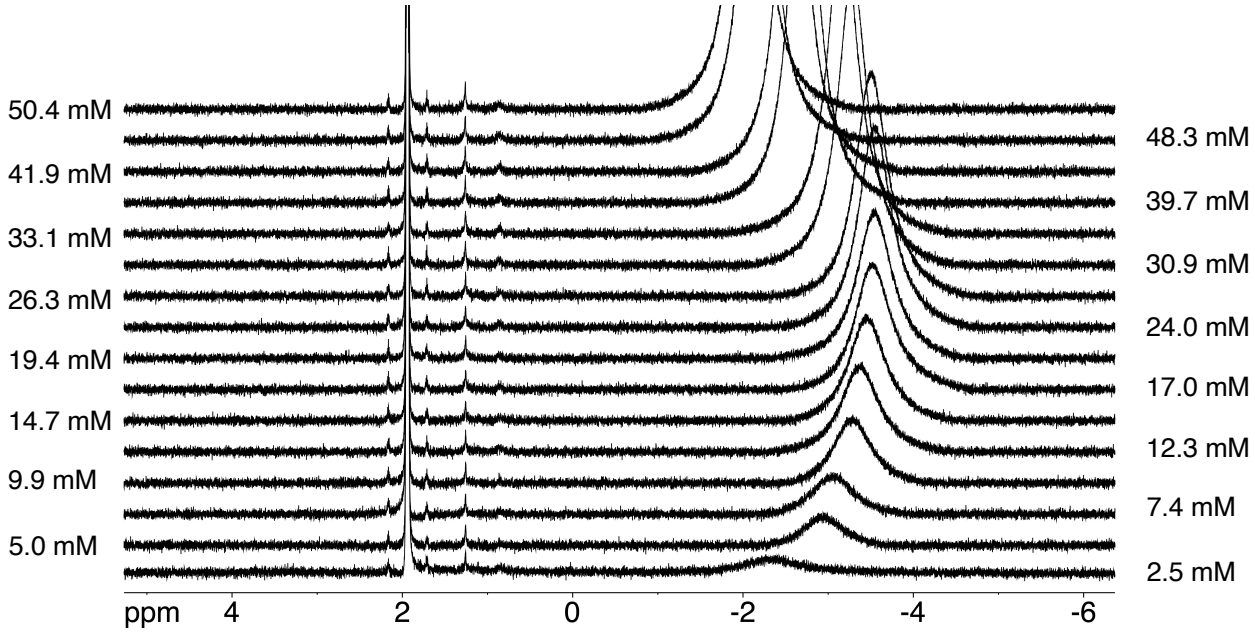

Figure 2.15. ^1H NMR titration of $FeCl_2$ in MeCN with $^tBuNH_2$ in CD_3CN. Concentration of $FeCl_2$ is 15.8 mM. Concentration of total $^tBuNH_2$ found on the sides of the spectra.

The calculated values for K_1, K_2, δ_{ML} and δ_{ML2} were obtained as an average of three titration experiments with the average of these values shown in Table 2.10. See Appendix B for the fitting protocol. The values for K_1 and K_2 at 25 °C are 914 ± 321 and 1213 ± 349, respectively. The chemical shifts for $FeCl_2(^tBuNH_2)$ and $FeCl_2(^tBuNH_2)_2$ are –2.78 ± 0.22 and –4.22 ppm ± 0.22, respectively. The values reported herein were averages from three different trials with the standard error being derived from the standard deviation of the three trials. Attempts to lower the temperature of the NMR spectrometer to reduce the rate of

exchange and to observe all species in solution were unsuccessful and attributed to the exchange still being fast at –20 °C.

Table 2.10. Equilibrium constants and chemical shifts for $FeCl_2(^tBuNH_2)$ and $FeCl_2(^tBuNH_2)_2$

Parameter	Calculated Value
K_1 (M^{-1})	914 ± 321
K_2 (M^{-1})	1213 ± 349
δ_{ML} (ppm)	–2.78 ± 0.22
δ_{ML2} (ppm)	–4.22 ± 0.22

2.2.6.4 Solid State Stability of 4

Compound **4** crystallizes as transparent needles but transforms to a light tan solid upon storage inside a –20 °C freezer over months. When **4** was prepared for elemental analysis, the colourless, transparent crystals turned into light grey powder after drying under vacuum over multiple days. The color changes and diminished crystallinity suggests oxidization or decomposition of **4** occurred, possibly due to loss of $^tBuNH_2$. The elemental analysis for C, H and N were all low, which provided evidence that the composition of the material that went through analysis was not pure **4** but likely a combination of **4** and $FeCl_2(^tBuNH_2)$ which is consistent with loss of $^tBuNH_2$. The experimental data of C, 32.51; H, 7.67; N, 9.13 can be fit with the amine stoichiometry range of 1.76 to 1.71 with the C, H and N composition being C, 32.621; H, 7.53; N, 9.51 and C, 32.14; H, 7.42; N, 9.37 respectively. Therefore, the elemental analysis and the color of **4** after drying is consistent with the weak binding and loss of $^tBuNH_2$.

2.2.7 Chapter Summary

The work presented in this chapter led to a more thorough investigation into the synthesis of iron–imide cubane–like clusters and a more complete characterisation of the redox members. The initial communication by the laboratories of Lee and Fenske did not

explore the synthetic conditions for these clusters. Parameters such as reaction solvent, reaction temperature, stoichiometry and purification protocols were systematically varied in this study to determine the optimal conditions for forming the iron–imide clusters.

The synthesis of $FeCl_2$ with two equivalents of LiNH^{t}Bu in THF at 90 °C for 16 hours, originally utilized by Duncan, was confirmed in this work to provide optimal conditions to form the iron-imide clusters. Only Li**2**, **3** and **4** were observed as products by ^{1}H NMR spectroscopy. Formation of **3** occurred only upon heating, whereas **4** was observed as a common coproduct. Monomer was synthesized directly by reacting $FeCl_2$ with three equivalents of ^{t}BuNH$_2$. The ^{t}BuNH$_2$ ligands in **4** undergo fast dynamic exchange on the timescale of the NMR experiment with the equilibrium of the two ligands binding modelled in this work.

Two additional redox members were isolated via oxidation and reduction of compound [Ph$_4$P]**2**, yielding **1** and [Ph$_4$P]$_2$**6**, respectively. It was initially believed that both **1** and Li**2** were present in the crude reaction mixture. However, further analysis revealed that Li**2** is the sole redox member produced directly, white partial oxidation to **1** occurs during the workup process, likely upon redissolution of the crude mixture in nonpolar solvents.

The iron-alkylimide redox series was characterized using a broad suite of physical techniques to examine both solid state and in solution phase properties. In solution identification was performed using 1H NMR and UV-vis spectroscopy and the solid state structure was determined using single crystal XRD analysis. Compounds **1** and [Ph$_4$P]$_2$**6** exhibit diamagnetic ground states while [Ph$_4$P]**2** displays a S = ½ ground spin state as confirmed by magnetic susceptibility measurements across the series and EPR measurements of [Ph$_4$P]**2**. The iron environments were probed using Mossbauer spectroscopy which showcased expected features for **1** and [Ph$_4$P]$_2$**6** but showed an asymmetric doublet feature for [Ph$_4$P]**2**.

2.3 Experimental Section

NMR spectra were obtained on Bruker 300 MHz Avance spectrometers at 25 °C with chemical shifts referenced to the residual protio signal of the deuterated solvent. UV-vis spectra were obtained using a Varian Cary 5000 UV-vis-NIR spectrophotometers and solutions were measured using cells with pathlength of 0.1 mm measured anaerobically. Electrochemical measurements were conducted inside a N_2 atmosphere glovebox. Measurements were conducted using a Biologic SP-150 potentiostat. Redox potentials were referenced using ferrocene/ferrocenium as the internal standard and converted to SCE. Elemental analysis measurements were conducted by the Center for Enabling New Technologies Through Catalysis at the University of Rochester on a PerkinElmer 2400 Series II analyzer. Magnetochemical analyses were conducted by the Brockhouse Institute for Materials Research at McMaster University on a Quantum Design SQUID magnetometer.

2.3.1 General Experimental Details

Synthetic operations were performed using standard Schlenk and glove box techniques under pure N_2 atmosphere. Reaction solvents (HPLC grade) (VWR: MeCN, benzene, Et_2O, CH_2Cl_2; Sigma-Aldrich: THF, HMDSO, *n*-pentane) and reagents were obtained from commercial sources and used as purchased unless otherwise indicated. Reaction solvents and ^{t}BuNH$_2$ reagent were purified by passage through desiccant columns (MBraun, SPS-800;benzene, Et_2O, *n*-pentane) or distillation in the presence of sodium benzophenone ketyl (THF), sodium metal (HMDSO), or CaH_2 (CH_2Cl_2, ^{t}BuNH$_2$) scavenger, and stored over 3 Å molecular sieves. Deuterated solvents (Sigma-Aldrich) were dried by successive storage over 3 Å molecular sieves (2 passes). LiNH^{t}Bu and nitrobenzenediazonium tetrafluoroborate were synthesized using literature preparations.[58,59] All other reagents were used without purification.

2.3.2 Preparation of Compounds

$Fe_4(\mu_3$-N^{t}Bu$)_4Cl_4$ (1). Preparation of 1 follows a slightly modified preparation created by Dr. Jeremiah Duncan. Solid LiNH^{t}Bu (2.670 g, 33.77 mmol) was added over 30 min. to an amber solution of $FeCl_3$ (2.751 g, 16.96 mmol) in THF (60 mL) with stirring,

resulting in an exothermic reaction with fuming and immediate darkening of the solution to a deep brown solution. The mixture was then sealed in a heavy walled glass pressure vessel and heated to 90 °C for 18 h. After cooling to room temperature, the solvent was removed under reduced pressure and the black residue dried i*n vacuo* for 6 h to remove trapped solvent. The residue was then suspended in benzene (60 mL) with stirring for 3 h and filtered, and the filtrate was washed further with benzene and *n*-pentane until the rinses were transparent (ca. 20 mL) to yield a gray-black solid. The solid was then taken up in MeCN (15 mL) and treated with 4-nitrobenzenediazonium tetrafluoroborate (0.5086 g, 2.15 mmol). The mixture was stirred for 4 h to give a brown-black solution with tan precipitate. The residue was then extracted with *n*-pentane (70 mL) and filtered through diatomaceous earth. Addition of HMDSO (10 mL) to the black-brown filtrate, followed by volume reduction to ca. 15 mL and storage at –20 °C for one day yielded black crystals that were isolated by filtration. Yield 0.717 g (0.608 mmol, 26.0%).

(Ph_4P)[$Fe_4(\mu_3$-$N^tBu)_4Cl_4$]([Ph_4P]2). Solid $LiNH^tBu$ (1.645 g, 20.8 mol) was added slowly over 30 minutes to a stirred amber suspension of $FeCl_3$ (1.688 g, 10.4 mmol) in THF (40 mL), resulting in an exothermic reaction with fuming and the immediate development of a deep brown solution color. The solution was then heated to 90 °C for 16 h, then allowed to cool to room temperature and the solvent removed in vacuo to give a black residue. The residue was stirred in DCM (40 mL) for 1 h, then filtered over diatomaceous earth to remove LiCl, with the bed rinsed with minimal DCM (10 mL) until the rinses were clear. The solvent was removed in vacuo to afford a black residue that was redissolved in DCM (15 mL) and was added to a solution of Ph_4PCl (0.5686, 1.5 mmol) in DCM (5 mL). The solution was filtered through diatomaceous earth and the bed was rinsed with DCM until rinses were clear. The volume of the combined filtrate and rinses was reduced in vacuo to 10 mL, and vapor diffusion of Et_2O into this solution at –13 °C yielded black crystals of **2** that were collected, rinsed with Et_2O, and dried in vacuo. A second crop of black crystals contaminated with light while crystals can be obtained from the mother liquor and purified by a further recrystallization via DCM/Et_2O vapor diffusion. Yield: 0.6058 g (0.613 mmol, 23.5%).

$FeCl_2(NH_2{}^tBu)_2$ (4). $^tBuNH_2$ (1.2 mL, 11.42 mmol) was added to a tan suspension of $FeCl_2$ (0.504 g, 3.98 mmol) in MeCN (30 mL), and the mixture stirred for 6 h to afford a

transparent tan solution. The solution was filtered over diatomaceous earth, and the volume was reduced (ca. 10 mL) in vacuo until light-colored microcrystalline solid appeared. Et_2O was added to enhance precipitation, and the mixture was held at –22 °C overnight. The precipitate was harvested, rinsed with Et_2O, and dried to afford tan crystals. Yield: 0.749 g (2.74 mmol, 69.1%).

$FeCl_3(THF)_2$ (5) $FeCl_3$ (217.3 mg) was added slowly to THF (5 mL) to afford an amber suspension. Red insoluble material was then filtered off to afford a green solution that upon volume reduction (ca. 1 mL) and storage at –15 °C for 6 days afforded light green crystals. Yield: 157.1 mg. ^{1}H NMR (300 MHz, 25 °C, C_6D_6): δ 36.63 (8H), 123.32 (8H)

$(Ph_4P)_2[Fe_4(\mu_3\text{-}N^tBu)_4Cl_4]$ ($[Ph_4P]_2$6). Benzophenone (49.6 mg, 0.272 mmol) and Na (6.8 mg, 0.296 mmol) were stirred together in THF (2.7 mL) 3 h, forming a dark blue stock solution forming $Na(Ph_2CO)$. To a suspension of **2** (114.6 mg, 0.116 mmol) and Ph_4PCl (40.5 mg, 0.108 mmol) in THF was added $Na(Ph_2CO)$ (1.4 mL, 0.140 M). After the initial addition, microcrystalline material precipitated out of solution immediately and the reaction stirred for 1 hour to ensure complete reduction of $[Ph_4P]$**2**. After the reaction time, the filtrate was left transparent brown, and the black crystalline solid was collected. The solid was purified by CH_3CN/Et_2O vapor diffusion at -13 °C to afford large black crystals. Yield: 68.0 mg (0.0458 mmol, 44.2%). Anal Calcd. for $C_{56}H_{76}N_4Cl_4Fe_4P_2$: C, 57.86; H, 5.77; N, 4.22. Found: C, 57.10: H, 5.54; N, 4.17.

$(Ph_4P)(Cp^*_2Co)[Fe_4(\mu_3\text{-}N^tBu)_4Cl_4]$ ($[Ph_4P][Cp^*_2Co]$6). To a solution of **2** (27.7 mg, 0.0280 mmol) in THF, Cp^*_2Co (10.3 mg, 0.0313 mmol) was added and allowed to stir for 30 min, yielding black microcrystalline precipitate and a transparent brown filtrate. The solid was isolated and purified by CH_3CN/Et_2O vapor diffusion at –13 °C to afford large black crystals that were characterized by ^{1}H NMR analysis. Yield: 19.2 mg (52%).

2.3.3 X-Ray Crystallography

Single crystals suitable for single crystal X-ray diffraction analysis were obtained from a $MeCN/Et_2O$ vapor diffusion at –15°C ($[Ph_4P]_2$**6**, as black blocks), storage of a concentrated THF solution at –15 °C (**5**, as light green plates), and from a $MeCN/Et_2O$

vapour diffusion at –15 °C (**4**, as colorless needles). Unit cell data and crystallographic data for **4** and $[Ph_4P]_2$**6** are found in Table 2.11 and Table 2.12, respectively.

Table 2.11. Selected crystallographic data for $FeCl_2(NH_2{}^tBu)_2$ (**4**)

Parameter	Original data set (2001)	Unit Cell (2019)
a, Å	12.078(2)	12.08(3)
b, Å	12.901(2)	12.89(3)
c, Å	18.348(3)	18.34(4)
α, °	94.460(5)	94.45(2)
β, °	95.046(8)	95.14(2)
γ, °	96.838(9)	96.89(3)
V, Å^3	2816.53	2814
T, K	200	273

Table 2.12. Crystallographic data summary for $[Ph_4P]_2[Fe_4(N^tBu)_4Cl_4]$ ($[Ph_4P]_2$**6**)

	$[Ph_4P]_2$**6**
Formula	$[Ph_4P]_2[Fe_4(N^tBu)_4Cl_4]$
MW	1328.45
Space group	$P2_1/n$ (no. 14)
a, Å	19.8534(13)
b, Å	15.0228(10)
c, Å	24.8990(17)
β, °	111.067(2)
V, Å^3	6929.9(8)
θ_{max}, °	28
$R_1(wR_2)$, %	6.51 (17.34)
Tot. data, %	99.9
S	1.057

2.3.4 Electrochemical Analysis

Cyclic voltammograms were recorded on a SP-150 potentiostat using platinum working and counter electrodes, and a nonaqueous $Ag/AgNO_3$ (0.01 M) reference electrode. Measurements for $[Ph_4P]_2$**6** were conducted using a standard three-electrode cell and 0.1 M

(n-Bu_4N)(ClO_4)(TBAP) supporting electrolyte in MeCN. To prevent contamination of the reference electrode with chloride, a dual compartment cell was used to separate the analyte solution (0.1 M(n-Bu_4N)Cl/MeCN), containing the working and counter electrodes, from the reference electrode (0.1 M TBAP/MeCN); a fine porosity frit connected the two compartments. Potentials were referenced internally to the ferrocene/ferrocenium ($Fc^{0/+}$) couple, then converted to the SCE scale ($Fc^{+/0}$ = +0.38 V vs SCE in 0.1 M TBAP/MeCN).

2.3.5 ^{1}H qNMR Analysis

In-situ ^{1}H NMR yields were calculated using the calibrated residual protio signal of the deuterated NMR solvent. NMR solvents used for qNMR analysis within this thesis (CD_3CN, C_6D_6 and THF-d_8 were all dried in the commercial bottle over sieves (except THF-d_8 that was purchased in an ampule)) and portioned into smaller bottles with sieves. Storing the NMR solvents over sieves kept the residual protio signal constant while if the solvent was stored over neutral alumina, the residual protio signal increased over time. The NMR calibrants used for CD_3CN were caffeine and 1,4-dinitrobenzene while just 1,4-dinitrobenzene was used to calibrate the residual protio signal for THF-*d8* and C_6D_6. To ensure complete dissolution of the calibrants, a pipette was used to stir the solution, and the solution was directly added into the NMR tube. The difference in concentration of CD_2HCN between the two calibrants used should not exceed 10%. The residual protio signal was then compared with different aliquots from the same stock bottle. The relaxation delay (d1) was determined for each NMR solvent by collecting ^{1}H NMR data at different d1 values to determine when the proton is relaxed. The optimal relaxation delay was determined to be 150 s, 300 s and 600 s for CD_3CN, THF-d_8 and C_6D_6, respectively.

Chapter 3: Polymorphism of Lithium *tert*-Butylamide

3.1.1 Introduction

Alkali metal organoamide compounds are utilized as strong Brønsted bases or as ligands in the synthesis of transition metal complexes. The most common alkali metal amides are lithium amides (LiNRR′), although sodium amides (NaNRR′) and potassium amides (KNRR′) have also been synthesized, albeit with less structural information reported.[60] The common syntheses of alkali metal organoamide compounds are highlighted in Scheme 3.1. Lithium amides are typically formed by the deprotonation of amines with *n*-BuLi (A.1), while sodium amides are generally prepared by reacting the amine with *n*-BuNa (B.1), $NaNH_2$ (B.2) or Na (B.3). Potassium amides can be synthesized by the reaction of lithium amides with potassium *tert*-butoxide (C.1) and by the reaction of amines with potassium metal (C.2) or with potassium hydride (C.3). In organic synthesis, disubstituted lithium amides (e.g. lithium diisopropylamide (LDA)) are widely used due to their strong Brønsted basicity, solubility in non-polar solvents, and non-nucleophilic nature. In inorganic synthesis, lithium amides (e.g. lithium bis(trimethylsilyl)amide (LiHMDS) and lithium *tert*-butylamide (LiNH^{t}Bu)) are employed as ligands in transition metal complexes or as precursors for inorganic clusters that contain the amide $(NRR')^{1-}$ or imide $(NR)^{2-}$ functionality.[60, 2]

[2] Preliminary work on the synthesis of LiNH^{t}Bu was performed by Dion Grobe. ^{1}H DOSY protocol was set up and validated by Dr. Blossom Yan.

Scheme 3.1. Common reactions in the formation of alkali metal organoamide compounds

A.1 $n\text{-BuLi} + \text{RR}'\text{NH} \longrightarrow \text{LiNRR}' + n\text{-Bu}$

B.1 $n\text{-BuNa} + \text{RR}'\text{NH} \longrightarrow \text{NaNRR}' + n\text{-Bu}$

B.2 $\text{NaNH}_2 + \text{RR}'\text{NH} \longrightarrow \text{NaNRR}' + \text{NH}_3$

B.3 $2\ \text{Na} + 2\ \text{RR}'\text{NH} \longrightarrow 2\ \text{NaNRR}' + \text{H}_2$

C.1 $\text{KO}^t\text{Bu} + \text{LiNRR}' \longrightarrow \text{KNRR}' + \text{LiO}^t\text{Bu}$

C.2 $2\ \text{K} + 2\ \text{RR}'\text{NH} \longrightarrow 2\ \text{KNRR}' + \text{H}_2$

C.3 $\text{KH} + \text{RR}'\text{NH} \longrightarrow \text{KNRR}' + \text{H}_2$

The structures of lithium amides can be categorized into two types: oligomers and polymers. Most structures of lithium amides reported are of the oligomer type in which the oligomers can be further split into the following categories: mononuclear[61,62] (**A**), four–[63–68] (**B**), six–[69,70] (**C**) or eight–[71](**D**) membered rings, six–[72–74] (**E**) and eight–[59,75] (**F**) membered cyclic ladders and a four rung ladder[76–81] (**G**) as shown in Figure 3.1. Disubstituted amides (LiNRR′) crystallized from noncoordinating solvents typically form six– and eight–membered rings while monosubstituted amides (LiNHR) crystallized from non-coordinating solvents typically form either an infinite polymer or cyclic ladder oligomer. When lithium amides are crystallized in the presence of chelating solvents, like tetramethylethylenediamine (TMEDA), both LiNRR′ and LiNHR form four-rung ladders and from coordinating solvents, dinuclear complexes, which result from coordination of lithium by the solvent. Mononuclear structures are usually observed from secondary lithium amides crystallized in the presence of crown ethers. The infinite polymer structure type is scarcer than the oligomer structure types.

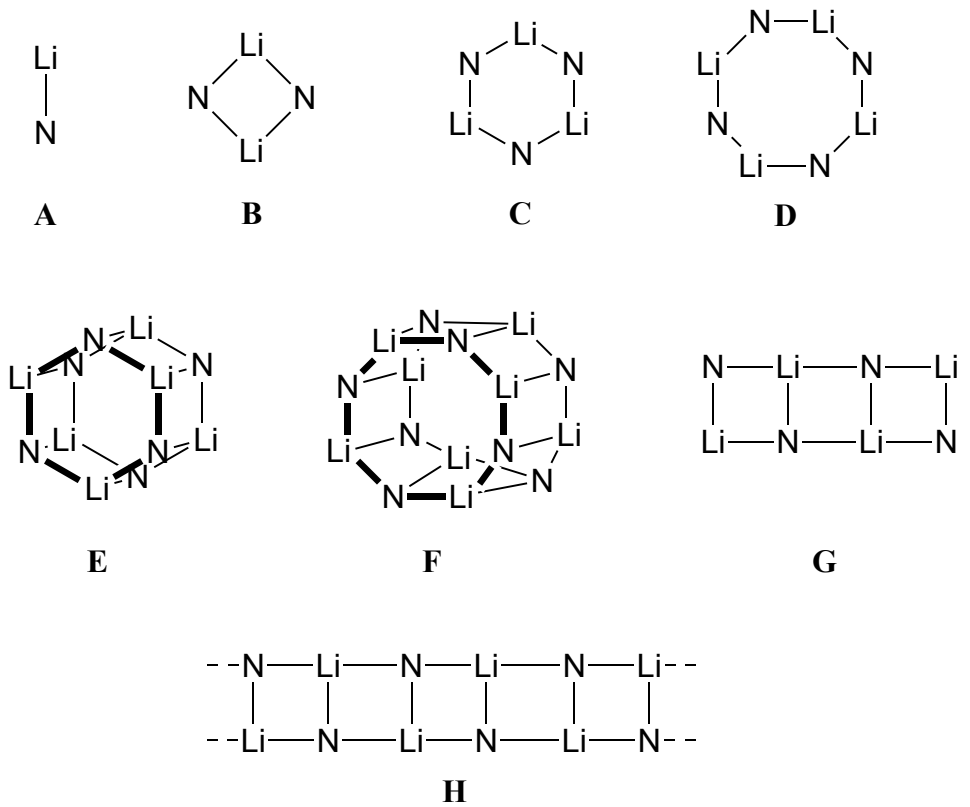

Figure 3.1. Common structure types of lithium amides characterized by single crystal X-ray diffraction analysis. Structure types include (A) mononuclear, (B) dinuclear, four-membered rings, (C) trinuclear, six-membered rings, (D), tetranuclear, eight-membered rings, (E) six membered, cyclic ladder (F) eight membered, cyclic ladder (G) four-rung ladder and (H) polymeric ladder. Nitrogen R groups omitted for clarity.

The ladder structure types shown follow the principles of ring-laddering, which describe the self-assembly of $(LiN)_2$ dimers as simplified in Scheme 3.2.[60,82–84] The size, reaction solvent, and stereochemistry of the amide influence the degree of ring-laddering observed.

Scheme 3.2. General example of ring-laddering

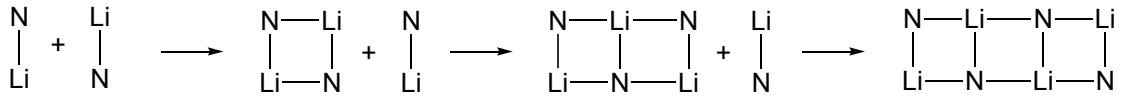

The in-solution structures of lithium amides may differ slightly from those observed in the solid state. The in-solution structures are determined using NMR spectroscopy,

specifically techniques such as diffusion-ordered spectroscopy (DOSY)[85–98] and isotopic labelling experiments with ^{6}Li and ^{15}N labels[99–108]. The DOSY experiments provide information about the molecular masses of these aggregates based on experimentally determined diffusion coefficients, while the NMR labelling experiments offer additional information on the lithium and nitrogen environments within these aggregates. However, there are inherent limitations in fully characterizing their structures in solution. DOSY does not provide any structural information about the aggregate in solution and relies on using precedent and an educated guess to determine a structure based on molecular mass. Isotopic labelling experiments do provide structural information but also requires inference to produce a structure that is consistent with the data. Despite these challenges, reported data suggest that the solution-state structures of lithium amides may closely resemble their solid-state counterparts.

3.1.2 Lithium *tert*-butylamide

The lithium amide of interest in our laboratory is lithium *tert*-butyl amide, [(LiNH^{t}Bu)$_8$·C$_6$H$_{14}$](**8**).[59] As discussed in Chapter 2, **8** serves as a nitrogen anion source in the synthesis of [Ph$_4$P]**2**. The synthesis of **8**, developed by Williard and coworkers proceeds via lithiation of ^{t}BuNH$_2$ by *n*-BuLi in hexanes (Scheme 3.1(A.1)). Crystallographic analysis revealed its solid-state structure to be the novel octameric cyclic ladder shown in Figure 3.2.

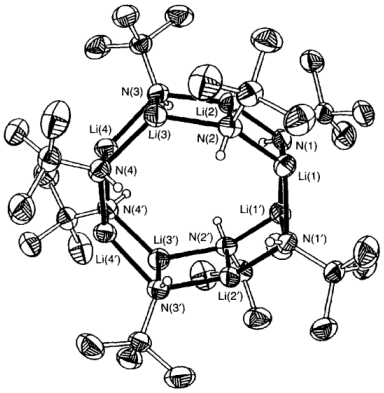

Figure 3.2. Published structure of [(LiNH^{t}Bu)$_8$·C$_6$H$_{14}$] (**8**). Barnett, N. D. R.; Clegg, W.; Horsburgh, L.; Lindsay, D. M.; Liu, Q.-Y.; Mackenzie, F. M.; Mulvey, R. E.; Williard P. G., *Chem. Commun.*, **1996**, *5*, 231–2322, with permission from The Royal Society of Chemistry.

Structure **8** was the first example of a large molecular aggregate of lithium amides, compared to the numerous reports of dinuclear lithium amide structures from crystallization from coordinating solvents and the handful of infinite polymeric structures from crystallization from non-coordinating solvents. Williard *et al*. also investigated the deprotonation of ^{t}BuNH$_2$ with other strong bases including *n*-BuNa and a mixture of *n*-BuNa and *n*-BuLi (reaction from Scheme 3.1 (B.1)).[80] These reactions yielded [(NaNH^{t}Bu)$_3$^{t}BuNH$_2$]$_\infty$, an infinite polymer containing Na and ^{t}BuNH$_2$ per three NaNH^{t}Bu units, and [(LiNa[NH^{t}Bu]$_2$)$_2$(TMEDA)$_2$], a four-rung ladder containing both Na^+ and Li^+ ions, with structures shown in Figure 3.3.

A

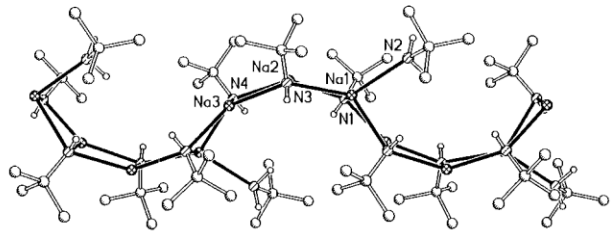

B

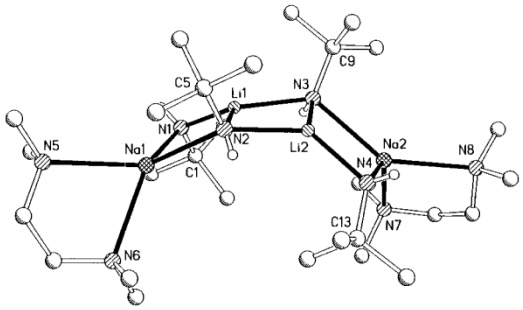

Figure 3.3. Crystal structures of other (^{t}BuHN)$^-$ compounds, [(NaNH^{t}Bu)$_3$^{t}BuNH$_2$]$_\infty$ and [(LiNa[NH^{t}Bu]$_2$)$_2$(TMEDA)$_2$]. Reproduced from Clegg, W.; Henderson, K. W.; Horsburgh, L.; Mackenzie, F. M.; Mulvey, R. E., *Chem. Eur. J.,* **1998**, 4 (1), 53–56, with permission from Wiley-VCH.

The synthesis of **8** in our lab led to the discovery of a second form of LiNH^{t}Bu with differing solubility properties from the original octameric cyclic ladder. Instead of the reported form, which is highly soluble in nonpolar solvents like pentane, LiNH^{t}Bu was isolated with an infinite polymeric ladder ((LiNH^{t}Bu)$_\infty$ (**9**)) structure that is insoluble in nonpolar solvents. Solubility was tested by attempted dissolution of the material in organic solvents, followed by filtration, solvent removal of the filtrate under reduced pressure and

addition of C_6D_6 to the reaction flask. This finding prompted an investigation into the reactivity of the second form and the relationship of **8** to **9**. Solid-state and solution characterization of **8** and **9** revealed that **8** can be converted to **9** using various methods.

3.2 Results and Discussion

3.2.1 Synthesis of Lithium *tert*-Butylamide

The synthesis of LiNH^{t}Bu (**8**), as described in the literature, involves the deprotonation of ^{t}BuNH$_2$ with one equivalent of *n*-BuLi in hexanes as shown in Scheme 3.3. The initial reaction is highly exothermic, necessitating careful control of the ^{t}BuNH$_2$ addition rate to prevent ^{t}BuNH$_2$ evaporation before the reagent reaches the reaction solution. After an hour, the solution is concentrated *in vacuo* until a white solid crystallizes out of solution. The solid is redissolved by gentle heating and placed at –20 °C overnight. The solid is then harvested via cannula filtration and the white powder is dried *in vacuo* to remove trapped hexanes.

Scheme 3.3. Literature synthesis of (LiNH^{t}Bu)$_8$ (**8**)

$$8\ n\text{-BuLi} + 8\ {}^t\text{BuNH}_2 \xrightarrow[\text{hexanes}]{} (\text{LiNH}^t\text{Bu})_8\ (\mathbf{8})$$

Our lab deviates from the reported preparation of **8** by employing a slight excess of ^{t}BuNH$_2$ in the reaction (~1.05 equivalents) to account for evaporation and ensure complete consumption of *n*-BuLi. However, when more than 1.05 equivalents of ^{t}BuNH$_2$ are used (ca. 1.10), white solid rapidly precipitated from the solution (within minutes) forming a colloidal suspension. Solvent removal of the white colloidal suspension *in vacuo* yielded a white powder with different solubility from the reported form. The second form is a white solid that is insoluble in low coordinating solvents like hexanes, pentane, toluene, benzene and ether. However, the new form displays solubility in THF and single crystals were grown via THF/pentane vapour diffusion. Single crystal X-ray diffraction analysis revealed that the structure of the second form is an infinite polymeric ladder, (LiNH^{t}Bu)$_\infty$ (**9**). Compound **9**

can be directly synthesized from the reaction of *n*-BuLi with 1.10 equivalents of $^{t}BuNH_2$ shown in Scheme 3.4.

Scheme 3.4. Synthesis of $(LiNH^{t}Bu)_{\infty}$ (**9**)

$$n\text{-BuLi} + 1.1\ ^{t}BuNH_2 \xrightarrow[\text{hexanes}]{} (LiNH^{t}Bu)_{\infty}\ (\mathbf{9})$$

Partial crystallographic data of a second form of **8** was footnoted by Williard and coworkers in the original $LiNH^{t}Bu$ communication.[59] Only the space group (*I*2/a), volume (4675(3) $Å^3$) and collection temperature (160 K) were reported in the footnote. This form was] obtained by dissolving the hexane-solvated cyclic ladder in toluene, and after volume reduction, led to the isolation of single crystals. Single-crystal X-ray diffraction analysis revealed a similar cyclic ladder structure as **8** but with no solvent present in the crystal lattice, $(LiNH^{t}Bu)_8$ (**10**).

3.2.2 Single Crystal X-ray Diffraction Analysis

The determination of structures was undertaken using single crystal XRD analysis. Single crystals of **9** and **10** were grown and the resulting structures are shown in Figure 3.4 and Figure 3.5 respectively. The metrics of **9** and **10** are shown in Table 3.1. The metrics of **9** are for one $LiNH^{t}Bu$ unit in the asymmetric unit of **9** while the metrics of **10** are an average of the four $LiNH^{t}Bu$ molecules in the asymmetric unit of **10**. The structure of **9** is an infinite, polymeric ladder where the nitrogen is in a four coordinate, tetrahedral environment and the lithium are in a three coordinate, almost trigonal planar geometry. The solid-state structure of compound **10** is like **8** as **10** displays an octameric, cyclic ladder structure.

Table 3.1. Selected distances (Å) and angles (º) for $(LiNH^{t}Bu)_{\infty}$ (**9**) and $(LiNH^{t}Bu)_8$ (**10**)

	$(LiNH^{t}Bu)_{\infty}$ (**9**)	$(LiNH^{t}Bu)_8$(**10**)
Li(1)–N(1/2/1')		2.0191(26)/2.0596(27)/2.0683(30)
Li(2)–N(1/2/3)		2.0622(26)/2.0430(26)/2.0561(29)
Li(3)–N(2/3/4)		2.0391(27)/2.0288(25)/2.0650(31)
Li(4)–N(3/4/4')		2.0408(27)/2.0225(25)/2.0547(25)
Li(1)–N(1)	2.0240(28)	
Li(1)–N(1)–Li(2/1')		72.14(10)/72.42(11)

	$(LiNH^tBu)_\infty$ (**9**)	$(LiNH^tBu)_8$(**10**)
Li(1/2)–N(2)–(2/3)		71.71(10)/70.66(10)
Li(2/3)–N(3)–Li(3/4)		70.60(10)/72.37(10)
Li(3/4)–N(4)–Li(4/4')		72.00(10)/71.77(11)
Li(1)–N(1)-Li(1’)	71.04(11)	
N(1)–Li(1)–N(1'/2)		107.52(11)/108.56(13)
N(1/2)–Li(2)–N(2/3)		107.54(12)/108.59(11)
N(2/3)–Li(3)–N(3/4)		109.82(11)/107.22(11)
N(3/4)–Li(4)–N(4/4')		108.40(11)/107.87(11)
N(1)–Li(1)–N(1’)	107.13(11)	

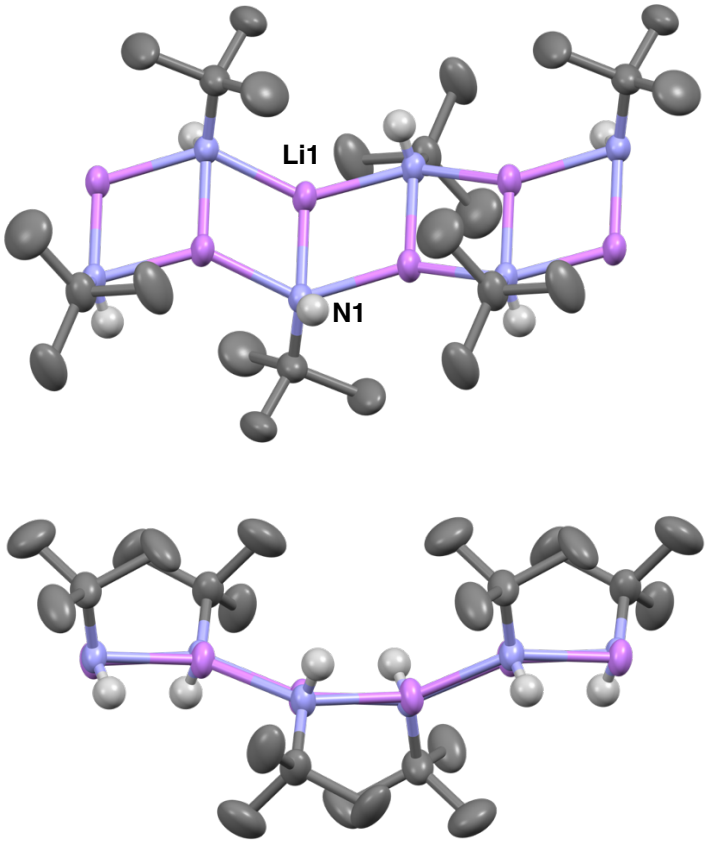

Figure 3.4. Structure of $(LiNH^tBu)_\infty$ (**9**) with thermal ellipsoids (50% probability level) and selected atom labels. For clarity, ^{t}Bu hydrogen atoms are not shown. One unit of $LiNH^tBu$ is present in the asymmetric unit with other atoms generated by crystallographic 2-fold rotation.

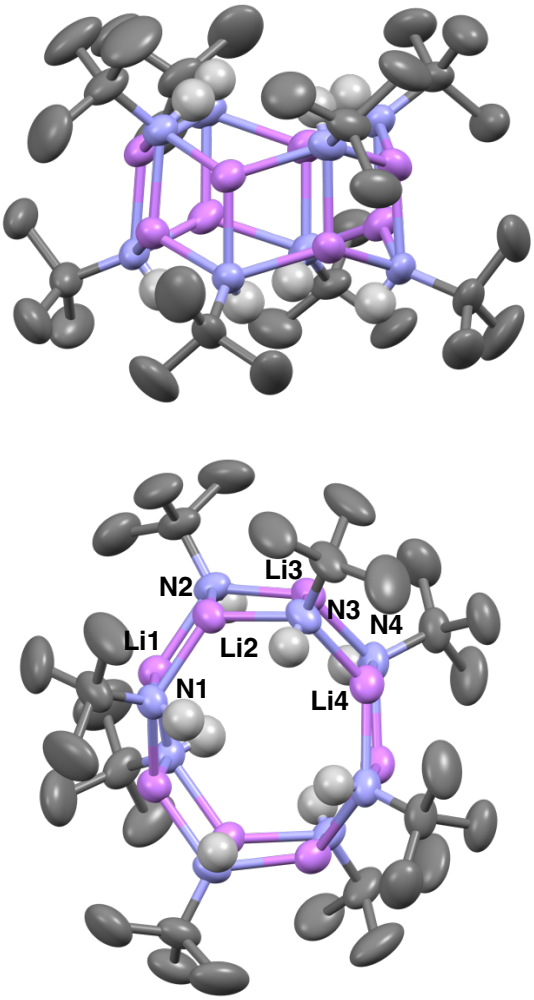

Figure 3.5. Structure of (LiNH^{t}Bu)$_8$ (**10**) with thermal ellipsoids (50% probability level) and selected atom labels. For clarity, ^{t}Bu hydrogen atoms are not shown. Four molecules of LiNH^{t}Bu are present in the asymmetric unit with other atoms generated by crystallographic 2-fold rotation.

The averaged metrics of Li–N, Li···Li, N···N, Li–N–Li and N–Li–N for **8**, **10** and **9** are presented in Table 3.2. Li–N–Li^a and N–Li–N^a bond angles are the angles within a Li_2N_2 diamond, while Li–N–Li^b and N–Li–N^b angles represent the angles between Li_2N_2 diamonds. The bond angle for **9** was measured from the generation of atoms by the crystallographic 2-fold rotation. These metrics do not significantly vary between the three forms which can signify that the ladder rungs for both the infinite polymer and cyclic ladder are the same. This

observation can relate both **8** and **10** to **9** with **9** being **8**/**10** unraveled from the cyclic form to a linear form.

Table 3.2. Selected averaged distances (Å) and angles (º) for $(LiNH^tBu)_8C_6H_{14}$ (**8**), $(LiNH^tBu)_\infty$ (**9**) and $(LiNH^tBu)_8$ (**10**)

Average Selected Metrics	**8**	**10**	**9**
Li–N (Å)	2.050(15)	2.047(17)	2.05(3)
Li–N–Li^a (°)	71.8(4)	71.7(7)	71.9(9)
N–Li–N^a (°)	108.2(5)	108.2(8)	108.1(9)
Li–N–Li^b (°)	122(4)	122(8)	n/a
N–Li–N^b (°)	124(3)	123(4)	n/a

Metrics for **8** and **10** were averaged from four molecules of $LiNH^tBu$

Shown in Figure 3.6 is the superposition of the 16 atom Li and N core of **8** (in green) and **10** (in purple) aligned to minimize the root-mean-square deviation (RMSD), which was calculated to be 0.1356 Å. Different orientations of **10** were tested to minimize the RMSD with the orientation shown providing the lowest RMSD value. The superposition reveals that the Li and N (16-atom cores) of **8** and **10** are nearly identical, with slight deviations likely arising from differences in data collection temperatures. The Li–N–Li^b angle of **10** showcased a larger standard deviation compared to **8**, likely due to **10** displaying a more oval shape compared to the circular shape of **8**.

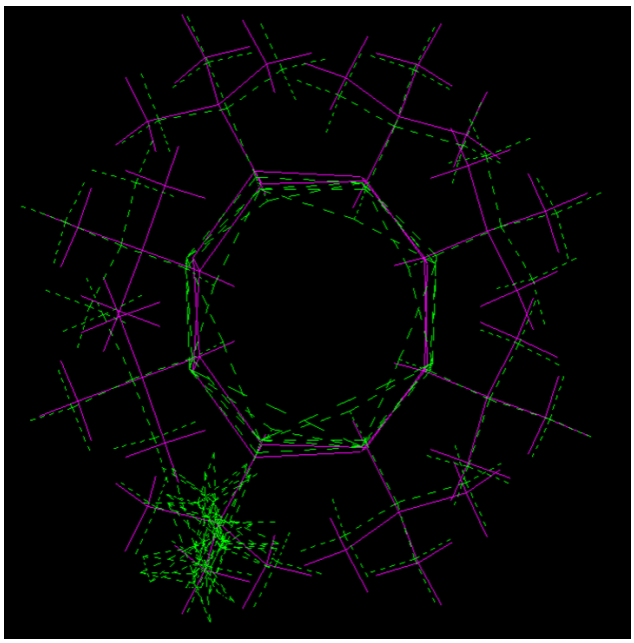

Figure 3.6. Superposition of the 16 atom Li_8N_8 core of **8** (green) and **10** (purple).

The metrics of **8**, **9** and **10** can also be compared to the other (^{t}BuHN)$^-$ structures published, $[(NaNH^tBu)_3{}^tBuNH_2]_\infty$ and $[(LiNa[NH^tBu]_2)_2(TMEDA)_2]$ shown in Figure 3.7. [80]

A

B

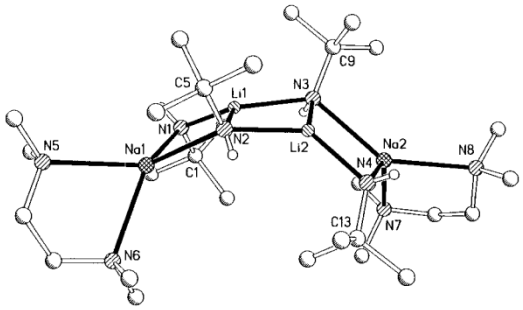

Figure 3.7. Crystal structures of other $^-$(NH^{t}Bu) compounds, $[(NaNH^tBu)_3{}^tBuNH_2]_\infty$ and $[(LiNa[NH^tBu]_2)_2(TMEDA)_2]$. Reproduced from Clegg, W.; Henderson, K. W.; Horsburgh, L.; Mackenzie, F. M.; Mulvey, R. E., *Chem. Eur. J.,* 1998, 4 (1), 53–56, with permission from Wiley-VCH.

The structure of $[(NaNH^tBu)_3{}^tBuNH_2]_\infty$ is an infinite polymeric structure, like the structure type of **9** except $[(NaNH^tBu)_3{}^tBuNH_2]_\infty$ contains one Na^+-coordinated with a $^tBuNH_2$ molecule per three $NaNH^tBu$. A comparison of structures **9** and $[(NaNH^tBu)_3{}^tBuNH_2]_\infty$ reveals distinct overall structure types. In the structure of **9**, the polymer consists of alternating cis and trans amido groups, with the arrangement shifting after each dimeric ring. Similarly, the structure of $[(NaNH^tBu)_3{}^tBuNH_2]_\infty$ contains both cis and trans amido groups; however, the pattern alternates following the sodium ion coordinated to $^tBuNH_2$. The structure of $[(NaNH^tBu)_3{}^tBuNH_2]_\infty$ can be visualized as a repeating unit of $((NaNH^tBu)_3{}^tBuNH_2)$ where each successive unit is flipped. Mulvey and coworkers attributed this change in orientation to the steric bulk of the solvating $^tBuNH_2$.[80]

The structure of $[(LiNa[NH^tBu]_2)_2(TMEDA)_2]$ is viewed as a four-rung ladder structure type. The sodium ions are at the ends of the ladder while the two lithium ions are found within the second and third ladder rung. The lithium ions are three coordinate, only coordinated by the nitrogen amides while the sodium ions are four coordinate, coordinated by two nitrogen amides and by one molecule of TMEDA each. Tabulated in Table 3.3 are selected interatomic distances and angles of $[(NaNH^tBu)_3{}^tBuNH_2]_\infty$ and $[(LiNa[NH^tBu]_2)_2(TMEDA)_2]$. The Na–N bond length in both $[(NaNH^tBu)_3{}^tBuNH_2]_\infty$ and $[(LiNa[NH^tBu]_2)_2(TMEDA)_2]$ exhibit longer lengths by 0.3 to 0.4 Å compared to Li–N bond lengths found in **8** and **9**. Comparing $[(NaNH^tBu)_3{}^tBuNH_2]_\infty$ and **9**, the M–N–M bond angle in **9** is smaller by 4 °while the N–M–N bond angle is larger by 5 °.

Table 3.3. Selected averaged interatomic distances (Å) and angles (°) of $[(NaNH^tBu)_3{}^tBuNH_2]_\infty$ and $[(LiNa[NH^tBu]_2)_2(TMEDA)_2]$

	$[(NaNH^tBu)_3{}^tBuNH_2]_\infty$	$[(LiNa[NH^tBu]_2)_2(TMEDA)_2]$
Na–N (Å)	2.420(64)	2.393(80)
Li–N (Å)		1.98(66)
Na–N–Na^a (°)	76.1(4)	
Na–N–Li^a (°)		
Li–N–Li^a (°)		71.8(6)
N–Na–N^a (°)	103(4)	89.85(21)
Na–N-Li^a (°)		77(3)
N–Li–N^a (°)		112(5)
Na–N–Na^b (°)	136(2)	
Li–N–Na (°)		130.7(1)
N–Na–N^b (°)	129(2)	

	$[(NaNH^tBu)_3{}^tBuNH_2]_\infty$	$[(LiNa[NH^tBu]_2)_2(TMEDA)_2]$
N–Li–N[b] (°)		130.1(1)

Values for $[(NaNH^tBu)_3{}^tBuNH_2]_\infty$ and $[(LiNa[NH^tBu]_2)_2(TMEDA)_2]$ determined from bond lengths and angles of one asymmetric unit for each. Asymmetric unit of $[(NaNH^tBu)_3{}^tBuNH_2]_\infty$ contains $(NaNH^tBu)_3{}^tBuNH_2$.

3.2.3 Conversion of Polymorphs

Compounds **8**, **9** and **10** can be classified as pseudo-polymorphs where each compound displays the same molecular formula with different molecular structure or crystal structures. The comparison of **8** and **9** is noteworthy as both compounds exhibit the same molecular formula but differ in how the atoms are arranged in the solid state (as discussed above). The formation and isolation of **9** led to the investigation of the relationship between **8** and **9**. The interconversion of the forms was undertaken to see if **8** could be opened to **9** and/or if **9** could be sliced and wrapped to form **8**. Numerous experiments were conducted to observe this polymorph conversion as summarized in Table 3.4. Different conditions such as solvent, temperature and addition of a donating solvent were tested/studied to observe the transformation. To our knowledge, while the interconversion of polymorphs with the same connectivity but different crystal structures has been reported, the ring opening and interconversion between structural polymorphs have not been reported in the literature. Only the conversion of **8** to **9** was observed and the conversion of **9** to **8** was not observed, highlighting the differences between the two forms.

PXRD analysis and ^{1}H NMR spectroscopy analyzed in C_6D_6 were used to verify if interconversion occurred as both **8** and **9** have distinct PXRD patterns (see section 3.2.4) and **8** displays solubility in C_6D_6 while **9** does not. Since the isolation of **9** is conducted via the addition of 1.1 equivalents of $^tBuNH_2$, the dissolution of **8** in hexanes followed by the addition of 0.1 equivalents of $^tBuNH_2$ led to the formation of a white colloidal solution. After solvent removal *in vacuo*, the dissolution of the white powder in C_6D_6 was attempted, but no signals were observed using ^{1}H NMR spectroscopy. Both **8** and **9** display solubility in THF and single crystals of **9** were obtained via THF/pentane vapour diffusion. This prompted an investigation into the structural changes that occur upon dissolving **8** in THF, followed by either solvent with removal under reduced pressure or recrystallization via THF/pentane vapour diffusion. A control was performed with **8** dissolved in hexanes which was allowed to

stand for 21 days. In this time, no precipitation was found. The methods outlined below provide a rationale for identifying **8** as the metastable form and **9** as the thermodynamic form.

Table 3.4. Polymorph conversion data of **8** to **9** using various methods

	Method	Solvent	Conc.	Temp.	Time	Determination of form	Yield
(i)[a]	Dissolution	THF	0.2 M	~25 °C	1 hr.	Solubility/PXRD	N/A
(ii)[b]	Vapor Diffusion	THF/Pentane	0.4 M	~25 °C	1 day	Solubility/PXRD	60%
(iii)[b]	0.1 equiv of $^{t}BuNH_2$	Hexanes	0.9 M	~25 °C	2 hr.	Solubility/PXRD	84%
(iv)[b]	0.1 equiv of THF	Hexanes	0.9 M	~25 °C	1 day	Solubility	76%
(v)[b]	Seed with $(LiNH^{t}Bu)_{\infty}$	Hexanes	0.8 M	~25 °C	20 days	Solubility	84%
(vi)[b]	Dissolution	Diethyl ether	0.4 M	~25 °C	1 hr.	Solubility	72%
(vii)	Solid-solid conversion	N/A	N/A	200 °C	1 hr.	Solubility/PXRD	~44%[b]

[a] After dissolution in THF, solvent removal was performed under reduced pressure to isolate white solid [b] White solid was present after reaction time. Solid was isolated by pipetting solvent and drying via box purging [c] conversion presumed to be quantitative

The observations from points (i) and (ii) can be rationalized as follows: dissolution of **8** in THF, a coordinating solvent, leads to the breakdown of the cyclic ladder structure into smaller oligomers. A common structural motif for lithium amides in coordinating solvents consists of dinuclear species with one or two THF molecules coordinating to the bridging lithium, which supports this rationale. Upon solvent removal or under crystallization conditions, the form that appears is the polymeric ladder due to the ring-laddering principle.

The synthesis of **9** requires excess $^{t}BuNH_2$ (ca. 1.1 equivalents of $^{t}BuNH_2$). To determine whether **9** forms directly from **8** or via a different reaction pathway, a catalytic amount (0.1 equivalents) of $^{t}BuNH_2$ and THF (another coordinating solvent) were added to **8** in hexanes. Observations from points (iii) and (iv) suggest that **8** initially forms in hexanes, while the addition of $^{t}BuNH_2$ (or THF), acting as both a coordinating solvent and ligand, catalyzes its transformation into **9**. The faster conversion of **8** to **9** in the presence of $^{t}BuNH_2$ compared to THF is attributed to the stronger donating ability of $^{t}BuNH_2$.

When **8** was dissolved in hexanes and left undisturbed for several weeks, no precipitation was observed. However, adding small amounts of **9** (spatula tip) to a solution of **8** in hexanes led to the precipitation of **9** within 20 days. This finding (v) suggests a seeding mechanism in which **9** provides a crystallographic template, facilitating the transformation of **8** into **9**.

The conversion of **8** to **9** was also tested in diethyl ether, another ethereal coordinating solvent. **8** displayed good solubility in diethyl ether but precipitated as **9** within an hour. This result (vi) is consistent with observations in THF. However, the lower polarity of diethyl ether and weaker coordination ability compared to THF likely provides insufficient stabilization for the ionic components, favoring precipitation as **9.**

Heating **8** to 200 °C provided further insights into the stability of these compounds. Solid **8**, heated for 1 hour at this temperature, converted to **9**. This result (vii) suggests that **8** represents a metastable form, while **9** is the thermodynamically favored form under these conditions. This thermodynamic relationship is further explored in Section 3.2.5.

Finally, **8** converts to **10** upon drying, as confirmed by PXRD analysis. This conversion is not unexpected, given that **8** and **9** share the same structural motif but differ in the presence of solvent within the crystal lattice.

3.2.4 Powder X-ray Diffraction Analysis

Experimental PXRD data for **8** and **9** are shown in Figure 3.8. Both phases have distinct PXRD patterns which allow PXRD analysis to be used to determine which form is present.

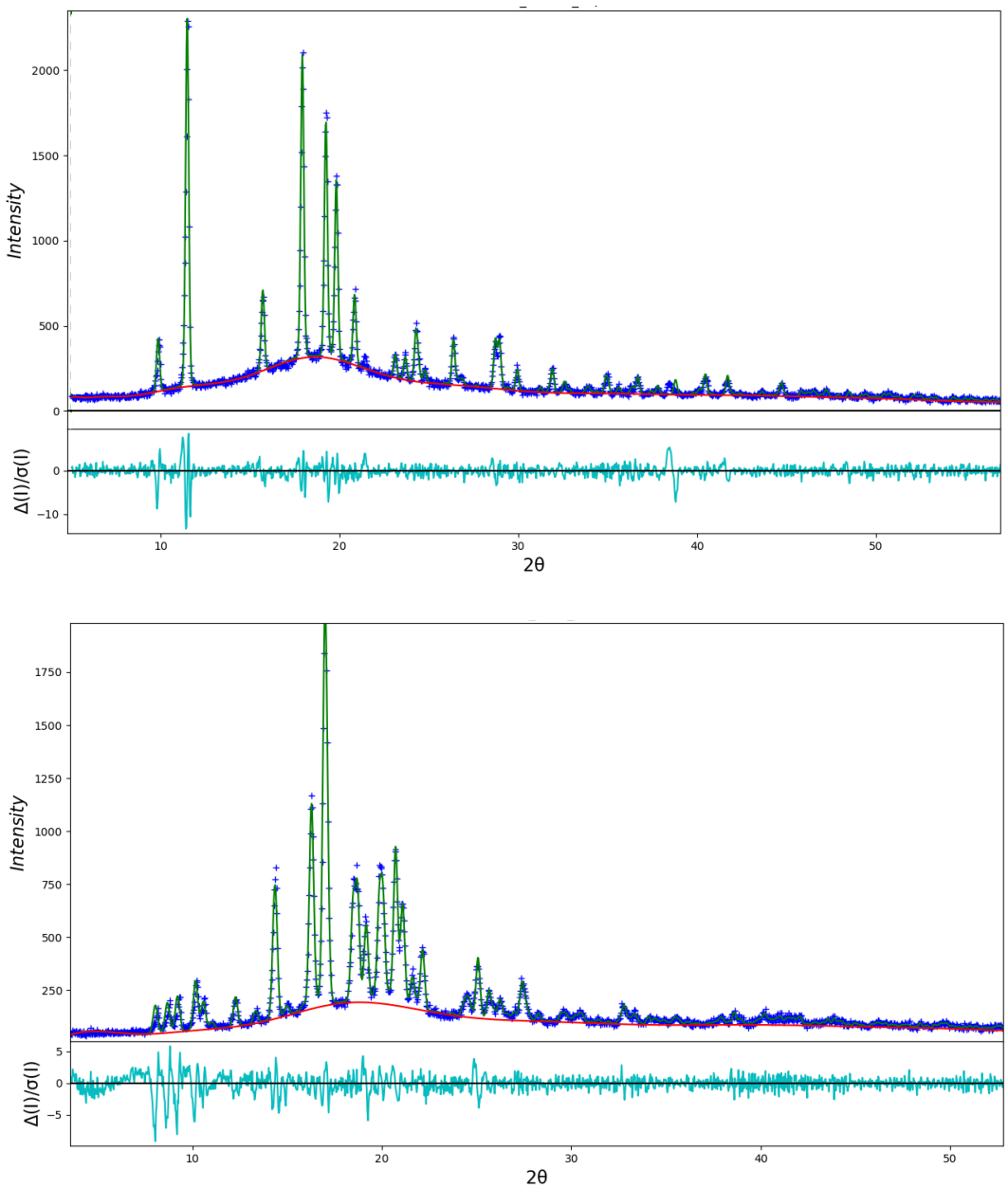

Figure 3.8. Fitted PXRD Data for $(LiNH^tBu)_8$ (**8**) and $(LiNH^tBu)_\infty$ (**9**). Experimental data shown as blue points, while the green line represents the calculated PXRD pattern based on single crystal X-ray diffraction data. The red line indicates the baseline correction, and the teal line shows the difference between the experimental and calculated patterns.

3.2.5 Differential Scanning Calorimetry Analysis

Differential scanning calorimetry (DSC) was performed on **9** and **8** to observe thermal properties as shown by the thermograms in Figures 3.9 and 3.10. Calorimetry data can be found in Table 3.5. DSC analysis on **9** was carried out under two different experimental conditions: (A) cooling immediately after the melting feature and (B) cooling approximately 25 °C after the melting feature, as shown in Figure 3.8.

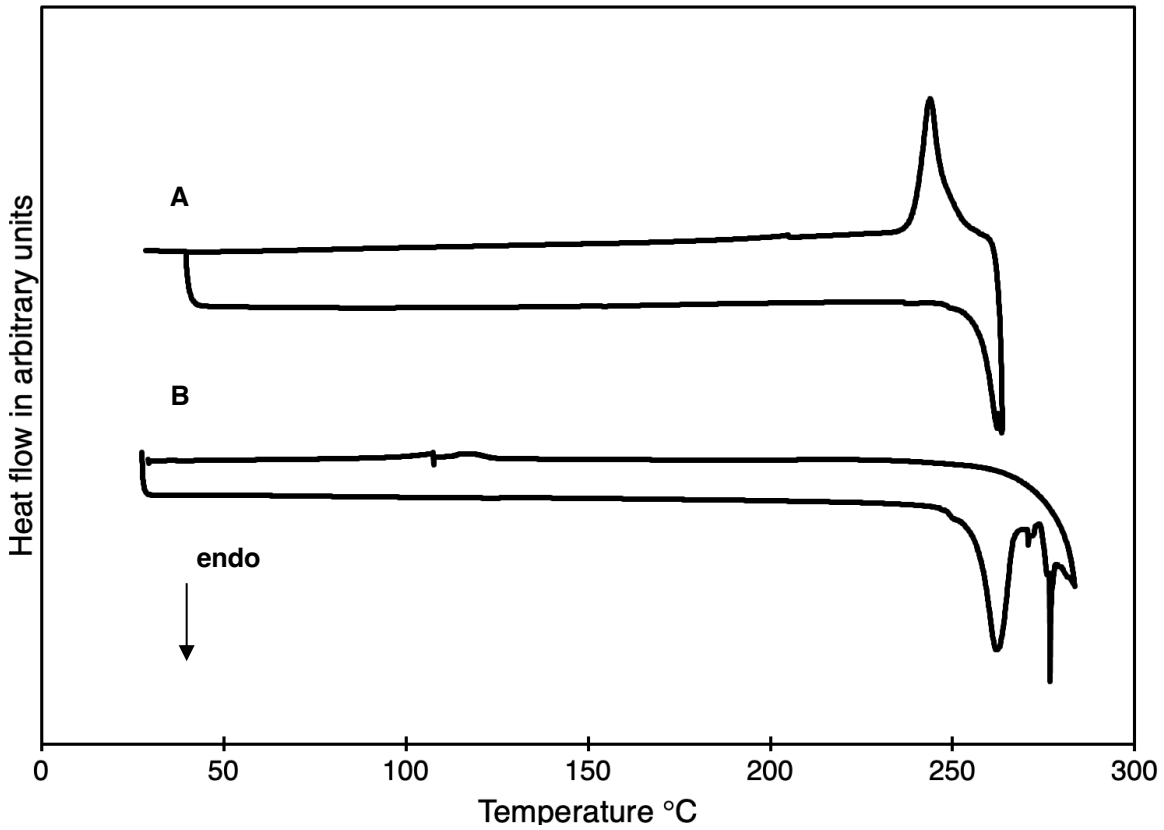

Figure 3.9. DSC curve at 10 °C/min for $(LiNH^tBu)_\infty$ (**9**). Parameters for run A: Mass of **9** was 3.6 mg, starting temperature set to 40 °C and ramp rate was 10.00 °C/min. Parameters for run B: Mass of **9** was 3.7 mg, starting temperature set to 40 °C and ramp rate was 10.00 °C/min.

The common feature in both thermographs of **9** was an endothermic peak with an onset temperature (T_e) at around 257 °C, consistent with melting of the material. When the DSC system was cooled immediately after melting, an exothermic peak at 248 °C was observed, consistent with the crystallization of the material. The similar T_e, maximum

temperatures (T_p) and enthalpy (peak area) for these endothermic and exothermic features provide supporting evidence that these peaks correspond to melting and crystallization. Heating the system beyond 260 °C, sharp endothermic peaks were observed, likely due to the decomposition of **9**. The small exothermic peak observed during the cooling on **B** at around 120 °C cannot be confidently assigned to **9** itself and is more likely a feature of its decomposition product.

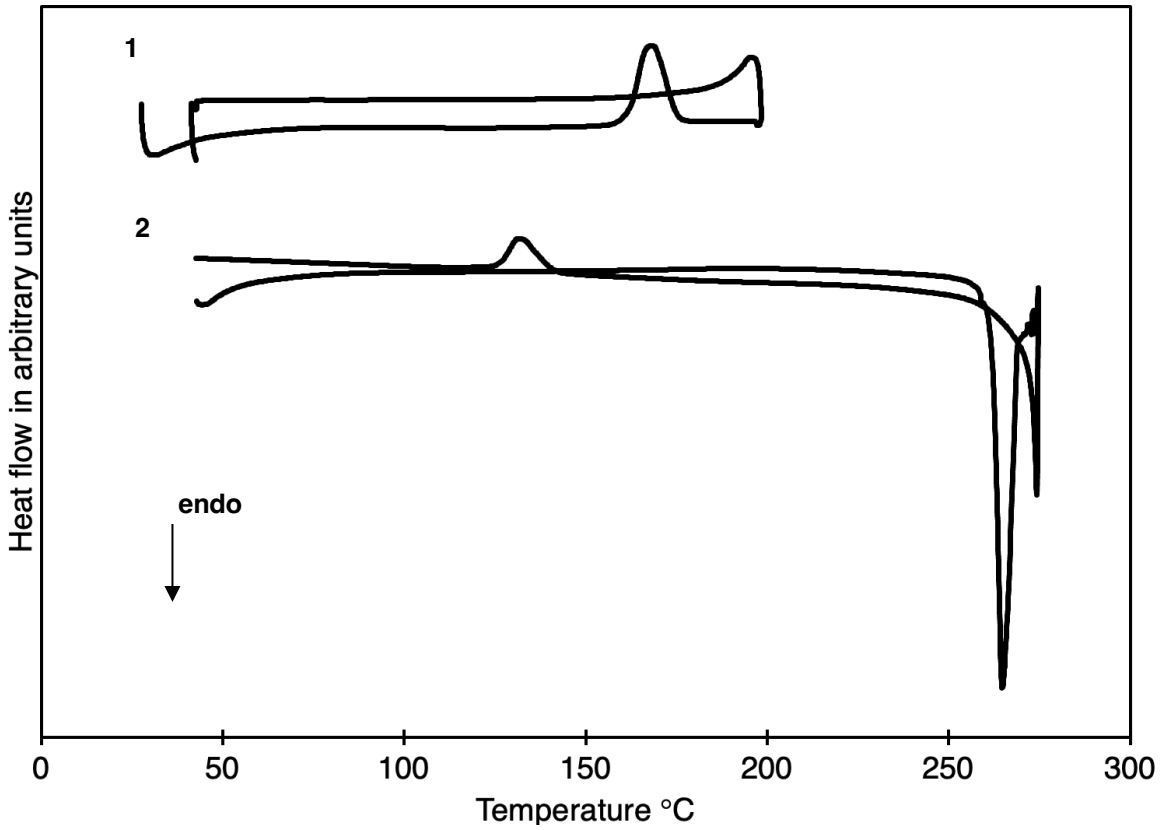

Figure 3.10. DSC curve at 10 °C/min for $(LiNH^tBu)_8$ (**8**). Mass of **8** was 3.5 mg. Starting temperature was 40 °C and ramp rate was 10.00 °C. 1 represents first heating and cooling cycle to 200 °C and 2 represents second heating and cooling cycle to 270 °C.

DSC measurements of **8** were conducted over two heating and cooling cycles. During the first heating cycle, the sample was heated to 200 °C, revealing an exothermic peak at approximately 160 °C. The system was then cooled to 50 °C before being reheated to 270 °C. During the second heating cycle, an endothermic peak was observed at approximately 257

°C, corresponding to the melting of **9**, followed by decomposition at higher temperatures. This behaviour is consistent with the exothermic peak at 160 °C representing the phase transition of **8** to **9**, followed by melting of **9** and subsequent decomposition. This conclusion is supported by the similarity in T_e value for **9** and similar decomposition features. Upon cooling back to 40 °C, an additional exothermic peak was detected at approximately 134 °C. However, this peak cannot be attributed to **9**, as the decomposition product could not be definitively identified. Notably, similar exothermic peaks were observed in the DSC measurements of **8** and **9** upon cooling when the temperature of the system exceeded 257 °C. This observation suggests that the exothermic peaks likely correspond to the same decomposition related feature.

Table 3.5. Calorimetry data for $(LiNH^tBu)_8$ (**8**) and $(LiNH^tBu)_\infty$ (**9**)

Compound			**Temperature (° C)**
8	**First Heating/Cooling Cycle**	T_e (onset temperature) (°C)	161.85
		T_p (maximum temperature) (°C)	167.83
		Enthalpy, (J/g)	39.34
8	**Second Heating/Cooling Cycle**	T_e (onset temperature) (°C)	256.95
		T_p (maximum temperature) (°C)	262.09
		Enthalpy, (J/g)	–71.89
8		T_e (onset temperature) (°C)	137.93
		T_p (maximum temperature) (°C)	131.19
		Enthalpy, (J/g)	10.71
9	**Conditions A Heating**	T_e (onset temperature) (°C)	257.69
		T_p (maximum temperature) (°C)	263.50
		Enthalpy, (J/g)	–61.77
9	**Conditions A Cooling**	T_e (onset temperature) (°C)	248.08
		T_p (maximum temperature) (°C)	243.80
		Enthalpy, (J/g)	71.56

Compound			Temperature (° C)
	Conditions B	T_e (onset temperature) (°C)	256.95
9	**Heating**	T_p (maximum temperature) (°C)	262.09
		Enthalpy, (J/g)	–71.89
	Conditions B	T_e (onset temperature) (°C)	n.o.
9	**Cooling**	T_p (maximum temperature) (°C)	n.o.
		Enthalpy, (J/g)	n.o.

3.2.6 ^{1}H NMR Spectroscopy

^{1}H NMR data for **8** and **9** are listed in Table 3.6.

Table 3.6. ^{1}H NMR data for $(LiNH^tBu)_8$ (**8**/**10**) and $(LiNH^tBu)_\infty$ (**9**)

Compound	^{1}H NMR, ppm
$(LiNH^tBu)_8$ (**8**/**10**)	1.37(9 H), –1.53 (1 H)[a]
	1.07 (9 H), –1.55 (1 H)[b]
$(LiNH^tBu)_\infty$ (**9**)	1.07 (9 H), –1.58 (1 H)[b]

[a]C_6D_6. [b]THF-d_8. 300 MHz, 25 °C.

^{1}H NMR spectra of **8** in C_6D_6 and **8** and **9** in THF-d_8 show two resonances in a 1:9 ratio, consistent with the amide proton and free rotation of ^{t}Bu in solution as shown in Figure 3.11. The amide proton signal appears at –1.5 while the ^{t}Bu signal appears at 1 ppm in THF-d_8 and 1.37 in C_6D_6.

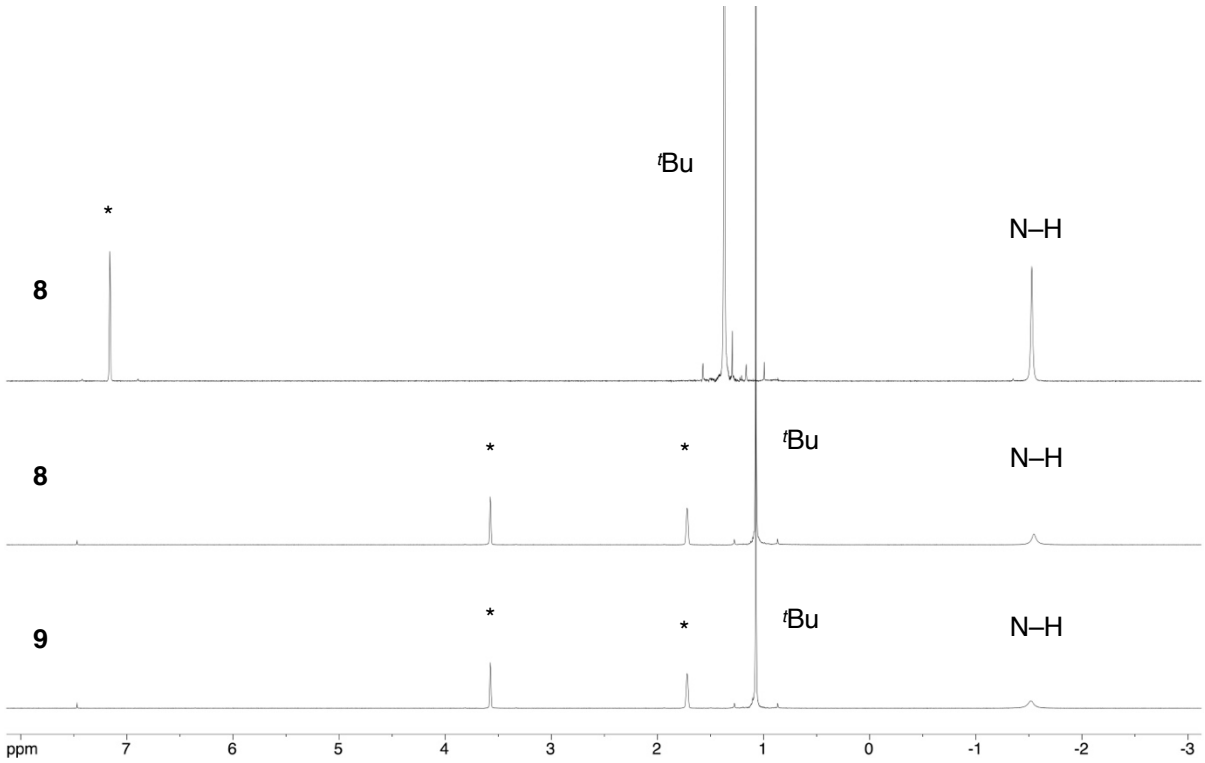

Figure 3.11. ^{1}H NMR (300 MHz, 25 °C) spectra of **8** in C_6D_6 and THF-d_8 and **9** in THF-d_8. * represents residual protio solvent resonance.

3.2.7 In Solution Molecular Mass Determination

To ascertain the identity of **8** and **9** in solution, ^{1}H diffusion-ordered spectroscopy (DOSY) analysis was utilized to determine the molecular masses of **8** in toluene-d_8 and THF-d_8 and **9** in THF-d_8 using the method developed by Williard *et al*. The determination of the solution-state structure of **8** in toluene-d_8 was attempted using isotopic labelling experiments by Collum and coworkers.[107] Collum and coworkers utilized ^{6}Li and ^{15}N isotopic labelling and NMR spectroscopy to probe the solution state structure. The resulting ^{6}Li and ^{15}N NMR spectrum at –30 °C revealed that both lithium and nitrogen are surrounded by three nitrogen and lithium, respectively, consistent with the complexes shown in Figure 3.12. Variable temperature measurements were performed to exclude rapid interaggregate site exchange, but the results led to no clear interpretation of the structure of **8** in toluene-d_8.

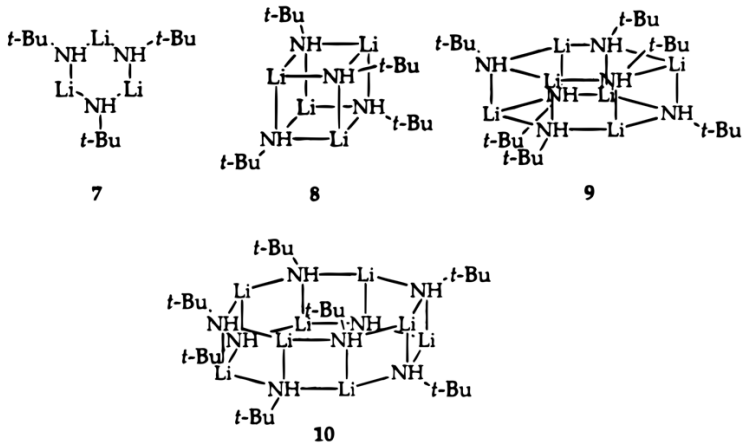

Figure 3.12. Likely structures of LiNH^{t}Bu in toluene-d_8 consistent with ^{6}Li and ^{15}N isotopic labelled NMR experiments. Reprinted (adapted) with permission from Aubrecht, K. B.; Lucht, B. L.; Collum, D. B. *Organometallics* **1999**, *18* (16), 2981–2987. Copyright 1999 American Chemical Society.

As the results of these labelling experiments were inconclusive, this led us to a further investigation of determining the species of LiNH^{t}Bu in solution using ^{1}H DOSY measurements.

3.2.7.1 ^{1}H DOSY Background

^{1}H DOSY is an NMR spectroscopy technique used to determine the diffusion behaviour of molecules in solution.[109] In recent years, this technique has been used as a tool to estimate the molecular mass of aggregates in solution. This method does not directly reveal the molecular mass of species in solution but determines the diffusion coefficients of those species which is then correlated to molecular mass.[90]

Diffusion in DOSY is measured using the pulsed field gradient method, where a linear magnetic field gradient is applied to the sample.[110] This gradient causes different positions within the sample to experience varying magnetic field strengths. The gradient is followed by a delay, which allows the molecules to move in solution. A second field gradient is then applied. If a molecule remains stationary during the delay, the second pulse cancels the effect of the first pulse, resulting in strong signal intensity for that molecule. Conversely, if the molecule has diffused, the phase shift changes, reducing the signal intensity. This

reduction in signal intensity is referred to as NMR signal attenuation. The rate of NMR signal attenuation is influenced by the size of the species and is directly related to its diffusion coefficient. For instance, a smaller molecular aggregate will diffuse faster during a DOSY experiment compared to a larger aggregate. Consequently, the signal of the smaller aggregate undergoes greater attenuation due to its faster diffusion.

Diffusion coefficients are determined using several mathematical equations and approximations. The Stokes – Einstein relation[111], Equation 3.1, relates the diffusion coefficients (D) obtained from DOSY analysis to the hydrodynamic radii (r)[112–114] of the species in solution, enabling the determination of molecular size from the diffusion coefficient. This relation is based on a sphere. This equation also incorporates the Boltzmann constant (k), the viscosity of the medium (η) and the temperature (T). This relationship assumes free diffusion and that the diffusion coefficient is measured in infinite dilution, where intermolecular interactions are negligible.

Equation 3.1.

$$D = (k\mathrm{T})/(6\pi\eta\mathrm{r}))$$

The diffusion coefficient (D) can be directly correlated to molecular mass (M) using the Power-Law relationship (Equation 3.2).[115] In this equation, A represent the proportionality constant, and α denotes the scaling component.

Equation 3.2.

$$D = AM^{\alpha}$$

Equation 3.2 can be linearized by applying the logarithm to both sides, resulting in Equation 3.3.

Equation 3.3.

$$\log D = a \log FW + b$$

Using Equation 3.3 and carefully selected internal standards, the empirical molecular masses of unknown aggregates can be determined by interpolating (or extrapolating) the calibration curve. This curve is created by correlating the molecular masses and experimentally determined diffusion coefficients of the internal standards. Williard and coworkers selected internal standards including benzene (78.11 g/mol), cyclooctene (110.2g/mol), 1-tetradecene (196.4 g/mol) and squalene (410.7 g/mol). These standards were chosen to cover a wide molecular mass range, remain unreactive with the analyte, and exhibit a similar shape to the analyte in solution. Internal standards were added to each NMR sample to minimize the effects of variations in sample preparation on the data analysis.

Figure 3.13 shows the ^{1}H DOSY spectrum of **9** in THF-d_8 along with the four internal calibrants. The ^{1}H DOSY spectrum is a pseudo 2D stacked spectrum consisting of 16 slices, each slice containing a 1D experiment measured at different gradient strengths. The x-axis represents the chemical shift and the y-axis in the spectrum is the log of the diffusion coefficients.

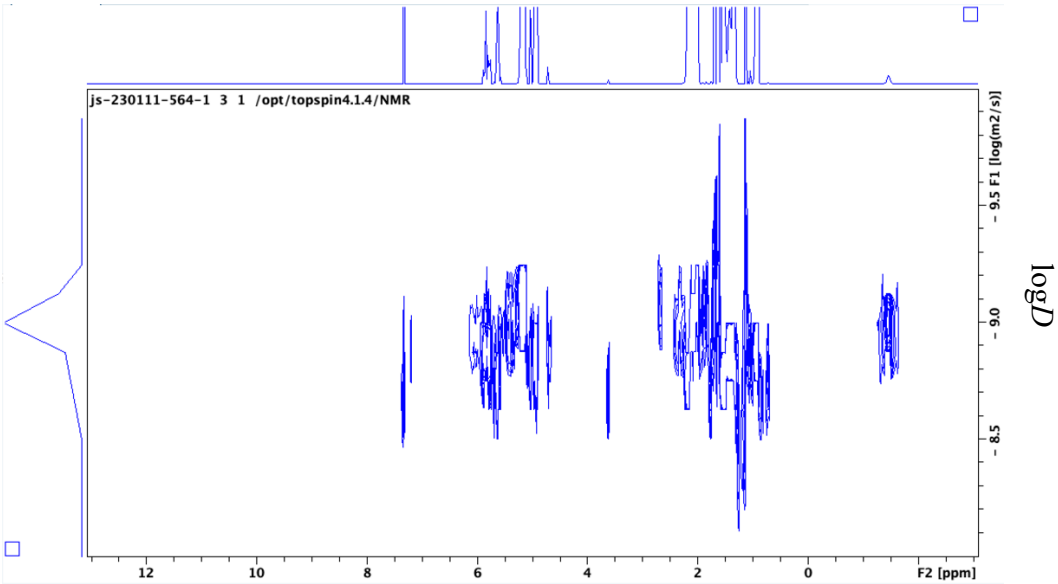

chemical shift

Figure 3.13. ^{1}H DOSY spectrum of **8** and four internal references in THF-d_8.

The diffusion coefficient was calculated utilizing the Stejskal-Tanner equation, Equation 3.4, where I is the signal intensity at a given gradient strength, I_0 is the initial signal intensity in the absence of a gradient, b is the diffusion weighting average and D is the diffusion coefficient.

Equation 3.4.

$$I = I_0 e^{-bD}$$

The diffusion weighted average, shown in Equation 3.5, is defined as:

Equation 3.5.

$$b = \gamma^2 g^2 \delta^2 \left(\Delta - \frac{\delta}{3}\right)$$

Where γ represents the gyromagnetic ratio of the nucleus, g represents the gradient strength, δ represents the duration of the gradient pulses and Δ represents the diffusion time.

3.2.7.2 Experimental Procedure and Considerations

The experimental setup and considerations were assisted by Dr. Blossom Yan. The two parameters optimized in the ^{1}H DOSY experiments are big delta (Δ) and small delta (δ). Δ is defined as the diffusion time (time between the end of the first gradient pulse and before the start of the second gradient pulse) while δ is defined as duration of the gradient pulse. Optimization of the ^{1}H DOSY experiments was performed by conducting 1D diffusion experiments at different gradient pulse strengths of 5% to 90% of the maximum gradient strength. Both Δ and δ were varied prior to the 2D experiment to optimize the dynamic range of the measurement. Figure 3.14 presents the Stejskal-Tanner plot of 1-tetradecene in THF-d_8. This plot illustrates the diffusion weighting factor (b-value) on the x-axis and the natural log of the signal intensity on the y-axis. The plot exhibits exponential decay, with the slope of the decay corresponding to the diffusion coefficient of the species. The Stejskal-Tanner plots were generated for all internal standards and samples to determine the diffusion coefficients.

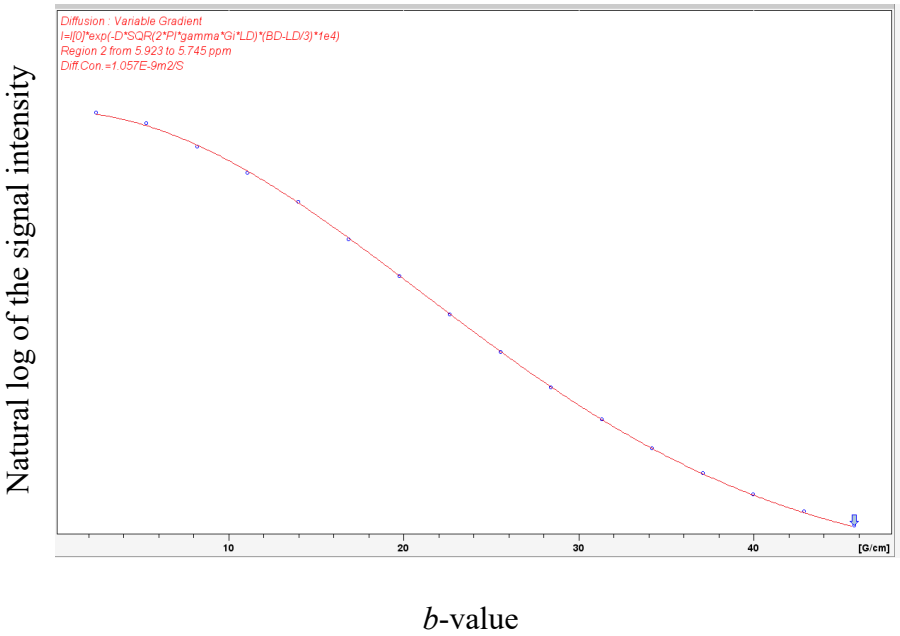

Figure 3.14. Stejskal-Tanner plot of 1-tetradecene in THF-d_8

Figure 3.15 shows a calibration curve plotting log *D* vs. log *MW* which was used to determine the molecular mass of **9** in THF-d_8. The four data points were treated with a linear regression, enabling the calculation of the molecular mass of **9**.

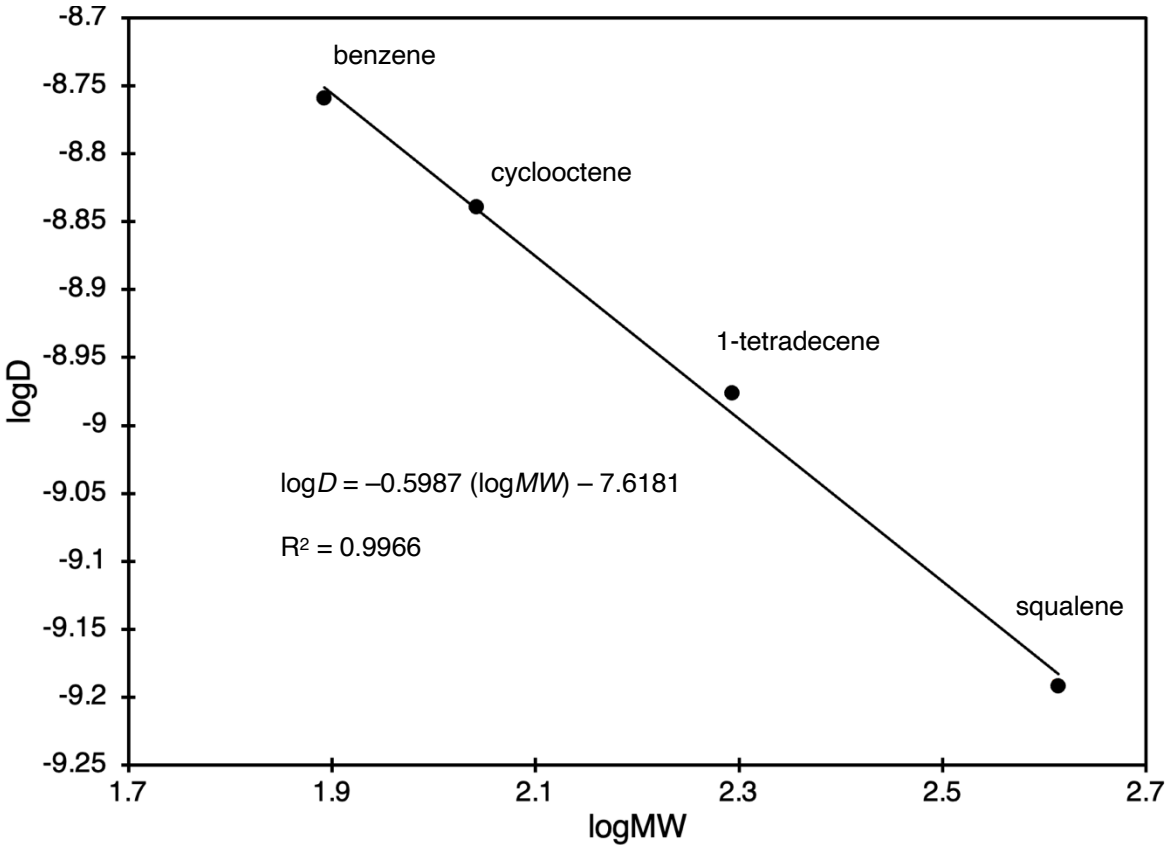

Figure 3.15. log D vs log MW DOSY molecular weight calibration curve.

The calculated molecular masses of each internal standard were determined using the calibration curve to confirm that the error in measurements did not exceed over 10% as shown in Table 3.7. A percent difference of 10% or less provides confidence in the reliability of this method for calculating molecular masses using the calibration curve. These percent differences are consistent with values reported in the literature.

Table 3.7. Percent differences of the actual and calculated molecular mass of benzene, cyclooctene, 1-tetradecene and squalene

Reagent	Diffusion Coefficient	Molecular mass	Calculated molecular mass	Percent Difference
benzene	1.74E-09	78	81	3.13
cyclooctene	1.45E-09	110	109	–0.67
1-tetradecene	1.06E-09	196	185	–5.58

Reagent	Diffusion Coefficient	Molecular mass	Calculated molecular mass	Percent Difference
squalene	6.44E-10	411	425	3.39

[a] Molecular masses were calculated using the following equation rearranged from the equation of the line from Figure 3.15: $\mathrm{MW} = 10^{\frac{\mathrm{LogD}+7.6181}{-0.5987}}$

3.2.7.3 Data Analysis and Interpretation

The experiments analyzed within this section are from the dissolution of **8** and **9** in THF-d_8 and **8** in toluene-d_8. The diffusion coefficients and determined molecular masses of the internal standards and LiNH^{t}Bu are shown in Table 3.8. For the measurement of **8** in toluene-d_8, benzene was not used as an internal standard as the resonances of benzene overlap with the resonances of the residual protio signal of toluene-d_8 in the ^{1}H NMR spectrum.

Table 3.8. Calculated diffusion coefficients and molecular masses of internal standards and **8** in THF-d_8 and toluene- d_8 and **9** in THF-d_8

	9 in THF-d_8		**8** in THF-d_8		**8** in toluene-d_8	
Compound	Calculated Diffusion Coefficient (m^2/s)	Calculated MW (g/mol)	Calculated Diffusion Coefficient (m^2/s)	Calculated MW (g/mol)	Calculated Diffusion Coefficient (m^2/s)	Calculated MW (g/mol)
Benzene	1.74E-09	81	1.75E-09	84	n/a	n/a
COE	1.45E-09	109	1.50E-09	108	1.44E-09	117
TEA	1.06E-09	185	1.12E-09	174	1.10E-09	175
SQUA	6.44E-10	425	6.30E-10	442	6.02E-10	432
LiNH$_t$Bu	8.00E-10	295	7.71E-10	318	4.69E-10	626

Benzene was not used as an internal standard for measurements in toluene-d_8 due to overlapping resonances.

Based on the ^{1}H DOSY data, the molecular mass of **8** in THF-d_8 and toluene-d_8 was determined to be 318 g/mol and 626 g/mol, respectively, whereas the molecular mass of **9** in THF-d_8 was determined to 295 g/mol as tabulated in Table 3.9.

Table 3.9. Calculated MW for **8** in toluene-d_8 and THF-d_8 and **9** in THF-d_8 using ^{1}H DOSY MW analysis

Solid State Form	NMR Solvent	Calculated MW	Theoretical Formula	Percent Difference
$(LiNH^tBu)_8$ (**8**)	toluene-d_8	626	$(LiNH^tBu)_8$	1.05%
$(LiNH^tBu)_8$ (**8**)	THF-d_8	318	$(LiNH^tBu)_2(THF\text{-}d_8)_2$	0.18%
$(LiNH^tBu)_\infty$ (**9**)	THF-d_8	295	$(LiNH^tBu)_2(THF\text{-}d_8)_2$	7.32%

Theoretical molecular mass of $(LiNH^tBu)_8$ is 632.56 g/mol. Theoretical molecular mass of $(LiNH^tBu)_2(THF\text{-}d_8)_2$ is 318.45 g/mol

The calculated molecular mass of **8** in toluene-d_8 is 626 g/mol, which is within experimental error (1.05%) of the actual molecular mass of **8** (MW = 632.56 g/mol). This agreement suggests that the solution-phase structure of **8** in toluene-d_8 closely resembles its solid-state structure. The molecular masses of **8** and **9** determined in THF-d_8 are within 10% experimental error of each other. Possible structure types of $LiNH^tBu$ in THF-d_8 are shown in Figure 3.16. Combined with the experimental observation that **9** crystallizes from **8** or **9** in THF/pentane vapour diffusion, this suggests that **8** and **9** are the same species in THF-d_8. Lithium amide complexes crystallized from THF, typically form dinuclear complexes with a four-membered Li_2N_2 ring structure, often coordinated to one or two THF molecules, making structure **A** the most likely structure in solution. This is consistent with the ring-laddering principle, where, upon crystallization, additional LiN units can polymerize with the Li_2N_2 ring to form the polymeric ladder. Structures **B** and **C**, with molecular masses of 316.28 g/mol, cannot be ruled out based solely on molecular mass. However, these structures are unlikely in THF due to the strong coordination of THF to lithium, which makes the existence of two-coordinate lithium species unlikely. Thus, structures **B** and **C** are not likely contenders.

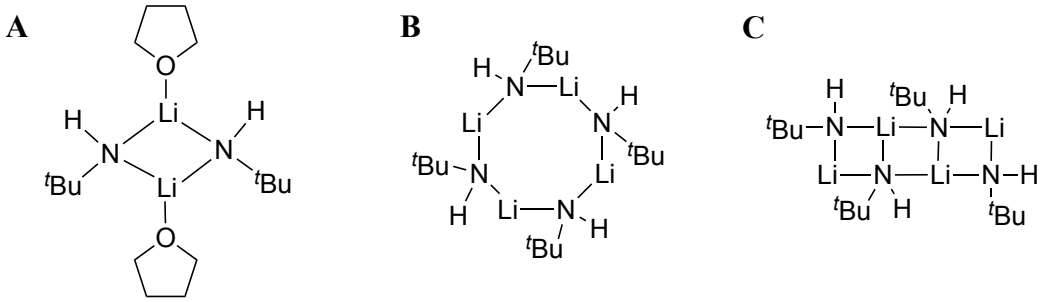

Figure 3.16. Structures consistent with the molecular mass of **8** and **9** in THF-d_8.

3.2.7.4 Literature Comparison

The DOSY method for determining molecular masses of aggregates in solution has been reported several times in the literature.[86–91,109,115] Initially, this method was used to measure the diffusion coefficient of *n*-BuLi in THF, but its application has since expanded to include estimating the molecular masses of various lithium salts in solution.[89,91] This approach has also been employed to investigate the molecular masses of lithium enolates and to elucidate the in-solution structure of LDA in the presence of different ethereal solvents. Like the work presented in this chapter, the percent error between the experimentally determined and predicted formula weights for internal standards and analytes was found to be around 10% but values around 20% have been reported. This level of accuracy lends confidence to the reliability of the reported results.

The determination of molecular masses of THF solvated species in THF-d_8 has also been reported in the literature.[87] For example, the molecular mass of isopropyllithium in THF has been shown to align with the expected values for the THF solvated species. A potential challenge when determining the molecular masses of metal-containing complexes in solution is the coordination of solvent molecules to the metal ion. In the case of lithium ions, THF is a well-known coordinating solvent, meaning the molecular mass of aggregates such as LiNH^{t}Bu in THF includes contributions from THF solvation. In theory, this coordination could complicate molecular mass determination due to potential chemical equilibrium between free THF and THF bound to the coordinately unsaturated lithium ions. However, this equilibrium process is not a concern in this case. The timescale of the THF solvation equilibrium is much faster than the timescale at which diffusion measurements are

conducted. Additionally, because the NMR solvent is THF-d_8 and there is an excess of solvent compared to LiNHtBu in solution, the equilibrium likely favors the THF-bond species. Consequently, the equilibrium process does not interfere with or affect the diffusion measurements, enabling the accurate determination of diffusion coefficients.

3.2.7.5 Chapter Summary

The work presented in this chapter led to the synthesis of a second polymorph of LiNH^{t}Bu, which adopts an infinite, polymeric ladder structure. This form can be synthesized quantitatively by reacting *n*-BuLi and 1.1 equivalents of ^{t}BuNH$_2$ in hexanes. As described in Chapter 2, **8** was used in the synthesis of [Ph$_4$P]**2** in THF. Experimental evidence showed that using **9** as the LiNHtBu reagent produced the same amount of [Li]**2** as using **8**, suggesting that the form of LiNH^{t}Bu does not alter the reaction chemistry in THF.

Compounds **8** and **10** exhibit similar structures in the solid state. Compound **10** adopts a cyclic ladder structure containing eight LiNH^{t}Bu units, while **9** displays an infinite, polymeric ladder structure. The Li–N bond length and N–Li–N/Li–N–Li bond angles are indistinguishable between the two forms.

Based on experimental and DSC data, **8** can be classified as the metastable polymorph, whereas **9** represents the thermodynamic polymorph. Compound **8** can be converted to **9** by several methods, including dissolution in hexanes followed by the addition of a donor solvent, seeding with **9**, heating to 200 °C, dissolution in diethyl ether or dissolution in THF followed by solvent removal under reduced pressure or pentane diffusion. The distinct PXRD patterns and solubility properties of **8** and **9** allow for two methods to distinguish between the two polymorphs.

Lastly, the solution phase characterization of both forms was explored using ^{1}H DOSY. The molecular mass of **8** in toluene-d_8 was determined to be 626 g/mol, consistent with its calculated molar mass of 632.56 g/mol. In THF-d_8, the molecular masses of compounds **8** and **9** were measured as 318 g/mol and 295 g/mol, respectively, approximately half the molecular mass of the cyclic ladder. Based on the solid-state structures of lithium amides crystallized from THF, the species in THF-d_8 is likely a four membered, dinuclear species with one THF-d_8 molecule coordinating per lithium atom. Experimental data showing

that compound **9** crystallizes from both **8** and **9** under THF/pentane vapor diffusion conditions further support the conclusion that **8** and **9** yield the same species in THF solution.

3.3 Experimental Section

3.3.1 General Experimental Details

General experimental details have been outlined in Chapter 2, Section 2.3.1. In addition, toluene (VWR, HPLC grade), was purified through desiccant columns (MBraun, SPS-800) and hexanes was distilled from CaH_2.

3.3.2 Preparation of Compounds

(LiNH^{t}Bu)$_8$·C$_6$H$_{14}$ (8). ^{t}BuNH$_2$ (0.176 mol, 18.5 mL, 1.07 equiv) was added dropwise to a solution of *n*-BuLi (0.165 mol, 103.0 mL 1.6 M, 1.00 equiv) in hexanes while stirring in a water bath. The reaction mixture was stirred for 1 h, after which the solvent was reduced in volume *in* vacuo (ca. 60 mL), leading to the formation of a cloudy solution containing white solid. The mixture was gently reheated until the solid dissolved, and the solution was then stored at –20 °C for 12 h, resulting in the formation of transparent crystals. The crystals were isolated by filtration, rinsed with cold hexanes, and dried to afford a white powder (9.52 g, 74.7%)

(LiNH^{t}Bu)$_\infty$ (9). ^{t}BuNH$_2$ (0.980 mol, 103 mL, 1.14 equiv) was added dropwise to a solution of *n*-BuLi (0.855mol, 506 mL, 1.6 M, 1.00 equiv) in hexanes over 4 h while the flask was chilled in a water bath. Within 1 h, the solution became opaque due to the formation of a white solid. After an after hour, the solvent was removed *in vacuo*, and the material was dried overnight. The resulting solid was collected to afford a white powder (59.565 g, 88%). Crystallization by THF/pentane vapor diffusion yielded colorless needs suitable for structural analysis. Anal. Calcd. for $C_9H_{10}LiN$: C, 60.76; H, 12.75; N, 17.71. Found: C, 60.67; H, 13.18; N, 17.38.

(LiNH^{t}Bu)$_8$ (10). **8** (530 mg) was dissolved in toluene (20 mL) and a small amount of yellow residue was filtered to afford a transparent, colorless solution. The solution was concentrated *in vacuo* to approximately 5 mL, leading to the formation of colourless crystals. The mixture was gently warmed to redissolve the crystals, cooled to –10 °C for 24 h, and

then filtered to afford colorless plates (178 mg). Anal. Calcd. for $C_9H_{10}LiN$: C, 60.76; H, 12.75; N, 17.71. Found: C, 59.20; H, 12.80; N, 17.09.

3.3.3 Elemental Analysis

The synthesis of **8** involves the use of commercially purchased *n*-BuLi which is known to contain a varying amount of LiCl contamination. Elemental analysis of **10** (recrystallized in toluene) revealed low readings analyzed for C, H and N. Values for the elemental analysis of **8** was not disclosed by the author but "satisfactory C, H, Li, N analyses" was stated.[59] If the C, H and N analysis had shown values higher than the theoretical, it could be theorized that residual toluene was present and the sample sent for elemental analysis had not been thoroughly dried. However, because the C, H and N readings were lower than expected, it is believed that inorganic contamination, likely from LiCl or other chloride anions, contributed to these results. Assuming the contamination is LiCl, the elemental analysis results can be mapped to estimate the contamination level. If 0.04 equivalents of LiCl are present per LiNH′Bu molecule, that corresponds to 0.32 equivalates per octamer or one LiCl per three octamers. At this level of contamination, the expected elemental analysis values would be 59.48% C, 12.47% H, and 17.34% N. Elemental analysis of the recrystallized ladder was satisfactory, indicating that the purification process (recrystallization via THF/pentane vapour diffusion) successfully removed any inorganic contamination.

3.3.4 X-Ray Crystallography

Single crystals suitable for single crystal X-ray diffraction analysis were obtained from storage of a concentrated toluene solution at –15 °C (**10**, as colorless blocks) and from THF/pentane vapour diffusion at –15 °C (**9**, as colorless needles). Data for single crystal x-ray diffraction were collected using Bruker SMART APEX diffractometer with an Oxford 700 Series cryostream cooler. Data sets were collected, indexed and processed using Bruker APEX2 software suites. Solutions were refined using Bruker SHELXTL. Crystallographic data for **8**, **9** and **10** are found in Table 3.10.

Table 3.10. Crystallographic data for $(LiNH^tBu)_\infty$ (**9**) and $(LiNH^tBu)_8$ (**10**)

	Published[59]	**10**	**9**
Formula	$(LiNH^tBu)_8$	$(LiNH^tBu)_8$	$(LiNH^tBu)_\infty$
Space group	*P*2/n (no. 13)	*C*2/*c* (no. 15)	*C*2/*c* (no. 15)
a, Å	12.000(8)	24.382(3)	18.495(2)
b, Å	12.547(7)	11.5121(12)	8.4883(10)
c, Å	18.339(12)	18.5413(3)	7.5922(9)
β, °	105.55(5)	115.510(3)	107.7941(17)
V, Å^3	2660.125	4697.0(8)	1134.9(2)
θ_{max}, °	N/A	28.00	26.00
$R_1(wR_2)$, %	5.2 (N/A)	5.58 (18.71)	5.11 (16.58)
Tot. data, %	N/A	100	100
S	N/A	1.051	1.097

PXRD data was collected on an INEL XRG 3000 diffractometer equipped with a Cu radiation source ($K\alpha_1\lambda$ = 1.54056, $K\alpha_2\lambda$ = 1.54439, 30 kV, 30 mA). PXRD samples were prepared inside an N_2 glovebox using the Flat Plate Method and Kapton film was used to seal the sample. Data was collected for 10 minutes. Data was analyzed using GSAS-II software fit using the Le Bail refinement method. The Kapton seal allowed for data to be collected for approximately 10 minutes, with visible decomposition (darkening of the white powder) occurring across the entire sample after this time. The data obtained from these experiments were sufficient to determine which form was synthesized, but more advanced fitting techniques (e.g. Rietveld fitting) were not used due to inadequate data quality.

3.3.5 Other Physical Measurements

DSC samples were prepared inside a glovebox by weighing the solid into a tared Tzero Aluminum Hermetic pan and the pan and lid were crimped sealed inside the glovebox. Data was collected on the TA Instruments DSC Q2000 with the ramp rate being 10 °C/min. N_2 gas was used as the chamber gas.

DOSY measurements were conducted on a 300 Avance NMR spectrometer. A 5 G/cmA *z*-axis gradient amplifier was employed, with the maximum gradient strength of 10 A. Experiments were performed using the standard pulse program (dstebpgp3s) using a double stimulated echo sequence, bipolar gradient pulses for diffusion and three spoil gradients. Gradient recovery delays were 200 μs. Diffusion coefficients were obtained using the T1/T2 analysis module in TopSpin.

Chapter 4: Synthesis of Di- and Trinuclear Iron (II) Complexes with Mixed Amide Ligation

4.1 Introduction

Homoleptic transition metal (bistrimethylsilylamide) ($M(N(SiMe_3)_2)_n$ complexes represent a fascinating class of compounds, distinguished by their unique structures and reactivity profiles. Three types of ($M(N(SiMe_3)_2)$) complexes have been identified: those containing one bistrimethylsilylamide ligand $M(N(SiMe_3)_2)$[116–119], two bistrimethylsilylamide ligands $M(N(SiMe_3)_2)_2$ [120,121], and three bistrimethylsilylamide $M(N(SiMe_3)_2)_3$[122,123] ligands as shown in Figure 4.1. These complexes provide synthetic benefits as precursors in ligand substitution reactions where the labile $[(Me_3Si)_2N]^-$ ligand can be replaced with a deprotonated protio-ligand. These complexes also exhibit solubility in nonpolar solvents, in contrast to the limited solubility typically observed for metal halides.

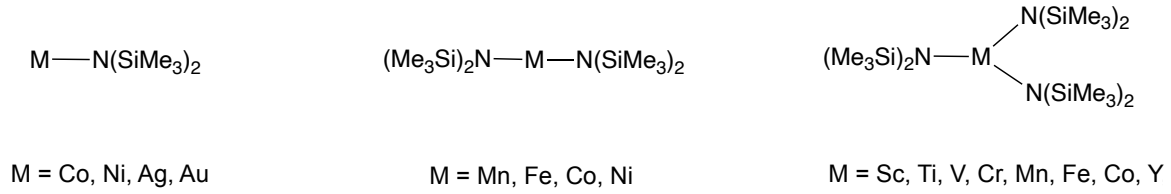

Figure 4.1. Structurally characterized transition metal (bistrimethylsilylamide) complexes.

The ($M(N(SiMe_3)_2)$) complex that is the focus of this chapter is iron (bistrimethylsilylamide) $[Fe(N(SiMe_3)_2)_2]$ (**11**), which was originally synthesized via a ligand exchange reaction between $FeBr_2(THF)_2$ with two equivalents of $Li(N(SiMe_3)_2)$ as shown by Scheme 4.1.[121] The synthesis of **11** demands meticulous handling, as it is highly air-sensitive and rapidly oxidizes upon exposure to oxygen. Work in our laboratory deviated from the original preparation by utilizing ferrous chloride as the Fe(II) precursor instead of $FeBr_2(THF)_2$.[3]

[3] The work presented in this chapter is built on work performed by Dr. Wei Zhang. Jay Bhagat is acknowledged for assistance with preliminary amine screening.

Compound **11** has been widely utilized as an Fe(II) synthon in the synthesis of Fe(II) complexes and has recently garnered interest as a precursor in the study of single molecule magnets; notably, a structurally similar compound has also shown promise as a single molecule magnet.[124–126,]

Scheme 4.1. Original synthesis of $Fe(N(SiMe_3)_2)_2$ (**11**)[121]

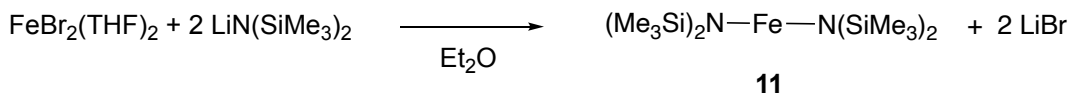

The solid-state structure of **11** exists as a dinuclear complex featuring two trigonal planar irons, two terminal $[(Me_3Si)_2N]^-$ ligands, and two bridging $[(Me_3Si)_2N]^-$ ligands.[127] In contrast to the solid state structure, the solution phase structure of **11** was determined to be mononuclear with a linear geometry and contained two $[(Me_3Si)_2N]^-$ ligands. This was determined using gas electron diffraction analysis, molecular weight determination using the Signer method and comparison of the ^{1}H NMR chemical shifts to related compounds that are mononuclear in the solid state. The mononuclear-dinuclear equilibrium was modelled using data obtained from ^{1}H NMR spectroscopy by Power and coworkers with the equilibrium expression shown in Equation 4.1.[127] At room temperature in toluene-d_8, **11** exists predominantly (99.9%) in the mononuclear form. The equilibrium is slow on the NMR timescale, allowing both the mononuclear and dinuclear forms to be observed at lower temperatures. The ^{1}H NMR chemical shift of the mononuclear form is ~60 ppm and the dinuclear form is at 4.62 ppm and –7.82 ppm.

Equation 4.1.

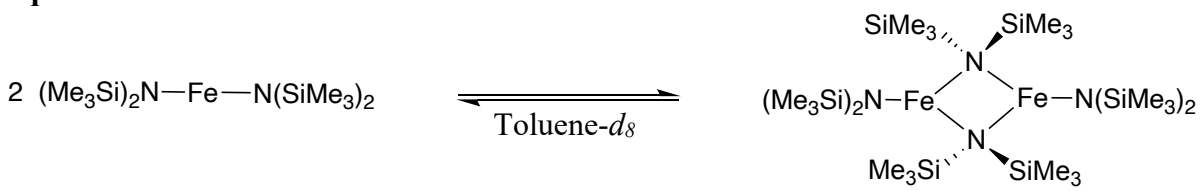

Compound **11** is routinely employed in protolytic ligand substitution reactions, where one or both $[(Me_3Si)_2N]^-$ ligands are substituted upon protonation of $[(Me_3Si)_2N]^-$ to $(Me_3Si)_2NH$ by a ligand with an acidic proton. The protonation of $[(Me_3Si)_2N]^-$ (and

subsequent deprotonation of the ligand with a more acidic proton) typically follows the relative pK_a values of the reactants as the incoming protio-ligand reagent contains a lower pK_a value compared to $(Me_3Si)_2NH$. Scheme 4.2 shows recent examples from 2024 of reactions between **11** and protonated ligands via double protolytic ligand substitution, yielding complexes devoid of $[(Me_3Si)_2N]^-$ ligation.[128,129] Reaction (**A**) demonstrates a straightforward protolytic ligand substitution, while (**B**) highlights more intricate reactivity involving the addition of one equivalent of base ($K(N(SiMe_3)_2)$). The double protolytic ligand substitution reaction was observed for **11**, as the labile $[(Me_3Si)_2N]^-$ ligands readily undergo exchange, efficiently leaving behind a discrete Fe(II) center.

Scheme 4.2. Selected examples of **11** used in double protolytic substitution reactions. (**A**) Reprinted from reference 128. (**B**) Reprinted (adapted) with permission from Stroek, W.; Rowlinson, N. A. V.; Hudson, L. A.; Albrecht, M. *Inorg. Chem.* **2024**, *63*, 17134–17140. Copyright 2024 American Chemical Society.

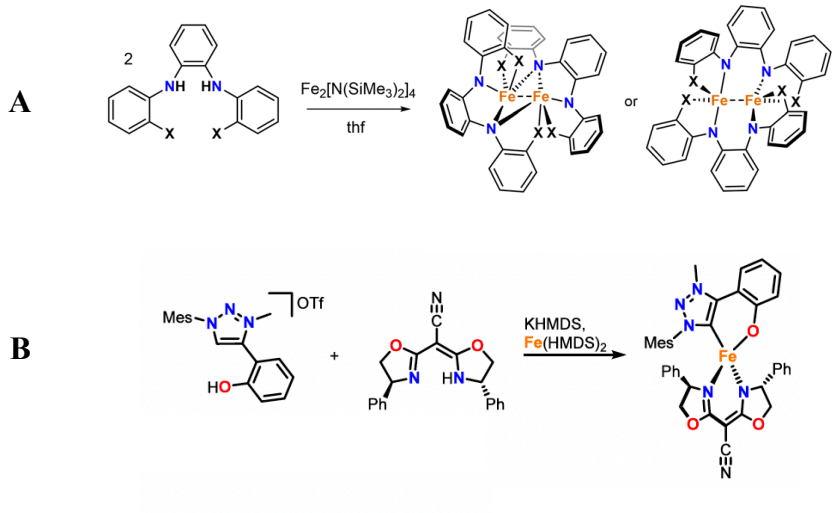

Another type of protolytic ligand substitution reaction is the single protolytic substitution reaction, which is less commonly reported in the literature compared to double substitution reactions. This reaction results in the replacement of only one of the two $[(Me_3Si)_2N]^-$ ligands, leaving the Fe(II) center coordinated to at least one $[(Me_3Si)_2N]^-$ ligand. Scheme 4.3 presents an example of a single protolytic ligand substitution reaction, in which **11** reacts with 2,4,6-tri-*tert*-butylphenol in a 1:1 stoichiometric ratio to form a disubstituted, dinuclear complex.[130] In this product, the bridging ligands are 2,4,6-tri-*tert*-butylphenoxide replacing $[(Me_3Si)_2N]^-$, while the terminal ligand remains as $[(Me_3Si)_2N]^-$.

The geometry of the complex resembles the solid state structure of **11** containing two, three coordinate trigonal planar irons ligated terminally by $[(Me_3Si)_2N]^-$ and two bridging ligands.

Scheme 4.3. Selected example of **11** reacting in a single protolytic substitution reaction

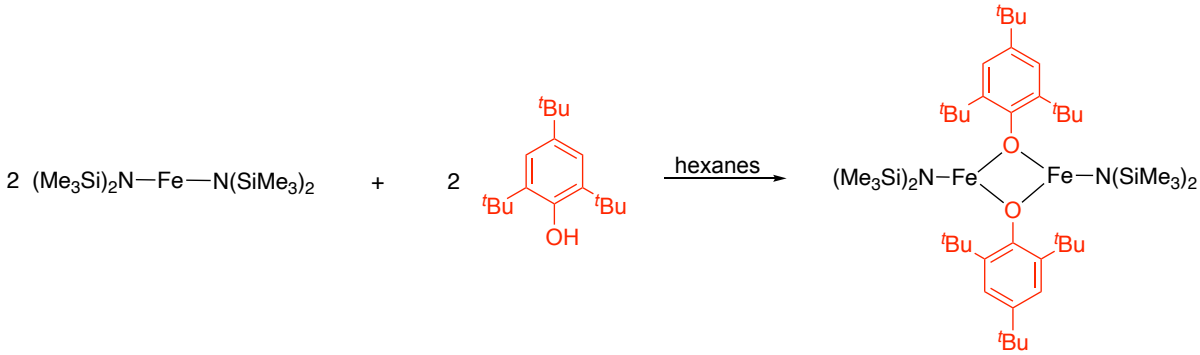

Tuning the stoichiometry of the protio-ligand to **11** leads to the formation of different structure types. Figure 4.2 highlights selected examples of products formed from the reaction of **11** with varying equivalents of protio-ligands that possess a more acidic proton than $(Me_3Si)_2NH$. A stoichiometry of 1:0.5 (**11**: protio-ligand) leads to the monosubstituted dinuclear complexes (**C**)[131], a stoichiometry of 1:1 (**11**: protio-ligand) leads to disubstituted dinuclear complexes (**A**, **B**, **D**, **E**), [130,132–134] and a stoichiometry of 1:1.3 (**11**: protio-ligand) leads to the trinuclear complexes (**F**)[135]. All products depicted in Figure 4.2 feature bridging ligands derived from the deprotonation of the protio-ligand.

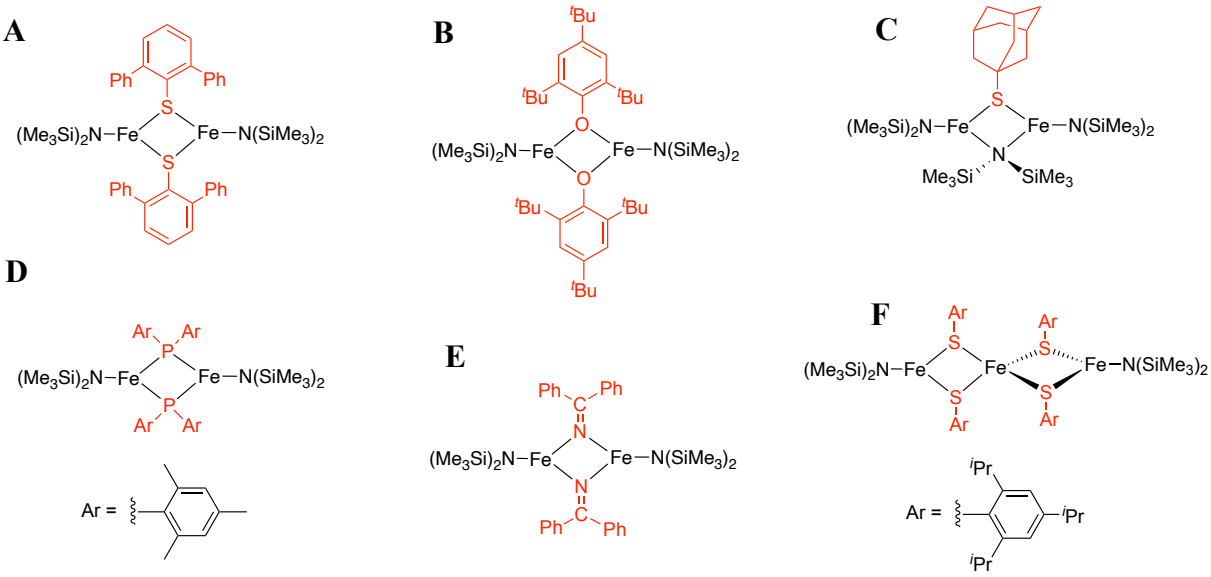

Figure 4.2. Select examples of di- and trinuclear complex from the protolytic ligand substitution reaction of **11** with ligands with acidic protons.

Among the examples shown above, the protio-ligand added to **11** possesses a more acidic proton relative to $(Me_3Si)_2NH$. Work in the Lee group demonstrated that the reaction of **11** with $^tBuNH_2$ results in the formation of the disubstituted, dinuclear complex $Fe_2(\mu\text{-}NH^tBu)_2[N(SiMe_3)_2]_2$ (**14-^{t}Bu**) as shown in Scheme 4.4.[26] To our knowledge, this was the first report of the formation of a dinuclear complex from reaction of **11** with a weaker acid than $(Me_3Si)_2NH$. This reaction is noteworthy for its quantitative nature as ^{1}H NMR spectroscopy confirms that **14-^{t}Bu** is the sole product formed.

Scheme 4.4. Synthesis of $Fe_2(\mu\text{-}NH^tBu)_2[N(SiMe_3)_2]_2$ (**14-^{t}Bu**)

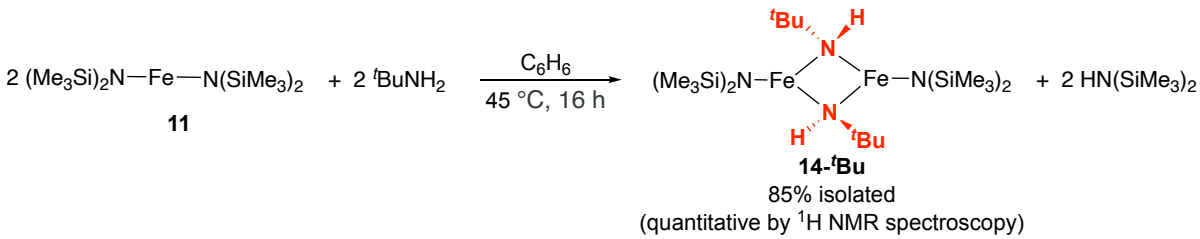

Compound **14-^{t}Bu** has been used in the Lee group as a precursor for synthesizing mixed imide-sulfide cubane clusters, as highlighted in Scheme 4.5. **14-^{t}Bu** reacts with sulfur via an oxidation addition reaction to form a triply bridged Fe(III) dinuclear complex. The intermediate can subsequently further react with $[Fe_4S_4Cl_4]^{2-}$ to produce the heteroleptic, mixed iron-imide-sulfide cubane cluster $[Fe_4(N^tBu)S_3Cl_4]^{2-}$.

Scheme 4.5. Synthesis of $[Fe_4(N^tBu)S_3Cl_4]^{2-}$

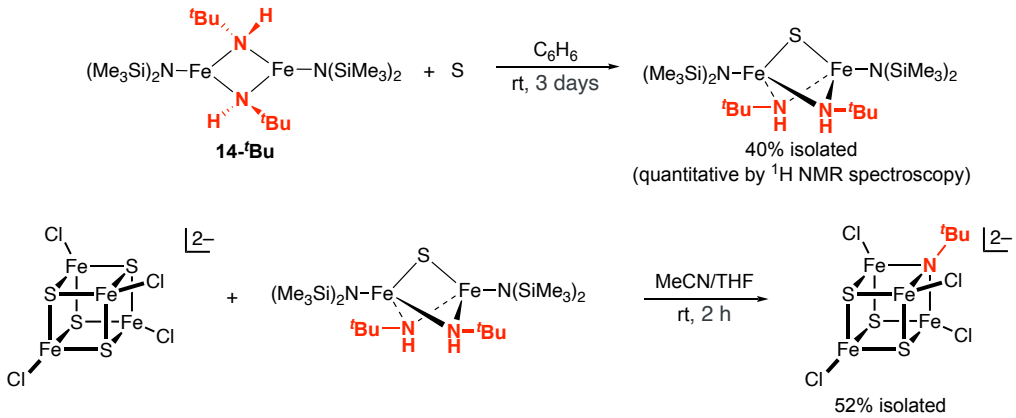

The formation of $[Fe_4(N^tBu)S_3Cl_4]^{2-}$ was particularly significant, as this cluster is isometric with the Fe_4S_3C subunit of the M-cluster making it an interesting subject for studies related to biological nitrogen fixation (discussed further in Chapter 5). Tuning the electronics and sterics of the bridging imide may be beneficial in modifying the properties of $[Fe_4(NR)S_3Cl_4]^{2-}$. To synthesize $[Fe_4(NR)S_3Cl_4]^{2-}$ or $[Fe_4(NAr)S_3Cl_4]^{2-}$ clusters, derivatives of **14-^{t}Bu** would be required, as the $(N\text{-}R)^{2-}$ functionally originates from **14-^{t}Bu**. The work presented in this chapter examines the reaction of **11** with different amines (Equation 4.2) to explore the formation of other disubstituted dinuclear species in this protonolysis reaction.

Equation 4.2.

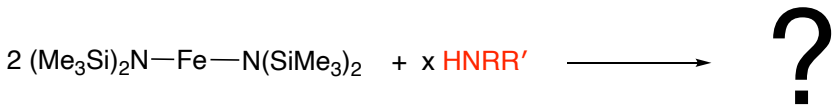

4.2 Results and Discussion

4.2.1 Synthetic Summary

The complexes prepared in this study were synthesized via the protonolysis reaction of **11** with aryl- or alkylamines. Some preliminary work was conducted by Dr. Wei Zhang and Jay Bhagat, with appropriate credit given where applicable.[27] The amines used – *tert*-butylamine, *tert*-amylamine, diisopropylamine, benzylamine, piperidine, aniline, *o*-toluidine,

p-toluidine, 2,4,6-trimethylaniline , 2,6-diisopropylaniline, *N*-methylaniline, *N*-methylbenzylamine – in this chapter are shown in Figure 4.3.

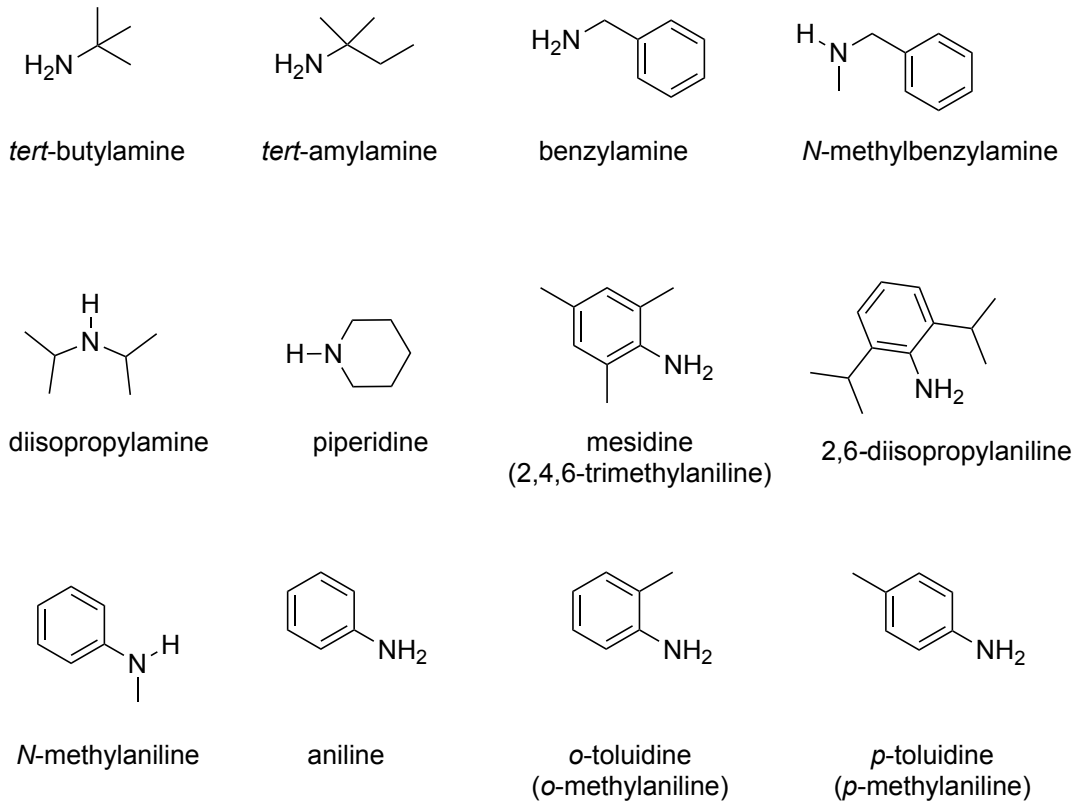

Figure 4.3. Structures of various amines tested in this study.

The properties of the amines examined included: (1) stoichiometry, (2) acidity, (3) steric effects of the amine, and (4) nitrogen substitution. The amines tested were categorized into different groups based on their structural and electronic characteristics. The shorthand notation for each amine is provided in brackets.

(i) **Primary alkylamines without α-protons**: *tert*-butylamine (^{t}Bu), *tert*-amylamine (^{t}Am),

(ii) **Primary alkylamines with α-protons**: benzylamine (Bn),

(iii) **Secondary alkylamines with α-protons**: diisopropylamine (DIPA), piperidine (pip),

(iv) **Primary arylamines with ortho protons**: aniline (Ph), *o*-toluidine (*o*-Tol), *p*-toluidine (*p*-Tol),

(v) **Primary arylamines without ortho protons**: 2,4,6-trimethylaniline (Mes) , 2,6-diisopropylaniline (DIPAni)

(vi) ***N*-methyl secondary amines**: *N*-methylaniline (NMePh), *N*-methylbenzylamine (NMeBn)

This study resulted in the isolation and characterization of five distinct complex types as shown in Scheme 4.6. These complexes include the mononuclear amine adduct complex $Fe(NRR')[N(SiMe_3)_2]_2$ (**12**), the monosubstituted dinuclear complex, $Fe_2(\mu\text{-}NRR')(\mu\text{-}N(SiMe_3)_2)[N(SiMe_3)_2]_2$ (**13**), the disubstituted dinuclear complex $Fe_2(\mu\text{-}NRR')_2[N(SiMe_3)_2]_2$ (**14**), the heteroleptic trinuclear complex $Fe_3(\mu\text{-}NRR')_4[N(SiMe_3)_2]_2$ (**15**), and the homoleptic trinuclear complex $Fe_3(\mu\text{-}NRR')_4[(NRR')]_2$ (**16**). These complexes were synthesized from the reaction of **11** with varying equivalents of amine in benzene at room temperature for 16 h unless noted otherwise. The ideal stoichiometries for complex formation are shown in Scheme 4.6.

Scheme 4.6. Ideal stoichiometries to form complexes observed

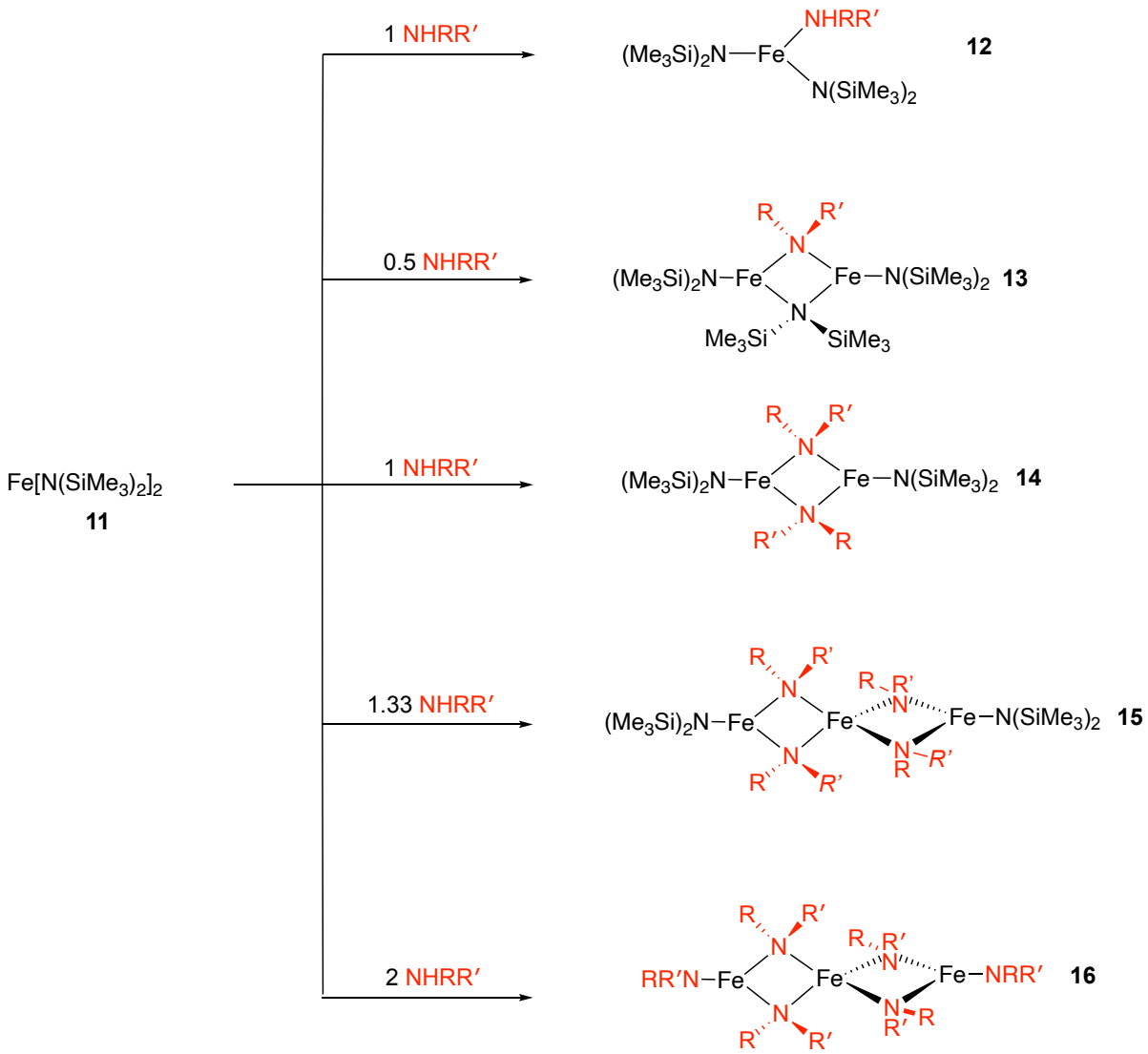

The products formed depended not only on the stoichiometry of amine to **11** but also on the properties of the amine added. These properties include:

(i) **Acidity**: The electronic properties, specifically the acidity of the amine, dictated the reaction rate. This was observed using ^{1}H NMR spectroscopy as well as visual indicators such as solution color and opacity. The addition of

alkylamines to **11** in benzene resulted in an initial light green solution, which transformed into a light blue solution for several minutes, indicative of amine adduct formation, before reverting to light green. The light green deepens to medium green for the dinuclear species and dark green for the trinuclear complexes over several hours. In contrast, the addition of arylamines to **11** in benzene generally caused the solution to darken from light green to deep green within minutes, with the light blue solution color not observed. ^{1}H NMR spectroscopy also showed that the dinuclear species formed more rapidly with arylamines than with alkylamines.

(ii) **Steric effects**: The steric properties of the amine influenced the product distribution. Great steric bulk on the amine favoured the formation of mononuclear amine adducts instead of di– and trinuclear species.

(iii) **Presence of ortho protons**: The presence of protons in the ortho position of arylamines led to the decomposition of the molecular species formed, resulting in ^{1}H NMR silent material and a black opaque solution, with the isolated material appearing as a black oil. In contrast, successfully synthesized and isolated complexes exhibited light blue or green colors in both solution and solid state. The black coloration and oily consistency were indicative of decomposition.

(iv) **Presence of protons on the α-carbon**: The presence of protons on the α-carbon of alkylamines led to decomposition, producing results like those observed in (iii).

(v) **Nitrogen substitution**: The degree of nitrogen substitution (primary vs. secondary) influenced the stabilization of the di- and trinuclear complexes. The decomposition observed in (iii) and (iv) could be prevented if the amine was a secondary amine. The current observation for this decomposition suggests that the presence of N–H bonds and ortho protons (or protons on the α-carbon) lead to decomposition.

This work also demonstrates the original complex synthesized by the Lee group, **14-^{t}Bu**, is not the most stable complex type observed in this study. While the ^{1}H NMR spectra of

other **14** complexes exhibit identifiable signal sets, these complexes are not stable in solution, as they readily convert to the trinuclear complex and not stable for isolation. The rationale for the instability of other disubstituted dinuclear complexes compared to **14-^{t}Bu** remains unclear.

The isolated and *in-situ* yields of the reaction of **11** with amines from this study are presented in Table 4.1. The data in the table includes the following classifications:

(i) **Isolated yield**: The complex was isolated as a crystalline solid. The isolated yield does not necessarily correspond to the *in-situ* yield, as these complexes are highly soluble in non-polar, unreactive solvents such as pentane.

(ii) ***In-situ* yield**: Determined using ^{1}H qNMR analysis, with the residual-protio signal of the C_6D_6 used as the internal calibrant.

(iii) **Observed**: ^{1}H NMR signals can be attributed to these complexes; however, obtaining ^{1}H NMR data for a pure sample was not possible due to the lack of crystallinity or instability of the species.

(iv) **Not observed**: The complex was not detected spectroscopically, but its existence is likely.

(v) **Not applicable**: The complex did not form, either due to steric constraints or decomposition.

(vi) **Undetermined**: The complex likely exists, but assigning ^{1}H NMR signals was not possible.

Table 4.1. Summary of outcomes in the reaction of **11** with various amines

Amine	Adduct (**12**)	Monosubstituted Dinuclear (**13**)	Disubstituted Dinuclear (**14**)	Trinuclear (**15**)
^{t}BuNH$_2$	observed	isolated yield 85%	isolated yield 81%	observed
^{t}AmNH$_2$	observed	isolated yield 54%	isolated yield 53%	undetermined
Benzylamine	not observed	*in-situ* yield 50%	not applicable	not applicable
DIPA	isolated yield 61%	not applicable	not applicable	not applicable
Piperidine	isolated yield 38%	isolated yield 55%	observed	isolated yield 25%

	Adduct (**12**)	Monosubstituted Dinuclear (**13**)	Disubstituted Dinuclear (**14**)	Trinuclear (**15**)
Aniline	not observed	*in-situ* yield 50%	not applicable	not applicable
p-toluidine	not observed	*in-situ* yield 52%	not applicable	not applicable
o-toluidine	not observed	*in-situ* yield 60%	not applicable	not applicable
Mesidine	not observed	isolated yield 54%	observed	isolated yield 28%
2,6-diisopropylaniline	not observed	isolated yield 58%	undetermined	observed***
N-methylaniline	not observed	*in-situ* yield 90%	undetermined	observed
N-methylbenzylamine	not observed	*in-situ* yield 92%	undetermined	observed

*** isolated as the homoleptic trinuclear complex **16**.

The protonolysis reactions by alkylamines, arylamines and N-methylamines are discussed below.

4.2.2 Protonolysis by Alkylamines

Preliminary studies conducted by Dr. Wei Zhang investigated the reactivity of **11** with varying equivalents of $^{t}BuNH_2$ and a structurally similar amine, $^{t}AmNH_2$.[27] Both amines contain a tertiary carbon bound to nitrogen, which was hypothesized to be necessary to form isolable complexes, as observed in the synthesis of Fe(III) complexes.[25] It was found that the addition of 0.5 equivalents of $^{t}BuNH_2$ to **11** in benzene at room temperature produced a green solution and yielded the stoichiometric monosubstituted dinuclear complex, $Fe_2(\mu\text{-}NH^{t}Bu)(\mu\text{-}N(SiMe_3)_2)[N(SiMe_3)_2]_2$ (**13-^{t}Bu**). Analogous to the protonolysis of **11** with $^{t}BuNH_2$, 0.5 equivalent and 1 equivalent of $^{t}AmNH_2$ to **11** in C_6D_6 yielded the monosubstituted dinuclear complex, $Fe_2(\mu\text{-}NH^{t}Am)(\mu\text{-}N(SiMe_3)_2)[N(SiMe_3)_2]_2$ (**13-^{t}Am**) and the disubstituted, dinuclear complex, $Fe_2(\mu\text{-}NH^{t}Am)_2[N(SiMe_3)_2]_2$ (**14-^{t}Am**) respectively. These results showcased that the formation of monosubstituted and disubstituted dinuclear complexes are controlled by stoichiometry as **14-^{t}Bu** (or **14-^{t}Am**) does not appear at 0.5 equivalents of

amine and that heat was necessary for the formation of **14**, otherwise the reaction does not go to completion.

Dr. Wei Zhang also investigated higher equivalents of $^{t}BuNH_2$ and isolated single crystals of the trinuclear complex $Fe_3(\mu\text{-}NH^{t}Bu)_4[N(SiMe_3)_2]_2$ (**15-^{t}Bu**) from the reaction of **11** with 2 equivalents of $^{t}BuNH_2$ in THF heated to 45 °C. This reactivity revealed some challenges and key observations:

(i) **Solvent dependence:** Dr. Wei Zhang proposed that THF was necessary for the formation of **15-^{t}Bu**, in contrast to the dinuclear complexes, which form in benzene.

(ii) **Incomplete conversion:** The reaction never produced pure **15-^{t}Bu**, always yielding a mixture of **14-^{t}Bu** and **15-^{t}Bu**, with **14-^{t}Bu** as the predominant product.

(iii) **Purification challenges:** Fractional crystallization of **15-^{t}Bu** can lead to crystals of mostly **15-^{t}Bu** but still contain **14-^{t}Bu** contamination due to the similar solubilities of **14-^{t}Bu** and **15-^{t}Bu** in pentane.

(iv) **Structural and spectroscopic analysis**: The crystal structure of **15-^{t}Bu** reveals the presence of two distinct diastereomers. The ^{1}H NMR spectrum of **15-^{t}Bu** exhibits three broad signals, though it remains unclear whether this broadness arises from the presence of different isomers in solution or from restricted rotation. Consequently, ^{1}H NMR spectroscopy cannot be reliably used to assess the purity of the complex.

Since the synthetic protocol for the formation of **15-^{t}Bu** did not achieve complete conversion of **14-^{t}Bu** to **15-^{t}Bu**, reaction parameters—including concentration, temperature (rt vs. 45 °C), stoichiometry and solvent (C_6D_6, THF-d_8) — were systematically varied to optimize the formation of **15-^{t}Bu**. The following observations are noted:

(i) **Concentration**: Increasing the initial reaction concentration by a factor of five did not result in a higher yield of **15-^{t}Bu** relative to **14-^{t}Bu**.

(ii) **Temperature:** Conducting the reaction at room temperature vs. 45 °C did not significantly alter the product distribution. Higher temperatures (> 45 °C) were not explored due to the potential decomposition of the complexes.

(iii) **Stoichiometry:** Increasing the amount of $^{t}BuNH_2$ (3 equivalents instead of 2 equivalents) in the initial reaction did not change the product distribution.

(iv) **Solvent effects:** Performing the reaction in THF-d_8 at 45 °C resulted in a faster formation of **15-^{t}Bu** compared to C_6D_6. However, after 24 hours, the yields of **15-^{t}Bu** in THF-d_8 and C_6D_6 were comparable.

(v) **Post-reaction amine addition:** Adding $^{t}BuNH_2$ to the isolated **14-^{t}Bu**/**15-^{t}Bu** crystals in THF-d_8 did not lead to more **15-^{t}Bu** being produced.

These results suggest that the reaction may reach equilibrium, where the observed **14-^{t}Bu** to **15-^{t}Bu** product ratio remains constant even with altered parameters. However, no definite evidence confirms this hypothesis. One experiment that was considered but not attempted – due to the inability to synthesize **15-^{t}Bu** in pure form – was the addition of HMDSA to **15-^{t}Bu** to determine whether the equilibrium would lead back to **14-^{t}Bu** formation.

Building upon Dr. Wei Zhang's successful work with alkylamines containing a tertiary carbon bound to nitrogen, the following discussion focuses on the reactivity of **11** with amines that contain α-protons which include benzylamine, DIPA and piperidine. The addition of 0.5 equivalents of benzylamine to **11** in benzene resulted in a color change from light green to opaque black within hours. The predominant resonances in the ^{1}H NMR spectrum were consistent with the formation of the monosubstituted, dinuclear complex ($Fe_2(\mu\text{-NHBn})(\mu\text{-N(SiMe}_3)_2)[N(SiMe_3)_2]_2$ (**13-Bn**), with an *in-situ* yield of 45%. The following observations were made:

(i) The opaque black solution starkly contrasts with the transparent light green color of **13-^{t}Bu**, **14-^{t}Bu**, **13-^{t}Am** and **14-^{t}Am**. It is believed that the opaque black coloration is due to decomposition products rather than **13-Bn**, accounting for the remaining 55% of **11**.

(ii) The *in-situ* yield of 45% is significantly lower than the nearly quantitative formation (> 90 %) of **13-^{t}Bu**, **14-^{t}Bu**, **13-^{t}Am** and **14-^{t}Am**.

(iii) Solvent removal *in vacuo* resulted in a black oil, in contrast to the green powders typically associated with isolable materials. Attempts to crystallize **13-Bn,** even with shorter reaction times to avoid the black opaque solution color, have thus far been unsuccessful.

The addition of 1 equivalent of benzylamine to **11** in benzene also resulted in the solution darkening from light green to opaque black within hours. However, ^{1}H NMR spectroscopy of the material revealed no predominant resonances aside from the signal corresponding to HMDSA. This result suggests that at higher benzylamine equivalents, no molecular complexes are formed, and decomposition is the likely reaction pathway.

The addition of one equivalent of DIPA to **11** in benzene produced a transparent light blue solution with the mononuclear, diisopropylamine adduct complex $Fe(NH(^iPr)_2)[N(SiMe_3)_2]_2$ (**12-DIPA**) formed as the sole product. The light blue solution color is indicative of adduct formation, consistent with the solution color of $Fe(N(SiMe_3)_2)_2(THF)$ (**12-THF**). This outcome differs significantly from the reactivity of **11** with $^tBuNH_2$ and $BnNH_2$, where the same stoichiometry (1:1) leads to the formation of **14-^{t}Bu** and decomposition, respectively. Compound **12-DIPA** can be crystallized from a concentration solution in pentane at –20 °C. Two factors are proposed to explain why higher-nuclearity complexes do not form in the synthesis of diisopropylamide-ligated complexes, even with higher equivalents of DIPA:

(i) The bulky isopropyl groups create a high-energy transition state for the proton transfer step, preventing further substitution.

(ii) Diisopropylamide is not an effective bridging ligand due to steric.

To overcome the proposed high-energy transition state, a solution of **12-DIPA** in benzene was heated to 45 °C over 16 h. However, no change in solution color to green—characteristic of higher nuclearity complexes— was observed, indicating that such complexes did not form

under these conditions. The ^{1}H NMR spectrum of the reaction also displayed the resonances consistent with **12-DIPA**.

Lastly, piperidine, a secondary alkylamine with protons on the α-carbons, was tested for reactivity. Surprisingly, the reaction of **11** with piperidine yielded three isolable types of iron complexes (mononuclear amine adduct, monosubstituted dinuclear, and trinuclear complexes). Noted below are the following observations:

(i) **0.5 equivalent of piperidine to 11**: produced the monosubstituted, dinuclear complex $Fe_2(\mu\text{-}N(CH_2)_5)(\mu\text{-}N(SiMe_3)_2)[N(SiMe_3)_2]_2$ (**13-pip**) quantitatively with the reaction being complete overnight.

(i) **1 equivalent of piperidine to 11 with a 16 h reaction time**: resulted in a mixture of **13-pip,** the disubstituted, dinuclear complex, $Fe_2(\mu\text{-}N(CH_2)_5)_2[N(SiMe_3)_2]_2$ (**14-pip**), and the trinuclear complex $Fe_3(\mu\text{-}N(CH_2)_5)_4[N(SiMe_3)_2]_2$ (**15-pip**) based on ^{1}H NMR data. While the stoichiometry suggested that **14-pip** should be the sole product, the presence of **15-pip** implies a lower reaction barrier for its formation compared to the analogues ^{t}BuNH$_2$ derived complex **15-^{t}Bu**. Piperidine is slightly less acidic compared to ^{t}BuNH$_2$, sterically distinct, and a secondary amine, leading to a difference in product distribution. Attempts to crystallize **14-pip** have been unsuccessful.

(ii) **1 equivalent of piperidine to 11 with a 1 h reaction time**: a light green solution formed, and light blue crystals were isolated after pentane/HMDSO vapour diffusion overnight at –15 °C. The crystal color and single crystal X-ray diffraction data confirmed the structure of the mononuclear amine adduct complex, $Fe(NH(CH_2)_5)[N(SiMe_3)_2]_2$ (**12-pip**). This adduct was the predominant product in the reaction mixture, which contained **11**, **12-pip** and **13-pip**. The slow reaction kinetics allowed the trapping of the piperidine adduct intermediate and dissolution of **12-pip** in C_6D_6 revealed its transformation to **13-pip** within hours. This transformation is discussed further in Section 4.2.6.

(iii) **1.33 equivalents of piperidine to 11**: The use of 1.33 equivalents of piperidine with **11** overnight led to the formation of $Fe_3(\mu\text{-}N(CH_2)_5)_4[N(SiMe_3)_2]_2$ (**15-pip**) with slight contamination of the dinuclear complex **14-pip**.

(iv) **2 equivalents of piperidine to 11**: **15-pip** was the sole product with an *in*-situ yield for this transformation being 95%, representing a near-quantitative conversion. The excess piperidine accelerated the reaction rate, enabling complete formation of **15-pip** overnight.

(v) The isolated yields of **13-pip** and **15-pip** were 55% and 25%, respectively, which is significantly lower than their *in-situ* yields. This discrepancy was attributed to the high solubility of these complexes in non-polar solvents, complicating their isolation.

These observations have led to the investigation in the protonolysis reaction of **11** with other alkylamines that contain α-protons to help provide more specific insight into the conditions for complex formation and decomposition.

4.2.2.1 Protonolysis by Alkylamines – Inconclusive Results

Protonolysis of **11** with cyclohexylamine, *n*-butylamine, *n*-octylamine and diethylamine was performed, although the results were less definitive compared to the other reactivity studies discussed. Shown in Figure 4.4 are the structures of these amines.

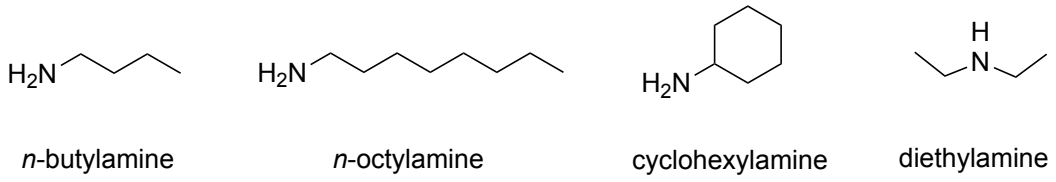

Figure 4.4. Molecular structures of *n*-butylamine, *n*-octylamine, cyclohexylamine, and diethylamine.

The reactivity of cyclohexylamine, *n*-butylamine and *n*-octylamine was investigated to determine whether α-proton decomposition was responsible for the observed reactivity

with benzylamine. Benzylamine is a more reactive amine, so the decomposition pathway may have been influenced by an alternative mechanism, not due to the α-protons. The following observations were made:

(i) NMR scale reactions (5- 10 mg of **11**) with 0.5 or 1 equivalents of cyclohexylamine, *n*-butylamine, or *n*-octylamine in C_6D_6 resulted in a light green solution and isotropically shifted NMR signals, consistent with complex formation. The many signals in the ^{1}H NMR spectrum made structure determination difficult.

(ii) Larger scale reactions (60-100 mg of **11**) with 0.5 equivalents of cyclohexylamine, *n*-butylamine, or *n*-octylamine in benzene yielded a transparent orange solution, with the material appearing as an oil after solvent removal under reduced pressure. It is unclear if the oily nature of the material is due to contamination or due to the dinuclear complexes with these substituents being oils.

(iii) Larger scale reactions (60-100 mg of **11**) with 1 equivalent of cyclohexylamine, *n*-butylamine, *n*-octylamine in benzene yielded opaque black solutions, with the material appearing as an oil after solvent removal under reduced pressure. This result is consistent with decomposition.

The protonolysis of **11** with diethylamine was attempted to determine the steric hindrance effect in inhibiting dinuclear complex formation. The addition of 0.5 and 1 equivalent of diethylamine to **11** resulted in transparent green solutions, rather than the expected light blue color indicative of the amine adduct. The ^{1}H NMR spectra contained numerous signals, but the predominant signals could not be reliably assigned. The reaction of **11** with 1 equivalent of diethylamine was examined with a 1 hour reaction time. The ^{1}H NMR spectrum of the material in C_6D_6 displayed broad signals in the expected chemical shift region for the amine adduct; however, crystallization attempts were unsuccessful in isolating the amine adduct.

The protonolysis reactions of **11** with cyclohexylamine, *n*-butylamine, or *n*-octylamine have led to inconclusive observations. Further work needs to be performed to understand the variables that are leading to decomposition with the upscale reactions. Further work will also be needed to isolate material from the reaction of **11** with diethylamine. The signal sets and color are evident that the mononuclear amine adduct **12** and at least the dinuclear monosubstituted complexes are also forming.

4.2.2 Protonolysis by Arylamines

Arylamines are generally more acidic than alkylamines, exhibiting p*Ka* values that are comparable to the p*Ka* of $(Me_3Si)_2NH$, which led to faster reaction times compared to alkylamines. This faster reaction rate is observed visually with the light green solution color of **11** darkening to dark green within minutes after the addition of arylamines and spectroscopically with the formation of **13** being complete within 2-3 hours. Dr. Wei Zhang observed the formation of a trinuclear complex upon reaction of **11** with 1.33 equivalents of mesidine, whereas the reaction of **11** with aniline resulted in no discernible ^{1}H NMR signals and the formation of an opaque, black solution, indicating decomposition. This differing reactivity prompted a more in-depth study of the interactions between **11** and arylamines.

The reactivity of **11** with mesidine in benzene at the following stoichiometries was worked on by Jay Bhagat and showcases the following observations:

(i) **0.5 equivalent to 11:** A transparent yellow-green solution formed within minutes, with the monosubstituted complex $Fe_2(\mu\text{-NHMes})(\mu\text{-N(SiMe}_3)_2)[N(SiMe_3)_2]_2$ (**13-Mes**) as the sole product. The reaction was complete within hours and **13-Mes** was formed quantitatively.

(ii) **1 equivalent to 11:** A dark green solution formed, exhibiting numerous sharp and broad resonances in the ^{1}H NMR spectrum, with both **13-Mes,** $Fe_3(\mu\text{-NHMes})_4[N(SiMe_3)_2]_2$ (**15-Mes**) and likely $Fe_2(\mu\text{-NHMes})_2[N(SiMe_3)_2]_2$ **14-Mes** present.

(iii) **1.33 equivalents to 11:** A dark green solution formed, exhibiting numerous sharp and broad resonances in the ^{1}H NMR spectrum. The predominant signal set corresponded to the trinuclear complex **15-Mes**.

(iv) **2 equivalents to 11:** A transparent solution formed with dark grey precipitation, indicating decomposition.

The numerous sharp and broad signals observed in the ^{1}H NMR spectra of **11** with 1 and 1.33 equivalents of mesidine suggest the presence of a secondary reaction pathway that is not observed with alkylamines. This secondary pathway may be attributed to the comparable acidity of arylamines to $(Me_3Si)_2NH$ leading to further reactivity. Solvent removal *in vacuo* and crystallization of the reaction of **11** with 1 equivalent of mesidine lead to the isolation of crystals of **13-Mes** and **15-Mes** with **14-Mes** not crystallizing from the solution. This result, along with the reaction of **11** with 1 equivalent of piperidine indicates that the disubstituted, dinuclear complex **14-Mes** is not the most stable complex formed.

The reactivity of **11** with 2,6-diisopropylaniline in benzene showcases similar reactivity as mesidine at 0.5 and 1 equivalents with the monosubstituted, dinuclear complex forming and numerous sharp and broad resonances forming. At 1.33 equivalent, the solution color develops to a deep red with the product isolated from the crude mixture being the homoleptic complex $Fe_3(\mu\text{-}NH(2,6\text{-}C_6H_3{}^iPr_2)_4[NH(2,6\text{-}C_6H_3{}^iPr_2)]_2$ (**16-DIPAni**). This is the only instance of homoleptic trinuclear complexes formed with the same bridging and terminal amide ligation. The deep red, opaque solution color contrasts with the transparent green solution observed with other complexes formed and it is a stark visual indicator of **16-DIPAni.**

The observations in the reactivity of **11** with mesidine and 2,6-diisopropylaniline reveals the following:

(i) The comparable acidity of arylamines compared to $(Me_3Si)_2NH$ likely allows for both bridging and terminal ligation of the deprotonated arylamine.

(ii) 2,6-diisopropylanilide provides sufficient steric bulk to stabilize the homoleptic trinuclear complex, leading to the stability and isolation of the complex.

The decomposition observed with 2 equivalents of mesidine may be attributed to point (ii), as terminal substitution likely occurs during protonolysis with mesidine; however, the methyl groups on mesidine do not provide sufficient steric bulk to stabilize the homoleptic trinuclear complex.

Dr. Wei Zhang's preliminary results with 1 equivalent of aniline to **11** and the recent results with mesidine have led to a further investigation with aniline and other aniline derivatives to determine if a trend can be discovered. The results are summarized below:

(i) **0.5 equivalents of aniline to 11:** Formation of an opaque black solution within hours and the formation of the mono-substituted dinuclear complexes with the following *in-situ* yields:
Aniline, $Fe_2(\mu\text{-NHPh})(\mu\text{-N(SiMe}_3)_2)[N(SiMe_3)_2]_2$ (13-Ph): 50%
***p*-toluidine, $Fe_2(\mu\text{-NH(4-C}_6H_4Me))(\mu\text{-N(SiMe}_3)_2)[N(SiMe_3)_2]_2$ (13-*p*-Tol)**: 52%
***o*-toluidine, $Fe_2(\mu\text{-NH(}o\text{-C}_6H_4Me))(\mu\text{-N(SiMe}_3)_2)[N(SiMe_3)_2]_2$ (13-*o*-Tol):** 66%

(ii) **1 equivalent of aniline, *p*-toluidine or *o*-toluidine:** Formation of an opaque black solution within hours and only HMDSA observed in the ^{1}H NMR spectrum.

The reactivity of **11** with aniline and *p*-toluidine resulted in the formation of **13** in similar amounts in solution, while the reaction with *o*-toluidine led to an increase in yield to 66%. The decomposition and *in-situ* yields led to the following insight:

(i) Substitution at the para position with a methyl group does not inhibit the decomposition pathway.

(ii) Substitution at one ortho position with a methyl group may inhibit the decomposition pathway, potentially due to steric effects or the absence of a proton inhibiting the decomposition pathway.

(iii) A comparison of these reactions with the protonolysis of **11** using mesidine demonstrates that substitution in both ortho positions result in more favorable reactivity.

4.2.3 Protonolysis by *N*-methylamines

The reaction of **11** with 0.5 equivalents of aniline and benzylamine led to the formation of the monosubstituted, dinuclear complex in approximately 50% *in-situ* yield. However, the reaction of **11** with 1 equivalent of aniline and benzylamine led to no resonances besides HMDSA when analyzed via ^{1}H NMR spectroscopy, indicating decomposition. In contrast, the protonolysis reaction of **11** with piperidine (secondary alkylamines with α-protons) led to the quantitative formation of **13-pip** and **15-pip**. These observations suggest that utilizing secondary derivatives of benzylamine and aniline may provide an avenue for isolating stable, higher nuclearity complexes. Simple secondary amines to investigate are those with a methyl substituent on the nitrogen, such as *N*-methylaniline and *N*-methylbenzylamine.

The addition of 0.5 equivalents of *N*-methylaniline or *N*-methylbenzylamine to **11** resulted in a light green solution and the quantitative formation of the monosubstituted, dinuclear complexes $Fe_2(\mu\text{-N(Me)Ph})(\mu\text{-N(SiMe}_3)_2)[\text{N(SiMe}_3)_2]_2$ (**13-NMePh**) and $Fe_2(\mu\text{-N(Me)Bn})(\mu\text{-N(SiMe}_3)_2)[\text{N(SiMe}_3)_2]_2$ (**13-NMeBn**). Upon solvent removal under vacuum, a light green powder remains. Attempts to crystallize **13-NMePh** and **13-NMeBn** have so far been unsuccessful, as a pentane/HMDSO diffusion at –15 °C does not yield crystals. This reactivity contrasts with that of **11** with 0.5 equivalents of aniline or benzylamine, which led to opaque, black solutions and the formation of a black oil after solvent removal.

Testing higher equivalents of *N*-methylaniline or *N*-methylbenzylamine compared to aniline and benzylamine showed distinct results. Specifically, the addition of 1.33 equivalents of *N*-methylaniline or *N*-methylbenzylamine to **11** resulted in a transparent green solution. Subsequent solvent removal under vacuum, redissolution in pentane, and a vapour evaporation with HMDSO at –15 °C yielded X-ray quality crystals, which identified the complexes of $Fe_3(\mu\text{-N(Me)Ph})_4\text{N(SiMe}_3)_2]_2$ (**15-NMePh**) and $Fe_3(\mu\text{-N(Me)Bn})_4\text{N(SiMe}_3)_2]_2$ (**13-NMeBn**), respectively. However, harvesting the crystals proved challenging, as they incorporated pentane within the crystal lattice and crystallinity was lost upon workup. Harvesting bulk crystalline material was not possible due to the pentane solvation.

Comparing the results of the protonolysis reaction of **11** with benzylamine/aniline versus *N*-methylbenzylamine/*N*-methylaniline highlights the effect of a proton on nitrogen in

this reaction. While the exact decomposition mechanisms of **11** with aniline and benzylamine remain unclear, it can be hypothesized that the decomposition pathways for both protonolysis reactions are different. The observations for each decomposition pathway are noted below:

(i) **Primary arylamines with ortho protons**: The comparable acidity of $(Me_3Si)_2NH$ with arylamines likely leads to terminal $(Me_3Si)_2N^-$ substitution followed by decomposition of the reactive three coordinate iron centers.

(ii) **Primary alkylamines with α-protons**: The logical decomposition pathway for primary alkylamines with α-protons would be a dehydrogenation reaction. As monosubstituted complexes with benzylamide can be detected, it is likely that the monosubstituted species is stable but further substitution (terminal or bridging) is leading to decomposition.

4.2.4 Complex Structures

Single crystal x-ray diffraction analysis is essential for determining the structural motifs of the complexes formed in this chapter, as the technique provides more reliable and definite results compared to other techniques. Although ^{1}H NMR spectroscopy can be used to determine the structures of the mononuclear and dinuclear complexes in solution, it has limitations, particularly for trinuclear complexes. The ^{1}H NMR data for the trinuclear complexes cannot be used to reliably determine structures due to the number of signals and the overlapping of the signals as discussed in Section 4.2.6.

4.2.4.1 Structures of Mononuclear Complexes

The first set of complexes analyzed within are the mononuclear amine adduct complexes (**12**). The structures of the two isolated mononuclear complexes, **12-pip** and **12-DIPA** are shown in Figures 4.5 and 4.6, respectively. **12-pip** contains one molecule of **12-pip** in the asymmetric unit and **12-DIPA** contains half a molecule in the asymmetric unit as the Fe-N_{amine} bond is located on a 2-fold axis. The crystallographic data for **12-DIPA** showcases disorder of the isopropyl substituents which can be attributed to the rotational freedom of the isopropyl groups.

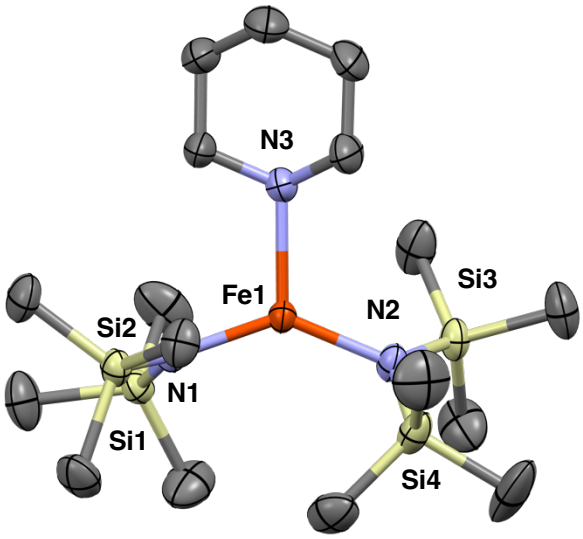

Figure 4.5. Structure of $Fe(NH(CH_2)_5)[N(SiMe_3)_2]_2$ (**12-pip**) with thermal ellipsoids (50% probability level) and selected atom labels. Hydrogen atoms are not shown.

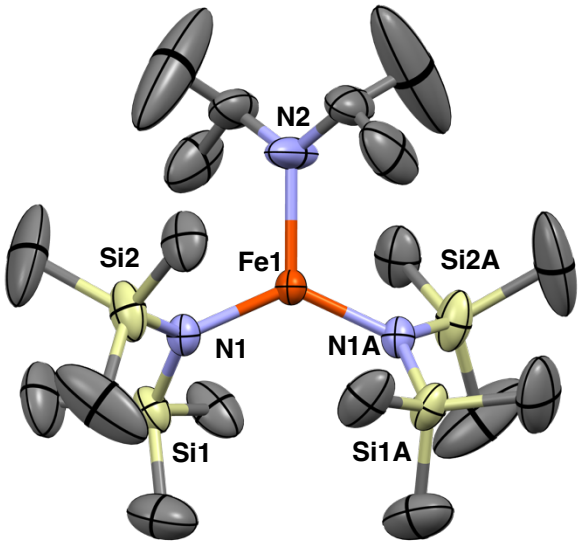

Figure 4.6. Structure of $Fe(NH(^iPr)_2)[N(SiMe_3)_2]_2$ (**12-DIPA**) with thermal ellipsoids (50% probability level) and selected atom labels. Hydrogen atoms are not shown. The asymmetric unit contains half of the **12-DIPA** molecule, with the remaining atoms generated by a crystallographic 2-fold rotation.

Selected metrics for **12-pip** and **12-DIPA** are tabulated in Table 4.2. Both **12-pip** and **12-DIPA** showcase trigonal planar, three coordinate iron atoms coordinated by two $N(SiMe_3)_2$ ligands and one amine. **12-pip** and **12-DIPA** contain two distinct Fe–N bonds, an iron–amide bond and an iron–amine bond, which can be distinguished by the bond length. The iron-amide bond lengths are shorter than the iron-amine bond lengths by approximately 0.2 Å.

Table 4.2. Selected distances (Å) and Angles (º) for $Fe(NH(CH_2)_5)[N(SiMe_3)_2]_2$ (**12-pip**) and $Fe(NH(^iPr)_2)[N(SiMe_3)_2]_2$ (**12-DIPA**)

	12-pip	**12-DIPA**
Fe(1)–N(1/q)	1.928(2)/1.926(1)	1.947(4)
Fe(1)–N(r)	2.137(2)	2.172(6)
N(1)–Si(1/2)	1.715(1)/1.707(1)	1.708(4)/1.723(4)
N(2)–Si(3/4)	1.714(1)/1.714(1)	
N(1)–Fe(1)–N(q)	137.78(6)	131.68(24)
N(1/2)–Fe(1)–N(q)	113.27(6)/108.94(6)	114.16(12)
Si(1/2)–N(1)–Fe(1)	115.23(8)/119.68(8)	122.87(21)/114.98(19)
Si(3/4)–N(2)–Fe(1)	124.83(9)/124.93(8)	
Si(1/3)–N(1/2)–Si(2/4)	114.01(7)/120.71(7)	121.93(22)

For **12-pip**: q = 2, r = 3; For **12-DIPA**: q = 1A, r = 2.The asymmetric unit of **12-DIPA** contains half the molecule as a 2-fold rotation axis runs along the $Fe\text{-}N_{amine}$ bond. The asymmetric unit of **12-DIPA** contains half the molecule as a 2-fold rotation axis runs along the $Fe–N_{amine}$ bond.

4.2.4.2 Structures of Dinuclear Complexes

The second set of complexes analyzed within are the dinuclear complexes (**13** and **14**). The two isolated disubstituted dinuclear complexes **14-^{t}Bu** and **14-^{t}Am** were structurally characterized by Dr. Jeremiah Duncan and Dr. Wei Zhang, respectively. Dr. Wei Zhang also structurally characterized the monosubstituted **13-^{t}Bu**. The structures of the four isolated monosubstituted, dinuclear complexes **13-pip**, **13-^{t}Am**, **13-Mes** and **13-DIPAni** are shown in Figures 4.7-4.10, respectively. The general structures of these complexes showcase essentially a planar Fe_2N_2 core with trigonal planar iron atoms and tetrahedral bridging amides. The structure of **13-Mes** contained half of the molecule in the asymmetric unit as a 2-fold rotation axis goes through the two bridging nitrogen atoms. The nitrogen atom being on a special position created two nitrogen sites and two carbon sites that are related by

symmetry which complicates the structural analysis of the molecule. Also, disorder was present for one of the trimethylsilyl groups of the terminal $N(SiMe_3)_2$ ligand.

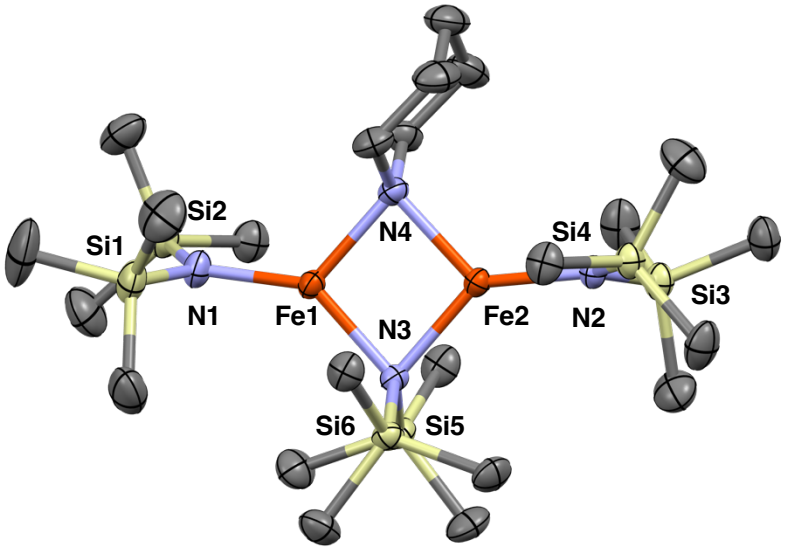

Figure 4.7. Structure of $Fe_2(\mu\text{-}N(CH_2)_5)(\mu\text{-}N(SiMe_3)_2)[N(SiMe_3)_2]_2$ (**13-pip)** with thermal ellipsoids (50% probability level) and selected atom labels. Hydrogen atoms are not shown.

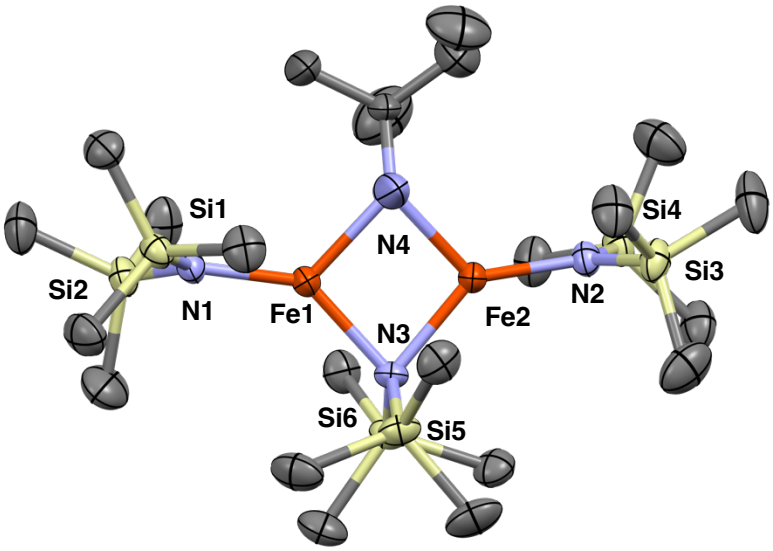

Figure 4.8. Structure of $Fe_2(\mu\text{-}NH^tAm)(\mu\text{-}N(SiMe_3)_2)[N(SiMe_3)_2]_2$(**13-^{t}Am**) with thermal ellipsoids (50% probability level) and selected atom labels. Hydrogen atoms are not shown.

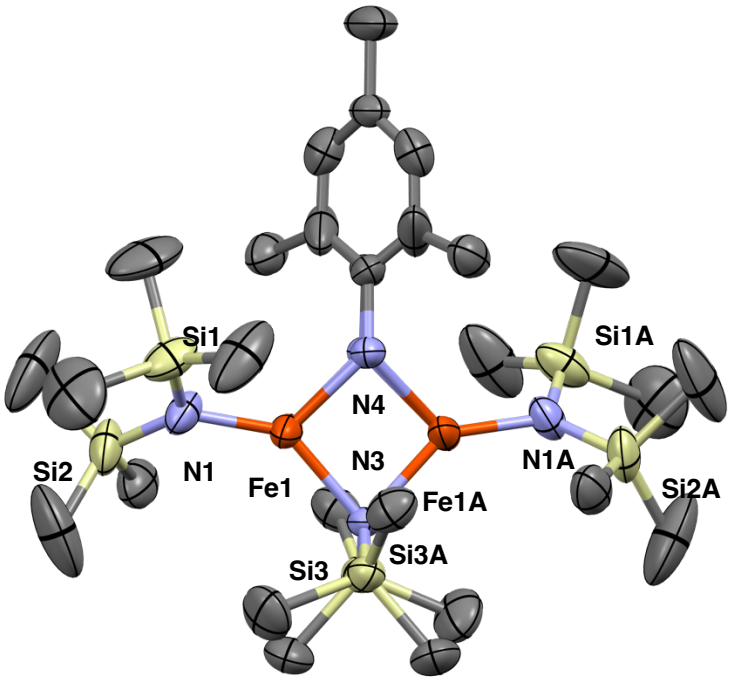

Figure 4.9. Structure of $Fe_2(\mu\text{-NHMes})(\mu\text{-N(SiMe}_3)_2)[\text{N(SiMe}_3)_2]_2$(**13-Mes**) with thermal ellipsoids (50% probability level) and selected atom labels. Hydrogen atoms are not shown. Half the molecule of **13-Mes** present in the asymmetric unit with other atoms generated by crystallographic 2-fold rotation.

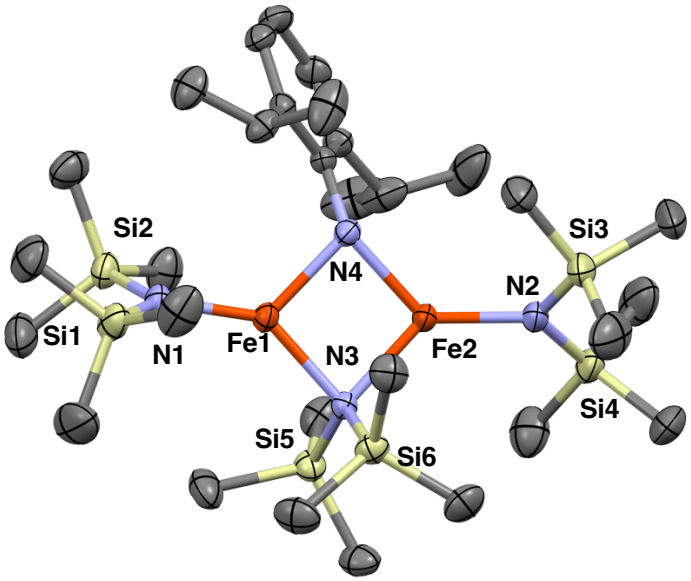

Figure 4.10. Structure of $Fe_2(\mu\text{-2,6-C}_6\text{H}_3{}^i\text{Pr}_2)(\mu\text{-N(SiMe}_3)_2)[\text{N(SiMe}_3)_2]_2$(13-DIPAni) with thermal ellipsoids (50% probability level) and selected atom labels. Hydrogen atoms are not shown.

The dinuclear complexes contain two trigonal planar iron centers that are edge fused via two bridging amide ligands. The iron atoms are three coordinate, and the bridging amides are both four coordinate. The monosubstituted dinuclear complexes contain one μ-N(SiMe$_3$)$_2$ ligand and the second bridging ligand being either an alkyl- (**13-pip** and **13-^{t}Am**) or arylamide (**13-Mes** and **13-DIPAni**). Selected metrics are tabulated in Tables 4.3-4.5. The terminal Fe–N(SiMe$_3$)$_2$ bond lengths are shorter than both the bridging Fe–N(SiMe$_3$)$_2$ and Fe–N(RR) by over 0.1 Å**.** The Fe···Fe distances for the alkylamide complexes are similar while the Fe···Fe distances are longer by 0.05 Å for **13-Mes** and by 0.1 Å for **13-DIPAni** when compared to the alkylamide complexes. The N···N distances are comparable for all structures.

Table 4.3. Selected distances (Å) and Angles (º) for Fe$_2$(μ-N(CH$_2$)$_5$)(μ-N(SiMe$_3$)$_2$)[N(SiMe$_3$)$_2$]$_2$ (**13-pip**) and Fe$_2$(μ-NH^{t}Am)(μ-N(SiMe$_3$)$_2$)[N(SiMe$_3$)$_2$]$_2$ (**13-^{t}Am**)

	13-pip	**13-^{t}Am**
Fe(1/2)–N(1/2)	1.9152(11)/1.9215(10)	1.9166(34)/1.9166(34)
Fe(1)–N(3/4)	2.0513(9)/2.0369(10)	2.0690(33)/2.0232(49)
Fe(2)–N(3/4)	2.0769(1)/2.0266(10)	2.0704(33)/2.0206(49)
Fe(1)···Fe(2)	2.7343(4)	2.7400(11)
N(3)···(N4)	3.049(1)	3.014(7)
N(1)–Si(1/2)	1.7268(12)/1.7205(12)	1.7227(38)/1.7282(36)
N(2)–Si(3/4)	1.7287(11)/1/7218(11)	1.7154(38)/1.7321(36)
N(3)–Si(5/6)	1.7710(10)/1.7702(10)	1.7642(35)/1.7778(36)
N(1/1/4)–Fe(1)–N(3/4/3)	139.23(5)/124.30(5)/96.46(4)	140.00(14)/124.22(17)/94.96(16)
N(2/2/4)–Fe(2)–N(3/4/3)	136.31(3)/127.71(4)/95.98(4)	138.97(14)/125.93(17)/94.96(16)
Si(1/3)–N(1/2)–Si(2/4)	123.02(6)/121.22(6)	122.16(20)/121.34(20)
Fe(1)–N(3/4)–Fe(2)	82.96(4)/84.58(4)	82.89(12)/85.31(20)
Si(1/2)–N(1)–Fe(1)	117.23(6)/119.72(6)	119.68(19)/118.01(2)
Si(3/4)–N(2)–Fe(2)	119.64(6)/118.97(5)	116.81(20)/121.74(19)

The asymmetric unit of **13-pip** and **13-^{t}Am** contains one molecule of **13-pip** and **13-^{t}Am** respectively

Table 4.4. Selected distances (Å) and Angles (º) for Fe$_2$(μ-NHMes)(μ N(SiMe$_3$)$_2$)[N(SiMe$_3$)$_2$]$_2$ (**13-Mes**)

	13-Mes
Fe(1)–N(1)	1.9077(38)
Fe(1)–N(2/3)	2.0795(34)/1.9563(51)
Fe(1)···Fe1A	2.7961(13)

	13-Mes
N(1)–Si(1/2)	1.7272(41)/1.7150(41)
N(2)–Si(3)	1.7653(27)
N(1/1)–Fe(1)–N(2/3)	140.82(16)/126.33(19)
Si(1)–N(1)–Si(2)	121.23(23)
Fe(1)–N(1)–Si(1/2)	119.33(22)/119.43(21)
Fe(1)–N(2/3)–Fe1_$1	84.49(17)/91.22(31)
N(2)–Fe(1)–N(3)	92.14(18)

The asymmetric unit of **13-Mes** contains half a molecule of **13-Mes**.

Table 4.5. Selected Distances (Å) and Angles (º) for $Fe_2(\mu\text{-}NH(2,6\text{-}C_6H_3{}^iPr_2)(\mu\text{-}N(SiMe_3)_2)[N(SiMe_3)_2]_2$ (**13-DIPAni**)

	13-DIPAni
Fe(1/2)–N(1/2)	1.9212(17)/1.9358(17)
Fe(1)–N(3/4)	2.0732(16)/2.0583(19)
Fe(2)–N(3/4)	2.0647(16)/2.1069(19)
Fe(1)···Fe(2)	2.8336(11)
N(3)···(N4)	3.023(3)
N(1)–Si(1/2)	1.7293(19)/1.7383(19)
N(2)–Si(3/4)	1.7360(20)/1.7341(20)
N(3)–Si(5/6)	1.7803(18)/1.7766(18)
N(1/1/4)–Fe(1)–N(3/4/3)	140.77(7)/125.16(7)/94.07(6)
N(2/2/4) –Fe(2)–N(3/4/3)	131.88(7)/129.99(8)/92.89(7)
Si(1/3)–N(1/2)–Si(2/4)	120.62(9)/118.50(9)
Fe(1)–N(3/4) –Fe(2)	85.35(6)/86.83(7)
Si(1/2) –N(1) –Fe(1)	120.92(10)/118.29(9)
Si(3/4) –N(2) –Fe(2)	119.22(10)/122.22(10)

The asymmetric unit of **13-DIPAni** contain one molecule of **13-DIPAni**.

4.2.4.3 Structures of Trinuclear Complexes

The trinuclear complexes are constructed of two sets of Fe_2N_2 dinuclear complexes fused at a central tetrahedral iron center. The terminal irons are ligated by one terminal $N(SiMe_3)_2$ ligand and two bridging ligands except in the case of **16-DIPAni** which has the terminal irons ligated by the same ligand as the bridging ligands. The central iron has a tetrahedral geometry coordinated to four bridging ligands. These trinuclear complexes can be categorized into two groups with one group containing bridging alkylamides (**15-pip**, **15-NMeBn**) and the second group containing bridging arylamides (**15-Mes**, **15-NMePh** and **16-DIPAni**). The structures of the trinuclear complexes are shown in Figure 4.11-4.15

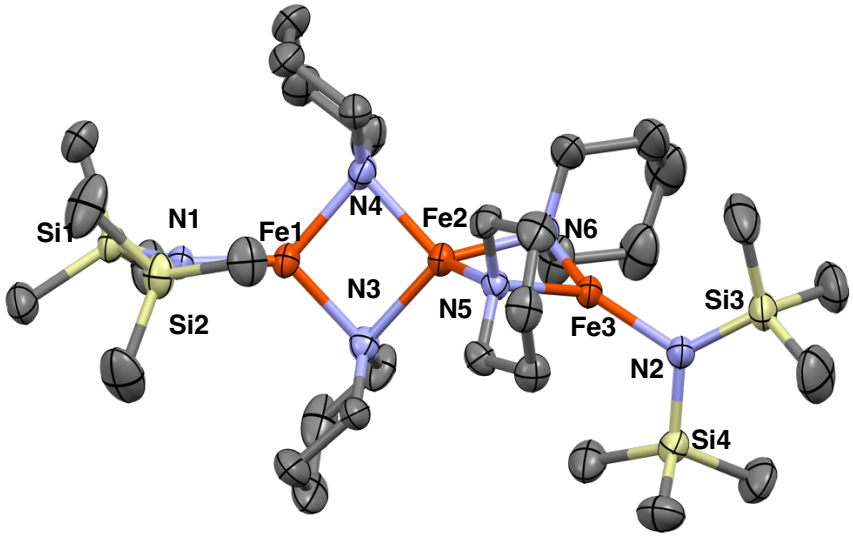

Figure 4.11. Structure of $Fe_3(\mu\text{-}N(CH_2)_5)_4[N(SiMe_3)_2]_2$ (**15-pip**) with thermal ellipsoids (50% probability level) and selected atom labels. Hydrogen atoms are not shown.

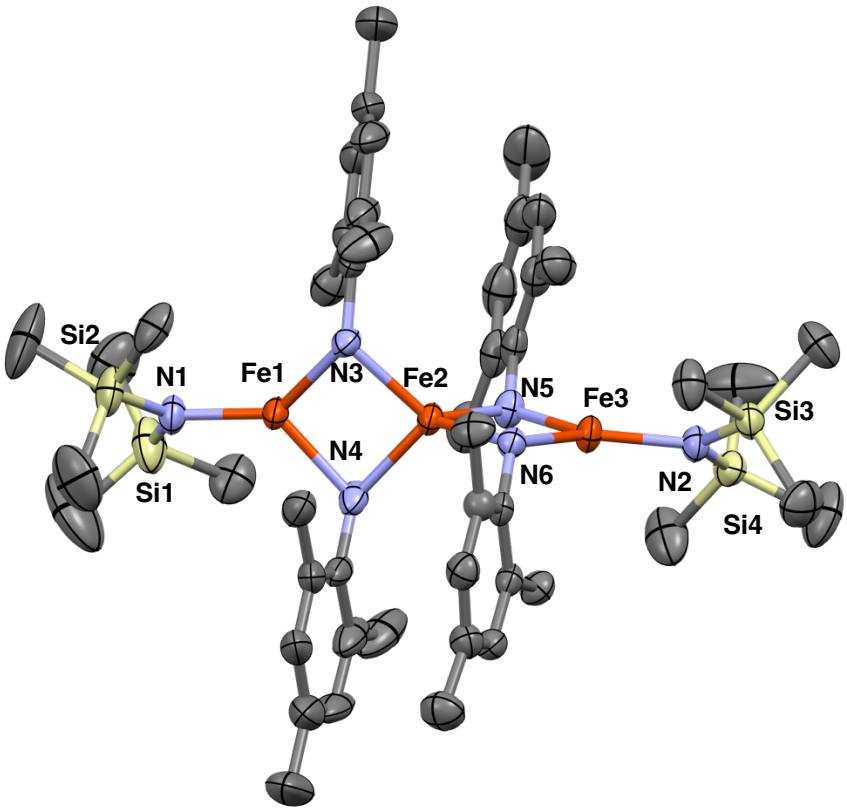

Figure 4.12. Structure of $Fe_3(\mu\text{-}NHMes)_4[N(SiMe_3)_2]_2$ (**15-Mes**) with thermal ellipsoids (50% probability level) and selected atom labels. Hydrogen atoms are not shown.

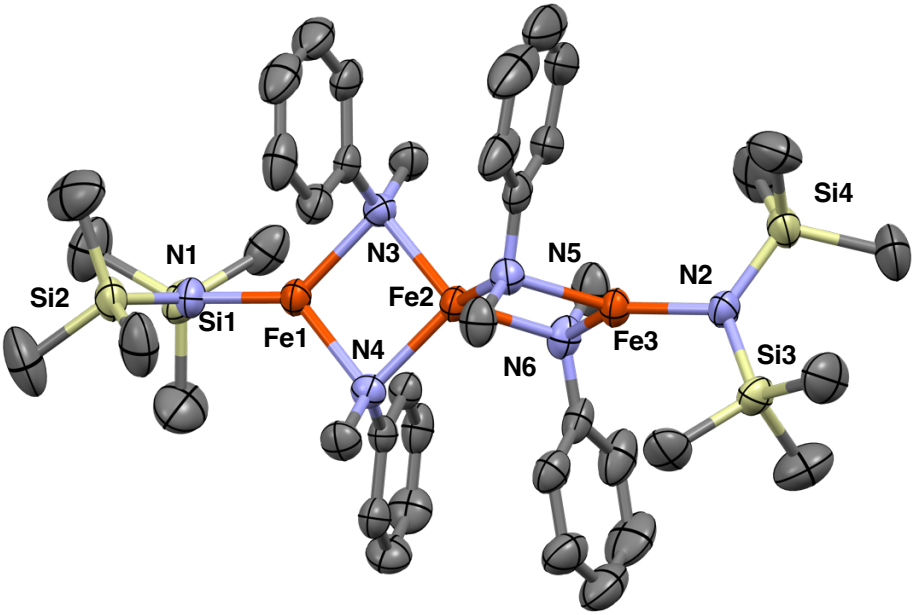

Figure 4.13. Structure of $Fe_3(\mu\text{-}N(Me)Ph)_4N(SiMe_3)_2]_2$ (**15-NMePh**) with thermal ellipsoids (50% probability level) and selected atom labels. Hydrogen atoms are not shown.

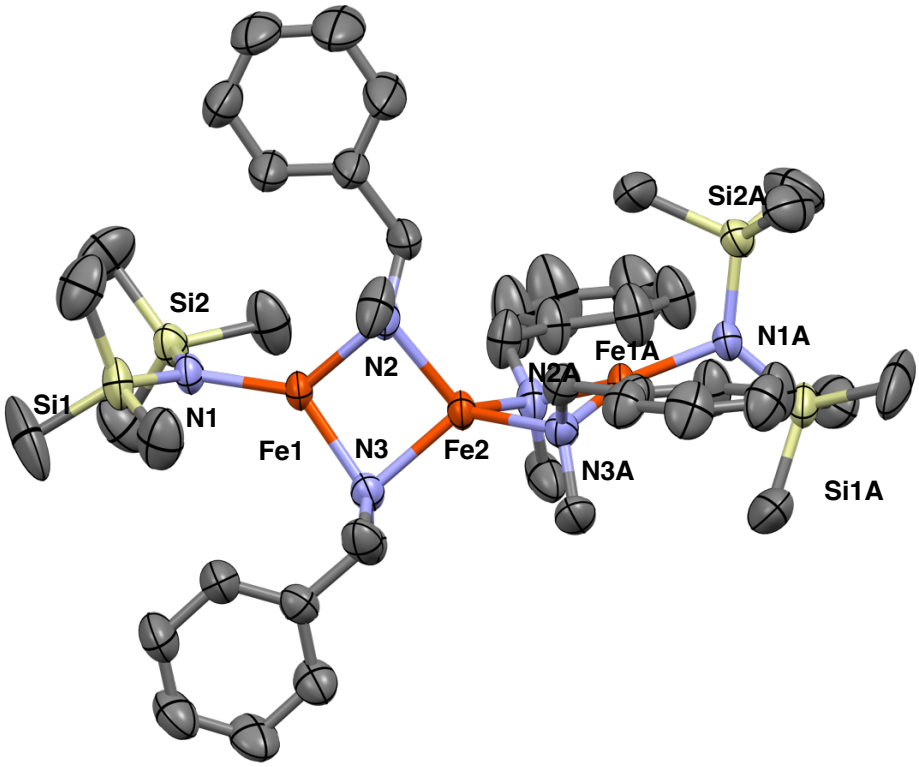

Figure 4.14. Structure of $Fe_3(\mu\text{-}N(Me)Bn)_4N(SiMe_3)_2]_2$ (**15-NMeBn**) with thermal ellipsoids (50% probability level) and selected atom labels. Hydrogen atoms are not shown. Half the molecule of **15-NMeBn** is present in the asymmetric unit with other atoms generated by crystallographic 2-fold rotation.

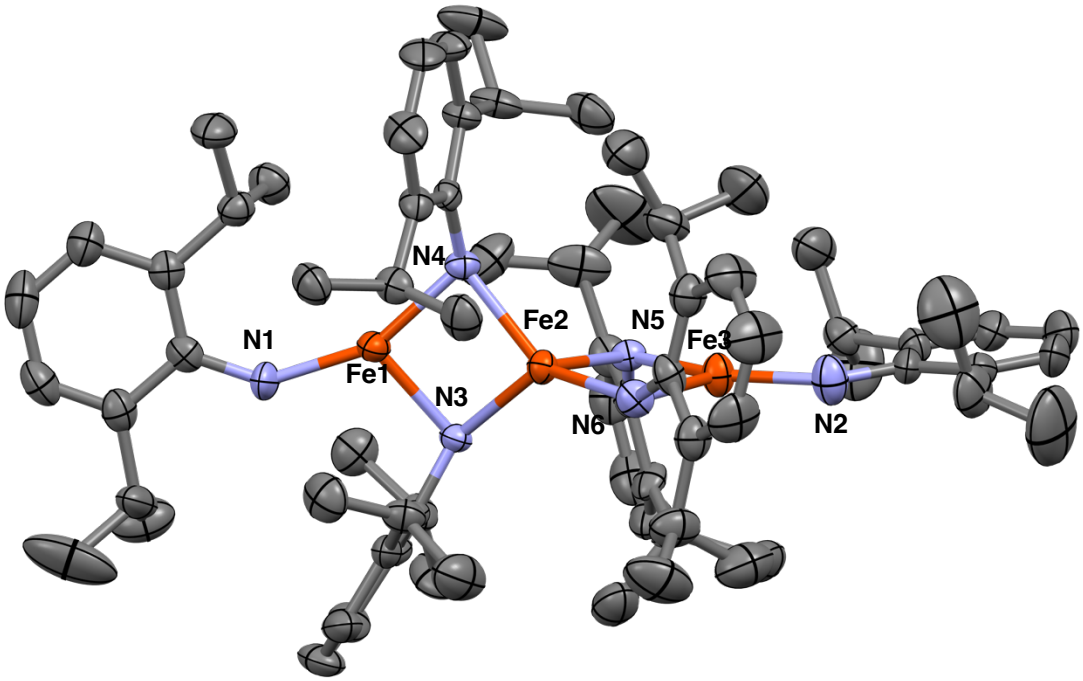

Figure 4.15. Structure of $Fe_3(\mu\text{-}NH(2,6\text{-}C_6H_3{}^iPr_2)_4[NH(2,6\text{-}C_6H_3{}^iPr_2)]_2$ (**16-DIPAni**) with thermal ellipsoids (50% probability level) and selected atom labels. Hydrogen atoms are not shown.

Select metrics for trinuclear complexes are found in Tables 4.6 to 4.8. Trends in the terminal Fe–N and bridging Fe–N bond lengths are analogous to the trends observed in the dinuclear complexes. The bond lengths in general are similar amongst the linear trinuclear complexes. The bigger deviation is present in the Fe–Fe–Fe angle which would ideally be 180 °. Only **15-NMePh** showcases a bond angle close to 180° with the other four trinuclear complexes have a Fe–Fe–Fe bond angle of 160° to 166°.

Table 4.6. Selected Distances (Å) and Angles (º) for $Fe_3(\mu\text{-}NHMes)_4[N(SiMe_3)_2]_2$ (**15-Mes**) and $Fe_3(\mu\text{-}N(Me)Ph)_4N(SiMe_3)_2]_2$ (**15-NMePh**)

	15-Mes	**15-NMePh**
Fe(1/3)–N(1/2)	1.9064(29)/1.9142(28)	1.9059(27)/1.9096(26)
Fe(1/2)–N(3)	2.0523(29)/2.0770(27)	2.0669(28)/2.0960(26)
Fe(1/2)–N(4)	2.0625(29)/2.0849(31)	2.0765(9)/2.0946(28)
Fe(2/3)–N(5)	2.0742(31)/2.0587(31)	2.0839(29)/2.0684(27)
Fe(2/3)–N(6)	2.0766(29)/2.0556(29)	2.0899(28)/2.0704(29)
Fe(1/2)···Fe(2/3)	2.8119(12)/2.8385(14)	2.8467(9)/2.8484(9)
N(3/5)···N(4/6)	3.002(5)/3.015(4)	3.043(4)/3.027(4)
Fe(1)–Fe(2)–Fe(3)	166.34(2)	178.71(3)

	15-Mes	15-NMePh
N(1)–Si(1/2)	1.7165(35)/1.7099(35)	1.7240(31)/1.7321(30)
N(2)–Si(3/4)	1.7207(32)/1.7196(31)	1.7304(28)/1.7244(29)
N(1/1/4)–Fe(1)–N(3/4/3)	137.28(12)/128/17(13)/94.22(11)	134.85(12)/130.60(12)/94.51(11)
N(2/2/6)–Fe(3)–N(5/6/5)	130.11(12)/136.12)/93.77(11)	135.12(12)/130.88(12)/93.98(11)
N(3/4)–Fe(2)–N(5/6)	126.51(13)/123.37(12)	109.62(11)/127.43(11)
N(3/5)–Fe(2)–N(4/6)	92.84(11)/92/70(11)	93.12(11)/92.96(11)
Si(1/3)–N(1/2)–Si(2/4)	125.21(18)/ 124.81(17)	124.41(16)/124.74(16)
Fe(1)–N(3/4)–Fe(2)	85.84(10)/85.37(11)	86.29(10)/86.08(10)
Fe(2)–N(5/6)–Fe(3)	86.75(12)/86.77(11)	86.63(11)/86.42(11)
Si(1/2)–N(1)–Fe(1)	118.93(17)/115.69(18)	118.11(16)/117.41(16)
Si(3/4)–N(2)–Fe(3)	117.87(16)/117.14 (17)	115.82(15)/119.44(15)

The asymmetric unit of **15-Mes** and **15-NMePh** contain one molecule.

Table 4.7. Selected Distances (Å) and Angles (º) for $Fe_3(\mu\text{-}N(CH_2)_5)_4[N(SiMe_3)_2]_2$ (**15-pip**) and $Fe_3(\mu\text{-}NH(2,6\text{-}C_6H_3{}^iPr_2)_4[NH(2,6\text{-}C_6H_3{}^iPr_2)]_2$ (**15-DIPAni**)

	15-pip	15-DIPAni
Fe(1/3)–N(1/2)	1.9223(33)/1.9303(34)	1.8737(78)/1.8850(84)
Fe(1/2) –N(3)	2.0253(34)/2.1053(33)	2.0521(18)/2.1131(69)
Fe(1/2) –N(4)	2.0364(36)/2.0896(35)	2.0173(71)/2.139(70)
Fe(2/3) –N(5)	2.1114(33)/2.0290(34)	2.1435(73)/2.0123(73)
Fe(2/3) –N(6)	2.0315(37)/2.0782(35)	2.0414(72)/2.0936(73)
Fe(1/2)···Fe(2/3)	2.7374(10)/2.7283(11)	2.8481(18)/2.8884(19)
N(3/5)···N(4/6)	3.0180(5)/3.020(5)	2.959(9)/2.97(1)
Fe(1)–Fe(2)–Fe(3)	165.76(3)	161.36(7)
N(1)–Si(1/2)	1.7274(35)/1.7181(36)	
N(2)–Si(3/4)	1.7201(34)/1.7227(36)	
N(1/1/4)–Fe(1)–N(3/4/3)	132.79(14)/130.47(14)/95.96(14)	112.38(31)/154.45(31)/93.16(28)
N(2/2/6)–Fe(3)–N(5/6/5)	131.52(14)/131.26(15)/96.10(13)	151.02(34)/116.43(32)/92.55(29)
N(3/4)–Fe(2)–N(5/6)	114.43(13)/109.94(14)	90.30(28)/135.08(30)
N(3/5)–Fe(2)–N(4/6)	92.00(14)/ 92.23(13)	88.47(36)/90.30(28)
Si(1/3)–N(1/2)–Si(2/4)	123.57(20)/124.41(20)	
Fe(1)–N(3/4)–Fe(2)	82.99(12)/83.12(13)	86.27(26)/86.86(26)

	15-pip	15-DIPAni
Fe(2)–N(5/6)–Fe(3)	82.41(12)/83.18(13)	88.00(27)/88.61(27)
Si(1/2)–N(1)–Fe(1)	119.81(19)/116.43(18)	
Si(3/4)–N(2)–Fe(3)	116.18(19)/119.40(19)/116.18(19)	

Table 4.8. Selected Distances (Å) and Angles (º) for $Fe_3(\mu\text{-}N(Me)Bn)_4N(SiMe_3)_2]_2$ (**15-NMeBn**)

	15-NMeBn
Fe(1)–N(1)	1.9064(33)
Fe(1/2)–N(2)	2.0083(37)/2.0904(37)
Fe(1/2)–N(3)	2.0385(38)/2.0763(35)
Fe(1)···Fe(2)	2.7301(7)
N(2)···N(3)	2.996(6)
Fe(1)–Fe(2)-Fe(1A)	159.98(8)
N(1)–Si(1/2)	1.7054(37)/1.7251(39)
N(1/1/2)–Fe(1)–N(3/2/3)	131.50 (15)/132.88(16)/95.56(15)
N(2)–Fe(2)–N(3)	91.98(14)
Si(1)–-N(1)–Si(2)	125.04(20)
Fe(1)–N(2/3)–Fe(2)	83.50(15)/83.13(14)
Si(1/2)–N(1)–Fe(1)	118.64(21)/116.26(19)

4.2.5 Isomers

The disubstituted, dinuclear complexes and trinuclear complexes can exist as distinct isomers due to variation in the spatial arrangement of the bridging amide substituents. The isolated disubstituted, dinuclear complexes (**14-*t*Bu** and **14-*t*Am**) can adopt either the cis or trans configuration as shown in Figure 4.16. In the solid state, both **14-*t*Bu** and **14-*t*Am** display the trans configuration. In solution, only one signal set is observed using ^{1}H NMR spectroscopy which can be due to the following reasons:

(i) Only one species is present in solution.

(ii) It is possible that both isomers are present in solution but undergo fast isomerization in the timescale of the NMR experiment.

(iii) Also, it is possible that the broad resonances for both the cis and trans configurations are present but overlapping.

The likely and simplest explanation is (i) but these other rationales ((ii) and (iii)) are possible.

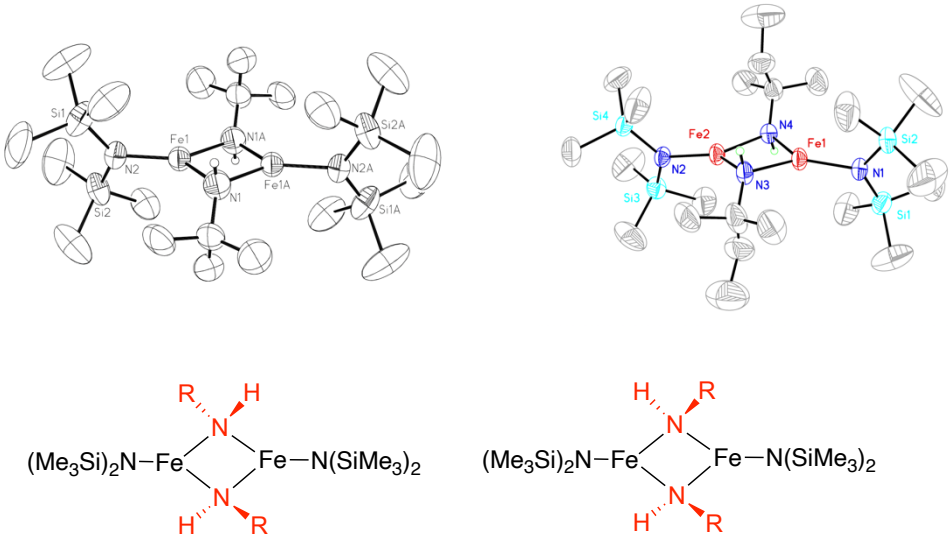

Figure 4.16. Structures of isolated heteroleptic dinuclear complexes (**14-^{t}Bu**[25] and **14-^{t}Am**[27]). Cis and trans configuration of the disubstituted, dinuclear complexes.

The trinuclear complexes present a more complex scenario. The linear trinuclear complexes are built by vertex fusion of two dinuclear rhombs at 90 °. Each dinuclear complex can either display the cis or trans configuration which leads to the possibility of different isomers. The four unique possible diastereomers are shown in Figure 4.17 with the point groups of C_1, C_2, D_2 and S_4. Among these, three of the diastereomers exist as enantiomeric pairs, further increasing the stereochemical complexity of these species. The possible combinations that lead to the four diastereomers are trans/cis, cis/cis and two trans/trans configurations. The structures can be visualized from the left of the depiction along the Fe–Fe–Fe vector to visualize the substituents' spatial arrangement.

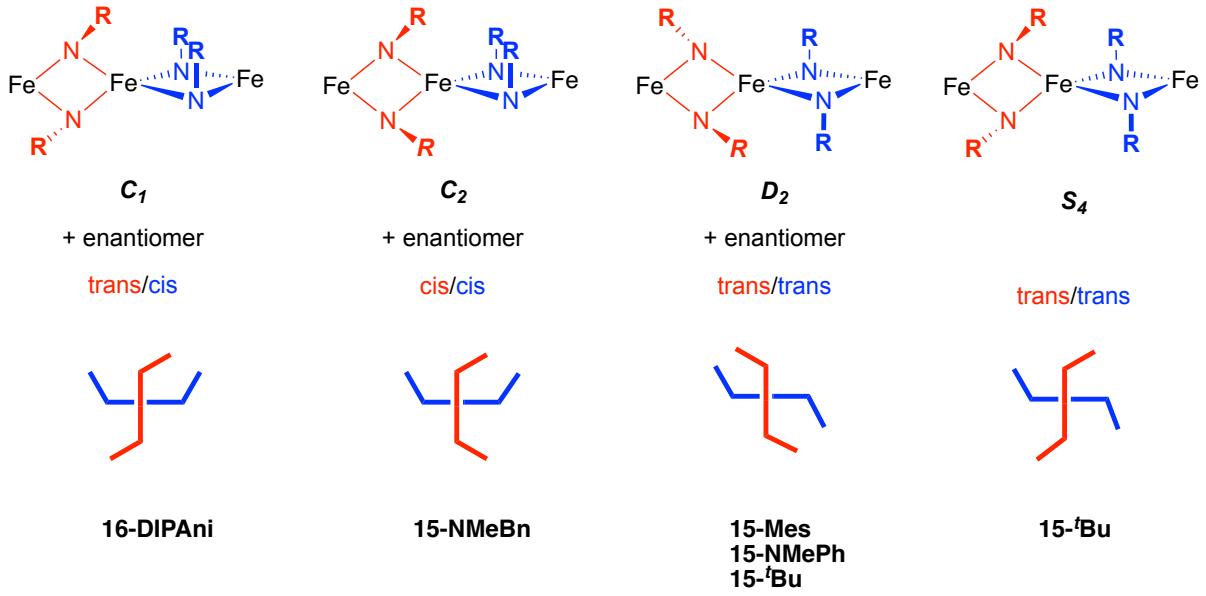

Figure 4.17. All possible diastereomers of the trinuclear complexes.

Five trinuclear complexes have been characterized in the solid state in this work with the structure of **15-^{t}Bu** obtained by Dr. Wei Zhang. The structure of **15-^{t}Bu** was unique as it showcased two isomers with the D_2 and S_4 isomers being observed. Compound **15-pip** contains the same substituent bound to the bridging amide which results in an idealized point group of D_{2d}. The other structures have also been observed in this work. The possibility of different diastereomers may be what complicates the ^{1}H NMR analysis (see Section 4.2.6) of the trinuclear complexes as the different isomers would showcase different ^{1}H NMR signal sets. It is also possible that different isomers are crystallized and what was selected for single crystal XRD analysis was only one isomer. Another structure of **15-Mes** was obtained by Dr. Wei Zhang which showed a similar unit cell as **15-Mes** reported in this work and a secondary structure of **16-DIPAni** was obtained which also showed a similar unit cell as the structure of **16-DIPAni** reported in this work. While a second data set was collected for only two complexes, the second data set contained the same unit cell, which may provide data that only one form crystallizes from solution.

4.2.6 Spectroscopic Properties

4.2.6.1 ^{1}H NMR Spectroscopy

^{1}H NMR spectroscopy was one of the primary tools used to assess the reactivity of **11** with amines. While the technique provides insight into the nuclearity and ligand environments, it does not allow for definite structural determination because of the number of resonances and the peak broadness. The chemical shift regions for mononuclear, dinuclear, and trinuclear complexes are distinct, allowing for ^{1}H NMR spectroscopy to serve as a valuable technique for distinguishing the nuclearity of the resulting species. The structures of complexes in solution are determined based on the number of signals, chemical shift regions, and peak integration. The general characteristics are summarized as follows:

(i) **Mononuclear**: The ^{1}H NMR spectra of mononuclear complexes serve as fingerprints, though the resonances are broad, making accurate integration challenging. These complexes display a single $SiMe_3$ signal, with amine resonances isotropically shifted. The solution color of mononuclear species is light blue, which contrasts with the green color of di- and trinuclear species.

(ii) **Dinuclear**: Most ^{1}H NMR signals for dinuclear species can be assigned to specific protons. These signals exhibit less shift, appearing within a narrower chemical shift range, and on average, are sharper than those of the mononuclear and trinuclear species.

(iii) **Trinuclear**: These species exhibit numerous signals spanning a wide chemical shift range (approximately +100 to –100 ppm). The presence of diastereomers in solution, along with restricted rotation due to steric hindrance from the amide substituents leads to overlapping resonances which complicates the interpretation of ^{1}H NMR data.

The mononuclear complexes **12-DIPA** and **12-pip** exhibit similar resonance distributions, as shown in Figure 4.18. The ^{1}H NMR spectrum of **12-DIPA** displays one broad resonance corresponding to $(Me_3Si)_2N^-$, along with a broad resonance attributed to the

CH and CH_3 signals of diisopropylamine. Similarly, **12-pip** exhibits one broad $(Me_3Si)_2N^-$ resonance, along with multiple CH_2 resonances that are significantly shifted downfield and upfield. The broad resonances and wide chemical shift range are consistent with a mononuclear species in solution, due to the presence of unpaired electrons on iron. Compound **12-pip** is not stable in solution and will convert to the higher nuclearity clusters, while compound **12-DIPA** remains stable in solution for several days.

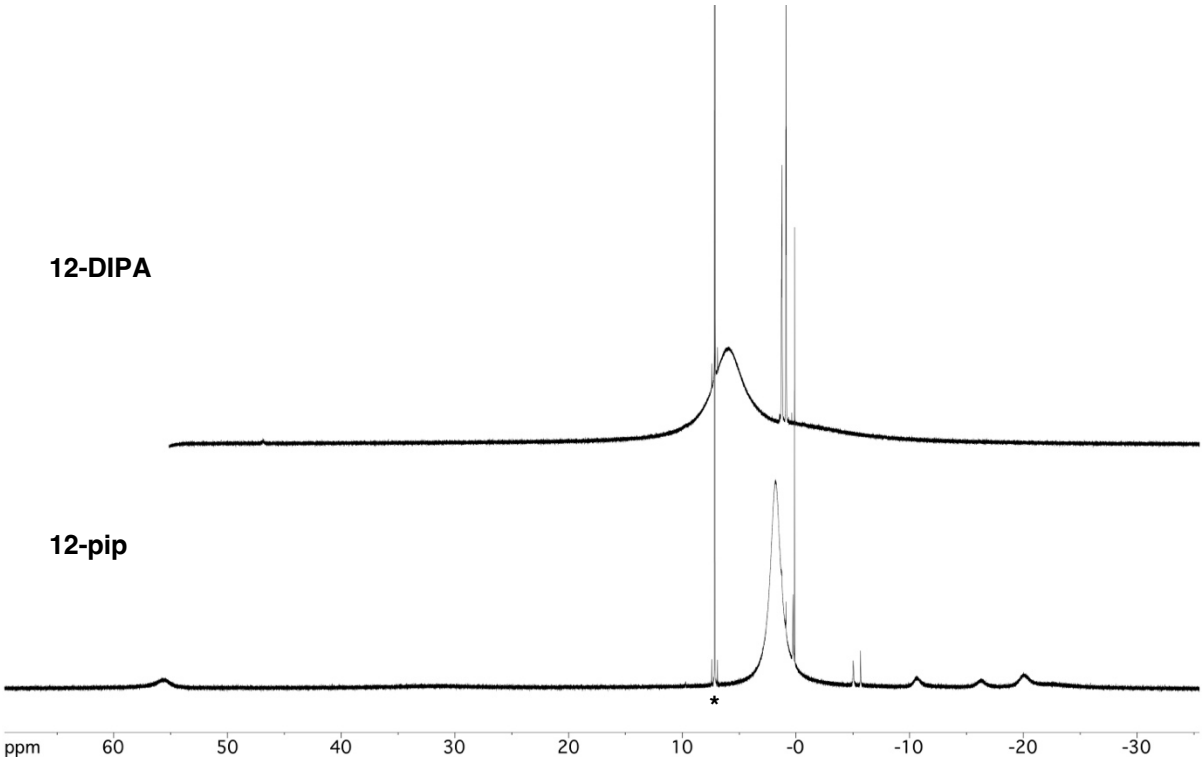

Figure 4.18. ^{1}H NMR spectra (298 K, 300 MHz) of **12-DIPA** and **12-pip** in C_6D_6. Residual protio signal indicated by *.

The coordination of amines to Fe(II) metal centers has been shown to contain weak binding and rapid exchange on the timescale of the NMR experiment (Chapter 2). This observation prompted an investigation into whether a dynamic equilibrium is present between **12-DIPA** and free DIPA in solution.

To determine whether a dynamic equilibrium is present in the formation of **12-DIPA**, stoichiometric titration of **11** with varying equivalents of DIPA was performed. Shown in Figure 4.19 is the ^{1}H NMR titration data and Figure 4.20 illustrates the relationship between the equivalents of DIPA added and the ^{1}H NMR chemical shift of the $SiMe_3$ signal. Upon addition of DIPA to **11**, a single resonance is observed, which can be attributed to the dynamic behaviour and fast exchange equilibrium of the system on the NMR timescale. The single resonance represents a weighted average of **12-DIPA** and free DIPA. These titration results indicate that one equivalent of DIPA is necessary to form **17**.

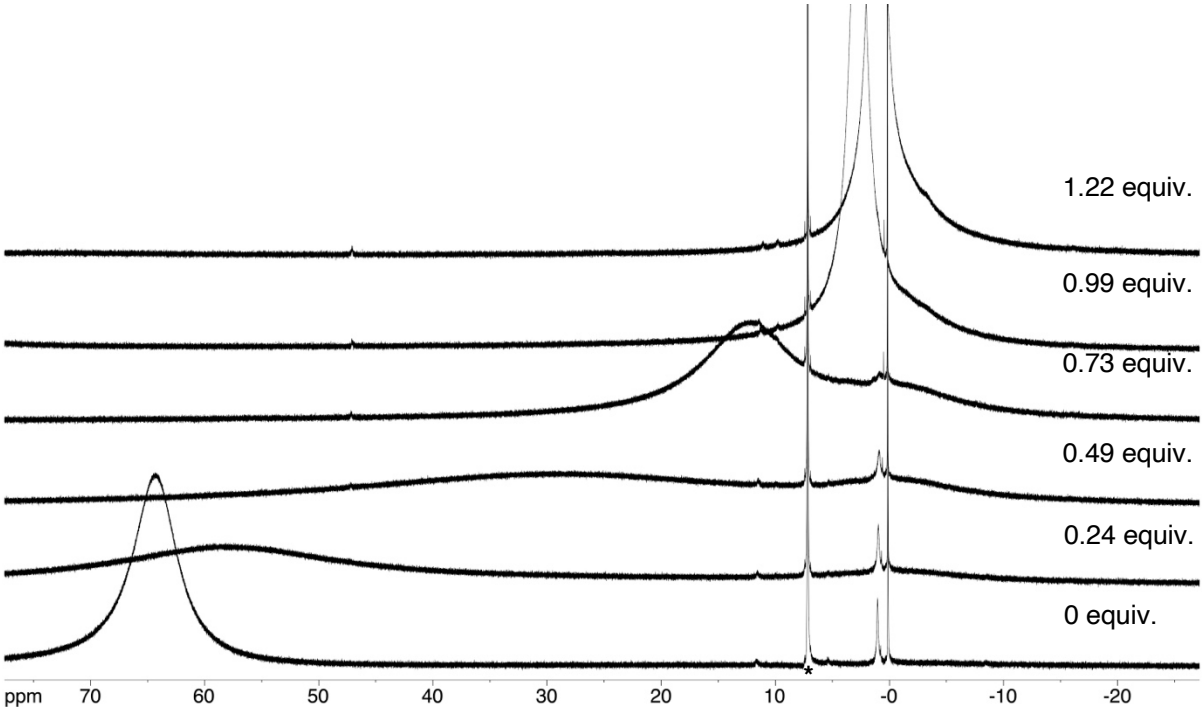

Figure 4.19. ^{1}H NMR titration of **11** with varying equivalents of DIPA in C_6D_6.

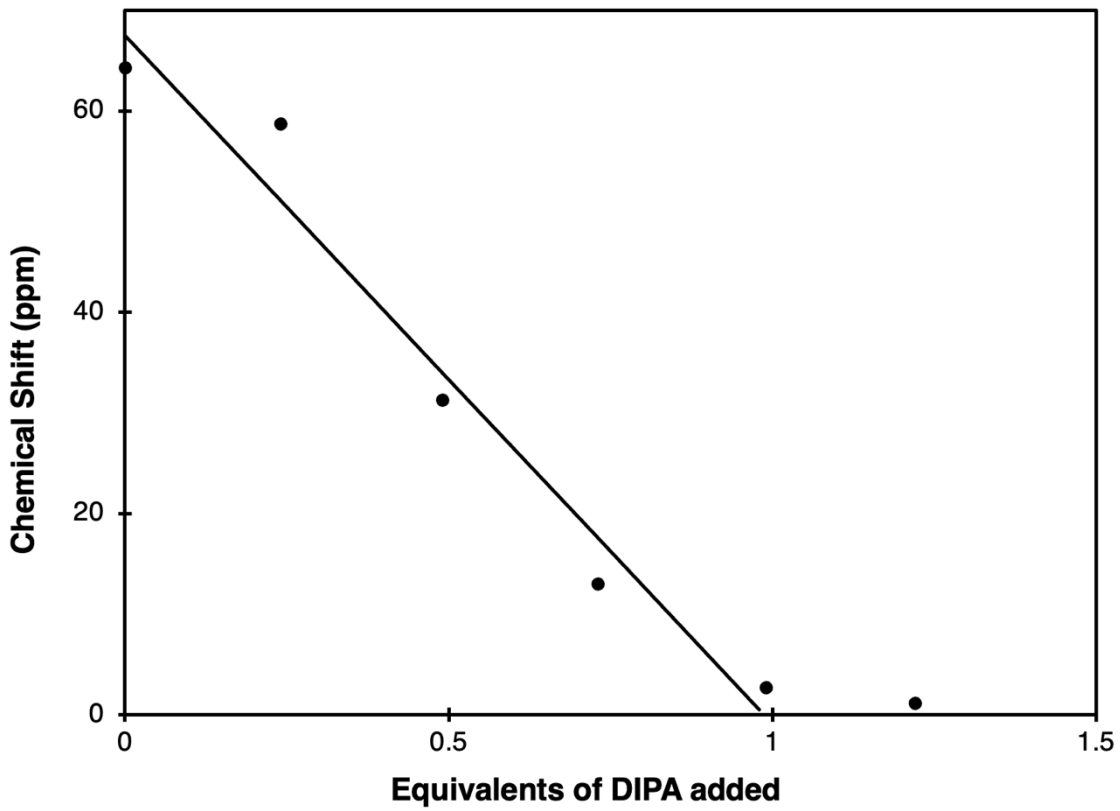

Figure 4.20. Chemical shift comparison of **11** in C_6D_6 with varying equivalents of DIPA.

The dinuclear complexes exhibit resonances with chemical shifts closer to that of $(Me_3Si)_2NH$ (0.10 ppm in C_6D_6), behaviour attributed to the presumed antiferromagnetic coupling of the iron centers at low temperatures, resulting in an $S = 0$ (diamagnetic) ground spin state. Interestingly, the monosubstituted complexes could exhibit one or two resonances for the terminal $(Me_3Si)_2N^-$ ligands. Both **13-*t*Bu** and **13-*t*Am** display two signals for the terminal $(Me_3Si)_2N^-$ likely due to restricted rotation of the Si–N bond in solution. Dr. Wei Zhang employed variable temperature ^{1}H NMR spectroscopy and observed that the two signals begin to shift at 55 °C, with partial overlap at 110 °C. Shown in Figure 4.21 are the ^{1}H NMR spectra of **13-*t*Bu**, **14-*t*Bu**, **13-*t*Am** and **14-*t*Am** in C_6D_6, where all signals are accounted for.

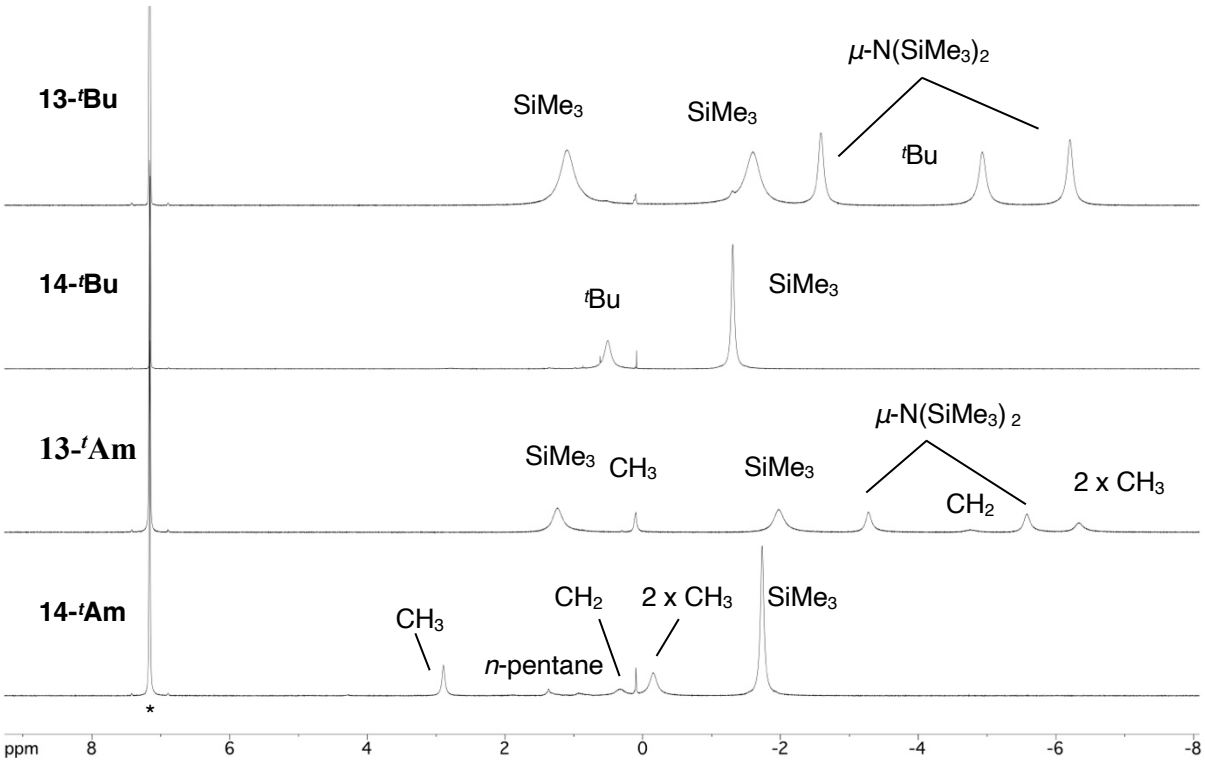

Figure 4.21. ^{1}H NMR spectra (298 K, 300 MHz) of **13-^{t}Bu**, **14-^{t}Bu**, **13-^{t}Am**, and **14-^{t}Am** in C_6D_6. Residual protio signal indicated by *.

The ^{1}H NMR spectrum for **13-pip** and **13-Bn** is shown in Figure 4.22. The observed signals are consistent with a monosubstituted dinuclear complex, as determined by the chemical shift range and peak integration. Some CH_2 resonances in **13-pip** remain unassigned, with four protons unaccounted for, likely due to signal broadening and overlap.

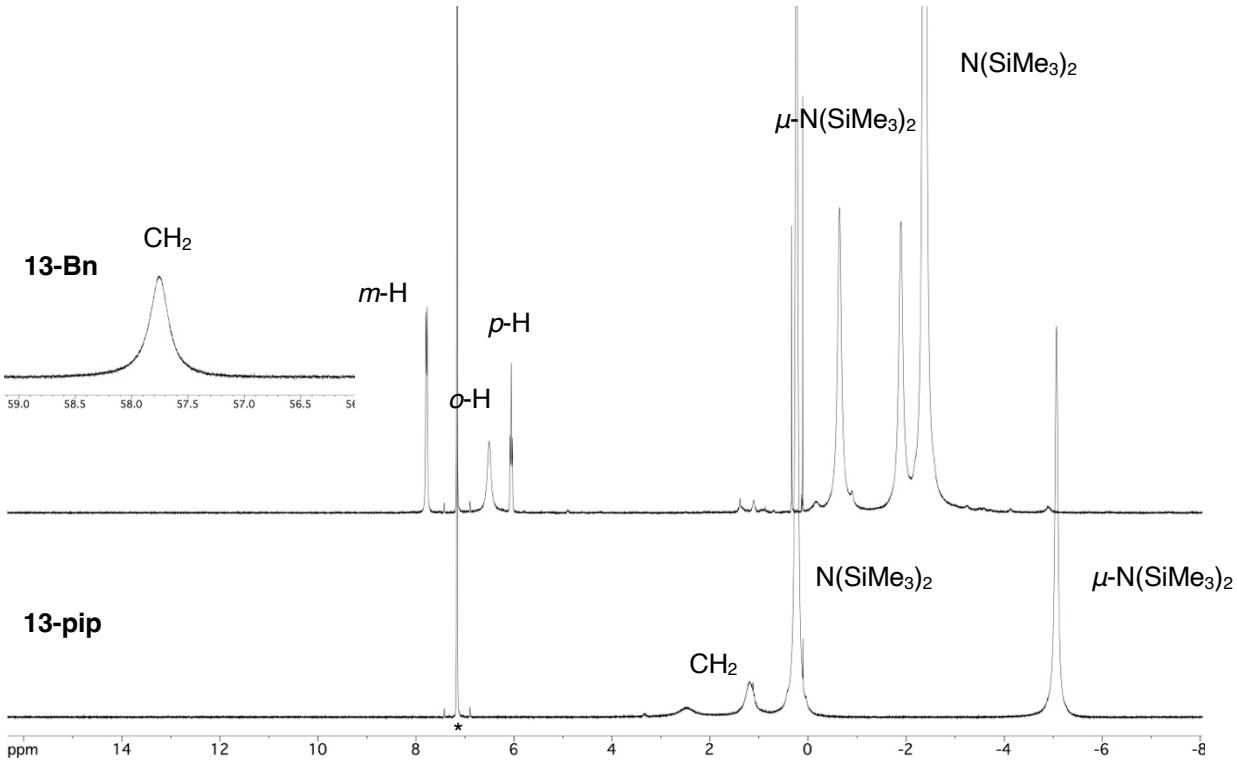

Figure 4.22. ^{1}H NMR spectrum (298 K, 300 MHz) of **13-Bn** and **13-pip** in C_6D_6. Residual protio signal indicated by *.

Figure 4.23 presents the ^{1}H NMR spectra of **13-Mes and 13-DIPAni**. While labelled resonances are identified, not all signals could be assigned. The isolated **13-Mes** and **13-DIPAni** complexes exhibit a single signal for the terminal $N(SiMe_3)_2$, suggesting a lower rotational barrier at room temperature compared to **13-^{t}Bu** and **13-^{t}Am.**

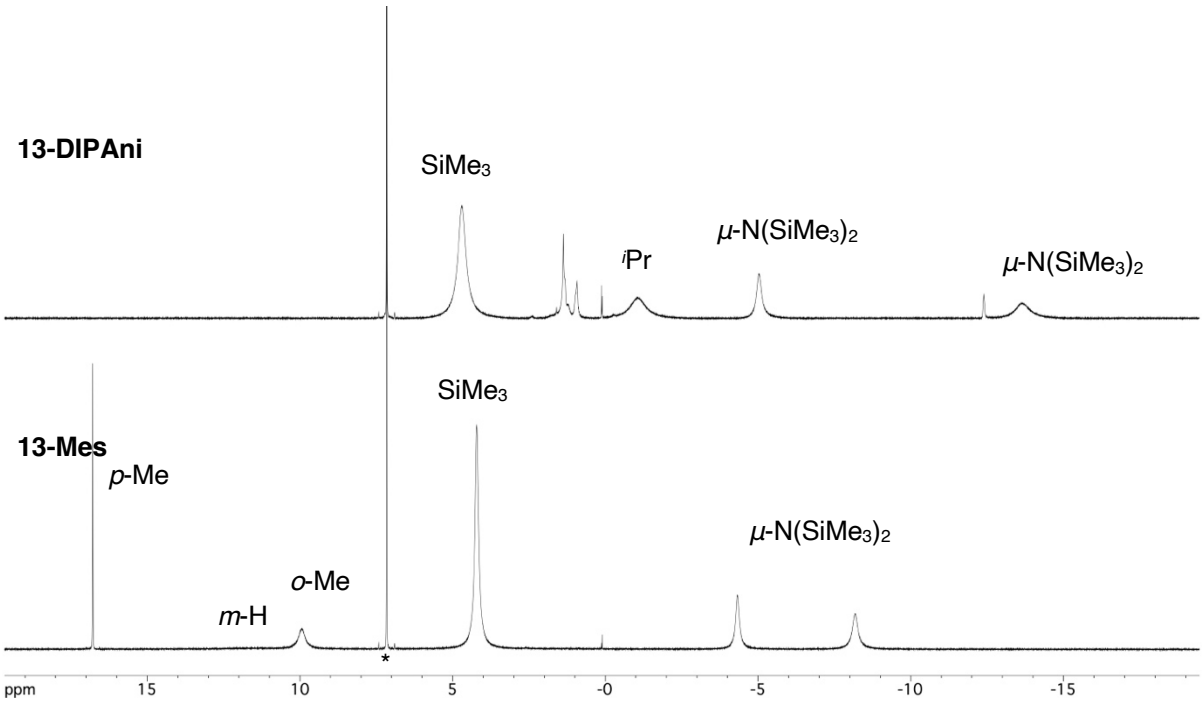

Figure 4.23. ^{1}H NMR spectra (298 K, 300 MHz) of **13-DIPAni** and **13-Mes** in C_6D_6. Residual protio signal indicated by *.

The ^{1}H NMR spectra for the *in-situ* generated monosubstituted dinuclear complexes (**13-Ph**, **13-*p*-tol**, **13-*o*-tol**, **13-NMePh** and **13-NMeBn**) are shown in Figures 4.24 and 4.25 respectively. All resonances can be accounted for with the expected integral ratios.

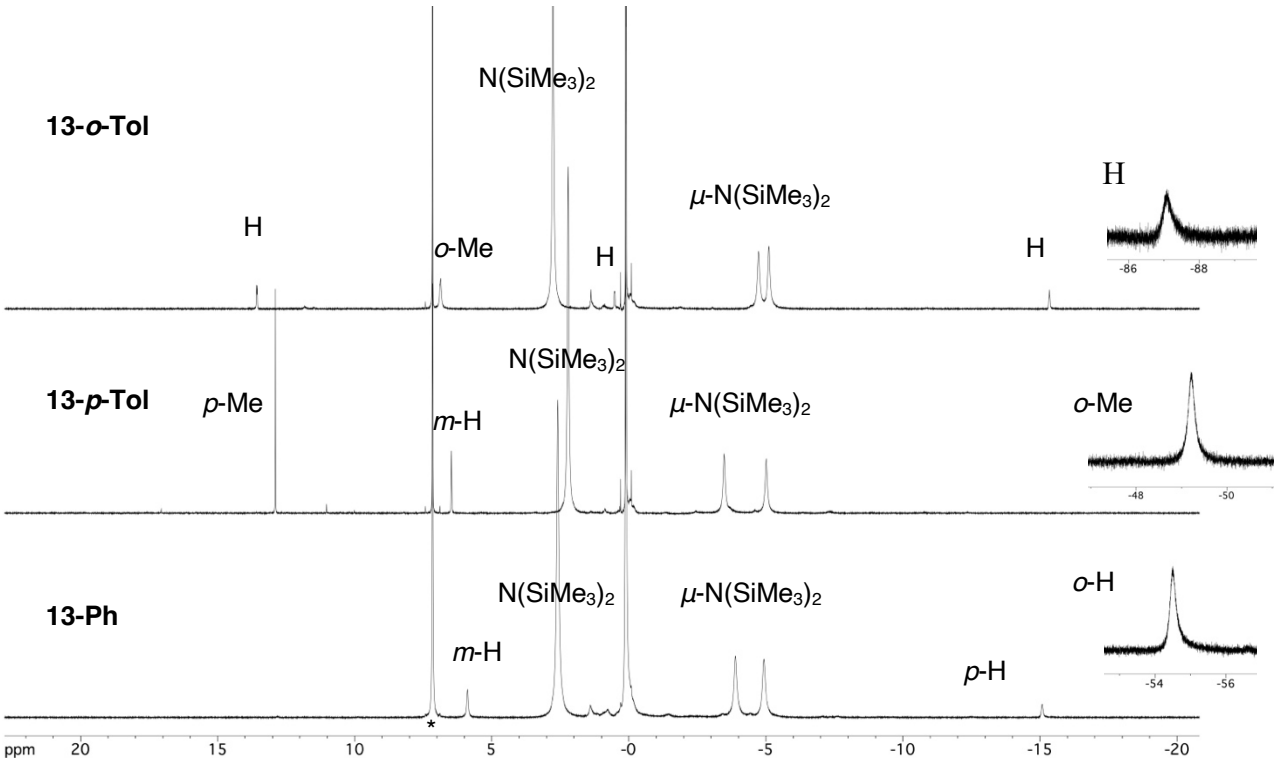

Figure 4.24. ^{1}H NMR spectra (298 K, 300 MHz) of **13-Ph**, **13-*p*-Tol** and **13-*o*-Tol**. Residual protio signal indicated by *.

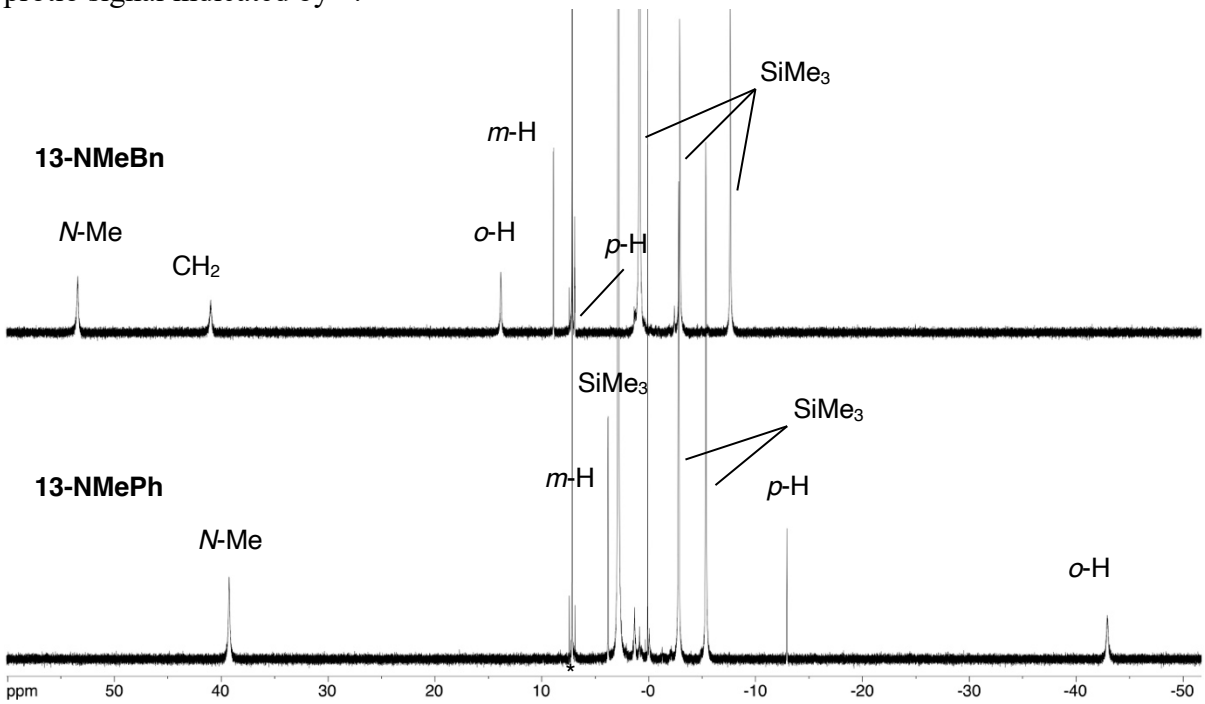

Figure 4.25. ^{1}H NMR spectra (298 K, 300 MHz) of **13-NMePh** and **13-NMeBn** in C_6D_6. Residual protio signal indicated by *.

Among the complexes synthesized in this chapter, the trinuclear complexes are the most challenging to interpret using ^{1}H NMR spectroscopy due to the following observations:

(i) Complexes contain three high spin, Fe(II) centers in either a trigonal planar or tetrahedral geometry, leading to unpaired electrons and paramagnetism in the ground state.

(ii) The likely presence of diastereomers.

(iii) The potential for restricted rotation of amide substitutions in solution due to the steric hindrance of the amide substituents.

These complexes exhibit isotopically shifted signals across a wide chemical shift range of 100 to –100 ppm. The trinuclear complexes with ^{1}H NMR resonances that can be interpreted or utilized as fingerprint resonances are **15-^{t}Bu, 15-pip and 15-Mes**.

Shown in Figure 4.26 is the ^{1}H NMR of crystalline **15-^{t}Bu**, which is contaminated with **14-^{t}Bu**. The presence of different diastereomers and the likely rotational barriers of the ^{t}Bu substituents complicate spectral analysis. However, the three broad resonances serve as fingerprint signals for **15-^{t}Bu.**

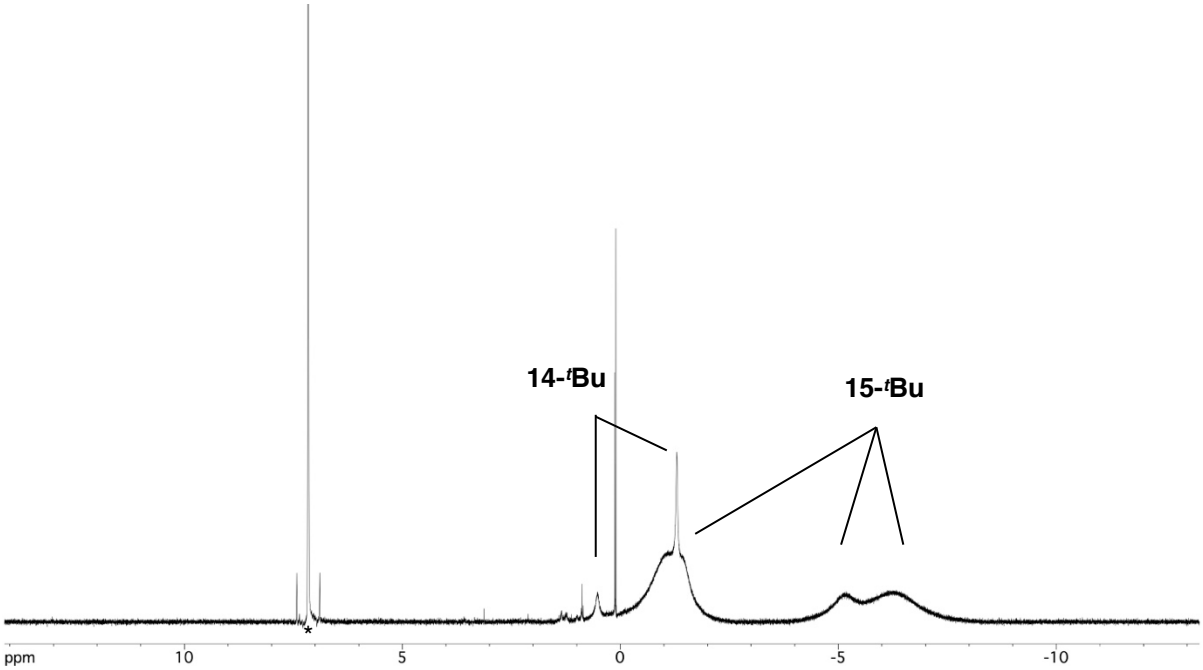

Figure 4.26. ^{1}H NMR spectrum (298 K, 300 MHz) of **15-^{t}Bu** in C_6D_6 contaminated with **14-^{t}Bu**. Residual protio signal indicated by *

The ^{1}H NMR spectrum of **15-pip** is shown in Figure 4.27. A single $SiMe_3$ resonance is observed along with five additional signals corresponding to the piperidine CH_2 protons. The broad peak widths of several signals and overlapping signals complicate the assignment of specific resonances to individual protons.

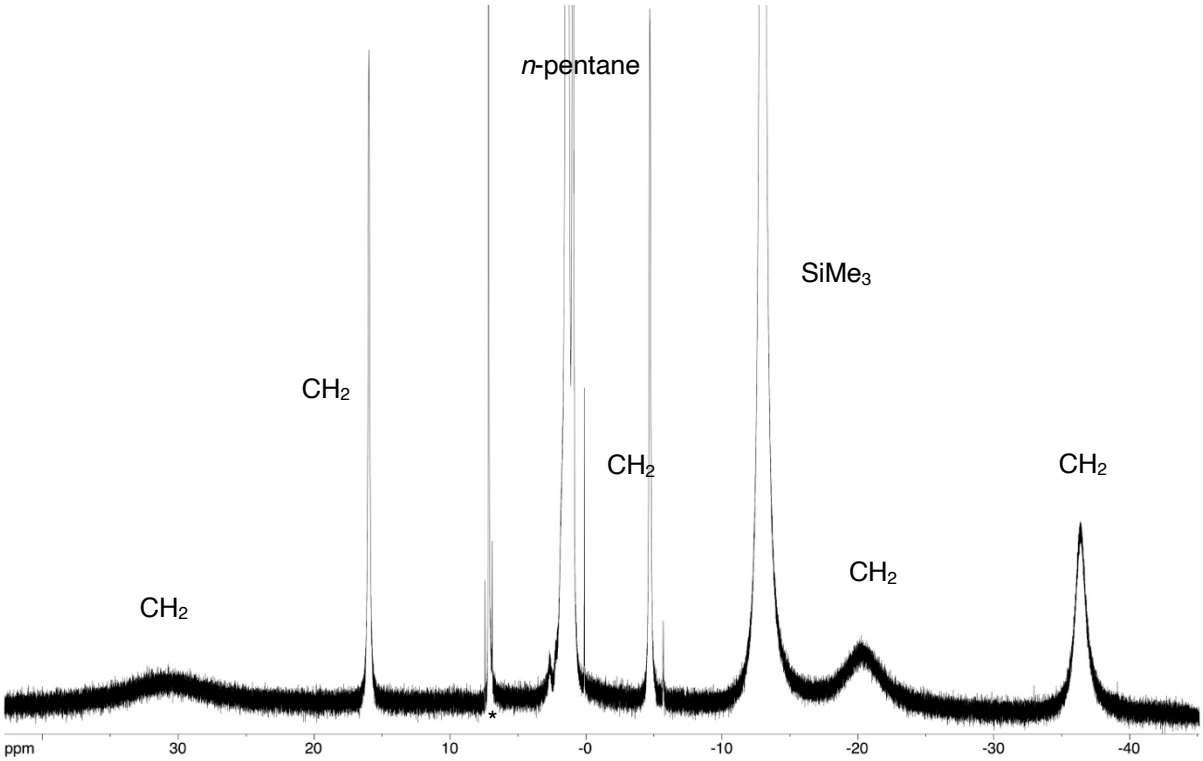

Figure 4.27. ^{1}H NMR spectrum (298 K, 300 MHz) of **15-pip** in C_6D_6. Residual protio signal indicated by *.

The ^{1}H NMR spectrum of a single crystal of **15-Mes** in C_6D_6 is shown in Figure 4.28. The signals are assigned to **15-Mes**, assuming free rotation of the terminal $N(SiMe_3)_2$ but restricted rotation of the mesityl groups. Since the four mesityl groups are symmetry-related, five signals corresponding to the mesityl groups are expected, along with one signal for the terminal $(Me_3Si)_2N^-$ resonance (excluding the amide protons). Minor, unassigned signals (circled in red) are present in the ^{1}H NMR spectrum. These four signals might correspond to a secondary isomer of **15-Mes**, with the remaining signals of this isomer being broad and not visible. Elemental analysis confirmed the purity of the sample, verifying that the spectrum of a presumed single crystal of **15-Mes** represents authentic **15-Mes**. Variable temperature (VT) NMR spectroscopy was performed to determine whether the secondary isomer signals would

convert to the predominant signal set. Heating the sample to 70 °C resulted in a shift of the signals for both isomers. Upon cooling to 25 °C, numerous additional signals appeared, which are attributed to the decomposition of **15-Mes**.

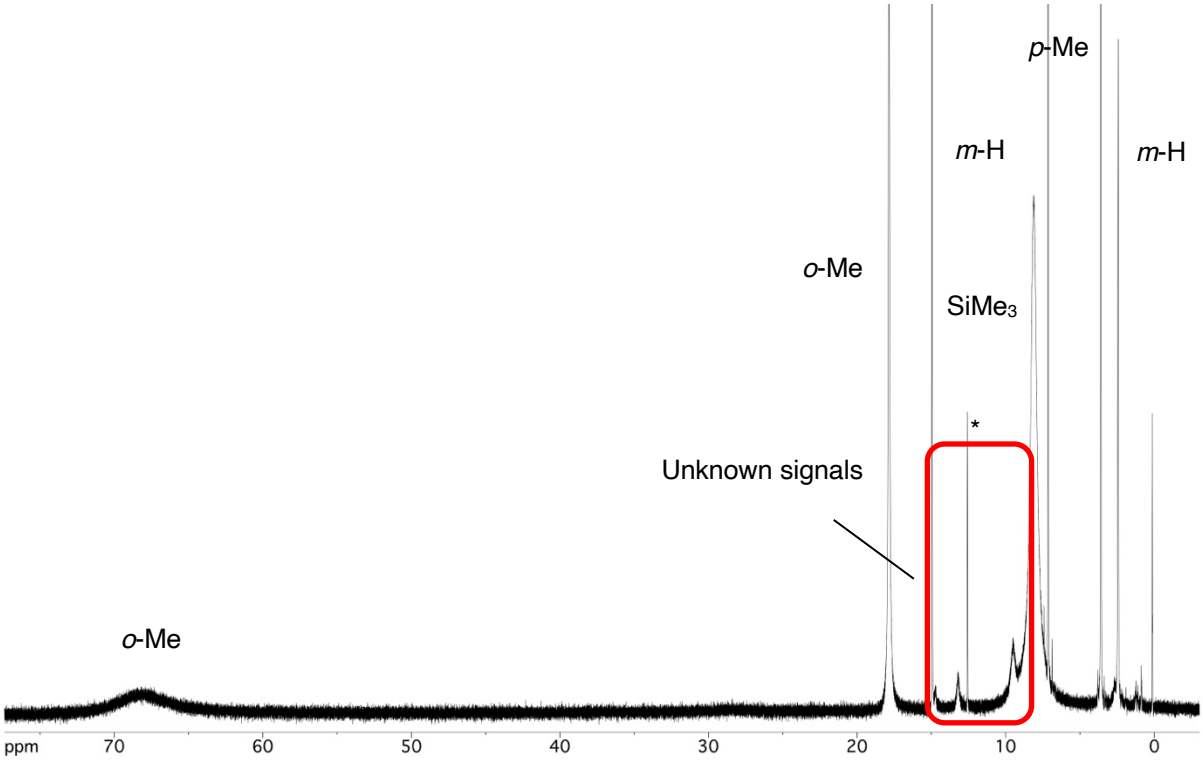

Figure 4.28. ^{1}H NMR spectrum (298 K, 300 MHz) of a single crystal of **15-Mes** in C_6D_6. Residual protio signal indicated by *.

The ^{1}H NMR spectra of crystalline **15-NMePh** and **15-NMeBn** are shown in Figure 4.29. Unlike the spectra of crystalline **15-Mes** and **15-pip**, the interpretation of the ^{1}H NMR signals for **15-NMePh** and **15-NMeBn** is challenging due to the presence of numerous broad and sharp signals. These signals span over a 100-ppm chemical shift range, consistent with expectations for trinuclear complexes.

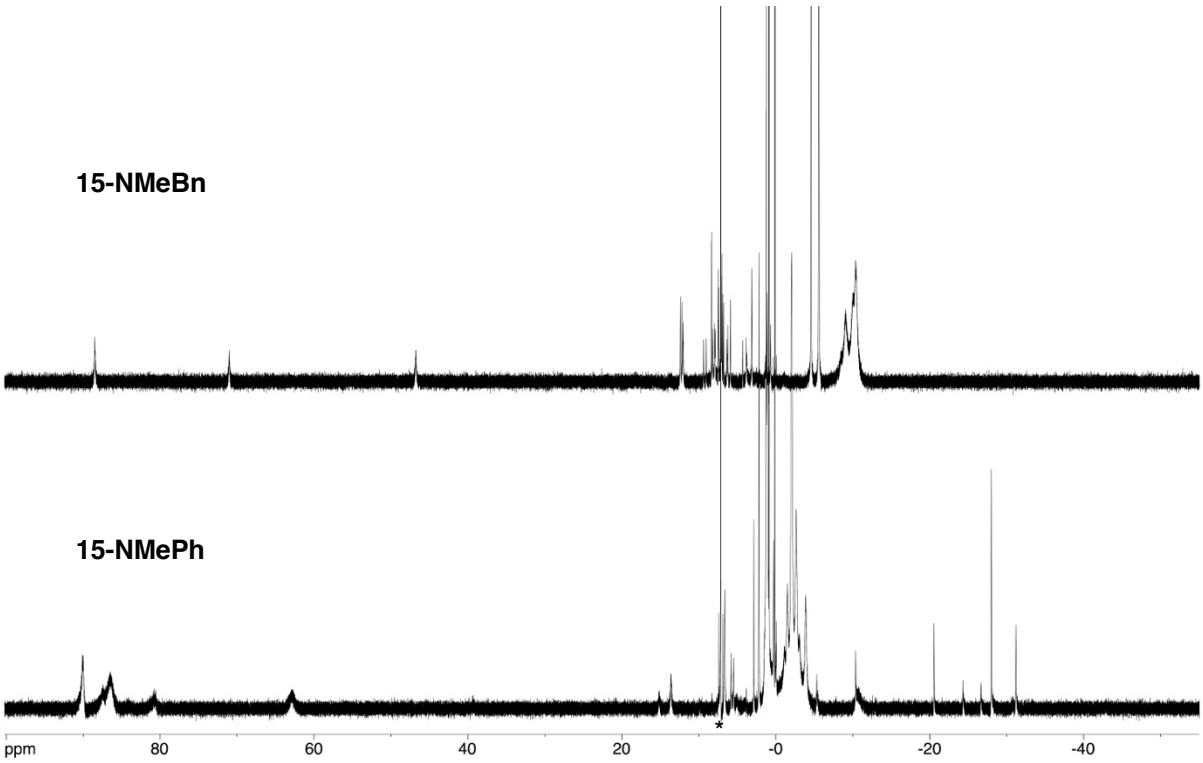

Figure 4.29. ^{1}H NMR spectra (298 K, 300 MHz) of a single crystal of **15-NMePh** (bottom) and **15-NMeBn** (top). Residual protio signal indicated by *.

Figure 4.15 presents the ^{1}H NMR spectra of the crude reaction mixture obtained from the reaction of **11** with 1.33 equivalents of 2,6-diisopropylaniline, along with the spectrum of crystalline **16-DIPAni** in C_6D_6. At present, the ^{1}H NMR spectra remain uninterpretable, making it uncertain whether crystallization of the crude material results in purification. The resonances observed in the spectrum of the single crystals closely resemble those of the crude mixture, suggesting that **16-DIPAni** may be the sole product formed in the reaction. However, without definitive signal assignment, qNMR analysis to determine the amount of **16-DIPAni** produced cannot be performed.

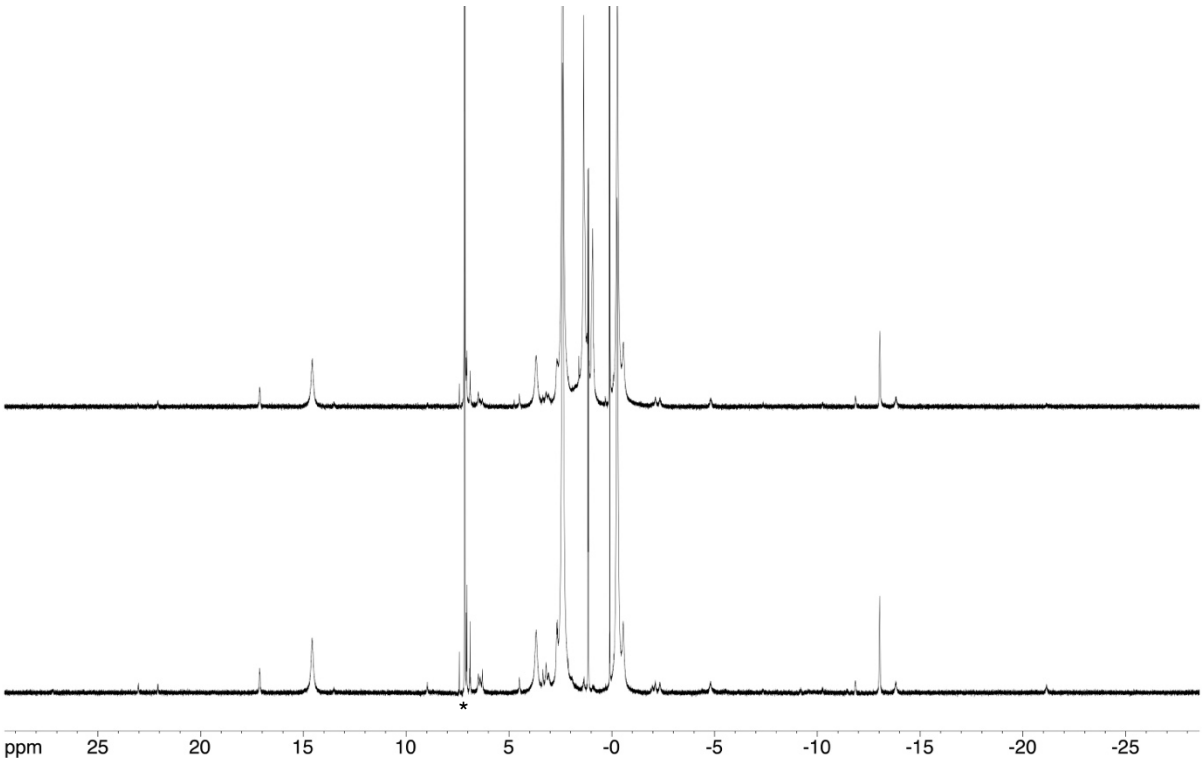

Figure 4.30. (top) ^{1}H NMR spectra (298 K, 300 MHz) of the crude reaction of **11** and 1.33 equivalents of 2,6-diisopropylaniline. (bottom) ^{1}H NMR spectra (298 K, 300 MHz) of single crystals of **16-DIPAni** in C_6D_6.

The inability to assign the resonances to **15-NMePh**, **15-NMeBn** and **16-DIPAni** presents a significant challenge, as ^{1}H NMR spectroscopy cannot be used to assess the purity of the material. Several factors may contribute to this issue:

(i) The crystals obtained through vapour diffusion may be contaminated with impurities from the mother liquor. Rinsing the harvested crystals to remove these impurities was not feasible, as even rinsing with cold HMDSO resulted in the dissolution of **15-NMePh**, **15-NMeBn** and **16-DIPAni**.

(ii) The harvested crystals may consist of multiple isomers, leading to the presence of more than one isomer signal set in the ^{1}H NMR spectra.

(iii) The compound may crystallize as a single isomer but undergo isomerization upon dissolution, leading to the formation of multiple isomers and multiple signals in the ^{1}H NMR spectra.

4.2.6.2 Electronic Properties

The compounds analyzed within this chapter exhibit various solution colors, including transparent blue (**12**), transparent light green (**13** and **15**), transparent dark green (**15**) or opaque red (**16**). The electronic absorption spectra of the isolated complexes, shown in Figures 4.31 to 4.36, serve as fingerprints for these species. The spectra of these complexes exhibit charge transfer bands, characterized by the high molar absorptivity (ε) values. Notably, ε values increase with nuclearity, following the trend: mononuclear < dinuclear < trinuclear.

The electronic absorption spectra of amine adduct complexes **12-pip** and **12-DIPA** are presented in Figure 4.31 and Figure 4.36, respectively. These spectra exhibit characteristic charge-transfer bands of mononuclear complexes, comparable to the absorption spectrum and solution color of **12-THF**. The light blue color of these complexes corresponds to minimal absorption in the visible region. Additionally, these complexes display relatively low absorbance in the ultraviolet region compared to the higher nuclearity complexes.

The electronic absorption spectra of the monosubstituted dinuclear species **13-pip**, **13-Mes**, **13-^{t}Bu, 13-^{t}Am** and **13-DIPAni** are shown in Figures 4.31–4.35, respectively. The monosubstituted complexes can be categorized based on the nature of the bridging ligands as either arylamides or alkylamides. Complexes with arylamide bridging ligands exhibit more intense absorbance in the ultraviolet region than those with alkylamide bridging ligands. The spectral patterns of the monosubstituted species are similar, each displaying three major features in the ultraviolet region. Disubstituted dinuclear species synthesized by previous group members, **14-^{t}Bu** and **14-^{t}Am**, exhibit similar spectral patterns, with two major features in the ultraviolet region and ε values comparable to those of the monosubstituted dinuclear complexes.

The electronic absorption spectra of the trinuclear species, **15-pip** and **15-Mes** are shown in Figure 4.31 and Figure 4.32 respectively. These complexes display the highest ε values, consistent with their increased nuclearity. The spectra of other trinuclear complexes, including **15-^{t}Bu**, **15-NMeBn**, **15-NMePh** and **16-DIPAni** were not analyzed by UV-vis

spectroscopy because their in-solution structures cannot be easily resolved, making spectral interpretation challenging.

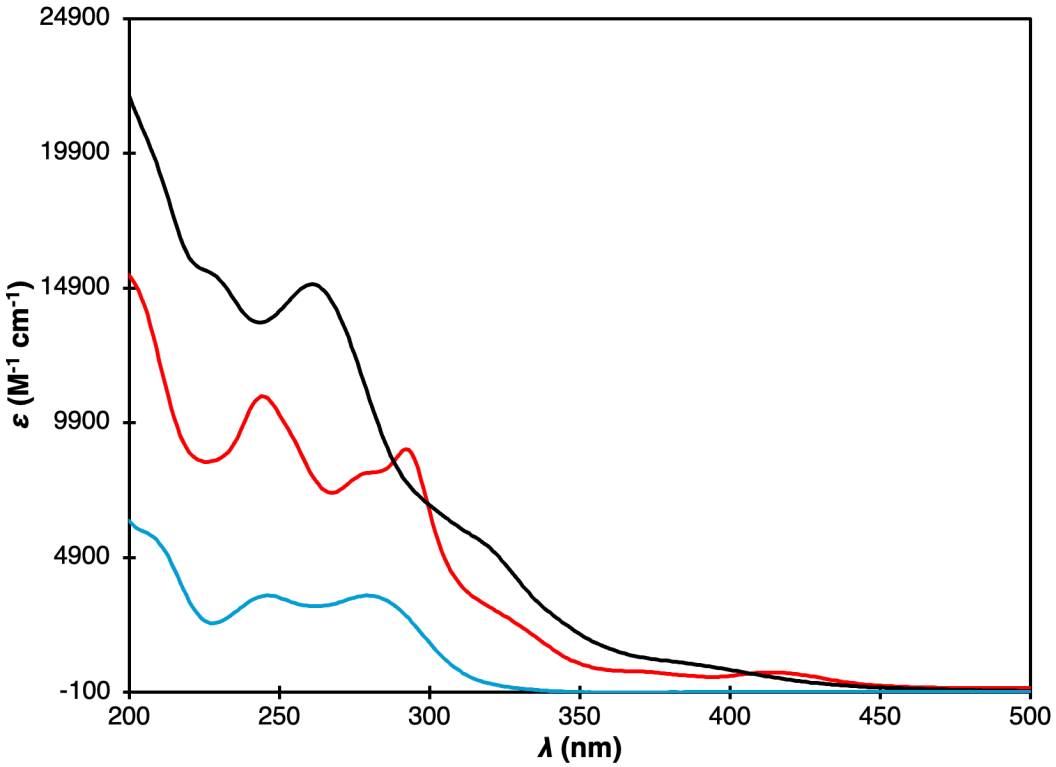

Figure 4.31. Electronic absorption spectra of **15-pip** (black), **13-pip** (red) and **12-pip** (blue) in *n*-pentane.

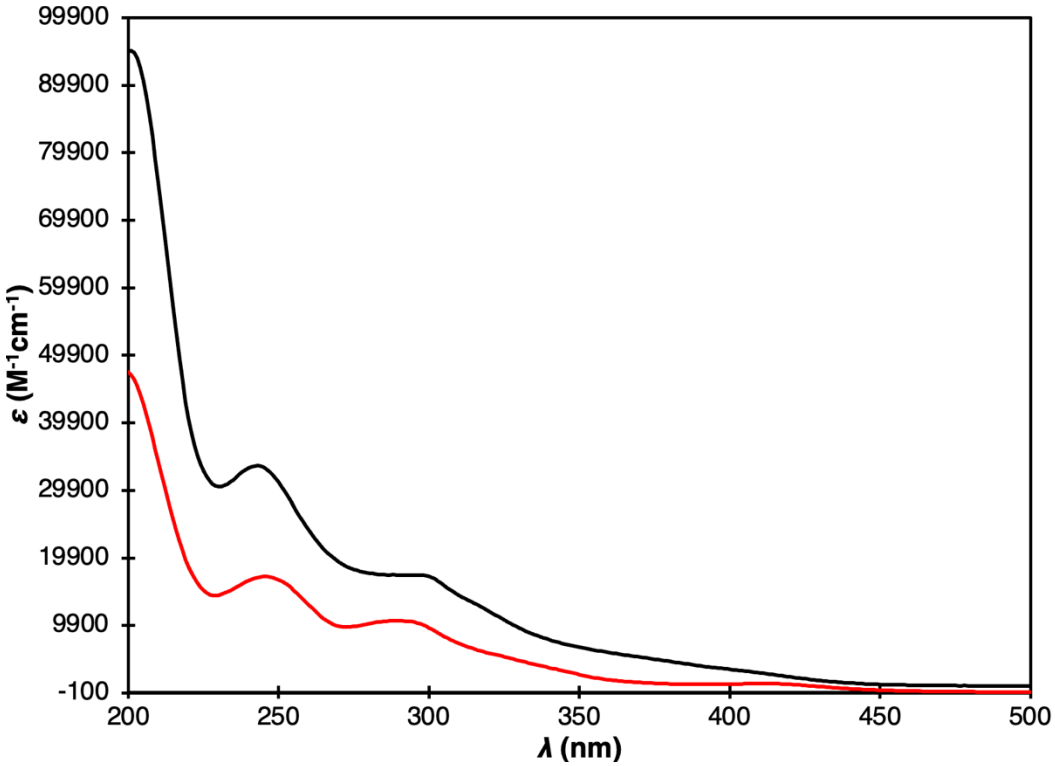

Figure 4.32. Electronic absorption spectra of **15-Mes** (black) and **13-Mes** (red) in *n*-pentane.

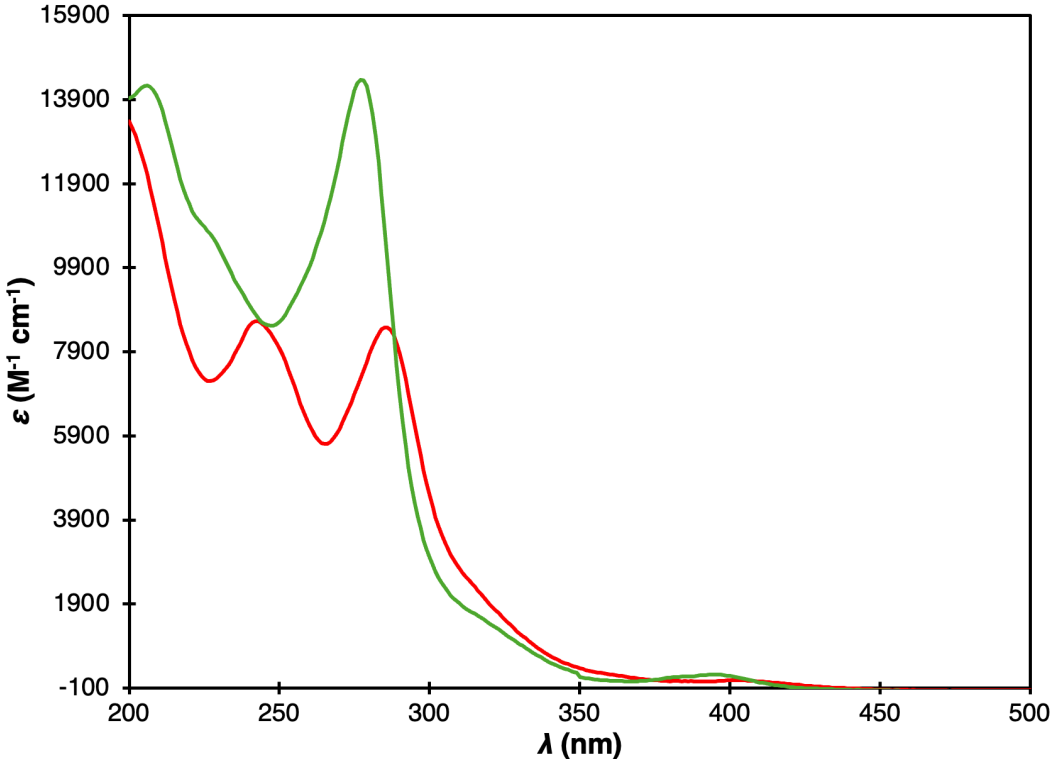

Figure 4.33. Electronic absorption spectra of **14-^{t}Bu** (green) and **13-^{t}Bu** (red) in *n*-pentane.

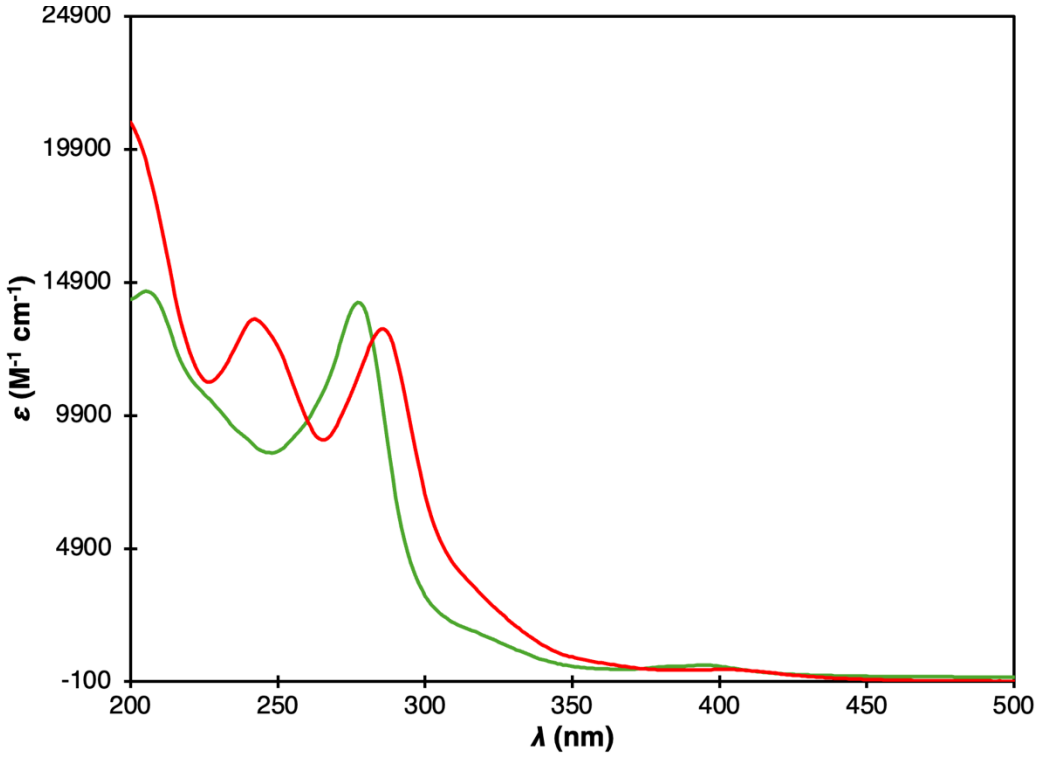

Figure 4.34. Electronic absorption spectra of **14-^{t}Am** (green) and **13-^{t}Am** (red) in *n*-pentane.

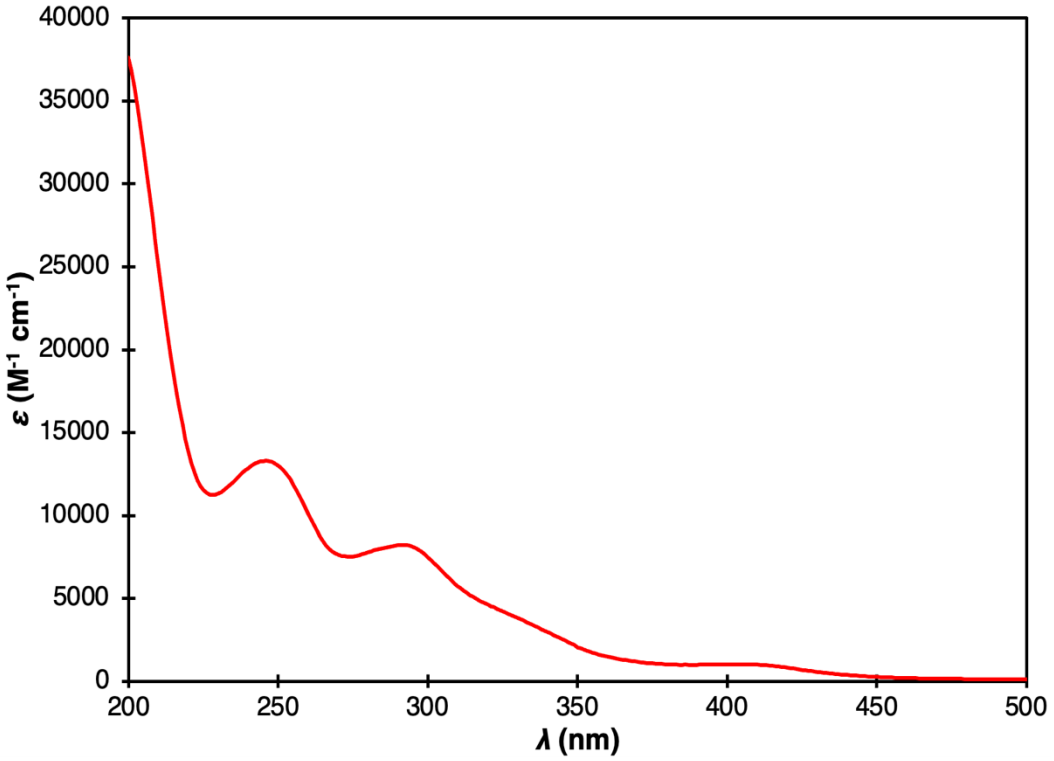

Figure 4.35. Electronic absorption spectra of **13-DIPAni** (red) in *n*-pentane.

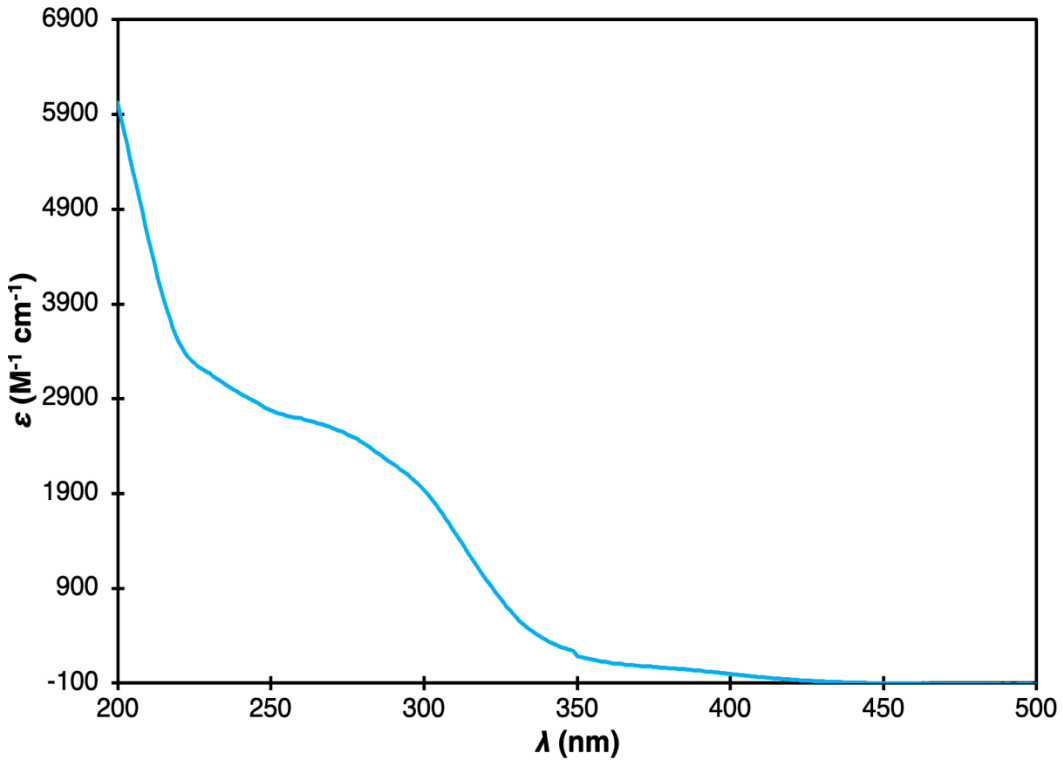

Figure 4.36. Electronic absorption spectra of **12-DIPA** (blue) in *n*-pentane.

4.2.7 Reactivity

4.2.7.1 Study of complex formation

The five types of complexes studied in this work include the mononuclear amine adduct (**12**), the monosubstituted dinuclear complex (**13**), the disubstituted dinuclear complex (**14**), the heteroleptic trinuclear complex (**15**) and the homoleptic trinuclear complex (**16**). Experiments were conducted to determine whether the mechanism of complex formation could be elucidated. The reaction of **11** with piperidine provided an ideal system for studying the stepwise formation of these complexes using ^{1}H NMR spectroscopy. When **11** was reacted with 1.33 equivalents of piperidine, the complexes appeared sequentially in the order: **12-pip**, **13-pip**, **14-pip** and finally **15-pip**.

Compound **12-pip** was determined to be metastable, as dissolution of the light blue, transparent crystals of **12-pip** in C_6D_6 resulted in a color change from transparent light blue

to transparent light green within an hour, indicating the formation of higher nuclearity complexes. The conversion of **12-pip** into higher nuclearity species was monitored using ^{1}H NMR spectroscopy. The summary of conversion is shown in Scheme 4.7 with the following observations highlighted:

(i) After 20 minutes, the ^{1}H NMR spectrum of **12-pip** in C_6D_6 displayed signal sets corresponding to **12-pip**, **13-pip** and **14-pip** in a 45:4:1 ratio, with **12-pip** remaining the dominant species.

(ii) After 24 hours, the signal set for **12-pip** disappeared, while those for **13-pip**, **14-pip** and **15-pip** appear in a 3:6:1 ratio, with **14-pip** as the dominant species. The presence of **15-pip** is unexpected, as a 1:1 stoichiometry should yield **14-pip** as the sole product. This observation suggests either the instability of **14-pip** or a low kinetic barrier for the formation of **15-pip**.

Scheme 4.7. Reactivity of **12-pip**

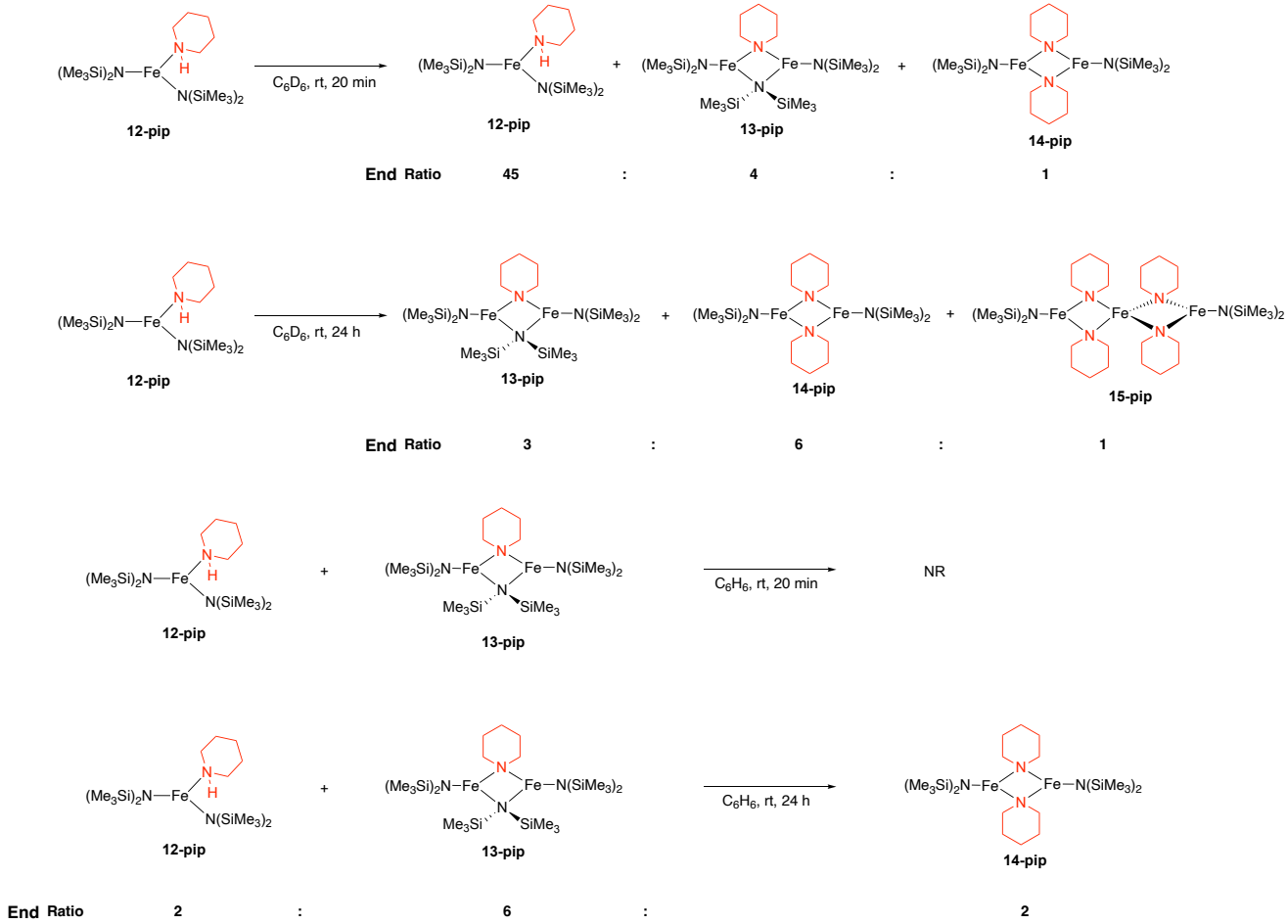

The reaction of **12-pip** with **13-pip** was conducted to determine whether the reaction rate favored the formation of **14-pip** or **15-pip** as shown in Scheme 4.8. The following observations were made:

(i) ^{1}H NMR analysis after 20 minutes showed no reaction.

(ii) After 24 hours, no **15-pip** was detected, and the formation rate of **14-pip** was slower than when free amine was added to **13-pip** or when pure **12-pip** was dissolved. The ratio of **12-pip**, **13-pip** and **14-pip** was 1:3:1 respectively.

These findings suggest that while **12-pip** is metastable, piperidine likely binds more tightly to the iron center, leading to a slower reaction rate with **13-pip**.

Scheme 4.8. Reactions of **13-pip** and **15-pip**

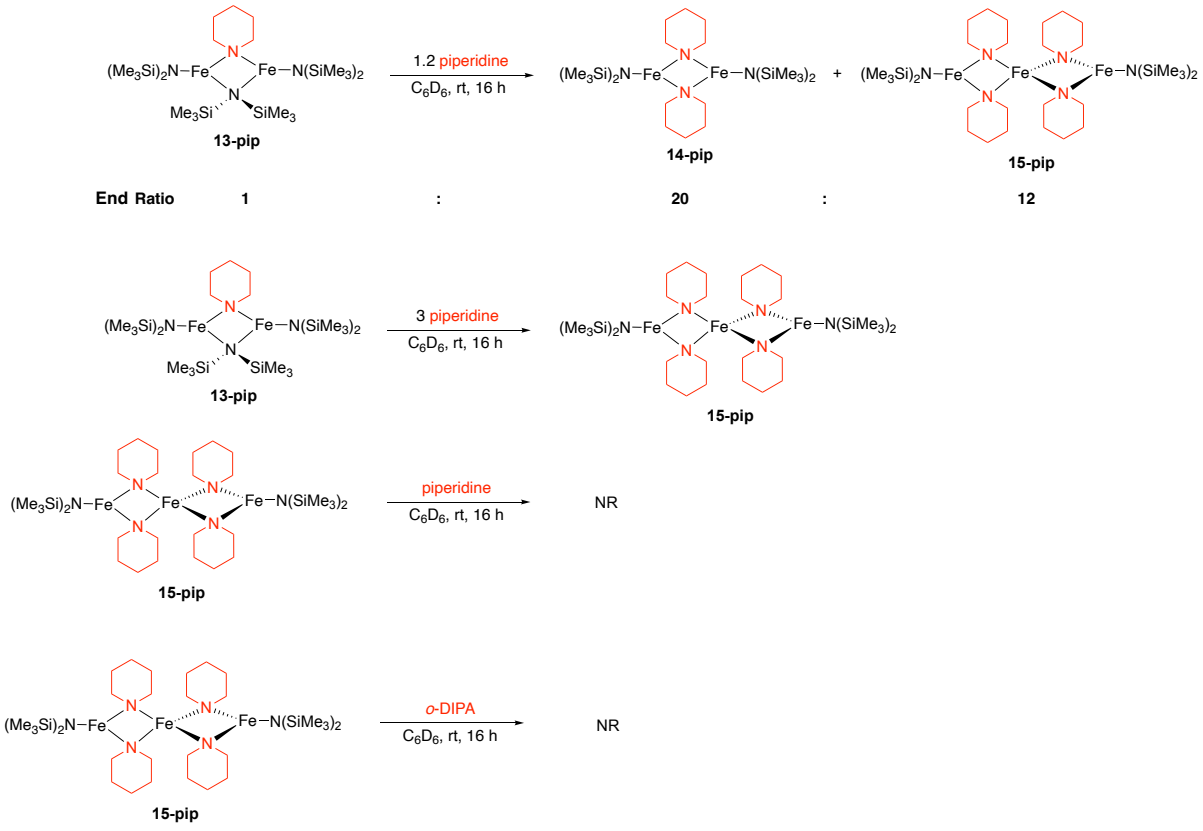

Work was performed by adding varying equivalents of piperidine to **13-pip** to determine if **14-pip** can be formed directly as attempts to isolate **14-pip** from **11** have been unsuccessful. The addition of 1.2 equivalents of piperidine to **13-pip** leads to the formation of **14-pip** and **15-pip**, suggesting either **14-pip** is metastable or a low kinetic barrier to form **15-pip** is present. Upon addition of 3 equivalents of piperidine to **13-pip** in C_6D_6, the signal set for **13-pip** decreases as the signal set of **14-pip** emerges. Due to the excess piperidine, **15-pip** appears and becomes the sole iron containing species after 16 hours.

The formation of **16-DIPAni** has led to the investigation into whether terminal substitution is possible for other trinuclear complexes and when terminal substitution occurs.

The only homoleptic complex isolated in this work is **16-DIPAni.** Two equivalents of piperidine and 2,6-diisopropylaniline were added to **15-pip** in C_6D_6. The addition of excess piperidine to **15-pip** did not result in terminal substitution, which is consistent with the absence of higher substituted complexes in the initial synthesis of **15-pip**, where excess piperidine was used. Similarly, the addition of 2,6-diisopropylaniline to **15-pip** did not induce terminal substitution. The hypothesis for the formation of **16-DIPAni** is that the comparable acidity and steric hindrance of $(Me_3Si)_2NH$ to 2,6-diiosopropylaniline stabilizes the terminal three-coordinate iron centres in **16-DIPAni**, suggesting that terminal substitution should occur on **15-pip**. The lack of terminal substitution with **15-pip** may be attributed to kinetic limitations as the reaction barrier to terminal substitute may be high due to the steric bulk of the piperamide CH_2 groups.

These results combined with the observations in early sections have led to the following conclusions:

(i) Formation of **12**:
   a. Reaction of **11** with alkylamines led to spectroscopic signatures of **12**. Isolation of **12** was performed with secondary amines like DIPA and piperidine.
   b. Reaction of **11** with arylamines does not lead to isolable **12** which is attributed to arylamines being more acidic, facilitating a faster proton transfer, which leads to the formation of **13**.

(ii) Formation of **13**:
   a. Protonolysis with both alkylamines and arylamides leads to the formation of **13**.
   b. Ortho protons on arylamines and α-protons leads to decomposition pathways with the formation of **13** not being quantitative.

(iii) Formation of **14**:
   a. Protonolysis with primary alkylamines without α-protons leads to isolable, stable **14**.

b. Protonolysis with primary alkylamines with α-protons and primary arylamines with ortho protons do not lead to the formation of **14**.

c. Protonolysis with mesidine and pieridine led to a signal set consistent with **14** but the species was not isolable.

(iv) Formation of **15**:

a. Protonolysis with secondary alkylamines, primary arylamines without ortho protons and secondary arylamines with ortho protons lead to the formation of **15**.

b. Not observed with protonolysis with primary alkylamines with α-protons or with primary arylamines with ortho protons

(v) Formation of **16**:

a. Only observed in the protonolysis with 2,6-diisopropylaniline

4.2.7.2 Complex Reactivity with Amines

The reaction of **11** with amines has showcased that the trinuclear species **15** likely forms through a stepwise formation starting with **12** to **13** to **14** to **15**. This has led to an investigation of the reactivity of **13** and **14** with amines to determine if the higher nuclearity complexes can form. The first set of experiments was using selected **13** and **14** and adding the same amine as the bridging amide. Shown in Scheme 4.9 are the various experiments that were undertaken. Highlighted are the various observations:

(i) **14-^{t}Bu** but not **15-^{t}Bu** can form quantitatively from **13-^{t}Bu**.

(ii) Addition of excess ^{t}BuNH$_2$ to **13-^{t}Bu** and **14-^{t}Bu** does not lead to a reasonable conversion to **15-^{t}Bu**.

(iii) **16-DIPAni** forms from reactivity of **13-DIPAni** with 2,6-diisopropylaniline.

(iv) **15-Mes** does not form quantitatively from reactivity of **13-Mes** with mesidine.

The reaction of one equivalent of ^{t}BuNH$_2$ with **13-^{t}Bu** resulted in an almost quantitative conversion to form **14-^{t}Bu**. In contrast, the reaction of one equivalent of

mesidine with **13-Mes** produced a mixture of signals. These multiple signals are consistent with those observed when **11** reacts with more than one equivalent of mesidine. These observations provide insight into the mechanism of complex formation (further discussed in Section 4.2.6). The results suggest that disubstituted complexes are likely formed after the monosubstituted species are generated, supporting a stepwise formation pathway.

The formation of **14-^{t}Bu** from **13-^{t}Bu** can be rationalized by protonation of the bridging $(Me_3Si)_2N^-$ to $(Me_3Si)_2NH$ followed by replacement of the amine by ^{t}BuHN$^-$. The exact mechanism of which bonds are breaking and forming at what point remains unclear. The formation of **16-DIPAni** from **13-DIPAni** and 2,6-diisopropylaniline showcases that the trinuclear complex forms from the monosubstituted dinuclear complex. The formation of **15-Mes** from **13-Mes** and mesidine reveals that the barrier to form **15-Mes** may be easier to overcome compared to the formation of **15-^{t}Bu**.

Scheme 4.9. Reactivity of **13** with the same amine

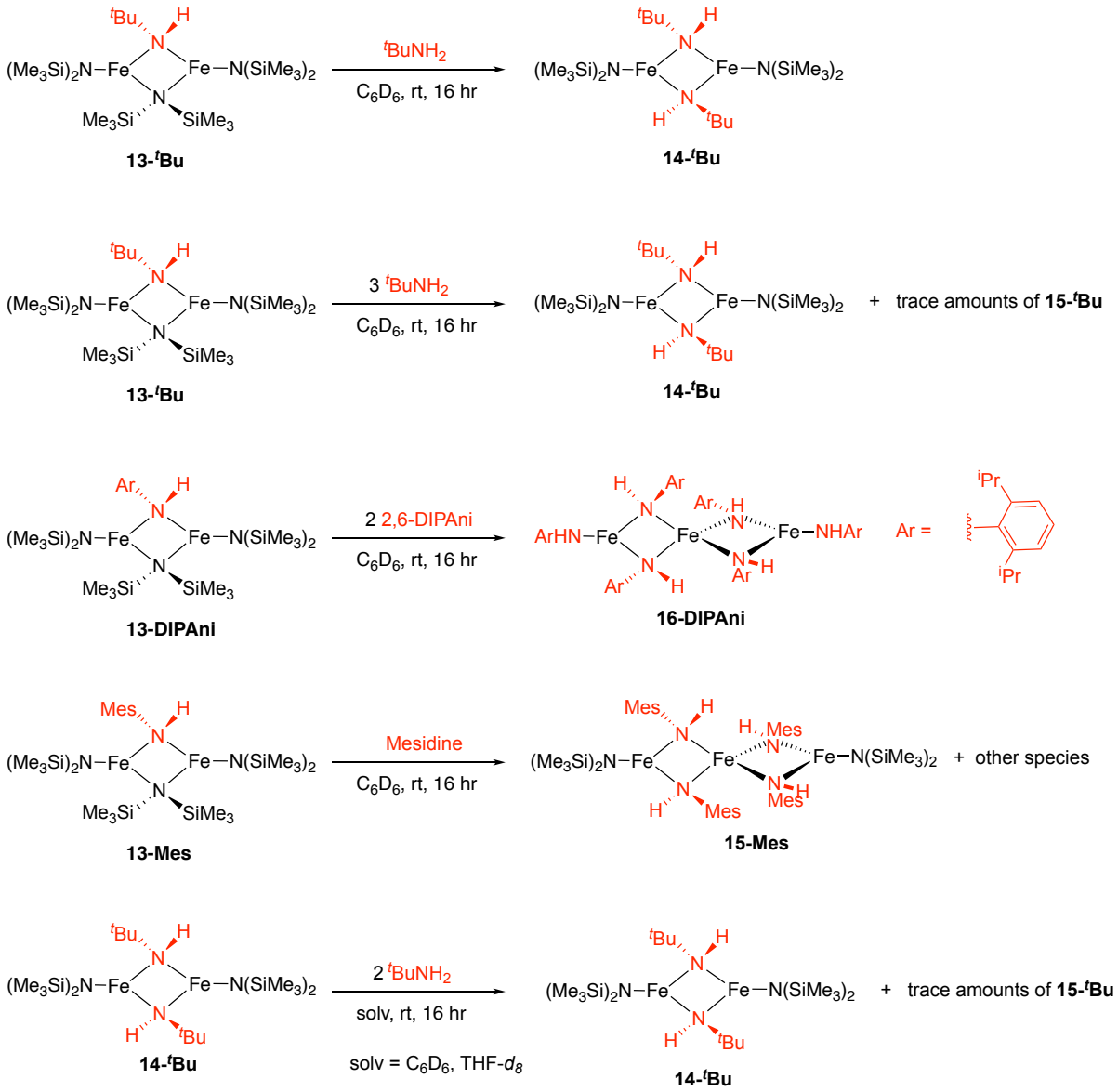

The second set of experiments analyzed involved the reactions of **13** with different amines as shown in Scheme 4.10. These reactions were performed in hopes to synthesize complexes with mixed bridging amide ligands.

Scheme 4.10. Reactivity of **13** with various amines

The reaction of **13-^{t}Bu** with one equivalent of ^{t}AmNH$_2$ initially led to the formation of all possible dinuclear complexes within this system, including **13-^{t}Am**, **14-^{t}Am**, **14-^{t}Bu**, and the heteroleptic bridging complex **14-^{t}Bu/^{t}Am**. After 24 hours, the only products observed were the disubstituted dinuclear complexes of **14-^{t}Bu**, **14-^{t}Bu/^{t}Am** and **14-^{t}Am** in a 1:2:1 ratio, corresponding to a statistical distribution. The presence of all dinuclear complexes at 15 minutes and only disubstituted complexes at 24 hours provides insight into the mechanism of complex formation and the following conclusions:

(i) If only **14-^{t}Bu/^{t}Am** was present in the ^{1}H NMR spectrum, it could be assumed that only the μ-N(SiMe$_3$)$_2$ undergoes protonation and substitution and the μ-NH^{t}Bu is inert.

(ii) The formation of **14-^{t}Am** is observed, which is likely through the formation of **13-^{t}Am**, from the replacement of the μ-NH^{t}Bu with ^{t}AmNH$_2$ and then the protonation and replacement of bridging (Me$_3$Si)$_2$N$^-$ with ^{t}AmNH$_2$.

(iii) During the process of (ii), the free ^{t}BuNH$_2$ can then react with **13-^{t}Bu** to form **14-^{t}Bu** or with the *in-situ* produced **13-^{t}Am** to form **14-^{t}Bu/^{t}Am**.

(iv) These reactions continue until all the bridging (Me$_3$Si)$_2$N$^-$ have been substituted and all the free amine has been deprotonated to form the amide.

The reaction of **13-^{t}Bu** with one equivalent of mesidine, an arylamine, was performed. This reaction was complete within 15 minutes, as no change in product distribution was observed after 24 hours. The faster reaction rate compared to the addition of ^{t}AmNH$_2$ to **13-^{t}Bu** can be attributed to the higher acidity of mesidine compared to ^{t}AmNH$_2$. At 15 minutes, numerous signals were observed in the ^{1}H NMR spectrum, with assignable signals corresponding to **13-^{t}Bu**, **14-^{t}Bu** and **15-Mes** with a product ratio of 3:2:1. Several additional signals could not be assigned to the ^{1}H NMR spectra; however, these signals have been previously observed in the reaction of **11** with one equivalent of mesidine. The reverse reaction of **13-Mes** and one equivalent of ^{t}BuNH$_2$ was performed and led to formation of **14-^{t}Bu** and **15-Mes** as the interpretable NMR signatures with many other signals also being

observed. The reaction was dominated by **14-^{t}Bu** but this was deceptive as the reaction of **13-Mes** and one equivalent of mesidine leads to numerous signals, likely secondary reaction pathways and decomposition with **14-Mes** not being as stable compared to **14-^{t}Bu**.

The reaction of **13-^{t}Bu** with benzylamine and DIPA is shown in Scheme 4.10. The addition of 1 equivalent of benzylamine to **13-^{t}Bu** leads to the formation of **14-^{t}Bu** and decomposition. At 15 minutes, many minor signals are observed with the predominant species being **14-^{t}Bu.** By 24 hours, the predominant signal set still corresponds to **14-^{t}Bu** with some minor signals and the solution color being black and opaque. The addition of one equivalent of DIPA to **13-^{t}Bu** leads to no reaction.

4.2.7.3 Cluster Reactivity

To determine if the monosubstituted dinuclear complexes were stable or would interact in ligand exchange, equimolar mixtures (1:1 mol ratios) of **13-^{t}Bu**:**13:^{t}Am**, **13-^{t}Bu**:**13-Mes** and **13-Mes**:**13-DIPAni** were prepared in C_6D_6. These experiments demonstrated that the complexes remain stable under these conditions, as no reactivity was observed in 24 hours. If ligand exchange had occurred, mixed disubstituted species and **11** would have been expected, as shown in Scheme 4.11.

Scheme 4.11. Intercluster reactivity of **13**

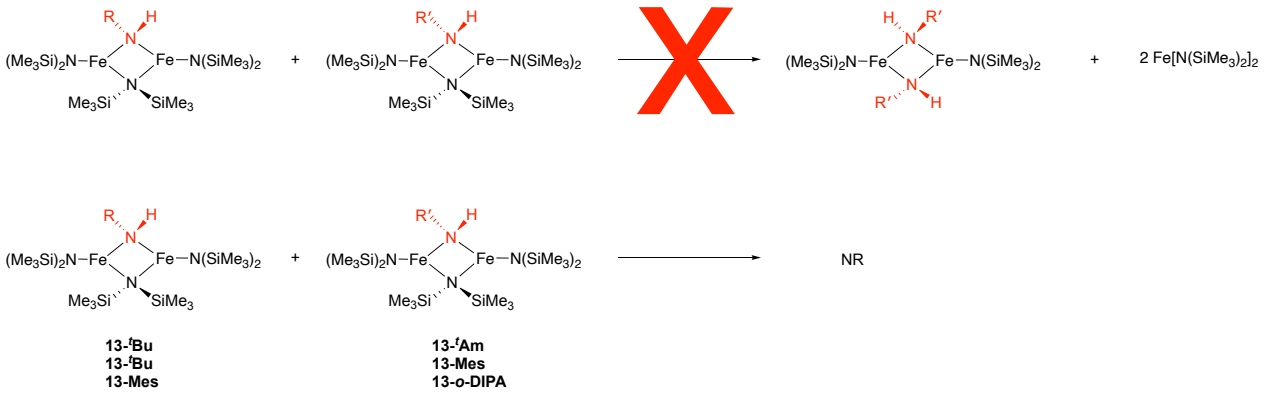

Interestingly, the dissolution of the disubstituted **13-^{t}Bu** in THF-d_8 led to its disproportionation into the monosubstituted **14-^{t}Bu** and **11**, as shown in Scheme 4.12. However, this reactivity was not observed when **14-^{t}Bu** was dissolved in THF-d_8, indicating a difference in stability or reactivity between these complexes under identical conditions.

Dissolution of **13-Mes** in THF-d_8 led to the formation of many signals that cannot be assigned to known complexes.

Scheme 4.12. Selected **13** and **14** complexes in THF-d_8

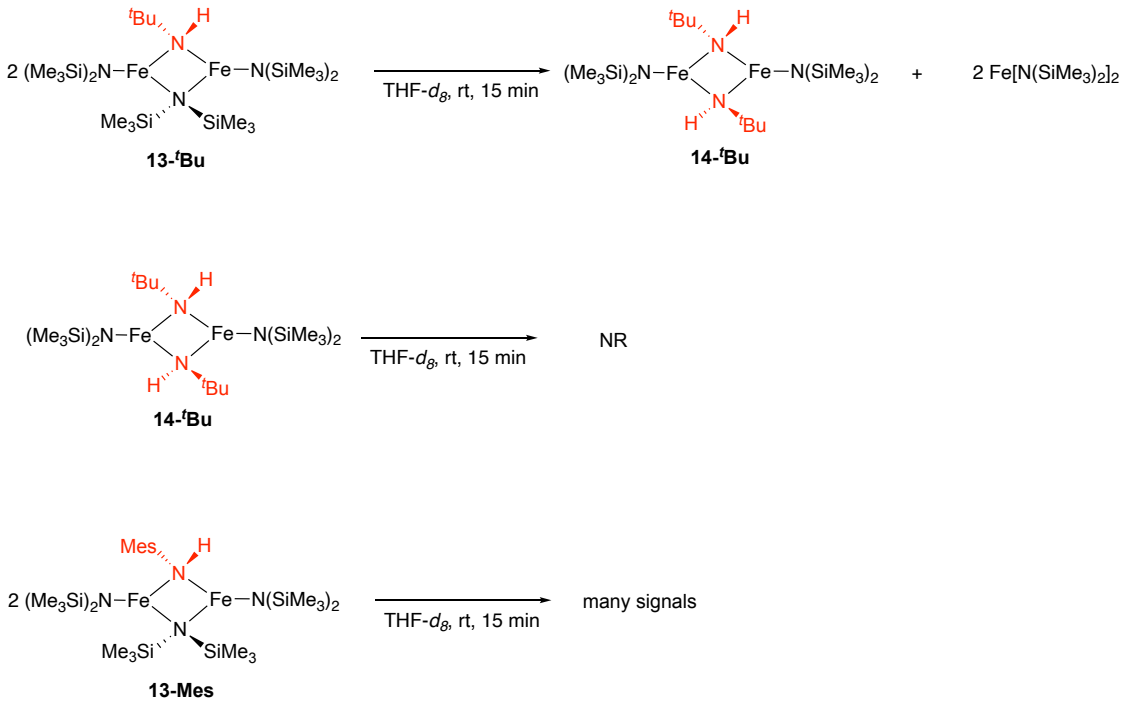

One of the precursors needed in the formation of $[Fe_4(N^tBu)S_3Cl_4]^{2-}$ is the triply bridged dinuclear complex which is formed by the oxidation addition of **14-^{t}Bu** with sulfur as shown in Scheme 4.13. The same reactivity was attempted with **13-^{t}Bu** and sulfur in C_6H_6 with no reactivity being observed.

Scheme 4.13. Oxidative addition reactions with sulfur

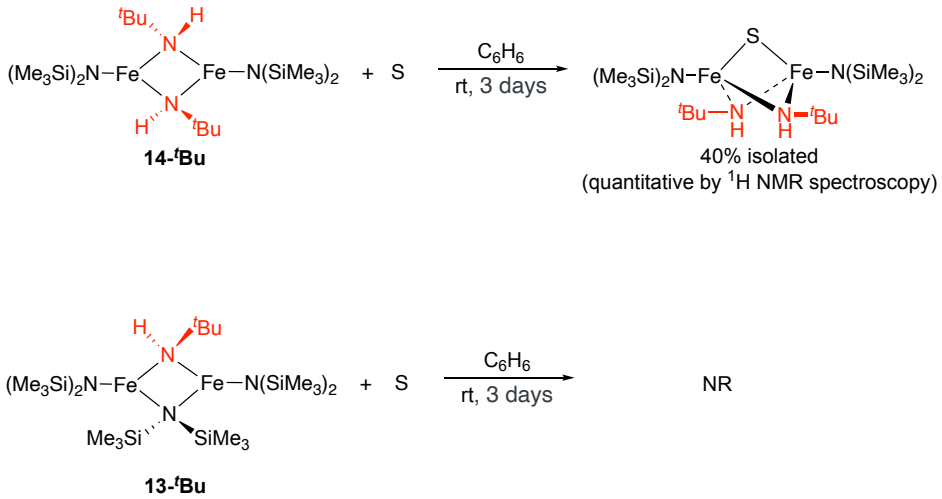

4.2.8 Chapter Summary

The work presented in this chapter led to the synthesis of mono-, di- and trinuclear Fe(II) complexes via the reaction of **11** with various amines. Unlike most previously reported systems formed by the protonolysis of **11** with protio ligands, the reactivity of **11** with less acidic protio-ligands remains underexplored. Work in the Lee laboratory led to the synthesis of **14-^{t}Bu**, which forms quantitatively from the reaction of **11** with ^{t}BuNH$_2$ in a 2:2 stoichiometry. The identify of the products formed depended on the stoichiometry of the amine relative to **11** and on several properties of the amine: its acidity, steric hindrance around the nitrogen and the degree of nitrogen substitution.

The amine to **11** stoichiometry dictated which product would form, assuming no competing side reactions. The products observed were an amine adduct complex, monosubstituted dinuclear complexes, disubstituted dinuclear complexes, heteroleptic trinuclear complexes and homoleptic trinuclear complexes. The amines employed in this study were grouped into four major categories: (1) primary alkylamines with tertiary α-carbons, (2) primary arylamines with ortho C-H bonds, (3) secondary alkylamines with primary or secondary α-carbons, and (4) secondary arylamines lacking ortho C-H bonds.

Generally, the reaction of **11** was slower with alkylamines than with arylamines, consistent with the greater acidity of the latter. Primary alkylamines bearing α-hydrogens and

primary arylamines bearing ortho hydrogens afforded non-quantitative formation of the monosubstituted dinuclear complex, followed by complete decomposition when higher equivalents of amine were used. This decomposition pathway was supressed when secondary alkyl- and arylamines were used

Two types of trinuclear complexes were isolated: heteroleptic trinuclear complexes that contained tms amide ligation and homoleptic trinuclear complexes. The homoleptic trinuclear complex was synthesized utilizing 2,6-diisopropylaniline as the protio-ligand. The steric bulk of the isopropyl group is proposed to stabilize the three-coordinate iron centers, enabling the isolation of the homoleptic trinuclear species.

The proposed transformation pathway proceeds through initial formation of an amine adduct, which converts sequentially into the monosubstituted dinuclear complex, then the disubstituted dinuclear complexes, and finally the heteroleptic trinuclear complex. This transformation was monitored by ^{1}H NMR spectroscopy, particularly in the piperidine series as three compounds of the set were isolated.

4.3 Experimental Section

4.3.1 General Experimental Details

Most standard experimental conditions have been reported in Chapter 2, Section 2.3.1. All amines used were distilled over CaH_2. Compound **11** was synthesized using the modified preparation using $FeCl_2$ as the iron source.[136] Compound **14-^{t}Bu** was synthesized using literature preparation and **13-^{t}Bu** and **14-^{t}Am** were synthesized using the preparation of Dr. Wei Zhang.[27] UV-vis spectra were obtained using a Varian Cary 5000 UV-vis-NIR spectrophotometer and solutions were measured using cells with pathlength of 0.1 mm.

General NMR assays. **11** was dissolved in C_6D_6 (500 μL) and neat amine was added by a microlitre syringe. The solution was then transferred to a Teflon-valved NMR tube. The ^{1}H NMR spectra were acquired after the following times: 15 min, 1 hour, 3 hours, 5 hours, 18 hours, 24 hours and 48 hours.

Titration of 11 with DIPA. **11** was dissolved in C_6D_6 and neat DIPA was injected into the Teflon-valved NMR tube via micro syringe.

4.3.2 Preparation of Compounds

General preparation of compounds. Solid **11** was stored in a Schlenk tube with a Teflon valve inside the glovebox. The Schlenk tube was removed from the glovebox, and the solid was melted using a heat gun. After placing the tube back into the glovebox, green **11** was then weighed into a vial using a pipette, and benzene was added directly to the vial, yielding a transparent, light green solution. Amine was then added neat to the solution of **11** yielding a color change, usually to transparent green. The solution was stirred overnight, and the solvent was removed under reduced pressure. The resulting green solid was redissolved in 2-3 mL of pentane, transferred to a 4 mL vial, and placed inside a 20 mL vial containing 5 mL of HMDSO to facilitate pentane/HMDSO evaporation. The vial was then stored at –20 °C, yielding large green crystals within days.

$Fe(NH(R)_2)[N(SiMe_3)_2]_2$ (12)

R = ^{i}Pr (12-DIPA). Reaction was performed in pentane (10 mL) with the amine to **11** stoichiometry being 2:1. The solution color was transparent light blue. Crystals were grown from a concentrated pentane solution. **11** (215.3 mg, 0.572 mmol, 1.0 equiv.); diisopropylamine (0.717 g/mL, 160 μL, 1.133 mmol, 1.98 equiv.); **12-DIPA** (167.0 mg, 61%). Anal. Calcd for $C_{18}H_{51}N_3Si_4Fe$: C, 45.16; H, 10.95; N, 8.78. Found: C, 45.22; H,11.51; N, 8.69.

R = pip (12-pip). Reaction was stopped after 1 hour. **11** (267.5 mg, 0.710 mmol, 1.0 equiv.); piperidine (0.862 g/mL, 70 μL, 0.709 mmol, 1.00 equiv.); C_6H_6 (10 mL); **12-pip** (140 mg, 43%) Anal. Calcd for $C_{18}H_{51}N_3Si_4Fe$: C, 45.16; H, 10.95; N, 8.78. Found: C, 45.22; H,11.51; N, 8.69.

$Fe_2(\mu\text{-}NRR')(\mu\text{-}N(SiMe_3)_2)[N(SiMe_3)_2]_2$ (13)

R = ^{t}Bu, R′ = H (13-^{t}Bu). Anal. Calcd for $C_{22}H_{64}N_4Si_6Fe_2$: C, 39.74; H, 9.70; N, 8.43. Found: C, 40.00; H, 9.80; N, 8.56.

R = ^{t}Am, R′ = H (13-^{t}Am). was synthesized analogously to **13-^{t}Bu** Anal. Calcd for $C_{23}H_{66}N_4Si_6Fe_2$: C, 40.70; H, 9.80; N, 8.25. Found: C, 40.66; H, 9.77; N, 8.30

R = pip (13-pip). Anal. Calcd for $C_{23}H_{40}N_4Si_6Fe_2$: C, 40.82; H, 9.53; N, 8.28. Found: C, 40.80; H, 9.555; N, 8.02

R = Bn, R′ = H (13-Bn). The addition of benzylamine to **11** in benzene led to the development of an opaque black solution within hours. Solvent removal under reduced pressure led to a black oil.

R = Mes, R′ = H (13-Mes). Instead of a neat amine addition, amine was added dropwise as a solution in benzene to control the rate of addition and reaction. The solution color evolved from light green (**11** in benzene) to a transparent, olive green color within an hour. Anal. Calcd for $C_{27}H_{66}N_4Si_6Fe_2$: C, 44.60; H, 9.15; N, 7.71. Found: C, 44.92; H, 9.13; N, 7.92.

R = 2,6-($C_6H_3{}^iPr_2$), R′ = H (13-DIPAni). 13-DIPAni was synthesized analogously to **13-Mes**

R = Ph, R′ = Me (13-NMePh). 13-NMePh was synthesized analogously to **13-Mes**

R = Bn, R′ = Me (13-NMeBn). 13-NMeBn was synthesized analogously to **13-Mes**

$Fe_2(\mu$-NRR′$)_2[N(SiMe_3)_2]_2$ (14)

R = ^{t}Am, (14-^{t}Am). Anal. Calcd for $C_{22}H_{60}N_4Si_4Fe_2$: C, 43.69; H, 10.00; N, 9.26. Found: C, 43.84; H, 10.15; N, 9.38.

$Fe_3(\mu$-NHR$)_4[N(SiMe_3)_2]_2$ (15)

R = Mes, R′ = H (15-Mes). Amine was added as a solution in benzene to a solution of **11** in C_6D_6. The light green solution of **11** deepened to olive green within hours. Anal. Calcd for $C_{48}H_{84}N_6Si_4Fe_3$: C, 56.25; H, 8.26; N, 8.20. Found: C, 56.47; H, 8.41; N, 8.03.

R = pip (15-pip). Amine is added in excess, 1:2 **11** to piperidine stoichiometry.

Anal. Calcd for $C_{32}H_{76}N_6Si_4Fe_3$: C, 46.60; H, 9.29; N, 10.19. Found: C, 46.97; H, 9.36; N, 9.96.

R = Ph, R′ = Me (15-NMePh). 15-NMePh was synthesized analogously to **15-Mes**

R = Bn, R′ = Me (15-NMeBn). 15-NMeBn was synthesized analogously to **15-Mes**

$Fe_3(\mu$-NH(2,6-$C_6H_3{}^iPr_2)_4$[NH(2,6-$C_6H_3{}^iPr_2)]_2$ (16)

R = 2,6-($C_6H_3{}^iPr_2$), R′ = H (16-DIPAni). 16-DIPAni was synthesized analogously to **15-Mes**. The light green solution deepened to opaque red within hours.

Spectroscopic data for select compounds found in Tables 4.9 and 4.10.

Table 4.9. ^{1}H NMR data for $Fe_2(\mu$-NH^{t}Bu$)_2$[N(SiMe$_3)_2]_2$ (**14-^{t}Bu**), $Fe_2(\mu$-NH^{t}Bu)(μ-N(SiMe$_3)_2$)[N(SiMe$_3)_2]_2$ (**13-^{t}Bu**), $Fe_3(\mu$-NH^{t}Bu$)_4$[N(SiMe$_3)_2]_2$ (**15-^{t}Bu**), $Fe_2(\mu$-NH^{t}Am)(μ-N(SiMe$_3)_2$)[N(SiMe$_3)_2]_2$ (**13-^{t}Am**), $Fe_2(\mu$-NH^{t}Am$)_2$[N(SiMe$_3)_2]_2$ (**14-^{t}Am**), Fe(NH(^{i}Pr$)_2$)[N(SiMe$_3)_2]_2$ (**12-DIPA**), Fe(NH(CH$_2)_5$)[N(SiMe$_3)_2]_2$ (**12-pip**), $Fe_2(\mu$-N(CH$_2)_5$)(μ-N(SiMe$_3)_2$)[N(SiMe$_3)_2]_2$ (**13-pip**), $Fe_3(\mu$-N(CH$_2)_5)_4$[N(SiMe$_3)_2]_2$ (**15-pip**), $Fe_2(\mu$-NHBn)(μ-N(SiMe$_3)_2$)[N(SiMe$_3)_2]_2$ (**13-Bn**), $Fe_3(\mu$-NHPh$)_4$[N(SiMe$_3)_2]_2$ (**13-Ph**), Fe(μ-NH(4-C_6H_4(Me)))(μ-N(SiMe$_3)_2$)[N(SiMe$_3)_2]_2$ (**13-*p*-Tol**), Fe(μ-NH(*o*-C_6H_4(Me)))(μ-N(SiMe$_3)_2$)[[N(SiMe$_3)_2]_2$ (**13-*o*-Tol**), $Fe_2(\mu$-NHMes)(μ-N(SiMe$_3)_2$)[N(SiMe$_3)_2]_2$ (**13-Mes**), $Fe_3(\mu$-NHMes$)_4$[N(SiMe$_3)_2]_2$ (**15-Mes**), $Fe_2(\mu$-N(Me)Ph)(μ-N(SiMe$_3)_2$)[N(SiMe$_3)_2]_2$ (**13-NMePh**), and $Fe_2(\mu$-N(Me)Bn)(μ-N(SiMe$_3)_2$)[N(SiMe$_3)_2]_2$ (**13-NMeBn**)

Complex	^{1}H NMR (C_6D_6, δ ppm)
14-^{t}Bu	0.513 (18 H, ^{t}Bu), –1.30 (36 H, SiMe$_3$)
13-^{t}Bu	1.10 (18 H, SiMe$_3$), –1.61 (18, H, SiMe$_3$), –2.59 (9 H), –4.93 (9 H), –6.20 (9 H)
15-^{t}Bu	–1.10 (27 H), –5.180 (9 H), –6.324 (18 H)
13-^{t}Am	1.24 (18 H), –0.10 (3 H), –1.98 (18 H), –3.23 (9 H), –4.75 (2 H), –5.49 (9 H), –6.24 (6 H)
14-^{t}Am	2.89 (6 H), 0.33 (4 H), –0.15 (12 H), –1.73 (36 H, SiMe$_3$)
14-^{t}Bu/^{t}Am	3.19 (3 H, CH$_3$), 1.87 (2 H, CH$_2$), 1.58 (6 H), -0.98 (9 H, ^{t}Bu), –1.29 (18 H, SiMe$_3$), –1.87 (18 H, SiMe$_3$)
12-DIPA	5.87, 1.65
12-pip	55.66 (3 H), 1.80 (36 H, SiMe$_3$), –10.61 (2 H), –16.24 (2 H), –20.06 (3 H)
13-pip	2.484 (2 H), 1.195 (4 H), 0.234 (36 H, SiMe$_3$), –5.066 (18 H, SiMe$_3$)
15-pip	31.60 (12 H), 15.97 (8 H), –4.72 (4 H), –13.02 (36 H, SiMe$_3$), –20.48 (8 H), –36.40 (8 H)
13-Bn	57.74 (2 H, CH$_2$), 7.79 (2 H, d, 6.78 Hz, *m*-H), 6.51 (2 H, *o*-H), 6.08 (1 H, t, 6.97, *p*-H) , 0.639 (9 H, SiMe$_3$), –1.89 (9 H, SiMe$_3$), –2.38 (36 H, SiMe$_3$)
13-Ph	5.89 (2 H, *m*-H), 2.59 (36 H, SiMe$_3$), –3.80 (9 H, SiMe$_3$), –4.93 (9 H, SiMe$_3$), –15.08 (1 H, *p*-H), –54.51 (2 H, *o*-H)

Complex	^{1}H NMR (C_6D_6, δ ppm)
13-*p*-Tol	12.89 (3 H, *p*-Me), 6.47 (2 H, *m*-H), 2.21 (36 H, $SiMe_3$), -3.480 (9 H, $SiMe_3$), –5.01 (9 H, $SiMe_3$), –49.238 (2 H, *o*-H)
13-*o*-Tol	12.58 (1 H), 6.87 (3 H, *o*-H), 2.76 (36 H, $SiMe_3$), 0.53 (1 H), –4.74 (9 H, $SiMe_3$), –5.11 (9 H, $SiMe_3$), -15.34 (1 H), –81.13 (1 H)
13-Mes	16.781 (3 H, *p*-Me), 12.063 (2 H br, *o*-H), 9.33 (6 H, *p*-Me), 4.211 (36 H, $SiMe_3$), –4.322 (9 H, $SiMe_3$), –8.175 (9 H, $SiMe_3$)
15-Mes	68.20 (12 H), 17.864 (12 H), 14.97 (4 H, *m*-H), 8.30 (36 H, $SiMe_3$), 3.60 (12 H), 2.44 (4 H, *m*-H)
13-NMePh	39.27 (3 H, *N*-Me), 3.80 (2 H, *m*-H), 2.84 (36 H, $SiMe_3$), –2.80 (9 H, $SiMe_3$), –5.33 (9 H, $SiMe_3$), –12.93 (1 H, *p*-H) –42.94 (2 H, *o*-H)
13-NMeBn	53.44 (3 H, *N*-Me), 41.00 (2 H, CH_2), 13.85 (2 H, *o*-H), 8.91 (2 H, *m*-H), 6.94 (1 H, *p*-H), 0.88 (36 H, $SiMe_3$), –2.91 (9 H, $SiMe_3$), –7.63 (9 H, $SiMe_3$)

Table 4.10. UV-vis Data for $Fe_2(\mu\text{-NH}^t\text{Bu})_2[N(SiMe_3)_2]_2$ (**14-^{t}Bu**), $Fe_2(\mu\text{-NH}^t\text{Bu})(\mu\text{-N}(SiMe_3)_2)[N(SiMe_3)_2]_2$ (**13-^{t}Bu**), $Fe_2(\mu\text{-NH}^t\text{Am})(\mu\text{-N}(SiMe_3)_2)[N(SiMe_3)_2]_2$ (**13-^{t}Am**), $Fe_2(\mu\text{-NH}^t\text{Am})_2[N(SiMe_3)_2]_2$ (**14-^{t}Am**), $Fe(NH(^i\text{Pr})_2)[N(SiMe_3)_2]_2$ (**12-DIPA**), $Fe(NH(CH_2)_5)[N(SiMe_3)_2]_2$ (**12-pip**), $Fe_2(\mu\text{-N}(CH_2)_5)(\mu\text{-N}(SiMe_3)_2)[N(SiMe_3)_2]_2$ (**13-pip**), $Fe_3(\mu\text{-N}(CH_2)_5)_4[N(SiMe_3)_2]_2$ (**15-pip**), $Fe_2(\mu\text{-NHMes})(\mu\text{-N}(SiMe_3)_2)[N(SiMe_3)_2]_2$ (**13-Mes**), $Fe_3(\mu\text{-NHMes})_4[N(SiMe_3)_2]_2$ (**15-Mes**) and $Fe_2(\mu\text{-NH}(2,6\text{-}C_6H_3{}^i\text{Pr}_2)(\mu\text{-N}(SiMe_3)_2)[N(SiMe_3)_2]_2$ (**13-DIPAni**)

Complex	λ_{max},nm (ε_M,L·mol^{-1}·cm^{-1})
14-^{t}Bu	209 (14 000), 229 (10 500), 277 (14 400) 393 (250)
13-^{t}Bu	245 (8 500), 285 (8 500), 407 (75)
13-^{t}Am	242 (11 000), 284 (10 600), 408 (830)
14-^{t}Am	242 (17 900), 285 (17 300),405 (464)
12-DIPA	281 (2 400), 384 (50)
12-pip	207 (5 700), 246 (3 500), 280 (3 500)
13-pip	244 (11 000), 277 (8 000), 294 (8 800). 328 (2 500), 273 (660), 419 (610)
15-pip	230 (15 200), 263 (15 000), 320 (5 300), 401 (710)
13-Mes	246, (17 100), 292 (10 500), 416 (1230)
15-Mes	244 (33 500), 300 (17 000), 387 (4 100)

Complex	λ_{max},nm (ε_M,L·mol^{-1}·cm^{-1})
13-DIPAni	247 (13 300), 295 (8 100), 329 (3 900), 414 (960)

4.3.3 X-Ray Crystallography

Single crystals suitable for single crystal X-ray diffraction analysis were obtained from storage of a concentrated pentane solution at –20 °C (**12-DIPA**, as transparent light blue blocks) and from a pentane/HMDSO evaporation at –20 °C (**12-pip** as light blue plates; **13-pip**, **13-^{t}Am**, **15-pip** as green blocks; **13-DIPAni** and **13-Mes** as olive green rods; **15-Mes** as dark green blocks; **15-NMePh** and **15-NMeBn** as green plates**; 16-DIPAni** as red rods). Data for single crystal x-ray diffraction were collected using Bruker SMART APEX diffractometer with an Oxford 700 Series cryostream cooler. Data sets were collected, indexed and processed using Bruker APEX2 software suite. Crystallographic structure solutions were refined using Bruker SHELXTL software package. Crystallographic data is tabulated in Table 4.11 to 4.13

Table 4.11. Crystallographic data for Fe(NH(^{i}Pr)$_2$)[N(SiMe$_3$)$_2$]$_2$ (**12-DIPA**) and Fe(NH(CH$_2$)$_5$)[N(SiMe$_3$)$_2$]$_2$ (**12-pip**)

	12-DIPA	**12-pip**
Formula	Fe(NH(^{i}Pr)$_2$)[N(SiMe$_3$)$_2$]$_2$	Fe(NH(CH$_2$)$_5$)[N(SiMe$_3$)$_2$]$_2$
Space group	*C2/c*	*P2$_1$/n*
a, Å	8.364(5)	11.481(1)
b, Å	18.136(10)	21.284(3)
c, Å	19.705(11)	11.789(1)
β, °	100.408(15)	103.520(3)
V, Å^3	2939.81	2800.84
θ_{max}, °	26	28
R_1(wR_2), %	7.33(15.72)	3.01(9.17)
Tot. data, %	99.9	99.0
S	1.180	1.2975

Table 4.12. Crystallographic data for $Fe_2(\mu\text{-}NH^tAm)(\mu\text{-}N(SiMe_3)_2)[N(SiMe_3)_2]_2$ (**13-^{t}Am**), $Fe_2(\mu\text{-}N(CH_2)_5)(\mu\text{-}N(SiMe_3)_2)[N(SiMe_3)_2]_2$ (**13-pip**), $Fe_2(\mu\text{-}NHMes)(\mu\text{-}N(SiMe_3)_2)[N(SiMe_3)_2]_2$ (**13-Mes**), and $Fe_2(\mu\text{-}NH(2,6\text{-}C_6H_3{}^iPr_2)(\mu\text{-}N(SiMe_3)_2)[N(SiMe_3)_2]_2$ (**13-DIPAni**)

	13-^{t}Am	**13-pip**	**13-Mes**	**13-DIPAni**
Formula	$Fe_2(\mu\text{-}NH^tAm)(\mu\text{-}N(SiMe_3)_2)[N(SiMe_3)_2]_2$	$Fe_2(\mu\text{-}N(CH_2)_5)(\mu\text{-}N(SiMe_3)_2)[N(SiMe_3)_2]_2$	$Fe_2(\mu\text{-}NHMes)(\mu\text{-}N(SiMe_3)_2)[N(SiMe_3)_2]_2$	$Fe_2(\mu\text{-}NH(2,6\text{-}C_6H_3{}^iPr_2)(\mu\text{-}N(SiMe_3)_2)[N(SiMe_3)_2]_2$
Space group	*P-1*	*P-1*	*C2/c*	*P2₁/n*
a, Å	9.061(3)	8.992(1)	19.605(4)	11.886(7)
b, Å	14.654(4)	14.902(2)	14.459(3)	10.546(6)
c, Å	14.84(4)	14.975(2)	17.505(3)	35.67(2)
α, °	95.834(8)	79.491(3)	90	90
β, °	91.526(9)	83.203(3)	122.258(4)	92.15(2)
γ, °	90.797(9)	85.456(3)	90	90
V, Å^3	1960.16	1955.53	4196.03	4468.66
θ_{max}, °	26	30	28	26
$R_1(wR_2)$, %	5.85(13.70)	2.57(7.62)	5.15 (16.78)	3.13(6.51)
Tot. data, %	99.4	100	99.9	99.8
S	1.383	1.007	1.032	1.181

Table 4.13. Crystallographic data for $Fe_3(\mu\text{-}NHMes)_4[N(SiMe_3)_2]_2$ (**15-Mes**), $Fe_3(\mu\text{-}N(CH_2)_5)_4[N(SiMe_3)_2]_2$ (**15-pip**), $Fe_3(\mu\text{-}N(Me)Bn)_4N(SiMe_3)_2]_2$ (**15-NMeBn),** $Fe_3(\mu\text{-}N(Me)Ph)_4N(SiMe_3)_2]_2$ (**15-NMePh**), and $Fe_3(\mu\text{-}NH(2,6\text{-}C_6H_3{}^iPr_2)_4[NH(2,6\text{-}C_6H_3{}^iPr_2)]_2$ (**16-DIPAni**)

	15-Mes	**15-pip**	**15-NMeBn**	**15-NMePh**	**16-DIPAni**
Formula	$Fe_3(\mu\text{-}NHMes)_4[N(SiMe_3)_2]_2$	$Fe_3(\mu\text{-}N(CH_2)_5)_4[N(SiMe_3)_2]_2$	$Fe_3(\mu\text{-}N(Me)Bn)_4N(SiMe_3)_2]_2$	$Fe_3(\mu\text{-}N(Me)Ph)_4N(SiMe_3)_2]_2$	$Fe_3(\mu\text{-}NH(2,6\text{-}C_6H_3{}^iPr_2)_4[NH(2,6\text{-}C_6H_3{}^iPr_2)]_2$
Space group	*P2₁/c*	*P2₁/c*	*C2/c*	*P2₁/n*	*P-1*
a, Å	12.646(7)	13.582(5)	31.285(5)	17.498(4)	16.182(3)
b, Å	39.84(2)	11.107(4)	8.649(2)	17.105(4)	16.569(3)
c, Å	12.468(7)	30.858(11)	20.238(3)	18.245(4)	18.105(3)
α, °	90	90	90	90	115.0184(6)
β, °	113.469(15)	97.930(10)	106.909(5)	106.337(7)	97.232(6)

	15-Mes	**15-pip**	**15-NMeBn**	**15-NMePh**	**16-DIPAni**
γ, °	90	90	90	90	101.563(6)
V, Å^3	5762.31	4610.55	5239.60	5240.24	4186.43
θ_{max}, °	28	26	26	28	26
R_1(wR_2), %	6.21 (17.11)	6.28 (20.24)	6.15(13.76)	5.37(11.61)	5.55(10.10)
Tot. data, %	100	98.9	100	100	99.99
S	1.023	1.002	1.405	1.166	1.235

Chapter 5: Synthesis and Stability Study of Oxidized and Reduced Iron-Imide-Sulfide Clusters

5.1 Introduction

5.1.1 Cofactors in nitrogenases

Nitrogenases are a class of enzymes found in certain prokaryotes that catalyze nitrogen fixation, converting atmospheric dinitrogen (N_2), which is biologically inaccessible, into ammonia (NH_3), a biologically accessible form. This transformation is essential, as nitrogen is a key component of amino acids and nucleic acids, the building blocks of life. Nitrogen fixation also occurs through two other known processes. The first process that is a major contributor to nitrogen fixation is the industrial Haber-Bosch process, which converts N_2 to NH_3, [137–139] and the second process that is a minor contributor is lighting induced conversion in the Earth's atmosphere, which transforms N_2 to nitrogen oxides (NO_x). Both nitrogenase enzymes and the Haber-Bosch process produce comparable amounts of fixed nitrogen, while the lighting-induced pathway contributes only a minor fraction of the total fixed nitrogen.

Currently, three forms of the nitrogenase enzyme are known: molybdenum (Mo) nitrogenase, vanadium (V) nitrogenase, and iron-only (Fe-only) nitrogenase. The dominant form found in nature is Mo-nitrogenase; however, under Mo-limiting conditions, V-nitrogenase is expressed. Similarly, Fe-only nitrogenase is expressed under conditions limiting in both Mo and V.[4] The limiting stoichiometry for the conversion is shown in Equation 5.1:

Equation 5.1

$$N_2 + n\,H^+ + 2n\,ATP + n\,e^- \rightarrow 2\,NH_3 + m\,H_2 + 2n\,ADP + 2n\,P_i$$

[4] The work presented in this chapter is built on unpublished results from Lay Ling Tan. Dion Grobe is acknowledged for experimental assistance.

The coefficients in Equation 5.1 are as follows: $n = 8$ and $m = 1$ for Mo-nitrogenase, $n = 12$ and $m = 3$ for V-nitrogenase, and $n = 24$ and $m = 9$ for Fe-only nitrogenase.[140] The efficiency of nitrogen fixation, defined as the N_2:H_2 production ratio, differs among the enzymes and is 1:1 for Mo-nitrogenase, 1:3 for V-nitrogenase, and 1:9 for Fe-only nitrogenase. As the mechanism of biological nitrogen fixation remains unresolved, the difference in catalytic efficiency among the nitrogenase isoforms also remains unexplained.

Many advances in understanding this essential process were performed which revealed the structures of the metalloclusters in the protein using single crystal X-ray diffraction analysis. The three metalloclusters are the F-cluster, P-cluster and M-cluster for the Mo-nitrogenases as shown in Figure 5.1. The F-cluster and the P-cluster of the V-nitrogenase are the same as the Mo-nitrogenase with the M-cluster of the V- nitrogenase containing a bridging carbonate instead of one of the bridging sulfides. The structure of the F-cluster is analogous to the Fe_4S_4 redox cofactors found in ferredoxins while the P- and M-clusters are novel for their more complex structure.

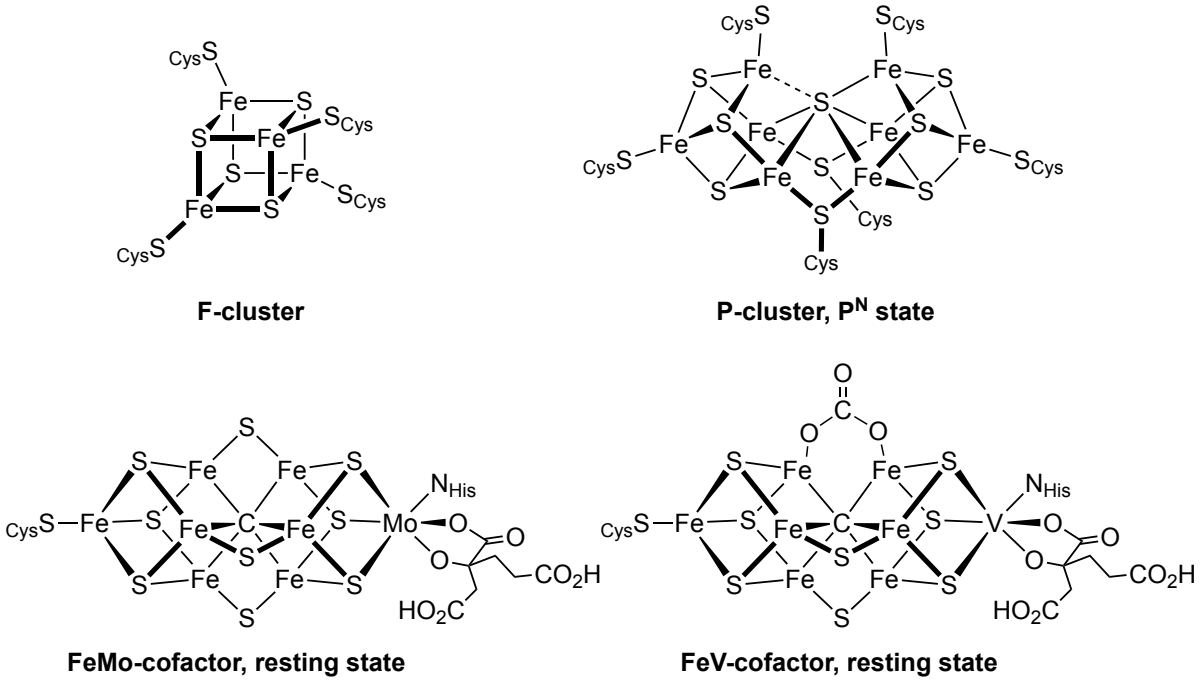

Figure 5.1. Metalloclusters found in Mo-nitrogenase and V-nitrogenase.

The structure of the F-cluster is an [Fe_4S_4] cubane-like cluster with terminal cysteine thiolate ligands on the iron atoms. The P-cluster with core composition of [Fe_8S_7], contains a double cubane fused at a sulfide vertex with two bridging cysteine thiolate ligands. The M-cluster with core composition [$MoFe_7S_9C$] can be viewed as two cubanes with core compositions of [$MoFe_3S_3$] and [Fe_4S_3] fused at a carbide vertex with three bridging sulfides. The F-cluster and P-cluster are responsible for electron transport while the M-cluster is believed to be the active site for biological nitrogen fixation, as evident by biochemical, genetic, spectroscopic and crystallographic evidence.

5.1.2 Nitrogenase active site

One of the genetic/biochemical evidence supporting the M-cluster as the active site for N_2 fixation was provided by Hawkes, McLean, and Smith.[141,142] The MoFe protein from a *nifV*$^-$ strain was purified and found to reduce C_2H_2 but not N_2. Additionally, under CO inhibition, this protein did not produce H_2. The M-cluster from this protein was isolated and subsequently inserted into the MoFe protein synthesized by a *nifB*$^-$ strain. The *nifB*$^-$ strain MoFe protein did not contain a M-cluster. The resulting *nifB*$^-$ MoFe protein containing the *nifV*$^-$ M-cluster exhibited the same characteristics as the MoFe protein generated from a *nifV*$^-$ strain: it reduced C_2H_2 but not N_2 and did not produce H_2 under CO inhibition. These findings provided strong evidence that the M-cluster is responsible for N_2 fixation. Spectroscopic evidence further supporting the M-cluster as the active site for dinitrogen fixation was obtained from CO inhibition studies of the MoFe protein. CO is a well-known inhibitor of Mo-nitrogenase. EPR, ENDOR, ^{13}C labelled and IR spectroscopy studies were conducted to investigate CO binding in the MoFe protein.[143–149] Under both low and high CO concentrations, characteristic spectroscopic signals of the MoFe protein's M cluster were altered, indicating electronic and structural changes. At low CO concentrations, N_2 fixation was still possible, albeit with reduced efficiency, whereas at high CO concentrations, N_2 fixation was completely inhibited.

These studies and others provided compelling evidence that the M-cluster is responsible for biological nitrogen fixation. This conclusion was further supported by single

crystal X-ray diffraction analysis, which confirmed reactivity and atom/molecule binding to two iron atoms within the M-cluster, accompanied by the displacement of a sulfide ligand as shown in Figure 5.2. Current evidence suggests that under specific conditions, the μ-sulfides in the M-cluster are labile, a phenomenon not previously observed in iron-sulfur chemistry. The lability of μ-sulfides may create an open coordination site on iron atoms, which are otherwise coordinatively saturated in a tetrahedral geometry. To date, four examples of μ-sulfide lability in the MoFe protein have been reported which include substitution with selenium (Se)[150], CO[151], N_2[152] and two CO[153]. It has also been demonstrated that all three μ-sulfides could be replaced. Specifically, selenium from selenocyanate ($SeCN^-$) was incorporated into these positions within FeMoco under turnover conditions.

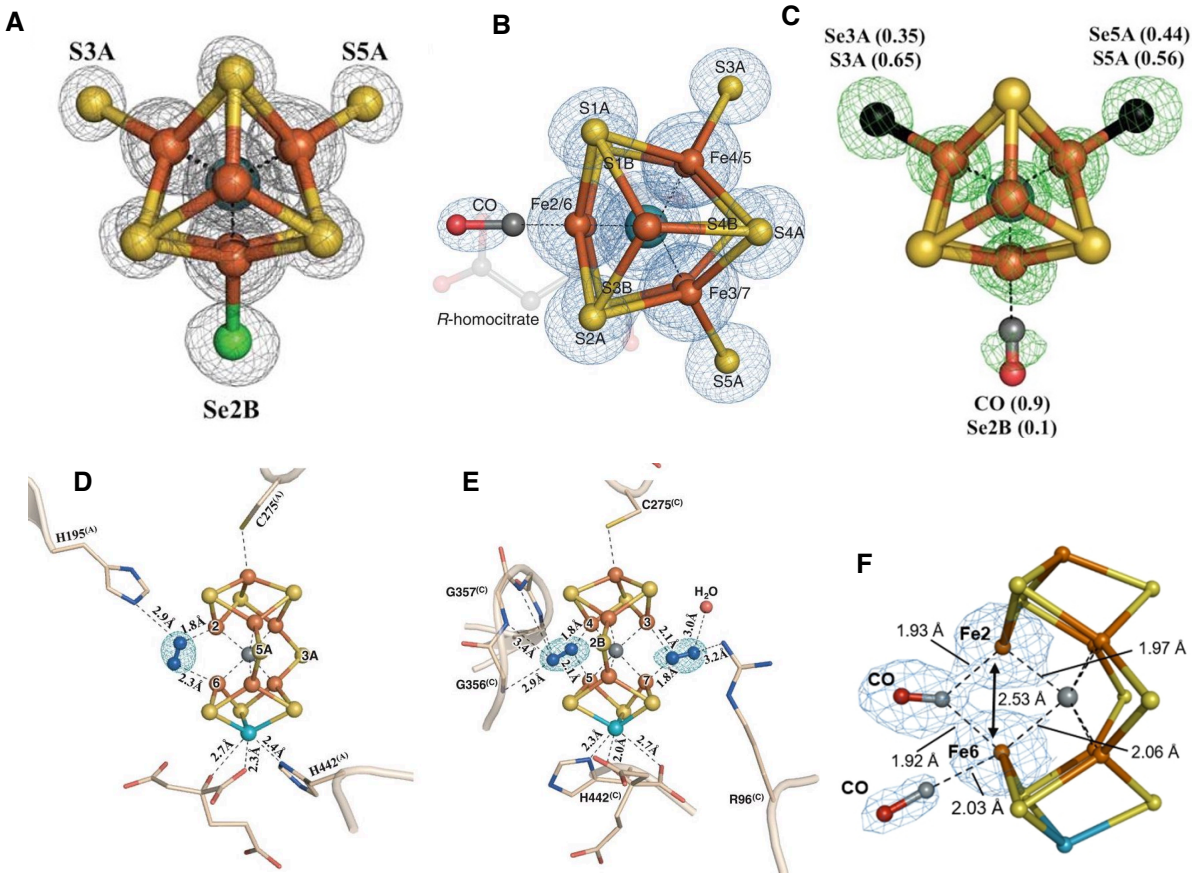

Figure 5.2. Structure of FeMoco under turnover conditions. Figure **A** and **C** taken from Reference 150. Figure **B**: Reprinted with permission from Spatzal, T.; Perez, K. A.; Einsle. O; Howard, J. B.; Rees, D. C, *Science*, 2014, *345*, 1616–1620. © 2020 The Authors, some rights reserved, exclusive licensee American Association for the Advancement of Science.

Figure **D** and **E:** Reprinted with permission from Kang, W.; Lee, C. C.; Jasniewski, A. J.; Ribbe, M. W.; Hu, Y., *Science*, 2020, *368*, 1381–1385. © 2020 The Authors, some rights reserved, exclusive licensee American Association for the Advancement of Science. Figure **F** taken from Reference 153.

Although crystallographic evidence suggests N_2 binding to the M-cluster, this interpretation remains contested.[154–156] The observed binding modes do not align with those found in known metal-dinitrogen complexes.[157] Figure 5.2 illustrates two M-cluster configurations: in one, a single bridging sulfide is replaced, and in the other, two are replaced. Given the size and complexity of the protein, and the similarity in electron density between N_2 and S^{2-}, it is plausible that the electron density assigned to N_2 could correspond to disordered S^{2-}.

5.1.3 Synthetic Analogues

Despite the genetic, spectroscopic, and crystallographic evidence, many aspects of biological nitrogen fixation remain poorly understood. One approach to investigating this process is through the study of isolated cofactors. The isolation of pure M-cluster requires extensive purification from the biochemical assembly, a process that is both labor-intensive and prone to impurities.[158,159] Additionally, the isolated M-cluster is stable for only one minute in the presence of oxygen, a few hours in protic solvents, and up to ten days in aprotic solvents, making its handling particularly challenging. Even though the M-cluster can be isolated, the structure of the isolated M-cluster remains undetermined and isolated M-cluster appears to be inactive to nitrogen fixation. An alternative approach to studying the mechanism of dinitrogen reduction involves the use of synthetic analogues.

Synthetic analogues are small molecules designed to better understand the chemistry of biological cofactors, such as those found in nitrogenase. These analogues can be employed in several ways including the following contexts: (i) "the deduction of minimal site structure (where unknown) based on coincident model-biomolecule properties or (where known) required for the execution of biological function." (ii) "the detection of the influence of the biomolecular environment on the intrinsic properties of the site as represented by the model." and (iii) "the broad exploration of fundamental chemistry as motivated by a biological system, with the immediate goal of establishing possibilities and methodologies that

ultimately will lead to corroborative synthetic analogues and a chemical understanding of the inspiration system".[160,161]

5.1.4 Synthetic Analogues of FeMoco

Over the years, numerous models of the M-cluster have been reported. These models share key features with the M-cluster which include multinuclear metal complexes, high-spin iron centers, sulfide bridges and either contain integration of a light 2p element, integration of a heterometal or contain a double cubane structure type. The work presented in Figure 5.3 spans more than two decades and involves contributions from various research laboratories.[21,162–167] These models are a specific subset that fulfill the criteria above, as many other complexes that can be viewed as models of the M-cluster have been reported.

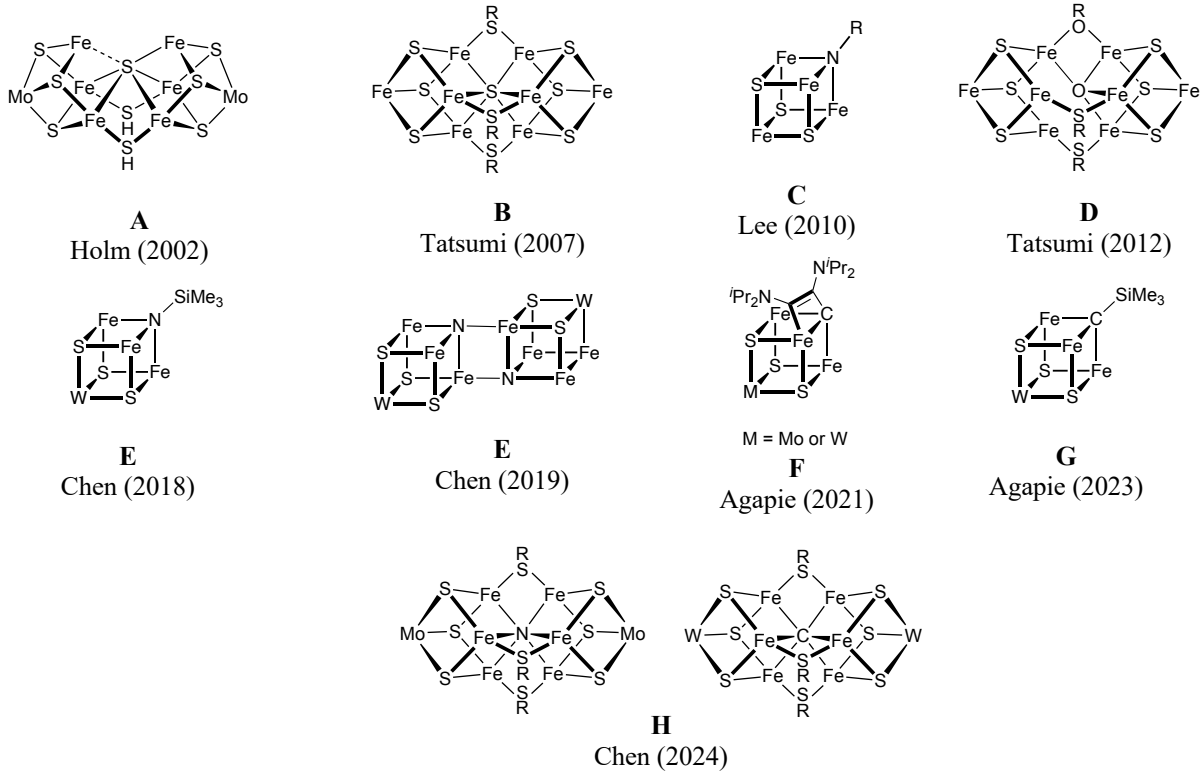

Figure 5.3. Structures of synthetic analogues of FeMoco in historical order.

As mentioned previously, work in the Lee group led to the synthesis and characterization of an iron-imide-sulfide cubane compound class. One member of the compound class is particularly noteworthy for its potential use as a model for half the M-

cluster. Figure 5.4 presents the superposition of the $[Fe_4S_3N]$ core of $[Fe4S_3(N^tBu)Cl_4]^{2-}$ and the $[Fe_4S_3C]$ subunit of the M-cluster, with a RMSD of 0.047 Å for the eight-atom core. [26] This indicates that the $[Fe_4S_3N]$ core is isometric with one half of the M-cluster. Similarly, the basic μ_3-N^{t}Bu ligand carries a formal charge of 2– per cubane, while the μ_6-carbide in the M-cluster has a charge of 4– distributed across two cubanes, further reinforcing the structural and electronic parallels between the two clusters.

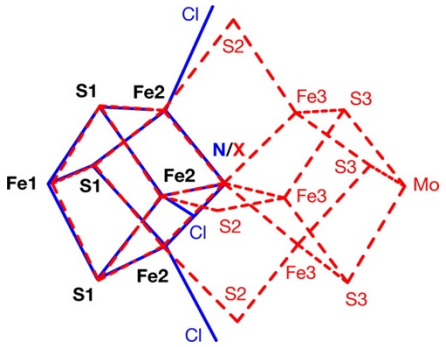

Figure 5.4. Superposition of the $[Fe_4S_3N]$ core and the $[Fe_4S_3C]$ subunit of FeMoco. The RMSD is 0.047 Å for the eight core atoms. Reprinted (adapted) with permission from Chen, X. D.; Zhang, W.; Duncan, J. S.; Lee, S. C. *Inorg. Chem.* **2012**, *51* (23), 12891–12904. Copyright 2012 American Chemical Society.

To further increase the structural and electronic resemblance of $[Fe_4S_3(N^tBu)Cl_4]^{2-}$ with the M-cluster, functionalization with thiolate ligands was performed. Thiolate ligands were selected due to their relevance in the $[Fe_4S_3C]$ subunit of the M-cluster, where one iron is coordinated by cysteine thiolate, and three iron centers are bridged by sulfides. As the target complex serves as an analogue of one half of the M-cluster, the 1– charge of the thiolate approximates the 2– charge of a sulfide in a single cubane, allowing thiolates to act as both electronic and structural surrogates for the μ-sulfide bridges. Thiolate ligands typically form stronger bonds with iron compared to chloride ligands, offering enhanced stability. While $[Fe_4(N^tBu)S_3Cl_4]^{2-}$ exhibits quais-reversible reduction potentials, incorporation of iron-thiolate bonds is expected to stabilize the complex, potentially leading to reversible redox processes, analogous to those observed in $[Fe_4S_4]$ clusters.

5.2 Results and Discussions

5.2.1 Synthesis of Starting Material

The published synthesis of $[Et_4N]_2[Fe_4(N^tBu)S_3Cl_4]$ ($[Et_4N]_2$**19**) is shown in Scheme 5.1. This preparation utilizes $[Et_4N]_2[Fe_4S_4Cl_4]$ ($[Et_4N]_2$**18**) and the triply bridged, iron(II) complex $Fe_2(\mu\text{-}NH^tBu)_2S[N(SiMe_3)_2]_2$ (**17**). The original preparation of **19** employed the $(Et_4N)^+$ salt of **18**. Compounds **18** and **19** will refer to the cluster anion in $[Et_4N]_2$**18**/$[Ph_4P]_2$**18** $[Et_4N]_2$**19**/$[Ph_4P]_2$**19** respectively when the results pertain to cluster regardless of the counterion.

Scheme 5.1. Synthesis of $[Fe_4(N^tBu)S_3Cl_4]^{2-}$ **(19)**

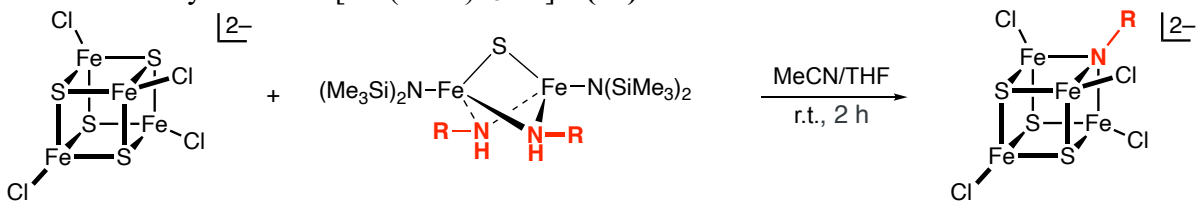

The many reported synthetic protocols to form $[Et_4N]_2$**18** can be challenging, as the preparations often require multiple steps and/or may yield material of insufficient purity.[168–170] The work described in this chapter presents a modified approach that utilizes $[Ph_4P]_2$**18** to synthesize $[Ph_4P]_2$**19**. The literature-reported synthesis of $[Ph_4P]_2$**18** is advantageous, as it follows a one-pot procedure (Equation 5.2) from simple starting material, enabling the production of gram-scale crystalline material within a day, in contrast to the multi-week synthesis required for $[Et_4N]_2$**18**.[171] Amanda Kwan, an undergraduate researcher in the lab, attempted to synthesize $[Et_4N]_2$**18** using $FeCl_2$, KSPh, Et_4NCl and S. This did not lead to isolable material which demonstrated the necessary use of $[Ph_4P]Cl$ as the counterion source.

Equation 5.2.

$$4\ FeCl_2 + 6\ KSPh + 2\ [Ph_4P]Cl + 4\ S \longrightarrow [Ph_4P]_2[Fe_4S_4Cl_4] + 6\ KCl + 3\ PhSSPh$$

The synthesis of $[Et_4N]_2$**19** (Scheme 5.1) via the reaction of $[Et_4N]_2$**18** with **17** afforded an isolated yield of ~50%. The remainder of the reaction mass consisted of the di-*tert*-butylimide cluster $[Fe_4(N^tBu)_2S_2Cl_4]^{2-}$, as well as an insoluble black residue containing iron and sulfur. Separation of $[Et_4N]_2$**19** from $[Fe_4(N^tBu)_2S_2Cl_4]^{2-}$ was achieved via a solid-

liquid extraction using DCM. While both clusters dissolved in DCM, $[Et_4N]_2$**19** spontaneously crystallized from the solution due to its lower solubility relative to the byproduct. Lay Ling Tan, a previous member of the group, later discovered that increasing the reaction concentration, reducing the reaction time from 8 hours to 2 hours, and using a larger volume of DCM improved the protocol, enabling more efficient isolation of pure $[Et_4N]_2$**19**.

The synthesis of $[Ph_4P]_2$**19** followed a slightly modified protocol. Compared to $[Et_4N]_2$**18**, $[Ph_4P]_2$**18** exhibits lower solubility in acetonitrile, meaning a suspension of $[Ph_4P]_2$**18** in MeCN was added to a solution of **17** in THF. The protocol developed by Tan – incorporating her optimized concentration and shortened reaction time – was applied to optimize the amount of **19** formed. This method yielded only trace amounts of $[Fe_4(N^tBu)_2S_2Cl_4]^{2-}$, likely due to slower reaction kinetics associated with the biphasic nature of the system. The minimal formation of this byproduct rendered a solid-liquid extraction step unnecessary, simplifying the isolation process. $[Ph_4P]_2$**19** demonstrated high crystallinity, with microcrystals (via MeCN/Et_2O two solvent recrystallization) and macrocrystals (via Et_2O vapour diffusion into MeCN) obtained. The isolated yield for this preparation was 50%, comparable to that of $[Et_4N]_2$**19**.

Although tetraphenylphosphonium salts of clusters can be highly crystalline perhaps due to the comparable sizes of the counterion and cluster, the use of tetraphenylphosphonium as a counterion can introduce complications. Reduction of clusters with $[Ph_4P]^+$ as the counterion with strong alkali metal reductants (e.g. KC_8, $Na[Ph_2CO]$) led to the reduction of some tetraphenylphosphonium cation to triphenylphosphine**.** To mitigate this reactivity, the tetraphenylphosphonium counterion can be replaced with a less reactive organic counterion, such as tetraethylammonium, as shown in Scheme 5.2. Counterion metathesis can be achieved by reacting $[Ph_4P]_2$**19** with two equivalents of $NaBPh_4$ in MeCN, generating $[Na]_2$**19** in solution while precipitating crystalline $(Ph_4P)(BPh_4)$ as a coproduct. Subsequent reaction of $[Na]_2$**19** with Et_4NCl yields the tetraethylammonium salt in solution, with NaCl precipitating as a coproduct. Ensuring complete removal of $(Ph_4P)(BPh_4)$ is crucial to prevent contamination of the desired crystalline salt. Removal of remaining $(Ph_4P)(BPh_4)$ can be

performed by volume reduction of the MeCN solution under reduced pressure to allow for crystallization of $(Ph_4P)(BPh_4)$ as $[Et_4N]_2$**19** is readily soluble in MeCN.

Scheme 5.2. Counterion metathesis reaction

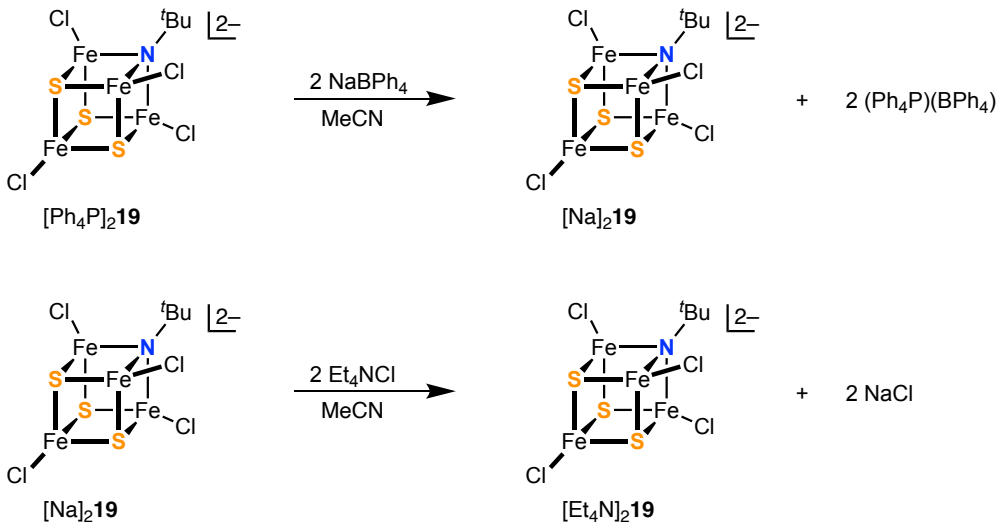

Purity determination of $[Et_4N]_2$**18** and $[Et_4N]_2$**19** can be potentially difficult using spectroscopic techniques. $[Et_4N]_2$**18** contains no protons on the complex, meaning ^{1}H NMR spectroscopy cannot be used to probe the purity of the complex and the *tert*-butyl resonance of $[Et_4N]_2$**19** is broad, meaning integration of this resonance led to inconsistent values. Assessing the purity of the complexes can be performed using ^{1}H NMR titration experiments with 4 equivalents of NaSPh. Using an excess of thiolate in these titration experiments is recommended, as these reactions are conducted on a small scale, and complete reactivity of the clusters is essential for accurate analysis. This reaction leads to the substitution of the terminal chlorides with thiolate ligands, leading to spectroscopic signatures that can be utilized to determine cluster purity. The aromatic signals are sharper relative to the ^{t}Bu resonance allowing for more reliable integration of peaks for absolute purity and relative purity in comparison to the counterion signals. This approach enables a more accurate determination of the counterion-to-cluster ratio and improves the precision of quantitative NMR measurements.

5.2.2 Thiolate Ligation of $Fe_4(N^tBu)S_3$ Clusters

The formation of the thiolate ligated clusters proceeds via a ligand metathesis reaction between **19** and sodium thiolate, as illustrated in Scheme 5.3.

Scheme 5.3. Ligand exchange reaction of **19** with arylthiolate

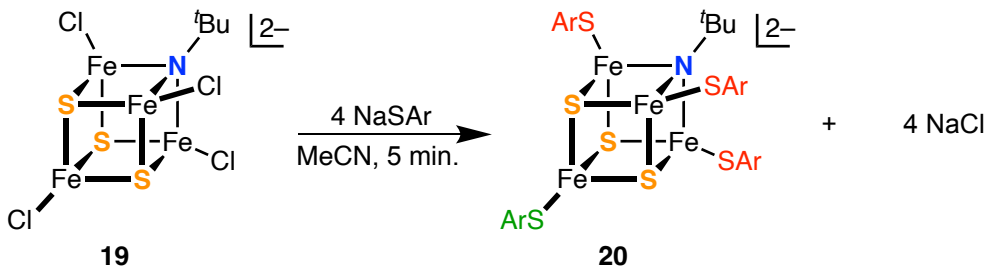

A solution of **19** in MeCN is added to a suspension of sodium thiolate in MeCN, resulting in a rapid color change from deep brown to golden black. NaCl, formed as a byproduct, is removed by filtration, and the thiolate ligated cluster is crystallized via a two-solvent recrystallization process using MeCN/Et_2O. The resulting crystalline product is stable in the solid state at –20 °C for several months. The thiolate ligands used in this study include benzene thiolate, mesityl thiolate, 4-chlorobenzene thiolate, 2,6-dichlorobenzene thiolate and *p*-methylbenzene thiolate with the structures of the ligands shown in Figure 5.5. These relatively simple thiolate ligands were chosen to study as they represented simple changes to the electronic and steric properties when compared to benzene thiolate.

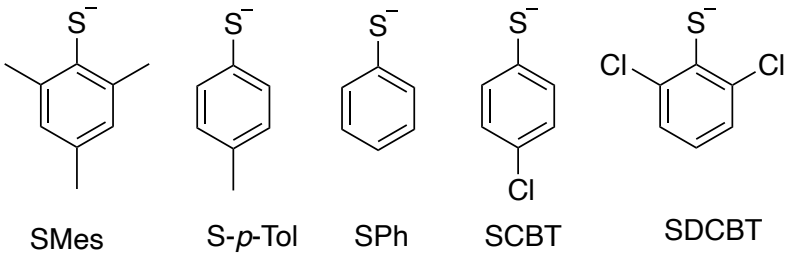

Figure 5.5. Thiolates utilized as ligands in this chapter. Thiolates include mesityl thiolate (SMes), 4-methylbenzene thiolate (S-*p*-Tol), benzene thiolate (SPh), 4-chlorobenzene thiolate (SCBT), and 2,6-dichlorobenzene thiolate (SDCBT).

Tan initially synthesized $[Et_4N]_2[Fe_4(N^tBu)S_3(SPh)_4]$ ($[Et_4N]_2$**20-Ph**) and $[Et_4N]_2[Fe_4(N^tBu)S_3(SMes)_4]$ ($[Et_4N]_2$**20-Mes**), both as the tetraethylammonium salts. Tetraphenylphosphonium proved advantageous in the synthesis of **20-Ph**, as this compound exhibited excellent crystallinity and was isolated as an analytically pure sample. However, initial crystallization attempts for **20-DCBT**, **20-CBT** and **20-*p*Tol** were unsuccessful with tetraphenylphosphonium as the counterion because the products tended to form oils under the recrystallization conditions with $MeCN/Et_2O$. To address this issue, tetraethylammonium was employed instead, which led to the successful isolation of crystalline, pure $[Et_4N]_2[Fe_4(N^tBu)S_3(S(2,6\text{-}C_6H_3Cl_2))_4]$ ($[Et_4N]_2$**20-DCBT**), $[Et_4N]_2[Fe_4(N^tBu)S_3(S(4\text{-}C_6H_4Cl))_4]$ ($[Et_4N]_2$**20-CBT**) and $[Et_4N]_2[Fe_4(N^tBu)S_3(S(4\text{-}C_6H_4Me))_4]$ ($[Et_4N]_2$**20-*p*Tol**).

5.2.3 Spectroscopic Properties

Complexes were identified in solution using ^1H NMR and UV-vis spectroscopy. ^1H NMR spectroscopy was utilized as the primary tool for rapid identification and quantitation of the clusters and to observe chemical reactivity. The thiolated clusters with the Fe_4NS_3 core analyzed in this chapter include **20-Ph**, **20-Mes**, **20-DCBT**, **20-CBT** and **20-*p*Tol**. Tan synthesized and performed the primary characterization of $[Et_4N]_2$**20-Ph** and $[Et_4N]_2$**20-Mes**. The resulting ^1H NMR spectra of these clusters, shown in Figure 5.6, display isotropically shifted signals that are consistent with a C_{3V} symmetric cluster.

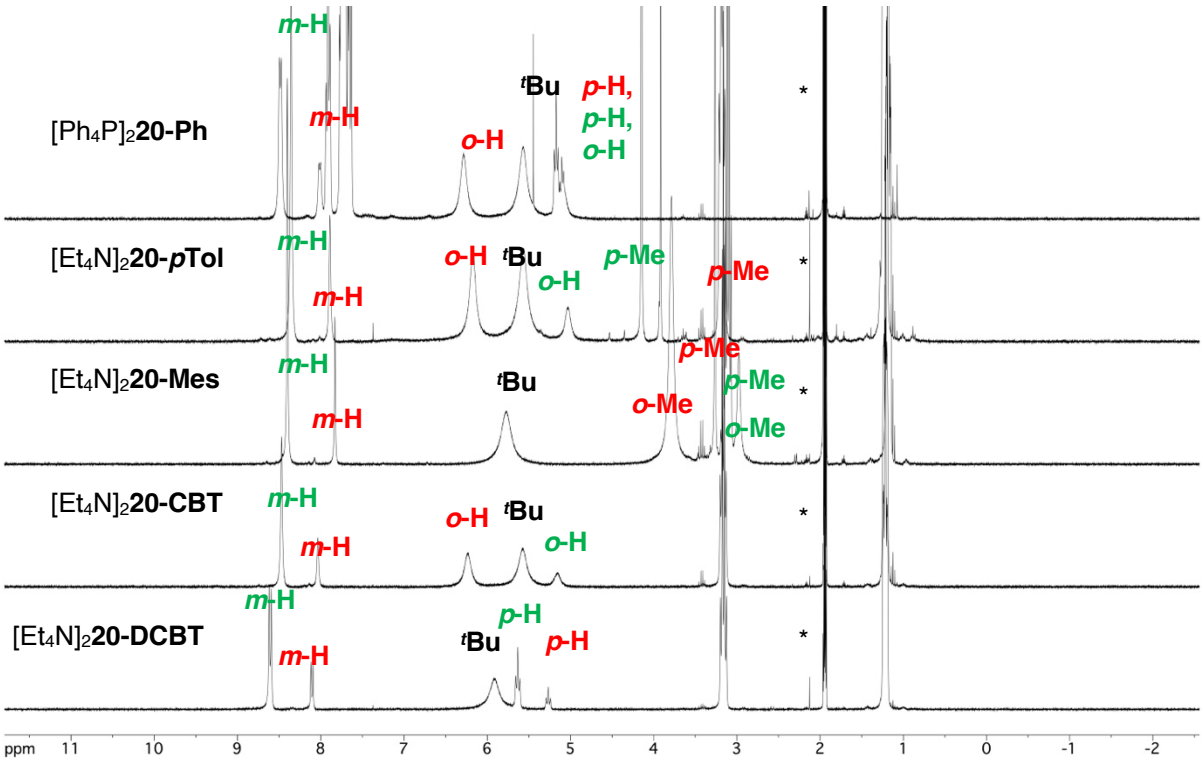

Figure 5.6. ^{1}H NMR Spectra (298 K, 300 MHz) of $[Ph_4P]_2$**20-Ph**, $[Et_4N]_2$**20-*p*Tol**, $[Et_4N]_2$**20-Mes**, $[Et_4N]_2$**20-CBT**, and $[Et_4N]_2$**20-DCBT**. Residual protio signals of CD_3CN are marked by *. Resonances corresponding to ligand environments bound to the three equivalent Fe sites are indicated in red; those corresponding to the unique Fe site are indicated in green.

The electronic properties of select clusters are shown in Figure 5.7. Compounds $[Ph_4P]_2$**19** and $[Ph_4P]_2$**20-Ph** display similar sharp features at 275, 268 and 228 nm as seen in the electronic absorption spectra of $[Ph_4P]$**2** and $[Ph_4P]_2$**6** which correspond to the $[Ph_4P]^+$ cation. Compound $[Ph_4P]_2$**19** displays nearly no absorbance in the visible region, correlating with the brown/black solution color while the thiolate ligated clusters $[Ph_4P]_2$**20-Ph**, $[Et_4N]_2$**28**, and $[Et_4N]_2$**20-*p*Tol** showcase absorbance in the tail of the visible region, correlating with the yellowish black solution color. The features in the spectrum of $[Et_4N]_2$**28** are blue shifted compared to $[Ph_4P]_2$**20-Ph** and $[Et_4N]_2$**20-*p*Tol.**

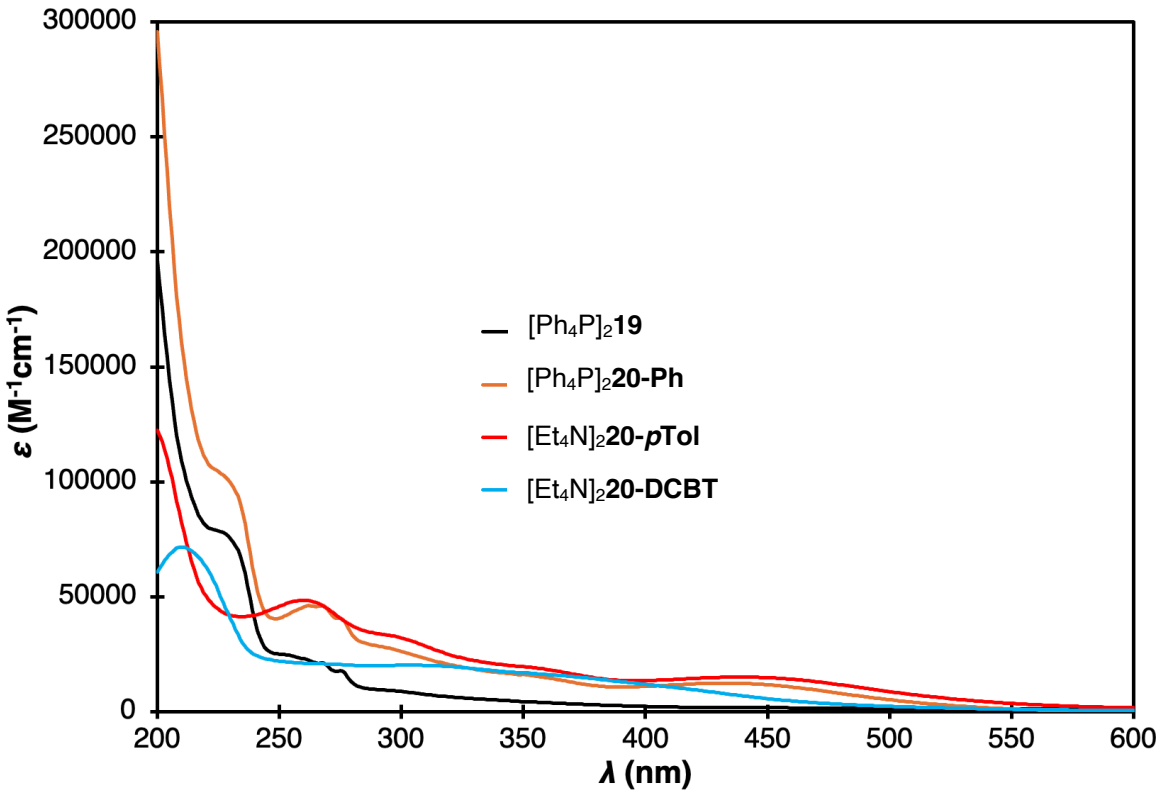

Figure 5.7. Solution UV-vis absorption spectra of $[Ph_4P]_2[Fe_4(N^tBu)S_3Cl_4]$ ($[Ph_4P]_2$**19**, black), $[Ph_4P]_2[Fe_4(N^tBu)S_3(SPh)_4]$ ($[Ph_4P]_2$**20-Ph**, orange), $[Et_4N]_2[Fe_4(N^tBu)S_3(S(4\text{-}C_6H_4Me))_4]$ ($[Et_4N]_2$**20-*p*Tol**, red), and $[Et_4N]_2[Fe_4(N^tBu)S_3(S(2,6\text{-}C_6H_3Cl_2))_4]$ ($[Et_4N]_2$**20-DCBT**, blue) in pentane.

5.2.4 X-ray Crystallography

X-ray diffraction analysis was performed to verify product identities. Tan collected and analyzed the X-ray diffraction data for $[Et_4N]_2$**20-Ph** and $[Et_4N]_2$**20-Mes**. The solid-state structures of $[Et_4N]_2$**20-DCBT** and of $[Et_4N]_2$**20-*p*Tol** are shown in Figures 5.8 and 5.9, respectively. Selected distances and angles for $[Et_4N]_2$**20-DCBT** and $[Et_4N]_2$**20-*p*Tol** are tabulated in Table 5.1.

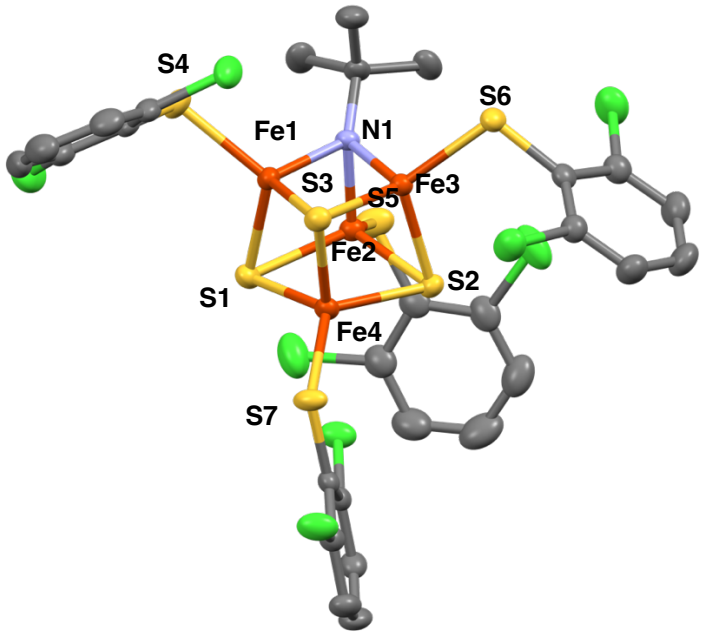

Figure 5.8. Structure of anion in $[Et_4N]_2[Fe_4(N^tBu)S_3(S(2,6\text{-}C_6H_3Cl_2))_4]$ ($[Et_4N]_2$**20-DCBT**) with thermal ellipsoids (50% probability level) and selected atom labels. For clarity, hydrogen atoms are not shown.

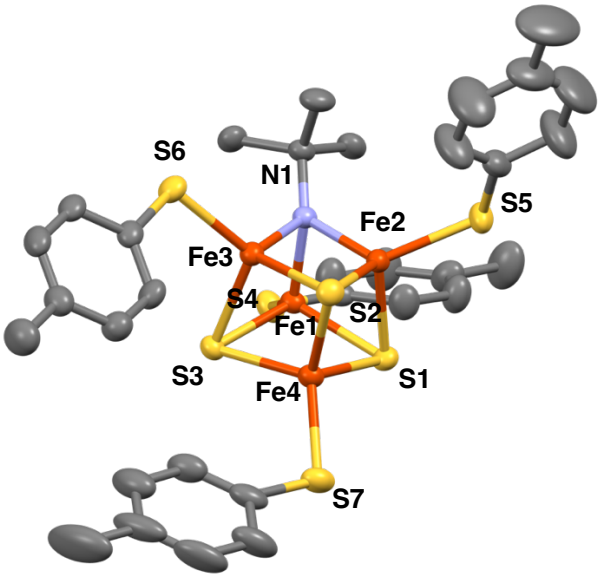

Figure 5.9. Structure of anion in $[Et_4N]_2[Fe_4(N^tBu)S_3(S(4\text{-}C_6H_4Me))_4]$ ($[Et_4N]_2$**20-*p*Tol**) with thermal ellipsoids (50% probability level) and selected atom labels. For clarity, hydrogen atoms are not shown.

Table 5.1. Selected Distances (Å) and Angles (º) for $[Et_4N]_2[Fe_4(N^tBu)S_3(S(2,6\text{-}C_6H_3Cl_2))_4]$ ($[Et_4N]_2$**20-DCBT**) and $[Et_4N]_2[Fe_4(N^tBu)S_3(S(4\text{-}C_6H_4Me))_4]$ ($[Et_4N]_2$**20-*p*Tol**)

	$[Et_4N]_2$**20-DCBT**	$[Et_4N]_2$**20-*p*Tol**
Fe(1/2/3-N(1)	1.9508(18)/1.9694(19)/1.9369(19)	1.9735(15)/1.9726(16)/1.8980(16)
Fe(2/3/4)–S(2)	2.2804(9)/2.2941(7)/2.2762(8)	2.2580(7)/2.3202(8)/2.3165(7)
Fe(1/3/4)–S(3)	2.2673(8)/2.2877(8)/2.3519(8)	2.2603(7)/2.3253(7)/2.3241(7)
Fe(1/2/4)–S(1)	2.3173(9)/2.3001(8)/2.2911(8)	2.305(7)/2.3206(7)/2.2342(7)
Fe(1/2/3/4)–S(4/5/6/7)	2.3009(8)/2.2910(8)/2.2982(8)/2.3136(7)	2.2740(7)/2.2724(7)/2.2866(8)/2.2781(8)
Fe(1)···Fe(2/3/4)	2.6684(7)/2.6187(6)/2.7868(7)	2.6791(8)/2.6372(7)/2.7575(7)
Fe(2)···Fe(3/4)	2.6421(6)/2.7233(7)	2.6111(6)/2.7495(8)
Fe(3)···Fe(4)	2.8085(8)	2.7652(6)
N(1)···S(1/2/3)	3.293(2)/3.287(2)/3.285(2)	3.320(2)/3.290(2)/3.270(2)
S(1)···(2/3)	3.631(1)/3.615(1)	3.579(1)/3.570(1)
S(2)···S(3)	3.579(1)	3.672(1)
S(1/2/3)-Fe(4)–S(2/3/1)	105.32(3)/ 101.27(3)/102.26(3)	103.67(3)/104.63(3)/103.07(3)
S(1)–Fe(1)–S(3)	104.09(3)	102.87(3)
N(1)-Fe(1)-S(1/3)	100.63(6)/102.03(6)	101.49(5)/100.92(5)
S(1)–Fe(2)–S(2)	104.88(2)	102.80(3)
N(1)-Fe(2)-S(1/2)	100.65(6)/101.07(6)	100.98(5)/101.89(5)
S(2)–Fe(3)–S(3)	102.71(3)	104.47(3)
N(1)-Fe(3)-S(2/3)	101.61(6)/101.75(6)	102.06(5)/101.00(5)
Fe(1/2/4)–S(1)–Fe(2/4/1)	70.61(3)/72.76(2)/74.42(2)	70.79(2)/74.24(3)/74.80(2)
Fe(2/3/4)–S(2)–Fe(3/4/2)	70.56(2)/73.40(2)/75.83(2)	69.53(2)/73.22(2)/73.88(2)
Fe(1/3/4)–S(3)–Fe(3/4/1)	70.18(2)/74.19(2)/74.49(2)	70.2(2)/72.99(2)/73.94(2)
Fe(1/2/3)–N(1)–Fe(2/3/1)	85.79(7)/85.12(7)/84.69(7)	85.52(6)/84.82(6)/85.85(6)
S(4)–Fe(1)–S(1/3)	114.38(3)/120.39(3)	115.64(3)/102.87(2)
S(4)–Fe(1)–N(1)	112.84(6)	121.25(5)
S(5)–Fe(2)–S(1/2)	116.45(3)/116.73(3)	104.44(3)/123.07(3)
S(5)–Fe(2)–N(1)	114.75(6)	120.26(5)
S(6)–Fe(3)–S(2/3)	114.34(3)/120.71(3)	114.49(2)/114.54(2)
S(6)–Fe(3)–N(1)	113.27(6)	118.3(5)
S(7)–Fe(4)–S(1/2/3)	123.33(3)/121.70(3)/97.95(3)	111.6(3)/115.94(2)/116.40(2)
S(7)–Fe(4)–S(1/2/3)	123.33(3)/121.70(3)/97.95(3)	111.6(3)/115.94(2)/116.40(2)

Selected mean distances and angles for $[Et_4N]_2$**20-DCBT** and $[Et_4N]_2$**20-*p*Tol** are tabulated in Tables 5.2 and 5.3 respectively. The bond angle metrics for both $[Et_4N]_2$**20-DCBT** and $[Et_4N]_2$**20-*p*Tol** display the largest deviations. Bond angles for the terminal ligands are more sensitive to changes in packing of the substituents in the solid state. Most metrics are indistinguishable between the two clusters with the Fe–$S_{thiolate}$ bond length being shorter by 0.23 Å for $[Et_4N]_2$**20-DCBT** compared to $[Et_4N]_2$**20-*p*Tol**. The metrics with the largest deviations are the bond angles which are known to be easily distorted. This can be attributed to the packing of the ligands.

Table 5.2. Selected averaged distances (Å) and angles (º) for $[Et_4N]_2$**20-DCBT**

	n^a	Mean of n^b	Range^c
Fe–N	4	1.952(16)	1.9508–1.9694
Fe–S	9	2.296(25)	2.2673–2.3519
Fe–$S_{thiolate}$	4	2.301(9)	2.2910–2.3136
Fe···Fe	6	2.71(8)	2.6187–2.7868
N···S	3	3.288(4)	3.285–2.293
S···S	3	3.61(3)	3.579–3.631
S–Fe–S	6	103(1)	101.27–105.32
N–Fe–S	6	101.3(6)	100.63–102.03
Fe–S–Fe	9	73(2)	70.18–75.83
Fe–N–Fe	3	85.2(6)	84.69–85.79
S–Fe–$S_{thiolate}$	9	116(8)	97.95–123.33
N–Fe–$S_{thiolate}$	3	114(1)	112.84–114.75

[a]Number of independent values corresponding to the metric type. [b]Arithmetic mean, with uncertainty representing the standard deviation from the mean. [c]Range of independent values.

Table 5.3. Selected average distances (Å) and angles (º) for $[Et_4N]_2$**20-*p*Tol**

	n^a	Mean of n^b	Range^c
Fe–N	4	1.948(43)	1.898–1.9735
Fe–S	9	2.296(35)	2.2342–2.3253
Fe–$S_{thiolate}$	4	2.278(6)	2.2724–2.2866
Fe···Fe	6	2.70(7)	2.6111–2.7652
N···S	3	3.29(3)	3.27–3.32
S···S	3	3.61(6)	3.57–3.672
S–Fe–S	6	104(1)	102.8–104.63
N–Fe–S	6	101.4(5)	100.92–102.06
Fe–S–Fe	9	72(2)	69.53–74.8
Fe–N–Fe	3	85.4(5)	84.82–85.85
S–Fe–$S_{thiolate}$	9	113(6)	102.87–123.07
N–Fe–$S_{thiolate}$	3	120(2)	118.3–121.25

[a]Number of independent values corresponding to the metric type. [b]Arithmetic mean, with uncertainty representing the standard deviation from the mean. [c]Range of independent values

5.2.5 Redox Properties

Tan collected the cyclic voltammograms of $[Et_4N]_2$**20-Ph** and $[Et_4N]_2$**20-Mes** in MeCN (Figure 5.10). Both compounds exhibit electrochemically reversible reduction and oxidation processes at –1.32 and –1.50 V vs. SCE and –0.14 and –0.34 V vs. SCE, respectively, as verified by $i_{pa}/i_{pc} = 1$ for $\upsilon = 10$ to 1000 mV/s and $E_{1/2}$ and ΔEp largely independent of υ. Compared to the chloride-ligated complex **19**, which displays a quasi-

reversible reduction potential at –1.16 V vs. SCE, $[Et_4N]_2$**20-Ph** and $[Et_4N]_2$**20-Mes** show more negative reduction potentials, shifted by –0.16 and –0.34 V, respectively. Similar trends have been observed in the Fe_4S_4 core, where terminal thiolate ligands with $^-$SPh and $^-$SMes shifts the reduction potential by –0.18 V and –0.38 V, respectively, relative to **19**.

The reduction potentials of **20-Ph** and **20-Mes** are ~300 mV more negative than those of $[Fe_4S_4(SPh)_4]^{2-}$ and $[Fe_4S_4(SMes)_4]^{2-}$, which is attributed to stronger electron donating character of the *tert*-butylimide ligand. Comparing the electrochemical behaviour of $[Et_4N]_2$**20-Ph** and $[Et_4N]_2$**20-Mes**, the latter displays both more negative reduction and oxidation potentials, consistent with the more electron-donating nature of the $^-$SMes ligand relative to $^-$SPh.

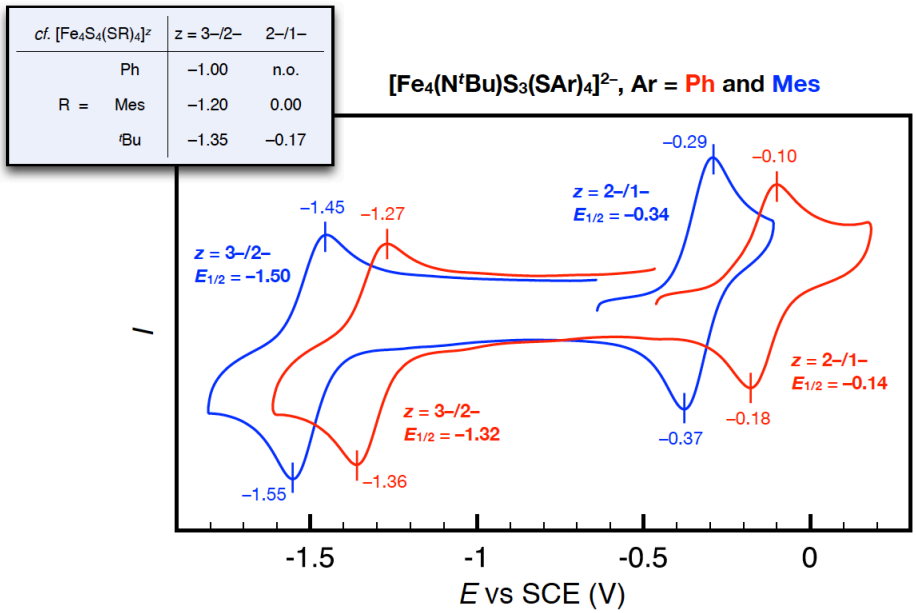

Figure 5.10. Cyclic voltammograms (0.1 M (n-Bu_4N)ClO_4 supporting electrolyte in MeCN, 100 mV/s scan rate) of $[Et_4N]_2$**20-Ph** and $[Et_4N]_2$**20-Mes**.

The cyclic voltammograms of $[Et_4N]_2$**20-CBT**, $[Et_4N]_2$**20-*p*Tol** and $[Et_4N]_2$**20-DCBT** are shown in Figures 5.11, 5.12 and 5.13. Compounds $[Et_4N]_2$**20-CBT** and $[Et_4N]_2$**20-*p*Tol** exhibit electrochemically reversible reduction and oxidation potentials, as verified by i_{pa}/i_{pc} = 1 for υ = 10 to 1000 mV/s and $E_{1/2}$ and ΔEp largely independent of υ. The z = 2–/3– reduction potential for $[Et_4N]_2$**20-CBT** and $[Et_4N]_2$**20-*p*Tol** are –1.24 V and –1.36 V vs. SCE

respectively. The observed shift in reduction potential is attributed to the electronic nature of the thiolate ligand: more electron-donating ligands generally shift the redox potential to more negative values. In contrast, the cyclic voltammogram of $[Et_4N]_2$**20-DCBT** displays an irreversible reductive transformation, with a reduction potential of –1.33 V vs. SCE– comparable to that of **20-Ph**. Due to the irreversibility, an accurate $E_{1/2}$ value cannot be determined. It was hypothesized that the additional electron withdrawing groups on the aromatic ring would render it less donating, thereby shifting the reduction potential to more positive values. However, this trend was not observed experimentally with **20-DCBT**, and the underlying rationale remains unclear. Electrochemical data of select compounds and redox agents are tabulated in Table 5.4

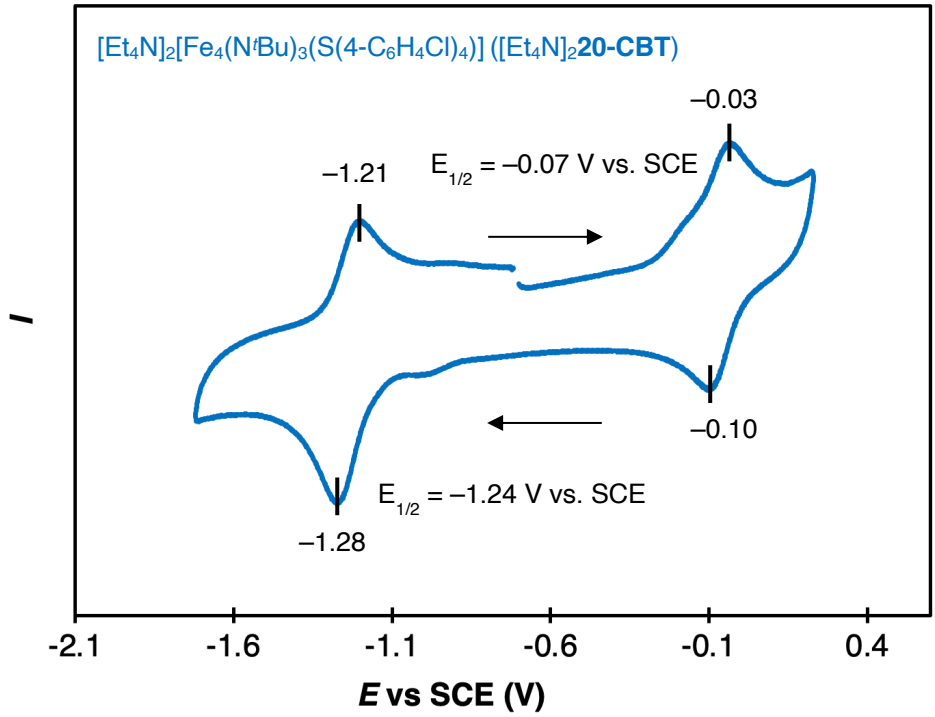

Figure 5.11. Cyclic voltammogram (0.1 M (n-Bu_4N)ClO_4 supporting electrolyte in MeCN, 100 mV/s scan rate) of $[Et_4N]_2$**20-CBT**.

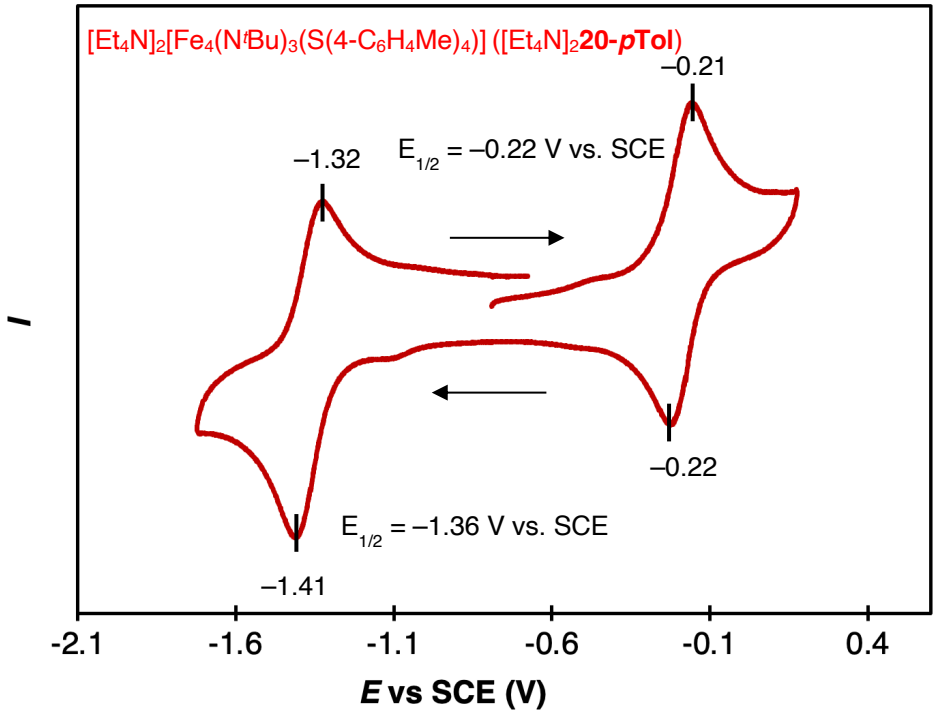

Figure 5.12. Cyclic voltammogram (0.1 M (n-Bu_4N)ClO_4 supporting electrolyte in MeCN, 100 mV/s scan rate) of $[Et_4N]_2$**20-*p*Tol**.

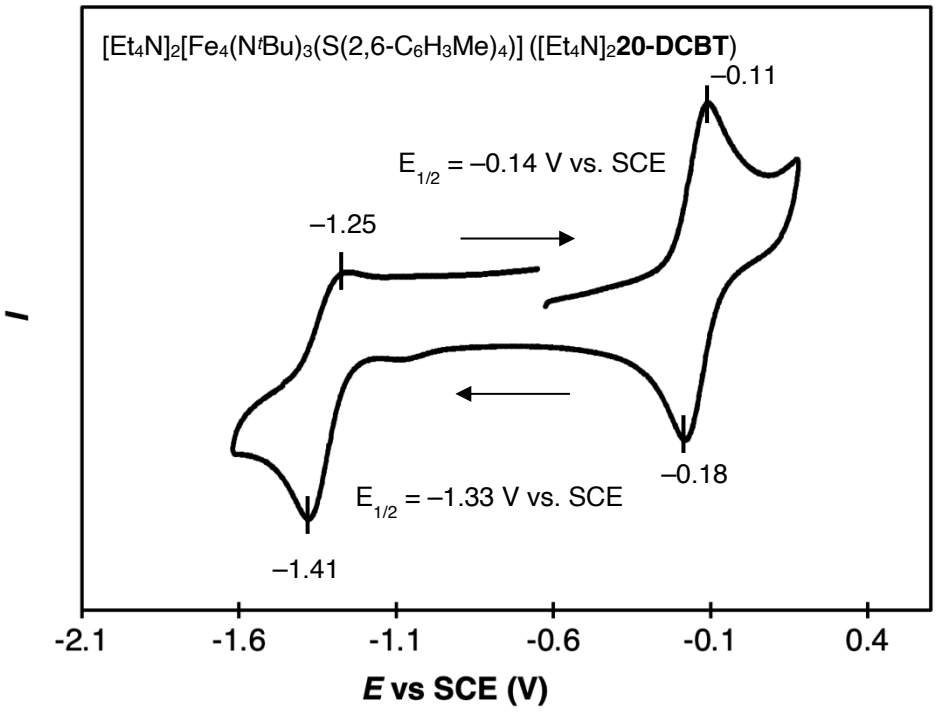

Figure 5.13. Cyclic voltammogram (0.1 M (n-Bu_4N)ClO_4 supporting electrolyte in MeCN, 100 mV/s scan rate) of $[Et_4N]_2$**20-DCBT**.

Table 5.4. Electrochemical data for select $[Fe_4S_4]$ clusters, $[Fe_4(N^tBu)S_3]$ clusters and redox agents (vs. SCE). Solvent is MeCN unless otherwise noted.

Compound	z = 2–/3–	z = 1–/2–
$[Fe_4S_4Cl_4]^{2-}$ [b]	–0.82*	n.o.
$[Et_4N]_2[Fe_4(N^tBu)S_3Cl_4]$ ($[Et_4N]_2$**19**)[c]	–1.16*	n.o.
$[Fe_4S_4(SBn)_4]^{2-}$ [a,d]	–1.25	n.o
$[Fe_4S_4(SPh)_4]^{2-}$ [e]	–1.00	n.o.
$[Fe_4S_4(SPh)_4]^{2-}$ [a,d,f]	–1.04	n.o.
$[Ph_4P]_2[Fe_4(N^tBu)S_3(SPh)_4]$ ($[Ph_4P]_2$**20-Ph**)	–1.33	–0.14
$[Et_4N]_2[Fe_4(N^tBu)S_3(SPh)_4]$ ($[Et_4N]_2$**20-Ph**)[h]	–1.32	–0.14
$[Fe_4S_4(SMes)_4]^{2-}$ [,g]	–1.20	0.00
$[Et_4N]_2[Fe_4(N^tBu)S_3(SMes)_4]$ ($[Et_4N]_2$**20-Mes**)[h]	–1.50	–0.32
$[Et_4N]_2[Fe_4(N^tBu)S_3(S(2,6\text{-}C_6H_3Cl_2))_4]$ ($[Et_4N]_2$**20-DCBT**)	–1.33**	–0.14
$[Fe_4S_4(S(4\text{-}C_6H_4Cl))_4]^{2-}$ [a,f]	–0.95	n.o
$[Et_4N]_2[Fe_4(N^tBu)S_3(S(4\text{-}C_6H_4Cl))_4]$ ($[Et_4N]_2$**20-CBT**)	–1.24	–0.07
$[Fe_4S_4(S(4\text{-}C_6H_4Me))_4]^{2-}$ [a,f]	–1.09	n.o
$[Et_4N]_2[Fe_4(N^tBu)S_3(S(4\text{-}C_6H_4Me))_4]$ ($[Et_4N]_2$**20-*p*Tol**)	–1.36	–0.22
$[Et_4N]_3[Fe_4(N^tBu)S_3(S(4\text{-}C_6H_4Me))_4]$ ($[Et_4N]_3$**32**)	–1.36	–0.20
	Redox Potential[i]	
Cp^*_2Co	–1.54	
Fc^+	0.40	
[Acenaphthylenide]$^{-}$ [j]	–1.89	

* represents a quasi-reversible redox transformation.** represents an irreversible potential [a]electrochemistry solvent was DMF.[b]Reference [170], [c]Reference [26], [d]Reference [172], [e]Reference [173] , [f]Reference [174] , [g]Reference [175], [h]data collected by Lay Ling Tan, [i] Reference[176], [j]electrochemistry solvent was THF.

5.2.6 Synthesis of Oxidized Clusters

The common redox couples observed with $[Fe_4S_4(SCys)]^z$ cofactors are the z =1–/2– and the z = 2–/3– redox couples. There have been many reports of isolated, well studied, $[Fe_4S_4(SR)_4]^{3-}$ clusters but not $[Fe_4S_4(SR)_4]^{1-}$ clusters.[177] The first report of an isolable, oxidized $[Fe_4S_4(SAr)_4]^{1-}$ cluster was reported by Millar and coworkers.[43,178] Millar and coworkers utilized both 2,4,6- triisopropylbenzene thiolate ($^-$STipp) and mesitylbenzene thiolate as terminal ligands onto the Fe_4S_4 cluster core. The isolated materials displayed electrochemical reversibility in the z = 1–/2– redox couple and oxidation of $[Fe_4S_4(STipp)_4]^{2-}$ with ferrocenium tetrafluoroborate ($Fc(BF_4)$) led to the formation of $[Fe_4S_4(STipp)_4]^{1-}$. The

compound of $[Fe_4S_4(STipp)_4]^{1-}$ was determined to be more stable compared to $[Fe_4S_4(SMes)_4]^{1-}$, and these oxidized clusters are more stable in these solvents in the order of DMF<<MeCN<DCM with no stability found in methanol.

The synthesis of oxidized Fe_4S_4 clusters was also reported by the laboratory of Lee[49] and the laboratory of Tatsumi[179]. The oxidized Fe_4S_4 cluster reported by the Lee group, $[Fe_4S_4(N(SiMe_3)_2)_4]^{1-}$, had terminal ligation with $^-N(SiMe_3)_2$ which likely protected and stabilized the oxidized cluster core. Tatsumi and coworkers leveraged this compound by reacting $[Fe_4S_4(N(SiMe_3)_2)_4]^{1-}$, with various thiols to form the terminal thiolate ligated cluster $[Fe_4S_4(SAr)_4]^{1-}$. Tatsumi and coworkers further investigated the stability of the thiolate ligated oxidized clusters and determined that the instability of the clusters in stronger donating solvents is likely due to the coordination of the solvent to the electrophilic iron centers, leading to degradation of the cluster and the release of free thiolate.

The synthesis of oxidized clusters with the $Fe_4N(^tBu)S_3$ core was initially undertaken and performed by Lay Ling Tan. She determined that while $[Et_4N]_2$**20-Ph** displayed electrochemically reversible oxidation potentials, the oxidation of **20** with ferrocenium in CD_3CN led to a signal set that can be interpreted to the oxidized $z = 1-$ species but the species decomposed rapidly in CD_3CN to form numerous weak signals that cannot be assigned to the $z = 1-$ cluster. Compound $[Et_4N]_2$**20-Mes** also displayed electrochemically reversible oxidation potentials and the oxidation of $[Et_4N]_2$**20-Mes** with $Fc(BF_4)$ in DCM led to the formation and isolation of $[Et_4N]_2$**21** (Scheme 5.4).

Scheme 5.4. Oxidation of $[Et_4N]_2$**20-Mes** with $Fc(PF_6)$

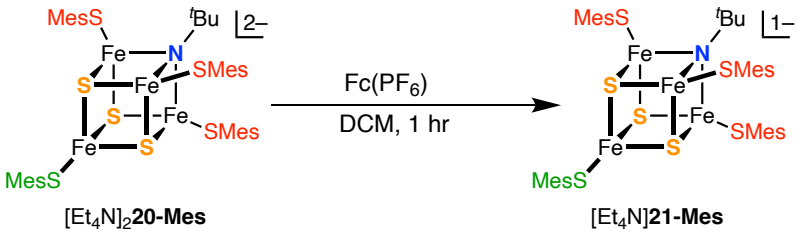

$[Et_4N]_2$**20-Mes** $[Et_4N]$**21-Mes**

$[Et_4N]_2$**20-Mes** unlike $[Et_4N]_2$**20-Ph**, displays solubility in DCM. DCM is a beneficial solvent as DCM is weakly coordinating and relatively non-nucleophilic, meaning solvent attack on the oxidized cluster core is unlikely, increasing the solution stability of $[Et_4N]$**21-**

Mes. The difference in stability of $[Fe_4(N^tBu)S_3(SPh)_4]^{1-}$ and $[Et_4N]$**21-Mes** can be attributed to two properties:

(i) The steric demand of the methyl groups on $^-$SMes better shield the cluster core from solvent induced nucleophilic attack compared to the protons on $^-$SPh.

(ii) The increased electron donating ability of $^-$SMes enhances stabilization of the oxidized cluster core relative to $^-$SPh ($E_{1/2}$ for z =2–/3– redox couple = –1.50 V vs. SCE for **20-Mes** and –1.32 V vs. SCE for **20-Ph**).

The ^{1}H NMR spectrum of the oxidized state $[Et_4N]$**21-Mes** is shown in Figure 5.14. Based on the number of resonances, chemical shift positions and resonance integrations, the spectrum is consistent with $[Et_4N]$**21-Mes**. The resonances are more isotropically shifted compared to $[Et_4N]_2$**20-Mes**, which is consistent with its non-zero ground spin state.

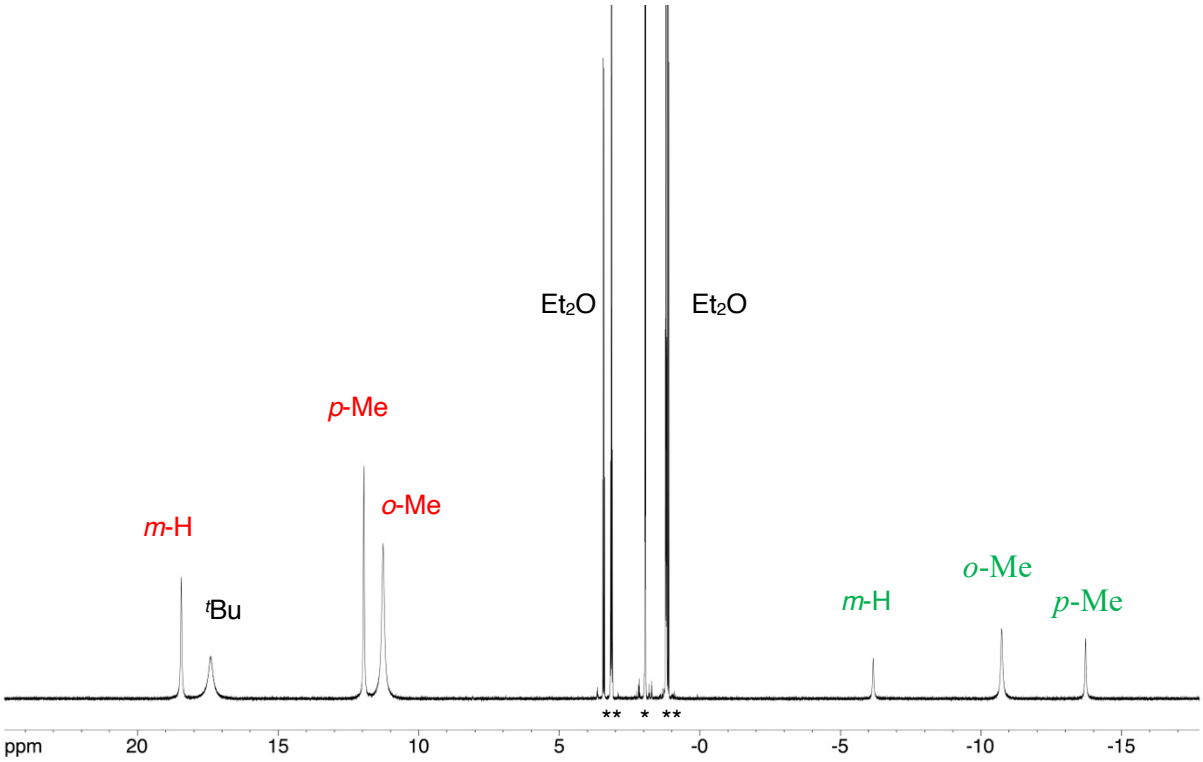

Figure 5.14. ^{1}H NMR spectra (298 K, 300 MHz) of $[Et_4N]$**21-Mes** in CD_3CN. Residual protio signal indicated by *. Counterion resonances indicated by **. Resonances corresponding to ligand environments bound to the three equivalent Fe sites are indicated in red; those corresponding to the unique Fe site are indicated in green.

Crystallization of [Et_4N]**21-Mes** can be challenging, as the purification system tends to lead to oiling of the material from solution. Slow addition of ether to a concentrated solution of [Et_4N]**21-Mes** in THF facilitated crystal formation. If crystalline material does not form on the first attempt, removing the solvent under reduced pressure and resetting the recrystallization process–potentially with scratching the glass–can lead to crystal growth.

5.2.7 Synthesis and Stability Studies of $[Fe_4S(N^tBu)(SPh)_4]^{3-}$

The M-cluster of nitrogenase is proposed to undergo reduction under turnover conditions, during which substrates bind to the metal centers. The $[Fe_4N(^tBu)S_3L_4]^{2-}$ cluster serves as a synthetic analogue of the $[Fe_4S_3C]$ core of the M-cluster; thus, the isolation and characterization of reduced $[Fe_4N(^tBu)S_3L_4]^{3-}$ species may provide valuable insight into the iron environments of FeMoco under turnover conditions. The approach for obtaining isolable reduced material can be adapted from established protocols in Fe_4S_4 chemistry. Reduced Fe_4S_4 clusters are synthesized through two main pathways, as shown in Scheme 5.5: (i) self-assembly starting from ferrous chloride[45] and, (ii) reduction of the z = 2– cluster to form the z = 3– cluster[180]. Generally, $[Fe_4S_4(SAr)_4]^z$ clusters exhibit a z = 2–/3– reduction potential around –1.00 V vs. SCE and are formed by the reduction pathway (ii). $[Fe_4S_4(SR)_4]^z$ (where R = alkyl) clusters exhibit a z = 2–/3– reduction potential around –1.30 V vs. SCE and are formed by the self-assembly pathway (i) as pathway (ii) did not lead to isolable complexes.

The reduction potential of **20-Ph** (–1.32 V vs. SCE in MeCN) falls within the same range as that of $[Fe_4S_4(SR)_4]^z$ clusters suggesting that direct reduction of **20-Ph** to isolate the reduced cluster may be challenging. However, the synthesis of reduced $Fe_4(N^tBu)S_3$ clusters cannot proceed via pathway (i), as the formation of mixed imide-sulfide clusters requires controlled synthetic conditions rather than self-assembly. This leaves pathway (ii) as the only route to isolate reduced Fe_4NS_3 clusters.

Scheme 5.5. Synthetic methods to synthesize $[Fe_4S_4(SPh)_4]^{3-}$

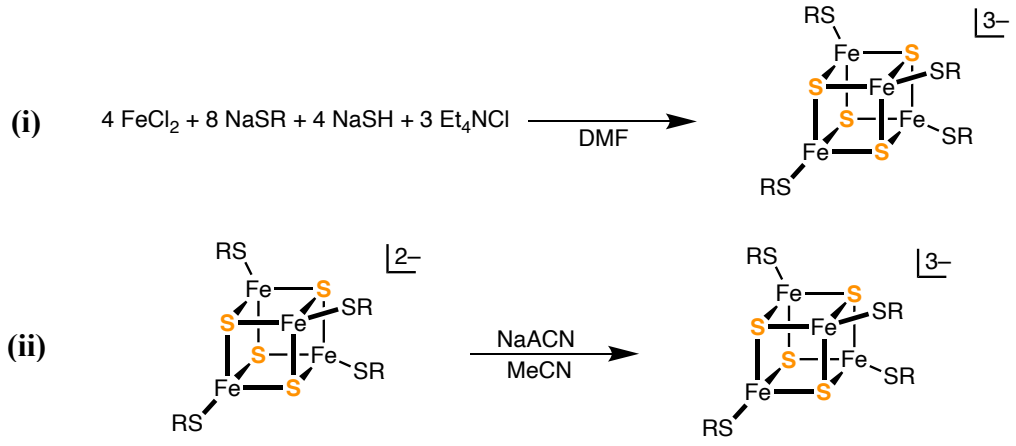

Tan reduced $[Et_4N]_2$**20-Ph** in MeCN using NaACN (prepared in THF) as illustrated in Scheme 5.6. After solvent removal *in vacuo* and redissolution in CD_3CN, analysis by ^1H NMR spectroscopy revealed numerous weak signals that could not be assigned to **22-Ph** or to reduced clusters. The presence of 0.5 molecules of thiolate per reduced cubane cluster was also present in the ^1H NMR spectrum. The detection of free thiolate was unexpected as it can be assumed that decomposition products would likely scavenge free thiolate. This outcome of thiolate loss was not reported in the study of $z = 3-$ Fe_4S_4 clusters. Interestingly, Tan observed the reappearance of the starting cluster upon oxidation of the reduced solution with $Fc(PF_6)$. This suggested that the cluster core remained intact during decomposition, as complete degradation would likely prevent cluster reassembly upon oxidation. Reduction with NaACN has previously been successful in synthesizing the reduced homoleptic core $[Fe_4S_4(SPh)_4]^{3-}$ (**24-Ph**) from reduction of the normal state cluster $[Fe_4S_4(SPh)_4]^{2-}$ (**23-Ph**) in MeCN. However, the differing outcome for **20-Ph** may be attributed to its more negative reduction potential compared to **23-Ph** leading to the instability of the reduced cluster or that NaACN is a strong reductant that is leading to over-reduction of the cluster to more reduced redox states.

Scheme 5.6. Previous reduction and oxidation work by Tan

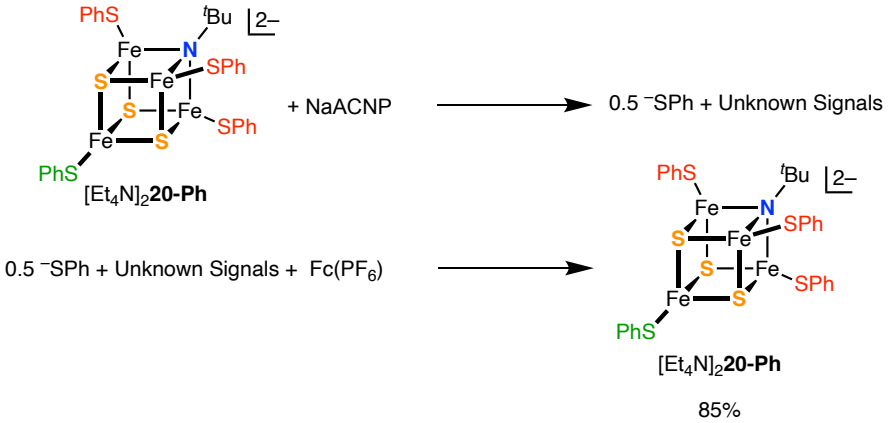

To test the second possibility, milder reducing agents that can be easily administrated were considered. Cp^*_2Co was chosen as the reductant which has a redox potential of –1.51 V vs. SCE in MeCN. [176] This reagent has been successfully employed in the reduction of $[Ph_4P]$**2** to $[Ph_4P]_2$**6** (Chapter 2) and may be suitable for the reduction of **20-Ph**. However, a limitation of Cp^*_2Co is that the reducing potential may not be sufficiently negative to fully reduce **20-Ph** as reducing with Cp^*_2Co will lead to a **22-Ph**:**20-Ph** ratio of 40:1.[5]

A reduction titration experiment was performed by undergraduate researcher Dion Grobe. The addition of sub-stoichiometric to excess equivalents of Cp^*_2Co dissolved in C_6D_6 was added to a solution of **20-Ph** in CD_3CN. Increasing the amount of reductant to **20-Ph** led to the signal set progressively shifting more isotropically, indicative of a change in the redox state of the cluster. Around 1.2 equivalents of reductant, the signals stopped moving, meaning the redox reaction was completed. The z =3– cluster was formed and can be assigned based on the number of signals for a C_{3v} symmetric cluster, the signal range and signal integration. Only one signal set was observed in these titration experiments sub-stoichiometrically, showing that the signal is a weighted average of both the z = 2– and 3– clusters and that the redox equilibrium is fast on the timescale of the NMR experiment.

The reduction of $[Ph_4P]_2$**20-Ph** with 1.05 equivalents of Cp^*_2Co in CD_3CN (Figure 5.15) yielded a signal set assignable to $[Ph_4P]_2[Cp^*_2Co]$**22-Ph** with a conversion yield between 70 to 80 % determined by ^1H qNMR analysis.

[5] $\log\{[A^+]/[A]\} = 8.47\ \Delta E°'$

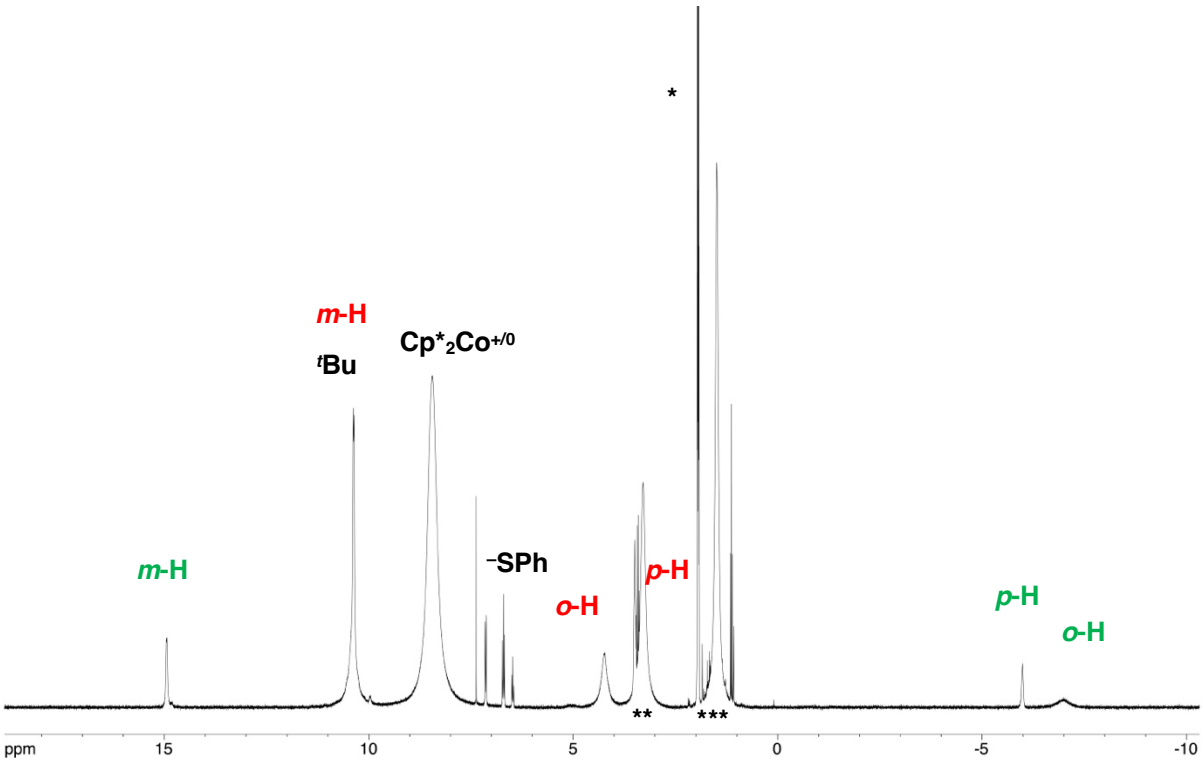

Figure 5.15. ^{1}H NMR spectrum (298 K, 300 MHz) of $[Et_4N]_2$**20-Ph** with 1.2 equivalents of Cp_2*Co in CD_3CN. Residual protio signal indicated by *. Counterion resonances indicated by **. Resonances corresponding to ligand environments bound to the three equivalent Fe sites are indicated in red; those corresponding to the unique Fe site are indicated in green.

Scheme 5.7. Reduction of $[Et_4N]_2$**20-Ph** in CD_3CN with 1 equivalent of Cp^*_2Co and subsequent oxidation with $Fc(PF_6)$

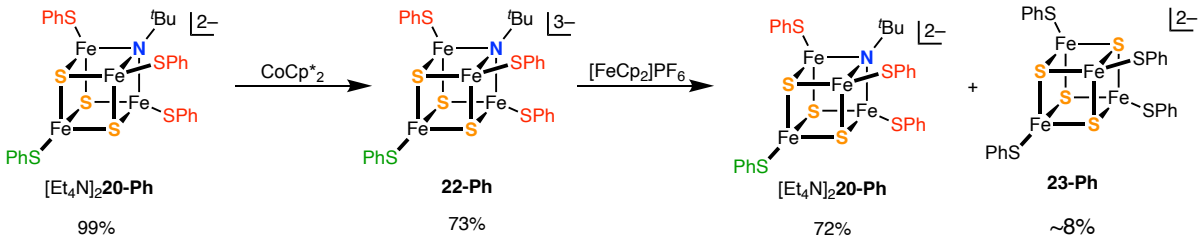

The stoichiometric reduction of **20-Ph** has been performed on the NMR scale using two different methods: (i) the addition of a solution of **20-Ph** in CD_3CN to solid Cp^*_2Co, or (ii) the addition of a solution of Cp^*_2Co in C_6D_6 to a solution of **20-Ph** in CD_3CN. These reactions yield the z = 3– cluster (**22-Ph**) along with free thiolate, analyzed by ^{1}H NMR assay (Figure 5.16). The values listed under the compound numbers of Scheme 5.7 display the

absolute yield of each component determined by ^{1}H NMR analysis. The *in-situ* yield after reduction is between 70-80% with the presence of 0.5 to 1 molecule of free thiolate per observed cluster. The free thiolate present corresponds to 25 – 50% of the total thiolate available after the decomposition of **20-Ph**. The free thiolate observed in the reduced spectrum likely originates from the decomposition of the 20-30% of **20-Ph.** Oxidation of the reduced solution after 15 minutes using 1 equivalent of $Fc(PF_6)$ produced **20-Ph** in a 72% yield based on starting cluster amount, along with $[Fe_4S_4(SPh)_4]^{2-}$ (**23-Ph**) in approximately 8% yield. The formation of **23-Ph** was unexpected, as the reduced cluster $[Fe_4S_4(SPh)_4]^{3-}$ (**24-Ph**) was not detected in the spectra and the only species detected in the ^{1}H NMR spectrum were **23-Ph**, excess Cp^*_2Co and $^-$SPh. This suggests that **23-Ph** is not formed via the oxidation of **24-Ph**, but rather through a secondary pathway, likely involving the oxidation of ^{1}H NMR silent species leading to the generation of **23-Ph**. The underlying cause of partial cluster decomposition upon reduction remains unclear.

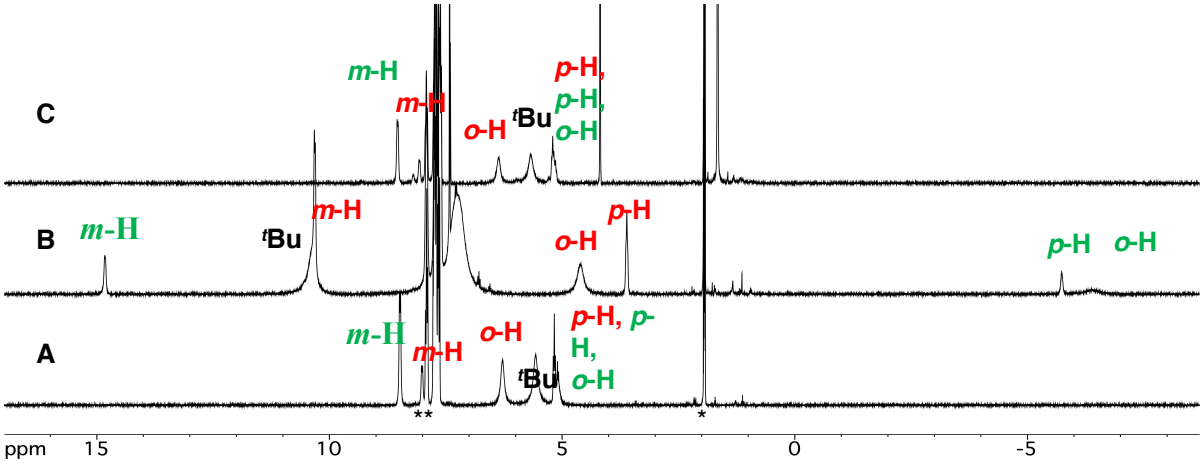

Figure 5.16. (A) ^{1}H NMR (298 K, 300 MHz) spectrum of $[Ph_4P]_2$**20-Ph**. (B) ^{1}H NMR (298 K, 300 MHz) spectrum of $[Ph_4P]_2$**20-Ph** and 1.1 equivalents of Cp^*_2Co. (C) ^{1}H NMR (298 K, 300 MHz) spectrum of the oxidation of (B) with $Fc(PF_6)$. Residual protio signal indicated by *. Counterion resonances indicated by **. Resonances corresponding to ligand environments bound to the three equivalent Fe sites are indicated in red; those corresponding to the unique Fe site are indicated in green.

The *in-situ* generated **22-Ph** appears to be unstable in CD_3CN as storage of the reduced solution in a sealed tube inside the glovebox overnight led to the signal set attributed to **22-Ph** shifting towards the signal positions of the z = 2– species as shown in Figure 5.17.

This observation likely indicates partial oxidation of z = 3– to 2– with the appearance of only a single signal set resulting from a redox equilibrium between the z = 3–/2– clusters, also observed in the reduction titration experiments. When this signal set is used as a reference, only ~30% of **20-Ph**/**22-Ph** can be accounted for while the ^{1}H NMR spectrum contains numerous new weak signals. Scheme 5.8 illustrates the reactions carried out in this experiment with absolute purity (initial **20-Ph**) or conversion yields (**22-Ph**) noted. Reduction and oxidation were performed by the addition of a Cp^*_2Co solution in C_6D_6 and $Fc(PF_6)$ solution in CD_3CN. These reduction/oxidation experiments were repeated in triplicate to confirm the findings.

Not only does the concentration of **22-Ph** decrease over time, but the amount of free thiolate increases over time as well. Initially, 1 equivalent of free thiolate is present per equivalent of **22-Ph** at the first reduction time point. After 16 h, the concentration of free thiolate increases by the same molar amount as the decrease in **22-Ph** concentration. This observation suggests that the increase in free thiolate over time arises from the lability of the$^-$ SPh ligand.

Scheme 5.8. (**A**) Reduction of $[Et_4N]_2$**20-Ph** in CD_3CN with 1 equivalent of Cp^*_2Co. (**B**) Oxidation of reduced solution with 1 equivalent of $Fc(PF_6)$.

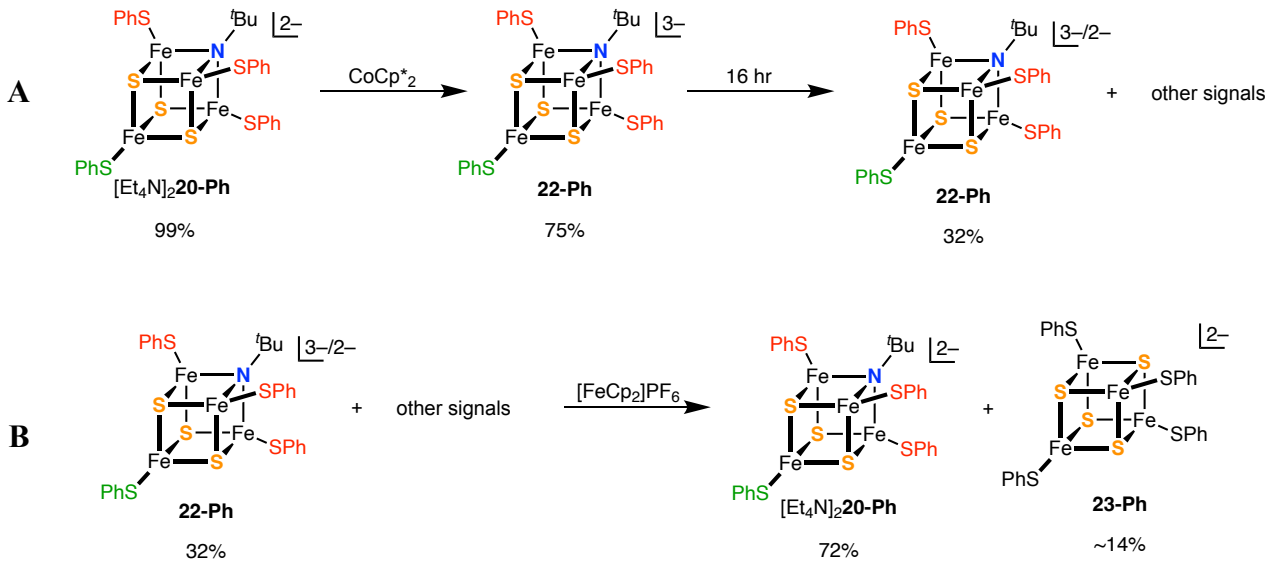

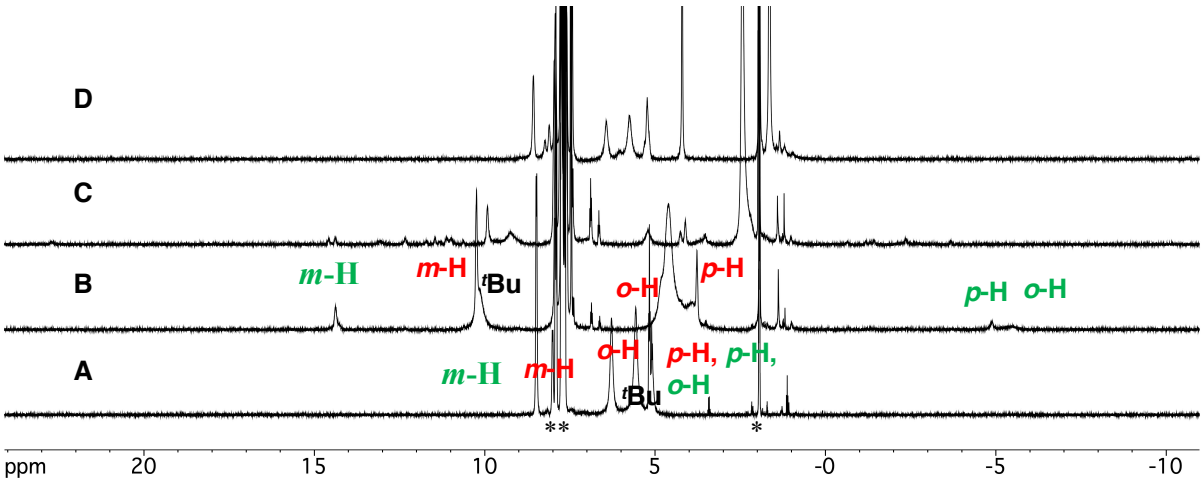

Figure 5.17. (**A**)^{1}H NMR spectrum (298 K, 300 MHz) of $[Ph_4P]_2$**20-Ph** (**B**) ^{1}H NMR (298 K, 300 MHz) spectra of $[Ph_4P]_2$**20-Ph** and 1.1 equivalents of Cp^*_2Co producing $[Ph_4P][Cp^*_2Co]_2$**22-Ph**. (**C**) ^{1}H NMR spectrum of B after 16 h. (**D**) ^{1}H NMR spectrum after oxidation with 1.1 equivalents of $Fc(PF_6)$. Residual protio signal indicated by *. Counterion resonances indicated by **. Resonances corresponding to ligand environments bound to the three equivalent Fe sites are indicated in red; those corresponding to the unique Fe site are indicated in green.

Reoxidation of the reduced solution after 16 hours with one equivalent of $Fc(PF_6)$ recovered approximately stoichiometric amounts of the reduced cluster with no free thiolate. This result is interesting as only 32% of the cluster can be accounted for immediately before reoxidation. If the decomposition of **23-Ph** led to the destruction of the $Fe_4N(^tBu)S_3$ cluster core and was irreversible, reoxidation would not be expected to recover **20-Ph.** This highlights an intriguing possibility, that the recovery of **20-Ph** upon reoxidation suggests that the decomposition species retains the $[Fe_4N(^tBu)S_3]$ cluster core. This highlights that the presence of **23-Ph** after oxidation is not related to the decomposition product of the reduced **22-Ph** but likely due to the initial reduction.

Excess reductant was utilized in the formation of **22-Ph** to ensure complete reduction of **20-Ph** to **22-Ph**. The equivalents of Cp^*_2Co were altered as it was possible that using excess equivalents of reductant was facilitating the decomposition of **22-Ph**. 0.9 equivalents and 3 equivalents of Cp^*_2Co were used which did not alter the decomposition rate of **20-Ph**, the amount of free thiolate, and the numerous signals correlated to the decomposition products.

The presence of free thiolate in the reduced cluster stability study may provide insight into the mechanism of cluster decomposition. $^{-}$SPh is classified as a π-donating, anionic ligand. Since free thiolate is present upon cluster reduction, it can be presumed that the charged donating ligand becomes more labile which is inducing the formation of the decomposition product. σ-donating or π-accepting neutral ligands may lead to the stabilization of the reduced cluster core. The ligands chosen were bipy, $P(Cy)_3$, CN(2,6-Xy) and these were added to the reduced cluster solution and monitored using ^{1}H NMR spectroscopy over 24 hours. The ^{1}H NMR spectrum of these experiments displayed the same signal sets for the decomposition product of **22-Ph** and the same rate of decomposition, indicating the addition of a trapping ligand was unsuccessful in stabilizing the reduced core. The addition of excess $^{-}$SPh was performed to slow down the rate of decomposition but was unsuccessful.

$[Et_4N]_2[Cp^*_2Co]$**22-Ph** can be isolated as a powder upon solvent removal under reduced pressure. The powder of $[Et_4N]_2[Cp^*_2Co]$**22-Ph** is stable in the solid state when stored at –15 °C for at least three days. Multiple attempts were made to crystallize $[Et_4N]_2[Cp^*_2Co]$**22-Ph** and $[Et_4N]_3$**22-Ph** through two-solvent recrystallization using MeCN/Et_2O and vapour diffusion of MeCN/Et_2O which was unsuccessful. Further analysis has not been conducted on $[Et_4N]_2[Cp^*_2Co]$**22-Ph** because pure, crystalline material could not be obtained.

5.2.8 Synthesis and Stability Studies of $[Fe_4S_4(SR)_4]^{1+}$ Clusters

The instability of **22-Ph** in CD_3CN prompted an investigation into whether $[Et_4N]_2$**24-Ph** exhibits similar instability. Given the structural relationship between $[Et_4N]_2$**20-Ph** and $[Et_4N]_2$**22-Ph**, studying the stability of $[Et_4N]_3$**24-Ph** is particularly significant, as the primary distinction between the two clusters lies in the presence of the *tert*-butylimide ligand. The reduction of $[Et_4N]_2$**23-Ph** with Cp^*_2Co was performed using the same reaction protocol used in the reduction of **20-Ph** with Cp^*_2Co, shown in Scheme 5.9. $[Et_4N]_2$**23-Ph** contains a z = 2–/3– reduction potential at –1.00 V vs. SCE which is ~300 mV more positive compared to **23-Ph.** The starting purity of **23-Ph** was 94% but the material is

presumed to be analytically pure with the deviation being explained by gravimetric error in the qNMR protocol.

Scheme 5.9. Reduction of $[Et_4N]_2$**23-Ph** in CD_3CN with 1 equivalent of Cp^*_2Co and subsequent oxidation with $Fe(PF_6)$

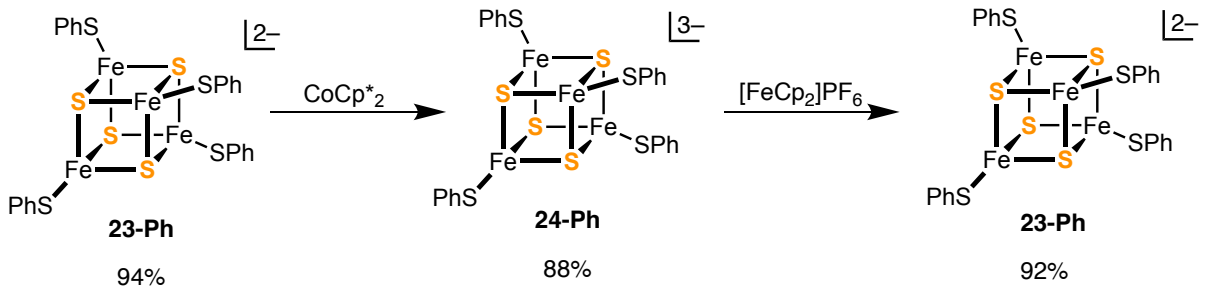

The resulting reduction and subsequent oxidation of $[Et_4N]_2$**23-Ph** is shown in Figure 5.18. The initial reduction of **23-Ph** to form **24-Ph** leads to a drop in the absolute concentration from 94% to 88%. Oxidation of the reduced cluster within 30 minutes leads to formation of **23-Ph** in a 92% absolute yield with the presence of small amounts of $^-$SPh.

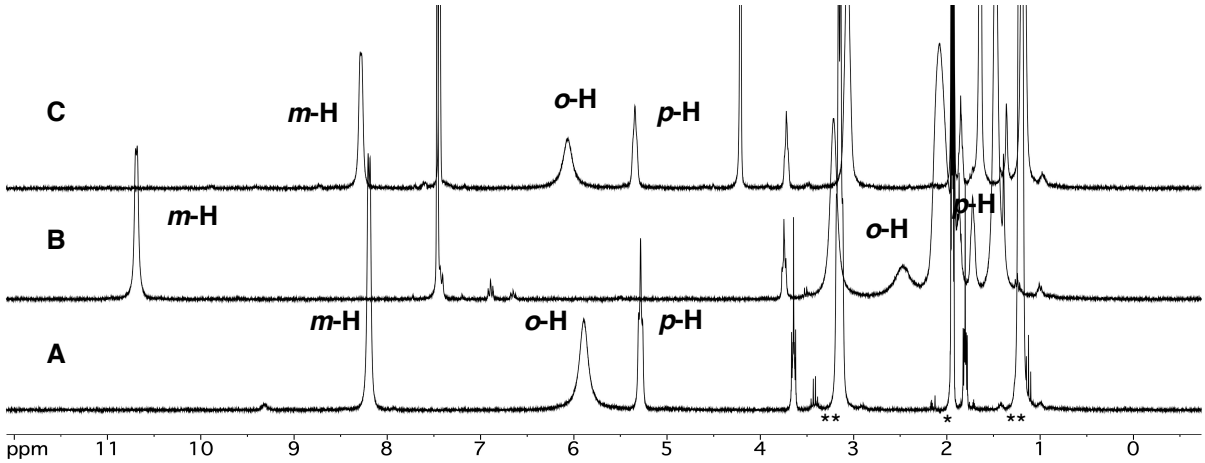

Figure 5.18. (**A**) ^{1}H NMR spectrum (298 K, 300 MHz) of $[Et_4N]_2$**23-Ph**. (**B**) ^{1}H NMR spectrum (298 K, 300 MHz) of $[Et_4N][Cp^*_2Co]$**24-Ph** generated from reduction of $[Et_4N]_2$**23-Ph** with Cp^*_2Co. (**C**) ^{1}H NMR spectrum (298 K, 300 MHz) of $[Et_4N]_2$**23-Ph** generated from oxidation of B with $Fe(PF_6)$. Residual protio signal indicated by *. Counterion resonances indicated by **.

The stability of **24-Ph** was tested by allowing the *in-situ* generated **24-Ph** to sit in the NMR tube overnight as shown in Figure 5.19 and highlighted in Scheme 5.10. The concentration of **24-Ph** was observed to decrease from 85% to 78%. This decrease is not as significant as observed in the stability studies of **22-Ph**. No other signals are observed in the ^{1}H NMR spectra of the reduced cluster after 16 hours. The absolute yield after oxidation is higher than the starting purity of **23-Ph** which is attributed to error in the qNMR measurements. From these results, it can be concluded that **24-Ph** is relatively stable in CD_3CN unlike **22-Ph**.

Scheme 5.10. (**A**) Reduction of $[Et_4N]_2$**23-Ph** in CD_3CN with 1 equivalent of Cp^*_2Co in C_6D_6. (**B**) Oxidation of (A) with 1 equivalent of $Fc(PF_6)$ in CD_3CN

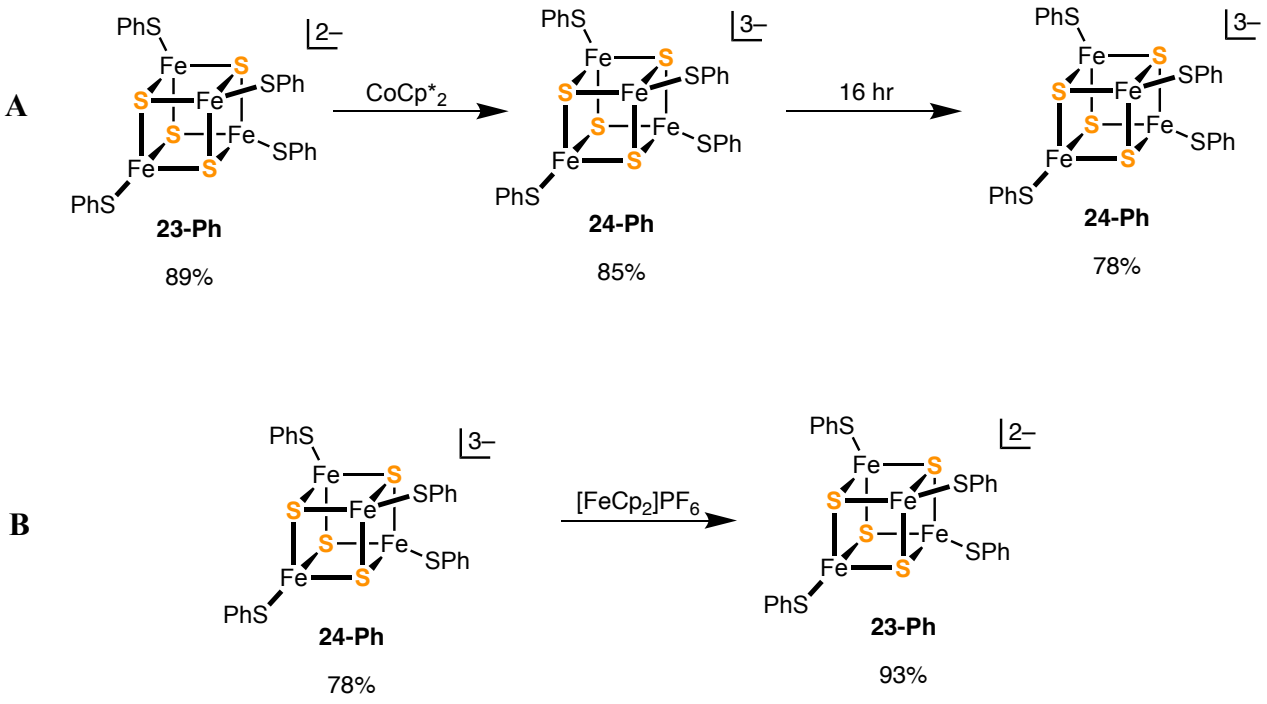

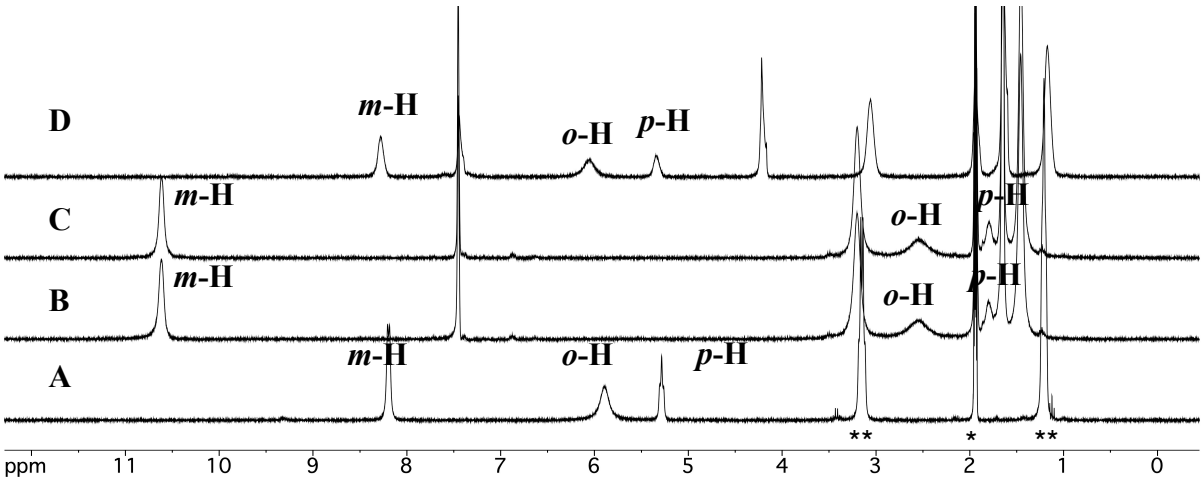

Figure 5.19. (**A**) ^{1}H NMR spectrum (298 K, 300 MHz) of $[Et_4N]_2$**23-Ph**. (**B**) ^{1}H NMR spectrum (298 K, 300 MHz) of $[Et_4N][Cp^*_2Co]$**25** generated from reduction of $[Et_4N]_2$**23-Ph** with Cp^*_2Co. (**C**) ^{1}H NMR spectrum (298 K, 300 MHz) of C after 16 hours. (**D**) ^{1}H NMR spectrum (298 K, 300 MHz) of $[Et_4N]_2$**23-Ph** generated from oxidation of C with $Fc(PF_6)$. Residual protio signal indicated by *. Counterion resonances indicated by **.

As discussed previously, the synthesis of iron-sulfur clusters with thiolate ligation and z = 2–/3– reduction potential greater than –1.30 V vs. SCE requires self-assembly protocols rather than reduction of the normal state (z = 2–) cluster in MeCN. The instability of **20-Ph** may be attributed to its more negative reduction potential, leading to thiolate loss followed by decomposition. Compound $[Et_4N]_2[Fe_4S_4(SBn)_4]$($[Et_4N]_2$**23-Bn**) was synthesized which displays a more negative z = 2–/3– reduction potential of –1.25 V vs. SCE. The z = 3– cluster was directly synthesized by reduction of the z = 2– cluster but the more negative reduction potential resembles that of **20-Ph** (z =2–/3– redox couple = 1.32 V vs. SCE) than **23-Ph** (z =2–/3– redox couple = 1.00 V vs. SCE). The reduction of **23-Bn** was performed in CD_3CN with 1.05 equivalents Cp^*_2Co, resulting in a shifted signal set in the ^{1}H NMR spectrum (Figure 5.20). consistent with the literature report of the z = 3– cluster $[Fe_4S_4(SBn)_4]^{3-}$(**24-Bn**). Unlike the reduction of **20-Ph**, the reduction of **23-Bn** did not result in the appearance of free thiolate. However, compound **24-Bn** was found to exhibit instability in CD_3CN, as its concentration decreased from 9.57 mM to 5.54 mM overnight. This decrease in the concentration of the reduced cluster is comparable to the decomposition observed for **22-Ph**. The decomposition product of **24-Bn** appears to be ^{1}H NMR silent material, as no additional signals were detected after 16 hours.

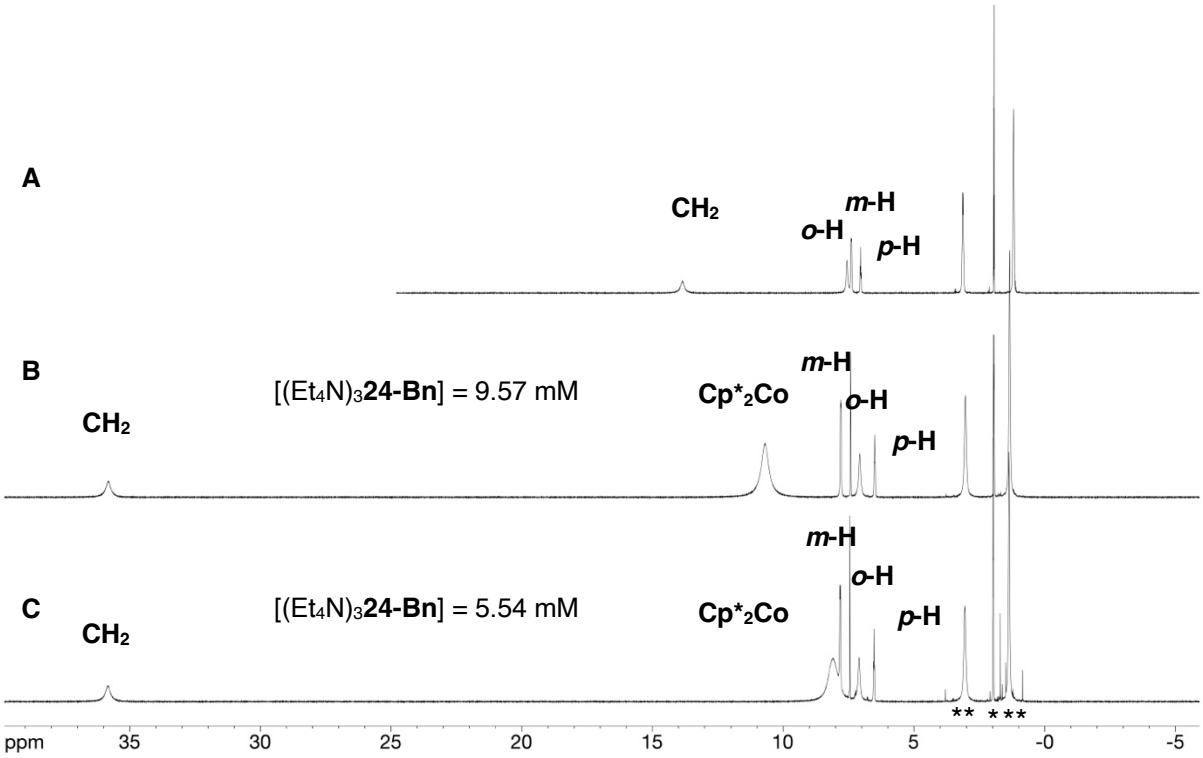

Figure 5.20. (**A**) ^{1}H NMR spectrum (298 K, 300 MHz) of $[Et_4N]_2$**23-Bn**. (**B**) ^{1}H NMR spectrum (298 K, 300 MHz) of $[Et_4N]_3$**24-Bn** generated from reduction of $[Et_4N]_2$**23-Bn** with Cp^*_2Co after 30 minutes. (**C**) ^{1}H NMR spectrum (298 K, 300 MHz) of $[Et_4N]_3$**24-Bn** generated from reduction of $[Et_4N]_2$**23-Bn** with Cp^*_2Co after 16 hours. Residual protio signal indicated by *. Counterion resonances indicated by **.

5.2.9 Synthesis and Stability Studies of $[Fe_4S_3(N^tBu)(SAr)_4]^{3-}$ Clusters

Work in the synthesis of reduced clusters was undertaken by reducing the $[Fe_4(N^tBu)S_3]^{2+}$ cluster with different arylthiolate ligands that varied in electronics and sterics. Changing the thiolate ligand to 2,6-dichlorobenzenethiolate (DCBT) and 4-chlorobenzenethiolate (CBT) may be advantageous as the z = 2–/3– reduction potential should be less negative compared to **20-Ph**. Changing the thiolate ligand to be more donating, like mesityl thiolate and *p*-methylbenzene thiolate was utilized to observe if a stronger ligand would lead to an increase in stability.

The cyclic voltammetry data of $[Et_4N]_2$**20-DCBT** showcased an irreversible reduction potential at around –1.31 V vs. SCE. This was unexpected as the addition of the Cl groups that are electron withdrawing via induction should lead to a less negative reduction potential.

The reduction of $[Et_4N]_2$**20-DCBT** led to decomposition of the normal state cluster and the presence of free thiolate. Adding additional equivalents of Cp^*_2Co led to the destruction of more $[Et_4N]_2$**20-DCBT**. The reduction titration experiment is shown in Figure 5.21. Attempts to re-oxidize the decomposed solution did not result in the reappearance of $[Et_4N]_2$**20-DCBT**, suggesting that the cluster core degrades after reduction. In contrast to the reduction of **20-Ph** and **23-Ph** with Cp^*_2Co, no spectroscopic evidence of the z = 3– cluster was observed during the reduction of $[Et_4N]_2$**20-DCBT**. It is possible that the reduction of $[Et_4N]_2$**20-DCBT** initially generates the z = 3– cluster, which subsequently undergoes thiolate loss, leading to complete cluster decomposition.

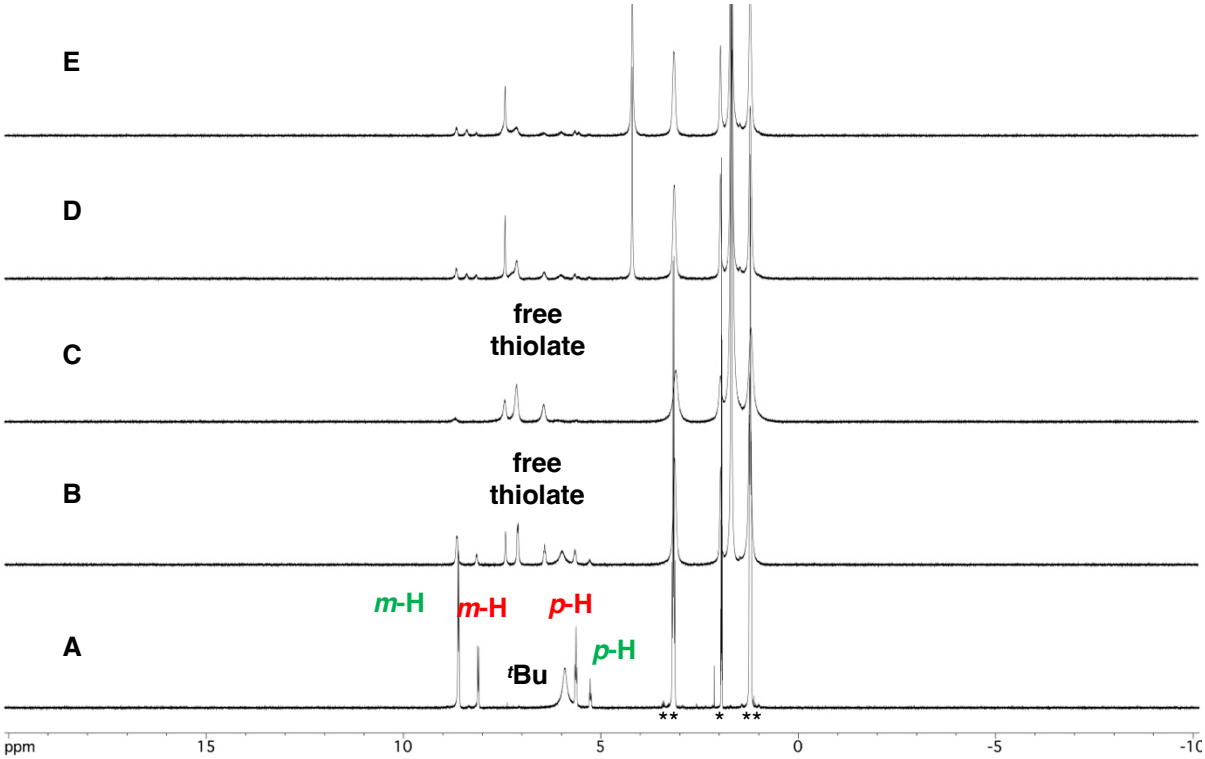

Figure 5.21. Reduction and oxidation of $[Et_4N]_2$**20-DCBT** in CD_3CN (298 K, 300 MHz). (**A**) ^1H NMR spectrum of $[Et_4N]_2$**20-DCBT**. (**B**) Addition of 1 equivalent of Cp^*_2Co. (**C**) Addition of 2nd equivalent of Cp^*_2Co. (**D**) Addition of 1 equivalent of $Fc(PF_6)$. (**E**) Addition of a 2nd equivalent of $Fc(PF_6)$. Residual protio signal indicated by *. Counterion resonances indicated by **. Resonances corresponding to ligand environments bound to the three equivalent Fe sites are indicated in red; those corresponding to the unique Fe site are indicated in green.

The ligand 2,6-dichlorobenzene thiolate was tested on Fe_4S_4 to determine if the instability of reduced **20-DCBT** was due to the bridging tert-butylimide or characteristic of the ligand. Compound $[Ph_4P]_2[Fe_4S_4(S(o\text{-}C_6H_3Cl_2)_4]$ ($[Ph_4P]_2$**23-DCBT**) was synthesized and crystallized. $[Ph_4P]_2$**23-DCBT** was reduced by one equivalent of Cp^*_2Co in CD_3CN and the reaction was monitored using ^1H NMR spectroscopy (Figure 5.22). With one equivalent of Cp^*_2Co, the signals observed are for $[Ph_4P]_2$**23-DCBT** and free thiolate. Allowing the reaction to stand for 16 hours does not alter the product distribution but the peaks sharpen after 16 hours, which can be attributed to insoluble material generated setting to the bottom of the NMR tube. These results reveal that the ligand, 2,6-dichlorobenzene thiolate, is not a suitable ligand for the reduced cluster cores as the increase in cluster charge leads to an increase in lability of this ligand.

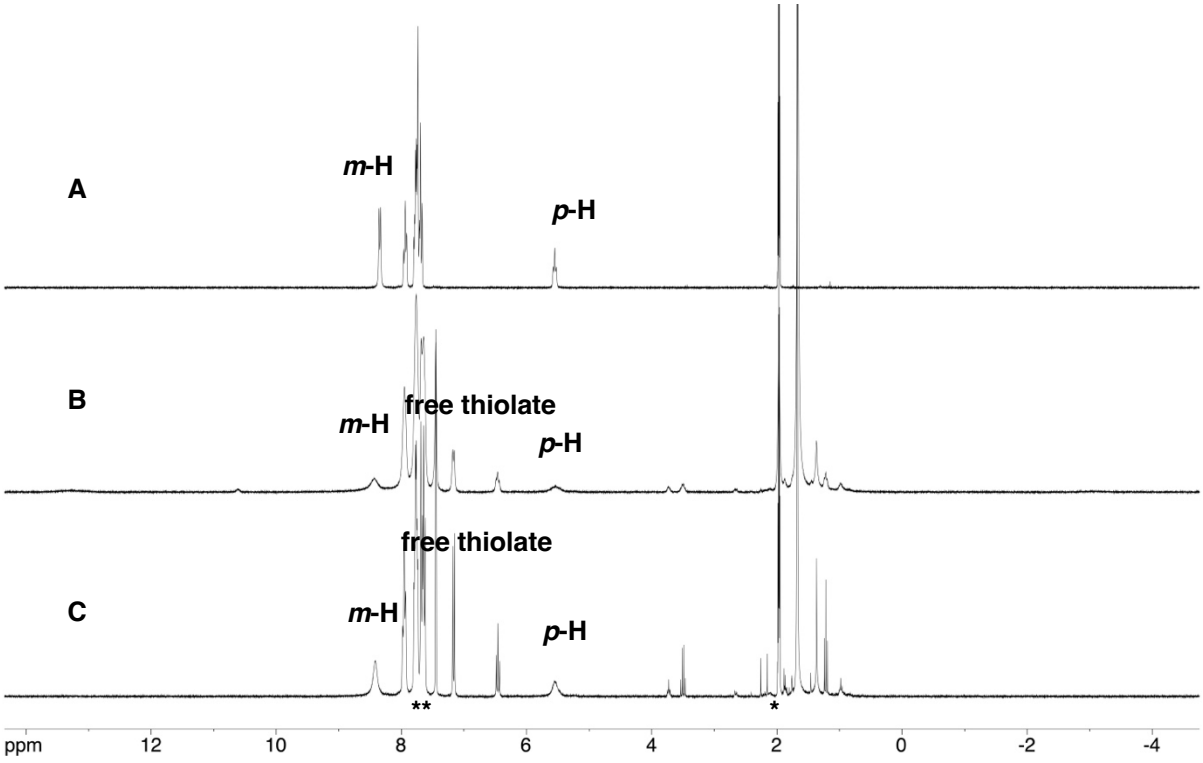

Figure 5.22. (**A**) ^1H NMR spectrum (298 K, 300 MHz) of $[Et_4N]_2$**23-DCBT**. (**B**) ^1H NMR spectrum (298 K, 300 MHz) of $[Et_4N]_2$**23-DCBT** and 1 equivalent Cp^*_2Co after 15 minutes. (**C**) ^1H NMR spectrum (298 K, 300 MHz) of $[Et_4N]_2$**23-DCBT** and 1 equivalent Cp^*_2Co after 16 hours. Residual protio signal indicated by *. Counterion resonances indicated by **.

The reversible reduction potential of $[Et_4N]_2$**20-CBT** is –1.24 V vs. SCE, which is 80 mV less negative compared to $[Et_4N]_2$**20-Ph.** This less negative reduction potential is attributed to the electron-withdrawing nature of Cl. As the chloro substituent is in the para position, it should not exert steric influence, unlike 2,6-dichlorobenzenethiolate which has the chloro groups ortho to the sulfur anion. The reduction potential of –1.24 V vs. SCE is sufficiently low to achieve a conversion of 194:1 of z = 2– : z = 3– when Cp^*_2Co is used as the reductant. Crystallization of $[Et_4N]_2$**20-CBT** proved to be difficult, so the thiolate ligated complex was generated *in-situ* by thiolate ligand substitution of the chloro complex $[Et_4N]_2$**19** with 4-chlorobenzenethiolate. The reduction of $[Et_4N]_2$**20-CBT** with one equivalent of Cp^*_2Co is shown in Figure 5.23. In the resulting ^1H NMR spectrum, the signals attributed to z = 3– cluster was not observed, and numerous signals spanning the region of 0 to 14 ppm are present as well as an increase in free thiolate. This observation reveals that a less negative z = 2–/3– reduction potential compared to **20-Ph** may not be beneficial in stabilizing the reduced cluster. A plausible explanation is that 4-chlorobenzenethiolate is a less strongly binding ligand compared to benzenethiolate, leading to greater lability upon reduction and, consequently, more rapid cluster decomposition.

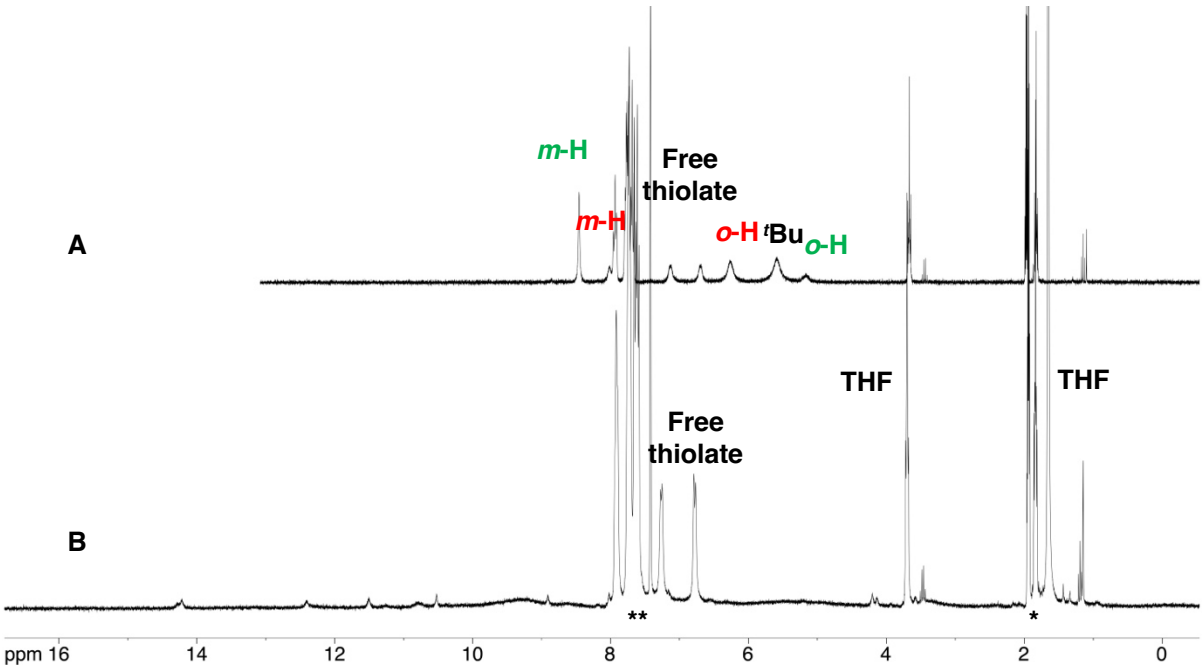

Figure 5.23. (**A**) ^{1}H NMR (298 K, 300 MHz) spectrum of the reaction of $(Ph_4P)_2$**19** and 4.1 equivalents of Na(4-C_6H_4Cl). (**B**) ^{1}H NMR (298 K, 300 MHz) spectrum after addition of one equivalent of Cp*$_2$Co. Residual protio signal indicated by *. Counterion resonances indicated by **. Resonances corresponding to ligand environments bound to the three equivalent Fe sites are indicated in red; those corresponding to the unique Fe site are indicated in green.

Reduction experiments for $[Et_4N]_2$**20-Mes** and $[Et_4N]_2$**20-*p*Tol** required a separate reduction protocol, as their reduction potentials were too negative for effective use of Cp*$_2$Co as a reductant. The reductant used in the initial synthesis of $[Et_4N]_3$**24-Ph** was NaACN in hexamethylphosphoramide (HMPA).[180] Later reports described the synthesis of $[Et_4N]_3$**24-Ph** via reduction of $[Et_4N]_2$**23-Ph** in MeCN using NaACN prepared in THF.[181,182] While this latter method resulted in a lower yield of $[Et_4N]_3$**24-Ph**, it avoided the use of HMPA–a high boiling, environmentally hazardous solvent. Given the instability of **22-Ph** in MeCN, switching the reaction solvent to HMPA was deemed beneficial for the isolation of reduced cluster. To monitor the reduction in HMPA by ^{1}H NMR spectroscopy, solvent suppression techniques were employed to minimize the HMPA resonance, as solvent removal under reduced pressure was not feasible. While solvent suppression may result in the loss of signals near the suppressed peak–thereby limiting its utility for structural elucidation–it remains valuable for assessing the formation of known complexes.

Reduction of **23-Ph** was carried out in HMPA with NaACN. An aliquot (500 μL) of the reaction mixture in HMPA was withdrawn, and 50 μL of C_6D_6 was added to the NMR tube to provide a deuterium signal for spectrometer locking. Unexpectedly, the addition of a small amount of C_6D_6 induced precipitation of microcrystalline material within the NMR tube. Isolation and NMR analysis of this solid revealed the reduced cluster $[Et_4N]_3$**24-Ph**. The same protocol of reduction in HMPA followed by addition of C_6D_6 was tested for $[Et_4N]_2$**20-Ph** to determine whether the reduced cluster could be similarly isolated. However, $[Et_4N]_2$**22-Ph** did not precipitate from solution but was observed using solvent suppression ^{1}H NMR spectroscopy. $[Et_4N]_2$**20**-Mes was subjected to the same reduction protocol as $[Et_4N]_2$**20-Ph** and led to a signal set that may be consistent with $[Et_4N]_2$**22-Mes,** but material could not be isolated upon addition of solvents like C_6H_6 or THF.

Reduction of $[Et_4N]_2$**20-*p*Tol** in HMPA with NaACN yielded the most promising outcome, as the addition of THF to the solution induced crystallization of $[Et_4N]_3$**22-*p*Tol**. The microcrystalline material upon drying, formed a black powder. When dissolved in CD_3CN, the material displayed isotropically shifted signals consistent with the z = 3– cluster. Because HMPA is not a desirable solvent, alternative conditions were explored. $[Et_4N]_2$**20-*p*Tol** and Et_4NCl were suspended in THF, with minimal amounts of MeCN added to the mixture to dissolve the cluster. $Na[Ph_2CO]$ was then introduced to the THF/MeCN mixture, resulting in the rapid precipitation of black solid within minutes. When redissolved in CD_3CN, the black solid exhibited signals corresponding to the z = 3– cluster. These findings demonstrate that an alternative reductant and solvent system can be used to generate the z = 3– cluster as isolable solid.

Like the instability observed in $(Et_4N)_2(CoCp^*_2)$**22-Ph** in MeCN, allowing the NMR solution to sit overnight inside the glovebox led to decomposition of the z = 3– cluster, as evidenced by the appearance numerous signals in the ^{1}H NMR spectrum as shown in Figure 5.24. These numerous signals currently cannot be assigned to known compounds.
The isolation of $[Et_4N]_3$**22-*p*Tol** was unexpected given the lack of crystallinity observed for $[Et_4N]_3$**22-Ph**.

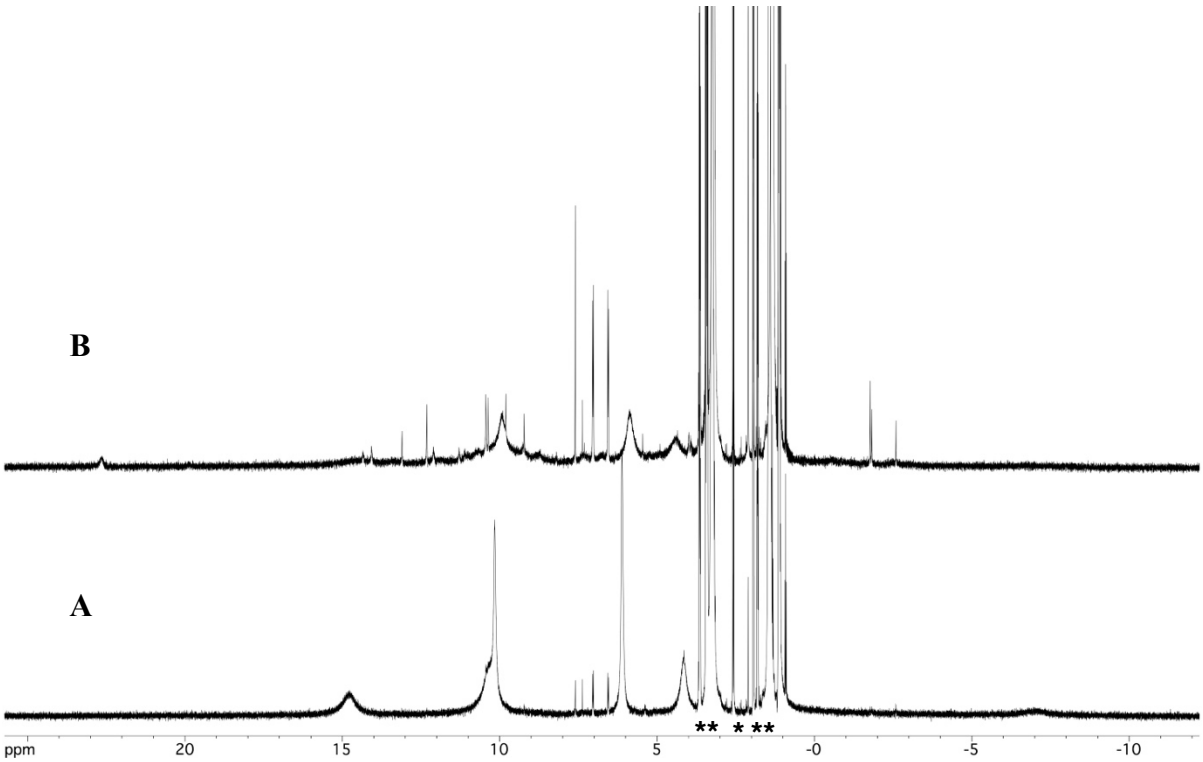

Figure 5.24. (**A**) ^{1}H NMR (298 K, 300 MHz) spectrum of crystalline $[Et_4N]_3$**22-*p*Tol** in CD_3CN after 15 minutes. (**B**) ^{1}H NMR (298 K, 300 MHz) spectrum of crystalline $[Et_4N]_3$**22-*p*Tol** in CD_3CN after 16 hours. Residual protio signal indicated by *. Counterion resonances indicated by **.

5.2.10 Ground Spin State Determination

Magnetic susceptibility measurements were conducted on polycrystalline $[Et_4N]_2$**20-Mes** and $[Et_4N]$**21-Mes** to determine their magnetic properties and the ground spin states. Other z = 2– clusters synthesized within this chapter were not subjected to magnetochemical analysis; precedent from Fe_4S_4 literature and the ^{1}H NMR data suggest that these clusters exhibit a diamagnetic ground spin state.[2,183] The magnetic susceptibility plot (Figure 5.25) shows lower molar magnetic susceptivity for $[Et_4N]_2$**20-Mes** compared to the oxidized $[Et_4N]$**21-Mes**. The magnetic susceptibility data for $[Et_4N]_2$**20-Mes** is similar to the data obtained for **1** and $[Ph_4P]_2$**6** (Chapter 2), highlighting a ground spin state of S = 0 for $[Et_4N]_2$**20-Mes**. The magnetic susceptibility of $[Et_4N]_2$**20-Mes** increases as the temperature approaches 2 K from a minimum around 50 K, which can likely be attributed to magnetic iron contamination. The magnetic moment derived from the Curie-Weiss analysis for

[Et_4N]**21-Mes** and [Et_4N]$_2$**20-Mes** at 2 K is 3.2 BM and 0.62 BM respectively. The magnetic moment of [Et_4N]**21-Mes** rises to approximately 4 BM at 50 K and stays constant up to 300 K.

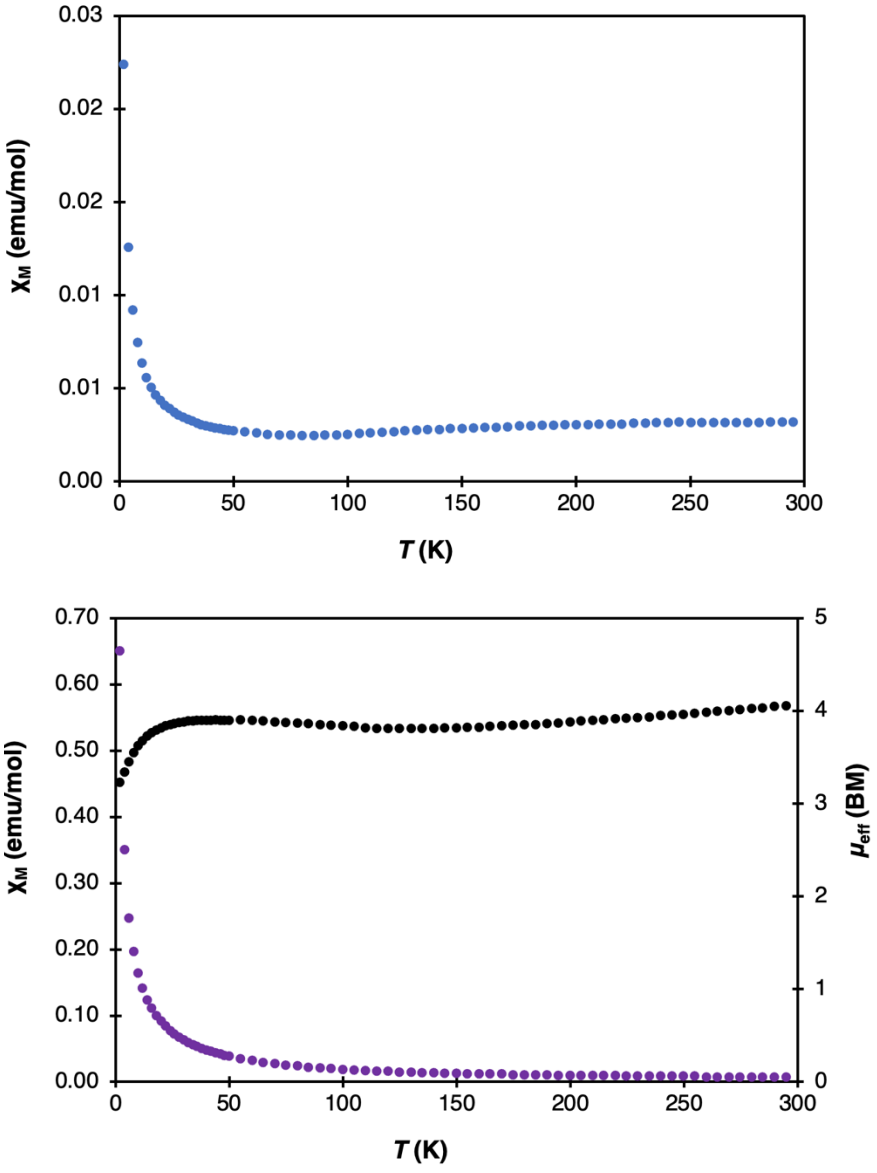

Figure 5.25. Temperature dependence plot of the magnetic susceptibilities of polycrystalline [Et_4N]$_2$[Fe_4(N^tBu)S_3($SMes$)$_4$] ([Et_4N]$_2$**20-Mes**, blue) and [Et_4N][Fe_4(N^tBu)S_3($SMes$)$_4$] ([Et_4N]**21-Mes**, purple). The magnet moment of [Et_4N]**21-Mes** is plotted in black.

Magnetic susceptibility measurements of [Et_4N]**21-Mes** follow a linear Curie-Weiss relationship ($\chi^M = C/(T-\theta)$; C = 2.00 emu K/mol, θ = –1.75 K) at low temperatures (2-50 K) and an almost linear relationship between 2 K to 300 K (Figure 5.26). A Curie constant of 2.00 emu K/mol is consistent with a ground spin state of S = 3/2. The coefficient of determination (R^2) for the temperature dependence of the inverse molar susceptibility plot to 300 K is 0.9958, which displays a linear fit and good correlation. This linear relationship is unusual compared to the magnetic susceptibility data of [Ph_4P]**2** (Chapter 2) and other Fe_4S_4 clusters with non S = 0 ground spin states, which typically exhibit curvature in the data at higher temperatures due to the population of higher-energy states.[181,182] The temperature dependence of the reciprocal molar susceptibility plot of [$Fe_4S_4(STipp)_4]^{1-}$ begins curving at around 100 K which is roughly the temperature the data of [Ph_4P]**2** begins to curve.[184]

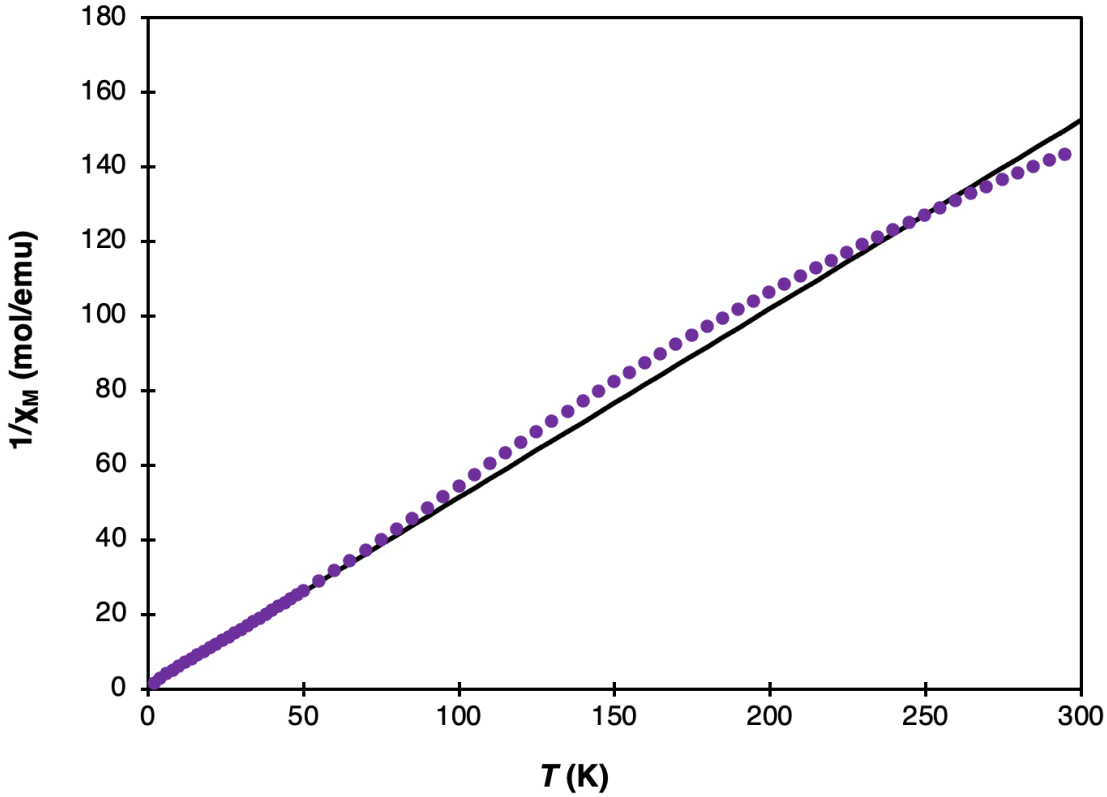

Figure 5.26. Temperature dependence plot of the reciprocal magnetic susceptibility of polycrystalline [Et_4N][$Fe_4(N^tBu)S_3(SMes)_4$] ([Et_4N]**21-Mes**). The solid line indicates the linear least-squares fit (y = 0.51 x + 0.88; C = 2.00 emu K/mol, θ = –1.75 K) to the data between T = 2 – 50 K. Data is consistent with a S=3/2 ground spin state.

The EPR spectrum of [Et_4N]**21-Mes** was collected and analyzed by Dr. Harald Kelm and Prof. Hans-Jörg Krüger. The odd-spin cluster [Et_4N]**21-Mes** displays a rhombic EPR signal at g = 1.99, 3.40 4.35 in 0.2 M TBAP/DMF glass at X-band frequency at 4 K (Figure 5.27), consistent with a ground spin state of S = 3/2.

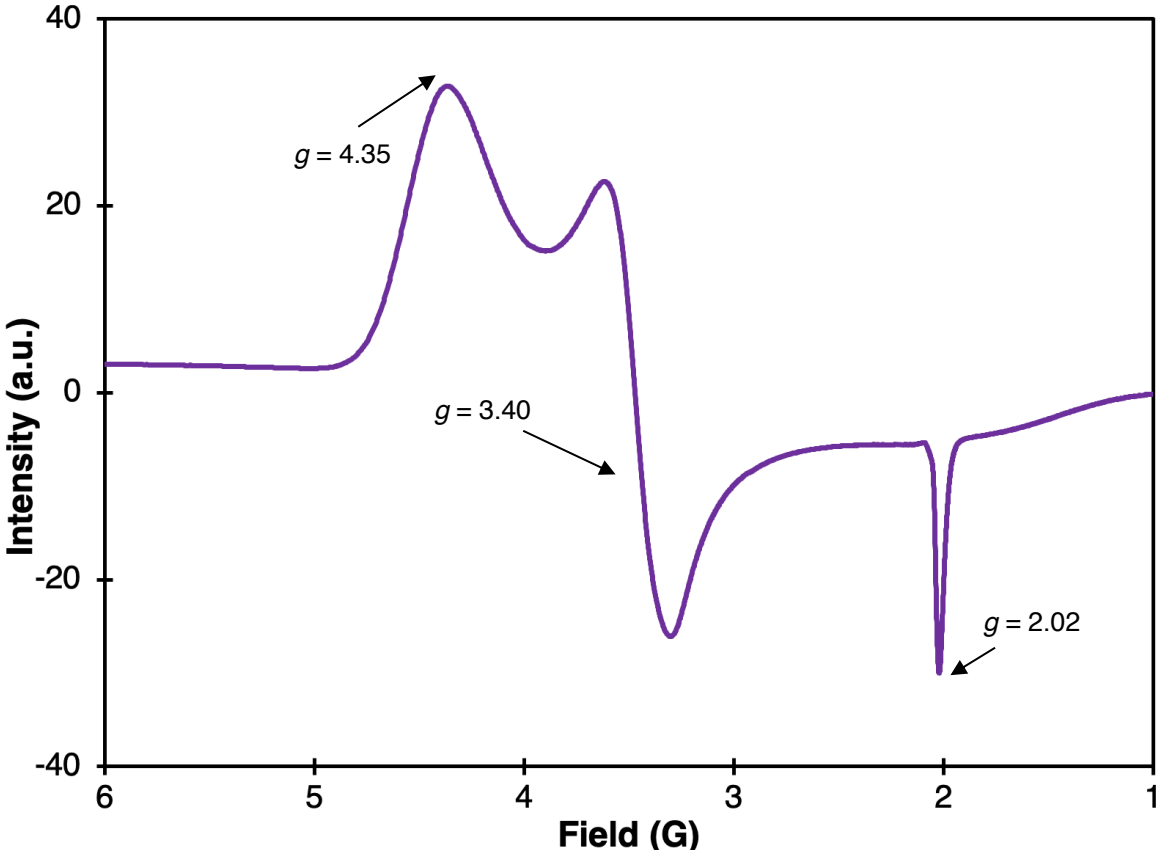

Figure 5.27. X-band EPR spectrum (4 K, 0.2 M TBAP/DMF) of [Et_4N]**21-Mes**.

$[Fe_4S_4]^{2+}$ clusters with a ground spin state of S = 0 can be modelled as two sets of antiferromagnetically coupled $[Fe_2S_2]^{1+}$ dinuclear complexes, as shown in Figure 5.28.[183,185] The mixed valent $[Fe_2S_2]^{1+}$ complex formally contains one Fe(III) and one Fe(II) but the ions undergo spin-dependent electron delocalization, also known as double exchange, to lead to a pair of $Fe^{2.5+}$ centers.[2] The two $Fe^{2.5+}Fe^{2.5+}$ dinuclear complexes then antiferromagnetically couple to form a S = 0 ground spin state. $[Fe_4S_4]^{1+/3+}$ clusters with a ground spin state of S = ½ can be viewed as one dinuclear $[Fe_2S_2]^{1+}$ subunit coupled to two Fe^{2+} ions in the case of

$[Fe_4S_4]^{3+}$ and two Fe^{3+} ions in the case of $[Fe_4S_4]^{1+}$. This model is applicable for both $[Fe_4S_4]^{1+/3+}$ clusters that display a ground spin state of $S = ½$.

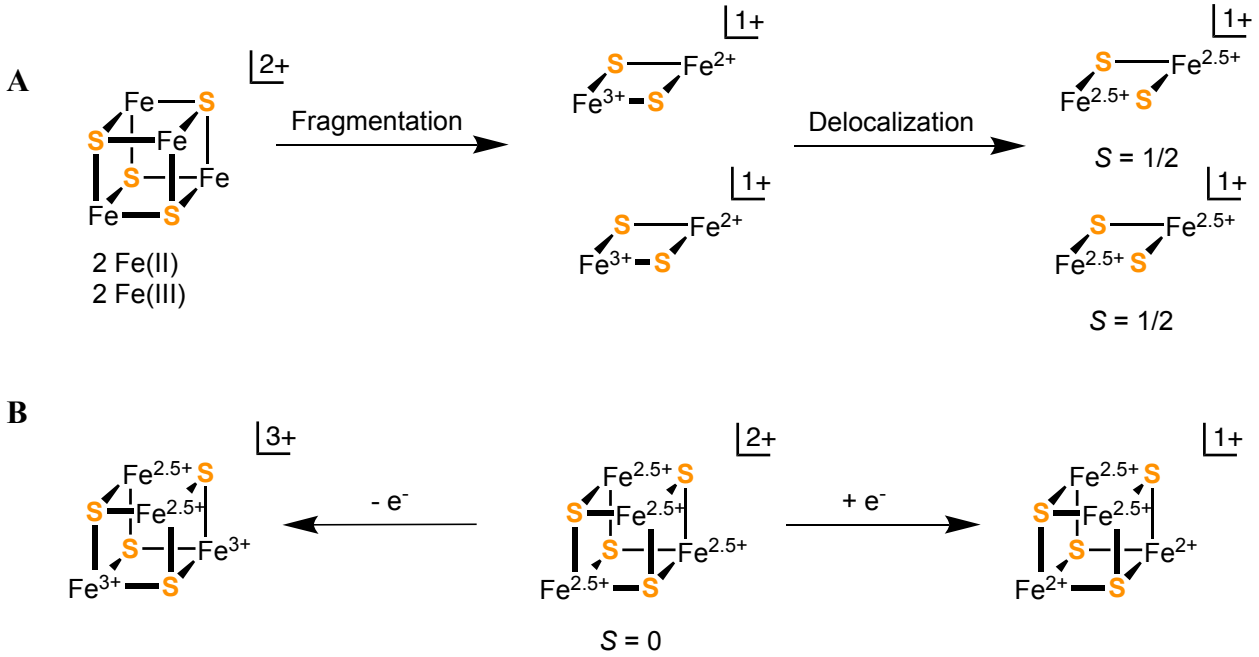

Figure 5.28. (A) Conceptualization of the delocalization in $[Fe_4S_4]^{2+}$ clusters. **(B)** Delocalization and localization patterns in $[Fe_4S_4]^{1+/2+/3+}$ clusters.

Compound $[Et_4N]$**21-Mes** with core composition $[Fe_4(N^tBu)S_3]^{3+}$ cannot be modelled the same as $[Fe_4S_4]^{3+}$ since the ground spin state of $[Et_4N]$**21-Mes** was determined to be $S = 3/2$. To our knowledge, the limited subset of $[Fe_4S_4]^{3+}$ clusters all display a $S = ½$ ground spin state based on EPR spectroscopy.[49,178,179,186] To model the $S = 3/2$ ground spin state of $[Et_4N]$**22**, the complex needs to be fragmented into a $[Fe_3S_3(N^tBu)]^{1+}$ fragment and an Fe^{2+} unit, as shown in Figure 5.29. The $[Fe_3S_3(N^tBu)]^{1+}$ fragment formally contains three Fe(III) ions with the ground spin state modelled as $S = 1/2$ based on biological precedent of $[Fe_3S_4]^{1+}$ clusters. [187–189] The tetrahedral Fe^{2+} unit can be modelled as a $S = 2$ ground spin state based on the electron count and d-splitting of the Fe^{2+} unit. The antiferromagnetic coupling of the $S = 2$ Fe^{2+} unit and the $S = 1/2$ $[Fe_3S_3(N^tBu)]^{1+}$ fragment leads to an overall ground spin state of $S = 3/2$.

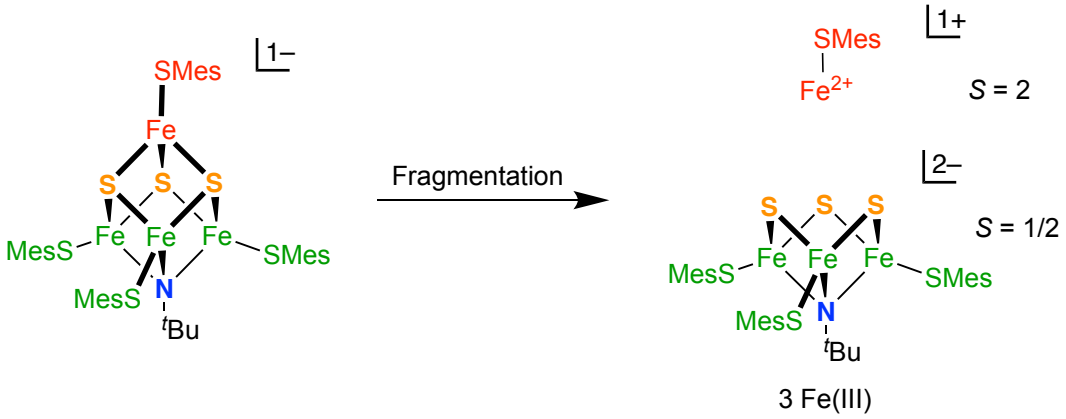

Figure 5.29. Conceptual fragmentation of [Et_4N]**21-Mes** into Fe^{2+} and [$Fe_3(N^tBu)S_4$].

^{1}H NMR data supports this model. Figure 5.30 presents ^{1}H NMR data of the normal state [Et_4N]$_2$**20-Mes,** [Et_4N]$_2$**20-Ph** and the oxidized [Et_4N]**21-Mes** and reduced **22-Ph** complexes. Ideally, the ^{1}H NMR data of [Et_4N]**21-Mes** would be compared to other oxidized clusters with the [$Fe_4(N^tBu)S_3$]$^{3+}$ cluster core but no other compounds currently exist. The ^{1}H NMR data of [Et_4N]**21-Mes** will be compared to **22-Ph** which contains an odd d count of electrons and a likely non-zero ground spin state. For **22-Ph**, the meta signals for the phenyl ring on the unique and three equivalent iron sites shift downfield, while the ortho and para signals shift upfield consistent with a system in which four iron atoms undergo exchange coupling. In contrast, for [Et_4N]**21-Mes**, all aromatic signals on the unique site shift upfield, whereas the three equivalent site signals shift downfield. This difference in ^{1}H chemical shifts in [Et_4N]**21-Mes** provides data that supports the fragmentation of [Et_4N]**21-Mes** into [$Fe_3S_3(N^tBu)$]$^{1+}$ and Fe^{2+} fragments.

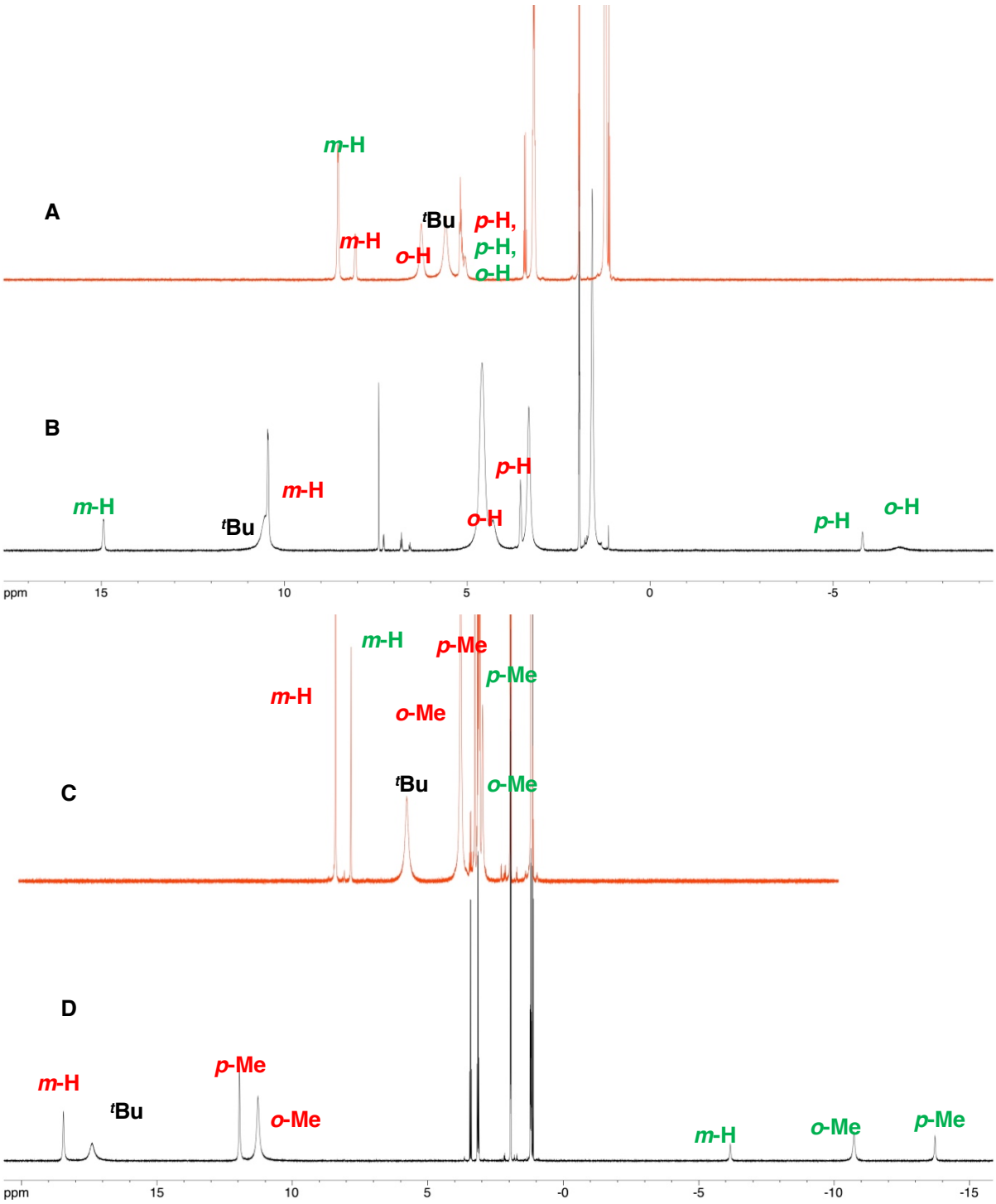

Figure 5.30. ^{1}H NMR (298 K, 300 MHz) spectra of $[Et_4N]_2$**20-Ph** (A), $[Et_4N]_2[Cp^*_2Co]$**22-Ph** (B), $[Et_4N]_2$**20-Mes** (C) and $[Et_4N]$**21-Mes** (D). Resonances corresponding to ligand environments bound to the three equivalent Fe sites are indicated in red; those corresponding to the unique Fe site are indicated in green.

This fragmentation model was proposed in the study of $[NiFe_3S_4(SEt)_3L]^{1+}$ clusters as shown by the structure in Figure 5.31.[190] Upon change of redox state, all resonances attributed to the ligand on Ni shifted in the same direction and all resonances attributed to the ligand on the Fe shifted in the same direction.

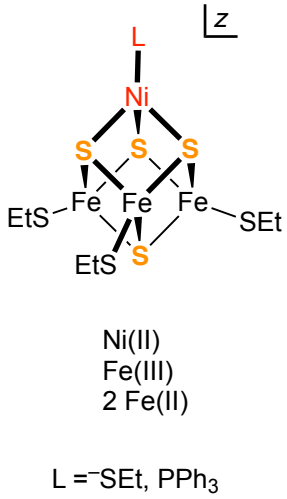

Figure 5.31. Literature model with Ni^{2+} and Fe_3S_4 fragmentation

5.2.11 Chapter Summary

The work presented in this chapter led to the synthesis of oxidized and reduced iron-imide-sulfide clusters. The normal state $z = 2-$ cluster was derivatized with a series of thiolate ligands including benzene thiolate, *p*-methylbenzene thiolate, *p*-chlorobenzene thiolate, 2,4,6-trimethylbenzene thiolate and 2,6 dichlorobenzene thiolate. These ligands were selected due to the relevance of sulfur based anionic donors in the nitrogenase enzyme. The set of arylthiolate ligands varied in both electronic properties and steric profiles, allowing for the modulation of the cluster' electrochemical behaviour. This study employed $[Ph_4P]^+$ as the counterion, in contrast to previously reported protocols that utilized $[Et_4N]^+$. The oxidized cluster was synthesized by treating $[Et_4N]_2$**20-SMes** with $FcPF_6$. The ground spin state of the oxidized cluster determined to be $S = 3/2$ via magnetic susceptibility measurements and EPR spectroscopy.

The reduced cluster of **22-SPh** was obtained by reduction of $[Et_4N]_2$**20-SPh** with one equivalent of $CoCp^*_2$. The resulting cluster was not isolable and decomposed in solution over hours to a new signal set and to free benzene thiolate. After 16 hours, the ^{1}H NMR spectrum displayed weak signals attributed to the z = 3– cluster and when the solution was re-oxidized, more z = 2– cluster was present at the 16 hour mark, suggesting reformation of $[Et_4N]_2$**20-SPh**. This decomposition and instability was not observed with the homoleptic Fe_4S_4 clusters under identical conditions. Substitution of the cluster with weaker donor ligands such as 2,6-dichlorobenzene thiolate and 4-chlorobenzene thiolate led to further destabilization of the reduced cluster. In contrast, use of 4-methylbenzne thiolate enabled the isolation of crystalline material that exhibited similar decomposition to **22-SPh**.

5.3 Experimental Section

5.3.1 General Experimental Details

The following details are added to the procedures explained in Chapter 2. $[Ph_4P]_2$**18** was synthesized using a literature protocol.[171] NaSPh was synthesized by reaction of HSPh with and NaSMes was synthesized by reaction of HSMes with NaH in THF. NaSBn, NaS(4-C_6H_4Cl), NaS(4-C_6H_4Me) and NaS(2,6-$C_6H_3Cl_2$) were synthesized using similar protocols to the synthesis of NaSMes.

5.3.2 Preparation of Compounds

Reduction followed by oxidation ^{1}H NMR Assay experiments of $[Ph_4P]_2$20. A stock solution of $[Ph_4P]_2$**20** was prepared by dissolving microcrystalline $[Ph_4P]_2$**20** (24.4 mg, 0.0162 mmol, 10.8 mM) in CD_3CN (1.5 mL) with stirring using a miniature stir bar. Once fully dissolved after 5 minutes, 450 µL of this stock solution was transferred via syringe to an NMR tube to collect a reference ^{1}H NMR spectrum. A reducing stock solution was then prepared by dissolving Cp^*_2Co (5.2 mg, 0.0158 mmol, 35.08 mM) in C_6D_6 (0.450 µL) using a microlitre syringe. An oxidizing stock solution was prepared by dissolving $(PF_6)F_C$ (5.2 mg, 35.69 mM) in CD_3CN (450 µL) following the same procedure as the Cp^*_2Co stock

solution. From the $[Ph_4P]_2$**20** stock solution, two 450 μL aliquots were extracted and transferred to separate vials, each containing a miniature stir bar. For the first reduction experiment, 150 μL of the Cp^*_2Co stock solution was added to the first vial containing $[Ph_4P]_2$**20** and stirred for ~5 minutes. After stirring, 450 μL of the solution was extracted via syringe and transferred to an NMR tube, with the ^1H NMR spectrum collected within 5 minutes. In the second vial containing $[Ph_4P]_2$**20**, 150 μL of the Cp^*_2Co stock solution was added and stirred for 5 minutes. Subsequently, 150 μL of the $(PF_6)F_C$ stock solution was injected into the vial and stirred for another 5 minutes. Finally, 450 μL of the oxidized solution was extracted via syringe, and its ^1H NMR spectrum was collected.

The overnight oxidation experiments and assays of $[Et_4N]_2$20-SPh were prepared analogously except with the oxidizing stock solution prepared the next day for the overnight experiments.

$Fe_2(\mu\text{-}NH^tBu)_2S[N(SiMe_3)_2]_2$ (17). Compound **17** was synthesized using a modified literature preparation.[26] After the addition of S_8 to the reaction of $^tBuNH_2$ and **11**, the solution was stirred 3 days. The solvent was then removed *in vacuo* and redissolved in pentane. Filtration through diatomaceous earth followed by solvent removal under reduced pressure led to the isolation of material that is pure enough for subsequent use.

$(Ph_4P)_2[Fe_4(N^tBu)S_3Cl_4]$ ($[Ph_4P]_2$19). A suspension of $[Ph_4P]_2$**18** (1.277 g, 1.08 mol) in MeCN (18 mL) is added to a solution of **35** (0.797 mg, 1.3) in THF (7 mL). The suspension is allowed to stir for 2.25 hours, and the solvent is removed in vacuo to afford black powder. MeCN (10 mL) is then added to the black solid and allowed to stir for 1 hour. The solution is filtered over celite to afford black insoluble material and a black solution. The solvent is then removed, the solid is redissolved in MeCN (15 mL), filtered over celite and diethyl ether (25 mL) is added until black microcrystalline material appears. The solution is then stored at –15 °C overnight and filtration the next day led to black microcrystalline material (0.654 g, 50%). Anal. Calcd for $C_{52}H_{49}N\ Cl_4Fe_4P_2S_3$: C, 51.56; H, 4.08; N, 1.16. Found: C, 51.36; H, 4.07; N, 1.13.

$(Et_4N)_2[Fe_4(N^tBu)S_3Cl_4]$ ($[Et_4N]_2$19). A solution of $Na(BPh_4)$ (368.4 mg, 1.077 mmol) in MeCN (6 mL) was added to solution of $[Ph_4P]_2$**20** (651 mg, 0.538 mmol) in MeCN

(12 mL) and allowed to stir for 1 h to produce a black solution with considerable amounts of brown insoluble material. The suspension was filtered over diatomaceous earth and a solution of $(Et_4N)Cl$ (180.7 mg, 1.09 mmol) in MeCN (5 mL) was added with the resulting solution allowed to stir for another hour. The solution was filtered over diatomaceous earth, volumed reduced until white solid appeared and filtered to remove the contaminating white solid. Et2O (15 mL) was added dropwise, and the solution was cooled to –20 °C for 24 h. Filtration, followed by rinsing the crystals with Et_2O yielded black, microcrystalline material (0.330 mg, 77%).

$(Ph_4P)_2[Fe_4(N^tBu)S_3(SPh)_4]$ ($[Ph_4P]_2$20-Ph). A solution of $[Ph_4P]_2$**19** (124.5 mg, 0.103 mmol) in MeCN (3 mL) was added to a suspension of NaSPh (56.3 mg, 0.426 mmol) in MeCN (1 mL) and stirred for 45 minutes. The solution color changed from brown black to golden-black within seconds. The reaction mixture was then filtered over celite, and diethyl ether (10 mL) was added to the filtrate, affording microcrystalline black material. The mixture was stored at –15 °C overnight, yielding microcrystals (122 mg, 79%) collected by filtration and rinsed with Et_2O. Anal. Calcd for $C_{76}H_{69}NFe_4P_2S_7$: C, 60.61; H, 4.62; N, 0.93. Found: C, 60.42; H, 4.65; N, 0.84.

Compounds **$(Et_4N)_2[Fe_4(N^tBu)S_3(SAr)_4]$**. **Ar = Ph** (**20-Ph**) Anal. Calcd for $C_{44}H_{69}N_3Fe_4S_7$: C, 48.58; H, 6.39; N, 3.86. Found: C, 48.61; H ,6.42; N, 3.82., **Mes** (**21**) Anal. Calcd for $C_{56}H_{93}N_3Fe_4S_7$: C, 53.54; H, 7.46; N, 3.35. Found: C, 53.18; H ,7.61; N, 3.65., **2,6-$C_6H_3Cl_2$ (20-DCBT), 4-C_6H_4Cl (20-CBT), 4-C_6H_4Me (20-*p*Tol), $(Et_4N)_2[Fe_4S_4(SBn)_4]$ (23-Bn) and $(Ph_4P)_2[Fe_4S_4(S(2,6\text{-}C_6H_3Cl_2)_4]$ (23-DCBT) were synthesized using analogues methods to $[Ph_4P]_2$20**.

$(Et_4N)[Fe_4(N^tBu)S_3(SMes)_4]$ ($[Et_4N]$21-Mes). A solution of $[Et_4N]_2$**20-Mes** (270.7 mg, 0.215 mmol) in 13 mL of DCM was added to a suspension of $[Fe(C_5H_5)_2]PF_6$ (73.5 mg, 0.222 mmol) in DCM (2 mL). The reaction mixture was stirred for 50 minutes and then filtered over celite. The solvent was removed under reduced pressure, and the residue was allowed to dry for four hours. The resulting solid was extracted in THF (10 mL), and the insoluble white/tan solid was removed by filtration. The filtrate was concentrated, and Et_2O (50 mL) was added. The solution was placed in a freezer overnight, yielding crop 1 (30 mg). An additional 20 mL of diethyl ether was added to the mother liquor, and the solution was

returned to the freezer for 2 hours, yielding crop 2 (94.5 mg). The combined mass of both crops was 124.5 mg, corresponding to a 51.3% yield.

$(Et_4N)_3[Fe_4(N^tBu)S_3(S(4\text{-}C_6H_4Me)_4]$ ($[Et_4N]_3$20-*p*Tol). Acenaphthalene (24.0 mg, 0.158 mmol) and Na (3.6mg, 0.157 mmol) were stirred together in HMPA (0.840 mL) for 18 h, forming a dark brown solution. To a solution of $[Et_4N]_2$**20-*p*Tol** (26.9 mg, 0.024 mmol) and Et_4NCl (4.1 mg, 0.025 mmol) in HMPA (1 mL), NaACN (0.145 mL, 0.027 mmol) was dropwise added and the solution was allowed to stir for 1 hr. 3 mL of THF was added dropwise to precipitate out impure black solid (44 mg).

Spectroscopic data for select compounds are displayed in Tables 5.5 and 5.6.

Table 5.5. ^{1}H NMR data for $[Ph_4P]_2[Fe_4(N^tBu)S_3Cl_4]$ ($[Ph_4P]_2$**19**), $[Ph_4P]_2[Fe_4(N^tBu)S_3(SPh)_4]$ ($[Ph_4P]_2$**20-SPh**), $[Et_4N]_2[Fe_4(N^tBu)S_3(SMes)_4]$ ($[Et_4N]_2$**20-Mes**), $[Et_4N]Fe_4(N^tBu)S_3(SMes)_4]$ ($[Et_4N]$**21-Mes**), $[Et_4N]_2[Cp^*_2Co][Fe_4(N^tBu)S_3(SPh)_4]$ ($[Et_4N]_2[Cp^*_2Co]$**22-Ph**), $[Et_4N]_2[Fe_4S_4(SPh)_4]$ ($[Et_4N]_2$**23-Ph**), $[Et_4N]_3[Fe_4S_4(SPh)_4]$ ($[Et_4N]_3$**24-Ph**), $[Et_4N]_2[Fe_4S_4(SBn)_4]$ ($[Et_4N]_2$**23-Bn**), $[Et_4N]_2[Cp^*_2Co][Fe_4S_4(SBn)_4]$ ($[Et_4N]_2[Cp^*_2Co]$**24-Bn**), $[Et_4N]_2[Fe_4(N^tBu)S_3(S(2,6\text{-}C_6H_3Cl_2))_4]$ ($[Et_4N]_2$**20-DCBT**), $[Ph_4P]_2[Fe_4S_4(S(2,6\text{-}C_6H_3Cl_2)_4]$ ($[Ph_4P]_2$**23-DCBT**), $[Et_4N]_2[Fe_4(N^tBu)S_3(S(4\text{-}C_6H_4Cl))_4]$ ($[Et_4N]_2$**20-CBT**), $[Et_4N]_2[Fe_4(N^tBu)S_3(S(4\text{-}C_6H_4Me))_4]$ ($[Et_4N]_2$**20-*p*Tol**)

Compound	^{1}H NMR (CD_3CN, δ ppm)
$[Ph_4P]_2$**19**	5.46 (9 H, ^{t}Bu)
$[Ph_4P]_2$**20**	8.48 (6 H, *m*-H), 8.01 (2 H, *m*-H), 6.28 (6 H, *o*-H), 5.57 (9 H, ^{t}Bu), 5.19-5.08 (6 H, *o*, *p*, *p*-H)
$[Et_4N]_2$**20-Mes**	8.40 (6 H, *m*-H), 7.83 (2 H, *m*-H), 5.77 (9 H, ^{t}Bu), 3.79 (18 H *o*-H), 3.26 (9 H, *p*-H), 3.16 (3 H *p*-H). 2.98 (6 H *o*-H)
$[Et_4N]$**22**	18.42 (6 H, *m*-H), 17.37 (9 H ^{t}Bu), 11.93 (9 H, *p*-Me), 11.25 (18 H, *o*-Me), –6.13 (2 H, *m*-H), –10.71 (6 H, *o*-Me), –13.69 (3 H, *p*-Me)
$[Et_4N]_2[Cp^*_2Co]$**22-Ph**	14.77 (2 H, *m*-H), 10.40 (15 H, *m*-H, ^{t}Bu), 4.34 (6 H, *o*-H), 3.58 (3 H, *p*-H), –5.55 (1 H, *p*-H), –6.54 (2 H, *o*-H)
$[Et_4N]_2$**23-Ph**	8.22 (8 *m*-H), 5.92 (8 H, *o*-H), 5.3 (4 H, *p*-H)
$[Et_4N]_3$**24-Ph**	10.64 (8 H, *m*-H), 2.59 (8 H, *o*-H), 1.83 (4 H, *p*-H)
$[Et_4N]_2$**23-Bn**	13.86 (8 H, CH_2), 7.56 (8 H, *o*-H), 7.41 (8 H, *m*-H), 7.04 (4 H, *p*-H)

Compound	^{1}H NMR (CD_3CN, δ ppm)
$[Et_4N]_2[Cp^*_2Co]$**24-Bn**	35.81 (8 H, CH_2), 7.81(8 H, *m*-H), 7.08 (8 H, *o*-H), 6.50 (4 H, *p*-H)
$[Et_4N]_2$**20-DCBT**	8.61 (6 H, *m*-H), 8.10 (2 H, *m*-H), 5.91 (9 H, ^{t}Bu), 5.63 (3 H, *p*-H), 5.27 (1 H, *p*-H)
$[Et_4N]_2$**29**	8.31 (8 H, *m*-H), 5.52 (4 H, *p*-H)
$[Et_4N]_2$**20-CBT**	8.47 (6 H, *m*-H), 8.04 (2 H, *m*-H), 6.23 (6 H, *o*-H), 5.58 (9 H, ^{t}Bu), 5.15 (2 H, *o*-H)
$[Et_4N]_2$**20-*p*Tol**	8.36 (6 H, *m*-H), 7.89 (2 H, *m*-H), 6.19 (6 H, *o*-H), 5.57 (9 H), 5.03 (2 H, *o*-H), 4.14 (9 H, *p*-Me), 3.92 (3 H, *p*-Me)

Table 5.6. UV-vis Data for $[Ph_4P]_2[Fe_4(N^tBu)S_3Cl_4]$ ($[Ph_4P]_2$**19**), $[Ph_4P]_2[Fe_4(N^tBu)S_3(SPh)_4]$ ($[Ph_4P]_2$**20-Ph**), $[Et_4N]_2[Fe_4(N^tBu)S_3(S(2,6\text{-}C_6H_3Cl_2))_4]$ ($[Et_4N]_2$**20-DCBT**) and $[Et_4N]_2[Fe_4(N^tBu)S_3(S(4\text{-}C_6H_4Me))_4]$ ($[Et_4N]_2$**20-*p*Tol**)

Compound	electronic absorption: λ, nm (ε_M , $L\cdot mol^{-1}\cdot cm^{-1}$
$[Ph_4P]_2$**19**	260 (2 100), 230 (78 000)
$[Ph_4P]_2$**20-Ph**	150 (14 800), 350 (16 000), 300 (26 000), 240 (42 000)
$[Et_4N]_2$**20-DCBT**	350 (16 500), 200; (71 000)
$[Et_4N]_2$**20-*p*Tol**	450 (14 600); 350(20 000); 300, (32 000); 240, (42 000)

5.3.3 X-ray Crystallography

Single crystals suitable for single crystal X-ray diffraction analysis were obtained from a MeCN/Et_2O vapor diffusion at –15°C ($[Et_4N]_2$**20-DCBT** and $[Et_4N]_2$**20-*p*Tol**, as black blocks). Unit cell data and crystallographic data for $[Et_4N]_2$**20-DCBT** and $[Et_4N]_2$**20-*p*Tol** are found in Table 5.7.

Table 5.7. Crystallographic data summary for $[Et_4N]_2[Fe_4(N^tBu)S_3(S(2,6\text{-}C_6H_3Cl_2))_4]$ ($[Et_4N]_2$**20-DCBT**) and $[Et_4N]_2[Fe_4(N^tBu)S_3(S(4\text{-}C_6H_4Me))_4]$ ($[Et_4N]_2$**20-*p*Tol**)

	$[Et_4N]_2$**20-DCBT**	$[Et_4N]_2$**20-*p*Tol**
Formula	$[Et_4N]_2[Fe_4(N^tBu)S_3(S(2,6\text{-}C_6H_3Cl_2))_4]$	$[Et_4N]_2[Fe_4(N^tBu)S_3(S(4\text{-}C_6H_4Me))_4]$
Space group	*P2(1)/c*	*P2(1)/c*
a, Å	21.849(5)	18.148(5)
b, Å	12.454(3)	11.805(3)
c, Å	22.229(6)	26.483(7)
β, °	107.719(7)	95.022(7)
V, Å^3	5761.50	5651.79
θ_{max}, °	28	28
$R_1(wR_2)$, %	3.12 (7.89)	3.09 (8.11)
Tot. data, %	99.99	99.9
S	1.030	1.022

Chapter 6: Synthesis of Iron-Imide-Sulfide Complexes with Bulky Thiolate Ligands

6.1 Introduction

6.1.1 Site Differentiation of Fe_4S_4 Clusters

Fe–S clusters with a $[Fe_4S_4]^z$ core typically exist in a charge state of $z = 2+$, with the iron atoms formally adopting 2 Fe(II) and 2 Fe(III) oxidation states. The initial studies of reduced $[Fe_4S_4]^{1+}$ clusters were conducted using thiolate ligands, while phosphines and NHC ligands have since been recognized as valuable for synthesizing the reduced cluster.[191–193] Another key aspect of reduced Fe–S cluster research is their role in small molecule activation. Small molecules such as N_2 and CO serve as substrates for nitrogenase enzymes, making their interactions with multinuclear iron complexes particularly insightful for understanding the activity of these enzymes.[194–196]

The Fe_4S_4 clusters possess a T_d symmetric core, in which all four iron atoms are equivalent. To isolate one iron atom for reactivity, either complex tridentate ligands or bulky monodentate ligands have been employed. The first reported method for site differentiation was developed by Holm and coworkers, who utilized a tridentate thiolate ligand to selectively passivate three of the four iron sites, as illustrated by the first example shown in Figure 6.1.[20,193,197–200] While effective, this approach requires multi-step ligand synthesis, making it synthetically challenging.

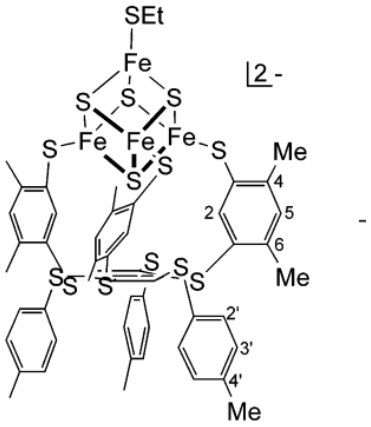

Figure 6.1. Schematic of a site differentiated iron-sulfur cluster from the Holm group. Reprinted (adapted) with permission from Rao, P. V.; Holm, R. H. *Chem. Rev.* **2004**, *104*, 527–559. Copyright 2004 American Chemical Society.

A second approach to achieving site differentiation involves the use of bulky monodentate ligands, such as NHCs and phosphines.[191,192]These neutral, sigma-donating ligands are advantageous because they stabilize the reduced cluster core, allowing access to lower core redox states. The first tetrasubstituted NHC-ligated Fe–S cluster was reported by Holm and coworkers. The Suess laboratory later expanded on this work by employing more sterically hindered NHC ligands to achieve tri-substitution.[201–206] Suess and coworkers also reported a 3:1 site differentiated iron-sulfur cluster, as shown in Figure 6.2.

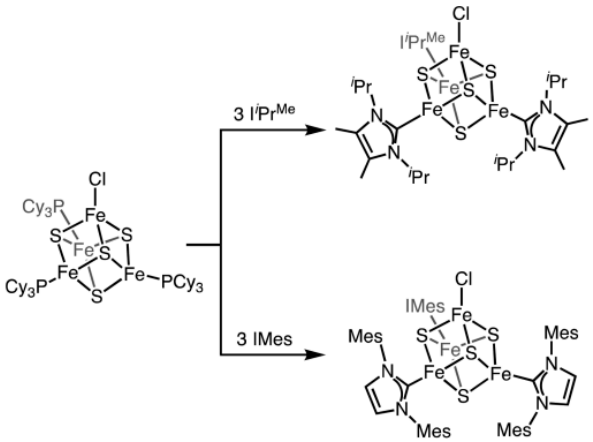

Figure 6.2. Synthesis of site-differentiated Fe_4S_4 cluster with bulky NHC ligation. Reprinted (adapted) with permission from Brown, A. C.; Suess, D. L. M., *Inorg. Chem.* **2019**, *58*, 5273–5280. Copyright 2019 American Chemical Society.

This 3:1 site differentiated cluster reported by the Suess laboratory has shown promise in small molecule reactivity as Suess and coworkers reported CO bound to the site differentiated iron atom, as shown in Figure 6.3.[207] The C–O bond length observed in the solid state was longer than the bond found in CO and the IR peaks of the CO-ligated compound were consistent with an activated bond. Similarly, when using bulky ligands, Suess observed N_2 bound to two [Fe_3MoS_4] cubane clusters (Figure 6.3).[208]

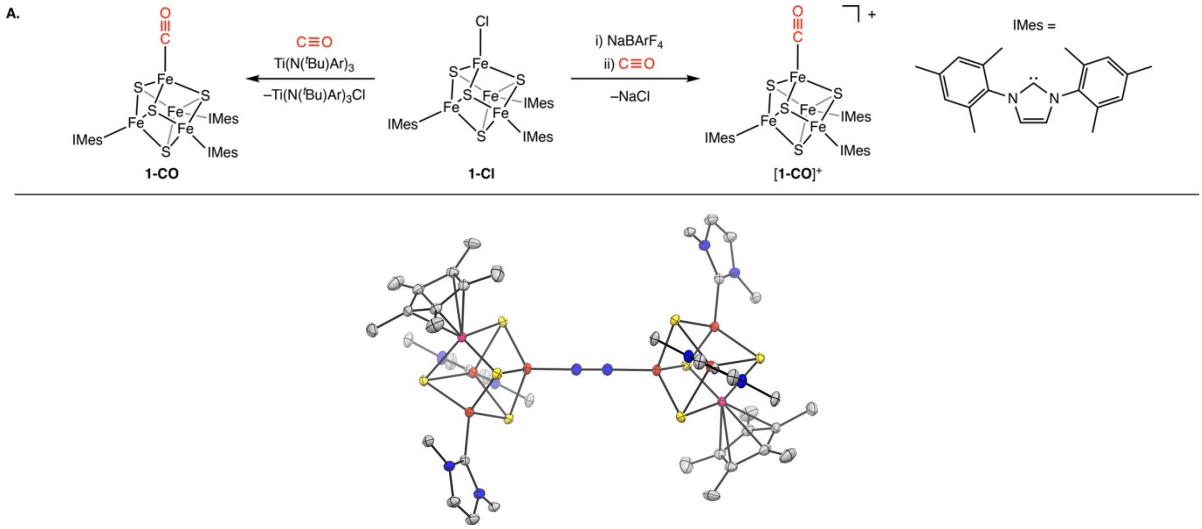

Figure 6.3. Schematic of CO and N_2 bound to synthetic iron-sulfur and iron-molybdenum-sulfur cubane clusters. Top figure: reprinted (adapted) from Brown, A. C.; Thompson, N. B.; Suess, D. L. M. *J. Am. Chem. Soc.* **2022**, *144* (20), 9066–9073. Copyright 2022 American Chemical Society. Bottom figure: reproduced with permission from McSkimming et al., *Nature Chemistry*, **2021**, *13(7)* , 666–670, Springer Nature.

6.1.2 Bulky thiolates

Another class of monodentate ligands that can lead to site differentiation are bulky thiolate ligands. Bulky thiolate ligands have been observed to stabilize low coordinate mononuclear and dinuclear complexes, and lead to the formation of 3:1 site differentiated Fe–S clusters. The thiolate ligand of interest, 2,6-dimesitylbenzene thiolate ($^{-}$SDmp), has been utilized for its bulky nature, as shown by the two-coordinate, mononuclear iron complexes highlighted in Figure 6.4.[209]

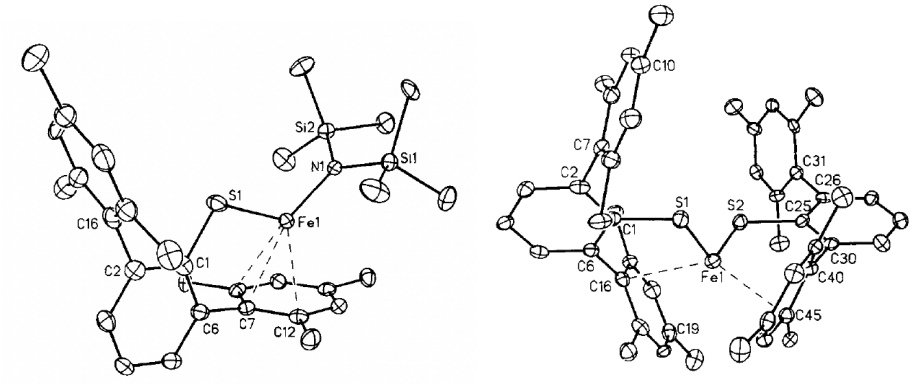

Figure 6.4. Structures of mononuclear iron complexes ligated with $^{-}$SDmp. Reproduced from Ellison, J. J.; Ruhlandt-Senge, K.; Power, P. P., *Angew. Chem. Int. Ed.*, **1994**, 33, 1178–1180, with permission from Wiley-VCH.

The thiolate ligand $^{-}$SDmp was shown to form both tetrasubstituted and trisubstituted Fe_4S_4 clusters in work reported by Tatsumi and Ohki as shown in Figure 6.5.[210] Tatsumi and Ohki reacted $Fe_4S_4(N(SiMe_3)_2)_4$ with 2,6-dimesitylbenzenethiol, leading to a protolytic ligand substitution reaction in which the $^{-}N(SiMe_3)_2$ ligand was replaced by $^{-}$SDmp. This outcome was expected, as the $^{-}N(SiMe_3)_2$ ligand serves as a labile placeholder (as discussed in Chapter 4) for protolytic ligand substitutions. This reaction yielded the trisubstituted, site-differentiated cluster instead of the tetrasubstituted cluster. When $Fe_4S_4(N(SiMe_3)_2)_4$ was first reduced by one electron to form $[Fe_4S_4(N(SiMe_3)_2)_4]^{-}$ and then subjected to the same deprotonation reaction, the resulting product was the tetrasubstituted cluster. Tatsumi and co-workers discovered that the tetrasubstituted cluster was unstable and, under appropriate conditions, reverted to the 3:1 site-differentiated cluster. These findings are significant, as they demonstrate that $^{-}$SDmp can be utilized to achieve site differentiation in Fe_4S_4 clusters, suggesting that a similar approach may be applicable to $Fe_4N(^{t}Bu)S_3$ clusters.

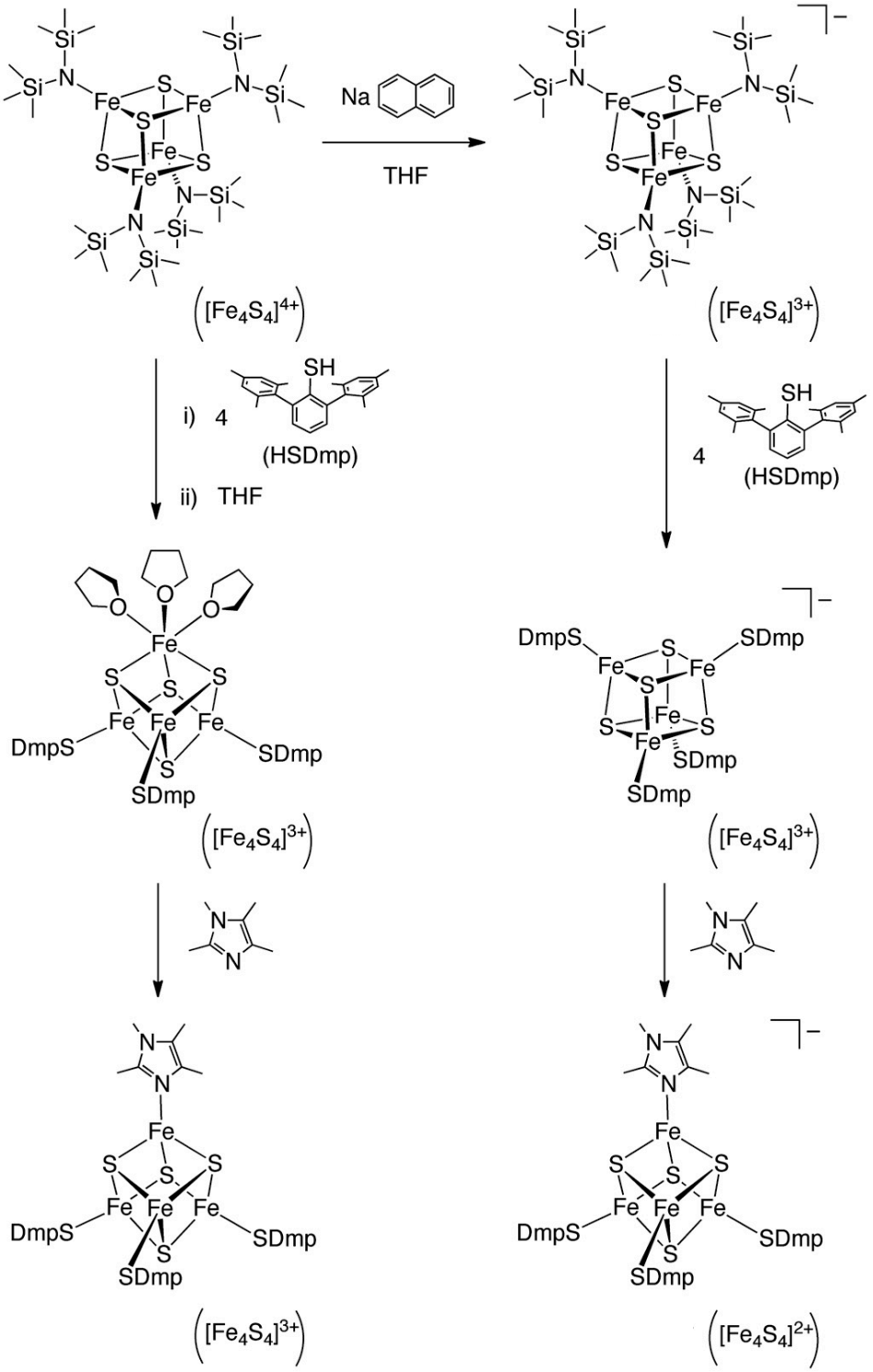

Figure 6.5. Synthesis of site differentiated Fe_4S_4 clusters with $^-$SDmp. Reproduced from Ohki, Y.; Tanifuji, K.; Yamada, N.; Imada, M.; Tajima, T.; Tatsumi, K. *PNAS* **2011**, *108*, 12635–12640. Copyright 2011 National Academy of Sciences.

The second instance of $^{-}$SDmp being utilized as a ligand on Fe_4S_4 led to the isolation of five members of a redox series ($[Fe_4S_4(SDmp)_4]^z$ (z = 0 – 4–)), as shown in Figure 6.6.[186] Unlike the work of Tatsumi and Ohki, in which the protolytic ligand substitution resulted in thiolate incorporation onto the Fe_4S_4 cluster, the synthesis of $[Fe_4S_4(SDmp)_4]^{2-}$ was achieved through controlled synthetic protocols. $^{-}$SDmp was first employed as a ligand to form a mononuclear species, which subsequently led to the formation of a dinuclear species and finally, a tetranuclear species with a z = 2– cluster charge and two associated potassium ions. Crystallographic analysis revealed that the K^+ ions are stabilized by coordination to the aromatic rings of the $^{-}$SDmp ligands. This interaction enhances the solubility of the compounds in relatively nonpolar solvents such as toluene, which starkly contrasts with the solubility of $[Fe_4(N^tBu)S_3(SPh)_4]^{2-}$ which is insoluble in toluene. The formation of the other members of the redox series was achieved through stepwise reduction or oxidation of the initial cluster.

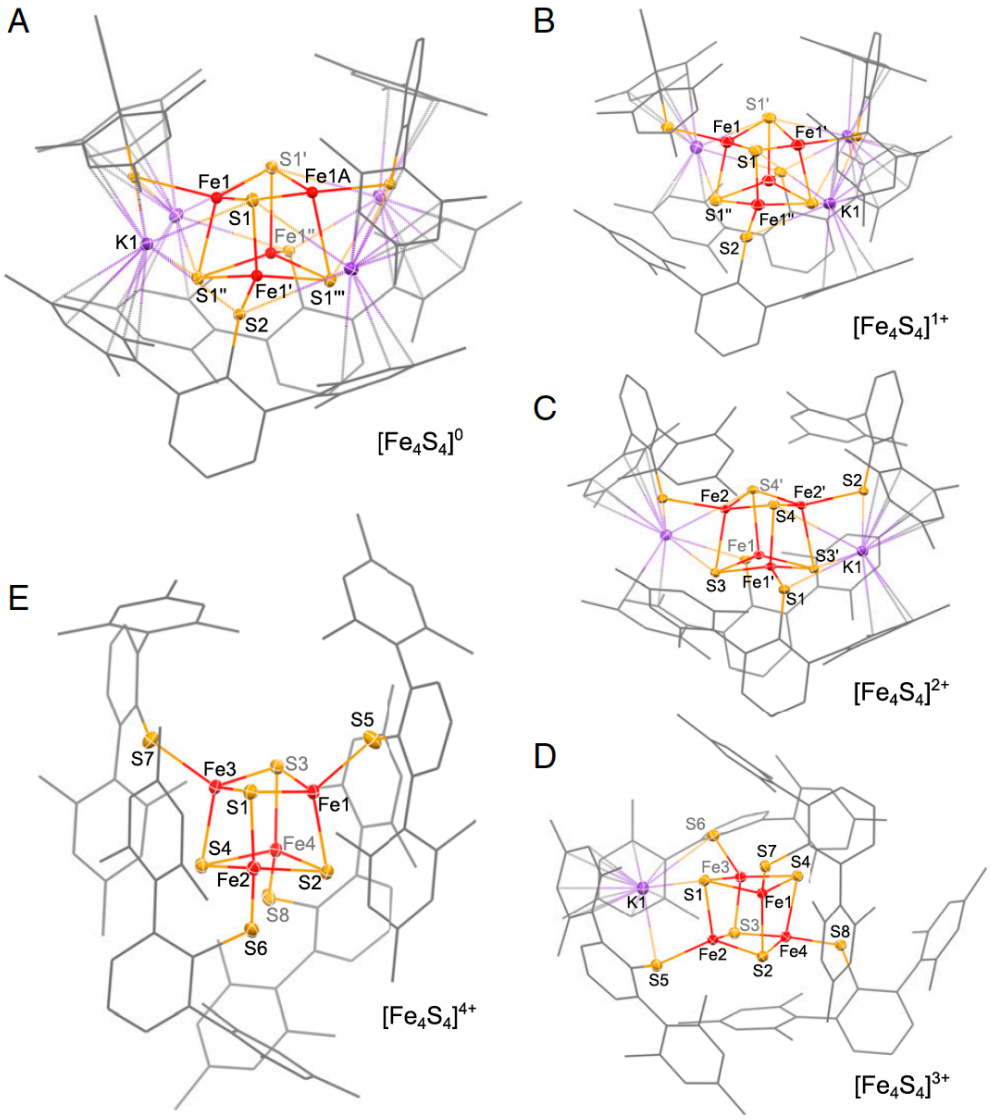

Figure 6.6. Crystal structures of $[Fe_4S_4(SDmp)_4]^z$ in five charge states (z = 0 to 4–). Reproduced from Grunwald, L.; Clémancey, M.; Klose, D.; Dubois, L.; Gambarelli, S.; Jeschke, G.; Wörle, M.; Blondin, M.; Mougel, V. *PNAS* **2022**, *119 (31).* Copyright 2022 National Academy of Sciences.

6.1.3 Proposal

As discussed in Chapter 5, the $[Fe_4(N^tBu)S_3]$ cluster core serves as a model for the $[Fe_4S_3C]$ subunit of the active site in nitrogenase enzymes. While the use of simple arylthiolate ligands has yielded reduced clusters (**22-Ph**, **22-*p*Tol**), purification and further characterization of these clusters was not achieved. An alternative strategy for isolating

reduced clusters involves the incorporation of bulkier thiolate ligands. These ligands offer a promising approach by either:

(i) protecting the cluster from undesired decomposition and/or

(ii) selectively substituting three of the four iron atoms, leaving one site available for further reactivity.

The objective of this chapter is to investigate the use of bulky thiolate ligands to achieve selective iron site differentiation. If tetrasubstitution occurs, this may lead to a synthetic route for the preparation and study of reduced clusters, as outlined in Scheme 6.1.

Scheme 6.1. Proposed reactivity of $[Et_4N]_2$**19** with NaSDmp

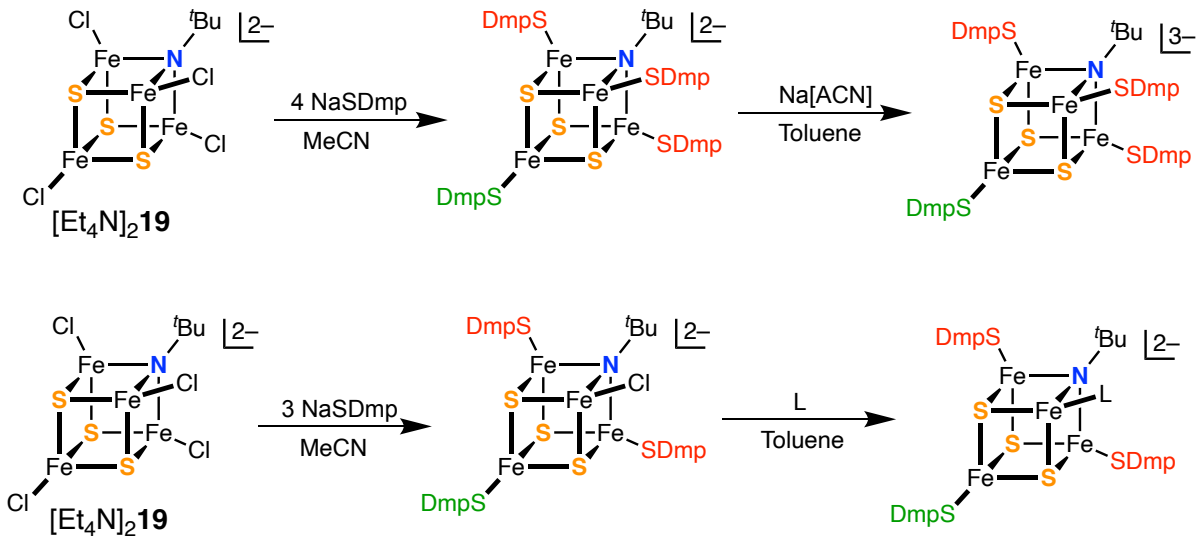

6.2 Results and Discussion

The bulky thiolate ligands chosen in this study include 2,4,6-triphenylbenzene thiolate (STriph) and 2,6-dimesitylbenzene thiolate ($^{-}$SDmp) (Figure 6.7). Preliminary tests were performed with $^{-}$STriph as it was prepared in-house by Dr. Mike Zdilla, a former member of the Lee group.

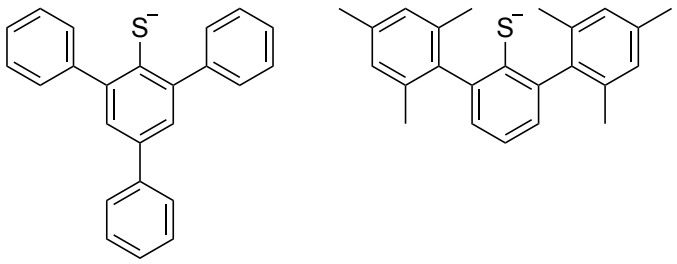

Figure 6.7. Thiolate ligands utilized within this chapter.

6.2.1 Reactivity with ⁻STriph

Preliminary work reacting $[Et_4N]_2$**19** with four equivalents of ⁻STriph led to the synthesis of the tetrasubstituted species, $[Et_4N]_2[Fe_4(N^tBu)S_3(STriph)_4]$ ($[Et_4N]_2$**20-Triph**). The ⁻STriph ligand was generated *in-situ* by reacting HSTriph with one equivalent of $Na(N(SiMe_3)_2)$ and the reaction with $[Et_4N]_2$**19** was allowed to stir for 1 hour. The ^{1}H NMR spectrum of this cluster showcased numerous signals with the majority being difficult to assign. Confirmation of tetra-substitution was achieved by analyzing the meta protons of the benzene bound to the sulfur anion. Based on the precedent established in Chapter 5, the meta signals were consistent with a tetrasubstituted cluster. To validate this assignment, oxidation of the cluster was performed using $Fc(PF_6)$ yielding $[Et_4N][Fe_4(N^tBu)S_3(STriph)_4]$($[Et_4N]$**34**). The ^{1}H NMR of $[Et_4N]$**34** yielded more isotropically shifted resonances consistent with a non-zero ground spin state. These results indicate that the ⁻STriph ligand does not provide sufficient steric bulk, suggesting that a more sterically demanding ligand may be required for further modifications.

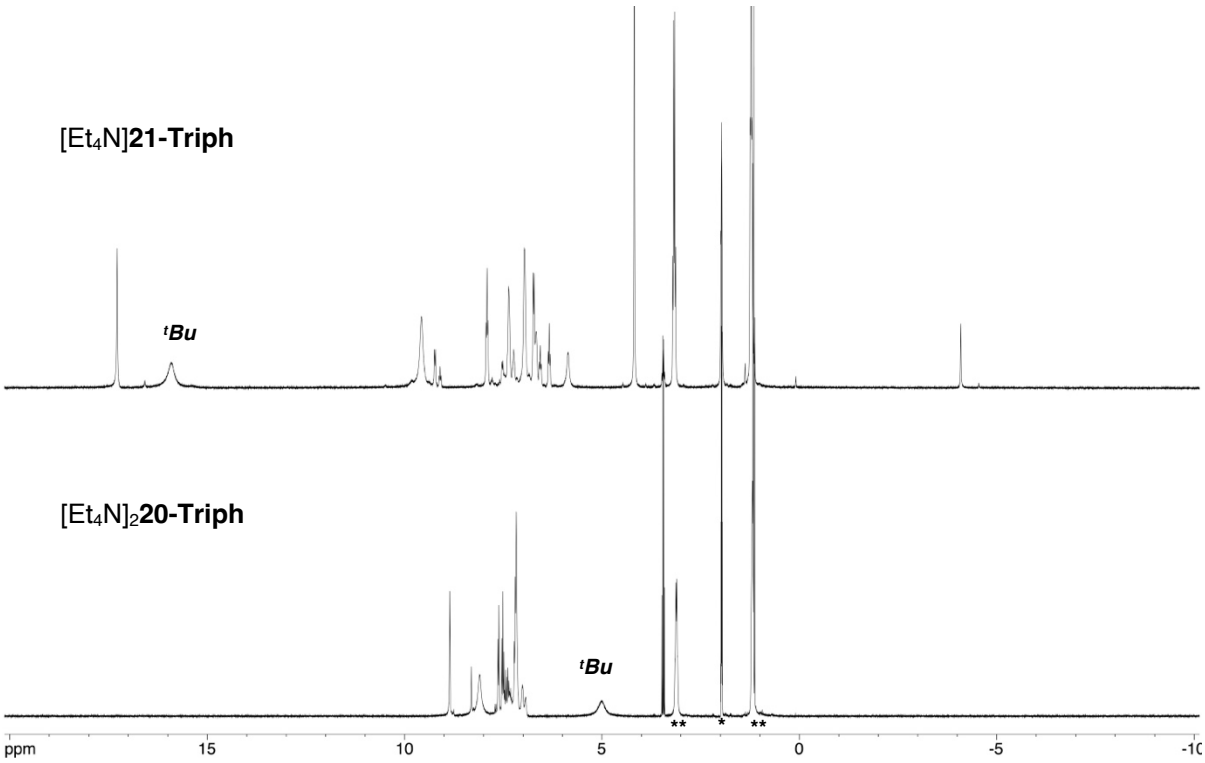

Figure 6.8. ^{1}H NMR (298 K, 300 MHz) spectrum of $[Et_4N]_2$**20-Triph** and $[Et_4N]$**21-Triph** in CD_3CN. Residual protio signal indicated by *. Counterion resonances indicated by **.

6.2.2 Reactivity of Fe_4NS_3 with 2,6-dimesitylbenzene thiolate

The literature precedent with $^-$SDmp and Fe–S cubane clusters provide evidence that three or four $^-$SDmp ligands may bind to the $Fe_4(N^tBu)S_3$ cluster. The inclusion of a single *tert*-butylimide ligand in the cluster core creates a distinct steric environment compared to the bridging sulfides. Based on this structural framework, the iron atom distal to the t*ert*-butylimide is referred to as the distal iron, while the three iron atoms bound to the imide are termed proximal irons. The two distinct iron sites, several substitution patterns and many protons on the $^-$SDmp ligand may lead to complex ^{1}H NMR data. Illustrated in Figure 6.9 are all possible species with varying amounts of $^-$SDmp ligation.

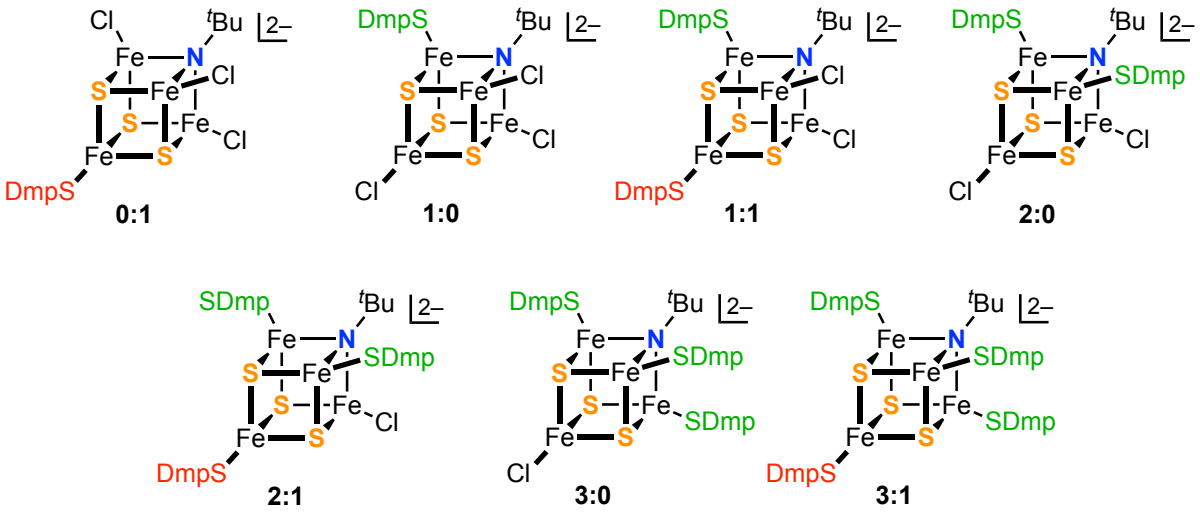

Figure 6.9. All possible substitution patterns with $^{-}$SDmp onto the Fe_4NS_3 core. Shorthand denotes which iron site (proximal vs. distal) is substituted.

To determine the number of ligands bound to the metal center, ^{1}H NMR experiments were conducted by varying the stoichiometry from 1 to 5 equivalents of $^{-}$SDmp per cluster as shown in Figure 6.10. Given the multiple proton environments in $^{-}$SDmp, the meta and para protons of the benzene backbone were used as key indicators to assess ligand binding. Additionally, the ^{t}Bu signal, while broad, indicates how many species are present in solution.

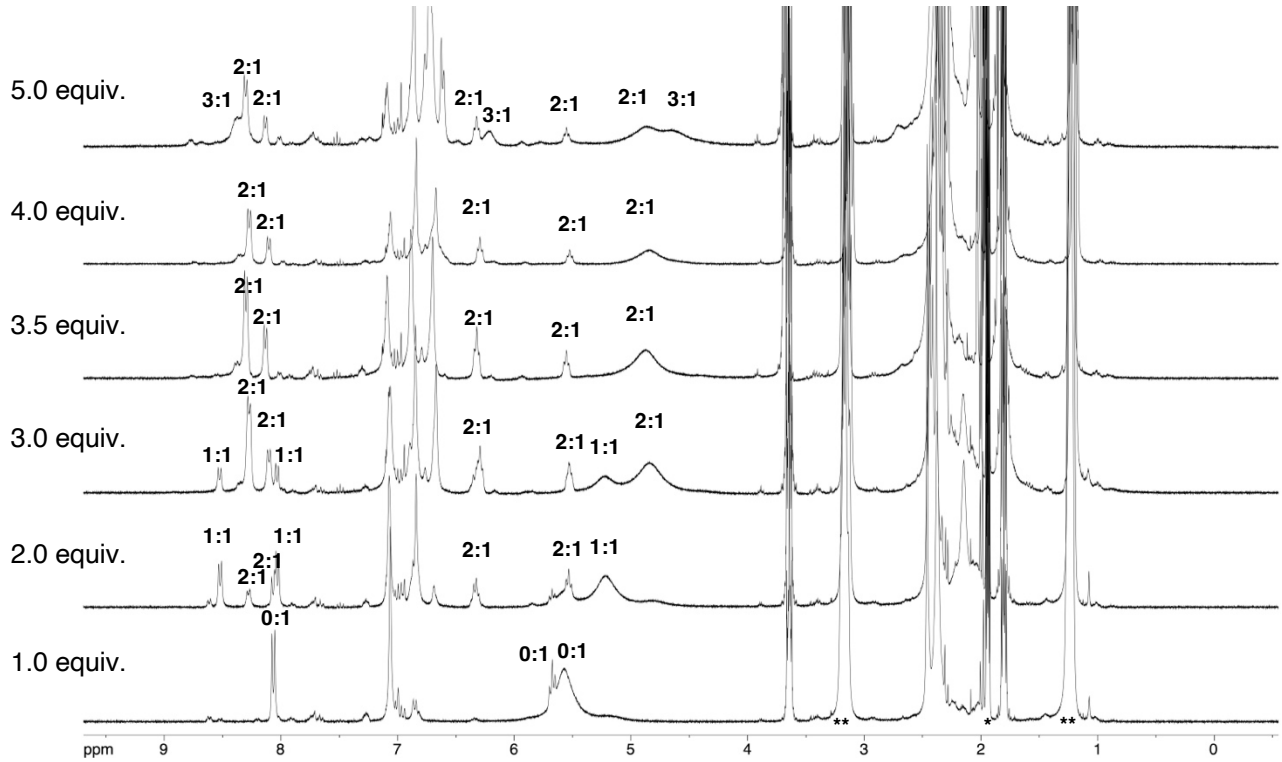

Figure 6.10. Stoichiometry investigation of $[Et_4N]_2$**19** with varying equivalents of $^{-}$SDmp in CD_3CN. Residual protio signal indicated by *. Counterion resonances indicated by **.

The potential products observed in this region include 1:0, 1:1, 2:1 and 3:1 being the predominant products. These products are formed and increase/decrease in concentration depending on the amount of thiolate added. With one equivalent of $^{-}$SDmp, the first species to form is likely 0:1 as the three equivalent iron atoms are next to the bulky tert-butylimide group. As the equivalents increase, new signal sets show up that are consistent with 1:1, 2:1 and lastly 3:1 complex. Interestingly, the meta and para signals set for 3:1 are broad. This broadness may be indicative of a dynamic equilibrium between the bound and free ligand undergoing exchange. The exchange observed can be rationalized based on the steric bulk of the ligand creating enough steric hindrance to destabilize the 3:1 complex. Each spectrum shown in Figure 6.10 is from a different experimental run. Allowing the NMR tube to stand inside of the glovebox overnight does not lead to a change in the product distribution, highlighting the stability of the species. The assignable single sets are tabulated in Table 6.1.

Table 6.1. ^{1}H NMR data for likely $^-$SDmp ligated species

Species	^{1}H NMR (CD_3CN, δ ppm)
0:1	8.06 (2 H, *m*-H), 5.67 (1 H, *p*-H), 5.57 (9 H, ^{t}Bu)
1:1	8.52 (2 H, *m*-H), 8.03 (2 H, *m*-H), 5.220 (9 H, ^{t}Bu)
2:1	8.27 (4 H, *m*-H), 8.10 (2 H, *m*-H), 6.29 (2 H, *p*-H), 5.52 (1 H, *p*-H), 4.84 (9 H, ^{t}Bu)
3:1	8.35 (6 H, *m*-H), 6.17 (3 H, *p*-H), 4.61 (9 H, ^{t}Bu)

Crystallization attempts to isolate the 2:1 species has not been successful which can be attributed to the bulky nature of $^-$SDmp increasing the solubility of the species in non-polar deeming vapour diffusions unsuccessful.

6.2.3 Future Work

This preliminary work demonstrated that the 2:1 site differentiation of $[Fe_4(N^tBu)S_3]$ is possible with $^-$SDmp as the terminal ligand. Next steps for this work will include the crystallization of the 2:1 species followed by redox and reactivity studies. The use of inorganic counterions like alkali metal cations (Li^+, Na^+, and K^+) will lead to an increase in solubility in non-polar solvents which will lead to isolation of crystalline material. Once pure, isolable 2:1 is synthesized, the next steps should include

(i) isolating more reduced states to study the influence of the *tert*-butylimide in the reduced cluster core.

(ii) Test the possibility of small molecule (CO, $^-$CN, N_2) reactivity with 2:1

6.3 Experimental Section

HSTriph and HSDmp were synthesized using the literature procedures.[209,211] NaSDmp were synthesized using analogous protocols detailed in Chapter 5. $Na(N(SiMe_3)_2)$ was synthesized via reaction of $HN(SiMe_3)_2$ with $NaNH_2$. Compounds $[Et_4N]_2$**20-Triph** and $[Et_4N]$**21-Triph** were synthesized analogously to $[Et_4N]_2$**20-Mes** and $[Et_4N]$**21-Mes**.

6.4 Final Words

The work presented in this thesis focused on the synthesis and characterization of iron-imide cubane clusters, iron-amide di– and tri– nuclear complexes, iron-imide-sulfide clusters and lithium amides.

Chapter 2 describes the optimized synthesis and characterization of the $[Ph_4P]$**2** and its redox members. The $[Ph_4P]$**2** cluster is formed via the reaction of $FeCl_3$ with two equivalents of $LiNH^tBu$ in THF at 90 °C for 16 hours. $[Ph_4P]$**2** can be oxidized and reduced to form **1** and $[Ph_4P]_2$**6** ,respectively. This work highlights the challenges of synthesizing iron–imide clusters from simple precursors. Although a balanced chemical equation can be written to predict the formation of **1** as the sole product, experimental outcomes show that multiple products are formed and are not mass balanced, illustrating the complexity of this synthetic chemistry. Future directions for this work include reactivity studies involving the $[Fe_4(N^tBu)_4]^z$ core with a variety of ligands.

Chapter 3 investigates the polymorphism of $LiNH^tBu$, a reagent employed in the synthesis of $[Ph_4P]$**2**. While this compound has been previously reported to adopt a cyclic, octameric ladder structure, a second polymorph with a polymeric infinite ladder structure was synthesized. DSC confirmed that the cyclic ladder is the metastable form, whereas the polymeric ladder is the thermodynamic form. The transformation between polymorphs was also observed synthetically, either by heating the cyclic ladder beyond the phase transition temperature or by adding donor ligands. The solution state structures of both forms in THF-d_8, as well as the cyclic ladder in toluene-d_8, was characterized by ^{1}H DOSY analysis. This study emphasizes the caution in the presence of polymorphs as a reagent may form as different polymorphs with different solubilities.

Chapter 4 discussed the synthesis of mono–, di– and trinuclear complexes from the reaction of **11** with various amines. While the reactivity of **11** with protio-ligands more acidic than HN(SiMe3)2 has been previously studied, less acidic protio-ligands have not been explored. The identity of the products formed in this work depended on the amine to iron stoichiometry, as well as the acidity, steric hindrance and substitution at the amine nitrogen. This work highlights the complexity of protonolysis reactions involving **11** and amines. Future work should include magnetic susceptibility measurements to determine the ground

state spin configurations of the resulting complexes. The potential of using these compounds are precursors for higher nuclear clusters should be explored.

Chapter 5 focuses on the synthesis of oxidized and reduced iron–imide–sulfide clusters with core composition $[Fe_4S_3(N^tBu)]^z$. The oxidized cluster was synthesized using $^-$SMes as the terminal thiolate ligand. The reduced clusters, prepared using $^-$SPh and $^-$S-*p*-Tol as terminal ligands, were unstable in CD_3CN. Over time, these reduced species decomposed, as evidenced by the appearance of free thiolate and new ^{1}H NMR signals. For the cluster ligated with $^-$SPh, reoxidation of the degraded solution regenerated the normal state cluster. Future work in this area should explore the use of bulkier thiolate ligands and inorganic counterions, which may improve solubility in non-polar solvents and increase the stability of the reduced clusters. This would facilitate purification and further characterization.

The mechanism of biological nitrogen fixation remains poorly understood despite decades of dedicated research. The study of mixed iron-amide and iron-imide-sulfide clusters offers structural and electronic benchmarks for understanding the role of the μ_6-carbide in the active site of the nitrogenase enzyme and on potential binding modes of nitrogen in biological nitrogen fixation. The results presented in this dissertation highlight the influence of imide/amide ligation on redox behaviour, structural diversity, and electronics in Fe based complexes. These findings contribute to the foundational understanding of Fe–N bonding motifs in complex, multielectron systems. Advancing this knowledge is essential not only for modeling the nitrogenase cofactors, but also for designing next-generation catalysis in small molecule reactivity.

References

1) Rees, D. C.; Howard, J. B. *Science* **2003**, *300*, 929–931

2) Beinert, H.; Holm, R. H.; Münck, E. *Science* **1997**, *277*, 653–659

3) Johnson, D. C.; Dean, D. R.; Smith, A. D.; Johnson, M. K. *Annu. Rev. Biochem.* **2005**, *75*, 247–282

4) Watenpaugh, K. D.; Sieker, L. C.; Jensen, L. H. *J. Mol. Biol.* **1979**, *131*, 509–522

5) Herriott, J. R.; Sieker, L. C.; Jensen, L. H. *J. Mol. Biol.* **1970**, *50,* 391–406

6) Carter Jr, W.; Kraut, J.; Freer, S. T.; Alden, R. A.; Sieker, L. C.; Adman, E.; Jensen, L. H. *Proc. Nat. Acad. Sci USA* **1972**, *69,* 3526–3529

7) Sieker, L. C.; Adman, E.; Jensen, L. H. *Nature* **1972**, *235*, 40–43

8) Robbins, A. H.; Stout, C. D. *PROTEINS: Structure, Function, and Genetics* **1989**, *5*, 289–312

9) Robbins, A. H.; Stour, C. D. *J. Biol. Chem.* **1985**, *260*, 2328–2333

10) Einsle, O.; Tezcan, F. A.; Andrade, S. L. A.; Schmid, B.; Yoshida, M.; Howard, J. B.; Rees, D. C. *Science* **2002**, *297*, 1696–1700

11) Dean, D. R.; Bolin, J. T.; Zheng, L. *J. Bacteriol* **1993**, *175*, 6737–6744

12) Georgiadis, M. M.; Komiya, H.; Chakrabarti, P.; Woo, D.; Kornuc, J. J.; Rees, D. C. *Science* **1992**, *257*, 1653–1659

13) Kim, J.; Rees, D. C. *Nature* **1992**, *360*, 553–560

14) Herskovitz, T.; Averill, B. A.; Holm, R. H.; Iberst, J. A.; Phillips, W. D.; Weiher, J. *Proc. Nat. Acad. Sci. USA* **1972**, *69* (9), 2437–2441

15) Hagen, K. S.; Watson, A. D.; Holm, R. H. *J. Am. Chem. Soc* **1983**, *105*, 3905–3913

16) Averill, B. A.; Herskovitz, T.; Holm, R. H.; Ibers, J. A. *J. Am. Chem. Soc* **1972**. 3523–3534

17) Zhou, J.; Holm, R. H. *J. Am. Chem. Soc* **1995**, *117*, 11353–11354

18) Lane, R. W.; Ibers, J. A.; Frankel, R. B.; Holm, R. H. *Proc. Nat. Acad. Sci. USA* **1975**, *72* (8), 2868–2872

19) Mayerle, J. J.; Frankel, R. B.; Holm, R. H.; Ibers, J. A.; Phillips, W. D.; Weiher, J. F.; Philips, W. D. *Proc. Nat. Acad. Sci. USA* **1973**, *70* (8), 2429–2433

20) Stack, T. D. P.; Holm, R. H. *J. Am. Chem. Soc* **1987**, *109* (3), 2265

21) Zhang, Y.; Zuo, J. L.; Zhou, H. C.; Holm, R. H. *J. Am. Chem. Soc.* **2002**, *124* (48), 14292–14293.

22) Duncan, J. S.; Nazif, T. M.; Verma, A. K.; Lee, S. C. *Inorg Chem* **2003**, *42* (4), 1211–1224

23) Duncan, J. S.; Zdilla, M. J.; Lee, S. C. **2007***, 46 (4)*, 1071–1080

24) Verma, A. K.; Nazif, T. N.; Achim, C.; Lee, S. C. *J. Am. Chem. Soc.* **2000**, *122 (44)*, 11013–11014

25) Duncan, J. S. *Iron-imide and Iron-imide-sulfide Clusters: First Generation Synthetic Model Compounds of the Nitrogenase Active Site;* Princeton University: Princeton, NJ, **2003**

26) Chen, X. D.; Zhang, W.; Duncan, J. S.; Lee, S. C. *Inorg. Chem.* **2012**, *51* (23), 12891–12904

27) Zhang, W. *Synthesis and Characterization of Iron-Amide and Iron-Imide-Sulfide Clusters*; University of Waterloo: Waterloo, ON, **2011**

28) Chen, X. D.; Duncan, J. S.; Verma, A. K.; Lee, S. C. *J. Am. Chem. Soc.* **2010**, *132* (45), 15884–15886

29) Lichtenberg, C.; Prokopchuk, D. E.; Adelhardt, M.; Viciu, L.; Meyer, K.; Grützmacher, H. *Chem. Eur. J.* **2015**, *21* (44), 15797–15805

30) Zdilla, M. J.; Verma, A. K.; Lee, S. C. *Inorg. Chem.* **2011**, *50* (4), 1551–1562

31) Verma, A. K.; Lee, S. C. *J. Am. Chem. Soc*. **1999**, *121*, 10838–10839

32) Link, H.; Decker, A.; Fenske, D. *Z. Anorg. Allg. Chem.* **2000**, *626*, 1567–1574

33) Riese, U.; Harms, K.; Pebler, J.; Dehnicke, K. *Z. Anorg. Allg. Chem.* **1999**, *625*, 746–754

34) Lichtenberg, C.; Garcia Rubio, I.; Viciu, L.; Adelhardt, M.; Meyer, K.; Jeschke, G.; Grützmacher, H. *Angew. Chem. Int. Ed.* **2015**, *127* (44), 13204–13209

35) Lee, S. C.; Lo, W.; Holm, R. H. *Chem. Rev.* **2014**, *114,* 3579–3600

36) Rao, P. V.; Holm, R. H. *Chem. Rev.* **2004**, *104*, 527–559

37) Boncella, A. E.; Sabo, E. T.; Santore, R. M.; Carter, J.; Whalen, J.; Hudspeth, J. D.; Morrison, C. N. *Coord. Chem. Rev.* **2022**, 1–71

38) Tanifuji, K.; Ohki, Y. *Chem. Rev.* **2020**, *120*, 5194–5251

39) Yang, H. J.; Yoon, S. W.; Park, H. S.; Lee, K. H.; Hur, N. H. *J. Appl. Polym. Sci.* **2019**, *136* (39), 1–7

40) Ivaika, L. V.; Streltsova, N. R.; Belskii, V. K.; Storozhe. Žurnal obŝej himii **1987**, *57(7)*, 1600–1605

41) Wong, G. B.; Bobrik, M. A.; Holm, R. H. I. B.; Bobrik, A.; Holm, R. H. *Inorg. Chem.* **1978**, *17(3)*, 578–584

42) Hagen, K. S.; Uddin, M. A. *Inorg. Chem.* **2008**, *47* (24), 11807–11815

43) O'Sullivan, T.; Millar, M. *J. Am. Chem. Soc.* **1985**, *107,* 4096–4097

44) Tan, L. L.; Holm, R. H.; Lee, S. C. *Polyhedron* **2013**, *58*, 206–217

45) Hagen, K. S.; Watson, A. D.; Holm, R. H. *Inorg. Chem.* **1984**, *23*, 2984–2990

46) Laskowsji, E. J.; Frankel, R. B.; Gillum, W. O.; Papaefthymiou, G. C.; Renaud, J.; Ibers, J. A.; Holm, R. H. *J. Am. Chem. Soc.* **1978**, *100 (17)*, 5322–5337

47) Mascharak, P. K.; Hagen, K. S.; Spence, J. T.; Holm, R. H. *Inorg. Chim. Acta.* **1983**, *80*, 157–170

48) Carney, M. J.; Papaefyhymiou, G. C.; Whitener, M. A.; Spartalian, K.; Frankel, R. B.; Holm, R. H. *Inorg. Chem.* **1988**, *27*, 346–352

49) Sharp, C. R.; Duncan, J. S.; Lee, S. C. *Inorg. Chem*. **2010**, *49* (14), 6697–6705

50) Thrane, N.; Trumpy, G. *Phys. Rev. B* **1970**, *1*, 153–155

51) Blume M. *Phys. Rev. Lett.* **1967**, *18*, 305–308

52) Declercq, J. P.; Feneau-Dupont, J.; Ladriere, J. *Polyhedron* **1943**, *14*, 1943–1952

53) Wignall, J. W. G. *J. Chem. Phys.* **1966***, 44*, 2462–2467

54) Lijima, S.; Mizutani, F.; Mitsumi, M.; Matsumoto, N.; Okawa, H. *Inorg. Chim. Acta.* **1996**, *253*, 47–51

55) Blume M. *Phys. Rev. Lett.* **1964**, *14 (4)*, 96–98

56) Traub, M. *The Synthesis of Iron Amine, Amide, and Imide Complexes From Ferric Chloride and Lithium tertiary-Butyl Amide;* Princeton University: Princeton, NJ, **2001**

57) Thordarson, P. *Chem. Soc. Rev.* **2010**, *40*, 1305–1323

58) Elofson, R. M.; Gadallah, F. F. *J. Org. Chem.* **1969**, *34 (4)*, 854–857

59) Barnett, N. D. R.; Clegg, W.; Horsburgh, L.; Lindsay, D. M.; Liu, Q.-Y.; Mackenzie, F. M.; Mulvey, R. E.; Williard P. G. *Chem. Commun.* **1996**, *5*, 2321–2322

60) Lappert, M. F. *Metal Amide Chemistry*; Wiley, 2009

61) Barr, D.; Clegg, W.; Mulvey, R. E.; Snaith, R. *J. Chem. Soc., Chem. Commun.* **1984**, *7*, 469–470

62) Barr, D.; Clegg, W.; Mulvey, R. E.; Snaith, R.; Wright, D. S. *J. Chem. Soc. Chem. Commun.* **1987**, *10*, 716–718

63) Clegg, W.; Horsburgh, L.; Liddle, S. T.; Mackenzie, F. M.; Mulvey, R. E.; Robertson, A. **2000**, 1225–1231

64) Armstrong D. R.; Baker, D. R.; Craig, F. J.; Mulvey, R. E. *Polyhedron* **1996**, *15 (20)*, 3533–3542

65) Barr, D.; Clegg, W.; Mulvey, R. E.; Snaith, R. *J. Chem. Soc. Chem. Commun,* **1984**, 285–287

66) Kennedy, A. R.; Klett, J.; O'Hara, C. T.; Mulvey, R. E.; Robertson, G. M. *Eur J Inorg. Chem.* **2009**, *33*, 5029–5035

67) Lappert, M. F.; Slade, M. J.; Singh, A.; Atwood, J. L.; Rogers, R. D.; Shakir, R. *J. Am. Chem. Soc.* **1983**, *105*, 302–304.

68) Williard, P. G.; Liu, Q–Y. *J. Am. Chem. Soc.* **1993**, *115*, 3380–3381

69) Rogers, O. D.; Atwood, J. L.; Grüning, R. *J. Organomet. Chem.* **1978**, *157,* 229–237

70) Barr, D.; Clegg, W.; Mulvey, R. E.; Snaith, R. *J. Chem. Commun.* **1984**, 469–470

71) Lappert, M. F.; Slade, M. J.; Singh, A. *J. Am. Chem. Soc.* **1982**, *105*, 302–304

72) Gade, L. H.; Mahr, N. *J. Chem. Soc., Dalton Trans.,***1993**, *4*, 489–494

73) Barr, D.; Clegg, W.; Hodgson, S. M.; Lamming, G. R.; Mulvey, R. E.; Scott, A. J.; Snaith, R.; Wright, D. S. *Angew. Chem. Int. Ed. Engl.* **1989**, *28*, 1241–1243

74) Goodwin, C. A. P.; Joslin, K. C.; Lockyer, S. J.; Formanuik, A.; Morris, G. A.; Ortu, F.; Vitorica-Yrezabal, I. J.; Mills, D. P. *Organometallics* **2015**, *34* (11), 2314–2325

75) Henderson, K. W.; Williard, P. G. *Organometallics* **1999**, *18* (26), 5620–5626

76) Clegg, W.; Horsburgh, L.; Mackenzie, F. M.; Mulvey, R. E. *J. Chem. Soc. Chem. Commun.* **1995**, *19*, 2011–2012

77) Chen, H.; Bartlett, R. A.; Rasika Dias, V.; Olmstead, M. M.; Power, P. P. *Inorg. Chem.* 1**991**, *30*, 2487–2494

78) Boche, G.; Langlotz, I.; Marsch, M.; Harms, K.; Nudelman, N. E. S *Angew. Chem. Int. Ed. in Engl.* **1992**, *31* (9), 1205–1207

79) Vestergren, M.; Eriksson, J.; Hilmersson, G.; Håkansson, M. *J. Organomet. Chem.* **2003**, *682*, 172–179

80) Clegg, W.; Henderson, K. W.; Horsburgh, L.; Mackenzie, F. M.; Mulvey, R. E. *Chem. Eur. J.* **1998**, *4(1),* 53–56

81) Armstrong, D. R.; Barr, D.; Clegg, W.; Hodgson, S. M.; Mulvey, R. E.; Reed, D.; Smith, R.; Wright, D. S. *J. Am. Chem. Soc.* **1989**, *111*, 4719–4727

82) Bond, A. D. *Cryst. Growth Des.* **2005**, *5* (2), 755–771

83) Mulvey, R. E. *Chem. Soc. Rev.* **1991**, *20*, 167–209

84) Armstrong, D. R.; Barr, D.; Clegg, W.; Mulvey, R. E.; Reed, D.; Snaith, R.; Wade, K. *J. Chem. Soc., Chem. Commun.* **1986**, *11*, 869–870

85) Tai, O.; Hopson, R.; Williard, P. G. *J. Org. Chem.* **2017**, *82* (12), 6223–6231

86) Li, D.; Keresztes, I.; Hopson, R.; Williard, P. G. *Acc. Chem. Res.* **2009**, *42* (2), 270–280

87) Barozzino-Consiglio, G.; Hamdoun, G.; Fressigné, C.; Harrison-Marchand, A.; Maddaluno, J.; Oulyadi, H. *Chem. Eur. J.* **2017**, *23* (51), 12475–12479

88) Zaccaria, F.; Zuccaccia, C.; Cipullo, R.; Macchioni, A. *Chem. Eur. J.* **2019**, *25* (42), 9930–9937

89) Hamdoun, G.; Sebban, M.; Cossoul, E.; Harrison-Marchand, A.; Maddaluno, J.; Oulyadi, H. *Chem. Commun.* **2014**, *50* (32), 4073–4075

90) Li, D.; Kagan, G.; Hopson, R.; Williard, P. G. *J. Am. Chem. Soc.* **2009**, *131* (15), 5627–5634

91) Keresztes, I.; Williard, P. G. *J. Am. Chem. Soc.* **2000**, *122*, 10228–10029

92) Su, C.; Hopson, R.; Williard, P. G. *J. Am. Chem. Soc.* **2013**, *135* (33), 12400–12406

93) Armstrong, D. R.; Harris, C. M. M.; Kennedy, A. R.; Liggat, J. J.; McLellan, R.; Mulvey, R. E.; Urquhart, M. D. T.; Robertson, S. D. *Chem. Eur. J.* **2015**, *21* (41), 14410–14420

94) Li, W.; Kagan, G.; Hopson, R.; Williard, P. G. *Arkivoc* **2011**, *2011* (5), 180–187

95) Su, C.; Hopson, R.; Williard, P. G. *J. Am. Chem. Soc.* **2013**, *135* (38), 14367–14379

96) Raya-Baron, A.; Ona-Burgos Pascual; Fernandez Ignacio. Diffusion NMR Spectroscopy Applied to Coordination and Organometallic Compounds. *Annual Reports on NMR Spectroscopy;* Elsevier, **2019**; pp 125–191

97) Guang, J.; Liu, Q.; Hopson, R.; Kagan, G.; Li, W.; Monroe, T. B.; Williard, P. G. *J. Am. Chem. Soc.* **2016**, *138* (46), 15177–15188

98) Guang, J.; Liu, Q. P.; Hopson, R.; Williard, P. G. *J. Am. Chem. Soc.* **2015**, *137* (23), 7347–7356.

99) Parsons, J. L.; Fortunak, J. M.; Dorow, R. L.; Harris, G. D.; Kauffman, G. S.; Nugent, W. A.; Winemiller, M. D.; Briggs, T. F.; Xiang, B.; Collum, D. B. *J. Am. Chem. Soc.* **2001**, *123* (37), 9135–9143

100) Johansson, A.; Davidsson, Ö. *Chem. Eur. J.* **2001**, *7* (16), 3461–3465

101) Granander, J.; Sott, R.; Hilmersson, G. *Chem. Eur. J.* **2006**, *12* (15), 4191–4197

102) Tomasevich, L. L.; Collum, D. B. *J. Org. Chem.* **2013**, *78* (15), 7498–7507

103) Rutherford, J. L.; Collum, D. B. *J. Am. Chem. Soc.* **2001**, *123* (2), 199–202

104) Eriksson, J.; Arvidsson, P. I.; Davidsson, Ö. *J. Am. Chem. Soc.* **2000**, *122,* 9310–9311

105) Arvidsson, P. I.; Davidsson, Ö. *Angew. Chem.* **2000**, *112* (8), 1527–1530

106) Rutherford, J. L.; Collum, D. B. *J. Am. Chem. Soc.* **1999**, *121* (43), 10198–10202

107) Aubrecht, K. B.; Lucht, B. L.; Collum, D. B. *Organometallics* **1999**, *18* (16), 2981–2987

108) Hédouin, M.; Barthelemy, A. L.; Vanthuyne, N.; Besrour, H.; Maddaluno, J.; Magnier, E.; Oulyadi, H. *Angew. Chem.* **2023**, *62* (5)

109) Morris, K. F.; Johnson Jr, C. S. *J. Am. Chem. Soc.* **1992**. *114*, 3139–3141

110) Johnson, C. S. *Prog. Nucl. Magn. Reson. Spectrosc.* **1999**, *34*, 203–256

111) Cohen, Y.; Avram, L.; Frish, L. *Angew. Chem. Int. Ed.* **2005**, *44*, 520–554

112) Tanner, J. E. *Rev. Sci. Instrum.* **1965**, *36* (8), 1086–1087

113) Stejskal, E. O.; Tanner, J. E. *J. Chem. Phys.* **1965**, *42* (1), 288–292

114) Stejskal, E. O. *J. Chem. Phys.* **1965**, *43* (10), 3597–3603

115) Chen, A.; Wu, D.; Johnson, C. S. *J. Am. Chem. Soc.* **1995**, *117*, 7965–7970

116) Bunge, S. D.; Just, O.; Rees, W. S. *Angew. Chem. Int. Ed.* **2000**, *39* (17), 3082–3084

117) Faust, M.; Bryan, A. M.; Mansikkamäki, A.; Vasko, P.; Olmstead, M. M.; Tuononen, H. M.; Grandjean, F.; Long, G. J.; Power, P. P. *Angew. Chem. Int. Ed.* **2015**, *127* (44), 12914–12917

118) Hitchcock, P. B.; Lappert, M. F.; Pierssens, L. J.-M. *Chem. Commun.* **1996**, *6*, 1189–1190

119) Ohki, Y.; Shimizu, Y.; Araake, R.; Tada, M.; Sameera, W. M. C.; Ito, J.; Nishiyama, H. *Angew. Chem. Int. Ed.* **2016**, *128* (51), 16053–16057

120) Burger, H.; Wannagat, U. *Monatshhefte für Chemie* **1963,** *95*, 1099–1102

121) Andersen, R. A.; Faegri, Jr. K.; Green, J. C.; Haaland, A.; Lappert, M. F.; Leung, W.-P.; Rypdal, K. *Inorg. Chem.* **1988**, *27*, 1782–1786

122) Bradley, D. C.; Copperthwaite, R. G.; Extine, M. W.; Reichert, W. W.; Chisholm, M. H. Transition Metal Complexes of Bis(Trimethyl-silyl)Amine (1,1,1,3,3,3-Hexamethyldisilazane). In *Inorganic Syntheses*; 1978; Vol. 18, pp 112–120

123) Hitchcock, P. B.; Huang, Q. G.; Lappert, M. F.; Wei, X. H. *J. Mater. Chem.* **2004**, *14*, 3266–3273

124) Zadrozny, J. M.; Atanasov, M.; Bryan, A. M.; Lin, C. Y.; Rekken, B. D.; Power, P. P.; Neese, F.; Long, J. R. *Chem. Sci.* **2013**, *4* (1), 125–138

125) Zadrozny, J. M.; Xiao, D. J.; Atanasov, M.; Long, G. J.; Grandjean, F.; Neese, F.; Long, J. R. *Nat. Chem.* **2013**, *5* (7), 577–581

126) Atanasov, M.; Zadrozny, J. M.; Long, J. R.; Neese, F. A. *Chem. Sci.* **2013**, *4* (1), 139–156

127) Olmstead, M. M.; Power, P. P.; Shoner, S. C. *Inorg. Chem.* **1991**, *30,* 2547–2551

127) Stroek, W.; Rowlinson, N. A. V.; Hudson, L. A.; Albrecht, M. *Inorg. Chem.* **2024**, *63*, 17134–17140

128) Spielvogel, K. D.; Campbell, E. J.; Chowdhury, S. R.; Benner, F.; Demir, S.; Hatzis, G. P.; Petras, H. R.; Sembukuttiarachchige, D.; Shepherd, J. J.; Thomas, C. M.; Vlaisavljevich, B.; Daly, S. R. *Chem. Commun.* **2024**, *60* (64), 8399–8402

130) Barlett, R. A.; Ellison, J. J.; Power, P. P.; Shoner, S. C. *Inorg. Chem.* **1991**, *30*, 2888–2894

131) Pryadun, R.; Holm, R. H. *Inorg. Chem.* **2008**, *47* (8), 3366–3370

132) Sieg, G.; Pessemesse, Q.; Reith, S.; Yelin, S.; Limberg, C.; Munz, D.; Werncke, C. G. *Chem. Eur. J.* **2021**, *27* (67), 16760–16767

133) Chen, H.; Olmstead, M. M.; Pestana, D. C.; Power, P. *Inorg. Chem.* **1991**, *30*, 1783–1787

134) Ohta, S.; Ohki, Y.; Ikagawa, Y.; Suizu, R.; Tatsumi, K. *J. Organomet. Chem.* **2007**, *692* (21), 4792–4799

135) Macdonnell, F. M.; Ruhlandt-Senge, K.; Ellison, J. J.; Holm, R. H.; Power, P. P. *Inorg. Chem.* **1995**, *34*, 1815–1822

136) Zdilla, M. J. *Exploration of Weak-Field Iron-Nitrogen Clusters: Nitrogenase-Inspired Synthetic Inorganic Chemistry;* Princeton University: Princeton, NJ, **2005**

137) Haber, V. F. Zur Geschicte Des Ammoniakverfahrens. **1923**

138) Haber, V. F. Uber Die Darstellung Des Ammoniaks Stickstoff Und Wasserstoff. **1922**

139) Chen, J. G.; Crooks, R. M.; Seefeldt, L. C.; Bren, K. L.; Morris Bullock, R.; Darensbourg, M. Y.; Holland, P. L.; Hoffman, B.; Janik, M. J.; Jones, A. K.; Kanatzidis, M. G.; King, P.; Lancaster, K. M.; Lymar, S. V.; Pfromm, P.; Schneider, W. F.; Schrock, R. R. *Science* **2018**, *360*

140) Jasniewski, A. J.; Lee, C. C.; Ribbe, M. W.; Ribbe, M. W.; Hu, Y. *Chem. Rev*. **2020**, *120*, 5107–5157

141) Hawkes, T. R.; Mclean, P. A.; Smith, B. E. *Biochem. J.* **1984**, *217*, 317–321

142) Burgess, B. K. *Chem. Rev.* **1990**, *90,* 1377–1406

143) Pollock, R. C.; Lee, H.-I.; Cameron, L. M.; DeRose, V. J.; Hales, B. J.; Orme-Johnson, W. H.; Hoffman, B. M. *J. Am. Chem. Soc.* **1995**, *117*, 8686–8687

144) Davis, L. C.; Henzl, M. T.; Burris, R. H.; Orne-Johnson, W. H. *Biochemistry* **1979**, *18*, 4860–4869

145) Cameron, L. M.; Hales, B. J. *Biochemistry* **1998**, *37*, 9449–9456

146) George, S. J.; Ashby, G. A.; Wharton, C. W.; Thorneley, N. F. *J. Am. Chem. Soc.* **1997**, *119*, 6450–6451

147) Maskos, Z.; Hales, B. J. *J. Inorg. Biochem.* **2003**, *93*, 11–17

148) Yan, L.; Dapper, C. H.; George, S. J.; Wang, H.; Mitra, D.; Dong, W.; Newton, W. E.; Cramer, S. P. *Eur. J. Inorg. Chem.* **2011**, 2064–2074

149) Lee, H.-I.; Cameron, L. M.; Hales, B. J.; Hoffman, B. M. *J. Am. Chem. Soc.* **1997**, *119,* 10121–10126

150) Spatzal, T.; Perez, K. A.; Howard, J. B.; Rees, D. C. *Elife* **2015**

151) Spatzal, T.; Perez, K. A.; Einsle. O; Howard, J. B.; Rees, D. C. *Science* **2014**, *345* (6204), 1616–1620

152) Kang, W.; Lee, C. C.; Jasniewski, A. J.; Ribbe, M. W.; Hu, Y. *Science* **2020**, *368,* 1381–1385

153) Buscagan, T. M.; Perez, K. A.; Maggiolo, A. O.; Rees, D. C.; Spatzal, T. *Angew. Chem. Int. Ed.* **2021**, *60*, 5704–5707

154) Peters, J. W.; Einsle, O.; Dean, D. R.; DeBeer, S.; Hoffman, B. M.; Holland, P. L.; Seefeldt, L. C. *Science* **2021**, 371

155) Kang, W.; Lee, C. C.; Jasniewski, A. J.; Ribbe, M. W.; Hu, Y. *Science* **2021**, 371

156) Bergmann, J.; Oksanen, E.; Ryde, U. *J. Biol. Inorg. Chem.* **2021**, *26*, 341–353

157) Nishibayashi, Yoshiaki. *Transition Metal-Dinitrogen Complexes : Preparation and Reactivity*; Wiley-VCH Verlag GmbH & Co., 2019.

158) Smith, B. E.; Durrant, M. C.; Fairhurst, S. A.; Gormal, C. A.; Grö, K. L. C.; Henderson, R. A.; Ibrahim, S. K.; Le Gall, T.; Pickett, C. J. *Coord. Chem. Rev.* **1999**, *185–186*, 669–687

159) Shah, V. K.; Brill, W. J. *Proc. Natl. Acad. Sci. USA* **1977**, *74 (8)*, 3249–3253

160) Ibers, J. A.; Holm, R. H. *Science* **1980**, *209*, 223-235.

161) Lee, S. C.; Holm, R. H. *PNAS* **2003**, *100*, 3595-3600.

162) Xu, Y.-Y.; Jiang, X.-L.; Chai, J.-L.; Qiu, S.-J.; He, J.; Xu, G.; Wei, J.; Yu, Q.-X.; Zhang, H.-Y.; Li, Y.; Zhang, X.-W.; Cao, G.-L.; Li, Y.; Cui, Y.-S.; Xu, C.-Q.; Li, J.; Chen, X.-D. *Controlled Synthesis of Cluster Mimics of Nitrogenase FeMo-Cofactor*, Ver. 1. *ChemRxiv*, 2024. https://doi.org/10.26434/chemrxiv-2024-sk258

163) Xu, G.; Zhou, J.; Wang, Z.; Holm, R. H.; Chen, X. *Angew. Chem. Int. Ed.* **2019**, *58*, 1649–16473

164) Scott, A. G.; Agapie, T. *J Am Chem Soc* **2023**, *145* (1)

165) Le, L. N. V; Bailey, G. A.; Scott, A. G.; Agapie, T. *PNAS* **2021**, *118 (49)*

166) Ohki, Y.; Ikagawa, Y.; Tatsumi, K. *J. Am. Chem. Soc.* **2007**, *129* (34), 10457–10465

167) Ohta, S.; Ohki, Y.; Hashimoto, T.; Cramer, R. E.; Tatsumi, K. *Inorg. Chem.* **2012**, *51 (21)*, 11217–11219

168) Kanatzidis, M. G.; Hagen, W. R.; Dunham, W. R.; Lester, R. K.; Coucouvanis, D. *J. Am. Chem. Soc.* **1984**, *107*, 953–961

169) Schüren, A. O.; Gramm, V. K.; Dürr, M.; Foi, A.; Ivanović-Burmazović, I.; Doctorovich, F.; Ruschewitz, U.; Klein, *Dalton Trans.* **2015**, *45 (1),* 361–375

170) Geoffrey Wong, I. B.; Bobrik, A.; Holm, R. H. *Inorg. Chem.* **1977**, *17 (3)*, 578–584

171) Appelt, R.; Vahrenkamp, H. Cyanometal-Substituted Derivatives of the Fe_4S_4 Cluster Core. In *Inorganic Syntheses*; Shapley, J. R., Ed., Wiley: New York, 2002; Vol. 34, pp 163–167

172) DePamphilis, B. V; Averill, B. A.; Herskovitz, T.; Que Jr, L.; Holm, R. H. *J. Am. Chem. Soc*. **1974**, *96 (13)*, 4159–4167

173) Zhou, C.; Raebiger, J. W.; Segal, B. M.; Holm, R. H. *Inorganica Chim. Acta* **2000**, *300–302*, 892–902

174) Mayerle, J. J.; Denmark, S. E.; DePamphilis, B. V; Ibers, J. A.; Holm, R. H. *J. Am. Chem. Soc.* **1975**, *97 (5)*, 1032–1045

175) Zhou, J.; Scott, M. J.; Hu, Z.; Peng, G.; Münck, E.; Holm, R. H. *J. Am. Chem. Soc*. **1992**, *114*, 10843–10854

176) Connelly, N. G.; Geiger, W. E. *Chem. Rev.* **1996**, *96,* 877–910

177) Rao, P. V.; Holm, R. H. *Chem. Rev.* **2004**, *104*, 527–559

178) Papaefthymiou, V.; Millar, M. M.; Münck, E. *Inorg. Chem.* **1986**, *25*, 3010–3014

179) Tanifuji, K.; Yamada, N.; Tajima, T.; Sasamori, T.; Tokitoh, N.; Matsuo, T.; Tamao, K.; Ohki, Y.; Tatsumi, K. *Inorg. Chem.* **2014**, *53* (8), 4000–4009

180) Cambray, J.; Lane, R. W.; Wedd, A. G.; Johnson, R. W.; Holm, R. H. *Inorg. Chem.* **1977**, *16* (10), 2565–2571

181) Carney, M. J.; Papaefthymiou, G. C.; Frankel, R. B.; Holm, R. H. *Inorg. Chem.* **1989**, *28*, 1497–1503.

182) Carney, M. J.; Papaefthymiou, G. C.; Whitener, M. A.; Spartalian, K.; Frankel, R. B.; Holm, R. H. *Inorg. Chem.* **1988**, *27*, 346–352

183) Papaefthymiou, G. C.; Laskowski, E. J.; Frota-Pessôa, S.; Frankel, R. B.; Holm, R. H. *Inorg. Chem.* **1982**, *21*, 1723–1728

184) Jordanov, J.; Roth, E. K. H.; Fries, P. H.; Noodlemanld, L. *Inorg. Chem.* **1990**, *29*, 4288–4292

185) Mouesca, J.-M.; Lamotte, B. *Coord. Chem. Rev.* **1998**, *178–180*, 1573–1614

186) Grunwald, L.; Clémancey, M.; Klose, D.; Dubois, L.; Gambarelli, S.; Jeschke, G.; Wörle, M.; Blondin, M.; Mougel, V. *PNAS* **2022**, *119 (31)*

187) Kent, T. A.; Huynh, B. H.; Münck, E. *Proc. Natl. Acad. Sci.* **1980**, *77 (11)*, 6574–6576

188) Huynh, B. H.; Moura, J. J.; Moura, I.; Kent, T. A.; LeGall, J.; Xavier, A. V.; Münck, E. *J. Biol. Chem.***1980**, *255* (8), 3242–3244

189) Emptage, M. H.; Kent, T. A.; Huynh, B. H.; Rawlings, J.; Orme-Johnson, W. H.; Münck, E. *J. Biol. Chem***. 1980**, *255* (5), 1793–1796

190) Ciurli, S.; Ross, P. K.; Scott, M. J.; Yu, S.-B.; Holm, R. H. *J. Am. Chem. Soc.* **1992**, *114*, 5415–5423

191) Deng, L.; Majumdar, A.; Lo, W.; Holm, R. H. *Inorg. Chem.* **2010**, *49* (23), 11118–11126

192) Zhou, H. C.; Holm, R. H. *Inorg. Chem.* **2003**, *42* (1), 11–21

193) Weigel, J. A.; Holm, R. H. *Inorg. Chem.* **1991**, *113*, 4184–4191

194) Jasniewski, A. J.; Lee, C. C.; Ribbe, M. W.; Ribbe, M. W.; Hu, Y. *Chem. Rev.* **2020**, *120*, 5107–5157

195) Burgess, B. K.; Lowe, D. J. *Chem. Rev.* **1996**, *96,* 2983–3011

196) Dance, I. *Chem. Commun.* **2013**, *49* (93), 10893–10907

197) Stack, T. D. P.; Holm, R. H. *J. Am. Chem. Soc.* **1988**, *110*, 2484–2494

198) Stack, T. D. P.; Weigel, J. A.; Holm, R. H. *Inorg. Chem.* **1990**, *29*, 3745–3760

199) Ciurli, S.; Carrié, M.; Weigel, J. A.; Carney, M. J.; Stack, T. D. P.; Papaefthymiou, G. C.; Holm, R. H. *J. Am. Chem. Soc.* **1990**, *112*, 2654–2664

200) Zhou, J.; Hu, Z.; Mu, E.; Holm, R. H. *J. Am. Chem. Soc* **1996**, *118*, 1966–1980

201) Brown, A. C.; Suess, D. L. M. *J. Am. Chem. Soc.* **2020**, *142* (33), 14240–14248

202) Ye, M.; Brown, A. C.; Suess, D. L. M. *J. Am. Chem. Soc.* **2022**, *144* (29), 13184–13195

203) Bostelaar, T. M.; Brown, A. C.; Sridharan, A.; Suess, D. L. M. *Nat. Synth.* **2023**, *2* (8), 740–748

204) Brown, A. C.; Suess, D. L. M. *Inorg. Chem.* **2023**, *62* (5), 1911–1918

205) Sridharan, A.; Brown, A. C.; Suess, D. L. M. *Angew. Chem. Int. Ed.* **2021**, *60* (23), 12802–12806

206) Brown, A. C.; Suess, D. L. M. *Inorg. Chem* .**2019**, *58* (8), 5273–5280

207) Brown, A. C.; Thompson, N. B.; Suess, D. L. M. *J. Am. Chem. Soc.* **2022**, *144* (20), 9066–9073

208) McSkimming, A.; Suess, D. L. M. *Nat. Chem.* **2021**, *13* (7), 666–670

209) Ellison, J. J.; Ruhlandt-Senge, K.; Power, P. P. *Angew. Chem. Int. Ed.* **1994**, *33* (11), 1178–1180

210) Ohki, Y.; Tanifuji, K.; Yamada, N.; Imada, M.; Tajima, T.; Tatsumi, K. *PNAS* **2011**, *108 (31)*, 12635–12640

211) Ruhlandt-Senge, K.; Power, P. P. *Bull. Soc. Chim. Fr.* **1992**, *129*, 594

212) Pokhodnya, K. I.; Bonner, M.; DiPasquale, A. G.; Rheingold, A. L.; Her, J. H.; Stephens, P. W.; Park, J. W.; Kennon, B. S.; Arif, A. M.; Miller, J. S. *Inorg. Chem*. **2007**, *46* (7), 2471–2477

Appendix A: Reactivity of [Ph_4P]2 with KC_8

Reactivity studies of [Ph_4P]**2** were performed with various reagents to determine the reactivity profile of these iron-alkylimide clusters. Previous work by Dr. Jeremiah Duncan discovered that [Ph_4P]**2** can react with NaSPh to form the tetrathiolated cluster. Initial reduction studies of [Ph_4P]**2** was performed with varying equivalents of KC_8 in THF. The utilization of three equivalents led to resonances consistent with one THF bound on the [$Fe_4(N^tBu)_4$] core to form [$Fe_4(\mu_3\text{-}N^tBu)_4Cl_3(THF)_2]^z$ (**7**). Four signals were observed in the ^{1}H NMR spectra with two broad signals downfield that integrated to 27 H and 9 H and two signals upfield that integrated to 4 H and 4 H as shown in Figure A.1. This signal set is consistent with a C_{3V} symmetric cluster with the unique iron site coordinating to THF.

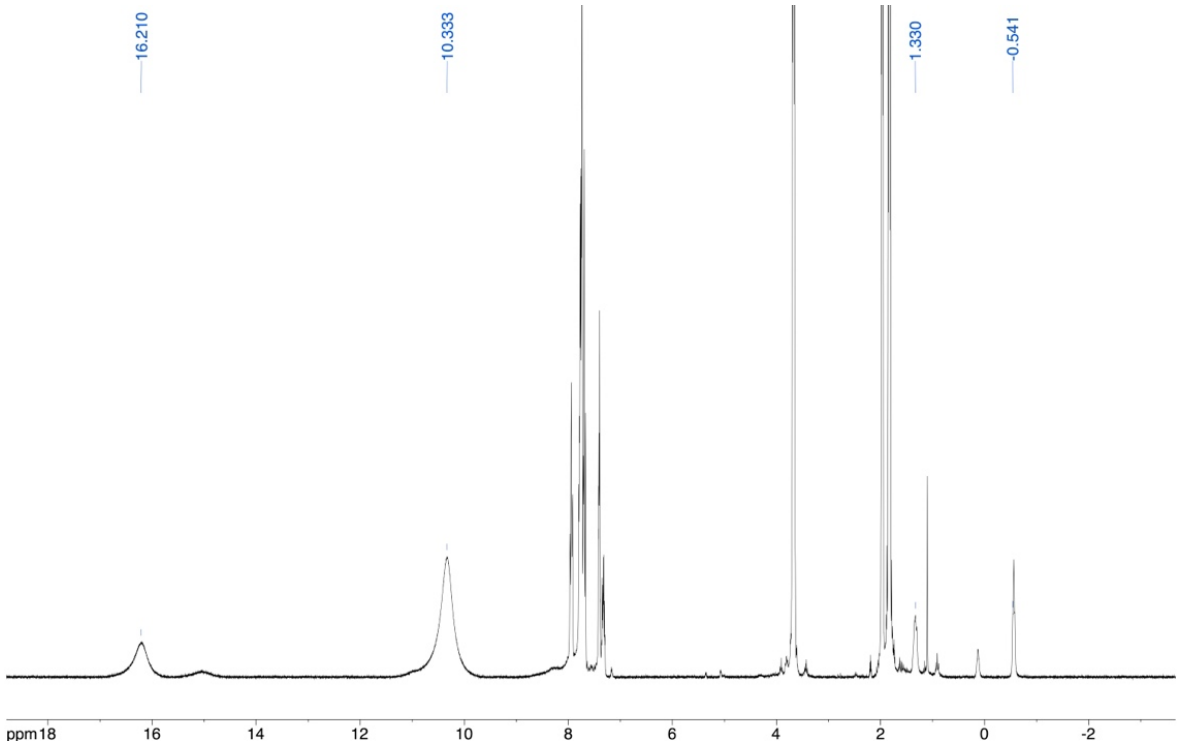

Figure A.1. ^{1}H NMR spectra of [Ph_4P]**2** and 3 equivalents of KC_8 in CD_3CN. Signal set for the new species highlighted with peak positions shown.

Reaction parameters were tested to optimize the conversion to **7** and the observation summary is found below:

(i) **Stoichiometry**: three equivalents of KC_8 led to the most conversion to **7** (~65% based off starting material). Using fewer equivalents of reductant led to a mixture of **7** and starting material $[Ph_4P]$**2**.

(ii) **Reaction time**: Longer reaction time led to more side products, consistent with decomposition and overall less **7** produced.

During the time of reduction study, THF used in the reaction chemistry was collected from our solvent purification system (SPS). Distilled THF was then utilized with the formation of $[Fe_4(N^tBu)_3Cl_3(THF)]^z$ not appearing under the same reaction conditions as the THF collected from the SPS contained contaminants. THF from the SPS was collected and the solvent was removed under reduced pressure resulting in a colourless oil. The ^1H NMR of the colourless oil was collected in $CDCl_3$ and shown in Figure A.2. The three predominant resonances observed were determined to be γ-butyrolactone using ^1H, ^{13}C, HMBC, HMQC and COSY with many NMR signals seen being attributed to likely polymeric material.

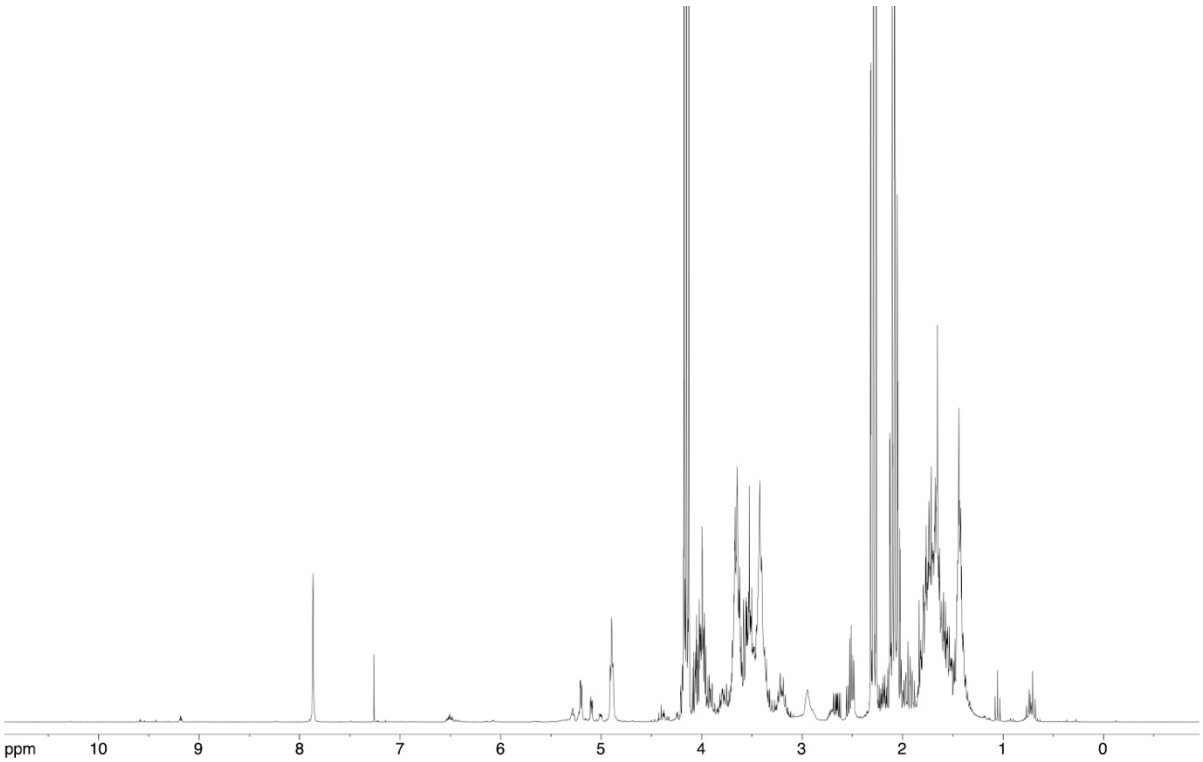

Figure A.2. ^1H NMR spectra (300 MHz, 298 K) of residual oil from THF collected from SPS in $CDCl_3$.

The reaction of $[Ph_4P]$**2** with one or two equivalents of KC_8 in distilled THF lead to the decomposition of tetraphenylphosphonium to triphenylphosphine instead of reduction of the cluster to **6**. This differing reactivity of KC_8 compared to $Na(Ph_2CO)$ can be attributed to KC_8 being a more potent reductant compared to $Na(Ph_2CO)$ and that $[Ph_4P]$**2** is reduced by $Na(Ph_2CO)$ before reduction of the counterion can happen.

Direct synthesis to form $[Fe_4(N^tBu)_3Cl_3(THF)]^z$ was attempted which included the following experiments:

(i) Salt metathesis of $[Ph_4P]$**2** with $KBPh_4$ (or $NaBPh_4$) followed by reducing with Cp^*_2Co.

(ii) Addition of γ-butyrolactone

(iii) Addition of dibenzo-18-crown-6

(iv) Addition of γ-butyrolactone and dibenzo-18-crown-6

The rational with (i) was reducing $[Ph_4P]$**2** with the counterion being $(Na)^+$ would push the reaction to release NaCl and create a vacant site on iron. This was not successful and it was hypothesized that since $[Fe_4(N^tBu)_3Cl_3(THF)]^z$ was formed in the presence of K (and likely $(K)^+$ ions) that switching to $KBPh_4$ would lead to reactivity. This was not observed with $(K)^+$ as the counterion. The addition of γ-butyrolactone, dibenzo-18-crown-6 and dibenzo-18-crown-6/ γ-butyrolactone mixture with Cp^*_2Co to $[Ph_4P]$**2** led to the reduction of $[Ph_4P]_2$**6**.

6.4.1.1 Reactivity Studies with Other Ligands

As the transformation of $[Ph_4P]$**2** to **7** disappeared with pure, distilled THF, the direct synthesis of $[Fe_4(N^tBu)_3Cl_3(THF)]^z$ was attempted. it was attempted to directly synthesize $[Fe_4(N^tBu)_3Cl_3(THF)]^z$. The salts of $Ag(PF_6)$ and $Tl(PF_6)$ were explored as chloride abstractors. Unsurprisingly, the addition of $Ag(PF_6)$ led to the oxidation of $[Ph_4P]$**2** to **1** and $[Ph_4P]_2$**6** to $[Ph_4P]$**2** with one equivalent or **1** with two equivalents of $Ag(PF_6)$. It was rationalized that the oxidation of $(Ag)^+$ to Ag is more favourable than Ag^+ acting as a chloride abstractor to form AgCl. It was expected that $Tl(PF_6)$, a reagent not utilized as an oxidant would lead to chloride abstractor to form TlCl but oxidation also occurred. No reactivity was observed between elemental sulfur or BnN_3 with $[Fe_4(\mu_3\text{-}N^tBu)_4Cl_4]^z$, regardless of the redox state.

Appendix B: $FeCl_2(NH_2{}^tBu)_2$ Titration Data

B.1. Titration protocols

^{1}H NMR titration experiments were performed in triplicate, following best practices to ensure reliability of the obtained values.[57] Two primary limitations of these experiments were the unknown solubility of $FeCl_2$ in MeCN and the exact volume of $^tBuNH_2$ added to the $FeCl_2$ stock solution. To the best of our knowledge, the solubility of $FeCl_2$ in MeCN has not been thoroughly investigated. The highest reported concentration of $FeCl_2$ in MeCN was 158 mM at reflux temperature,[212] and this solution was filtered twice, likely due to saturation.

In our titration experiments, a 15-30 mM solution of $FeCl_2$ in MeCN was prepared and the concentration was validated via spectrophotometric titrations. This concentration range was chosen to remain well within both the solubility limits of $FeCl_2$ in CD_3CN and the dynamic range of the NMR spectrometers. An alternative titration method – titrating $^tBuNH_2$ with a concentration stock solution of $FeCl_2$ – was not pursued, as the maximum solubility $FeCl_2$ in CD_3CN was insufficient to allow for accurate measurement using this approach.

The iron concentration was held constant throughout the titration, as the $^tBuNH_2$ stock solution was prepared using the $FeCl_2$ stock solution. The concentration of iron was therefore assumed to remain constant during data analysis. The quantity of $^tBuNH_2$ added was based on a sub stoichiometric titration experiment, which was selected because the largest changes in the ^{t}Bu chemical shift occurred at sub stoichiometric equivalents of $^tBuNH_2$.

Data fitting was carried out using a custom Python script. The equations used (shown below) were implemented in Python, and the input variables included the $FeCl_2$ concentration, the concentration of $^tBuNH_2$, and the observed chemical shift (δ_{obs}) at each titration point. The unknown parameters – K_1, K_2, δ_{ML}, and $\delta_{ML\ 2}$– were determined for each titration experiment. Equations (1) and (2) display the stepwise equilibrium used to model the titration data. Equations (3) and (4) represent the equilibrium expressions for (1) and (2), respectively. Equations (5) and (6) represent the possible products containing Fe and $^tBuNH_2$. Equations (7) and (8) represent the expressions to calculate the equilibrium concentrations of $FeCl_2{}^tBuNH_2$ and $FeCl_2(^tBuNH_2)_2$, respectively. Equation (9) is utilized to

determine the concentration of free $^{t}BuNH_2$ at equilibrium with that concentration being used in equation (7) and (8) to determine the equilibrium concentrations of $FeCl_2{}^{t}BuNH_2$ and $FeCl_2(^{t}BuNH_2)_2$. Equation (14) is built by combining Equation (10) – (13) and is manipulated to create equation (15). In the python script, the combinations of K_1 and K_2 were varied in a range. Each combination of K_1 and K_2, led to the determination of equilibrium concentrations of $^{t}BuNH_2$, $FeCl_2{}^{t}BuNH_2$ and $FeCl_2(^{t}BuNH_2)_2$. These values were then utilized in Equation 15 and equation (12) and (13) to calculate δ_{ML} and δ_{ML2}.

Initial estimates for K_1 and K_2 were manually inputted and varied from 10 M^{-1} to 1,000,000 M^{-1}. For each pair of K_1 and K_2 values, δ_{ML}, δ_{ML2} and calculated δ_{obs} were obtained. The sum of squared residuals between experimental and calculated δ_{obs} values was then plotted as a function of K_1 and K_2 to generate a 2D contour map. The optimal values of K_1 and K_2 were selected from the region corresponding to the lowest residuals, and the script was rerun to determine the best-fit parameters (K_1, K_2, δ_{ML}, and δ_{ML2}) for each titration experiment. The independent calculated parameters are found in Table B.1

Table B.1. Averaged and independent calculated titration data

	Average Value	Standard Deviation	Standard error	%Standard Error
K_1[a]	914	557	321	32.2%
K_2[a]	1213	605	349	28.8%
δ_{ML}	-2.78	0.38	0.22	7.9%
δ_{ML2}	-4.22	0.37	0.22	5.1%
	Titration 1	Titration 2	Titration 3	
K_1[a]	282	1331	1129	
K_2[a]	682	1086	1871	
δ_{ML}	-2.36	-2.86	-3.11	
δ_{ML2}	-4.64	-4.07	-3.94	
Sum of the residuals squared	0.018	0.082	0.059	

[a] Temperature of the NMR spectrometer is 24.5 °C

Titration of $FeCl_2$ with $^{t}BuNH_2$

General procedure. A fixed quantity of $FeCl_2$ (8.6 mg, 0.0679 mmol) was added to CD_3CN (3 mL) and stirred for 3 h until complete dissolution was observed, affording a tan,

transparent solution. Two 950 µL aliquots were transferred via syringe into screw-cap NMR tubes for use in the ^{1}H NMR titration experiments. Screw cap NMR tubes were preferred over those with rubber septa, as inverting solutions in tubes capped with septa resulted in darkening of the NMR solution, consistent with decomposition. The ^{t}BuNH$_2$ stock solution was prepared by the addition of ^{t}BuNH$_2$ (40 µL, 0.381mmol) to 600 µL of the FeCl$_2$ solution. Aliquots of the ^{t}BuNH$_2$ stock solution were added successively to the screw-cap NMR tubes. After each addition, the tubes were sealed and inverted to ensure thorough mixing. The ^{1}H NMR spectrum was recorded within 5 min of each addition. Amounts of FeCl$_2$ and ^{t}BuNH$_2$ for the three titration runs are tabulated in Table B.2.

Table B.2. Amounts and concentrations of FeCl$_2$ and ^{t}BuNH$_2$ for each titration run

	Titration 1	Titration 2	Titration 3
FeCl$_2$, mg	8.6	6.0	8.2
FeCl$_2$, mmol	0.0679	0.0473	0.0645
[FeCl$_2$]$_0$, mM	22.6	15.8	21.6
^{t}BuNH$_2$, μL	40	40	40
^{t}BuNH$_2$, mmol	0.381	0.381	0.381
[^{t}BuNH$_2$]$_0$, mM	595	595	595

A.2. ^{1}H NMR Titration Data

The calculated data for titration 1 ([^{t}BuNH$_2$]$_{eq}$, [FeCl$_2$^{t}BuNH$_2$]$_{eq}$, [FeCl$_2$(^{t}BuNH$_2$)$_2$]$_{eq}$ and δ_{calc}) for titrations 1, 2 and 3 are found in Table B.3, B.4 and B.5, respectively.

Table B.3. Calculated data for titration 1

[FeCl$_2$]$_0$, mM	[^{t}BuNH$_2$]$_0$, mM	δ_{obs} ppm	[^{t}BuNH$_2$] mM	[FeCl$_2$^{t}BuNH$_2$] mM	[FeCl$_2$(^{t}BuNH$_2$)$_2$] mM	δ_{calc} ppm	% Diff
22.6	5.0	-2.838	0.19	3.27	0.77	-3.073	7.9
22.6	7.4	-3.014	0.28	4.27	1.43	-3.192	5.7
22.6	9.9	-3.23	0.36	5.07	2.23	-3.288	1.8
22.6	12.3	-3.323	0.45	5.67	3.09	-3.363	1.2
22.6	14.7	-3.385	0.54	6.14	4.01	-3.425	1.2
22.6	17.0	-3.476	0.63	6.46	4.95	-3.476	0.0

$[FeCl_2]_0$, mM	$[^tBuNH_2]_0$, mM	δ_{obs} ppm	$[^tBuNH_2]$ mM	$[FeCl_2{}^tBuNH_2]$ mM	$[FeCl_2(^tBuNH_2)_2]$ mM	δ_{calc} ppm	% Diff
22.6	19.4	-3.48	0.74	6.69	5.99	-3.522	1.2
22.6	21.7	-3.546	0.85	6.81	7.02	-3.561	0.4
22.6	24.0	-3.566	0.98	6.84	8.09	-3.595	0.8
22.6	30.9	-3.717	1.49	6.39	11.51	-3.668	1.3
22.6	35.3	-3.718	2.00	5.69	13.81	-3.688	0.8
22.6	41.9	-3.62	3.44	4.12	17.17	-3.644	0.7
22.6	56.6	-3.133	12.97	1.34	21.14	-2.973	5.2
22.6	57.7	-2.964	13.95	1.26	21.25	-2.909	1.9
22.6	76.4	-2.219	31.81	0.57	22.01	-2.006	10.1

Table B.4. Calculated data for titration 2

$[FeCl_2]_0$, mM	$[^tBuNH_2]_0$, mM	δ_{obs} ppm	$[^tBuNH_2]$ mM	$[FeCl_2{}^tBuNH_2]$ mM	$[FeCl_2(^tBuNH_2)_2]$ mM	δ_{calc} ppm	% Diff
15.8	5.0	-2.940	0.26	2.89	0.92	-3.109	5.6
15.8	7.4	-3.058	0.38	3.65	1.69	-3.238	5.7
15.8	9.9	-3.279	0.51	4.20	2.60	-3.337	1.7
15.8	12.3	-3.361	0.65	4.54	3.56	-3.411	1.5
15.8	14.7	-3.441	0.80	4.73	4.58	-3.469	0.8
15.8	17.0	-3.514	0.97	4.78	5.62	-3.513	0.0
15.8	19.4	-3.547	1.18	4.70	6.76	-3.548	0.0
15.8	24.0	-3.554	1.77	4.19	9.02	-3.578	0.7
15.8	26.3	-3.506	2.21	3.78	10.15	-3.567	1.7
15.8	30.9	-3.281	3.68	2.74	12.24	-3.462	5.4
15.8	33.1	-3.163	4.78	2.25	13.04	-3.358	6.0
15.8	39.7	-2.698	9.62	1.24	14.42	-2.893	7.0
15.8	41.9	-2.582	11.54	1.05	14.65	-2.726	5.4
15.8	48.3	-2.165	17.50	0.71	15.05	-2.282	5.3
15.8	50.4	-2.065	19.51	0.64	15.13	-2.153	4.2

Table B.5. Calculated data for titration 3

$[FeCl_2]_0$, mM	$[^tBuNH_2]_0$, mM	δ_{obs} ppm	$[^tBuNH_2]$ mM	$[FeCl_2{}^tBuNH_2]$ mM	$[FeCl_2(^tBuNH_2)_2]$ mM	δ_{calc} ppm	% Diff
21.6	5.0	-3.203	0.20	3.23	0.79	-3.078	4.0
21.6	7.4	-3.307	0.29	4.19	1.46	-3.199	3.3
21.6	9.9	-3.352	0.38	4.96	2.28	-3.296	1.7
21.6	12.3	-3.464	0.47	5.54	3.15	-3.370	2.7
21.6	14.7	-3.493	0.56	5.96	4.09	-3.432	1.7
21.6	17.0	-3.517	0.66	6.26	5.04	-3.483	1.0
21.6	19.4	-3.599	0.78	6.45	6.09	-3.529	2.0
21.6	21.7	-3.642	0.90	6.53	7.13	-3.567	2.1
21.6	24.0	-3.671	1.04	6.52	8.22	-3.600	2.0
21.6	30.9	-3.714	1.62	5.93	11.67	-3.666	1.3
21.6	35.3	-3.626	2.24	5.13	13.96	-3.674	1.3
21.6	41.9	-3.401	4.06	3.49	17.18	-3.587	5.3
21.6	56.6	-2.629	14.71	1.14	20.37	-2.815	6.8
21.6	57.7	-2.541	15.72	1.07	20.45	-2.751	7.9
21.6	76.4	-1.726	33.75	0.51	21.07	-1.873	8.2

A.3. Full Mathematical Expression for 1:2 Binding

$$\mathrm{M} + \mathrm{L} \leftrightharpoons \mathrm{ML} \tag{1}$$

$$\mathrm{ML} + \mathrm{L} \leftrightharpoons \mathrm{ML_2} \tag{2}$$

$$K_1 = \frac{[ML]}{[M][L]} \tag{3}$$

$$K_2 = \frac{[\mathrm{ML_2}]}{[\mathrm{ML}][\mathrm{L}]} \tag{4}$$

$$[\mathrm{M}^0] = [\mathrm{M}] + [\mathrm{ML}] + [\mathrm{ML_2}] \tag{5}$$

$$[\mathrm{L}^0] = [\mathrm{L}] + [\mathrm{ML}] + 2[\mathrm{ML_2}] \tag{6}$$

$$[\mathrm{ML}] = \frac{K_1[M^0][L]}{K_1K_2[L]^2 + K_1[L] + 1} \tag{7}$$

$$[\mathrm{ML_2}] = \frac{K_1 K_2 [M^0][L]^2}{K_1 K_2 [L]^2 + K_1 [L] + 1} \tag{8}$$

$$K_1 K_2\ [\mathrm{L}]^3 + K_1 (2K_2 [\mathrm{M}^0] - K_2 [\mathrm{L}^0] + 1)[L]^2 + (K_1 [\mathrm{M}^0] - K_1 [\mathrm{L}^0] + 1)[\mathrm{L}] - [\mathrm{L}^0] = 0 \tag{9}$$

$$\delta_{obs} = \frac{[L]}{[L^0]} \delta_L + \frac{[ML]}{[L^0]} \delta_{ML} + \frac{2[ML_2]}{[L^0]} \delta_{ML_2} \tag{10}$$

$$\Delta\delta_{obs} = (\delta_{obs} - \delta_L) \tag{11}$$

$$\Delta\delta_{ML} = (\delta_{ML} - \delta_L) \tag{12}$$

$$\Delta\delta_{ML_2} = \left(\delta_{ML_2} - \delta_L\right) \tag{13}$$

$$\Delta\delta_{obs} = \frac{[ML]}{[L^0]} \Delta\delta_{ML} + \frac{2[ML_2]}{[L^0]} \Delta\delta_{ML_2} \tag{14}$$

$$\frac{[ML]}{[ML^0]\Delta\delta_{obs}} = \frac{1}{\Delta\delta_{ML}} - \frac{2[ML_2]}{[L^0]\Delta\delta_{obs}} \times \frac{\Delta\delta_{ML_2}}{\Delta\delta_{ML}} \tag{15}$$

A.4. Contour maps and residual plots

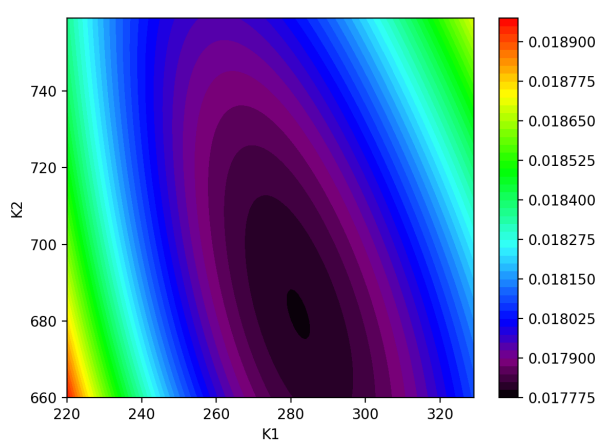

Figure B.1. Titration 1 residuals contour map.

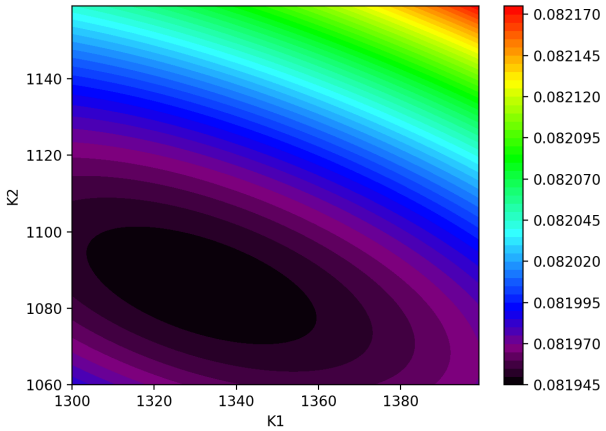

Figure B.2. Titration 2 residuals contour map.

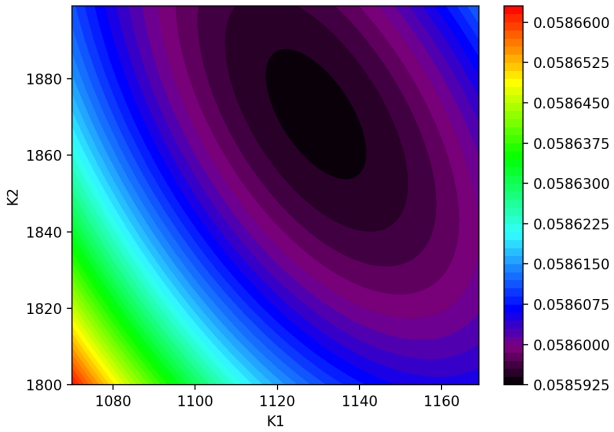

Figure B.3. Titration 3 residuals contour map.

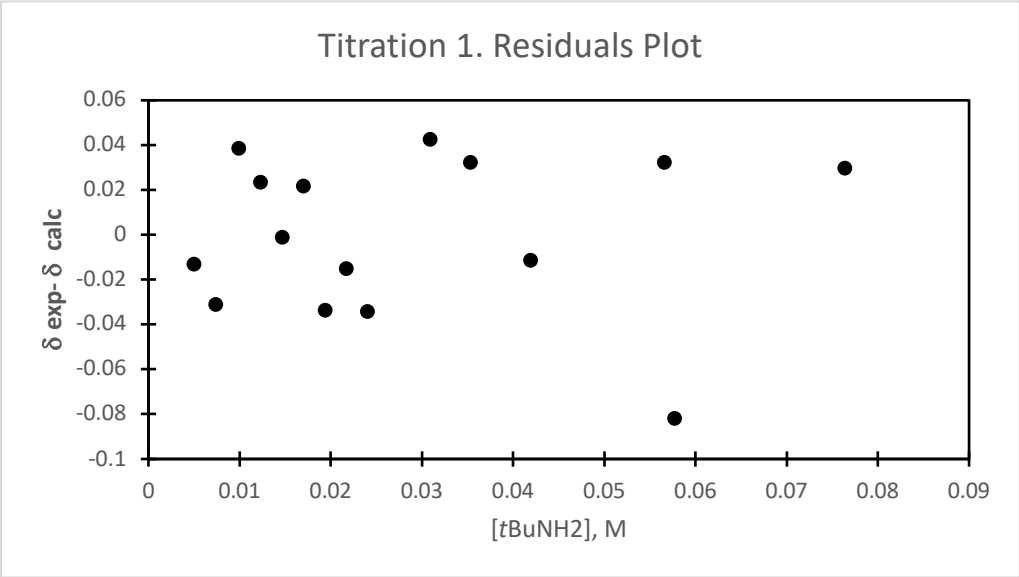

Figure B.4. Residual plot for titration 1.

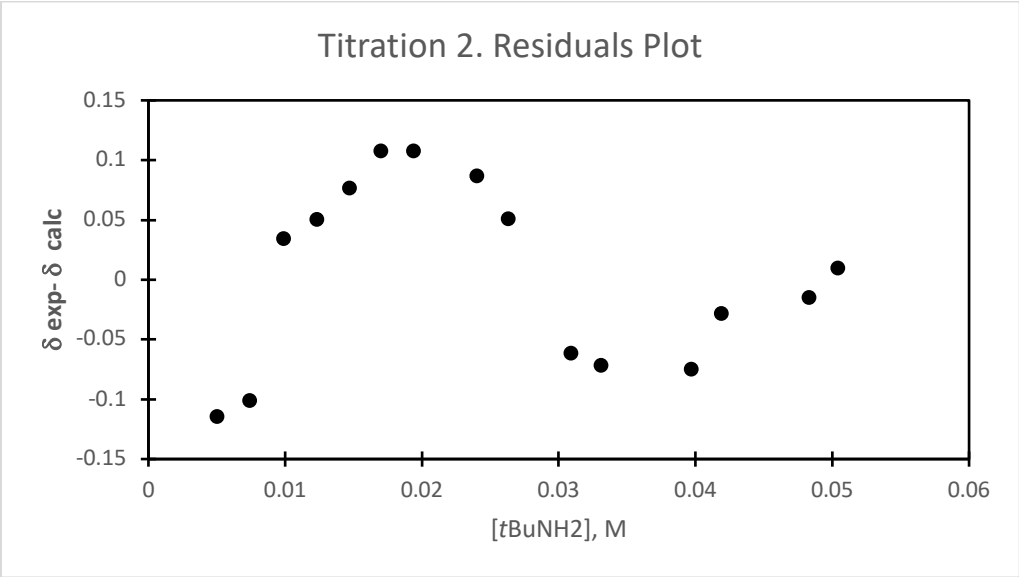

Figure B.5. Residual plot for titration 2.

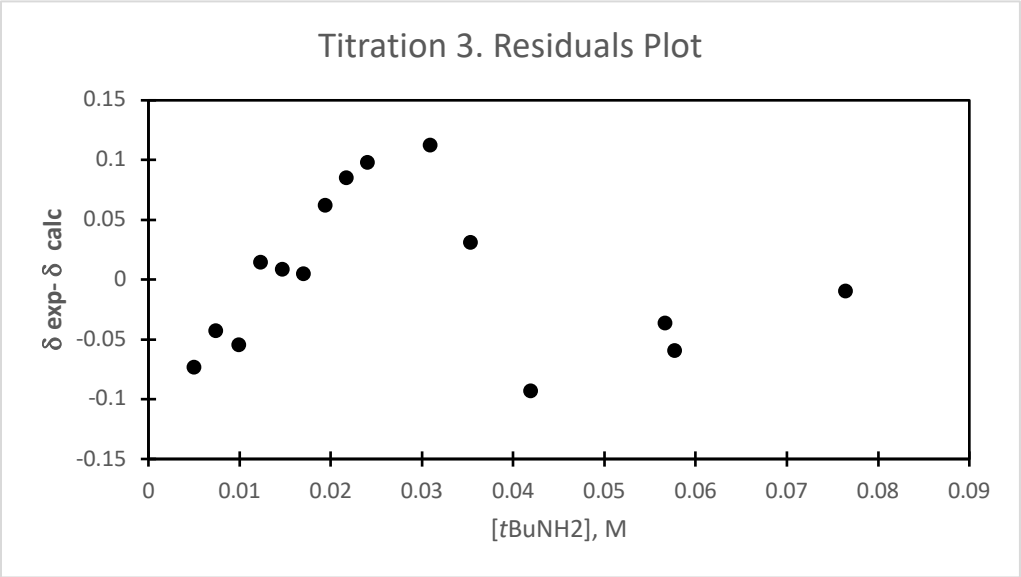

Figure B.6. Residual plot for titration 3.

A.5 Spectrophotometric determination of iron

The concentration of $FeCl_2$ in MeCN was validated spectrophotometrically. A calibration curve was created using ferrous ammonium sulphate. Ferrous ammonium sulphate [$(NH_4)_2Fe(SO_4)_2(H_2O)_6$] (0.2031 g, 0.518 mmol) was added to a 500 mL volumetric flask containing 4 mL of H_2SO_4 and filled to the mark with deionized water. From the [$(NH_4)_2Fe(SO_4)_2(H_2O)_6$] solution, 1 mL, 5 mL, 10 mL, 15 mL, and 20 mL of the stock solution were added to 100 mL volumetric flasks creating solutions with concentrations 0.0104 mM, 0.0518 mM, 0.104 mM, 0.155 mM and 0.207 mM respectively. This step was performed three times to create three sets of solutions. 10 mL from each 100 mL volumetric flask was added to a 25 mL volumetric flask containing 1 mL of 10 % hydroxylamine hydrochloride, 1 mL of 0.25 % phenanthroline and 5 mL of sodium acetate buffer and filled to the mark with deionized water. The absorbance for each solution was measured and averaged from the three trials (Table B.6) and a calibration plot was produced (Figure B.7). From the calibration plot, the line of best fit is y=11.509x-0.0014.

Table B.6. Tabulated absorbances

Concentration (mM)	Trial 1 Absorbance	Trial 2 Absorbance	Trial 3 Absorbance	**Average** Absorbance
0.00414	0.04677	0.04567	0.0408	0.04441
0.02072	0.23757	0.23947	0.2394	0.23881
0.04144	0.47745	0.47745	0.47761	0.47750
0.06215	0.71018	0.71637	0.70984	0.71213
0.08287	0.95187	0.95158	0.95395	0.95247

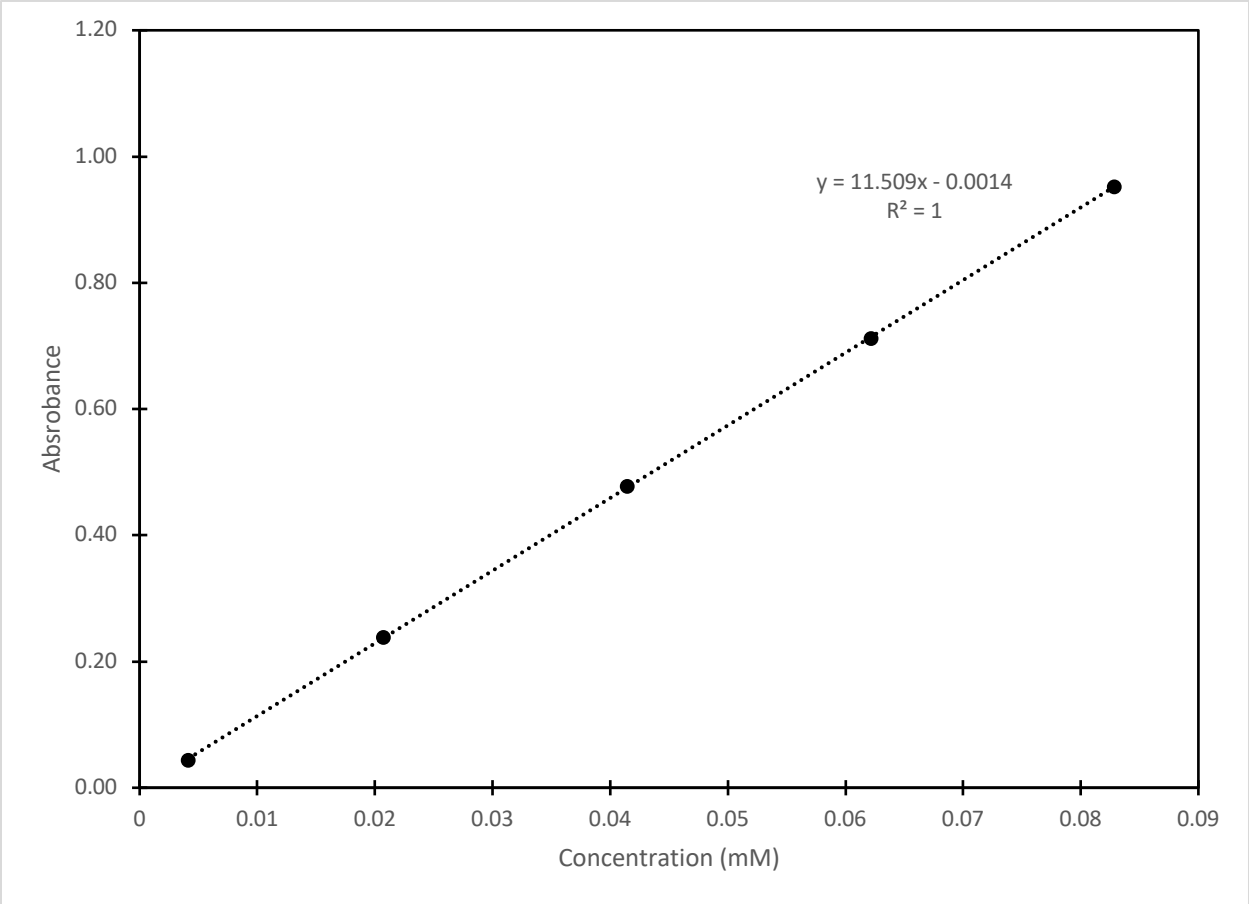

Figure B.7. Calibration plot of Fe^{2+} in MeCN.

A.6. $FeCl_2$ in MeCN solubility check

$FeCl_2$ was added (34.6 mg, 0.273 mmol) to MeCN (8.663 g, 11.02 mL) and the tan suspension was allowed to stir for 19.5 h resulting in a tan, transparent solution. The solution was then filtered and 50 μL was injected into a 25 mL volumetric flask containing 1 mL of 10 % hydroxylamine hydrochloride, 1 mL of 0.25 % phenanthroline, 5 mL of sodium acetate buffer and filled to the mark with deionized water. The absorbance of the solution was recorded two times (0.5639 and 0.5605) and averaged to give a $FeCl_2$ concentration of 24.48 mM (Calculated conc: 24.77 mM, % Diff: 1.2 %)

$FeCl_2$ was added (33.6 mg, 0.265 mmol) to MeCN (7.1761 g, 9.1299 mL) and the tan suspension was allowed to stir for 6.5 h resulting in a tan, transparent solution. Half the solution was filtered, and the other half was not filtered. From the filtered and unfiltered solutions, 50 μL was injected into separate 25 mL volumetric flask containing 1 mL of 10 % hydroxylamine hydrochloride, 1 mL of 0.25 % phenanthroline, 5 mL of sodium acetate buffer and filled to the mark with deionized water. The absorbance of the filtered solution was recorded two times (0.6462 and 0.6459) and averaged to give a $FeCl_2$ concentration of 28.13 mM (Calculated conc: 29.04 mM, % Diff: 3.1%). The absorbance of the unfiltered solution was recorded two times (0.6490. 0.6494) and averaged to give a $FeCl_2$ concentration of 28.27 mM (Calculated conc: 29.04 mM, % Diff: 2.7%)

$FeCl_2$ was added (34.1 mg, 0.269 mmol) to MeCN (6.9072 g, 8.7878 mL) and the tan suspension was allowed to stir for 2 h resulting in a tan, transparent solution The solution was then filtered and 50 μL was injected a 25 mL volumetric flask containing 1 mL of 10 % hydroxylamine,1 mL of 0.25 % phenanthroline, 5 mL of sodium acetate buffer and filled to the mark with deionized water. The absorbance of the solution was recorded two times (0.6983 and 0.6933) and averaged to give a $FeCl_2$ concentration of 30.30 mM (Calculated conc: 30.62 mM, % Diff: 1.1%)

Appendix C: ^{1}H DOSY Data

The remaining ^{1}H DOSY data is found in this appendix.

Table C.1. Masses, volumes and NMR parameters

	8 in toluene-d_8	**8** in THF-d_8	**9** in THF-d_8
LiNH^{t}Bu (mg)	6.0	5.0	5.8
Benzene (µL)	n.a	4	4
1-Tetradecene (µL)	50	50	50
Cyclooctene (µL)	25	25	25
Squalene (µL)	30	30	30
NMR solvent (µL)	450	450	450
δ (ms)	80	80	80
Δ (µs)	700	700	700

C.1 Molecular weight determination of 9 in THF-d_8.

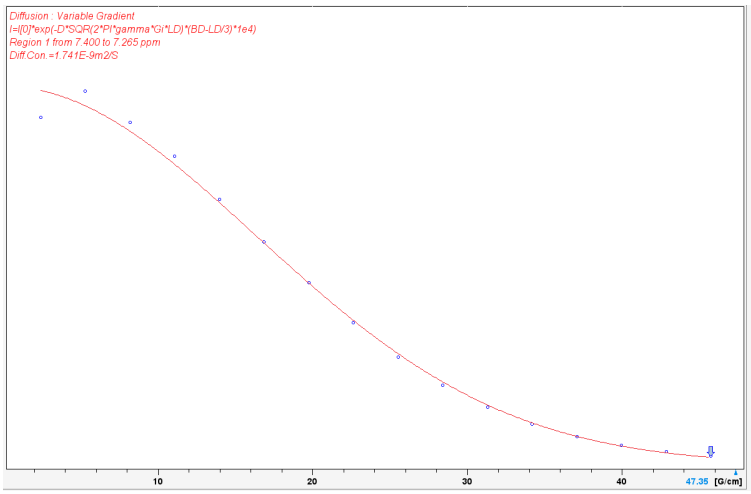

Figure C.1. Stejskal-Tanner plot of benzene in THF-d_8.

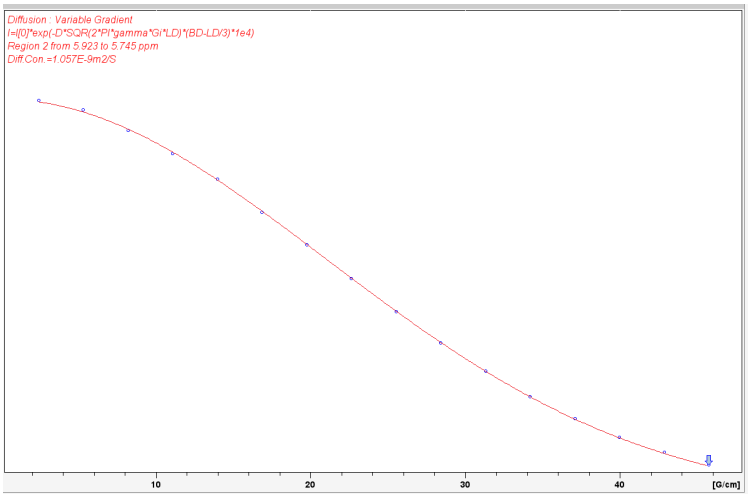

Figure C.2. Stejskal-Tanner plot of 1-tetradecene in THF-d_8.

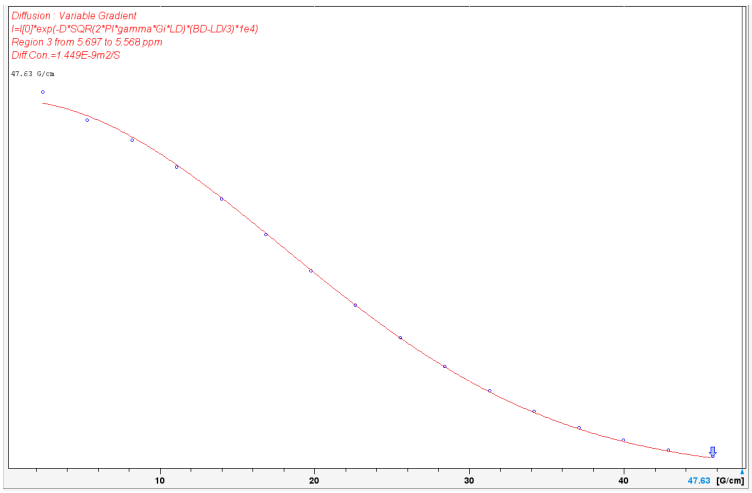

Figure C.3. Stejskal-Tanner plot of cyclooctene in THF-d_8.

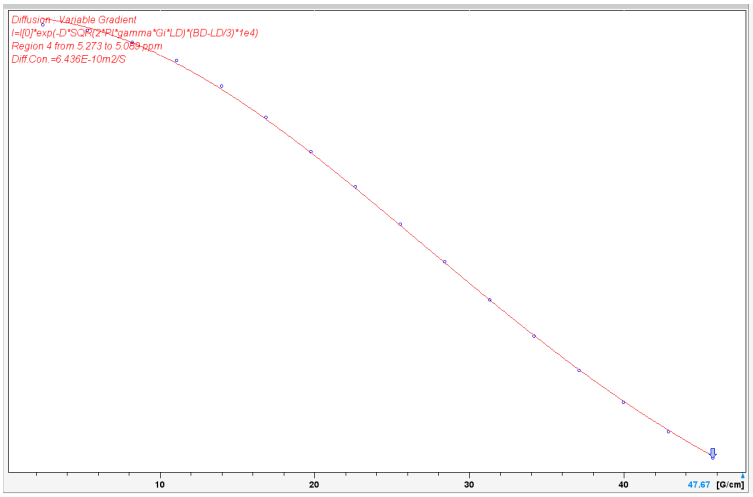

Figure C.4. Stejskal-Tanner plot of squalene in THF-d_8.

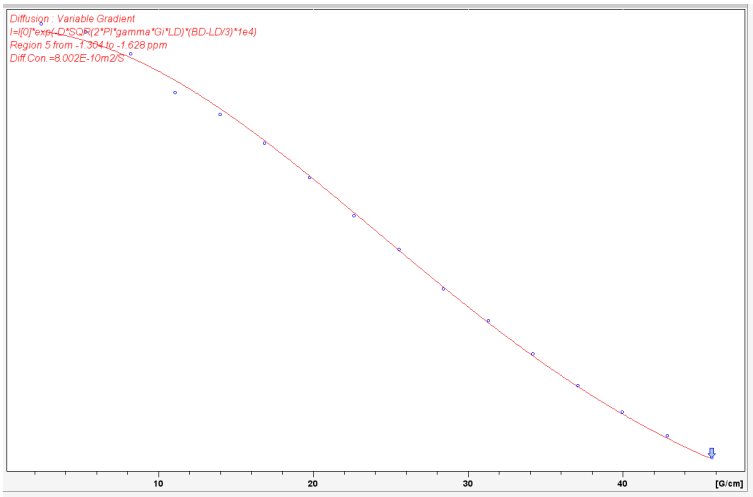

Figure C.5. Stejskal-Tanner plot of **9** in THF-d_8.

C.2 Molecular weight determination of 8 in THF-d_8.

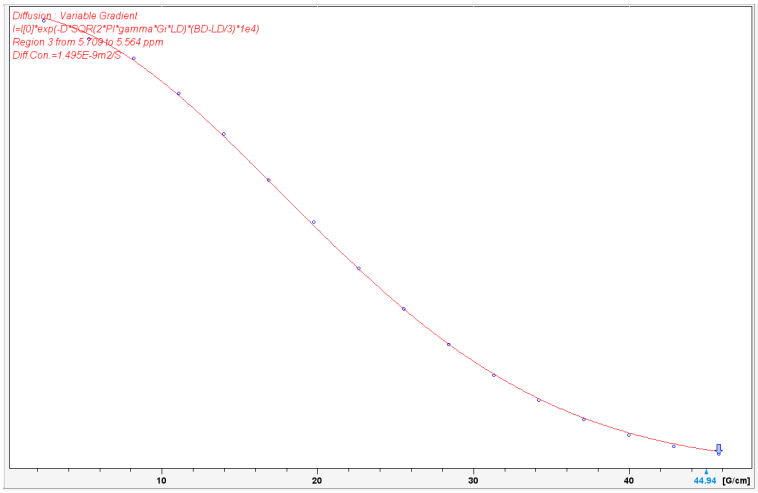

Figure C.6. Stejskal-Tanner plot of cyclooctene in THF-d_8.

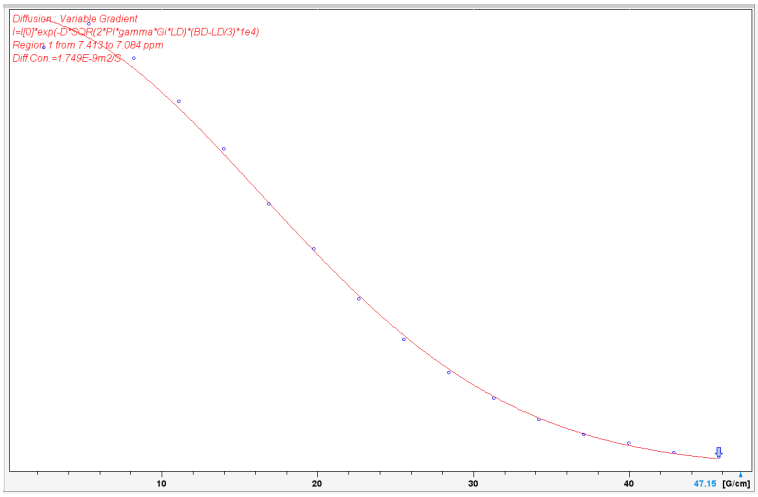

Figure C.7. Stejskal-Tanner plot of benzene in THF-d_8.

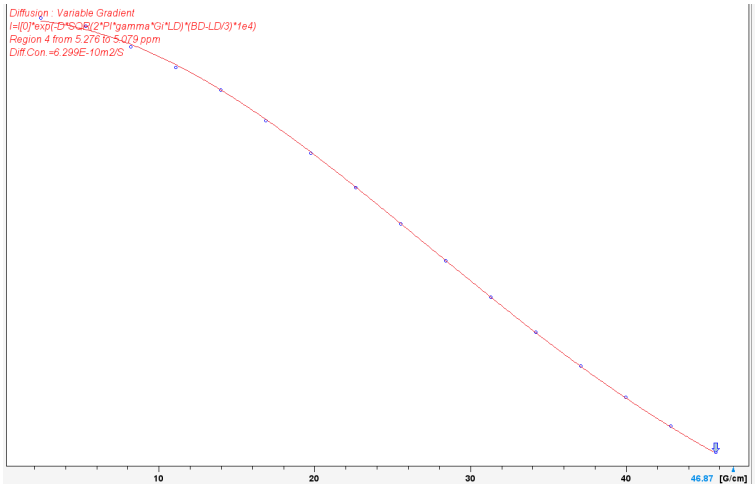

Figure C.8. Stejskal-Tanner plot of squalene in THF-d_8.

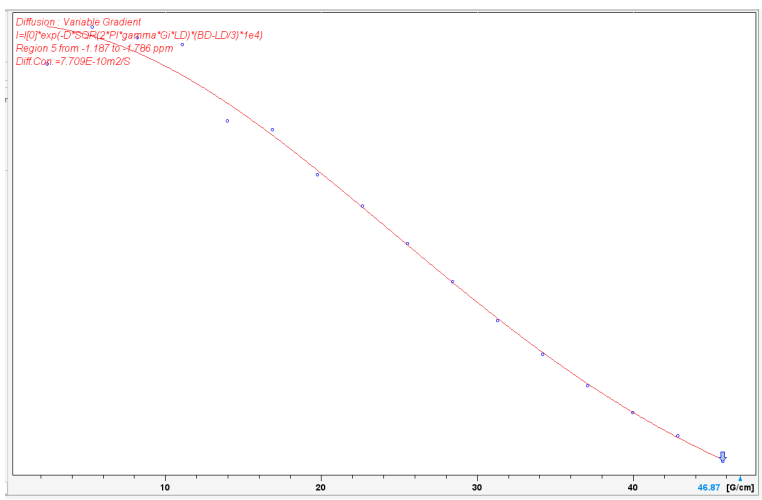

Figure C.9. Stejskal-Tanner plot of 8 in THF-d_8.

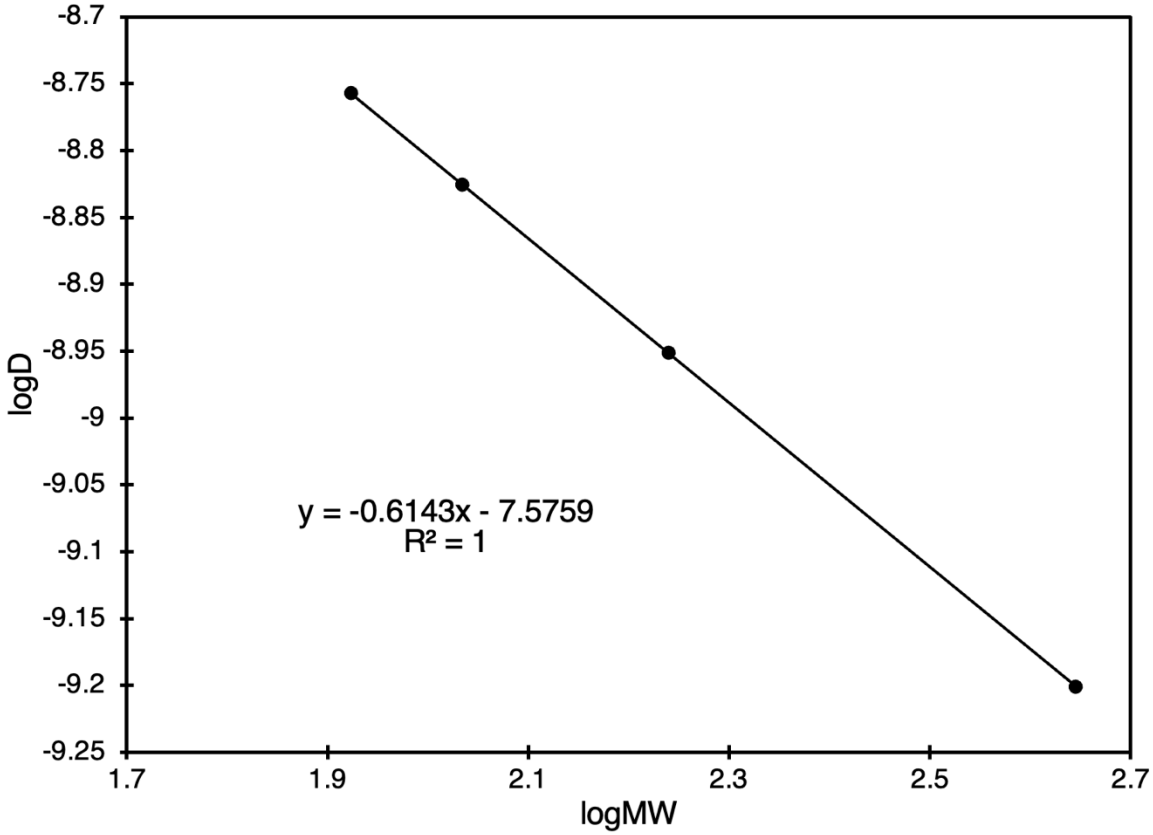

Figure C.10. log D vs log MW DOSY molecular weight calibration curve.

Table C.2. Percent differences of the actual and calculated molecular mass of benzene, cyclooctene, 1-tetradecene and squalene

Reagent	Diffusion Coefficient	Molecular mass	Calculated molecular mass	Percent Difference
benzene	1.75E-09	78	84	7.24
cyclooctene	1.50E-09	110	108	–1.87
1-tetradecene	1.12E-09	196	174	–11.62
squalene	6.30E-10	411	442	7.52

[a]Molecular masses were calculated using the following equation rearranged from the equation of the line from Figure C.10: $\mathrm{Mw} = 10^{\frac{\mathrm{LogD}+7.5759}{-0.6.143}}$

C.3 Molecular weight determination of 8 in toluene-d_8.

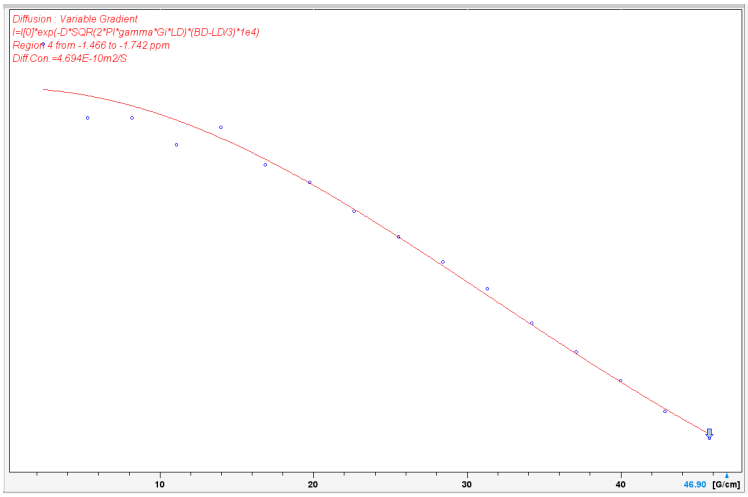

Figure C.11. Stejskal-Tanner plot of **8** in toluene-d_8.

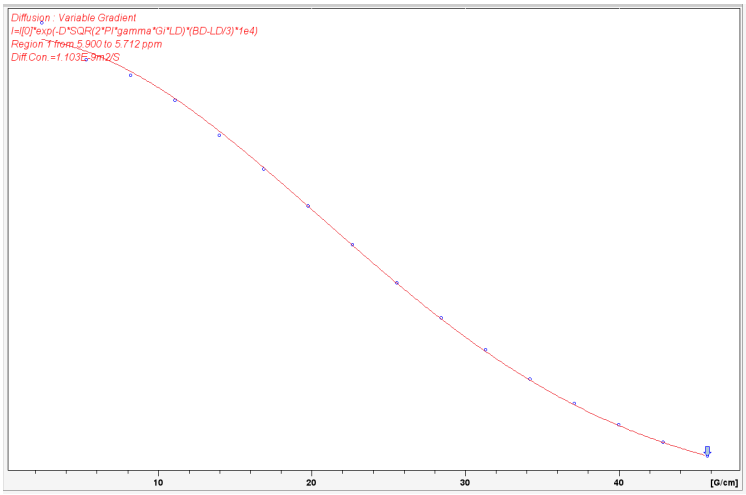

Figure C.12. Stejskal-Tanner plot of 1-tetradecene in toluene-d_8.

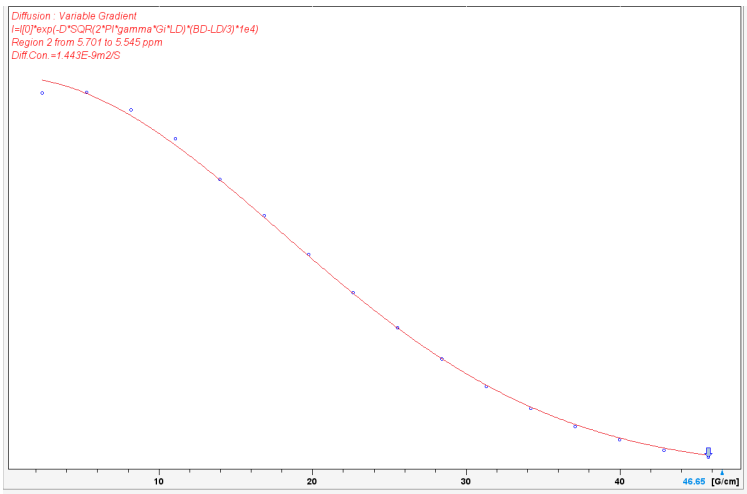

Figure C.13. Stejskal-Tanner plot of cyclooctene in toluene-d_8.

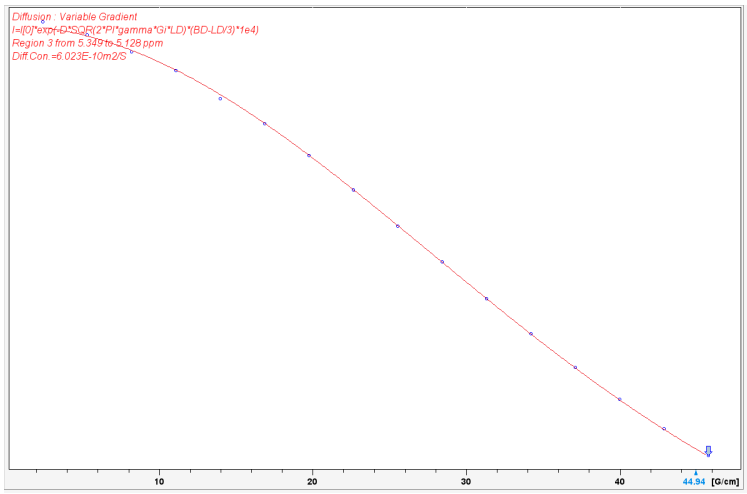

Figure C.14. Stejskal-Tanner plot of squalene in toluene-d_8.

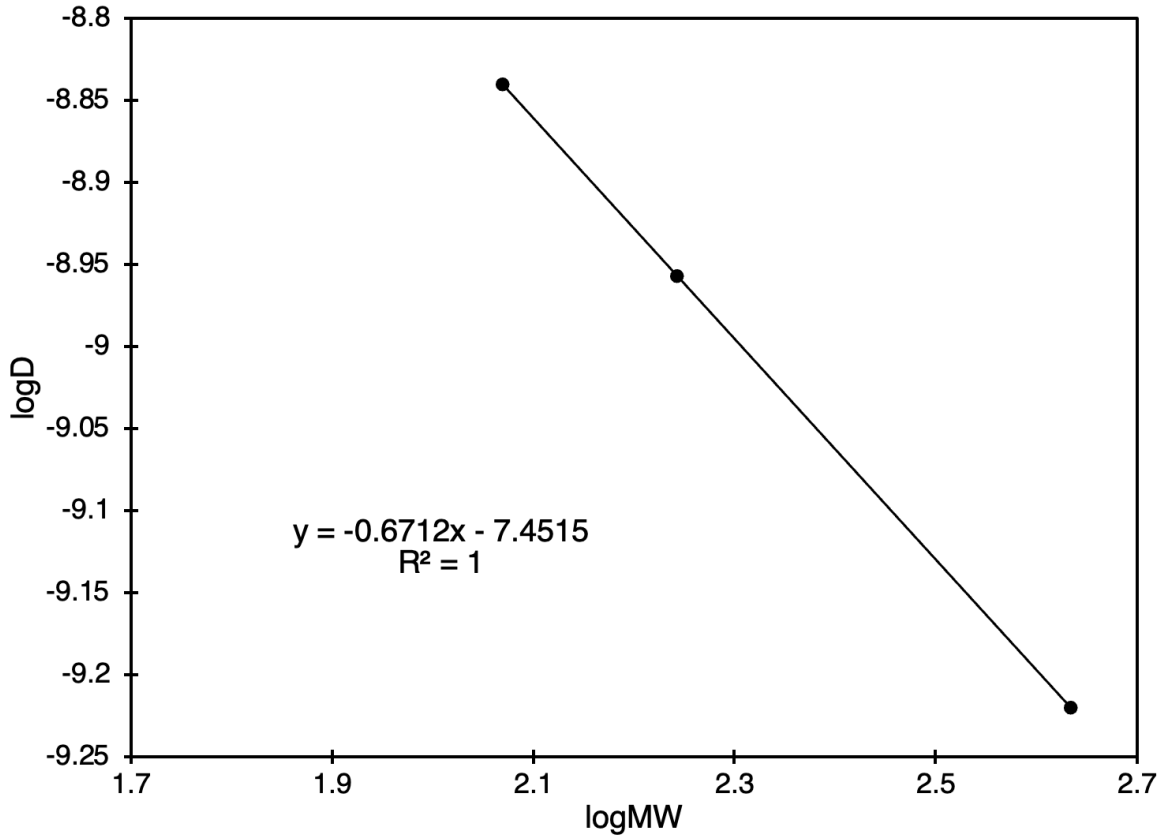

Figure C.15. log D vs log MW DOSY molecular weight calibration curve.

Table C.3. Percent differences of the actual and calculated molecular mass of cyclooctene, 1-tetradecene and squalene

Reagent	Diffusion Coefficient	Molecular mass	Calculated molecular mass	Percent Difference
cyclooctene	1.44E-09	110	17	6.58
1-tetradecene	1.10E-09	196	175	-10.74
squalene	6.02E-10	411	432	5.12

[a]Molecular masses were calculated using the following equation rearranged from the equation of the line from Figure C.15: $\mathrm{Mw} = 10^{\frac{\mathrm{LogD}+7.4515}{-0.6712}}$